

**Distributed Snowpack Simulation Using Weather Radar  
with an Hydrologic - Land Surface Scheme Model**

by

**Steven Richard Fassnacht**

**A thesis  
presented to the University of Waterloo  
in fulfilment of the  
thesis requirement for the degree of  
Doctor of Philosophy  
in  
Civil Engineering**

**Waterloo, Ontario, Canada, 2000**

**©Steven Richard Fassnacht, 2000**



**National Library  
of Canada**

**Acquisitions and  
Bibliographic Services**

**395 Wellington Street  
Ottawa ON K1A 0N4  
Canada**

**Bibliothèque nationale  
du Canada**

**Acquisitions et  
services bibliographiques**

**395, rue Wellington  
Ottawa ON K1A 0N4  
Canada**

*Your file Votre référence*

*Our file Notre référence*

**The author has granted a non-exclusive licence allowing the National Library of Canada to reproduce, loan, distribute or sell copies of this thesis in microform, paper or electronic formats.**

**The author retains ownership of the copyright in this thesis. Neither the thesis nor substantial extracts from it may be printed or otherwise reproduced without the author's permission.**

**L'auteur a accordé une licence non exclusive permettant à la Bibliothèque nationale du Canada de reproduire, prêter, distribuer ou vendre des copies de cette thèse sous la forme de microfiche/film, de reproduction sur papier ou sur format électronique.**

**L'auteur conserve la propriété du droit d'auteur qui protège cette thèse. Ni la thèse ni des extraits substantiels de celle-ci ne doivent être imprimés ou autrement reproduits sans son autorisation.**

**0-612-51194-4**

**Canada**

**The University of Waterloo requires the signatures of all persons using or photocopying this thesis. Please sign below, and give address and date.**

## **ABSTRACT**

**Fassnacht, Steven Richard, 2000.**

*Distributed Snowpack Simulation Using Weather Radar with an Hydrologic - Land Surface Scheme Model.* Unpublished Ph.D. thesis, Department of Civil Engineering, University of Waterloo, Waterloo, ON, Canada, xxv, 276pp, 199 figures, 26 tables, 4 appendices.

Snow serves as a reservoir of water for the earth. In fact, the volume of water stored in the snowpack and the timing of the snowmelt runoff are crucial to water supply. To determine runoff volumes, empirical relationships have been developed that relate snow accumulations at point locations to downstream flows. However, modelling of the snowmelt process is required to generate peak flow estimates. Typically an hydrological model is initiated when the snowpack accumulation has reached a maximum. Another approach has been to model the snow processes through the winter, from accumulation through to melt.

Continuous hydrological modelling requires precipitation and other meteorological data that are representative of the study watershed. Point measurements from precipitation gauges are often spatially unrepresentative and there are often systematic biases, such as wind undercatch when measuring snowfall. Weather radar has been used to overcome issues related to gridding point precipitation data, however to date weather radar has not provided winter precipitation estimates for hydrological modelling. In this research, weather radar is used as the winter precipitation input to model the snowpack throughout the snow season in order to produce streamflow estimates.

The King City Radar, which is located north of Toronto and operated by the Meteorological Service of Canada (Environment Canada), covers a majority of central southwestern Ontario. The radar images used in this research were derived from the hourly average of 2 by 2 km 10 minute Constant Altitude Plan Projection Images obtained from the conventional scan. Five watersheds are located to the west of the radar: Thames, Maitland, Saugeen, Nottawasaga, and the Grand Rivers. The focus of this research is primarily the Upper Grand River for a five year study period from 1993 through 1997.

The snowpack is modelled continuously over the winter using the linked WATFLOOD and CLASS models (WAT\_CLS3). The WATFLOOD model, developed at the University of



**Waterloo, provides the horizontal water balance and streamflow routing, while the CLASS model, developed by Environment Canada, provides the vertical water and energy balance.**

**To improve the streamflow and snowpack property estimates, the radar data have been adjusted to consider a local scaling phenomenon, the occurrence of mixed precipitation at warmer than freezing air temperatures, and the shape of snow particles occurring at colder temperatures. Six snow processes have been modified or added to the CLASS model, including the disaggregation of soil properties for snowcovered and snow-free areas, the occurrence of mixed precipitation near the surface, the variation of fresh snow density as a function of temperature, the variation of the maximum attainable snowpack density as a function of landcover type, snowfall canopy interception, and redistribution of blowing snow. The radar data adjustments are tested in terms of accumulation comparisons with what is considered to be accurate gauge estimates, and runoff volumes generated from WAT\_CLS3 simulation. The modelling improvements are compared in terms of simulated streamflows, snowpack and shallow soil layer properties.**

**While it was difficult to choose an optimal radar adjustment strategy, it was shown that addressing the local scaling issue yielded accumulation underestimates and the subsequent consideration of mixed precipitation provided improved estimates. The subsequent consideration of snow particle shape did not further improve the radar accumulation estimates.**

**From the hydrological modelling using the different radar datasets, the raw and the scaling removed radar datasets produced, on average, the best simulated streamflow volume estimates, yet the annual variability was greater than for the temperature adjustment schemes. The consideration of particle shape yielded a slight increase in runoff volume over the consideration of mixed precipitation. Since the phase and shape of falling precipitation can vary rapidly temporally and spatially, further investigation is required to examine the applicability of hourly averages for sub-hourly physical processes such as mixed precipitation and changes in the shape of snow crystals.**

**Since the water balance closed within 5% over a four year period using the WAT\_CLS3 model, the model translates precipitation into runoff and evapotranspiration appropriately without losing or storing excess water. Once the meteorological data were corrected, the most**

significant improvement to the streamflow hydrograph occurred as a result of the splitting of the soil state variables. The redistribution of snow from the bare or crop/low vegetation areas to the forest resulted in a delay in the streamflow snowmelt peak and altered the depth and snow water equivalence (SWE) of either snowpack. While the delaying of the peak is appropriate, the simple distribution technique did not represent the actual transport of snow, and in most cases overestimated movement. Variation in the maximum allowable snowpack density altered streamflow and snowpack depth, but not the SWE. The addition of mixed precipitation into CLASS provided a more realistic representation of the precipitation near the surface, however, the impact on the streamflow was small. For the variation in the fresh snow density, the actual depth of snow was only different immediately after an event. The introduction of a snowfall specific canopy interception formulation had minimal impact on the streamflow, and estimation of the composition of the forests and the canopy parameters was more important to snowpack development.

Secondary results from this research included the development of a method to estimate the daytime cloud cover fraction for computing longwave radiation, the derivation of a relationship for the relative specific surface area as a function of formation temperature, and the collection of fresh snow density data in order to assess the applicability of several existing functions.

This thesis has illustrated that ground based weather radar can be used as the winter precipitation input to a hydrological model, however, the radar data should be adjusted to consider the variability in phase and shape of winter hydrometeors. One new snow process has been added and five other processes have been enhanced in the CLASS model. All of these processes should be incorporated into hydrological models.

## **ACKNOWLEDGMENTS**

I would like to thank my supervisors, Professors E.D. (Ric) Soulis and Nick Kouwen, for their supervision throughout this research. Together from two different approaches, this project was able to be completed; one helped push to the finish and the other helped dot all the I's. I was fortunate to be able to work with each of them on different aspects of this research. Thanks are also due to Professor Lennox for his careful listening and helpful advice.

I appreciated the assistance of a number of individuals with the data collection, even if not all were used in this thesis. In particular, I would like to recognize Terry Ridgway's help with data collection and instrumentation, as well as the introduction to snow surveying.

The people of the Remote Sensing Laboratory aided in the modelling. Frank Seglenieks provided insight into the WATFLOOD model and Ken Snelgrove helped take away my unfounded fear of UNIX and introduced me to the CLASS model. Ted Whidden fixed a coding problem and helped alleviate my dread of the CLASS model. Jayson Innes wrote several pieces of code to manipulate radar data at the start, and helped with other related work at the end.

General inspiration was provided by various members of the Water Resources Group, including but not limited to Eric Hood, DJ Miln Harvey, and David Brush.

A thank you is due to Gerhard Kohnen who always emphasized work etiquette. He was the first to make me ponder snow and the perplexities of its scale by stating that 'snow is the great equalizer.'

This research was supported by Atmospheric Environment Service (now called the Meteorological Service of Canada or MSC) Science subventions and by the MSC-CRYSYS funding acquired by Professor Ellsworth LeDrew (University of Waterloo Geography). Various agencies provided data that were used in this thesis, and their assistance is acknowledged with thanks: the radar images were provided by MSC King City Radar; meteorologic data were provided by MSC-Downsview; streamflow data were measured by Water Survey of Canada and the Grand River Conservation Authority (GRCA); and snowcourse data were collected by the GRCA and supplied by Streamflow Forecast Centre of the Ontario Ministry of Natural Resources.

## **DEDICATION**

**To anyone who can see beyond what can be seen, and can see what is.**

# TABLE OF CONTENTS

TABLE OF CONTENTS .....	ix
LIST OF FIGURES .....	xii
LIST OF TABLES .....	xxii
LIST OF SYMBOLS .....	xxv
<b>1.0 INTRODUCTION .....</b>	<b>1</b>
1.1 OBJECTIVES .....	6
1.2 RATIONALE .....	7
1.3 SCOPE OF THESIS .....	8
<b>2.0 BACKGROUND .....</b>	<b>10</b>
2.1 SNOW PROCESSES .....	10
2.1.1 Precipitation Formation and Growth .....	11
2.1.2 Hydrometeors .....	13
2.1.2a <i>Snowfall</i> .....	13
2.1.2b <i>Mixed Precipitation</i> .....	13
2.1.3 Snow Accumulation .....	14
2.1.3a <i>Fresh Snow Density</i> .....	15
2.1.4 Snowfall Interception .....	17
2.1.5 Snowpack Metamorphosis .....	16
2.1.6 Snowcover Movement and Sublimation .....	18
2.1.6a <i>Non-Transport Sublimation</i> .....	19
2.1.6b <i>Redistribution</i> .....	21
2.1.6c <i>Transport Sublimation</i> .....	23
2.1.7 Snowmelt and Runoff .....	24
2.2 MEASUREMENT TECHNIQUES .....	26
2.2.1 Precipitation Measurement .....	27
2.2.1a <i>Precipitation Gauges</i> .....	27
2.2.1b <i>Snow Accumulation Sampling</i> .....	30
2.2.1c <i>Ground-based Weather Radar</i> .....	30
2.2.1d <i>Weather Radar Solid Precipitation Measurement</i> .....	33
2.2.2 Snowpack Assessment .....	38
2.2.2a <i>Snowcourses</i> .....	39
2.3 HYDROLOGIC SNOWPACK MODELLING .....	39
2.3.1 CLASS .....	40
2.3.2 WATFLOOD .....	42
2.3.3 WATFLOOD/CLASS Linkage .....	43
2.4 SCOPE OF THE INVESTIGATION .....	44

<b>3.0</b>	<b>STUDY SITE AND DATASET</b>	56
3.1	STUDY SITE	56
3.2	DATASET	59
3.2.1	Radar Imagery	59
3.2.2	Meteorological Gauges	60
3.2.3	Snowcourse Data	60
3.2.4	Hydrometric Data	60
3.2.5	Period of Study	63
<b>4.0</b>	<b>METHODOLOGY</b>	65
4.1	METEOROLOGICAL DATA ASSEMBLY	65
4.1.1	Precipitation Gauge Data Adjustment	66
4.1.2	Meteorological Data Gridding	68
4.1.3	Longwave Radiation Estimation	69
4.1.4	Radar Winter Precipitation Data Adjustment	72
4.1.4a	<i>Scaling</i>	73
4.1.4b	<i>Mixed Precipitation</i>	74
4.1.4c	<i>Snow Crystal Particle Shape</i>	78
4.1.4d	<i>Other Factors</i>	83
4.1.4e	<i>Summary of Alternatives</i>	83
4.2	MODELLING CHANGES AND ADDITIONS	84
4.2.1	Mixed Precipitation	84
4.2.2	Fresh Snow Density	86
4.2.3	Maximum Snowpack Density	87
4.2.4	Canopy Snowfall Interception	87
4.2.5	Redistribution	88
4.2.6	Split State Variables	90
4.3	RESULTS COMPARISON	91
<b>5.0</b>	<b>RESULTS AND DISCUSSION</b>	93
5.1	RADAR ESTIMATION OF WINTER PRECIPITATION	93
5.1.1	Winter Precipitation Accumulation	94
5.1.1a	<i>Raw Radar</i>	95
5.1.1b	<i>Scaling Removal Radar</i>	96
5.1.1c	<i>Mixed Precipitation Adjustment</i>	96
5.1.1d	<i>Mixed Precipitation and Particle Shape Adjustment</i>	100
5.1.1e	<i>Additional Adjustment Variations</i>	104
5.1.1f	<i>Summary of Winter Precipitation Accumulation</i>	105
5.1.2	Runoff Comparison	106
5.1.3	Radar Data Assessment	110
5.2	METEOROLOGICAL DATA IMPROVEMENTS	112
5.3	MODELLING IMPROVEMENTS	116
5.3.1	Split State Variables	117

5.3.2	Mixed Precipitation	117
5.3.3	Fresh Snow Density	119
5.3.3a	<i>Fresh Snow Density and Air Temperature Relationship</i>	119
5.3.3b	<i>Fresh Snow Density Influence on Modelling</i>	122
5.3.4	Maximum Snowpack Density	123
5.3.5	Canopy Snowfall Interception	124
5.3.6	Redistribution	125
5.3.6a	<i>Redistribution of Snow from Open Areas</i>	126
5.3.6b	<i>Minimum Snow Depth for Complete Snowcover Variation</i>	127
5.3.7	Other Cold Processes	128
5.4	OTHER CONSIDERATIONS	129
5.4.1	Multi-year Simulations	130
5.4.2	Initial Conditions	132
5.4.3	Comparison to WATFLOOD results	133
5.5	SUMMARY OF RESULTS	133
<b>6.0</b>	<b>CONCLUSIONS AND RECOMMENDATIONS</b>	<b>197</b>
6.1	CONCLUSIONS	198
6.1.1	Radar Snowfall Estimation	198
6.1.2	Distributed Snowpack Modelling	202
6.1.3	Secondary Results	204
6.2	RECOMMENDATIONS	205
<b>7.0</b>	<b>REFERENCES</b>	<b>208</b>
<b>APPENDIX A:</b>	<b>CODING SPECIFICS</b>	<b>218</b>
A.1	MIXED PRECIPITATION	218
A.2	VARIABLE FRESH SNOW DENSITY	219
A.3	MAXIMUM SNOW DENSITY	220
A.4	SNOWFALL CANOPY INTERCEPTION	220
A.5	REDISTRIBUTION	222
A.6	SPLIT STATE VARIABLES	223
<b>APPENDIX B:</b>	<b>CURVE FITTING</b>	<b>225</b>
B.1	MIXED PRECIPITATION	225
B.1.1	Smoothing of the Data	225
B.1.2	Selection of a Suitable Function	226
B.1.3	Smoothed Curve Representation	228
B.2	PARTICLE SHAPE CURVE	229
<b>APPENDIX C:</b>	<b>ADDITIONAL RESULTS</b>	<b>232</b>
<b>APPENDIX D:</b>	<b>DATA COLLECTED</b>	<b>274</b>

# LIST OF FIGURES

	page
1-1 Average annual percent precipitation as snow based on the Canadian Climate Normals (data from Environment Canada, 1998a) .....	3
1-2 Hourly precipitation at a 10 km resolution across the five central southwestern study basins for January 26 <sup>th</sup> 1996 at 13:00 EST derived from (a) gridded gauge data, and (b) radar estimates .....	5
1-3 Hourly precipitation at a 10 km resolution across the five central southwestern study basins for January 28 <sup>th</sup> 1996 at 03:00 EST derived from (a) gridded gauge data, and (b) radar estimates .....	5
1-4 Schematic of the general research methodology, illustrating the two research components and their specifics. The three different stages are data, modelling, and results .....	9
2-1 Ice-crystal growth faces nomenclature .....	47
2-2a Ice-crystal type of as a function of temperature and degree of supersaturation (from Mason <i>et al.</i> , 1963) .....	48
2-2b Dominant growth direction and the major growth axis a function of temperature	48
2-2c Maximum and minimum ice crystal growth rates as a function of temperature from data compiled by Ono (1970) .....	49
2-2d Linear ice crystal growth rates for the basal plane (columnar crystal) and prism face (planar crystal) as a function of temperature (from Lamb and Scott, 1971)	49
2-3 The International classification for solid precipitation (from National Research Council, 1954) .....	50
2-4 Magono and Lee (1966) classification of natural snow crystals .....	51
2-5 Average percentage probability of snow versus temperature based on 1000 observations in the US (from Auer, 1974), from data collected by the US Army Corps of Engineers (1956), and from two meteorologic stations (AROSA and DAVOS) in Switzerland (after Rohrer, 1989). The two curves for AROSA are winter and summer averages. It should be noted that all curves have been smoothed to enable a single plot comparison .....	52
2-6a Variation in fresh snow density per hour (except for the samples collected on 1-2/3/76) over the duration each storm event (data from Goodison <i>et al.</i> , 1981) .....	52
2-6b Variation in fresh snow density accumulated from the beginning of each storm event (data from Goodison <i>et al.</i> , 1981) .....	53
2-7 Fresh snow density as a function of air temperature observed by Diamond and Lowry (1953) and Schmidt and Gluns (1989). The Hedstrom and Pomeroy (1998) function was derived from the these data, while the Alta function by La Chapelle (1961) was derived from data collected at the Alta Avalanche Study Center .....	53



2-8a	The effect of wind speed on the catchment of precipitation gauges (after <i>Larson and Peck, 1974</i> ) .....	54
2-8b	Various methods to overcome wind turbulence effects about precipitation gauges (from <i>Sumner, 1988</i> and <i>Dingman, 1994</i> ) .....	54
2-8c	Under-catch of five gauges as a function of gauge mouth wind speed (after <i>Yang et al., 1999</i> ) .....	55
2-8d	Ratio of bush gauge to DFIR gauge as a function of wind speed for different precipitation types, using equations from <i>Yang et al. (1993)</i> .....	55
3-1	Map of central south-western Ontario illustrating the location of the study basins and the meteorological stations. The coverage of the AES King City Radar extends to the edge of the figure .....	57
3-2	Location of the eight hydrometric stations within the Upper Grand River basin. The four-digit numbers (2001-2012) in this figure correspond to the <i>GRCA snowcourses</i> listed in Table 3-3, while the single-digit numbers (1-8) correspond to the <i>WSC streamflow gauges</i> listed in Table 3-4 .....	62
3-3a	Seasonal snow depths in the northern section of the Upper Grand River basin at the snowcourse located at Corbetton (GRCA 2004) for the five winters .....	64
3-3b	Seasonal snow depths in the middle section of the Upper Grand River basin at the snowcourse located at Cananagigue (GRCA 2002) for the five winters .....	64
3-3c	Seasonal snow depths in the southern section of the Upper Grand River basin at the snowcourse located at Cambridge (GRCA 2001) for the five winters .....	64
4-1a	Linear representation and polynomial curve fit to the percentage probability of snow versus temperature plot derived by <i>Auer (1974)</i> .....	76
4-1b	Distribution of above freezing observed temperatures at the 3 study sites for observed data. The exponential pdf is derived from the mean of the data. The observed temperature frequencies were generated by 0.25 degree increments of the 3640 average hourly temperatures .....	77
4-2a	Distribution of below freezing observed and smoothed temperatures at the 3 study sites for observed data. The observed temperature frequencies are generated by 0.25 degree increments of the 12670 average hourly temperatures, and the smoothed data are 1.0 degree increments. The exponential pdf is derived from the mean of the below freezing data and the polynomial curve fit is a fourth-order polynomial fit to the smoothed data .....	79
4-2b	Snow-crystal particle shape adjustment curves: <i>original</i> from <i>Ono (1970)</i> crystal growth rate curve; <i>needle</i> to invert the original curve in the temperature range of maximum basal plane growth (columnar crystals); <i>capped column</i> to consider the shape irregularities (and protrusions) of the crystals that grow and/or conglomerate at temperatures where growth rates are equal in the basal and prism faces; and <i>proposed</i> to smooth the various curves. This adjustment curve is based on larger specific surface area to mass ratios (SSA) for more irregular crystals .....	81

4-2c	Comparison of the initial non-weighted particle shape adjustment curve (same as $PS_{proposed}$ in Figure 4-2b) to the transformed temperature weighted PS curve . . .	82
4-3	Schematic of snow redistribution from open areas to forested areas . . . . .	89
5-1	Snowfall radar versus “bush” gauge accumulation comparison for January 1993 at the Wormwood site . . . . .	142
5-2	Percent absolute difference in the raw radar data versus the gauge accumulation as a function of time . . . . .	142
5-3a	Seasonal snowfall accumulation raw radar versus “bush” gauge ( $\rho^2 = 0.178$ ) . . .	143
5-3b	Scale adjusted seasonal radar-gauge snowfall comparison ( $\rho^2 = 0.335$ ) . . . . .	143
5-3c	Seasonal snowfall adjusted for scale and mixed precipitation using Auer’s temperature curve with a constant factor for rain ( $\rho^2 = 0.595$ ) . . . . .	143
5-3d	Seasonal snowfall adjusted for scale and mixed precipitation using Auer’s temperature curve and precipitation rate ( $\rho^2 = 0.474$ ) . . . . .	143
5-3e	Seasonal snowfall adjusted for scale, mixed precipitation (Auer with constant rain factor), and snowflake particle shape ( $\rho^2 = 0.593$ ) . . . . .	143
5-3f	Seasonal snowfall adjusted for scale, mixed precipitation (Auer with variable R), and snowflake particle shape ( $\rho^2 = 0.471$ ) . . . . .	143
5-4a	Monthly snowfall accumulation raw radar versus “bush” gauge ( $\rho^2 = 0.089$ ) . . .	144
5-4b	Scale adjusted seasonal radar-gauge snowfall comparison ( $\rho^2 = 0.272$ ) . . . . .	144
5-4c	Monthly snowfall adjusted for scale and mixed precipitation using Auer’s temperature curve with a constant factor for rain ( $\rho^2 = 0.470$ ) . . . . .	144
5-4d	Monthly snowfall adjusted for scale and mixed precipitation using Auer’s temperature curve and precipitation rate ( $\rho^2 = 0.405$ ) . . . . .	144
5-4e	Monthly snowfall adjusted for scale, mixed precipitation (Auer with constant rain factor), and snowflake particle shape ( $\rho^2 = 0.472$ ) . . . . .	144
5-4f	Monthly snowfall adjusted for scale, mixed precipitation (Auer with variable R), and snowflake particle shape ( $\rho^2 = 0.406$ ) . . . . .	144
5-5a	Weekly snowfall accumulation raw radar versus “bush” gauge ( $\rho^2 = 0.081$ ) . . .	145
5-5b	Scale adjusted seasonal radar-gauge snowfall comparison ( $\rho^2 = -0.008$ ) . . . . .	145
5-5c	Weekly snowfall adjusted for scale and mixed precipitation using Auer’s temperature curve with a constant factor for rain ( $\rho^2 = 0.326$ ) . . . . .	145
5-5d	Weekly snowfall adjusted for scale and mixed precipitation using Auer’s temperature curve and precipitation rate ( $\rho^2 = 0.342$ ) . . . . .	145
5-5e	Weekly snowfall adjusted for scale, mixed precipitation (Auer with constant rain factor), and snowflake particle shape ( $\rho^2 = 0.341$ ) . . . . .	145
5-5f	Weekly snowfall adjusted for scale, mixed precipitation (Auer with variable R), and snowflake particle shape ( $\rho^2 = 0.351$ ) . . . . .	145
5-6	Histogram of winter radar precipitation rates for the three UW gauge sites. The bin interval is 0.1 mm/h. While the radar rate is measured in 0.5 mm/h increments, the radar data are a weighted average across the 3 by 3 pixels centred above the desired location (see section 3.1.4e) . . . . .	146

5-7a	Seasonal radar snowfall adjusted for mixed precipitation using Auer's curve with precipitation rate to a maximum rain factor of 2.03 ( $\rho^2 = 0.518$ )	147
5-7b	Monthly radar snowfall adjusted for mixed precipitation using Auer's curve with precipitation rate to a maximum rain factor of 2.03 ( $\rho^2 = 0.405$ )	147
5-7c	Weekly radar snowfall adjusted for mixed precipitation using Auer's curve with precipitation rate to a maximum rain factor of 2.03 ( $\rho^2 = 0.158$ )	147
5-8a	Seasonal radar snowfall adjusted for mixed precipitation (variable rain factor to a max. of 2.03) and particle shape using $T_{\text{dewpoint}}$ ( $\rho^2 = 0.402$ )	147
5-8b	Monthly radar snowfall adjusted for mixed precipitation (variable rain factor to a max. of 2.03) and particle shape using $T_{\text{dewpoint}}$ ( $\rho^2 = 0.275$ )	147
5-8c	Weekly radar snowfall adjusted for mixed precipitation (variable rain factor to a max. of 2.03) and particle shape using $T_{\text{dewpoint}}$ ( $\rho^2 = 0.166$ )	147
5-9a	The distributions for the OVER and UNDER estimated precipitation data	148
5-9b	The initial non-weighted particle shape adjustment curve and the difference between the OVER and UNDER estimated precipitation data	148
5-10a	December 1993 to April 1994 observed (solid) and simulated (dashed) streamflow at the Grand River at Galt derived from uncorrected gauge data	149
5-10b	December 1993 to April 1994 observed (solid) and simulated (dashed) streamflow at the Grand River at Galt derived from gauge data corrected to DFIR gauge	149
5-10c	December 1993 to April 1994 observed (solid) and simulated (dashed) streamflow at the Grand River at Galt derived from gauge data corrected to "bush" gauge	149
5-10d	December 1993 to April 1994 observed (solid) and simulated (dashed) streamflow at the Grand River at Galt derived from raw radar	150
5-10e	Grand River at Galt winter 1993/1994 hydrograph using the "no scaling" radar dataset	150
5-10f	Grand River at Galt winter 1993/1994 hydrograph using the "mixed precipitation using a constant rain factor" radar dataset	150
5-10g	Grand River at Galt winter 1993/1994 hydrograph using the "mixed precipitation using a constant rain factor and particle shape curve" radar dataset	151
5-10h	Grand River at Galt winter 1993/1994 hydrograph using the "mixed precipitation using a variable rain factor and particle shape curve" radar dataset	151
5-10i	December 1993 to April 1994 observed (solid) and simulated (dashed) streamflow at the Grand River at Galt derived from radar adjusted for mixed precipitation (variable rain factor) and particle shape	151
5-11	Observed versus calculated peak flow for the 1993 to 1997 winters using (a) uncorrected gauge data, (b) gauge data corrected to DFIR gauge, (c) gauge data corrected to "bush" gauge, (d) raw radar input, (e) scale adjusted radar, and (f) radar adjusted for mixed precipitation using Auer's curve with a constant rain factor (2.03), (g) radar adjusted for scale, mixed precipitation (constant R), and snowflake particle shape, (h) radar adjusted for mixed precipitation using Auer's temperature curve and precipitation rate, and (i) radar adjusted for scale, mixed precipitation (variable R), and snowflake particle shape precipitation modelling input	152

5-12a	Four-year water balance using WATFLOOD (Mackenzie River basin)	154
5-12b	Four-year water balance using WAT_CLS3 at one grid point in the Grand River	155
5-13a	Cumulative runoff volume from Jan. 1993 to April 1993 on the Eramosa River above Guelph	156
5-13b	Cumulative runoff volume from Nov. 1995 to April 1996 on the Speed River at Armstrong Mills	156
5-14a	Ratio of measured to computed clear-sky hourly shortwave radiation for the AES meteorological station at CARE over the winter of 1993, assuming that station data were collected at Local Apparent Time (LAT)	157
5-14b	Ratio of measured to computed clear-sky hourly shortwave radiation at Elora using LAT	157
5-14c	Ratio of measured to computed clear-sky hourly shortwave radiation at Toronto using LAT	157
5-15a	Ratio of measured to computed clear-sky hourly shortwave radiation for the AES meteorological station at CARE over the winter of 1993, assuming that station data were collected at Local Standard Time (LST)	158
5-15b	Ratio of measured to computed clear-sky hourly shortwave radiation at Elora using LST	158
5-15c	Ratio of measured to computed clear-sky hourly shortwave radiation at Toronto using LST	158
5-16a	Ratio of measured to computed clear-sky hourly radiation at CARE and Elora for November 3 (J=307) to December 21, 1995 (J=355)	159
5-16b	As in Figure C-4a, for December 22, 1995 (J=356) to February 7, 1996 (J=38)	159
5-16c	As in Figure C-4a, for February 8, 1996 (J=39) to March 19, 1996 (J=79)	159
5-16d	As in Figure C-4a, for March 20, 1996 (J=80) to April 30, 1996 (J=121)	159
5-17a	Ratio of measured to computed clear-sky hourly radiation at Toronto for November 3 (J=307) to December 21, 1994 (J=355)	160
5-17b	As in Figure C-5a, for December 22, 1994 (J=356) to February 7, 1995 (J=38)	160
5-17c	As in Figure C-5a, for February 8, 1995 (J=39) to March 20, 1995 (J=79)	160
5-17d	As in Figure C-5a, for March 21, 1995 (J=80) to April 30, 1995 (J=120)	160
5-18a	Third order polynomial fits for the maximum observed to computed shortwave radiation at the AES CARE and Elora meteorological stations (lower limit of $K_{obs}/K_{comp} > 0$ ; an upper limit of $K_{obs}/K_{comp} < 1$ )	161
5-18b	Third order polynomial fits for the maximum observed to computed short-wave radiation at the AES Toronto meteorological stations (lower limit of $K_{obs}/K_{comp} > 0$ ; an upper limit of $K_{obs}/K_{comp} < 1$ )	161
5-19a	Effect of cloud cover percentage used to calculate long wave radiation fluxes on initial spring peak for the Grand River at Galt in 1993 (March 24 <sup>th</sup> to April 9 <sup>th</sup> )	162
5-19b	As in Figure 5-19a, but for the entire snowmelt period (100, 30 and 0% cloud cover)	162
5-19c	As in Figure 5-19a, but for the entire snowmelt period (variable, 50, and 30% cloud cover)	162
5-20	The difference between the average temperature across the Southern Ontario	

study area as derived from gridded station data and as computed from the MC <sup>2</sup> model	163
5-21a Effects of data improvement and partitioning of soil parameters on the 1993 initial spring peak hydrograph (observed and three simulations) for the Grand River at Galt. The simulated hydrographs were modelled using “out-of-the-box” WAT_CLS3 with a limited meteorological dataset, an improved meteorological dataset, and WAT_CLS3 modified to differentiate between snow-covered and snow-free areas	163
5-21b Top layer soil temperature for the averaged soil properties (no snow processes) and the snowcovered area from the decoupling of soil properties (with snow processes)	164
5-21c Top layer soil liquid and frozen water content for the averaged soil properties (no snow processes) and the decoupling of the soil properties (with snow processes)	164
5-22a January to April 1993 observed streamflow and hydrographs simulated using different mixed precipitation scenarios for the Grand River at Galt	165
5-22b As in Figure 5-22a, but for the snowmelt period (March 20 <sup>th</sup> to the end of April)	165
5-22c As in Figure 5-22a and 5-22b, but specifically only the first snowmelt peak	166
5-23a Measured and computed snow depths for the mid Grand River snowcourse 2002 (north of Elmira) using different mixed precipitation scenarios for the Grand River at Galt	166
5-23b Measured and computed SWE, as per Figure 5-23b	167
5-24a Computed top layer soil temperature for the crop/low vegetation land cover type in the vicinity of GRCA snowcourse 2002, simulated using different mixed precipitation scenarios for the Grand River at Galt	167
5-24b Computed soil water content (liquid and liquid + ice), as per Figure 5-24a	168
5-25a Fresh snow density as a function of air temperature for the data collected in Waterloo during the winter of 1999, with the radar adjustment particle shape curve (outlined in section 3.1.4c)	168
5-25b Fresh snow density as a function of air temperature observed by Diamond and Lowry (1953), Schmidt and Gluns (1991), and in Waterloo during the winter of 1999. The Hedstrom and Pomeroy (1998) function was derived from the these data, while the Alta function by La Chapelle (1961) was derived from data collected at the Alta Avalanche Study Center. The particle shape curve was used to adjust the radar data, as outlined in section 3.1.4c	169
5-26a Effects of different fresh snow density formulations on the initial snowmelt peak on the Grand River at Galt in 1993	169
5-26b Effects of different fresh snow density formulations on the snow depth at snowcourse 2002	170
5-26c Effects of different fresh snow density formulations on the SWE at 2002	170
5-26d Effects of different fresh snow density formulations on the soil temperature	171
5-26e Effects of different fresh snow density formulations on the soil water content	171
5-27a Effect of variation in the maximum snow density on the initial snowmelt	

hydrograph on the Grand River at Galt in 1993 .....	172
5-27b Effect of variation in the maximum snow density on the snow depth at snowcourse 2002 .....	172
5-27c Effect of variation in the maximum snow density on the SWE .....	173
5-27d Effect of variation in the maximum snow density on the soil temperature ....	173
5-27e Effect of variation in the maximum snow density on the soil water content ...	174
5-28a Effects of different canopy snow interceptions formulations on the forest SWE, for forests throughout the basin that are 100% deciduous. The observed data are for a nearby snowcourse (2002) .....	174
5-28b Effects of different canopy snow interceptions formulations on the forest SWE, for forests throughout the basin that are 65% deciduous .....	175
5-28c Effects of different canopy snow interceptions formulations on the forest SWE, for forests throughout the basin that are 100% coniferous .....	175
5-28d Effects of the different canopy snow interception formulations on the simulated streamflow .....	176
5-29a Modelled snowmelt flow comparison of different canopy types, using the Hedstrom and Pomeroy (1998) canopy interception formulation .....	177
5-29b Effects of different canopy types throughout the basin on the forest SWE using the Hedstrom and Pomeroy (1998) canopy interception formulation .....	177
5-29c Effects of different canopy types throughout the basin on the forest top layer soil temperature using the Hedstrom and Pomeroy (1998) canopy interception formulation .....	178
5-29d Effects of different canopy types throughout the basin on the forest top layer soil water content using the Hedstrom and Pomeroy (1998) canopy interception formulation .....	178
5-30a Effects of simple redistribution on the 1993 initial snowmelt peak hydrograph (observed and five simulations) for the Grand River at Galt. The simulated hydrographs uses redistribution from the bare or crop/low vegetation land classes with different depth capacity limits .....	179
5-30b Effects of simple redistribution on the forest snowpack depth (near GRCA snowcourse 2002) from bare or crop/low veg. land cover for 150 and 250 mm accumulation limits .....	179
5-30c Effects of simple redistribution (location, date, and radar data as in Figure 5- 29a) with 250 mm depth capacity moving 0.1, 1, and 100% of the redistributable snow at each time step, plus the effect of variation in the $D_{100}$ with no redistribution .....	180
5-30d Effects of simple redistribution on the forest snowpack depth (near GRCA snowcourse 2002) with 250 mm depth capacity moving 0.1, 1, and 100% of the redistributable snow at each time step .....	180
5-31a Effects of varying the $D_{100}$ on the 1993 Grand River at Galt streamflow ....	181
5-31b Effects of varying the $D_{100}$ on the snow depth near snowcourse 2002 .....	181
5-31c Effects of varying the $D_{100}$ on the SWE .....	182
5-31d Effects of varying the $D_{100}$ on the soil temperature .....	182

5-31e	Effects of varying the $D_{100}$ on the soil water content	183
5-32	Five year continuous simulation for the Grand River at Galt	184
5-33a	Select poorly simulated annual hydrographs from the five year continuous simulation for the entire southern Ontario study area (drainage areas: Saugeen R. near Port Elgin = 3960 km <sup>2</sup> , Maitland R. above Wingham = 528 km <sup>2</sup> , Thames R. near Ealing = 1340 km <sup>2</sup> , and Thames R. at Ingersoll = 518 km <sup>2</sup> )	185
5-33b	The 1993 observed and simulated annual hydrographs from the five year continuous simulation for the entire southern Ontario study area, for the same watersheds as Figure 5-32a	186
5-34	(i) Simulated and observed cumulative runoff over time from 1993 through 1997, and (ii) simulated versus observed cumulative runoff, for (a) the Grand River at Galt (02GA003), (b) the Grand River near West Montrose (02GA034), (c) the Grand River at Marsville (02GA014), (d) the Eramosa River above Guelph (02GA029), (e) the Conestogo River above Drayton (02GA039), (f) the Speed River at Armstrong Mills (02GA040), (g) the Speed River below Guelph (02GA015), (h) Canangagique Creek near Elmira (02GA023), (i) the Pine River near Everett (02ED014), (j) the Saugeen River near Port Elgin (02FC001), (k) the Saugeen River near Walkerton (02FC002), (l) the South Saugeen River near Hanover (02FC012), (m) the Maitland River below Wingham (02FE002), (n) the Maitland River above Wingham (02FE005), (o) the Middle Maitland River near Belgrave (02FE008), (p) the Thames River near Ealing (02GD001), (q) the Middle Thames River at Thamesford (02GD004), (r) the North Thames River near Mitchell (02GD014), (s) the North Thames River near Thorndale (02GD015), and (t) the Thames River at Ingersoll (02GD016)	187
5-35	Variation in the early January 1993 hydrograph peak from the observed (solid black line), modelled assuming no snow on the ground on January 1 (dotted red line), and modelled assuming 10 cm of snow and 20mm of SWE everywhere (dashed green line). The watersheds are as in Figure 5-34	194
5-36	Comparison of simulated flows using WAT_CLS3 (short dashes) versus WATFLOOD (long dashes) for the Grand River at Galt	196
6-1	Summary of gauge versus radar accumulation population coefficient of determination ( $\rho^2$ ) and standard error of estimate (SEE) statistics	199
6-2a	Summary of average winter runoff volumes across the Grand River basin for different precipitation input data using the 'out-of-the-box' WAT_CLS3 model	200
6-2b	Summary of average runoff volumes across the Grand River basin for the 1993 through 1997 winters using different precipitation input data with the 'out-of-the-box' WAT_CLS3 model	201
6-3	Initial snowmelt hydrograph improvements (1993 Grand River at Galt)	203
B-1	Percent snow, rain and mixed precipitation as a function of air temperature from US Army Corps of Engineers (1956) data. The data were originally presented in tabular form. The <i>smoothed curve</i> presented is a smoothed	

	average of the percent snow and percent rain curves .....	225
B-2	Percent snow as a function of air temperature from 1000 meteorological observations in the US (Auer, 1974). The data were originally presented as a line segments .....	226
B-3	Percent snow as a function of air temperature at two locations in Switzerland (Rohrer, 1989). The summer and winter percent snow curves have been differentiated for the AROSA station. The data were originally presented as a series of bar charts for a temperature increment of 0.5°C. These ranges are presented as the average percent snow within each bin .....	227
B-4	The fit of four functions to the Auer (1974) smoothed curve .....	227
B-5	Percent snow as a function of air temperature from the five 6 <sup>th</sup> order polynomial curves fitted to the smoothed curves presented in Figures B-1 through B-3 .....	229
B-6	Three-dimensional representation of the directional average ice crystal growth rate as a function of formation temperature, based on the data compiled by Ono (1970) .....	230
B-7a	The fit of four functions to the particle shape curve (non-weighted in Figure 4-2c), across the entire temperature range .....	231
B-7b	The fit of the four functions to the particle shape curve (as above) for the maximum dendritic crystal growth range -17 and -14°C .....	231
C-1	Snowfall raw radar-gauge comparison at the Wormwood site for (a) February 1993 through (r) March 1997 .....	233
C-2	Snowfall raw radar-gauge comparison at the Greenoch site for (a) February 1995 through (g) December 1996 .....	242
C-3	Snowfall raw radar-gauge comparison at the Euclid site for (a) February 1997 and (b) March 1997 .....	245
C-4	Snowfall raw radar-gauge comparison at the CARE site for (a) February 1993, (b) March 1993, (c) 1994, and (d) 1995 .....	246
C-5a	Average, +/- 1 standard deviation, non-unity maximum, non-zero minimum ratio of measured to computed clear sky hourly radiation at Elora and CARE for November 3 (J=307) to December 21, 1995 (J=355) .....	249
C-5b	As in Figure C-7a, for December 22, 1995 (J=356) to February 7, 1996 (J=38) .....	249
C-5c	As in Figure C-7a, for February 8, 1996 (J=39) to March 19, 1996 (J=79) .....	250
C-5d	As in Figure C-7a, for March 20, 1996 (J=80) to April 30, 1996 (J=120) .....	250
C-6a	Water balance at one grid square in the Grand River basin for January to June 1993, before the incorporation of the advanced snow processes .....	251
C-6b	Annual water balance for 1993 in the Grand River, with snow processes incorporated .....	252
C-7a	Effects of different canopy snow interceptions formulations on the 1993 Grand River at Galt streamflow, for the forest that are 100% deciduous throughout the basin .....	253
C-7b	Effects of different canopy snow interceptions formulations on the forest	



	<b>snow depth near snowcourse 2002, for 100% deciduous forest</b> .....	<b>253</b>
<b>C-7c</b>	<b>Effects of different canopy snow interceptions formulations on the forest soil temperature for 100% deciduous forest</b> .....	<b>254</b>
<b>C-7d</b>	<b>Effects of different canopy snow interceptions formulations on the forest soil water content, for 100% deciduous forest</b> .....	<b>254</b>
<b>C-8</b>	<b>Comparison of simulated flows using WATFLOOD/CLASS (short dashes) versus WATFLOOD (long dashes) for (a) the Grand River near West Montrose (02GA034) through (s) the Thames River at Ingersoll (02GD016), as per the stations in Figure 5-34</b> .....	<b>255</b>

## LIST OF TABLES

	page
2-1	NRC Classification of Solid Precipitation (NRC, 1954) . . . . . 45
2-2	Radar reflectivity-precipitation rate coefficients in the $Z = AR^b$ relationship .. 46
2-3	A sample dataset for the CLASS 'BENCH.INI' parameter and initialization file for the beginning of the winter prior to accumulation, i.e., no snow, and for evergreen needleleaf trees . . . . . 46
2-4	Summary of the generalized components of WATFLOOD, CLASS, and the linked WATFLOOD/CLASS models . . . . . 47
3-1	Summary of climate normals across central south-western Ontario (data from Environment Canada, 1998b) . . . . . 58
3-2	Summary of the AES King City Weather Radar characteristics . . . . . 59
3-3	Summary of the meteorological gauges used in this research with the parameters used for the five winters indicated by an 'X' . . . . . 61
3-4	Description of the eight snowcourse locations within the Upper Grand River basin sampled by the Grand River Conservation Authority . . . . . 61
3-5	Description of the eight hydrometric stations operated by Water Survey of Canada within the Upper Grand River basin . . . . . 62
4-1	Summary of WAT_CLS3 meteorological data with units . . . . . 66
4-2	Bounds and coefficients for five percent probability of snow curves. Each curve is fit with a sixth order polynomial, yielding a percentage, $F(T_{min})$ , at the minimum temperature, $T_{min}$ , and a percentage, $F(T_{max})$ , at the maximum temperature, $T_{max}$ . To avoid round-off error when the percentage of snow approach 100% or 0%, the temperatures and corresponding percentages when the percent snow approaches 99% from below and 1% from above are used as limits . . . . . 78
4-3	The 17 adjustment procedures and corresponding figure number for seasonal, monthly and weekly snowfall accumulation comparisons . . . . . 85
4-4	Summary of precipitation input data for runoff volume comparison . . . . . 86
5-1	Summary of seasonal (columns 3 through 7) and monthly (8 through 12) comparison statistics for raw radar and various adjustment schemes versus gauge estimation. The statistics are weighted by the length of each record to account greater errors occurring at shorter intervals. The standard error of estimate (SEE) and coefficient of determination ( $r^2$ ) are based on the best-fit regression lines with the slope and y-intercept. The standard errors are normalized to values of mm/d . . . . . 135
5-2	Summary of seasonal (columns 3 through 6), monthly (7 through 10), and weekly (column 11 through 14) comparison statistics for raw radar and various

	adjustment schemes versus gauge estimation. The statistics are weighted by the length of each record to account greater errors occurring at shorter intervals. The mean difference (mean diff.), standard error of estimate (SEE) and coefficient of determination ( $r^2$ ) are based on the 1:1 line with a slope of unity through the origin (i.e., using an intercept of 0). The mean difference and standard errors are normalized to values of mm/d	136
5-3	Summary of seasonal (columns 3 through 7), monthly (8 through 12), and weekly (column 13 through 17) comparison statistics for combination adjustment schemes versus gauge estimation. The statistics are weighted by the length of each record to account greater errors occurring at shorter intervals. The mean difference (mean diff.), standard error of estimate (SEE) and coefficient of determination ( $r^2$ ) are based on the 1:1 line with a slope of unity through the origin (i.e., using an intercept of 0). The mean difference and standard errors are normalized to values of mm/d	137
5-4	Summary of peak flow statistics for all the five winters of peak flow data. The nine precipitation input data are as summarized in Table 3-4	137
5-5a	January 1993 to April 1993 winter runoff volumes (mm) at eight streamflow gauges (column 1) for the observed (column 2) and simulated runoff volumes based on the precipitation inputs summarized in Table 3-4	138
5-5b	December 1993 to April 1994 winter runoff volumes, as in Table 5-5a	138
5-5c	November 1994 to April 1995 winter runoff volumes, as in Table 5-5a	138
5-5d	November 1995 to April 1996 winter runoff volumes, as in Table 5-5a	138
5-5e	December 1996 to April 1997 winter runoff volumes, as in Table 5-5a	139
5-6	Average percent difference between the computed and observed runoff volumes at all hydrometric stations for the individual five years (8 datapoints), for all stations for the five years (40 datapoints), and for the total volume over the five winters (8 datapoints). The standard deviations are included for all runoff volumes and for the total station volumes	139
5-7a	Equations and for the third order polynomial fits of the form $K_{obs}/K_{comp} = a_3t_m^3 + a_2t_m^2 + a_1t + b$ for CARE and Elora, corresponding to the curves in Figure 5-18a	140
5-7b	Equations and for the third order polynomial fits of the form $K_{obs}/K_{comp} = a_3t_m^3 + a_2t_m^2 + a_1t + b$ for Toronto, corresponding to the curves in Figure 5-18b	140
5-8	Average cloud cover fraction at the AES CARE, Elora and Toronto meteorological stations as derived from the difference between measured shortwave and clear-sky shortwave radiation, using all data and daytime data. The adjusted method considers the fact that typically less than 100% of the theoretical clear-sky radiation reaches the earth's surface and that there are low morning and late afternoon short-wave measurement encountered during the winter and early spring	140
5-9	Fresh snow density data collected in Waterloo during winter 1999, including average temperature during each snowfall event, average depth, average SWE, maximum and	

<b>minimum fresh snow density limits</b> .....	<b>141</b>
<b>6-1 Summary of the influence of the incorporation of advanced snow processes on streamflow, snow depth and SWE in CLASS model</b> .....	<b>203</b>
<b>D-1a Raw fresh snow density data: mass, depth and area measurements for samples 1 through 5, with snowfall event start and end dates and times taken from sonic snow depth sampling at the University of Waterloo north campus weather station. Notes that event 2 occurred in 3 periods</b> .....	<b>274</b>
<b>D-1b Raw fresh snow density data: mass, depth and area measurements for samples 6 through 9, with snowfall event start and end dates and times taken from sonic snow depth sampling at the UW north campus weather station</b> .....	<b>275</b>
<b>D-1c Raw fresh snow density data: mass, depth and area measurements for samples 10 through 14, with snowfall event start and end dates and times taken from sonic snow depth sampling at the UW north campus weather station</b> .....	<b>276</b>

## LIST OF SYMBOLS

[UNITS: M = mass, L = length, T = temperature,  $\tau$  = time]

$a$	longest dimension of ice crystal growth in the basal plane [L]
$a$	height above the surface for wind speed measurement [L]
$a, b, c$	coefficients for the Anderson settling function, equation (2-7)
$a, b, c$	coefficients for particle shaped adjustment curve
$A$	radar power relationship constant
$a_{F_{s1}}$ -	
$a_{F_{s6}}$	coefficients for percent snow content in mixed precipitation computation
$A_{(forest)}$	area covered by forest [L <sup>2</sup> ]
$A_{(open)}$	open area [L <sup>2</sup> ]
$b$	dimension perpendicular to $a$ for ice crystal growth in the basal plane [L]
$b$	height above the surface for humidity and temperature measurements [L]
$b$	radar power relationship exponent
$b_{F_s}$	coefficient for percent snow content in mixed precipitation computation
$c$	prism face dimension for ice crystal growth [L]
$C$	radar unit-specific constant
$C_{can}$	canopy coverage fraction
$C_{cloud}$	cloud coverage fraction
$c_p$	specific heat capacity of air [M.L <sup>-1</sup> .T <sup>-1</sup> . $\tau^{-2}$ ]
$c_{suc}$	dimensionless snow unloading coefficient
$D_{100}$	minimum snowpack depth for complete snowcover [L]
$D_f$	diffusivity of water vapour in air
$d_s$	snow depth [L]
$d_s (forest)$	forest snow depth [L]
$d_s (open)$	open area snow depth [L]
$d_{s-NT\ max}$	maximum non-transport snow depth limit [L]
$e_a$	near surface vapour pressure of the air [M.L <sup>-1</sup> . $\tau^{-2}$ ]
$e_b$	vapour pressure at height $b$ [M.L <sup>-1</sup> . $\tau^{-2}$ ]
$e_o$	vapour pressure at the surface [M.L <sup>-1</sup> . $\tau^{-2}$ ]
$E_o$	eccentricity correction
$E_t$	equation of time [ $\tau$ ]
$F$	water vapour mass transfer rate [M.L <sup>-2</sup> . $\tau^{-1}$ ]
$f_1$	surface orientation function for incoming shortwave radiation estimation
$f_2$	cloud cover function for incoming shortwave radiation estimation
$F_{PS}$	particle shape adjustment factor
$F_{PS}'$	transformed particle shape adjustment factor
$F_s$	fraction of precipitation as snow
$F_s(T)$	fraction of precipitation as snow for a particular air temperature
$g$	acceleration due to gravity [L. $\tau^{-2}$ ]
$h^*$	height of the top of the saltating layer [L]

$h_a$	height of the wind speed measurement $a$ [L]
$h_b$	height of the wind speed measurement $b$ [L]
$I$	snow interception [M.L <sup>-2</sup> ]
$I^*$	maximum snow load [M.L <sup>-2</sup> ]
$I_o$	initial snow load [M.L <sup>-2</sup> ]
$I_{sc}$	solar constant ( $I_{sc} = 1367 \text{ W.m}^{-2}$ ) [M.τ <sup>-3</sup> ]
$J$	Julian date
$K$	refractive/absorptive property of reflecting rainfall
$K_{cs}$	clear sky shortwave radiation flux [M.τ <sup>-3</sup> ]
$K_{inc}$	theoretical incoming shortwave radiation [M.τ <sup>-3</sup> ]
$K_{meas}$	measured incoming shortwave radiation [M.τ <sup>-3</sup> ]
$k_o$	von Karman turbulence coefficient
$K_Q$	heat transfer from solar radiation [M.τ <sup>-3</sup> ]
$K_T$	thermal conductivity of air
$L_e$	local longitude
$L_{inc}$	incoming longwave radiation [M.τ <sup>-3</sup> ]
$L_s$	latent heat of sublimation
$L_{std}$	standard longitude
$LAI$	leaf area index
$LAT$	local apparent time [τ]
$M$	depth of melt water generated per unit time [L.τ <sup>-1</sup> ]
$M_W$	molecular weight of water vapour
$M_Q$	conversion factor for energy flux density to snowmelt density
$\bar{m}(z)$	mean particle mass at height $z$ [L]
$MF_i$	melt factor [L.T <sup>-1</sup> .τ <sup>-1</sup> ]
$p$	air pressure [M.L <sup>-1</sup> .τ <sup>-2</sup> ]
$P_r$	average return power from raindrop energy scatter
$PS_{capped\ column}$	ordinate value for capped column shaped particle adjustment curve
$PS_{needle}$	ordinate value for needle shaped particle adjustment curve
$PS_{original}$	ordinate value for original particle shape adjustment curve
$PS_{T-weighted}$	ordinate value for temperature weighted particle shape adjustment curve
$Q$	heat transfer rate [M.τ <sup>-3</sup> ]
$Q^*$	net all-wave radiation [M.τ <sup>-3</sup> ]
$q_b$	specific humidity at height $b$ [M.M <sup>-1</sup> ]
$Q_E$	latent heat flux [M.τ <sup>-3</sup> ]
$Q_G$	ground heat flux [M.τ <sup>-3</sup> ]
$Q_H$	sensible heat flux [M.τ <sup>-3</sup> ]
$Q_M$	energy available for melt [M.τ <sup>-3</sup> ]
$q_o$	specific humidity at the surface [M.M <sup>-1</sup> ]
$Q_R$	heat flux from rain [M.τ <sup>-3</sup> ]
$q_{salt}$	rate of saltating snow movement [M.L.τ <sup>-1</sup> ]

$q_{\text{susp}}$	rate of suspended snow movement [M.L. $\tau^{-1}$ ]
$q_{\text{subl}}$	rate of suspended snow movement [M.L. $\tau^{-1}$ ]
$q_T$	total blowing snow transport rate [M.L. $\tau^{-1}$ ]
$r$	distance from the sample volume of the radar unit [L]
$r$	radius of an ice sphere [L]
$R$	precipitation rate [L. $\tau^{-1}$ ]
$R$	universal gas constant
$R_{\text{mixed}}$	radar mixed precipitation rate [L. $\tau^{-1}$ ]
$R_s$	snowfall rate [L. $\tau^{-1}$ ]
$R_w$	winter Z-R derived precipitation rate [L. $\tau^{-1}$ ]
$S$	snowfall depth accumulation rate [L. $\tau^{-1}$ ]
$S_p$	trees species coefficient
$SWE_{\text{(forest)}}$	snow water equivalent in the forest [M.L $^2$ ]
$SWE_{\text{(open)}}$	snow water equivalent in the open area [M.L $^2$ ]
$t$	time [ $\tau$ ]
$T$	temperature [T]
$T_{0.01}$	temperature when snow fraction in mixed precipitation approaches 1% [T]
$T_{0.99}$	temperature when snow fraction in mixed precipitation approaches 99% [T]
$T_a$	air temperature at height $a$ [T]
$T_{\text{max}}$	daily maximum air temperature [T]
$T_{\text{mean}}$	mean daily air temperature [T]
$T_{\text{min}}$	daily minimum air temperature [T]
$T_{oi}$	temperature at which melt is initiated per land class $i$ [T]
$t_{\text{ASN}}$	time before or after solar noon [ $\tau$ ]
$\Delta t$	time increment [ $\tau$ ]
$U^*$	shear velocity [L. $\tau^{-1}$ ]
$U_{10}$	wind speed at a height of 10 metres [L. $\tau^{-1}$ ]
$U_a$	wind speed at height $a$ [L. $\tau^{-1}$ ]
$U_{\text{DFIR}}$	wind speed at DFIR gauge measurement height [L. $\tau^{-1}$ ]
$U_{\text{gauge}}$	wind speed at gauge height [L. $\tau^{-1}$ ]
$U_{\text{NIPHER}}$	wind speed at gauge height for a Nipher-shielded gauge [L. $\tau^{-1}$ ]
$U_p$	mean horizontal snow particle speed in the saltating layer [L. $\tau^{-1}$ ]
$W_p$	mean saltating snow particle weight per unit area [M.L. $\tau^{-1}$ ]
$z$	height above the ground surface [L]
$Z$	radar reflectivity
$z_b$	height of the top of the plume of particles diffusing into the atmosphere [L]
$z_d$	zero-plane displacement [L]
$z_o$	roughness height [L]
$\alpha$	slope azimuth (measured clockwise from north)
$\alpha_R$	rain adjustment constant
$\beta$	slope inclination angle
$\beta_R$	rain adjustment exponent

$\Gamma$	day angle
$\delta$	declination
$\epsilon_{at}$	integrated effective emissivity of the atmosphere and canopy
$\eta(z)$	suspended snow mass concentration at height $z$ [ $M.L^{-2}$ ]
$\theta_b$	potential temperature at height $b$ [T]
$\theta_o$	potential temperature at surface [T]
$\Lambda$	latitude
$\rho_d$	reference snow density in Anderson settling function, equation (2-7) [ $M.L^{-3}$ ]
$\rho_s$	density of snow [ $M.L^{-3}$ ]
$\rho_s (open)$	density of snow being transported from the open area [ $M.L^{-3}$ ]
$\rho_s (forest)$	density of snow in the forest [ $M.L^{-3}$ ]
$\rho_s (fresh)$	density of fresh snow [ $M.L^{-3}$ ]
$\rho_{wv}$	density of atmospheric water vapour [ $M.L^{-3}$ ]
$\sigma$	Stefan Boltzmann's constant ( $\sigma = 5.6697 \times 10^{-8} W.m^{-2}.K^{-4}$ )
$\sigma_{unsat}$	undersaturation of air with respect to water vapour
$\omega$	angular velocity of earth's rotation [ $\tau^{-1}$ ]

### Derivatives

$dL/dt$	average snow crystal growth rate [ $L.\tau^{-1}$ ]
$dm/dt$	change in mass with respect to time [ $M.\tau^{-1}$ ]
$du/dt$	change in internal energy with respect to time [ $M.\tau^{-3}$ ]

### Dimensionless parameters

$Nu$	Nusselt number
$Re$	Reynolds number
$Sh$	Sherwood number

### Subscripts

$i$	specific land class
$sat$	saturation level



# Chapter 1

## INTRODUCTION

---

*“When Man was still very young he had already become aware that certain elemental forces dominated the world womb. Embedded on the shores of their warm sea, the Greeks defined these as Fire and Earth and Air and Water. But at first the Greek sphere was small and circumscribed and the Greeks did not recognize the fifth elemental.*

*About 330 B.C., a peripatetic Greek mathematician named Pytheas made a fantastic voyage northward to Iceland and on into the Greenland Sea. Here he encountered the fifth elemental in all of its white and frigid majesty, ...”*  
(Mowat, 1975, p1)

Snow is a crucial component of the hydrologic cycle, especially in northern climates. Snowfall has an important social context; many humans have to live in a climate where snow is indicative of cold weather. Snowfall means shovelling, poor driving conditions, but in a positive sense, outdoor activities such as skiing or even snowball fights. In Canada, as little as 4% of the yearly precipitation falls as snow (Vancouver, BC) and as high as 91% is snowfall in the high Arctic (Alert, NWT), based on Climate Normals (Environment Canada, 1998a). These differences occur since the coastal areas of British Columbia receive large amounts of orographic rainfall (up to 3 m of total precipitation annually) and the climate is moderate, whereas in the far north temperatures are below freezing for 9 to 10 months of the year and parts are so arid that they are considered a desert (0.2 m total precipitation annually). Large regional variation is further augmented by significant local differences (Figure 1-1).

Hydrologically, snowfall implies immediate infiltration and runoff, or storage if the accumulation remains. Accumulation can be temporary as winter snowpacks or more permanent as storage in glaciers. Both accumulations are accompanied by snowmelt runoff and the associated streamflow in warm months. In the social context, resultant flooding can cause damage, displacement or even death. Climatologically, snowcover from snowfall accumulation

provides feedback from the surface to the atmosphere, and hence can be an indicator of climate change (Goodison *et al.*, 1999). Precipitation is a water flux. The snowcover, especially covered by fresh snow, has a much higher albedo than bare ground or liquid water, so that solar radiation absorption is significantly less, often reduced by as much as 50% (Walsh, 1984). Thus the underlying surface receives less short-wave radiation, whereas more is reflected back to the atmosphere. In areas of changing climate, for example where snowcover extents are diminishing over time, the ground will be warmer, and, as a result, there is more heating of the atmosphere. This may perpetuate further snowcover depletion, or be a result of climate warming. This can subtly impact human day-to-day life.

In Eurasia, the maximum snowcovered area (complete cover for at least several days) has decreased from approximately 19.5 million km<sup>2</sup> (with a variability from 17 to 23 million km<sup>2</sup>) between the years 1915 to 1965 to an average of 18.5 million km<sup>2</sup> in the 1970s and 1980s, and to approximately 17 million km<sup>2</sup> in the 1990s (Brown, 1997). On the other hand, the North American snow covered area has remained relatively constant at approximately 13 million km<sup>2</sup> with a variability from 11 to 17 million km<sup>2</sup>, over the same time period (Brown, 1997). Regular winter snow covers Canada, the northern US (almost all land above 40°N latitude), Scandinavia, former Soviet Union, China, and the Himalayan region (Walsh, 1984), which Dingman (1994) estimates to be 42% of the Northern Hemisphere.

From a water resources perspective snowmelt runoff produces a substantial portion of the annual streamflow in parts of the world that encounter sub-zero temperatures at times in the year, and prediction of runoff volumes is crucial for water management, such as flood forecasting and reservoir operation. In semi-arid regions, such as the prairies, Mackay (1970) estimated that 80% of the streamflow comes from the snowpack. Goodell (1966) approximated that 90% of the annual water yield in the high elevations of the Colorado Rockies is derived from snowfall. For a substantial area of the Northern Hemisphere that has a regular winter snow cover, more than half of the annual runoff is derived from snowmelt (L'vovich, 1974). This area includes most of Canada above 55°N latitude, Alaska, Scandinavia, and most of the former Soviet Union, and extending to high elevation zones, such as the northern US Rockies, the Sierra Nevadas, and the Himalayas.

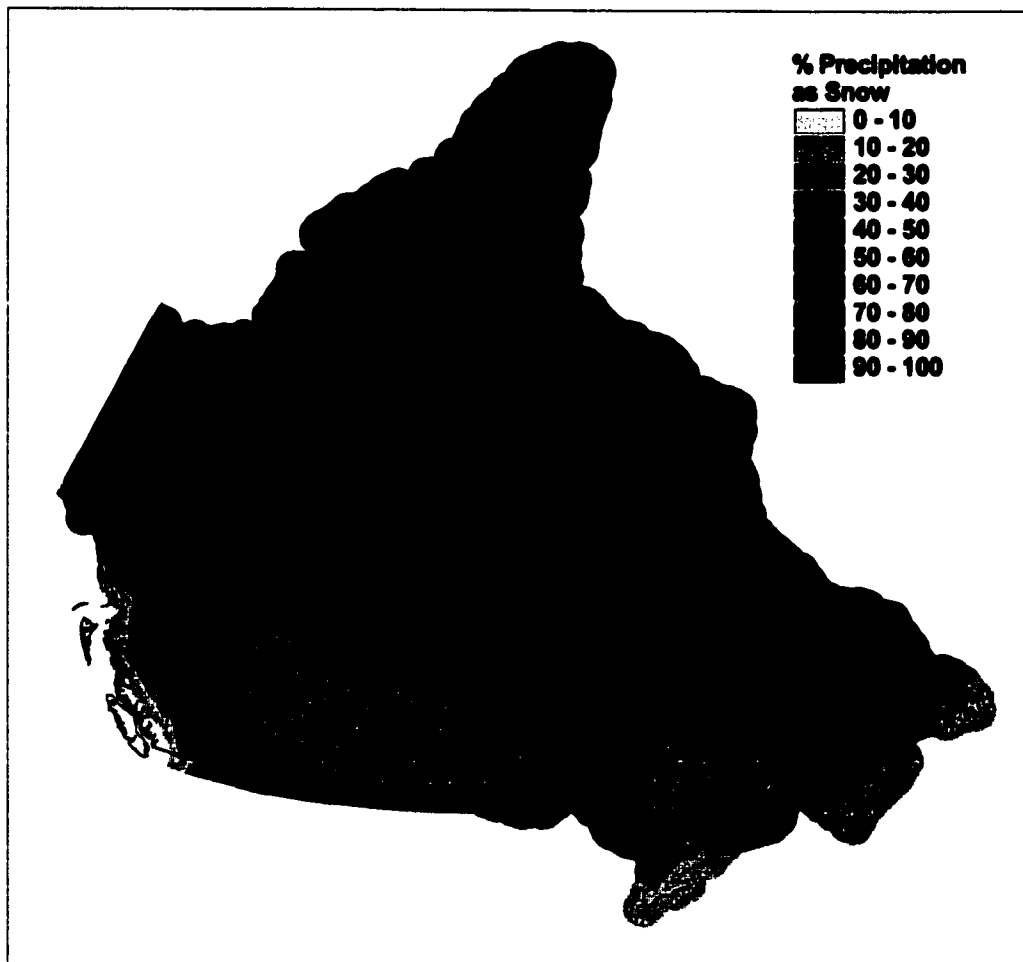


FIGURE I-1. Average annual percent precipitation as snow based on the Canadian Climate Normals (data from *Environment Canada, 1998a*).

To estimate the quantity of water produced from snowmelt runoff, several approaches have been used. Traditionally snowmelt modelling has been initiated at the maximum snowpack snow water equivalence (SWE), identified using snowcourse data, satellite estimation of SWE or snowcovered area (SCA), the persistence of above freezing temperatures, or even personal observation of the onset of melt. Determining the time at which maximum accumulation occurs and the SWE across a watershed at that time is difficult. An alternate modelling procedure is the continuous simulation of the snowpack from the initial accumulation through to the complete depletion of the pack. This, however, requires good estimates of snowfall, and adequate representation of all winter hydrologic processes.

Snowfall is measured at a location using a precipitation gauge. Systematic errors occur, such as wetting loss, evaporation, and wind induced under-catch, that result in underestimation of precipitation. The use of gauge shields, for example Alter and Nipher shields, increase snowfall catch, but still yield underestimates at gauge-mouth wind speeds greater than 2m/s. Goodison *et al.* (1998) have derived various equations to correct the estimates by considering wind speed. Areal estimation of snowfall is a subsequent problem related to gauge density across a watershed, and the technique used to grid the point data. The use of weather radar can overcome the gridding problem. For example, the 10km resolution gridded gauge precipitation, using the inverse squared distance approach, and the 10km radar precipitation for January 26<sup>th</sup> 1996 from 12:00 to 1:00 pm EST are presented in Figures 1-2a and 1-2b. From the various gauges across central southwestern Ontario, precipitation was only observed at north central gauge, around which the gridded precipitation is concentrated. Precipitation across the remainder of the domain is a result of gridding (Figure 1-2a). From the radar estimates, precipitation was only observed over the Toronto station in the eastern portion of the domain, just below the MSC King City radar. However, the radar precipitation near Toronto has often been observed to be urban clutter. On January 28<sup>th</sup> 1996 from 02:00 to 03:00 am EST, no precipitation was observed at any of the gauges and the gridding of the gauge data yielded no precipitation (Figure 1-3a). However, radar observations indicated the presence of precipitation, but not near the gauge locations (Figure 1-3b).

The processes that need to be represented for continuous winter hydrologic modelling include canopy interception, accumulation, pack metamorphosis, redistribution, and sublimation, as well as snowmelt, meltwater evaporation, and runoff. Most existing hydrologic models do not adequately simulate all winter processes, yet many nonetheless produce good hydrographs. For example, the WATFLOOD water balance hydrologic model, developed at the University of Waterloo, has been used to simulate streamflow starting at the onset of melt for Southern Ontario (eg., Donald, 1992; Seglenieks, 1994; Donald *et al.*, 1995), for the subarctic on tributaries to the Liard (Hamlin *et al.*, 1998), and throughout the winter for the Boreal Forest (eg., Whidden, 1999). Whidden (1999) has incorporated simple index methods to consider canopy interception and sublimation.

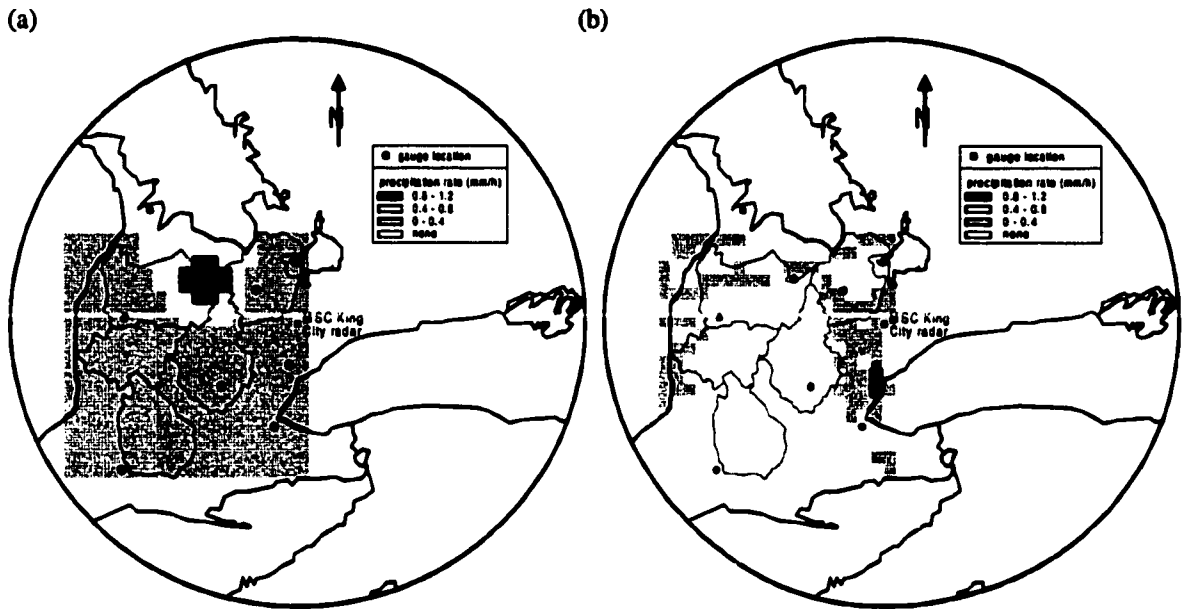


FIGURE 1-2. Hourly precipitation at a 10 km resolution across the five central southwestern study basins for January 26<sup>th</sup> 1996 at 13:00 EST derived from (a) gridded gauge data, and (b) radar estimates.

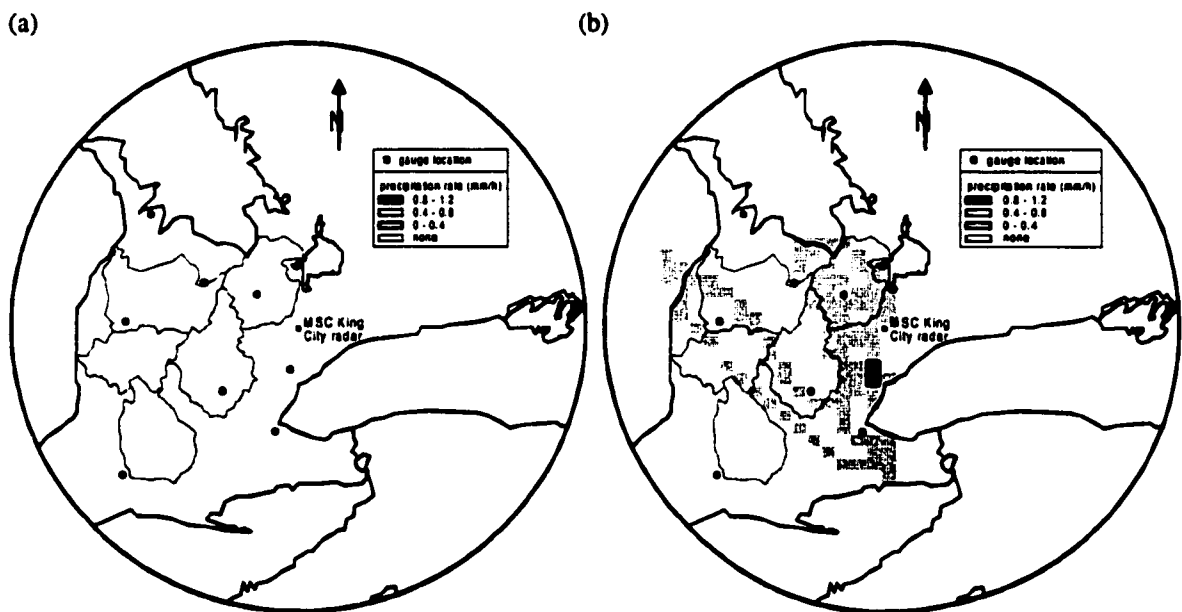


FIGURE 1-3. Hourly precipitation at a 10 km resolution across the five central southwestern study basins for January 28<sup>th</sup> 1996 at 03:00 EST derived from (a) gridded gauge data, and (b) radar estimates.

Another example is the Canadian Land Surface Scheme, CLASS, developed by the Atmospheric Environment Service (AES), which is a vertical energy and water balance model that incorporates some form of most winter processes (Verseghy, 1991). CLASS has been linked to WATFLOOD (Snelgrove, 1996; Soulis *et al.*, 2000) and together the linked model has been used to simulate winter processes and the related streamflow (Fassnacht *et al.*, 1998). There are various versions of CLASS and this research builds on version 2.6. The linked model will be called WAT\_CLS3 hereinafter.

## **1.1 OBJECTIVES**

The overall objective of this research is to model the snowpack throughout the snow season, using weather radar as the snowfall input, for the purpose of improved streamflow forecasting. Radar data are integrated across a watershed domain to provide winter precipitation, primarily snow, for hydrological modelling using the linked WAT\_CLS3 model.

The usefulness of weather radar to estimate winter precipitation is assessed in terms of snowpack accumulation compared to point gauge precipitation estimates, simulated snowpack development compared to observed snowcourse SWE and depth, and simulated runoff compared to observed hydrographs.

Various improvements are implemented in the CLASS model to more accurately represent snow processes. The significance of the model changes or additions is assessed using the “best” radar dataset developed from the above comparisons. The method for implementing the changes into the CLASS model is outlined to enable application by non-WAT\_CLS3 users.

The contributions of this research are the improvement of radar winter precipitation estimates, the successful use of radar precipitation as input for hydrological modelling for streamflow generation, and the incorporation of advanced winter processes into the CLASS model resulting in improved simulated snowpack and soil properties and improved streamflow estimates.

## **1.2 RATIONALE**

Precipitation estimates from gauge data can be insufficient to represent the pattern of observed precipitation; the representivity of the gauge data and the adequacy of point gauge data gridding. As well, weather radar coverage of the urban areas and population centres of Canada is a priority of the Meteorological Service of Canada, with the National Radar Project expected to provide radar coverage for 90% of the Canadian population by 2003 (Environment Canada, 1998b). Coverage will focus on the larger population areas and will use the American next generation weather radar system (NEXRAD) for overlap near the border. The NEXRAD system is also a priority for the US National Weather Service (NWS). The NWS has introduced the WSR-88D radar (Weather Service Radar commissioned in 1988 with Doppler capabilities) to upgrade its coverage of contiguous United States (National Weather Service, 1997a), with a goal of the program being the improvement of weather, hydrologic, and climate warnings and forecasts (National Weather Service, 1997b; 1999a). As well, Doppler Radar data are slated to be incorporated into operational mesoscale models by 2002 (National Weather Service, 1999b). Weather radar is thus a priority in Canada, for the Meteorological Service of Canada, and in the US, for the National Weather Service, and data from weather radar can be used as the precipitation input for hydrologic models.

Radar data are currently available in near real-time, thus the data can assist in nowcasting and forecasting. The data are available remotely and hence do not require labourious field surveys, i.e., snowcourses, nor *in situ* maintenance, i.e., gauges. Snow telemetry data (SNOTEL) have offered some promise, but are also not spatially distributed and often are located only within specific elevation zones.

While WATFLOOD does well at determining the water balance, and the distributed radar adds to this, the distribution of snowcover, especially between different land classes, and the different snowpack processes are not as adequately represented. CLASS, on the other hand, provides the platform to build upon the good horizontal water balance and routing of WATFLOOD to yield an adequate vertical water and energy balance. As well, CLASS is a priority for MSC as it is used with the Canadian General Circulation models (CGCM, CRCM),

and Numerical Weather Prediction models (GEM, MC<sup>2</sup>). Additions and changes to the physics in CLASS, developments in this thesis will potentially be contributing to the Canadian soil-vegetation-atmospheric-transfer scheme.

### **1.3 THESIS STRUCTURE**

Pertinent previous research is summarized in Chapter 2 with the literature review focused on physical snow processes, techniques for the measurement of snow, with an emphasis on radar-snow studies, and a brief evaluation of hydrologic models.

The specific study watershed is the Upper Grand River basin (above Galt-Cambridge). It is in central south-western Ontario, and within the coverage of the King City radar. The study area and the five winters of data (from November to April for 1992-93 through 1996-97) are discussed in Chapter 3.

Since there are various problems with the radar estimation of winter precipitation, several algorithms are developed to adjust the radar estimates. (Specifically, the radar data are adjusted to consider the occurrence of mixed precipitation at above freezing air temperatures and the implication of the shape of snow particles at below freezing air temperatures. A scaling phenomenon associated with the radar data is also discussed.) Chapter 4 addresses the methodology used to correct the gauge precipitation data and adjust the weather radar estimates. The snowpack processes from accumulation through snowmelt (such as metamorphosis, redistribution, and sublimation) are modelled using the energy approach in the vertical direction by CLASS, and horizontal water movement using WATFLOOD. Various modelling changes and additions that are incorporated into the CLASS model to more adequately represent snow processes are outlined in Chapter 4. A schematic of the research procedure followed in this thesis is presented in Figure 1-4. The focus is on the improvement of the radar data and the incorporation of advanced snow processes in the hydrologic model.

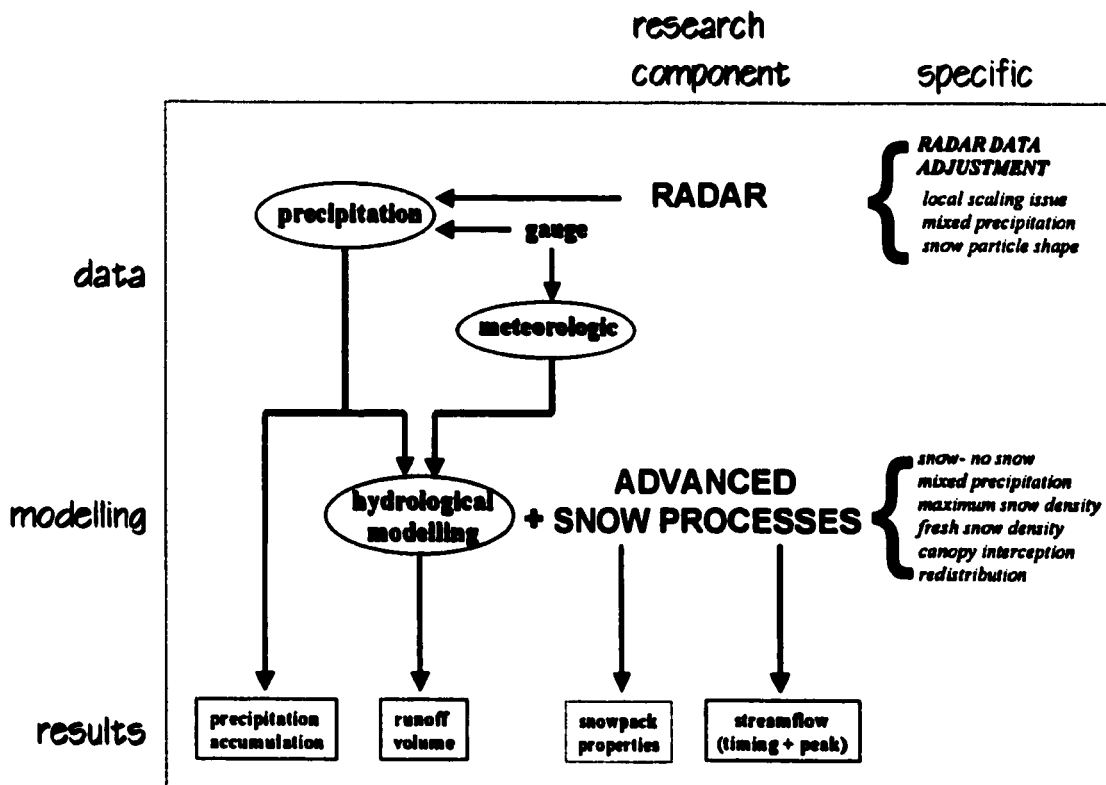
The success of radar adjustment algorithms and the modelling improvements is assessed in Chapter 5. For the radar algorithms, the radar snowfall accumulations are compared to



corrected precipitation gauge estimates, and the peak flows and runoff volumes are compared to flows measured at various hydrometric stations. The modelling improvements are examined in terms of snowpack characteristics (depth and SWE), and streamflow.

The conclusions and recommendations for future work are summarized in Chapter 6. Four Appendices have been included to present supplementary information. Appendix A lists the specific changes and additions in the CLASS model to consider advanced snow processes. The fitting of curves to derive relationships for data presented in the literature is explained in Appendix B. Additional results not presented in the main body are presented in Appendix C, and data collected specifically for this research are outlined in Appendix D.

FIGURE 1-4. Schematic of the general research methodology, illustrating the two research components and their specifics. The three different stages are data, modelling, and results.



# Chapter 2

## BACKGROUND

---

*“Although we may remember our childhood experience of [snow] with nostalgia, more and more we begin to think of snow with enmity. We cannot control snow, nor bend it to our will. The snow that fell harmlessly and beneficently upon the natural world our forefathers lived in has the power to inflict chaos on the mechanical new world we have been building.” (Mowat, 1975, p5)*

This chapter summarizes the state of knowledge of snow processes, the techniques used in the measurement of snowfall and snowpack properties, and the state of the model to be used in this research. The theory of precipitation formation is summarized to provide the background for a procedure to adjust radar snowfall estimates. The occurrence of mixed precipitation is discussed, as both background to a radar adjustment procedure, as well as an addition to modelling. Variation in fresh snow density, increases in canopy interception for snowfall, and variable maximum snow density are summarized as a precursor to modelling improvements. Snow redistribution and transport sublimation are also added to the model.

The snow measurement techniques focus on snowfall using precipitation gauges and weather radar, and the advantages and disadvantages of these methods are discussed. The linkage of the WATFLOOD/CLASS models are summarized with an emphasis on existing snow processes.

### 2.1 SNOW PROCESSES

Snow undergoes a variety of changes from formation in the clouds to melt. For hydrologic purposes, solid precipitation is accumulated, redistributed, metamorphosized, sublimated, and finally undergoes melt. The resulting liquid either infiltrates, runs off or is evaporated.

Once solid precipitation particles hit the ground, they melt if the surface is warmer than 0°C, otherwise they remain in their solid form. The crystals accumulate and, once the depth of crystals is greater than the height of the cover vegetation, complete snowcover occurs. Snow can also be intercepted by trees and accumulate and, in terms of mass, this can be an order of magnitude more than rainfall (Hedstrom and Pomeroy, 1997). As the snowpack depth increases, the particles in the matrix are altered. Once the snow is on the ground, the crystals begin to change shape and quickly bear little resemblance to the original snowflake shape. Wind redistribution, sublimation, the gravity force due to snow weight, and mid-season warm periods reshape snow crystals, both at the surface, and at depth. As the season progresses the crystals often become more rounded and the snowpack tends to be more dense.

Given adequate wind conditions, snow in exposed areas, such as fields and pastures, can be redistributed by erosion, transport, and deposition. The redistributed snow accumulates in areas of low wind, such as the edges of fields, in ditches, and along fences and treelines. A portion of the snowpack can also be lost to the atmosphere through sublimation, either during transport of snow, or directly from the snowpack surface.

Once warmer weather conditions begin to melt the snowpack, the meltwater that does not infiltrate into the ground or evaporate flows over the ground surface and contributes directly to streamflow. Often frozen saturated soil prevents most of the infiltration, yet deep snowpacks that accumulate on unfrozen or partial frozen soil act as insulators and inhibit further freezing.

### **2.1.1 Precipitation Formation and Growth**

Precipitation occurs as cloud droplets grow large enough that they can no longer be kept in suspension by updrafts. The formation and growth of cloud droplets thus determines the initial characteristics of any resultant hydrometeors (precipitation particles). The formation of cloud droplets is a result of the condensation of water vapour around a cloud condensation nuclei to form an aqueous droplet or sublimation of water vapour forms an ice crystal. Ice crystal formation can occur with the existence of supercooled liquid water between 0°C and -40°C by homogeneous, heterogeneous, contact, or ice nucleation (see Mason, 1971 or Sumner, 1988). Once formed, cloud droplets or ice crystals grow by condensation or collision and coalescence.

This second mechanism is the result of different particle sizes and masses in a cloud environment yielding various particle velocities. Beyond an approximate droplet diameter of 30 microns, growth by coalescence is preferential over condensation (Mason, 1971). Continued growth of cloud droplets forms potential hydrometeors. The two current theories that identify the growth of cloud droplets into precipitation particles are the growth of ice crystals at the expense of water drops (called the Bergeron-Findeisen Theory) and the coalescence of droplets due to collisions among falling droplets (called the Collision Theory).

Temperature is an important criterion governing the formation of water droplets in clouds. In clouds, ice crystals are predominant over supercooled water at temperatures below  $-22^{\circ}\text{C}$ , but occasionally as high as  $-9^{\circ}\text{C}$  (Sumner, 1988). Once formed, ice crystals grow readily by deposition of vapour onto their surface, however different temperatures cause different shapes of hexagonal crystals to form.

The actual shape of snow crystals was considered even before Kepler published his work entitled *The Six-cornered Snowflake* in 1611. The characteristic growth of ice crystals has been examined by numerous researchers, such as Nakaya (1954), Hobbs and Scott (1965), Ono (1970), Hobbs *et al.*, (1974), and Locatelli and Hobbs (1974). Ice crystals grow hexagonally in two dimensions and linearly in the third due to the matrix structure of ice molecules. The longest hexagonal dimension is given the symbol  $a$ , the perpendicular distance  $b$ , and the linear axis has a length  $c$ , as defined in soil science (see Figure 2-1). It is typically assumed that  $b$  can be calculated from geometry as one-half the square root of three, or approximately 0.866 of  $a$ .

Hobbs and Scott (1965) showed that the growth of ice crystals is initiated at the crystal edge. However, the molecular flux is temperature dependent, that is, the dominant migration direction to either the prism face or the basal plane, and the growth rate is governed by temperature. Figure 2-2a illustrates the type of ice-crystal as a function of temperature and degree of supersaturation, while Figure 2-2b presents the dominant growth direction and the major growth axis. Growth on the prism face results in hexagonal plates or planar crystals and is dominant between  $0^{\circ}\text{C}$  and  $-3^{\circ}\text{C}$  and between  $-10^{\circ}\text{C}$  and  $-21^{\circ}\text{C}$ , with a maximum growth rate occurring at  $-15^{\circ}\text{C}$  (see Figure 2-2c from Ono 1970). Columnar crystals occur as the molecular flux is primarily towards the basal plane. The dominant growth temperatures are  $-5$  to  $-9^{\circ}\text{C}$  and

possibly below  $-25^{\circ}\text{C}$ . Maximum growth occurs at  $-5^{\circ}\text{C}$  and yields thin needle-like crystals (Hobbs and Scott, 1965). The maximum growth rates in the basal and prism directions are plotted as function of temperature in Figure 2-2d.

To categorize the different snow crystals, the International Snow Classification for Solid Precipitation (National Research Council, 1954) defined 10 basic forms of solid precipitation (Figure 2-3 and Table 2-1). This was expanded by Nakaya (1954) and Magono and Lee (1966) to include up to 80 different snow crystal types, permitting a much more detailed classification of natural snow crystals (Figure 2-4). Flake characteristics are dependent upon the atmospheric conditions present during formation and growth. The structure of the lower atmosphere related to hydrometeors is defined as the region from cloud top to the ground surface. The height of the cloud top itself is a function of the atmospheric conditions that govern cloud growth and hence the formation of potential hydrometeor.

## **2.1.2 Hydrometeors**

### **2.1.2a Snowfall**

Once the downward forces (gravity and downdrafts) on a cloud particle become greater than the upward forces (drag, buoyancy and updrafts), the hydrometeor will fall, until either the particle evaporates or it reaches the ground. The actual falling crystals are often aggregates of various different crystal types. At warmer temperatures (between  $-5^{\circ}\text{C}$  and freezing), a fine film can form at the tips of crystals, in particular dendritic shaped flakes, melting from the high pressure gradients at these locations of high curvature (Nakaya, 1954). Crystals can aggregate as the film freezes when the crystals touch, as well, dendritic crystals may also mechanically interlock.

### **2.1.2b Mixed Precipitation**

If the snowflake falls through a quantity of air warmer than  $0^{\circ}\text{C}$ , the surface of the flake will become coated with a layer of melt water. If the flake continues to fall through warm air, it will melt into a liquid spheroid, or raindrop. The different forms of precipitation have been generalized by Rohrer (1989) based on temperature as follows: 1) rain, defined as any hydrometeor that is completely aqueous at ground level, when the near surface air temperature

is greater than +2°C; 2) a mixture of rain and snow called sleet, when the air temperature at ground level is between 0°C and +2°C; and 3) snow at temperatures below 0°C. Auer (1974) analyzed other data and showed that, below 0°C at ground level, no rainfall occurred and, above 6°C, no snowfall was observed. Auer's analysis illustrated that the probabilities of snow or rain occurring are equal at a temperature of +2.5°C. A plot of the mixed precipitation data collected by Auer (1974) and Rohrer (1989), as well as data from the US Army Corps of Engineers (1956), is presented in Figure 2-5. The differences between the three sets of observations indicate spatial and temporal dependence for the classifications.

At temperatures above freezing, the snow can become wet as snowflakes begin to melt, the flakes can be transformed into other forms of solid precipitation, such as ice pellets, or a mixed spectrum of solid and liquid hydrometeors can be observed. The occurrence of mixed shapes and phases of precipitation can result in a wide range of fall velocities, precipitation rates, and reflectivity signatures. With the exception of work by Stewart and his associates (see Stewart 1992 for details), especially related to weather radar physics, limited information exists in the literature regarding the characteristics of mixed precipitation. Stewart (1992) discussed the various particle configurations or types that can be expected in the transition region between snow and rain within an individual storm system. With respect to radar measurement of mixed precipitation, Stewart (1992) states that

*“The return energy from the radar depends on the size and composition of the target, the portion of the transmitted signal that is intercepted and the distance of the target. Although liquid water reflects much more power than the same mass of ice, a snowflake can partially melt or accrete many tiny drops from collision and confound measurement.”*

Overall, the near surface temperature and temperature variation to the cloud base are important factors in determining the precipitation particle type and the snow crystal shape. The shape, and more importantly type, will influence the reflectivity of the radar signal and hence the estimation of the water content.

### **2.1.3 Snowpack Accumulation**

Due to undulations in any topography and snowcover is not uniform, i.e., can be moved during descent, a lowest average depth of the snowpack ( $D_{100}$ ) needed to produce complete snowcover is defined. Donald (1992) assumed a  $D_{100}$  of 0.06 m for forest and 0.10 m for non-forest, since the surface characteristics of the forest floor are generally smoother than non-forested areas. The limits are also a function of snow redistribution (section 2.1.6b), especially for open areas.

### 2.1.3a Fresh Snow Density

If the depth of fresh snow on the ground is known, the amount of water or mass on the ground, called the snow water equivalent (SWE), is often derived using a density of 100 kg/m<sup>3</sup>. However, various experiments have shown that the density of new snow varies both spatially and temporally. Goodison *et al.* (1981) showed variations with time and throughout specific storm events (Figure 2-6a). The density of the accumulated snowpack increases with time, as the mass of the overlying new snow compresses the lower snow layers and these snow crystals alter their shape (Figure 2-6b).

Various attempts have been made to associate fresh snow density with observed air temperature. Diamond and Lowry (1953) expressed that the new snow density is likely a function of the size and type of snow crystal, and as stated in section 2.1.1, the type of snow crystal is a function of the formation temperature. Therefore, Diamond and Lowry (1953) plotted the air temperatures (taken when the densities were measured) versus the measured fresh snow density (see Figure 2-7). These data collected at the Central Sierra Snow Laboratory were later summarized in the US Army Corps of Engineers *Snow Hydrology* report (1956). For canopy interception experiments, Schmidt and Gluns (1991) measured snow depth and SWE with snowboards, as well as the temperature at the time of measurement. The fresh snow density can be computed from these data and plotted as a function of air temperature, as illustrated in Figure 2-7.

LaChapelle (1961), for the US Department of Agriculture, estimated the density of fresh snow,  $\rho_s(\text{fresh})$ , as a function of air temperature using data collected in Wasatch National Forest for air temperatures  $T_a$  in degrees Celsius, as follows:

$$\rho_s(\text{fresh}) = 50 + 1.7 \times (T_a + 15)^{1.5} \quad (2-1),$$

for air temperatures less than +2°C (La Chapelle, 1961). Hedstrom and Pomeroy (1998) summarized the data collected by Diamond and Lowry (1953) and Schmidt and Gluns (1991) and fitted a function in the form:

$$\rho_s(\text{fresh}) = 67.92 + 51.25 e^{(T_a / 2.59)} \quad (2-2).$$

These functions are illustrated in Figure 2-7.

#### 2.1.4 Snowfall Interception

Vegetation is a boundary between the atmosphere and the earth, and thus can be a significant detainer or retainer of precipitation. The interception of precipitation is a function of vegetation (tree, crop) type, stage of growth (i.e., time of year for all but conifers), and on a scale larger than individual plants, a function of the density of vegetation. Of particular interest are forests, since trees are larger, taller and their lifespan is measured in 10s to 100s of years, as compared to other plants. For example, crops are usually gone by the time the snow comes, and the rest of the ground cover either gets completely covered soon after the bare ground, or it's still close enough to the ground that it can be considered as part of the snowpack. While deciduous trees can trap more rain than coniferous trees in the summer and fall, due to the cupping by their broad leaves, in the winter conifers can collect snow between their needles much more efficiently than the leaf-less branches of the dormant deciduous trees. As snowflakes can aggregate during descent, they can also bridge between needles, and significant accumulation can occur on the branches. Whereas the interception of rainfall is a function of the leaf area index (the fraction of ground covered by leaves), the intercepted snowfall rate increases as interception increases until the branches become overloaded and the snowfall interception rate decreases. Hedstrom and Pomeroy (1997) illustrated that interception of snow in a coniferous canopy can be up to 10 times greater than the maximum rainfall interception. In terms of total water interception, Pomeroy and Gray (1995) stated that up to 60% of snowfall can be stored in forest canopies.



### 2.1.5 Snowpack Metamorphosis

As soon as snow accumulates, it undergoes change. The particles in the matrix are altered with the increased snowpack depth. Wind redistribution, sublimation, the gravity force due to snow weight, and mid season warm periods reshape both the basal and surface crystals of the snowpack. As the season progresses the crystals become more rounded and the snowpack becomes more dense. Associated with the densification is increased thermal conductivity, which changes the heat flux through the pack. There is also variation in the liquid-water flux and typically a decrease in the surface albedo.

Gold (1958) showed an increase in density from 200 to 300 kg/m<sup>3</sup> over 20 days due to compaction and wind forces, a subsequent increase to 400 kg/m<sup>3</sup> in 5 days due to partial melting, and developed a relationship snowpack density ( $\rho_s$ ) and time ( $t$ ):

$$\rho_s = 190e^{0.00112t} \quad (2-3).$$

Longley (1960) illustrated a maximum 290 and 370 kg/m<sup>3</sup> for late season snowpack samples. The data collected by Gold (1958) and Longley (1960) were used by Verseggy (1991) to derive an expression for the increase in snowpack density as a function of the snowpack density and the length of the time step as follows:

$$\rho_s(t+1) = [\rho_s(t) - 300]e^{-0.01\Delta t} + 300 \quad (2-4).$$

Jordan (1991) also assumed a maximum snowpack density of 300 kg/m<sup>3</sup> for snowpack modelling. However, the maximum density that may be observed in a snowpack varies with the location, land cover, and other factors. Pomeroy and Gray (1995) noted that during snowmelt, the density varies due to snowpack water storage and loss of meltwater, and commonly ranges between 350 and 500 kg/m<sup>3</sup>. The mean density of a Canadian Prairies shallow snowpack with limited melting has been given by Pomeroy and Gray (1995) as:

$$\rho_s = 239 + \frac{2.05}{d_s} \quad (2-5),$$

where the mean pack depth ( $d_s$ ) is less than 0.6 m. For a deeper snowpack ( $d_s > 0.6$  m) in an open environment, the density was expressed by Pomeroy *et al.* (1998) as:

$$\rho_s = 450 - \frac{204.7}{d_s} [1 - e^{-d_s/0.673}] \quad (2-6)$$

Tabler *et al.* (1990) demonstrated the same relationship format, however, 522 was used instead of 450. For forested areas, the maximum dry snow density has been approximated to be 250 kg/m<sup>3</sup> by Gray and Prowse (1993). Loth *et al.* (1993) used settling as a function of temperature and snow density, as derived by Anderson (1976):

$$\frac{1}{\rho(z, t)} \frac{\partial \rho(z, t)}{\partial t} = a e^{[-b (T_m - T(z, t)) - c (\rho(z, t) - \rho_d)]} \quad (2-7),$$

where  $a$ ,  $b$ , and  $c$  are coefficients,  $T_m$  is the melting temperature, and  $\rho_d$  is set at 150 kg/m<sup>3</sup>, with the maximum wet snow density less than 400 kg/m<sup>3</sup>.

### 2.1.6 Snowcover Movement and Sublimation

Sublimation is the phase change between solid and vapour and, for snow, contributes to the metamorphosis of snow crystals, the loss of mass from the snowpack, and occasionally the addition of mass to a snowpack. For snow, it occurs at the crystal scale, or finer, and is driven by atmospheric conditions, in particular, wind strength (speed), vapour pressure deficit (void space available for mass transport from the snow surface to the surrounding atmosphere), and energy available in terms of sensible heat to be used as latent heat (measurable as the temperature). The rate of sublimation is also influenced by the exposed surface area of individual particles (Fassnacht *et al.*, 1999). Mass loss from a snow surface may however not indicate a net loss, as ice molecules often sublime from areas of high curvature and re-sublimate in areas of lower curvature. This results in the metamorphosis or rounding of snow crystals. Sublimation can occur from a snowpack on the ground or intercepted by a canopy, or during the transportation of snow that is being blown from one location to another.

### 2.1.6a Non-Transport Sublimation

The mass and heat transfer equations that govern sublimation express the latent heat required for phase change and the energy available from the environment in terms of sensible heat. Sverdrup (1936) derived equations for air movement over snow by considering eddy conductivity. The amount of water transported away from or towards the surface was defined as a function of the eddy conductivity and the change in the specific humidity of air ( $q$ ) with respect to the height above the surface ( $z$ ). This mass transport ( $F$  with units of mass per time per area) explaining the vertical distribution and exchange of water vapour was given as:

$$F = \rho_{wv} k_o^2 \frac{U_a}{\ln\left(\frac{a+z_d}{z_o}\right)} \frac{q_b - q_o}{\ln\left(\frac{b+z_d}{z_o}\right)} \quad (2-8),$$

where  $\rho_{wv}$  is the density of water vapour (typical values lie between  $1.30$  to  $1.40 \times 10^{-3} \text{ g/cm}^3$ ),  $k_o$  is the von Karman turbulence coefficient (between  $0.38$  and  $0.41$ ),  $U_a$  is the wind velocity at height  $a$ ,  $z_o$  is the roughness height (Oke, 1987, gives a range between  $0.5$  to  $10.0 \times 10^{-4} \text{ m}$ ),  $z_d$  is the zero-plane displacement,  $b$  is the measurement height of  $q$ , and  $q_o$  is the specific humidity at the surface of the snow. The heat transported towards the surface ( $Q$  as energy per unit time per area) is a function of the specific heat capacity of air ( $c_p$ ), the eddy conductivity under stable air, and the change in the potential temperature of air ( $\theta$ ) with respect to the height above the surface. It is defined as:

$$Q = c_p \rho_{wv} k_o^2 \frac{U_a}{\ln\left(\frac{a+z_d}{z_o}\right)} \frac{\theta_b - \theta_o}{\ln\left(\frac{b+z_d}{z_o}\right)} \quad (2-9),$$

where the potential temperature ( $\theta_b$ ) is measured at height  $b$ . This potential temperature

considers the vertical atmospheric stability in terms of pressure change from the surface to the measurement height.

Light (1941) assumed no zero-plane displacement, and measurement of all environmental parameters at the same height above the surface ( $a$ ). The mass transfer equation (2-8) was rewritten as a function of vapour pressures at height ( $e_a$ ) and at the surface ( $e_o$ ), and air pressure ( $p$ ) as follows:

$$F = \frac{0.623}{p} \frac{\rho_{wv} k_o^2}{[\ln(a/z_o)]^2} U_a (e_a - e_o) \quad (2-10).$$

The lapse rate was assumed to be minimal for typical measurement heights, i.e., there was no significant atmospheric pressure change. Therefore the heat transfer equation (2-9) could be expressed as a function of the difference between the air temperature ( $T_a$ ) at height  $a$  and the surface temperature ( $T_o$ ) as follows:

$$Q = c_p \frac{\rho_{wv} k_o^2}{[\ln(a/z_o)]^2} U_a (T_a - T_o) \quad (2-11).$$

The sublimation rate is dictated by the limiting quantity of energy available (described in equation 2-11), and energy required based on the vapour pressure gradient (equation 2-10 multiplied by the latent heat of sublimation). However, these two quantities are not independent; the ambient vapour pressure, and hence the vapour pressure deficit, reflects the temperature, which adjusts to the available energy. Thus for steady state conditions, the available and required energy reach an equilibrium. This has prompted researchers to select the mass transfer approach for estimate of sublimation rates, since the surface air temperature in equation (2-11) is not readily or easily measured (eg. Williams, 1959), with a corresponding assumption of 100% humidity at the surface

### 2.1.6b Redistribution

A cohesionless snow crystal can begin to move when the shear stress induced by wind exceeds the friction forces between the particle and the surrounding crystals. The transport of snow crystals is a process similar to the aeolian transport of sand particles (as first detailed by Bagnold, 1941), or the movement of soil particles on the bed of a river (as described by Einstein, 1950). Pomeroy and Gray (1995) summarized the three modes of transport of individual particles as a function of the degree of movement, as follows: creep is the rolling movement along the surface, saltation is the jumping or skipping along the surface, and suspension is the turbulent diffusion of the particles at velocities close to the air speed. If the wind speed is sufficient, in areas exposed to substantial winds, a large quantity of snow particles can be moved if the particles begin to saltate. At increased wind speeds these particles can become suspended and the rate of transport increases.

Saltating snow, transported at a rate  $q_{salt}$  is a function of the wind speed, the characteristics of the snow surface (roughness, hardness), fetch distance, and other factors (Pomeroy and Gray, 1995). This saltating transport rate is expressed as:

$$q_{salt} = U_p \frac{W_p}{g} \quad (2-12),$$

where  $U_p$  is the mean horizontal snow particle velocity in the saltating layer,  $W_p$  is the mean snow saltating weight per unit snow surface area, and  $g$  is the acceleration due to gravity. The mean horizontal velocity is a function of the threshold friction velocity and the weight of saltating snow is a function of the flow shear stress on the snow particles (Pomeroy and Gray, 1995). Saltation occurs over a small height above the snow surface, whereas particles in suspension are carried at a height above the saltation layer. Therefore, the suspended snow transport rate ( $q_{susp}$ ) must be integrated from the top of the saltation layer ( $h^*$ ) to the top of the plume of particles diffusing into the atmosphere ( $z_b$ ), as defined by the following equation:

$$q_{susp} = \frac{u^*}{k_o} \int_{h^*}^{z_b} \eta(z) \ln\left(\frac{z}{z_o}\right) dz \quad (2-13),$$

where  $u^*$  is the shear velocity, and  $\eta(z)$  is the suspended snow mass concentration at height  $z$  (Pomeroy and Gray, 1995). Equations (2-7) and (2-8) can be combined to yield the total snow transport rate  $q_T$ . Various empirical relationships have been developed to calculate the transport rate of blowing snow for specific locations and snow surfaces. Pomeroy and Gray (1995) summarized five such relationships. The Canadian version for the Prairies, derived by Pomeroy *et al.* (1991), lies between the others. It expresses  $q_T$  (in kg/s/m) over a height of 0 to 5 m as a function of the 10 m wind speed,  $U_{10}$ , as follows:

$$q_T = 2.2 \times 10^{-6} U_{10}^{4.04} \quad (2-14).$$

Significant snow movement only occurs if a minimum wind speed is available to transport snow. Li & Pomeroy (1997) showed that the threshold wind speed for movement of snow particles at a measurement height of 10 m is usually greater than 5 m/s, with a few instances as low as 4 m/s.

The transport of snow results in a depletion of snow from an exposed location to an area where the surface characteristics are different such that suspension and/or saltation cannot be maintained. The exposed areas are typically open fields with significant fetch lengths, in order to enable an adequate boundary layer development for transport. The accumulating areas are often zones of increased surface roughness or with objects protruding from the snow surface such as ditches, fences, shrubs, trees, or structures.

Schroeter (1988) defined a limiting snow-catching, or accumulating capacity for various land cover types and land features (eg. ditches) and presented a redistribution model derived from sediment transport modelling using erodability (snowpack characteristics), wind speed, and land cover characteristics (fetch lengths and orientation with wind direction). Schroeter (1988) defined an open site as one with a fetch greater than 500 m. Due to the sparsity of meteorological and snowpack data for medium-sized watersheds (500 to 5000 km<sup>2</sup>), Donald

(1992) used Schroeter's depth limiting concept and estimated the depth capacity for non-forested areas to be 0.15 m, and unlimited for forested areas (set to 99.99 m in WATFLOOD).

Takeuchi (1980) illustrated that, for distances 200 to 400 m from the starting of drift snow, the snow depth was in equilibrium, i.e., the same quantity of snow blown out of the area was also blown into the area. Mass loss was a function of sublimation. For shorter distances there is a net erosion, and accumulation may occur for fetch lengths greater than 400 m (Takeuchi, 1980). However, larger sublimation losses are often associated with transport over these longer distances (Gray and Prowse, 1993).

### 2.1.6c Transport Sublimation

The sublimation of snow can account for a loss of 15 to 41% of the snowpack in certain areas of the Canadian Prairies (Pomeroy and Gray, 1995). A majority of this snow can be lost during redistribution. To understand the sublimation of blowing snow, Thorpe and Mason (1966) examined the sublimation from individual ice crystals. Similar to equations (2-8) and (2-9), the mass and heat transfer functions were developed for ice spheres as rates of mass change per unit time as:

$$\frac{\partial m}{\partial t} = 2\pi D_f r (\rho_{wv} - \rho_{wv(o)}) (Sh) \quad (2-15), \text{ and}$$

$$L_s \frac{\partial m}{\partial t} = 2\pi K_T r (T_o - T) (Nu) \quad (2-16),$$

respectively. In equations (2-15) and (2-16),  $r$  is the radius of the ice sphere,  $D_f$  is the diffusion coefficient of water vapour in air, and  $K_T$  is the air thermal conductivity. The Sherwood ( $Sh$ ) and Nusselt ( $Nu$ ) numbers are dimensionless indices used to describe the effect of wind ventilation. Using laboratory measurements, Thorpe and Mason (1966) estimated these indices from the Reynold's number. Schmidt (1972) added a solar radiation component ( $K_Q$ ) to the heat transfer equation, and applied Thorpe and Mason's work to blowing snow, using the assumption that

airborne snow concentrations were not large enough to cause significant particle interaction. The mass and heat transfer equations were combined to yield a single expression for the sublimation rate of suspended snow particles:

$$\frac{\partial m}{\partial t} = \frac{2 \pi \sigma_{unsat} - \frac{K_Q}{K_T T (Nu)} \left[ \frac{L_s M_W}{R_g T} - 1 \right]}{\frac{L_s}{K_T T (Nu)} \left[ \frac{L_s M_W}{R_g T} - 1 \right] + \frac{1}{D_f \rho_{wv(sat)}} (Sh)} \quad (2-17),$$

where  $\sigma_{unsat}$  is the undersaturation of the air,  $M_W$  is the molecular weight of water,  $R_g$  is the ideal gas constant, and  $\rho_{wv(sat)}$  is the saturated vapour density. Equation (2-17) can be used with data pertaining to the quantities of snow being transported, such as defined in equations (2-12) and (2-13), to determine the sublimation rate ( $q_{subl}$ ):

$$q_{subl} = \int_0^{z_b} \frac{d\bar{m}(z) / dt}{\bar{m}(z)} \eta(z) dz \quad (2-18),$$

where  $\bar{m}(z)$  is the mean particle mass at height  $z$  (Pomeroy and Gray, 1995).

### 2.1.7 Snowmelt and Runoff

Snowmelt is the change of state from solid to aqueous at air temperatures above 0°C, accompanied by runoff. It is induced when air temperatures and, in some instances, underlying soil temperatures rise above 0°C. Energy is available to warm the snow to 0°C and then alter the hexagonal molecular structure, thus changing state.

The energy is transferred to the snow surface and as melting begins, a boundary moves downward through the pack. Above this wetting front the temperature is 0°C and the pack is ripening. Below the wetting front, the lower pack is warming. In reality there exists a zone of



wet (aqueous) and dry (solid) snow. The aqueous areas have propagated beyond the wetting front due to preferential melting caused by snow density, porosity, grain size and shape heterogeneity.

Through the snow melting process, an iterative procedure accompanies pack densification. Portions of the aqueous phase above the wetting front refreeze and the released latent heat melts underlying snow particles and the soil surface. The wetting front continues to progress downward, given appropriate atmospheric conditions, until it approaches the underlying soil. The ground surface is usually below 0°C and energy is dissipated from the melt water to the soil creating a basal ice layer (Marsh, 1990). Some meltwater may infiltrate, depending on soil and pack characteristics. Water that cannot infiltrate or freeze will be available for runoff. The existence of a basal ice layer retards infiltration and serves to enhance runoff potential.

The snowmelt process can be considered as an energy balance in the terms of the energy available for melt,  $Q_M$ , as follows:

$$Q_M = Q^* + Q_H + Q_E + Q_R + Q_G - \frac{\partial u}{\partial t} \quad (2-19),$$

where  $Q^*$  is the net all-wave radiation,  $Q_H$  is the sensible heat flux,  $Q_E$  is the latent heat flux,  $Q_R$  is the heat flux from rain,  $Q_G$  is the ground heat flux at the snow-soil interface which is a sum of the stored sensible heat and the stored latent heat of fusion, and  $\partial u/\partial t$  is the rate of change of internal energy (Marsh, 1990).

For practical purposes, the snowmelt can be estimated using an index method. This uses temperature difference between atmospheric ( $T_a$ ) and the temperature ( $T_{oi}$ ) at which melt is initiated, and a melt factor ( $MF_i$ ) based on land classification (Donald, 1992), as follows:

$$M = MF_i (T_a - T_{oi}) \quad (2-20),$$

where the subscript  $i$  denotes the specific land class, and  $M$  is the depth of melt water generated by unit time. Since the air temperature is strongly correlated with all of the radiation fluxes

except shortwave radiation, this index method is a reasonable approximation for the quantity of melt for most land cover types. However, it does not work well for bare areas or glaciers where shortwave radiation fluxes dominate the melt. Furthermore, the melt factor must be calibrated for the time of year at which the melt is occurring. Typical melt factors for southern Ontario range from 0.10 mm/°C/hr for forests to 0.22 mm/°C/hr for bare areas (see Donald, 1992).

To improve the stability of  $MF_i$ , Rango and Martinec (1995) have proposed the incorporation of a net daily radiation component, as follows:

$$M = MF_i (T_a - T_{oi}) + M_Q Q^* \quad (2-21),$$

where  $M_Q$  is the conversion factor for energy flux density to snowmelt density. As expected, the addition of the radiation component to the snowmelt index model decreases the temperature melt factor, since representation of radiation shares in melt generation. For example, in modelling five basins in the lower Liard River Valley in the NWT with the temperature index model, Hamlin (1996) determined the  $MF_i$  to be 0.075 mm/°C/hr for deciduous/mixed and coniferous forests. For the temperature-radiation index model,  $MF_i$  decreased to 0.005 mm/°C/hr for deciduous/mixed forests and 0.035 mm/°C/hr for coniferous forests with  $M_Q$  values of 0.0112 and 0.070 mm/(W/m<sup>2</sup>)/hr for deciduous/mixed and coniferous forests, respectively. The variation in the  $MF_i$  and  $M_Q$  melt factors for the different forest types is a function of the canopy coverage and the aspect. Hamlin (1996) stated that the coniferous stands were more dense and grew on the north facing slopes, hence such areas received less radiation.

## 2.2 MEASUREMENT TECHNIQUES

Measurement of hydrologic quantities is difficult at best. The challenge is to determine the actual amount of water that is moving (eg. precipitation or runoff), or in storage (eg. SWE), which is known as the ground truth. This is often not quantifiable, therefore other methods have been established to capture a representative sample, either at a point, moving past a plane, or in a volume. For a method to be useful, its representivity must be assessed in terms of the associated

errors. This section will address the techniques used to evaluate the state of the snowpack, from accumulation (precipitation), to snowpack properties (depth, density), through to streamflow generated from runoff. The focus will be on standard measurement of solid and liquid water as mass, but not optical and thermal properties.

### **2.2.1 Precipitation Measurement**

Various techniques have been established to measure the quantity and rate of precipitation that falls over a certain area. To date ground based measurements such as gauges and radar, have been use to assess the quantity of precipitation falling.

#### **2.2.1a Precipitation Gauges**

The measurement of precipitation volumes and rates have traditionally been performed using collection gauges. Linsley *et al.* (1975) define any open receptacle with vertical sides as a collection gauge. For measurement of small precipitation increments, gauges have a large collecting mouth and a small measurement area, so that increments of 0.25 mm or less can be determined. There are three common types of gauges that can be used to measure precipitation rates: tipping bucket, weighing-type, and float recording. The tipping bucket collects a specific quantity of precipitation (0.1 mm depth) and the bucket is tipped sending an electrical impulse. Weighing-type and float recording gauges measure the increase in weight and depth.

There are several problems with precipitation gauges that prevent the data that they provide from being used as ground-truth: 1) small quantities of precipitation are difficult to measure; 2) measurement errors may be caused by instrumentation, calibration or related random errors; 3) under-catch due to wind; 4) splash and evaporation; and 5) spatial representivity. The first two errors are usually small and are often a result of carelessness. Wind influences however can introduce significant under-catch of precipitation (see Figure 2.8a). These influences are more pronounced for snowfall than rainfall, primarily due to the slower fall velocity of snow. Various methods have been devised to minimize the wind induced errors. These include the use of turf walls, rigid Nipher shields, hinged Alter shields, and ground level pit coverings (see Figure 2.8b). Each method has advantages and disadvantages in minimizing both wind and

splash/evaporation effects; however, it is beyond the scope of this discussion to evaluate the different techniques.

The systematic errors in precipitation measurement caused by wind and wetting and evaporation losses for solid precipitation have been studied by the World Meteorological Organization in the WMO Solid Precipitation Measurement Intercomparison project (Goodison *et al.*, 1998). The goals were to determine the various errors, derive correction methods, and establish a reference method for intercomparison of any precipitation gauge type. The various reference methods considered were the bush shield, the double fence shield, the forest clearing, the snow board, and the double gauge system. The study found that, while the natural bush shelter provided the best estimate of ground truth, such a setting was not available in all climatic regions (eg. high alpine and polar regions), and an artificial shield was recommended instead. The Tretyakov gauge with an octagonal vertical Double Fence was established as the Intercomparison Reference (DFIR) gauge. The final report summarized the catch ratio with respect to the DFIR gauge as a function of gauge height wind speed (see Figure 2.8c), and provided best fit regression equations for snow and mixed precipitation scenarios. Use of these equations will improve the under-estimation due to wind, however, other factors such as blowing snow should also be considered.

The Nipher-shielded gauge is used as the Canadian standard snow measurement gauge. Goodison *et al.* (1998) analyzed data from six gauges across Canada and derived the following relationship for the catch ratio of a Nipher-shielded gauge with respect to the DFIR gauge:

$$\frac{NIPHER}{DFIR} (\%)_{snow} = 100 - 0.44U_{gauge}^2 - 1.98U_{gauge} \quad (2-22),$$

where  $U_{gauge}$  is the wind speed at the gauge height (in m/s). For the occurrence of mixed precipitation, the maximum ( $T_{max}$ ) and minimum ( $T_{min}$ ) air temperatures were used with the wind speed to determine the catch ratio, as follows:

$$\frac{NIPHER}{DFIR} (\%)_{mixed} = 97.29 - 3.18U_{gauge} + 0.58T_{max} - 0.67T_{min} \quad (2-23).$$

While the DFIR gauge provides good estimates of snowfall, it must be adjusted to approximate the “true” snowfall, as measured in a sheltered bush. Golubev (1986) considered wind speed, air pressure, mean air temperature ( $T_{mean}$ ) and mean air humidity in adjusting the DFIR measurements. Goodison and Metcalfe (1992) simplified Golubev’s equation to consider only temperature and wind speed, yielding the catch ratio of a bush gauge to the DFIR gauge:

$$\frac{BUSH}{DFIR} (\%) = 100 + 0.5 \left( \frac{273}{273 + T_{mean}} \right)^2 U_{gauge}^2 \quad (2-24).$$

Yang *et al.* (1993) derived six different ratios between the bush gauge and DFIR for different types of precipitation. Plotting of these six relationships on the same axes (Figure 2.8d) illustrates that the differentiation of precipitation is only significant for blowing snow.

Other underestimation errors may be due to snow bridging across the gauge mouth or sticking to the sides of the gauge, and hence the precipitation is not weighed (Cole *et al.*, 1998). This has been partially overcome by the use of heated gauges that melt the frozen precipitation. The wetting loss has been measured to be 0.15 mm +/- 0.02 mm for the Nipher-shielded gauge, and 0.2 mm for the Tretyakov gauge used with the DFIR (Goodison, 1978). Goodison and Metcalfe (1992) state that Russia has used a wetting loss correction of 0.2 mm for liquid precipitation and 0.1 mm for solid precipitation. They subsequently recommend that 0.15 mm should be added to each observation to correct for wetting loss.

An important concern with precipitation gauges is spatial representivity. Kitchen and Blackall (1992) used a square grid of 16 gauges to illustrate the spatial error, as well as temporal errors, caused by using one gauge to estimate the rainfall over an area as small as 4 km<sup>2</sup>. The spatial and temporal heterogeneity of rainfall is one of the main sources of gauge representivity error. This is especially evident in convective type rainfall. The heterogeneity is less severe for long term-low intensity events, such as is typical for snowfall, with the exception of lake effect events. However winter storms are always more homogeneous than convective storms.

**2.2.1b Snow Accumulation Sampling**

The actual amount of snow that falls at a particular location is often measured by a snow ruler, a snow depth rod, or a snow board. These are manual measurements that require daily observation, and with the snow ruler and graduated rod one must infer the density of fresh snow to compute the SWE. These methods provide adequate snow depths, however the SWE measurements are less reliable. Since these measurements are performed at a point, they may not be representative. Also preferential melt or sublimation of the snow occur may occur at and around permanent snow depth rods or snow rulers.

A snowboard is useful to measure the SWE directly and, with a snow ruler, the depth. The SWE and depth are averaged across the surface of the snowboard, however these are manual observations, and to be representative rely in part on adequate placement. Metamorphosis of the snowpack often causes snow densification resulting in a depths and densities that may not be representative of the fresh snowfall.

Sonic sensors can measure snowpack depths without disturbing the snowpack and over an area from 0.2 to 2 m in diameter (Pomeroy and Gray, 1995), at a user-defined time interval. Many remote weather stations are currently incorporating this technology to generate depth-of-snow measurements. The primary error with the sonic sensor is the interruption of the sonic pulse downward to the snow and/or reflected back to the sensor by falling or blowing snow.

A device called a distrometer has been developed to measure the drop size distribution during a precipitation event. The unit measures the attenuation or interruption of an electromagnetic radiation signal as a hydrometeor passes through the beam. The distrometer can be a one metre square unit placed several metres above the ground surface. Although distrometers have seen limited use, they have illustrated that the drop size distribution is approximately logarithmic (Hindman *et al.*, 1994). Lundberg and Johansson (1994) describe a similar system that determines the precipitation type and intensity using light attenuation. This system uses two sets of light-diodes and photo-detectors placed orthogonally. The results are promising, but more research is required.

**2.2.1c Ground-based Weather Radar**

Weather radar operates by sending out a beam of electromagnetic radiation from a transmitter and detecting the quantity of energy reflected from hydrometeors using a receiver. The return time is a measure of distance. The strength of the return signal is an indication of the quantity of precipitation. Current weather radar systems use the following four operating bands: K-band (1 cm wavelength), X-band ( $\lambda \sim 3$ cm), C-band ( $\lambda \sim 5$ cm), and S-band ( $\lambda \sim 10$ cm). The K-band and X-band wavelengths are primarily used for short range (less than 50 km), low cost, urban systems, whereas, C and S band are applicable up to 200 km ranges. The shorter wavelength bands (K and X) are useful only for shorter distances due to the dissipation of the shorter wavelength signals in heavy rainfall.

Since the amount of energy reflected from raindrops is proportional to the sum of their diameters to the sixth power, larger raindrops within the sampling volume will strongly influence the reflectivity (Collier, 1991). The amount of energy returned is also proportional to the inverse of the square of the distance to the reflector. These factors can be summarized by the equation:

$$\overline{P}_r = \frac{C |K|^2 Z}{r^2} \quad (2-25),$$

where  $\overline{P}_r$  is the average return power from the raindrop energy scatter,  $Z$  is the radar reflectivity (proportional to sixth power of the raindrop diameter),  $K$  is the refractive/absorptive property of the reflecting rainfall,  $C$  is a radar unit-specific proportionality constant, and  $r$  is the distance from the sample volume of the radar unit. The average power return equation uses the following five assumptions: 1) the raindrops are assumed spherical, which is valid for raindrops smaller than 3 to 4 mm in diameter (see Doviak and Zrnic, 1984); 2) the sample volume is assumed to be homogeneous, which may introduce some edge or transition effect errors; 3) the sample volume is assumed to contain the same precipitation type (i.e., snow, sleet or rain); 4) the reflective power is assumed to be representative of the sample volume, since the radar pulse is averaged over a large number of individual pulses; and 5) the losses in the radar unit and calibration errors are assumed to be negligible. Attenuation of the radar beam due to the presence of atmospheric particulates must also be considered (see Collier, 1991).

The measurement of rainfall rates using radar reflectivity is based on the correlation between the radar reflectivity ( $Z$ ) and the rainfall rate ( $R$ ). Marshall and Palmer (1948) used the following power relationship:

$$Z = A R^b \quad (2-26),$$

with  $A$  empirically specified to be 200 and  $b$  to be 1.6. Numerous other values for  $A$  and  $b$  have been calculated since, partially related to the type of precipitation. A summary of relationships between radar reflectivity and rainfall rate were presented by Stout and Mueller (1968) and Wilson and Brandes (1979).

Problems associated with the estimation of precipitation using ground-based weather radar are due to the radar and its situation and due to the characteristics of the precipitation. The situation of the radar with respect to topographic features can introduce several errors. The radar beam may be blocked by topographic features or may not detect orographic precipitation falling beyond such features. Ground clutter, such as larger buildings in urban areas may be detected as continuous precipitation. Similarly, anomalous propagation (AP) may be received by the radar unit due to the presence of strong water vapour or temperature gradients, such as may exist over large lakes. The measurement of precipitation at larger distances may also be affected by the curvature of the earth and the divergence of the radar beam, causing measurement above the cloud tops. A final error that may be introduced is the receiving of radiation from the sun during sunrise or sunset. Errors in the interpretation of the return signal can also be created by the precipitation itself. Radar tends to over-estimate light rainfall (less than 0.1 mm/h) due to the lack of larger droplets. A more serious error is the bright band effect. If ice particles falling through the atmosphere begin to melt, there is a zone of wetted ice crystals in the atmosphere. The density differences between ice and water will yield large radar returns that appear as a band or zone of very high rainfall. The radar measurements above and below this band are unaffected.

The increase in computing power has enabled high speed manipulation of the raw radar data, improving the quality of the processed output. As well, the use of Doppler radar and



multi-parameter radar have addressed various problems. Doppler radar uses the interaction of radar wave energy with moving bodies. The movement of hydrometeors towards a radar unit will increase the return frequency, whereas particles moving away from the radar will have a slightly decreased frequency compared to the original signal. The frequency difference between the transmitted and return signal can thus quantify the movement of hydrometeors. Hence, Doppler radar can detect ground clutter and anomalous precipitation, since no Doppler shift is detected. Both conventional and Doppler radar can have a scanning radius of 200 km, however, the processing time required for Doppler images is significantly larger than conventional radar images. Multi-parameter radar uses independent measurement techniques from the same radar unit. Dual polarized radar uses the difference between radar reflectivity measured from orthogonal signals which is indicative of the shape of the hydrometeor. Dual band radar emits different wavelength signals and measures the wave phase shift and the attenuation differences between bands. The use of dual techniques is effective since the sampling of the same volume of hydrometeors by different, independent methods yields a smaller net variance than the either of the individual variances.

### *2.2.1d Weather Radar Solid Precipitation Measurement*

The use of ground-based radar to predict quantities of falling snow began in the mid-to-late 1940s with work near Montreal and Ottawa. In 1947, Marshall *et al.* measured rainfall rate with radar by the use of scattering theory to calculate the intensity of radiation scattered back from precipitation droplets. The following year Marshall and Palmer (1948) developed the now-famous reflectivity-rainfall rate ( $Z-R$ ) relationship and determined the power law coefficients to be  $A$  equal to 200 and  $b$  equal to 1.6. Most of the subsequent radar-precipitation research has focused on refinement of the  $A$  and  $b$  coefficients by investigation of reflectivity, precipitation rates, and precipitation particulate properties, such as, diameter, mass, fall velocity, particle size distribution and particle dielectric properties.

Langille and Thain (1951) used X-band radar to measure backscatter intensity, atmospheric snow densities and snowflake size distributions to compare to the theoretical formulation developed by Marshall *et al.* in 1947. The field results from four storm events were

in fair agreement with the theoretical formulations (Langille and Thain, 1951). Marshall and Gunn (1952) regressed Langille and Thain's data to develop Z-R relationships for each of the individual storm events. Although it was observed that, for equal precipitation rates, the return signal from snow was up to an order of magnitude less than the return for rain, Marshall and Gunn used the Marshall and Palmer (1948) coefficients ( $A$  of 200 and  $b$  of 1.6) and the Marshall *et al.* (1947) power return equation to illustrate a relationship between particle size and melted snow-particle diameter.

The diameter of melted snow particles were important factors for both Hooper and Kippax (1950) and Mason (1955) who investigated the bright band phenomena using radar, to examine the changes in particle size and fall velocity induced by mid-fall melting. They showed that the rain drops below the bright band had increased velocities and increased reflectivity and thus lower atmospheric densities than the snow particles above the melting layer. An increase in the predicted rain drop diameter given snowflake diameters usually occurs due to aggregation of snowflakes (Mason, 1955) and rain drops in the melt zone. The radar reflectivity within the bright band itself is usually greater than above or below this melt zone due to flatness of the snowflakes and the covering of the flakes by an aqueous layer.

The use of radar to investigate snow particle properties, in particular fall velocities, received significant attention due to the work by Marshall and others. For example, Langleben (1954) measured the terminal velocity of snowflakes using photographic techniques and compared these observations with radar echoes. These investigations have continued through to the present and have focused on the study of the ice crystal growth habits, particle size relationships and fall patterns and velocities. This research includes work by Nakaya (1954), Hobbs and Scott (1965), Magono and Lee (1966), Jayaweera and Cottis (1969), Warner and Gunn (1969), Ono (1970), Ohtake (1970), Auer and Veal (1970), Zikmunda and Vali (1972), Heymsfield (1972), Zikmunda (1972), Locatelli and Hobbs (1974), Hobbs *et al.* (1974), Passarelli (1978), Fujiyoshi and Wakahama (1985), and Hogan (1994).

Many of these snow particle investigations were subsequently used in conjunction with radar research to strengthen the theory and increase the snow sampling experiments for refinement of radar reflectivity-snow solid water equivalent precipitation rates. Gunn and

Marshall (1958) collected 20 sets of data based on particle type observations at ground level and considered the snowflake mass. They used the mass and the melted snow particle diameter to illustrate an initial Z-R correlation for a value of  $A$  of 600 and for  $b$  of 1.8 for the first 20 minutes of the event. This was followed by a sudden change to the Imai *et al.* (1955) relationship of  $A$  equal to 2150 and  $b$  equal to 1.8. This was attributed to the initial lack of aggregate snowflakes (Gunn and Marshall, 1958). They subsequently showed that the Z-R relationship for melted-snow was larger than for rain, as well, the reflectivity for a given snow precipitation rate was less than that for rain by a factor approximately equal to the ratio of the raindrop to snowflake fall velocity. A general Z-R relationship was developed for snow with  $A$  equal to 2000 and  $b$  equal to 2.0 (Gunn and Marshall, 1958). Austin (1963) examined the Marshall and Palmer and the Gunn and Marshall relationships and stated that since the former was for aggregated flakes and the later rain relation was for single flakes, it was recommended that  $A$  equal to 1000 and  $b$  equal to 1.6 was appropriate as an intermediate “catchall” relationship.

Kodaira and Inaba (1955) worked in conjunction with Imai *et al.* (1955) to illustrate that for a specific two hour event, studied on a minute by minute basis, and using an exponent  $b$  equal to 1.8, the coefficient  $A$  changed from 600 to 2400 to finally 1800.

Sekhon and Srivastava (1970) reevaluated the particle size distribution expressions initially presented by Marshall and Palmer (1948) to yield the Z-R coefficients of  $A$  equal to 780 and  $b$  equal to 2.21. They also concluded that the effective size or magnitude of the snow particle size distribution increased rapidly with the precipitation rate, that is, the increased precipitation rates were associated with larger snow particles. The coefficients derived by Sekhon and Srivastava agree with the data collected by such researchers as Imai *et al.* and Gunn and Marshall. Carlson (1968) collected his own dataset that resulted in the following coefficients: an  $A$  of 1000 and for a value of  $b$  of 2.67. However, Sekhon and Srivastava disagree with the Carlson results due to the sampling size required to validate his results.

Carlson and Marshall (1972) approached the measurement of snowfall by examining the accumulation of snowfall over a two day period, instead of the near-instantaneous particle methods used by previous researchers. They compared the snow-depth measurements at 140 locations within a 160 km radius to the summation of 22.5 minute CAPPI maps of the same area,

at different height intervals. The 140 snow-depth measurements were taken on a 24 hour basis and these values were divided by 10 to obtain estimates of SWE. The radar calibration used the Gunn and Marshall (1958)  $Z-R$  relationship, emphasizing the exponent  $b$  equal to 2.0. The study showed that an exponent slightly higher than 2.0 would yield better results. However, Carlson and Marshall state that their work is based on two snowfalls related to one storm event, and thus the shortcomings of using a single event dataset, as well as a 10:1 depth to SWE ratio, should be considered for a generalized application. Carlson and Marshall also emphasized the “intelligent use of reference gauges,” and illustrated that the accuracy of radar data decreased with distance.

Wilson (1974 and 1975) examined the radar accumulation of snowfall throughout the winter of 1972/73 near Oswego, NY in comparison to specially sited precipitation gauges within a 60 km radius of the radar apparatus. Wilson demonstrates that the radar precipitation estimates are less than the gauge measurements by a function of the distance from the radar installation. The increasing gauge-to-radar ratios were attributed to increasing height and width of the radar beam with increasing range. Wilson also found gauge-to-radar estimate differences for different storm types. The nature of the storm event dictated the level at which precipitation particles grew. Thus, for low cloud storms, the radar beam could sample at or above part of the particle growth layer and fall zone which Wilson attributed to a lower radar return signal. Wilson observed that storm systems at lower heights were often associated with spatial dendrite crystals that Ohtake and Henmi (1970) state should give higher reflectivity than plate or column crystals. The depth to SWE ratio was found to be dependent on the storm type, and hence the crystal type. Overall, Wilson recommends that a reference gauge should be used to calibrate the radar SWE estimates with consideration of distance, and that the best estimates are provided for large scale storm events with the majority of the particle growth occurring above a height of 2 km.

Peck *et al.* (1974) assisted in the placement of the special gauges used by Wilson (1974 and 1975). Their primary conclusion with respect to radar SWE estimation echoed Wilson’s concerns for the use of calibration precipitation gauges, and emphasized the importance of proper gauge placement.

Collier and Larke (1978) assessed the accuracy of using radar to measure snowfall

accumulation by calibration measurements at two different elevations and validation using numerous depth measurements, supplemented by gauge measurements. The analysis yielded good results with a correlation coefficient of 0.93. The important steps of the experiment were the use of ground measurements and the compensation for initial melting due to surface temperatures above freezing. They also used the radar reflectivities over a 4 by 4 km grid block to represent each ground measurement site in order to reduce the effects of wind transport of snow. The limitations of their analyses are the use of a linear elevation-melting temperature relationship, that is, a specific elevation contour as the boundary ground melt; the use of a constant close to 10:1 for snow depth to water conversion throughout; the limitation of range measurement to within 50 km of the installation; and the use of a single storm event for the experiment. The experimenters acknowledge that the spatial variability of the melting level was unknown.

For operational purposes, Boucher and Wieler (1985) changed the  $Z$ - $R$  relationship to:

$$Z = A S^b \quad (2-27),$$

where  $S$  is the snowfall depth rate and not the SWE rate. This relationship is useful for short range weather forecasting or for nowcasting and the related road advisories. For six storm events in Massachusetts, they found  $A$  equal to 5.07 and  $b$  equal to 1.65 with a correlation coefficient of 0.91. Boucher and Wieler (1985) agreed that the  $Z$ - $R$  relationship variation is due in part by the snow particle size distribution and fall speeds.

Fujiyoshi *et al.* (1990) illustrated the shortcomings of the previous  $Z$ - $R$  relationship determinations and attempted to redefine the coefficients for snowfall rate and accumulation by using a modern electronic precipitation gauge that had an apparent accuracy of 0.03 mm/h. Their observations are the most intense, and likely most accurate to date, and include the measurement of temperature, wind velocity and direction, relative humidity, atmospheric pressure, visibility and solar radiation. The comparison of radar imagery to surface snowfall measurements of rate and density resulted in a snowfall rate  $Z$ - $R$  relationship ( $A$  equal to 427 and  $b$  equal to 1.09) and a snowfall accumulation  $Z$ - $R$  relationship ( $A$  equal to 554,  $b$  equal to 0.88).

Although the investigation was very thorough, the dataset involves only three storm events in one specific area close to the radar installation.

Current research at the State University of New York at Syracuse has focused on the comparison of reflectivity to snowfall rates, SWE and snow depths for four different winter storm types that are encountered at or near the southeast Lake Ontario shore (Houck *et al.*, 1996). The radar data have been compared to snowboard, weighing gauge and weekly snowcourse data. It was proposed to incorporate radar-derived data into a geographical information system (GIS) for future use with a snowmelt model (Houck *et al.*, 1996), and to integrate all data into the system to produce a yearly snow database.

The advanced capabilities of weather radar are currently being explored to examine complex snowfall. For example, Ryzhkov and Zrníc (1998) used polarimetric radar to distinguish between rain and snow. They emphasized the importance of locating the transition zone between solid and liquid hydrometeors, especially the presence of a bright band. Another example is Matrosov (1998) who has shown that dual-wavelength radar (K and X-band) can be used to estimate snowfall rates. The difference between the reflectivities at the dual wavelengths yielded a snowflake size estimate that was combined with the longer wavelength reflectivity to approximate a snowfall rate (Matrosov 1998).

In general, the early snow-radar research attempted to define coefficients for the radar reflectivity-precipitation rate relationship based on different observations and theoretical analyses (see Table 2.1). Most of the recent research has used the established relationships, especially Sekhon and Srivastava (1970), to develop operational uses of snowfall accumulation estimation using radar. This research considers radar accumulation estimates for all winter precipitation. These data are used as the input to the WAT\_CLS3 hydrological model (section 2.3.3). The model will simulate streamflow hydrographs as well as the soil and snowpack properties.

### **2.2.2 Snowpack Assessment**

The depth and SWE of a snowpack can be assessed manually by using snowcourses, automatically with snow pillows and snow lysimeters, or remotely using airborne or space borne sensors. Since the snowpack data used in this research was collected as part of regular

snowcourse sampling, the discussion of snowpack assessment will be limited to snowcourses. Other methods are described in Goodison *et al.* (1981) and Pomeroy and Gray (1995).

### **2.2.2a Snowcourses**

Due to the cumulative nature of solid precipitation, the sampling of snow depths and SWE at specific snowcourse locations over the snow season are indicators of the changes in the snowpack properties. The snowcourse data are an average of 10 samples, and are typically taken on a 14-day basis during the winter and more frequently during melt periods.

The problems with snowcourse data are the temporal and spatial limitations. Since the snowcourses are often only sampled on a 14 day interval, any intermittent pack changes cannot be detected. The spatial problem is the same as the point estimation problem for a precipitation gauge. Redistribution of snow may be a problem, however the averaging of 10 samples and the siting of the snowcourses usually reduce the redistribution errors.

## **2.3 HYDROLOGIC SNOWPACK MODELLING**

Hydrologic modelling is the budgeting of the three different water phases and their interaction with air, vegetation and soil, by considering the conservation of mass and energy throughout the system, or by using parameter surrogates. The emphasis is placed on the movement of the aqueous phase at or near the soil interface over a specific watershed area. Hydrologic models attempt to integrate physical properties with physical processes to estimate water quantities, often through the manipulation of large datasets.

The various models can be classified based on process description, spatial and temporal scales, and solution technique (Singh, 1995). The hydrologic processes included determine the model complexity. Processes can be modelled in a lumped or distributed form. A distributed system considers the different land classes and land covers within a given area, as compared to lumping of an area. The scaling within a model is important for input requirements and output restriction. The temporal or spatial modelling scales may be determined by the limitations of

available data, stability criteria derived from the governing equations, or limitations in the governing equations themselves.

Of the 25 watershed models outlined in Singh (1995), only 11 include snow processes. Each of the models is able to melt an existing snowpack with the use of the energy method, a simplified energy method, or most commonly with the index temperature method. The snowpack depths and water equivalents are derived from snowcourse or remote sensing techniques, however, several models utilised meteorological data to accumulate snow over the winter season. Most models with accumulation capabilities do not consider all the various complex snow processes that occur throughout the accumulation and ablation season, as outlined in section 2.1. For example, Arnold and Williams (1995) state that the SWRBB model, which use the National Weather Services index snowmelt routine, lacks sublimation estimation. The index method has been extended in some models, such as SPUR-91, to differentiate between rain-on-snow melt at the surface and non-rain melt; however, midwinter thaw is typically not considered. The Canadian Land Surface Scheme (CLASS) model contains many of the vertical snow processes, as it models the water and energy balance. Since it is a convenient development platform that is already well developed and state of the art, and it is used across Canada, it will be reviewed in detail.

### **2.3.1 CLASS**

CLASS was developed by Environment Canada (Verseghy, 1991; Verseghy *et al.*, 1993). It is a physically-based one-dimensional column model, that is it represents average characteristics of a horizontal area. At the surface, each grid cell can be divided into as many as four subareas: bare soil, canopy covered, snow-covered, snow and canopy covered. There are three soil layers of variable depth for each grid cell. Soil layer thicknesses of 0.1, 0.25, and 3.75 m are the standard values, but Delage *et al.* (1999) recommended that layer thicknesses should be chosen such that the vegetation root zone is contained within an entire layer and hence does not occupy only part of a soil layer. In CLASS, water can either remain on the surface as ponded water, infiltrate into the soil and be stored, or drain out of the bottom soil layer as runoff. Within the soil, heat is transferred by conduction and soil moisture is moved according to Richards equation.



Each horizontal area or column can be divided into as many as four subareas: bare soil, canopy covered, snow-covered, snow and canopy covered. The canopy can be represented by up to four different vegetation types: coniferous, deciduous, crops and grasses.

A number of input parameters are used to describe the properties of the soil and canopy. Input parameters for the vegetation include canopy coverage, leaf area index, vegetation roughness, canopy mass, and rooting depth. To describe the soil, the following parameters are used: Clapp and Hornberger coefficients, saturated soil moisture content, saturated soil suction, saturated hydraulic conductivity, soil colour, soil drainage, a sand and a clay index. The colour index is used to define the ground albedo. The sand index is also used to define solid rock, organic matter and glacier land types.

The evolution of each soil layer is defined by the mean temperature and soil moisture content (liquid and frozen), and the evolution of the canopy is defined by the temperature, moisture storage (liquid and frozen), and the growth index. Since CLASS has been developed as a land surface scheme for GCMs, the average soil property (temperature and water content) across the four subareas is computed at the end of each time step. These properties and the average surface fluxes are used as the average grid feedback to a GCM. At present, CLASS uses these averages to initialize the soil properties at the beginning of subsequent time steps.

The evolution of the snowpack is defined by the temperature, SWE, density, and albedo. The snow depth is calculated from the SWE and density. CLASS considers the different thermal properties of falling precipitation, with 100% snow falling at air temperatures less than or equal 0°C, and 100% rain falling at warmer temperatures. The fresh snow density is assumed to be 100 kg/m<sup>3</sup>. The snowpack properties that are used in CLASS include the heat capacity, the thermal conductivity, and density flux out the bottom of the pack. The heat capacity and thermal conductivity are calculated as function of the snowpack density. As the snowpack ages, the snowpack density (Equation 2-4) and albedo are an exponential function of the time since accumulation. A  $D_{100}$  of 0.10 m is assumed for all land cover types (Verseghy, 1991). The loss of snow through sublimation is calculated using the bulk transfer formulae for sensible and latent heat, as presented in Equations (2-8) and (2-9), respectively.

The CLASS model requires various soil and landcover data, as well as information

pertaining to initial conditions. These data are contained in an initialization file (BENCH.INI), and data are given for each modelling element. The CLASS model has been developed to fit with the WATFLOOD modelling architecture and uses the GRU approach for each element. A sample of the initialization file for the beginning of a simulation, prior to any snow accumulation and for coniferous trees, is presented in Table 2-3.

Seven fields of meteorological data at half hour time intervals are required as input data. These data are air temperature, precipitation (partitioning of liquid and solid precipitation is optional), air pressure, specific humidity, wind speed (direction is optional), and short wave and (incoming or net) long wave radiation.

For streamflow generation, horizontal processes are required, as illustrated by Soulis *et al.* (1999). Snelgrove (1996) provided the linkage of CLASS (version 2.6) and WATFLOOD (version 7.73), and the version used in this research is called WAT\_CLS3.

### **2.3.2 WATFLOOD**

WATFLOOD was developed at the University of Waterloo as a flood forecasting model (Kouwen, 1988). The WATFLOOD model uses grouped response unit (GRU) approach to land cover types (see Kouwen *et al.*, 1993) that enables a distributed or mosaic modelling approach. This approach assumes that within a grid-element landcover dictates soil properties, and individual land cover areas in different locations in a grid can be grouped together. As the location of similar land cover areas within an element is not important, only the total fraction of each land cover type and the associated process parameters are required for each element. Land cover fractions and process parameters can vary across grid elements. By ignoring location, the GRU approach is very computationally efficient. While WATFLOOD can have between 1 (lumped approach) and 15 different land classes, often six land classes are sufficient. Grouped response units provide a simple alternative to hydrologic response units (HRUs) (Leavesley and Stannard, 1990) or representative elemental areas (REAs) (Wood *et al.*, 1990), since HRUs and REAs require the division of an element or subbasin into areas of uniform hydrological response, which may be difficult to determine. Conversely, GRUs can be assembled from remotely sensed images of land cover type, such as the LANDSAT Thematic Mapper satellite images.

Runoff is generated in WATFLOOD as surface runoff using a formulation of Manning's equation, as interflow from the excess water in the upper zone storage, and as groundwater flow from the excess water in the lower zone storage. Once the runoff reaches the stream channels, the streamflow is routed using a channel routing model.

The physical hydrologic processes are represented by index methods in WATFLOOD. Interception is modelled with a reservoir that has a fixed limit. Once the reservoir is full, precipitation can fall through the canopy. Evaporation occurs from the reservoir at the rate of potential evapotranspiration (PET). PET can be estimated from monthly climatic tables, or modelled using the Hargreaves (temperature) or the Priestley-Taylor (temperature and net radiation) index methods. The actual evapotranspiration is a reduction of the PET based on the available soil moisture and air temperature.

Snowmelt is generated using the temperature index approach (equation 2-20) or the temperature-radiation index approach (equation 2-21), and snow-covered depletion curves (see Donald *et al.* 1995). The snow-covered and snow-free areas are kept separate, enabling the use of different process parameters for each area.

### **2.3.3 WATFLOOD/CLASS Linkage**

WATFLOOD uses remotely sensed data where available enabling the modelling of watershed, and it is considered an operational model since it is computationally very fast. While the linkage of WATFLOOD/CLASS into WAT\_CLS3 results in runtimes that are more than an order of magnitude slower, the linkage integrates the two model into a physically-based framework that uses the vertical energy and water balances of CLASS and the horizontal water movement formulations of WATFLOOD (see Table 2-4). Essentially, the CLASS model replaces the vertical structure in WATFLOOD. Since CLASS and WATFLOOD both use a distributed or mosaic approach, the GRU approach is maintained in WAT\_CLS3.

The WATFLOOD model requires approximately 50 parameters to represent landcover, soil and vegetation characteristics, as well as runoff properties for overland flow and stream channel properties for streamflow routing. For this research, WATFLOOD will be used as a 'black box'. The runoff and stream channel properties that are used were derived by Kouwen

for standalone WATFLOOD simulation (see Kouwen, 1998 for sample parameter values). These parameters are not altered or optimized.

## **2.4 SCOPE OF THE INVESTIGATION**

This thesis focuses on precipitation data and modelling for spring flood prediction. The gauge precipitation data are corrected to consider wind under-catch, while the weather radar data are adjusted to consider a site specific scaling issues, under-estimation of mixed precipitation, and the reflectivity of different snow crystals. Gauge accumulations at several sites are compared to radar estimates for different lengths of accumulation.

The snowpack is modelled continuously throughout the winter using WAT\_CLS3, from initial accumulation to melt, to assess weather radar as a precipitation input. The runoff volumes computed using gauge precipitation and the different adjusted radar datasets are compared to the observed streamflow volumes at eight gauge locations.

The timing and the peaks of the modelled snowmelt streamflow, as well as the state of the snowpack throughout the winter, are examined. CLASS is modified to better represent some of the snow processes, and hence improve the timing and volume of the peak flow estimates. While CLASS uses a mosaic approach, the soil properties were averaged at the end of each time step, and these average values were used as approximations of the properties at the beginning of each time step. This initialization using averages is removed. The occurrence of mixed precipitation is added to precipitation input in CLASS. Other changes include implementing a variable fresh snow and maximum snowpack density, the differentiation between rainfall and snowfall canopy interception, redistribution of blowing snow, and transport sublimation.

TABLE 2-1. NRC Classification of Solid Precipitation (National Research Council, 1954).

Flake type	Additional remarks or assemblages
Plates	combination of plates, with or without very short connecting columns
Stellar Crystals	parallel stars with very short connecting columns
Columns	combination of columns
Needles	combination of needles
Spatial dendrites	spatial combinations of feathery crystals
Capped columns	columns with plates on one or both sides
Irregular particles	irregular aggregates of microscopic crystals
Graupel (soft hail)	isometric shape, central crystal cannot be recognized
Ice pellets	ice shell, inside mostly wet
Hail	

TABLE 2-2. Radar reflectivity-precipitation rate coefficients in the  $Z = AR^b$  relationship for snow unless otherwise specified.

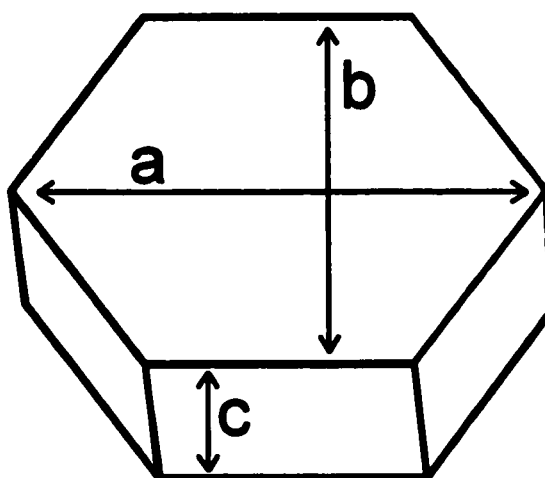
Researchers	A coefficient (constant)	b coefficient (exponent)	Comments
Marshall and Palmer (1948)	200	1.6	rainfall
Imai <i>et al.</i> (1955)	2150	1.8	storm average
Kodaira and Inaba (1955)	600, 2400, 1800	1.8	2-hr storm on a minute- minute comparison
Gunn and Marshall (1958)	2000	2	snowflake aggregates
Imai (1960)	540	2	dry snow
Imai (1960)	2100	2	wet snow
Carlson (1968)	1000	2.67	snowfall
Sekhon and Srivastava (1970)	1780	2.21	snowfall (Chicago area)
Carlson and Marshall (1972)	-	> 2.0	two snowfalls from one storm event
Richards and Crozier (1983)	295	1.43	southern Ontario rainfall
Boucher and Wieler (1985)	5.07	1.65	Z - snowfall depth rate, based on six 1978 storms
Fujiyoshi <i>et al.</i> (1990)	427	1.09	snowfall rate from 1 minute accumulation averages
Fujiyoshi <i>et al.</i> (1990)	554	0.88	snowfall accumulation for 30 minute averages

TABLE 2-3. A sample dataset for the CLASS 'BENCH.INI' parameter and initialization file for the beginning of the winter prior to accumulation, i.e., no snow, and for evergreen needleleaf trees.

parameter/characteristic	variable name	sample value
latitude	DEGLAT	43.75°
longitude	DEGLON	80.40°
reference height for air temperature, wind speed and humidity	ZREF	50.00 m
a switch for incoming versus net longwave radiation	ILW	1
number of vegetation types per GRU	ICAN	3
fraction of area (urban is an additional canopy type per land class)	FCAN	from 0 to 1
natural logarithm of roughness length of vegetation	LNZO	0.405
maximum leaf area index	LAMX	2.0
minimum leaf area index	LAMN	1.6
diurnally averaged, fully leafed, visible shortwave albedo	ALVC	0.03
diurnally averaged, fully leafed, near-IR shortwave albedo	ALIC	0.19
annual maximum above ground canopy mass	CMAS	25.0 kg/m <sup>2</sup>
maximum rooting depth	ROOT	1.0 m
soil colour and drainage parameter	SBND	9.0, 1.0
sigma value at midpoint of lowest GCM momentum layer	SGL	0.995
sigma value at midpoint of lowest GCM thermodynamic layer	SHL	0.995
sub-grid scale variance of topographic height	ENV	1.0
number of soil layers	IGND	3
fraction of sand, clay, and organic matter per layer	SOIL	3.0, 10.0, 0.0
initial soil layer temperatures	TBAR	12.75, 14.33, 7.40 °C
initial soil layer liquid water content	THLIQ	0.324, 0.303, 0.357
initial soil layer solid water content	THICE	0, 0, 0
average canopy temperature	TCAN	10.27 °C
average liquid stored in the canopy	WCAN	0.0019
average frozen water stored in the canopy	SCAN	0
average snowpack temperature	TSNO	0 °C
snow water equivalence SWE	SNO	0 m
average snowpack density	RHOS	100 kg/m <sup>3</sup>
all-wave snowcover albedo	ALBS	0.84
vegetation growth index	TT	0.000

**TABLE 2-4. Summary of the generalized components of WATFLOOD, CLASS, and the linked WATFLOOD/CLASS models.**

	WATFLOOD 7.73	CLASS 2.6	WAT_CLS3
vertical water balance	conceptual	physical	physical
horizontal water balance	✓		✓
energy balance		✓	✓
streamflow generation	✓		✓



**FIGURE 2-1. Ice-crystal growth faces nomenclature.**

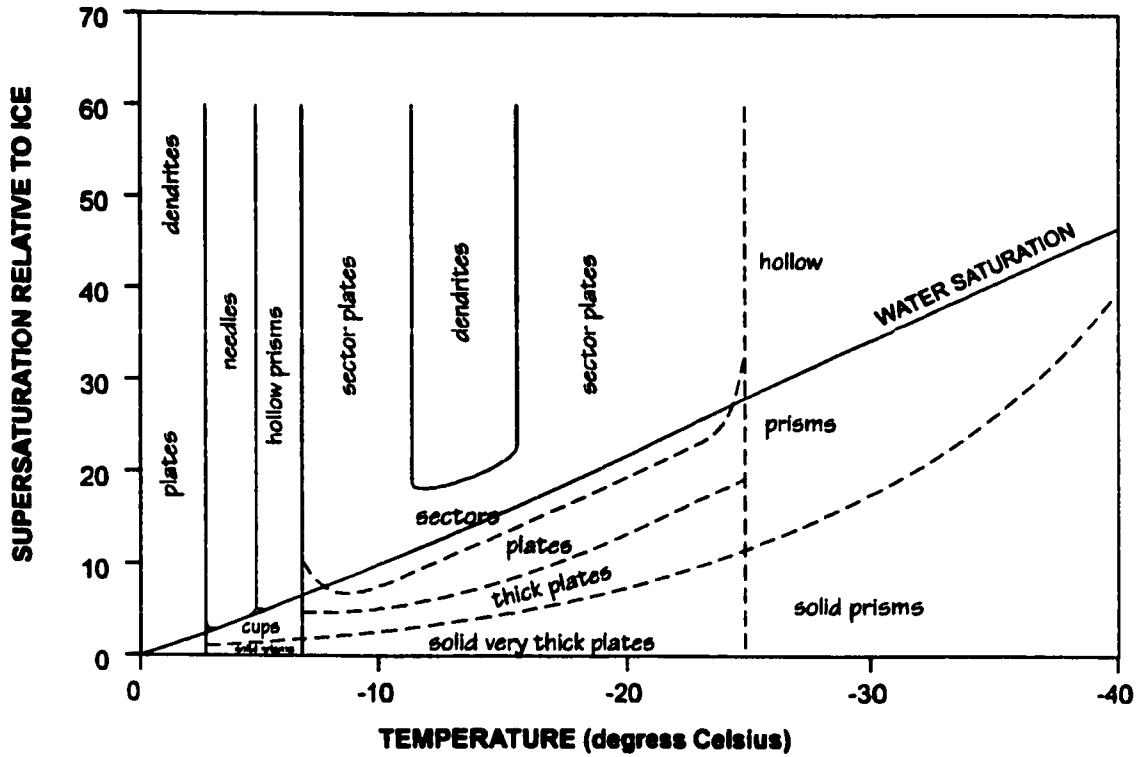


FIGURE 2-2a. Ice-crystal type of as a function of temperature and degree of supersaturation (from Mason *et al.*, 1963).

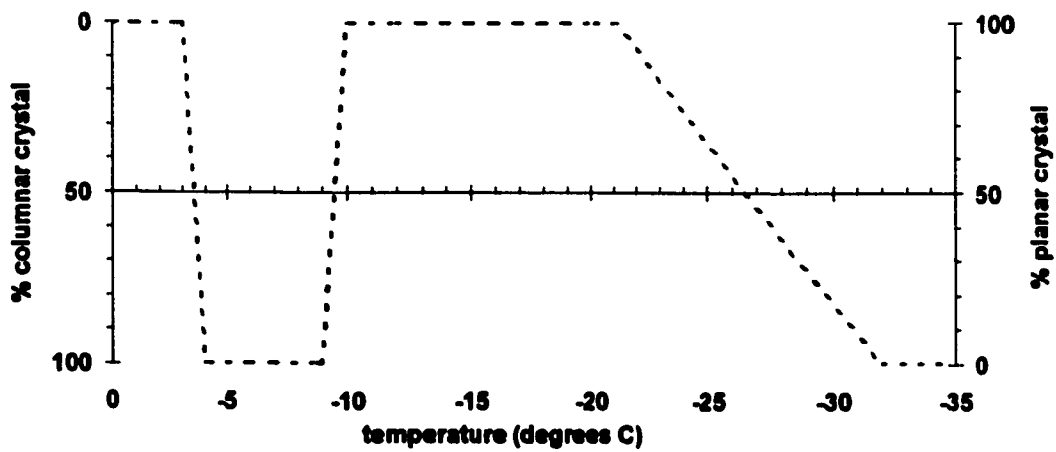


FIGURE 2-2b. Dominant growth direction and the major growth axis a function of temperature.



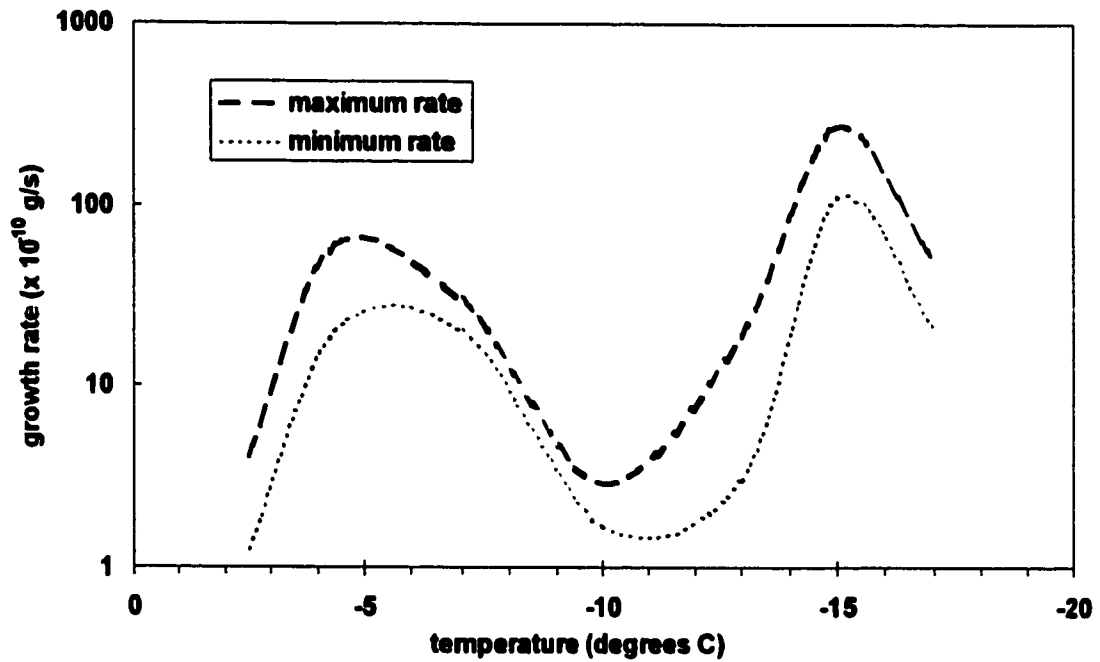


FIGURE 2-2c. Maximum and minimum ice crystal growth rates as a function of temperature from data compiled by Ono (1970).

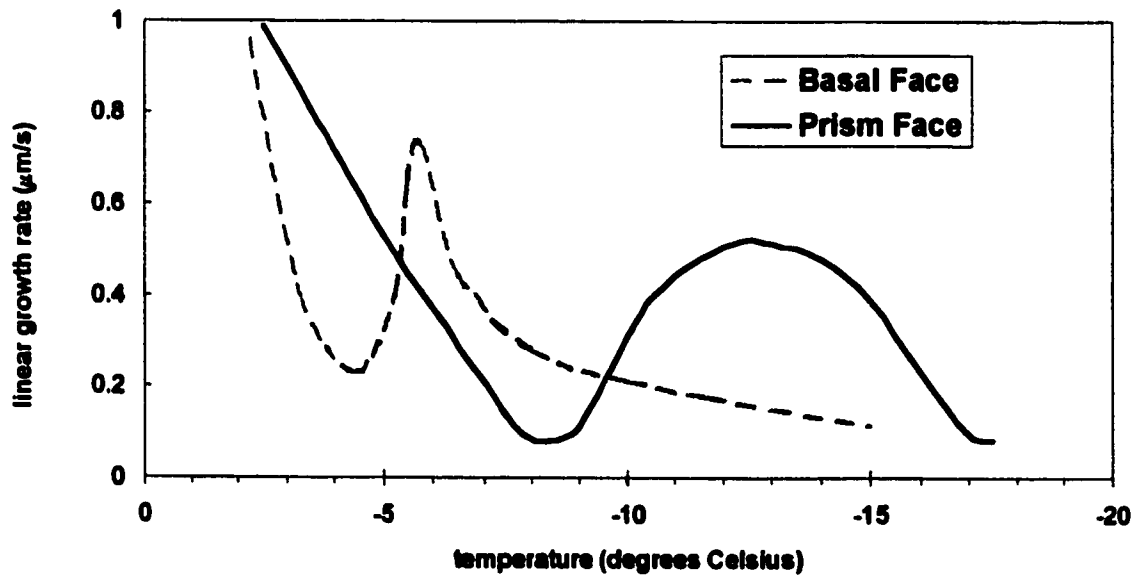


FIGURE 2-2d. Linear ice crystal growth rates for the basal plane (columnar crystal) and prism face (planar crystal) as a function of temperature (from Lamb and Hobbs, 1971).





















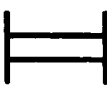

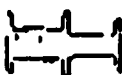

















symbolic representation	EXAMPLES			NAME	SYMBOL
				plate	F1
				stellar crystal	F2
				column	F3
				needle	F4
				spatial dendrite	F5
				capped column	F6
				irregular crystal	F7
				graupel	F8
				ice pellet	F9
				hailstone	F0

FIGURE 2-3. The International Classification for Solid Precipitation (from National Research Council, 1954).

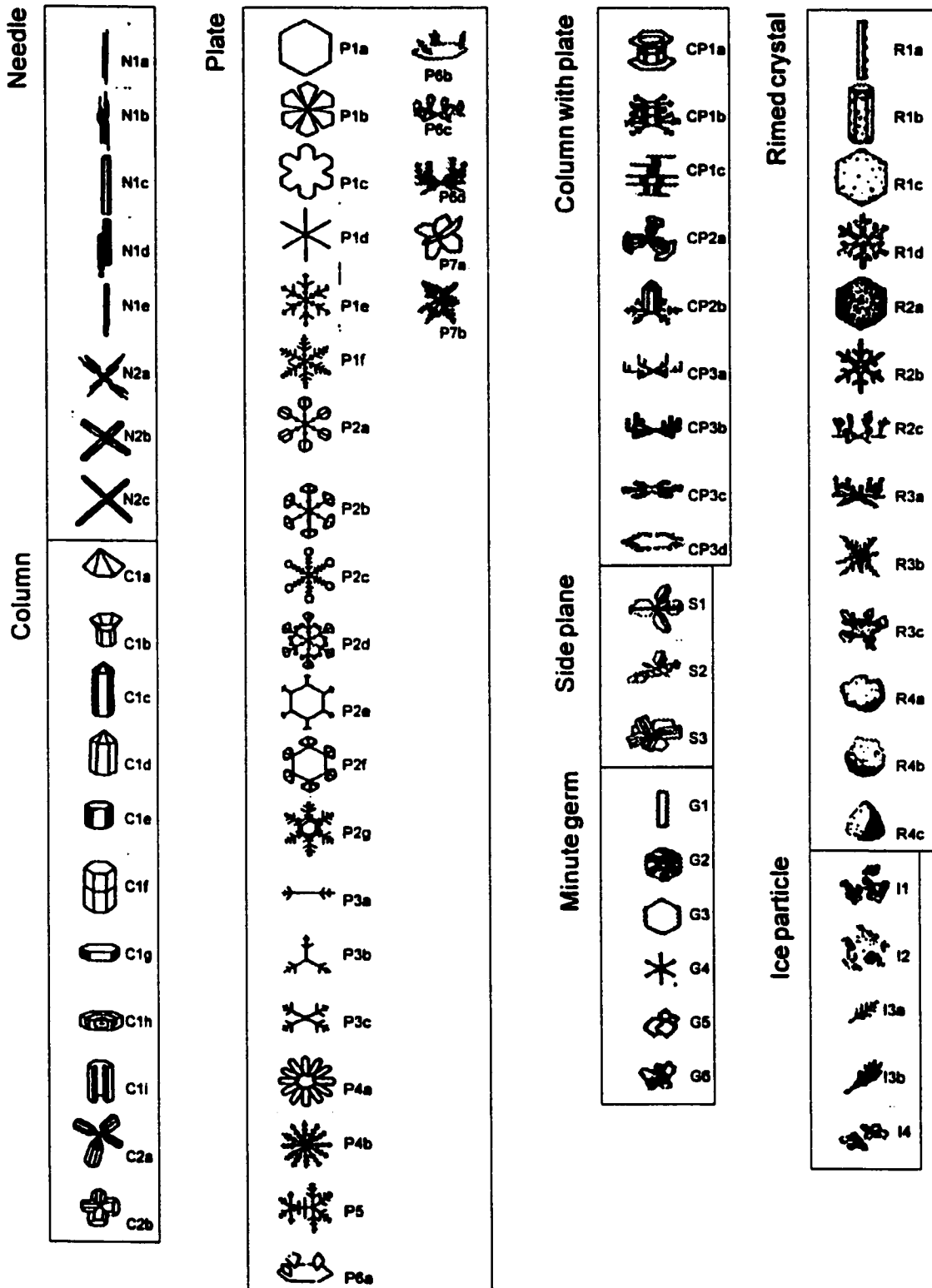


FIGURE 2-4. Magono and Lee (1966) classification of natural snow crystals.

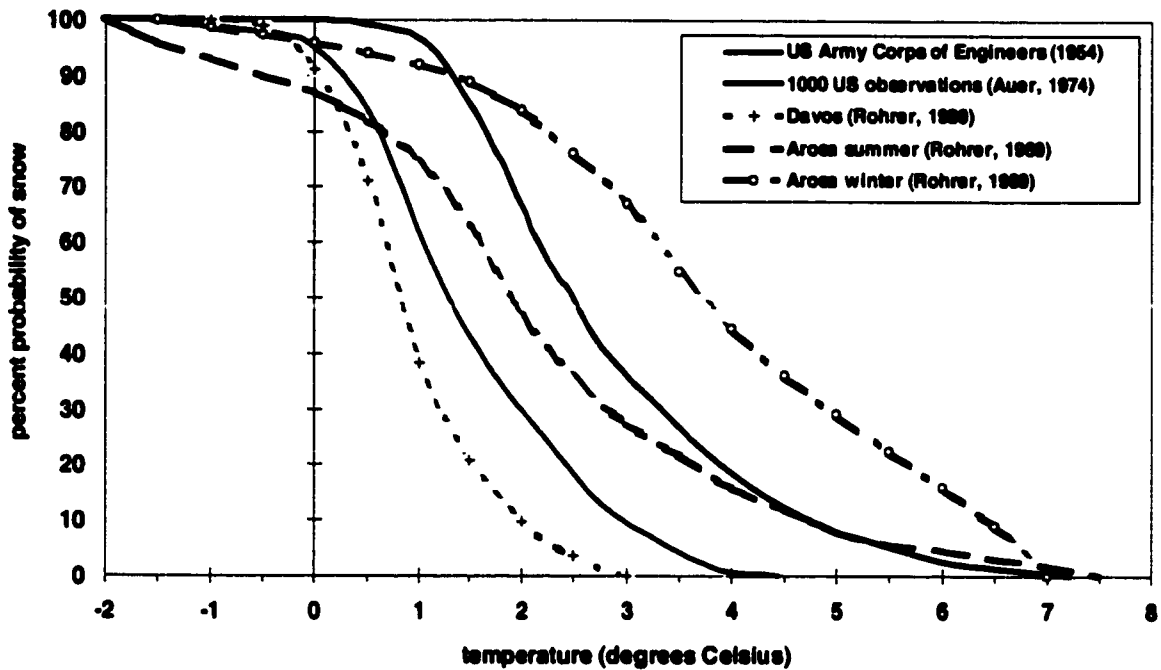


FIGURE 2-5. Average percentage probability of snow versus temperature based on 1000 observations in the US (from Auer, 1974), from data collected by the US Army Corps of Engineers (1956), and from two meteorologic stations (AROSA and DAVOS) in Switzerland (after Rohrer, 1989). The two curves for AROSA are winter and summer averages. It should be noted that all curves have been smoothed to enable a single plot comparison.

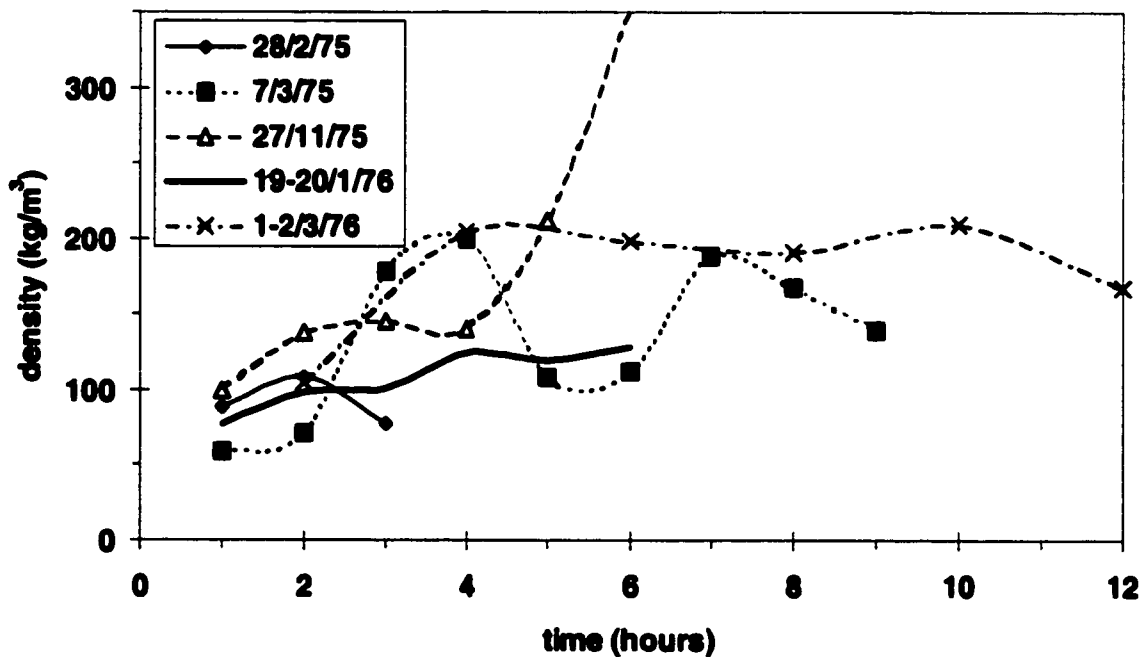


FIGURE 2-6a. Variation in fresh snow density per hour (except for the samples collected on 1-2/3/76) over the duration each storm event (data from Goodison *et al.*, 1981).

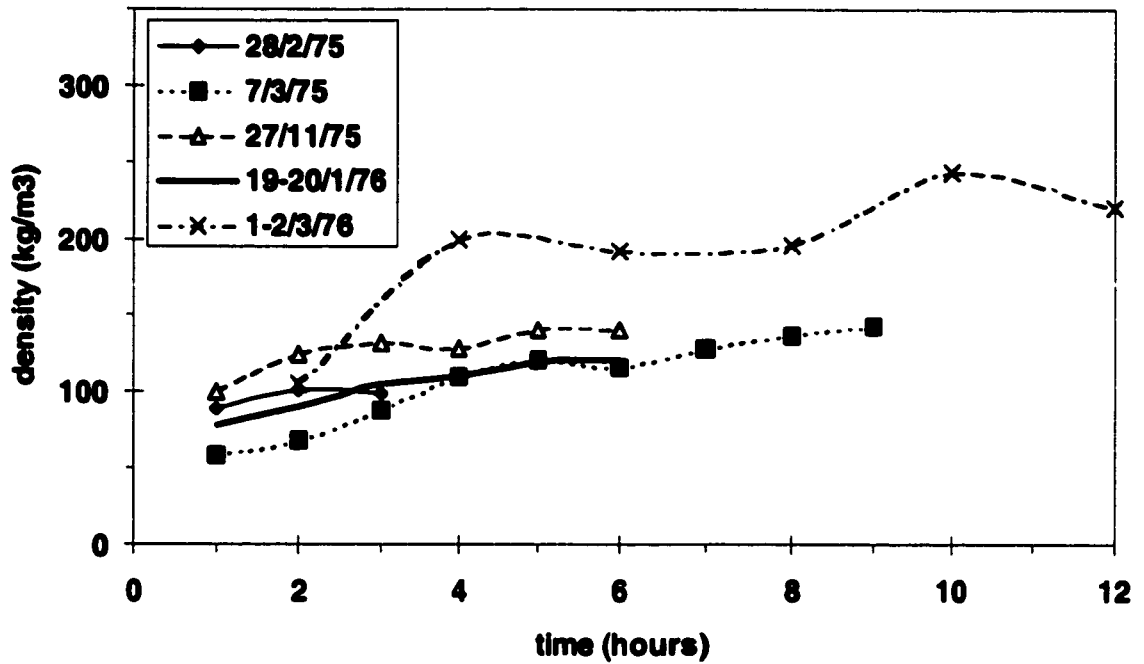


FIGURE 2-6b. Variation in fresh snow density accumulated from the beginning of each storm event (data from Goodison *et al.*, 1981).

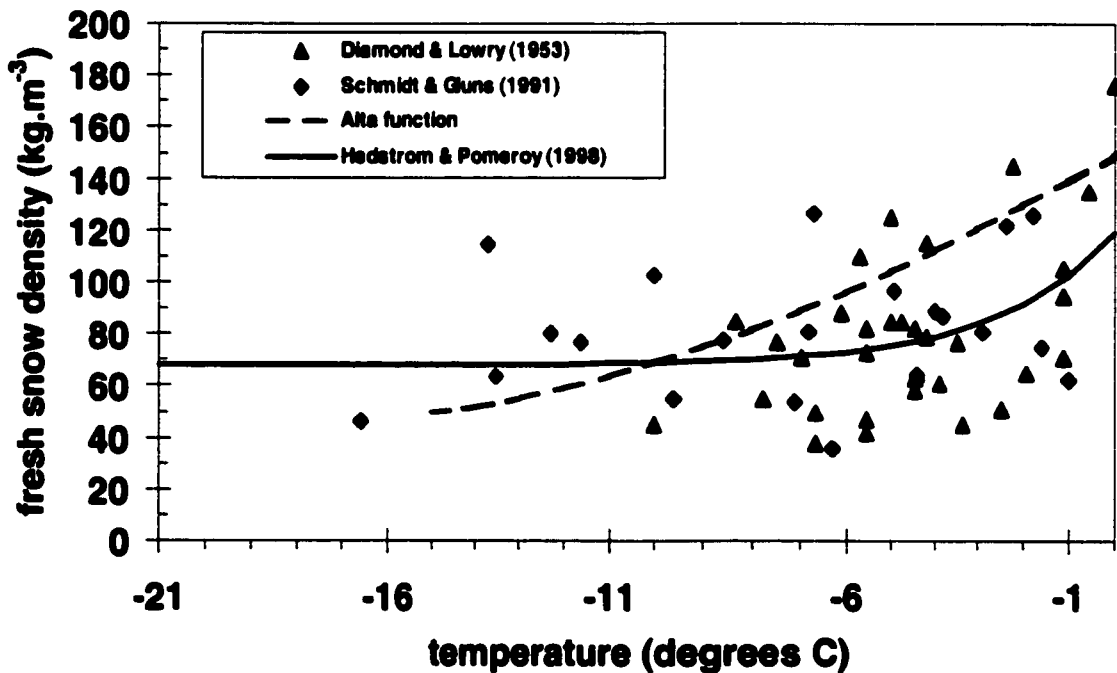


FIGURE 2-7. Fresh snow density as a function of air temperature observed by Diamond and Lowry (1953) and Schmidt and Gluns (1991). The Hedstrom and Pomeroy (1998) function was derived from these data, while the Alta function by La Chapelle (1961) was derived from data collected at the Alta Avalanche Study Center.

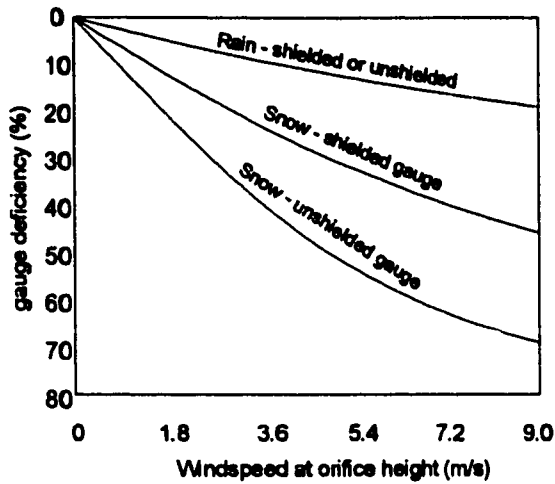


FIGURE 2-8a. The effect of wind speed on the catchment of precipitation gauges (from Larson and Peck, 1974).

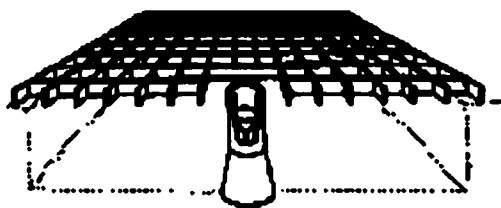
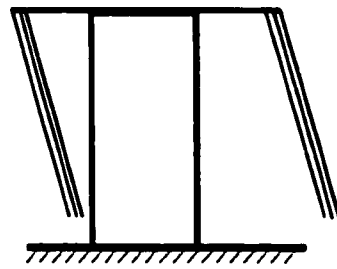
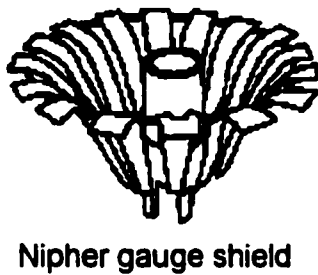
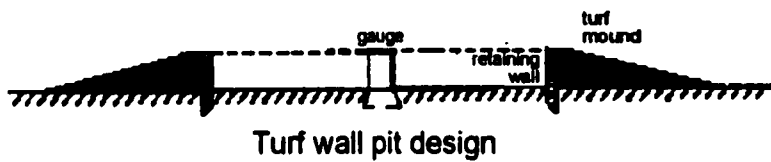


FIGURE 2-8b. Various methods to overcome wind turbulence effects about precipitation gauges (from Sumner, 1988 and Dingman, 1994).

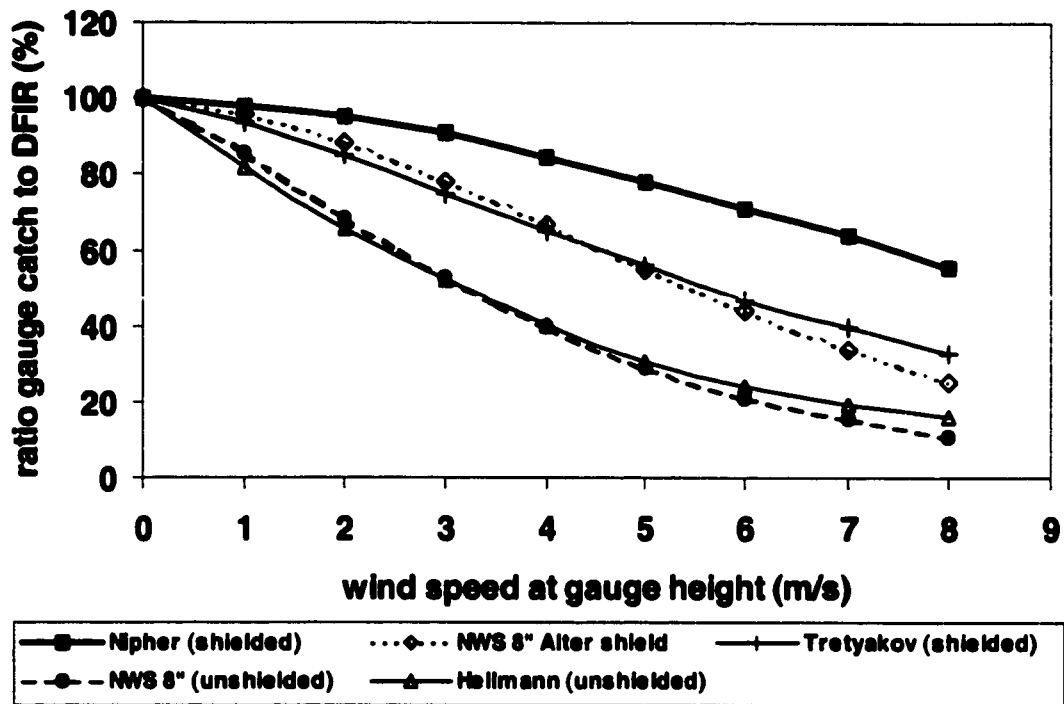


FIGURE 2-8c. Under-catch of five gauges as a function of gauge mouth wind speed (after Yang *et al.*, 1999).

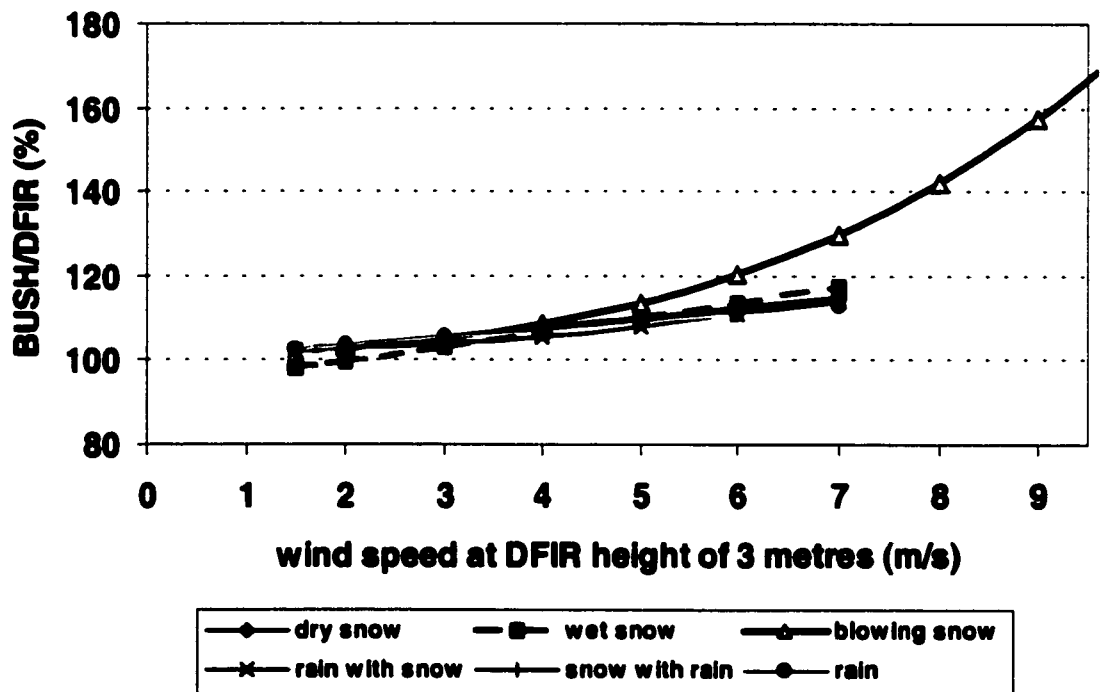


FIGURE 2-8d. Ratio of bush gauge to DFIR gauge as a function of wind speed for different precipitation types, using equations from Yang *et al.* (1993).

# Chapter 3

## STUDY SITE AND DATASET

*“The snow people know snow as they know themselves. In these days our scientists are busy studying the fifth elemental.” (Mowat, 1975, p8)*

### 3.1 STUDY SITE

This research focuses on central south-western Ontario (Figure 3-1). This area of Canada receives from 800 to 1000 mm of precipitation annually, of which a third often comes in the form of snow. The first snowfall can occur as early as late October, however, accumulation is sporadic until mid to late December. Winter can last until mid April, yet mid-winter melts periodically deplete the entire snowpack. On an average year, snowmelt begins in mid March in the south and by mid April in the northern part of the study area. While the winter is usually mild with minimum temperatures reaching -10 to -15°C, extended periods of -25 to -30°C have been observed. Substantial winds may lower such temperatures to wind chill temperatures below -40°C. A summary of the climate normals for the five Meteorological Service of Canada (MSC) meteorological stations used in this research (section 3.2.2) is presented in Table 3-1.

The five main watersheds in central south-western Ontario that have been modelled using WATFLOOD by Kouwen, and subsequently using WATFLOOD/CLASS by Snelgrove (1996) are the Grand, Maitland, Saugeen, Nottawasaga, and Upper Thames River basins. These basins are all within the coverage of the MSC King City Radar (section 3.2.1). This research concentrates on modelling the Upper Grand River watershed, since the hydrologic parameters have been well established for this basin (Kouwen, 1997). As well, the entire basin lies within 120 km of the King City Radar, which minimizes radar errors that occur at greater distances. For hydrologic modelling, 10 by 10 km grid elements are used with six different land cover types, as per Kouwen and Garland (1989). Most of this watershed is covered by crops and low vegetation (59%), with smaller regions of wetland (18%) and mixed deciduous-coniferous forest (14%). The remainder of the watershed comprises bare (8%) and impervious (1%) areas. The terrain in this portion of southern Ontario is glacial material, composed primarily of clayey till.



The precipitation in the area is caused by the meeting of frontal systems. The Jet Stream often runs near the area, as well in the winter Arctic systems meet warmer Maritime systems. In the summer localized convective thunderstorms can be frequent, however such storms are observed on occasion in the winter. Winter storms can be lake effect (such as Figure 1-2b and 1-3b), and snowfall is heaviest in the northern area and near Lake Huron.

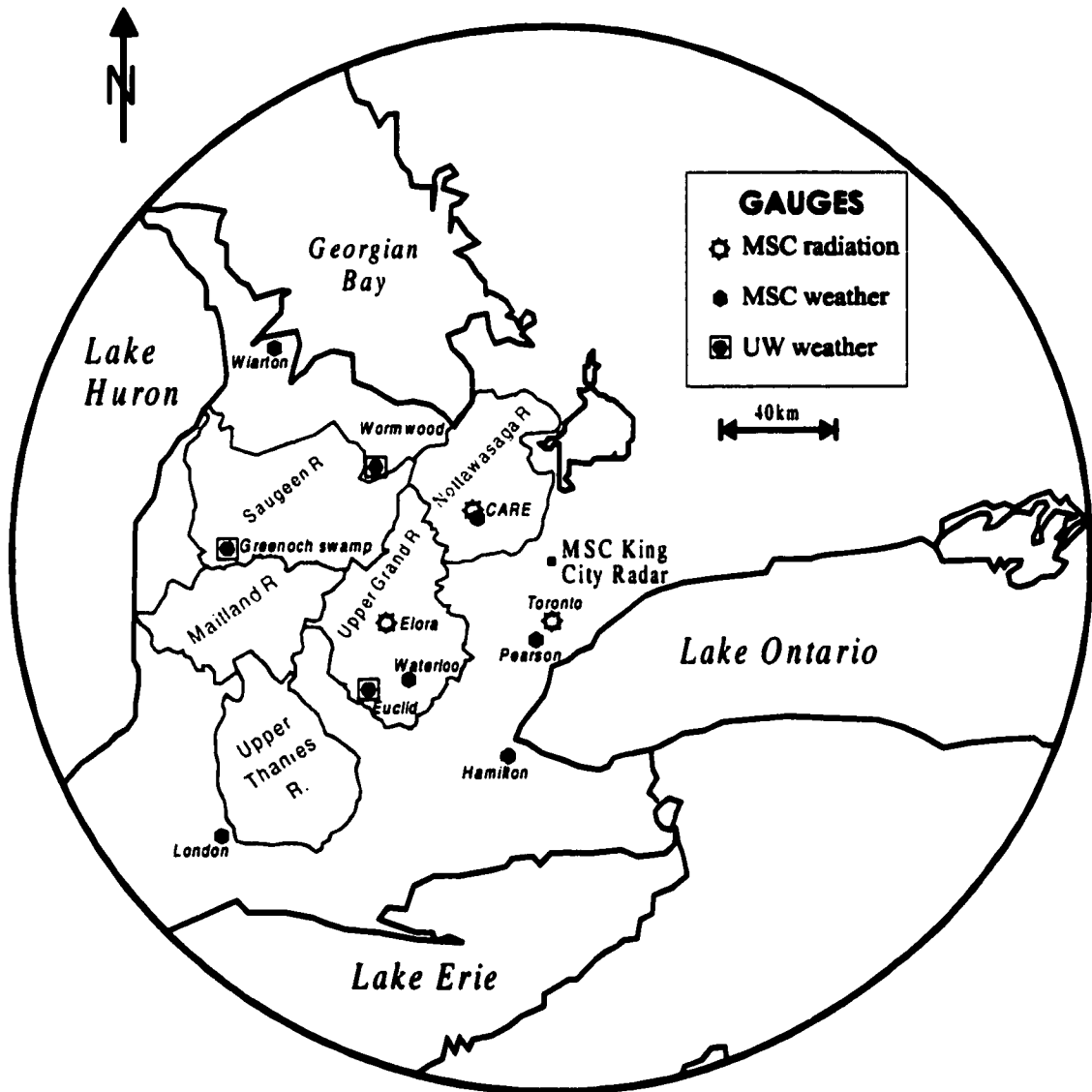


FIGURE 3-1. Map of central south-western Ontario illustrating the location of the study basins and the meteorological stations. The coverage of the MSC King City Radar extends to the edge of the figure.

TABLE 3-1. Summary of climate normals across central south-western Ontario (data from Environment Canada, 1998a).

	Jan	Feb	Mar	Apr	May	Jun	Jul	Aug	Sep	Oct	Nov	Dec	Year
<b>HAMILTON A</b> ( <i>latitude 43°10-N, longitude 79°56-W, elevation 237m, period of record 1959 to 1990</i> )													
max temp (°C)	-2.6	-1.6	3.7	11.3	18.5	23.5	26.4	25.3	20.7	13.9	7.2	0.5	12.2
min temp (°C)	-10.0	-9.8	-4.6	1.2	7.0	12.2	15.1	14.4	10.5	4.7	-0.2	-6.7	2.8
avg temp (°C)	-6.2	-5.6	-0.4	6.3	12.9	17.9	20.8	19.9	15.6	9.3	3.5	-3.1	7.6
Rainfall (mm)	22.2	24.6	50.5	66.5	70.1	78.4	81.0	84.7	83.5	65.8	69.6	46.4	743.3
Snowfall (cm)	41.8	32.0	22.3	7.3	0.5	0	0	0	0	1.1	9.8	37.6	152.4
Precip (mm)	61.3	53.5	73.7	74.3	70.7	78.4	81.0	84.7	83.5	66.3	80.2	82.8	890.4
<b>TORONTO PEARSON INT'L A</b> ( <i>lat. 43°40-N, long. 79°38-W, elev. 173m, record 1937 to 1990</i> )													
max temp (°C)	-2.5	-1.6	3.7	11.5	18.4	23.6	26.8	25.5	20.9	14.1	7.2	0.4	12.3
min temp (°C)	-11.1	-10.6	-5.3	0.6	6.1	11.1	14.2	13.4	9.4	3.6	-0.8	-7.4	1.9
avg temp (°C)	-6.7	-6.1	-0.8	6.0	12.3	17.4	20.5	19.5	15.2	8.9	3.2	-3.5	7.2
Rainfall (mm)	18.5	20.8	35.1	56.0	65.8	68.9	76.6	84.2	74.2	62.0	64.3	38.3	664.7
Snowfall (cm)	32.3	25.9	19.9	7.3	0.1	0	0	0	0	1.1	6.4	31.1	124.2
Precip (mm)	45.6	45.5	56.9	64.0	66.0	68.9	76.6	84.2	74.2	63.0	70.3	65.5	780.8
<b>WATERLOO WELLINGTON A</b> ( <i>lat. 43°27-N, long. 80°23-W, elev. 314m, record 1966 to 1990</i> )													
max temp (°C)	-3.3	-2.5	2.9	11.2	18.6	23.2	26.1	24.8	20.1	13.2	6.3	-0.5	11.7
min temp (°C)	-11.4	-11.2	-6.1	0.4	6.3	10.7	13.6	12.6	8.5	2.9	-1.3	-7.6	1.5
avg temp (°C)	-7.3	-6.8	-1.5	5.8	12.5	17.0	19.9	18.7	14.3	8.0	2.5	-4.0	6.6
Rainfall (mm)	20.2	26.5	49.2	64.4	75.8	79.5	90.4	93.3	89.6	69.8	71.8	43.1	773.6
Snowfall (cm)	39.9	33.4	21.9	8.1	0.4	0	0	0	0	0.6	12.7	41.0	158
Precip (mm)	54.3	55.6	72.7	72.6	76.3	79.5	90.4	93.3	89.6	70.4	83.1	79.2	917
<b>LONDON A</b> ( <i>lat. 43°02-N, long. 81°09-W, elev. 278m, record 1940 to 1990</i> )													
max temp (°C)	-2.8	-2.0	3.8	11.7	18.7	23.8	26.4	25.2	20.9	14.2	7.1	0.1	12.2
min temp (°C)	-10.7	-10.5	-5.0	0.7	6.4	11.6	14.2	13.3	9.6	3.9	-0.6	-7.1	2.1
avg temp (°C)	-6.7	-6.2	-0.5	6.2	12.6	17.7	20.3	19.3	15.3	9.1	3.3	-3.4	7.2
Rainfall (mm)	25.3	26.7	52.8	69.5	73.6	81.9	76.7	89.6	86.2	73.8	72.8	49.9	778.8
Snowfall (cm)	54.5	42.2	25.8	10.4	0.6	0	0	0	0	2.7	20.9	55.3	212.3
Precip (mm)	69.0	60.7	75.2	79.2	74.2	81.9	76.7	89.6	86.2	76.4	90.8	95.3	955.1
<b>WIARTON A</b> ( <i>lat. 44°45-N, long. 81°06-W, elev. 222 m, record 1947 to 1990</i> )													
max temp (°C)	-3.1	-2.9	2.1	9.6	16.2	21.2	24.2	23.1	19.1	13.1	6.3	-0.3	10.7
min temp (°C)	-11.1	-12.0	-7.1	-0.2	4.7	9.4	13.0	12.7	9.2	4.2	-0.6	-7.2	1.3
avg temp (°C)	-7.1	-7.4	-2.5	4.7	10.5	15.3	18.6	17.9	14.2	8.7	2.9	-3.7	6.0
Rainfall (mm)	15.1	17.2	31.8	53.7	65.4	71.4	71.3	88.6	107	85.5	72.2	37.5	717.1
Snowfall (cm)	116	71.2	44.1	12.4	1.3	0	0	0	0	3	39.5	109	396
Precip (mm)	94.0	63.4	67.0	64.4	66.7	71.4	71.3	88.6	107	88.2	104	113	999.5

## 3.2 DATASET

### 3.2.1 Radar Imagery

The radar operated by MSC near King City, Ontario is located at a latitude of 43° 57' 50" north and a longitude of 79° 34' 27". The installation is primarily a C-band radar (5.2 cm), although there are X-band capabilities. The radar produces products using both the conventional scan and the Doppler scan. In the conventional mode, the coverage is a radius of approximately 200 km (see Figure 3-1 for the extent of the conventional scan radar coverage), whereas the Doppler scan has a coverage radius of approximately 110 km. For the warm season, Richards and Crozier (1983) defined a set of  $Z$ - $R$  coefficients for the southern Ontario climatic areas as  $A$  equal to 295 and  $b$  equal to 1.43. For the cold season, the King City radar uses the  $Z$ - $R$  coefficients defined by Sekhon and Srivastava (1970) of  $A$  equal to 1780 and  $b$  equal to 2.21. The characteristics of King City radar are summarized in Table 3-2 (see Crozier *et al.*, 1991 for full details of the King City radar).

TABLE 3-2. Summary of the MSC King City Weather Radar characteristics.

parameter	units	conventional scan	Doppler scan
frequency	MHz	5625	5625
wavelength	cm	5.33 (C-band)	5.33
peak power	kW	260	260
pulse duration	ms	2	0.5
pulse length	m	600	150
range resolution	m	300	75
PRF	pps	250	892, 1190
scanning rate	rpm	6	0.75
reflector size		6.1m parabolic	
polarization		linear horizontal	
gain	dB	48	
beamwidth		0.65°	
radome		Fiberglas laminate	

The radar images used in this study are hourly 2 by 2 kilometre pixels that are derived by assigning the radial hit closest to centre of the square grid pixel from the average of the six 10 minute constant altitude plan position indicator images (CAPPI images). The CAPPIs are generated by combining the data from up to 24 different scan angles such that the scan height is 1.5 km above the ground during the summer and 1.0 km during the winter, since winter precipitation is closer to the ground. Beyond the limits of the desired CAPPI height, at approximately 84 km for the winter and 109 km for the summer, the 0.3 degrees scan is used. Use of the winter *Z-R* coefficients is identified in the data by the CAPPI number 3, whereas number 0 is used for the summer *Z-R* coefficients. The precipitation is given as depth of water in millimetres per hour for each pixel.

### **3.2.2 Meteorological Data**

There is a dense network of daily climate data available over southern Ontario, but few stations adequately measure meteorological parameters on an hourly basis. Only data from the synoptic stations and the three gauges operated by the University of Waterloo were available for this research (Figure 3-1). As summarized in Table 3-3, most parameters were measured at six to nine locations, with the exception of shortwave radiation that was only measured at three MSC stations. All data were collected according to national standards developed by MSC, including snowfall accumulation that was measured using Nipher-shielded Belfort precipitation gauges.

### **3.2.3 Snowcourse Data**

In Ontario, snowcourse data are collected by the Conservation Authorities on a biweekly basis, and occasionally more frequently during the snowmelt period. A description of the eight snowcourses operated within the Upper Grand River basin by the Grand River Conservation Authority (GRCA) are summarized in Table 3-4 and the locations are presented in Figure 3-2.

### **3.2.4 Hydrometric Data**

Streamflow is monitored at eight hydrometric stations within the Upper Grand basin (see Table 3-5 and Figure 3-2). The data are collected by the GRCA in conjunction with Water Survey of

Canada (WSC) according to WSC national standards. These data are archived by WSC and are available on the HYDAT CD-ROM (Environment Canada, 1997). Table 3-6 summarizes the 14 locations in the four other southern Ontario watersheds where streamflow is also simulated.

TABLE 3-3. Summary of the meteorological gauges used in this research with the parameters used for the five winters indicated by an 'X'.

station number	name	elevation (masl)	latitude (N)	longitude (W)	wind speed	pressure	temperature	relative humidity	precipitation	short-wave radiation
6158733	Toronto Pearson Int'l A	173	43°40'	79°38'	X	X	X	X	X	
6153194	Hamilton A	237	43°10'	79°56'	X	X	X	X	X	
6144475	London A	278	43°02'	81°09'	X	X	X	X	X	
6149387	Waterloo Wellington A	314	43°27'	80°23'	X	X	X	X	X	
6119500	Warton A	225	44°45'	81°06'	X	X	X	X	X	
6142285	Elora Research Station	376	43°39'	80°25'						X
6158350	Toronto	113	43°40'	79°24'						X
611KBE0	Egbert CARE	252	44°14'	79°47'	X	X	X	X	X	X
666UW01	Wormwood	432	44°19'	80°28'			X	X	X	
666UW02	Greenoch Swamp	275	44°04'	81°21'			X <sup>1</sup>	X <sup>1</sup>	X <sup>1</sup>	
666UW03	Waterloo Euclid	340	43°28'	80°32'			X <sup>2</sup>	X <sup>2</sup>	X <sup>2</sup>	

X<sup>1</sup> 1995 and 1996 only

X<sup>2</sup> 1997 only

TABLE 3-4. Description of the eight snowcourse locations within the Upper Grand River basin sampled by the Grand River Conservation Authority.

snowcourse number	snowcourse name	elevation (masl)	latitude (N)	longitude (W)
2001	Cambridge	290	43°23'	80°16'
2002	Canagagigue	404	43°38'	80°32'
2004	Corbetton	518	44°10'	80°18'
2005	Damascus	480	43°54'	80°29'
2006	Jessopville	495	44°04'	80°19'
2009	Rockwood	404	43°40'	80°13'
2010	Spring Creek	414	43°42'	80°47'
2012	Waldemar	454	43°54'	80°17'

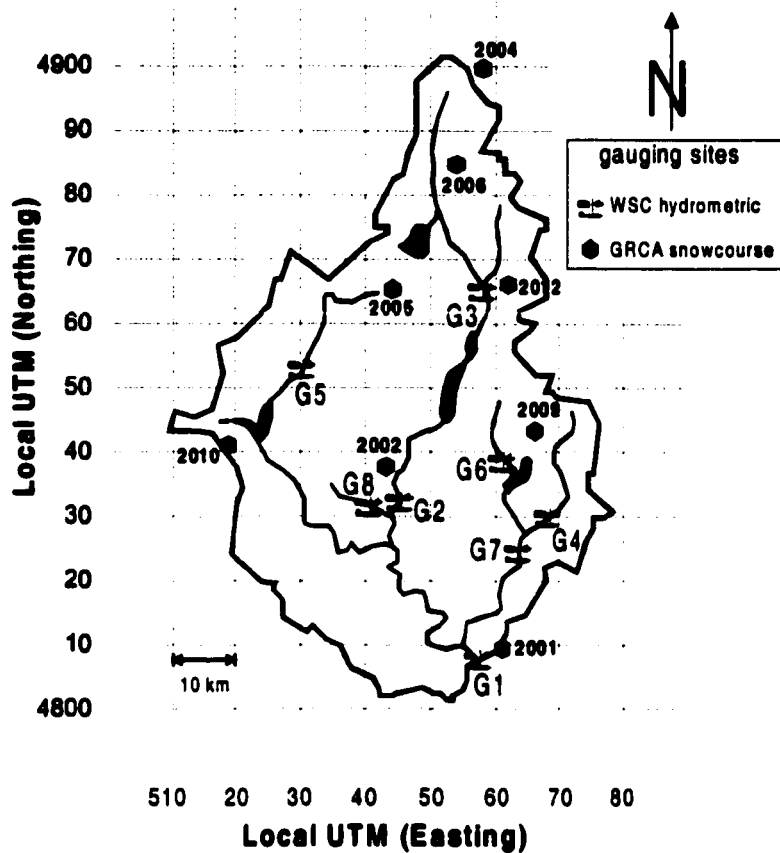


FIGURE 3-2. Location of the eight hydrometric stations within the Upper Grand River basin. The four-digit numbers (2001-2012) in this figure correspond to the *GRCA snowcourses* listed in Table 3-3, while the two-digit numbers (G1-G8) correspond to the *WSC streamflow gauges* listed in Table 3-4.

TABLE 3-5. Description of the eight hydrometric stations operated by Water Survey of Canada within the Upper Grand River basin, used in this study. The mean annual flow is based on the yearly average flow in  $\text{m}^3/\text{s}$  across the drainage area for the period of record.

gauge ID	gauge number	location	total drainage area ( $\text{km}^2$ )	latitude (N)	longitude (W)	mean annual flow ( $\text{mm}/\text{y}$ )	mean maximum daily flow ( $\text{m}^3/\text{s}$ )
G1	02GA003	Grand River at Galt	3520	43°21'10"	80°19'01"	325	485
G2	02GA034	Grand River near West Montrose	1170	43°35'06"	80°28'54"	388	188
G3	02GA014	Grand River at Marsville	694	43°51'43"	80°16'22"	372	176
G4	02GA029	Eramosa River above Guelph	236	43°32'52"	80°10'59"	341	24
G5	02GA039	Conestogo River above Drayton	272	43°46'58"	80°38'20"	418	104
G6	02GA040	Speed River at Armstrong Mills	167	43°38'19"	80°16'12"	410	40.2
G7	02GA015	Speed River below Guelph	593	43°31'30"	80°15'44"	310	57.2
G8	02GA023	Canagagigue Creek near Elmira	118	43°34'46"	80°30'30"	353	22.7

TABLE 3-6. Description of the 14 hydrometric stations used in this study that are operated by Water Survey of Canada within the Nottawasaga (N), Saugeen (S), Maitland (M), and Upper Thames (T) River basin. The mean annual flow is based on the yearly average flow in m<sup>3</sup>/s across the drainage area for the period of record.

gauge ID	gauge number	location	total drainage area (km <sup>2</sup> )	latitude (N)	longitude (W)	mean annual flow (mm/y)	mean maximum daily flow (m <sup>3</sup> /s)
N1	02ED003	Nottawasaga River near Baxter	1180	44°14'59"	79°49'20"	258	112
N2	02ED014	Pine River near Everett	195	44°11'58"	79°57'35"	363	17.5
N3	02ED026	Nottawasaga River at Hockley	173	44°01'27"	79°58'15"	359	18.4
S1	02FC001	Saugeen River near Port Elgin	3960	44°27'23"	81°19'36"	453	500
S2	02FC002	Saugeen River near Walkerton	2150	44°07'13"	81°06'55"	449	289
S3	02FC012	South Saugeen River near Hanover	635	44°05'55"	80°59'09"	591	133
M1	02FE002	Maitland River below Wingham	1630	43°53'12"	81°19'37"	438	335
M2	02FE005	Maitland River above Wingham	528	43°54'57"	81°15'50"	445	123
M3	02FE008	Middle Maitland River near Belgrave	648	43°48'46"	81°18'25"	458	142
T1	02GD001	Thames River near Ealing	1340	42°58'21"	81°12'35"	353	198
T2	02GD004	Middle Thames River at Thamesford	306	43°03'32"	80°59'18"	392	70.4
T3	02GD014	North Thames River near Mitchell	319	43°27'00"	81°12'20"	446	133
T4	02GD015	North Thames River near Thorndale	1340	43°08'57"	81°11'30"	410	337
T5	02GD016	Thames River at Ingersoll	518	43°02'20"	80°53'08"	359	62.9

### 3.2.5 Periods of Study

Five winters of data were used in this study. A winter was defined as the period commencing in the month in which there was snowfall accumulation recorded as part of the snowcourse sampling by the local conservation authority (see section 3.2.3) and terminated at the end of April. Figure 3-3a, b, and c illustrate the seasonal snow depths at selected snowcourse sites in the northern, middle and southern areas of the Upper Grand River basin. Based on these snow depths, the 1994 and 1997 winters were chosen as the period from December 1<sup>st</sup> through April 30<sup>th</sup>, and the 1995 and 1996 winters extended from November 1<sup>st</sup> through to April 30<sup>th</sup>. There was significant accumulation in December 1992 (winter of 1993) and snowcourse 2002 illustrates that there was a already small quantity of accumulation at the beginning of December (Figure 3-3b), but a majority of this snow melted by the end of the month. The period of study for the 1993 winter was chosen to commence in January with partial snowcover, since the radar data were not continuously available until January 1<sup>st</sup>, 1993.

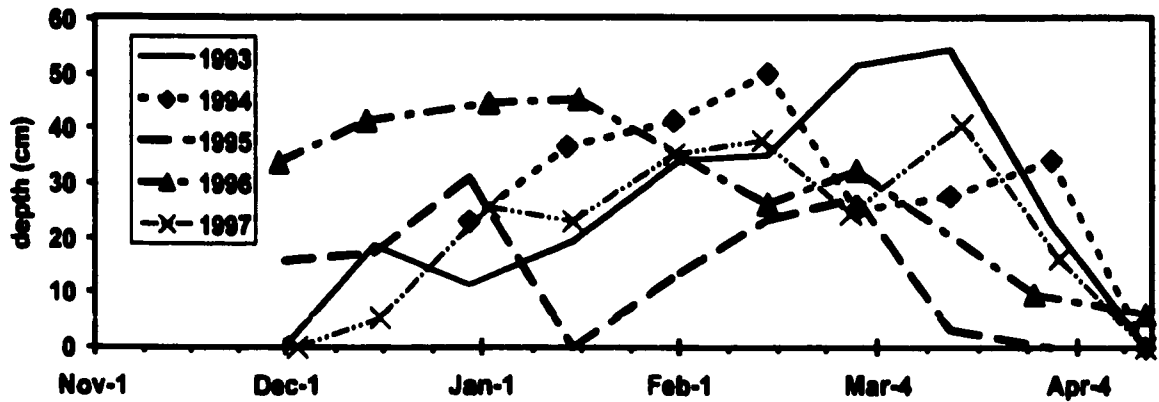


FIGURE 3-3a. Seasonal snow depths in the northern section of the Upper Grand River basin at the snowcourse located at Corbetton (GRCA 2004) for the five winters from 1993 to 1997.

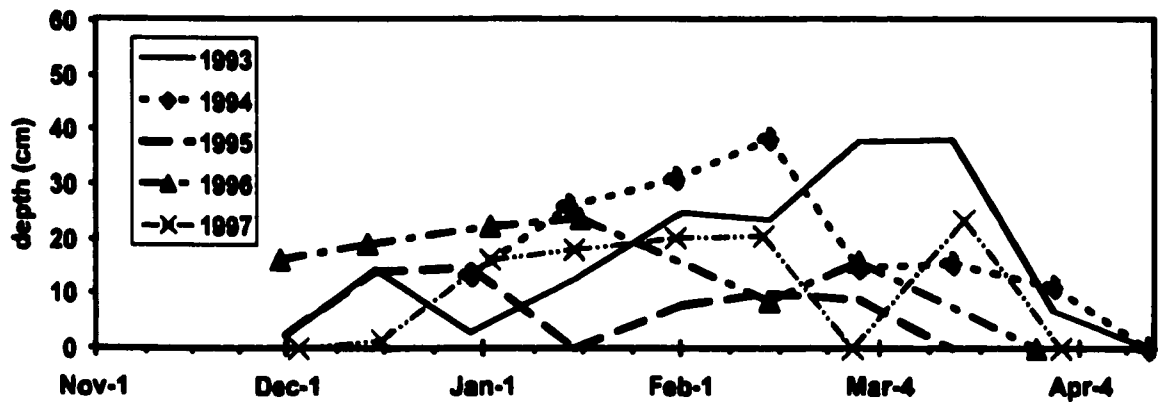


FIGURE 3-3b. Seasonal snow depths in the middle section of the Upper Grand River basin at the snowcourse located at Cananagigue (GRCA 2002) for the five winters from 1993 to 1997.

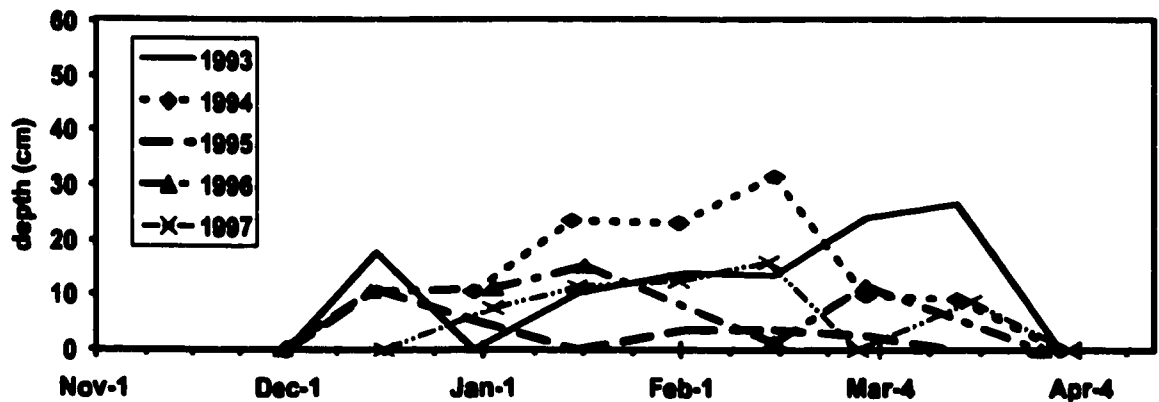


FIGURE 3-3c. Seasonal snow depths in the southern section of the Upper Grand River basin at the snowcourse located at Cambridge (GRCA 2001) for the five winters from 1993 to 1997.



# Chapter 4

## METHODOLOGY

---

*“Yukagir reindeer herdsman on the arctic coast of Siberia can tell the depth of snow cover, its degree of compactness, and the amount of internal ice crystallization it contains simply by glancing at the surface.” (Mowat, 1975, p8)*

This chapter outlines the methodology used to correct the gauge precipitation data, the various algorithms that were developed to adjust the radar data and to estimate cloud cover for calculating incoming longwave radiation; and presents the various modelling changes and additions that were incorporated into the CLASS model to more adequately represent snow processes. Specifically, the radar data are adjusted to consider the occurrence of mixed precipitation and the implication of the shape of snow particles. A scaling phenomenon associated with the local radar data is also discussed. The advanced snowpack processes considered are the occurrence of mixed precipitation, variable density of fresh snow, variable maximum snowpack density, increased canopy snowfall interception, the addition of redistribution and transport sublimation, and the use of split state soil parameters.

### 4.1 METEOROLOGICAL DATA ASSEMBLY

The hydrological parameters used in the study watershed were established by different studies (Tao and Kouwen, 1989 and Snelgrove, 1996). A brief description and the units for each of the nine meteorological data are presented in Table 4-1. With the exception of specific humidity and longwave radiation, all of the required meteorological data are usually measured at weather stations across Canada and archived on an hourly basis. The specific humidity was derived from air temperature and relative humidity; and the longwave radiation was computed from the air temperature and an estimate of the cloud cover, as per Dingman (1994).

TABLE 4-1. Summary of WATFLOOD/CLASS meteorological data with units.

data field	description	units
temperature	air temperature	K
precipitation: rain	mass of liquid precipitation	m/s
precipitation: snow	mass of solid precipitation	m/s
barometric pressure	air pressure	mb
specific humidity	specific humidity	kg/kg
wind speed from north	north component of wind speed measured at 10m height	m/s
wind speed from east	east component of wind speed measured at 10m height	m/s
shortwave radiation	user defined, but often given as incoming	W/m <sup>2</sup>
longwave radiation	user defined, but often given as incoming	W/m <sup>2</sup>

#### 4.1.1 Precipitation Gauge Data Adjustment

According to Louie (*pers. comm.*, 1999) and Environment Canada (1998c), hourly rainfall rates are measured using tipping bucket gauges, whereas snowfall rates are measured using Nipher-shielded gauges. Therefore, it was assumed that once precipitation occurred at temperatures below freezing (November 1<sup>st</sup> or later) the precipitation rates were measured using a Nipher-shielded gauge, and the appropriate wind and wetting loss corrections could be applied. It was also assumed that once the daily minimum temperatures no longer go below freezing (April 30<sup>th</sup> at the latest), precipitation data were collected using a tipping bucket gauge. For the winter, precipitation may occur at above freezing temperatures, i.e., it can rain in the winter. Since the winter precipitation data are collected using a Nipher-shielded gauge, the gauge correction was applied for air temperatures less than 2.2°C. This temperature is the 50% percent probability-of-snow from the Auer (1974) relationship (Figure 2-5). This threshold was the snow-rain division used by the biosphere-atmospheric-transfer-scheme (BATS) model (Yang *et al.*, 1998).

To correct the Nipher-shielded gauge data for wetting loss, 0.15mm can be added to each precipitation event, as per Goodison and Metcalfe (1992). For wind under-catch correction, the bush gauge was assumed to estimate “true” snowfall, thus the Nipher-shielded gauge data must be corrected to the Double Fence Intercomparison Reference (DFIR) gauge data and these data must be subsequently corrected to the bush gauge data. Equation (2-22) was inverted to yield:

$$\frac{DFIR}{NIPHER} = \frac{100}{100 - 1.98U_{gauge} - 0.44U_{gauge}^2} \quad (4-1).$$

Since all the bush to DFIR gauge relationships derived for various precipitation types by Yang *et al.* (1993) are similar, with the exception of the blowing snow scenario, an average relationship was derived for all expressions except blowing snow. As a second order polynomial, the average bush to DFIR gauge ratio takes the form:

$$\frac{BUSH}{DFIR} (\%)_{avg} = 99.04 + 1.639U_{gauge} + 0.0857U_{gauge}^2 \quad (4-2).$$

Prior to substitution of equation (4-1) into equation (4-2) to yield a relationship for the catch ratio of the bush gauge to the Nipher-shielded gauge, the wind speed at gauge height had to be made compatible. Since a logarithm wind velocity distribution was assumed above the ground surface, for wind speeds measured at different heights, the wind speed ( $U_a$ ) at one height ( $h_a$ ) could be defined as a function the wind speed ( $U_b$ ) at another height ( $h_b$ ) as follows:

$$U_a = U_b \left[ \frac{\log(h_a / z_o)}{\log(h_b / z_o)} \right] \quad (4-3),$$

where  $z_o$  is the roughness length. Goodison *et al.* (1998) defined  $z_o$  as 0.01 m for the winter and 0.03 m for the summer. Equation (4-1) assumes a wind speed ( $U_{NIPHER}$ ) measured at a gauge height of 2 m for the Nipher-shielded gauge, whereas equation (4-2) assumes a wind speed ( $U_{DFIR}$ ) measured at a gauge height of 3 m for Tretyakov in the DFIR. The height of the gauge mouth was not adjusted to consider the depth of snow accumulation. Using equation (4-3) for winter conditions, the wind speed at 2 m is approximately 93% of the wind speed at a 3m height, or specifically,

$$U_{DFIR} = 1.0765 U_{NIPHER} \quad (4-4).$$

Equation (4-4) can be substituted into equation (4-2) to yield:

$$\frac{BUSH}{DFIR} (\%) = 99.04 + 1.764U_{NIPHER} + 0.0993U_{NIPHER}^2 \quad (4-5),$$

which can be combined with equation (4-1) to yield the catch ratio expression:

$$\frac{BUSH}{NIPHER} (\%) = 100 \left[ \frac{99.04 + 1.764U_{NIPHER} + 0.0993U_{NIPHER}^2}{100 - 1.98U_{NIPHER} - 0.44U_{NIPHER}^2} \right] \quad (4-6).$$

Using regression analysis, this equation (4-6) was simplified to the catch ratio between bush and Nipher-shielded gauge:

$$\frac{BUSH}{NIPHER} (\%) = 106.2 - 2.228U_{NIPHER} + 1.807U_{NIPHER}^2 \quad (4-7).$$

#### 4.1.2 Meteorological Data Gridding

Numerous methods have been developed for the spatial interpolation of data, since the gridding of point data produces questionable areal estimates, especially where data are sparse, or in complex terrain. For the gridding of point precipitation data, Thiessen (1911) estimated the average areal precipitation for large areas. Since then, many of the interpolation schemes have focused on developing appropriate weighting functions for the distance weighting scheme (see Tabios and Salas, 1985; and Bussieres and Hogg, 1989 for a summary). The quality of the gridded precipitation with respect to the actual amount that fell over the same area is uncertain, as it is in part a function of the location, quantity, and quality of the point data. To this end, Marsh (1990) stated that for northern regions, "there is a drastic need to increase the density of

the precipitation network through the installation of remote stations or weather radars.”

For central south-western Ontario, Tao and Kouwen (1989) used an inverse squared distance interpolation to grid rainfall and temperature data for a 10 by 10 km grid. This method and grid size were used in this research across the same study area.

When there is precipitation recorded at any one gauge, the distance weighting computes a precipitation quantity across the entire gridding domain. As this is an error associated with the interpolation scheme, gridded precipitation less than 0.01 mm was assumed to be no precipitation and assigned a value of zero. For SWE measurements in Canada, a trace observation of snow is recorded 0.07 mm and 0.03 mm in the Arctic (Goodison *et al.*, 1998).

Various researchers have developed temperature corrections for elevation changes, such as Collier and Larke (1978) outlined in section 2.2.1d and the UBC Watershed Model (Quick, 1995). However, these corrections have not been applied to gridded data, especially where the change in relief is small (the elevation difference across the Southern Ontario study site is less than 200 m over 100 km, or 0.2%). Gridding of meteorological data from sparse station data have been performed by Solomon *et al.* (1968) considering the physiography of a domain, such as the distances from large water bodies and the height of intermediate obstacles. The resultant grids, however, have only been applied to map long term mean values (eg. Solomon, 1995).

### 4.1.3 Longwave Radiation Estimation

Longwave radiation is not routinely measured in Canada, while shortwave radiation is measured at approximately 90 locations (Environment Canada, 1998c). The incoming longwave radiation ( $L_{inc}$ ), however, can be derived from the near surface air temperature ( $T_a$ ) by the Stefan-Boltzmann equation, as follows:

$$L_{inc} = \epsilon_{at} \sigma T_a^4 \quad (4-8),$$

where  $\epsilon_{at}$  is the integrated effective emissivity of the atmosphere and canopy, and  $\sigma$  is the Stefan-Boltzmann constant ( $\sigma = 5.6697 \times 10^{-7} \text{ W.m}^{-2}.\text{K}^{-4}$ ) (Dingman, 1994). For no forest canopy, such

as meteorological stations, Croley (1989) estimated  $\epsilon_{at}$  as a function of the near surface vapour pressure ( $e_a$  in mb) and an estimate of the fraction of cloud cover ( $C_{cloud}$ ):

$$\epsilon_{at} = (0.53 + 0.065 e_a^{0.5}) (1 + 0.40 C_{cloud}) \quad (4-9).$$

Since the fraction of cloud cover is often unknown, it can be derived as a comparison of the measured solar radiation to the theoretical value.

For no canopy, the incoming solar radiation ( $K_{inc}$ ) can be expressed as follows:

$$K_{inc} = K_{cs}(\Lambda, J) f_1(\Lambda, \beta, \alpha) f_2(C_{cloud}) \quad (4-10),$$

where  $K_{cs}$  is the clear sky shortwave radiation flux,  $\Lambda$  is the latitude,  $J$  is the Julian date,  $\beta$  is the slope inclination angle,  $\alpha$  is the slope azimuth (measured clockwise from north), and  $f_1$  and  $f_2$  are functions (Dingman, 1994). The effect of cloud cover was expressed by Croley (1989) as:

$$f_2 = 0.355 + 0.68 (1 - C_{cloud}) \quad (4-11).$$

To determine  $f_1$ , eccentricity correction ( $E_o$ ), and declination ( $\delta$ ) are required. The eccentricity correction is a measure of the distance between the earth and the sun, and was approximated by Spencer (1971) as:

$$E_o = 1.000110 + 0.034221 \cos \Gamma + 0.001280 \sin \Gamma \\ + 0.000719 \cos 2\Gamma + 0.000077 \sin 2\Gamma \quad (4-12).$$

where the day angle ( $\Gamma$ ) is the position of the earth in its orbit, expressed by Iqbal (1983) as:

$$\Gamma = \frac{2\pi (J - 1)}{365} \quad (4-13).$$

The declination, in degrees, is the latitude at which the sun is directly overhead (solar noon) was estimated by Spencer (1971) as:

$$\begin{aligned} \delta = (180 / \pi) & (0.006918 - 0.399912 \cos \Gamma + 0.070257 \sin \Gamma \\ & - 0.006758 \cos 2\Gamma + 0.000907 \sin 2\Gamma \\ & - 0.002697 \cos 3\Gamma + 0.00148 \sin 3\Gamma) \end{aligned} \quad (4-14).$$

Using equation (4-11) in equation (4-10) with  $E_o$  and  $\delta$  (equations 4-12 and 4-14), yields the instantaneous extraterrestrial radiation flux (on a horizontal plane):

$$K_{inc} = I_{sc} E_o (\cos \delta \cos \Lambda \cos \omega t_{\Delta SN} + \sin \delta \sin \Lambda) \quad (4-15),$$

$$[0.355 + 0.68 (1 - C_{cloud})]$$

where  $I_{sc}$  is solar constant ( $I_{sc} = 1367 \text{ W.m}^{-2}$ ),  $\omega$  is the angular velocity of the earth's rotation ( $15^\circ \text{ h}^{-1}$ ), and  $t_{\Delta SN}$  is the time (in hours) before (negative) or after (positive) solar noon. If the measurement of solar radiation occurs with respect to local time at a measurement station, it is necessary to convert the measurement time to local apparent time ( $LAT$ ), which is a measure of  $t$ , i.e., it considers the local time of solar noon. Local apparent time was given by Iqbal (1983) as a function of local mean time and the equation of time ( $E_t$ ), as follows:

$$\begin{aligned} LAT &= \text{local mean time} + E_t \\ &= \text{local standard time} + \text{longitude correction} + E_t \\ &= \text{local standard time} + 4 (L_{std} - L_e) + E_t \end{aligned} \quad (4-16)$$

where  $L_{std}$  is the standard longitude ( $15^\circ \times$  the difference between local standard time and Greenwich Mean Time), and  $L_e$  is the local longitude. The equation of time is the discrepancy in the length of the solar day and the time at which solar noon occurs over the course of the year, and was approximated by Spencer (1971) as:

$$E_t = (0.000075 + 0.001868 \cos \Gamma - 0.032077 \sin \Gamma - 0.014615 \cos 2\Gamma - 0.04089 \sin 2\Gamma) (720 / \pi) \quad (4-17).$$

Therefore, using the equation of time (4-17) with equation (4-16) to calculate the local apparent time, and subtracting 12, yields the time from the daily solar noon.

Working backwards from measured values of incoming solar radiation at a specified time of day and year and at the specified location, the fraction of cloud cover (to be used in equation 4-9) can be estimated from equations (4-12) through (4-17) as a function of the measured incoming solar radiation ( $K_{meas}$ ) and the theoretical quantity ( $K_{inc}$ ), as follows:

$$C_{cloud} = 1 - \frac{1}{0.68} \left[ \frac{K_{meas}}{K_{inc}} - 0.355 \right] \quad (4-18).$$

#### 4.1.4 Radar Winter Precipitation Data Adjustment

Since solid precipitation accumulates over an entire winter in colder climates, the quantity of snow that falls in a single storm event is less significant in a hydrological sense than the seasonal accumulation. Although the characteristics of an individual snowfall are important to snowpack modelling, operationally, multiple event accumulation can be used with metamorphosis, redistribution, and sublimation routines to estimate the state of the pack, in particular the quantity of water remaining in the pack at the onset of spring melt. Therefore, to illustrate the usefulness of radar for snowfall estimation, seasonal, monthly and weekly radar estimates will be compared to gauge accumulation estimates.

The following three sections describe the method used to adjust the radar images for scaling problems, to consider the underestimation due to the occurrence of mixed precipitation and to consider the variation in reflectivity due to the different shapes of snow crystals. The fourth section summarizes all the different methods used to adjust the radar precipitation estimates, and to compare the results to gauge accumulations.



**4.1.4a Scaling**

For the King City Radar product used in this research, overestimation may occur as a result of forced over-scaling, which is a function of the occurrence of anomalous precipitation (AP) and the discretization of the precipitation rates. The radar product is represented as 28 incremental precipitation rates at a minimum rate of 0.5 mm per interval. This is based on 5-bit (0 - 31) data transmission. Forced over-scaling occurs when AP, intermittent clutter, or intense precipitation is present that produces a return signal that is larger than the maximum rate (13.5 mm) at the lowest rate increment (0.5 mm). This forces an increase in the scaling intervals to 1 mm, 2 mm or greater. This scaling increase may be appropriate for summer precipitation events, however, winter storms rarely produce hourly accumulation rates greater than 13.5 mm. To overcome the forced over-scaling, the radar data were reprocessed using only the lowest increment of 0.5 mm.

Initially, two scaling removal techniques were compared to assess the method that should be used to reduce the forced overscaling. The one method was removal of scaling from only the smallest bin increment and retaining the above minimum scaling for all other bins. For example, if the interval increased from 0.5 mm/h to 2.0 mm/h, all pixels with 2.0 mm/h would be reduced to 0.5 mm/h and all other pixels such as 4.0 or 6.0 mm/h will retain the precipitation rate of 4.0 or 6.0 mm/h. The second method was removal of scaling for all bins, such that for 2.0 mm/h intervals the minimum precipitation rate would become 0.5 mm/h, as previous, but the next bin (4.0 mm/h) would become 1.0 mm/h, 6.0 mm/h would become 1.5 mm/h, and so on. A comparison of accumulations produced by the two methods showed net monthly differences of 1% or less. Therefore, for computational simplicity, the complete scaling removal method was used in this study to adjust the raw radar data. Scaling removal was applied to all radar data in the winter dataset, specifically all data that used more winter coefficients ( $Z = 1780 R^{2.21}$ ), than summer coefficients ( $Z = 295 R^{1.43}$ ), i.e., three or more 3s in the CAPPI identification number.

Although the King City radar product was adjusted in December 1994 to only change the scaling for intense precipitation in the western portion of the coverage area, it is possible that AP or clutter in the western area could still cause unnecessary scaling. Although the forced over-scaling problem may occur only for the King City Radar data product, data users should be aware of the problem.

#### ***4.1.4b Mixed Precipitation***

Re-processing of the radar images is required to compensate for radar estimation errors due to the detection of mixed precipitation at air temperatures above freezing and the conversion of reflectivities using a solid precipitation  $Z-R$  relationship. The images can either undergo a different  $Z-R$  transformation during processing, or post-processing can be applied to images derived from the standard  $Z-R$  relationships. Since the state or condition of mixed precipitation is localized (Stewart and King 1987), the spatial distribution of temperature across the radar window is required for adequate adjustment of the precipitation rate. It would be difficult to adjust the  $Z-R$  relationship based on temperature while the precipitation map is being produced and archived since the temperature data are often not available in real-time. Instead, post-processing of the precipitation images can be performed once both the radar precipitation estimates have been reviewed and the temperature field has been developed across the desired domain. For hydrologic modelling, the precipitation-temperature adjustment can be undertaken during runtime, since both temperature and precipitation are modelling data inputs.

Various probability-of-snow versus temperature, presented in Figure 2.5, can be used to adjust the radar images due to underestimation from mixed and liquid precipitation. Since no curve exists for southern Ontario, and the data were not available, the probability curve derived by Auer (1974) was chosen. It was selected since it is based on 1000 observations in the US and was assumed to yield an average value. It is compared other curves in Figure 2.5. The other mixed precipitation curves are for mountainous environments.

Ideally a direct relationship could be developed between percentage snow in the precipitation versus radar precipitation rate adjustment, however, the  $Z-R$  precipitation - reflectivity relationship has only been established for pure solid precipitation and for pure liquid precipitation. As a first estimate, a linear interpolation has been assumed between percent snow or solid precipitation to determine the reflectivity adjustment across the temperature domain of mixed precipitation. Therefore the probability-of-snow versus temperature curve is used directly to estimate the adjustment to the precipitation rate.

A linear relationship has been used to approximate the curve derived by Auer (1974), as well a sixth order polynomial has been fitted (Figure 4-1a). To compare the linear approximation

to Auer's curve, the data from three gauge sites (for up to 5 winters) in southern Ontario (see section 3.1) were used to investigate winter (December to March) temperatures trends. For above 0°C temperatures, there is a greater probability of air temperatures closer to freezing than warmer temperatures (Figure 4-1b). Therefore the linear representation of Auer's curve should result in a similar temperature correction. Statistical analysis of these temperature data illustrates that an exponential distribution exists for temperatures above freezing (see Figure 4-1b), and this above-freezing temperature distribution was used to weight the fit of the polynomial curve in order to improve the representiveness of the sixth order polynomial. The resulting approximation of Auer's curve for the percent of snow content ( $F_s$ ) in mixed precipitation at an air temperature,  $T$ , can be written as follows:

$$F_s = 0.0202T^6 - 0.3660T^5 + 2.0399T^4 - 1.5089T^3 - 15.0387T^2 + 4.6664T + 100 \quad (4-19).$$

Below an air temperature of +0.45 degrees Celsius, it was assumed that there is 100% snow, and above +5.97 °C there is 100% rain. Other approximations of the Auer curve are presented in Appendix B.1.2.

In order to use only the fraction of snow and rain to adjust the winter  $Z-R$  derived precipitation ( $R_w$ ), that occurred at above freezing temperatures ( $\geq +0.45$  °C), the ratio of the summer to winter  $Z-R$  coefficients were compared. With the assumption of the same return signal and precipitation rate, the summer  $Z-R$  coefficients are 4.06 times larger than the winter coefficients. However, Kouwen (*pers. comm.*, 1998) stated that for hydrologic modelling using weather radar as input, radar rainfall, as provided by the King City radar, was often overestimated by a factor of two. Therefore, this ratio of coefficients was reduced to 2.03.

The constant rainfall factor of 2.03 is based on the assumption of the same return signal and precipitation rate. However, this only holds true for a precipitation rate of 0.24 mm/h. Therefore the  $R_w$  adjustment should include  $R_w$  to compute a conversion factor. Manipulation of the  $Z-R$  coefficients thus yielded the following new radar precipitation estimate ( $R_{mixed}$ ):

$$R_{mixed} = R_w \times \frac{F_S}{100} + \frac{(100 - F_S)}{100} \times \alpha_R R_w^{\beta_R} \quad (4-20),$$

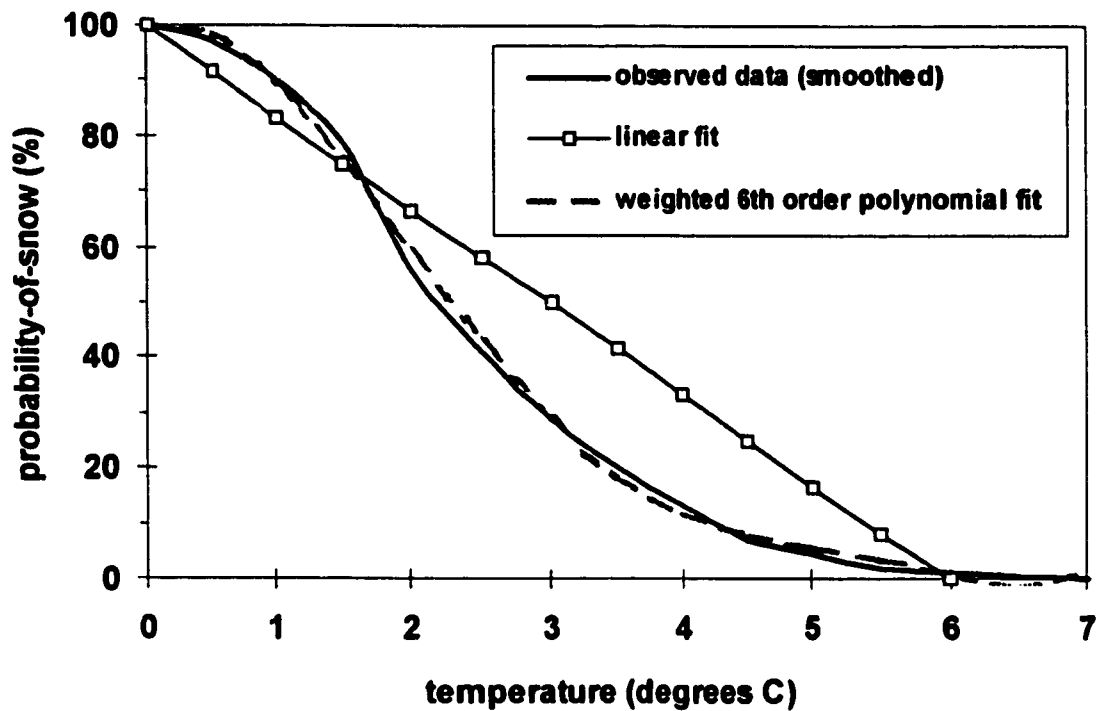


FIGURE 4-1a. Linear representation and polynomial curve fit to the percentage probability-of-snow versus temperature plot derived by Auer (1974).

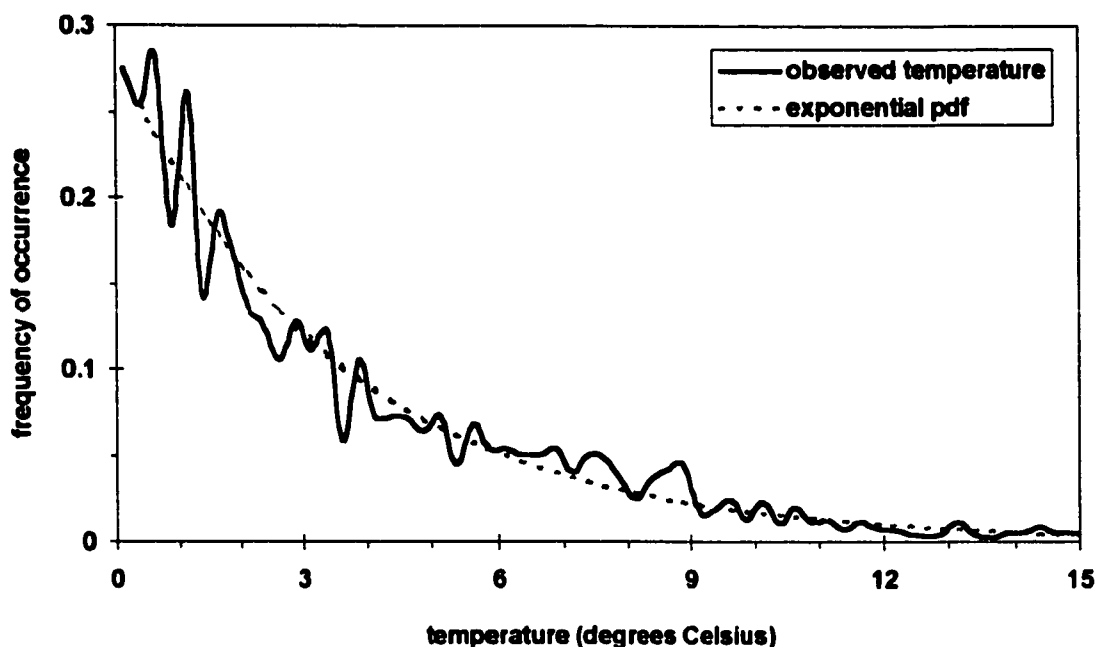


FIGURE 4-1b. Distribution of above freezing observed temperatures at the 3 study sites for the observed winter data (section 3.2.5). The exponential pdf is derived from the mean of the data. The observed temperature frequencies were generated by 0.25 degree increments of the 3640 average hourly temperatures.

where the rain adjustment constant ( $\alpha_R$ ) is equal to 2.165 and the rain adjustment exponent ( $\beta_R$ ) is equal to 1.545. Equation (4-20) can be used with the simplified ratio estimation by setting  $\alpha_R$  equal to 2.03 and  $\beta_R$  equal to 1.0.

The percent probability-of-snow from the US Army Corps of Engineers or the two stations in Switzerland (see Figure 2-5) could be used instead of Auer's curve. These curves could also be represented using sixth order polynomial functions of the form:

$$F_S(T) = a_{F_{s1}} T^6 + a_{F_{s2}} T^5 + a_{F_{s3}} T^4 + a_{F_{s4}} T^3 + a_{F_{s5}} T^2 + a_{F_{s6}} T + b_{F_s} \quad (4-21),$$

where  $a_{F_{s1}}$  through  $a_{F_{s6}}$  and  $b_{F_s}$  are coefficients. The values of these coefficients for the five percent probability-of-snow curves are presented in Table 4-2. The lower limit of sixth order polynomial curves, i.e., the occurrence of 100% snow, is presented in Table 4-2 to the nearest one-hundredth of a degree Celsius. The upper temperature limit for the occurrence of 100% rain is also presented in Table 4-2. To avoid computational errors that occur as a result of division

by a small number, the above lower and upper limits have also been determined for 99% snow (approaching from below, i.e., less than) and 1% snow (approaching from above, i.e., greater than), calculated from temperatures rounded to the nearest one-hundredth of a degree Celsius. The smoothing of the data presented in the literature and presented in Figure 2.5 and listed as a function in Table 4.2 are summarized in Appendix B.

TABLE 4-2. Bounds and coefficients for five percent probability-of-snow curves. Each curve is fit with a sixth order polynomial, yielding a percentage,  $F_S(T_{min})$ , at the minimum temperature,  $T_{min}$ , and a percentage,  $F_S(T_{max})$ , at the maximum temperature,  $T_{max}$ . To avoid round-off error when the percentage of snow approach 100% or 0%, the temperatures and corresponding percentages when the percent snow approaches 99% from below and 1% from above are used as limits.

	US Army Corps of Engineers	US observations (Auer, 1974)	Davos (Rohrer, 1989)	Arosa summer (Rohrer, 1989)	Arosa winter (Rohrer, 1989)
$a_1$	0.087	0.0202	1.257	0.0053	-0.0067
$a_2$	-0.909	-0.3660	-8.869	-0.1057	0.0826
$a_3$	2.471	2.0399	16.31	0.6117	-0.1596
$a_4$	2.987	-1.5089	10.39	-0.1331	-0.8291
$a_5$	-16.55	-15.038	-40.14	-5.914	-0.2474
$a_6$	-19.68	4.6664	-31.41	-10.12	-2.367
$b$	94.69	100	92.77	87.97	95.86
$T_{min}$ when $F_S(T)$ approaches 100%	-0.44	0.31	-0.99	-2.04	-1.44
$F(T_{min})$	99.9989	99.9743	99.7284	99.8435	99.9737
$T_{0.99}$ when $F_S(T)$ approaches 99%	-0.29	0.45	-0.39	-1.99	-1.13
$F(T_{0.99})$	98.95	98.99	98.76	98.96	98.99
$T_{max}$ when $F_S(T)$ approaches 0%	4.11	6.16	2.80	6.64	6.98
$F_S(T_{max})$	0.0057	0.0001	0.0582	0.0625	0.2026
$T_{0.01}$ when $F_S(T)$ approaches 1%	3.90	5.97	2.70	6.49	6.95
$F_S(T_{0.01})$	1.04	1.02	1.01	1.05	1.08

#### 4.1.4c Snowflake Particle Shape

Ohtake and Hemni (1970) showed that different snowflakes had different reflectivities for similar snowfall rates. While they developed different Z-R relationships for various snowflake shapes,

application of their coefficients requires knowledge of the type of falling crystal. Since the crystal shape can be approximated by the formation temperature, it will be assumed that if the lapse rate is constant throughout the winter, during precipitation events when the near surface air temperature is below freezing, then a relationship can be developed between reflectivity variations and air temperature. The intent is to develop a function with an average value of unity and a small amplitude, such as 0.2, that will adjust the hourly radar precipitation estimates.

The focus of the particle shape adjustment relationship will be between air temperatures of -1 and -20 °C, since a majority of the below freezing air temperature to be used in this analysis occurred in that range (Figure 4-2a). Since the temperature distribution data will be used to weight the particle shape curve, a fourth-order polynomial curve has been fit to the temperature distribution instead of using the lesser fitting exponential probability distribution function (see Figure 4-2a).

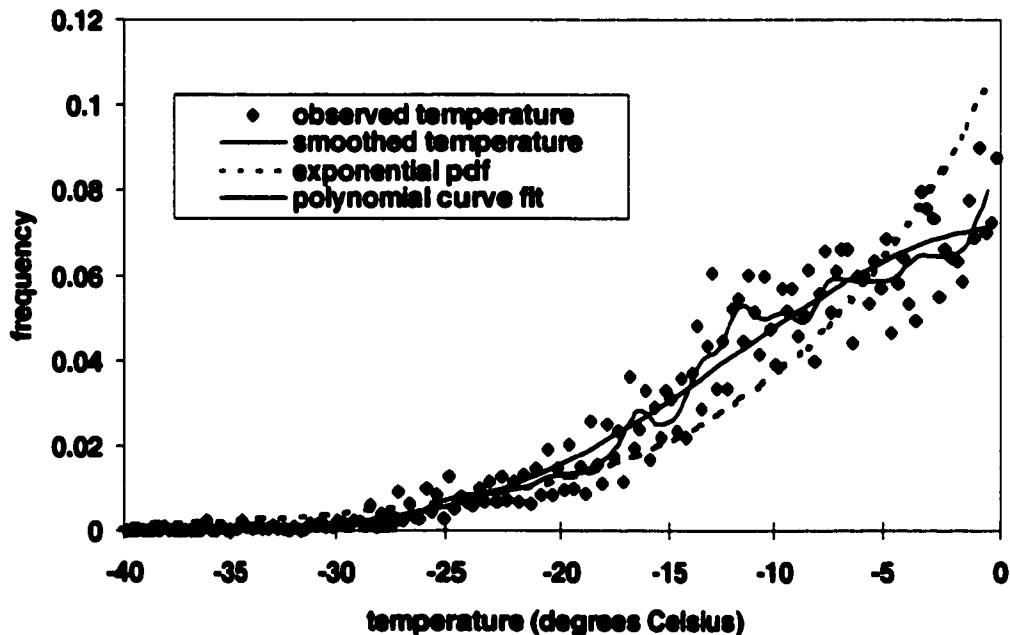


FIGURE 4-2a. Distribution of below freezing observed and smoothed temperatures at the 3 study sites for the observed winter data (section 3.2.5). The observed temperature frequencies are generated by 0.25 degree increments of the 12670 average hourly temperatures, and the smoothed data are 1.0 degree increments. The exponential pdf is derived from the mean of the below freezing data and the polynomial curve fit is a fourth-order polynomial fit to the smoothed data.

The proposed particle shape adjustment relationship (*PS* curve) is derived from Ono's (1970) summary of crystal growth rates (Figure 2-2c). The logarithm of the average of the maximum and minimum growth rates is used to form the basic *PS* curve. To reduce the overall amplitude of the curve, the logarithm is multiplied by a fraction. The first *PS* curve ( $PS_{original}$ ), based solely on growth rates, takes the following form:

$$PS_{original} = a \left[ \log \frac{\partial L}{\partial t} \times 10^{10} - b \right] + c \quad (4-22),$$

where the average growth rate is  $\partial L / \partial t$  in g/s, and  $a$ ,  $b$ ,  $c$  are adjustment coefficients. To yield a curve with an amplitude of less than 0.2 and an average value of unity,  $a$ ,  $b$  and  $c$  are set to 0.1, 1, and 1.05, respectively ( $PS_{original}$  in Figure 4-2b). The resultant curve however does not consider the difference between planar and columnar snow crystals. Columnar crystals, especially needles, are more regular in shape and have a smaller reflectible surface area per unit mass than planar crystals, in particular dendrites. Therefore from -1 to -11 °C, the original *PS* curve can be reflected about the line drawn between -1 and -11 (*adjustment factor* = 0.985 in Figure 4-2b) to create an adjustment curve,  $PS_{needle}$ . Between the flake formation temperatures of -8 and -11 °C, the intermediate  $PS_{needle}$  curve can be shifted up, i.e., assigned a greater surface area to consider the capped column and similar crystals that form at this transition temperature range (see  $PS_{capped\ column}$  in Figure 4-2b). Planar crystals have intricate shapes similar to capped columns, and therefore the  $PS_{capped\ column}$  curve should be shifted up in the area between -10 and -13 °C. Since, at temperatures below -21 °C, the crystals that form are significantly smaller than at higher temperatures, the adjustment factor can be assigned as close to unity (see Figure 4-2b). The proposed particle shape adjustment relationship, in terms of an adjustment factor ( $F_{PS}$ ), can be defined as a three term Fourier Series, as follows:

$$\begin{aligned} F_{PS} = & 1.011 - 0.030 \times \cos(0.331T + 0.418) + 0.015 \times \cos(2 \times 0.331T + 0.418) \\ & - 0.029 \times \cos(3 \times 0.331T + 0.418) + 0.123 \times \sin(0.331T + 0.418) \\ & + 0.009 \times \sin(2 \times 0.331T + 0.418) - 0.026 \times \sin(3 \times 0.331T + 0.418) \quad (4-23), \end{aligned}$$



for  $-21^{\circ}\text{C} \leq T \leq -1^{\circ}\text{C}$ .

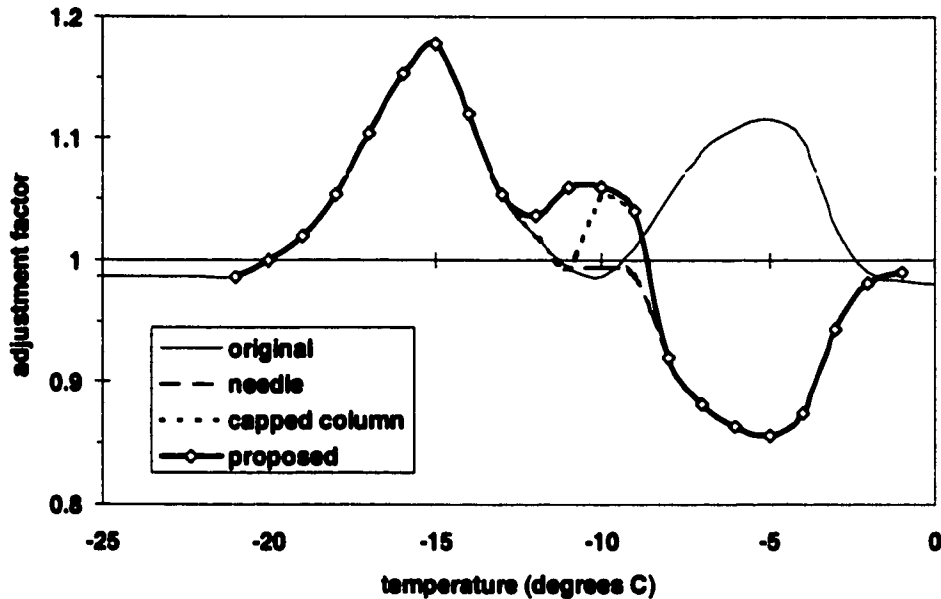


FIGURE 4-2b. The progression from the modified growth rate curve (derived from the logarithm of the average growth rates compiled by Ono, 1970) to the proposed particle shape adjustment curve, including intermediate modifications for needle and capped column type snow crystals.

The mass of a falling snowflake is determined from its reflectivity, which is a function of its volume-weighted surface area. Therefore, for a given reflectivity, a snowflake with a larger surface area will have less mass than a snowflake with a smaller surface area. Since the particle shape adjustment relationship or area adjustment factor (equation 4-23) defines a relative surface area for different snow crystal shapes based on temperature, the curve must be inverted to yield a mass adjustment factor. Given a reflectivity, the falling snowflake mass must be reduced for flakes with larger than average surface areas. Equation (4-23) can be modified using the below freezing temperature distribution (Figure 4-2a) to maintain no net adjustment, i.e., the area under the modified curve multiplied by the polynomial curve fit of the below freezing temperature distribution will be unity. The resultant transformed temperature weighted particle shape adjustment curve ( $PS_{T-weight}$ ) can be defined as an adjustment factor,  $F_{PS}$ , as follows:

$$\begin{aligned}
 F_{PS}' = & -1.75 \times [1.022 \\
 & - 0.018 \times \cos(0.333T + 0.341) + 0.006 \times \cos(2 \times 0.333T + 0.341) \\
 & - 0.029 \times \cos(3 \times 0.333T + 0.341) + 0.107 \times \sin(0.333T + 0.341) \\
 & + 0.015 \times \sin(2 \times 0.333T + 0.341) - 0.017 \times \sin(3 \times 0.333T + 0.341) - 1] + 1
 \end{aligned}
 \tag{4-24}$$

The difference between the initial non-weighted particle shape adjustment curve ( $F_{PS}$ ) and the transformed temperature weighted PS curve ( $F_{PS}'$ ) considers the reflectivity from various snowflake surface areas formed at different temperatures (Figure 4-2c).

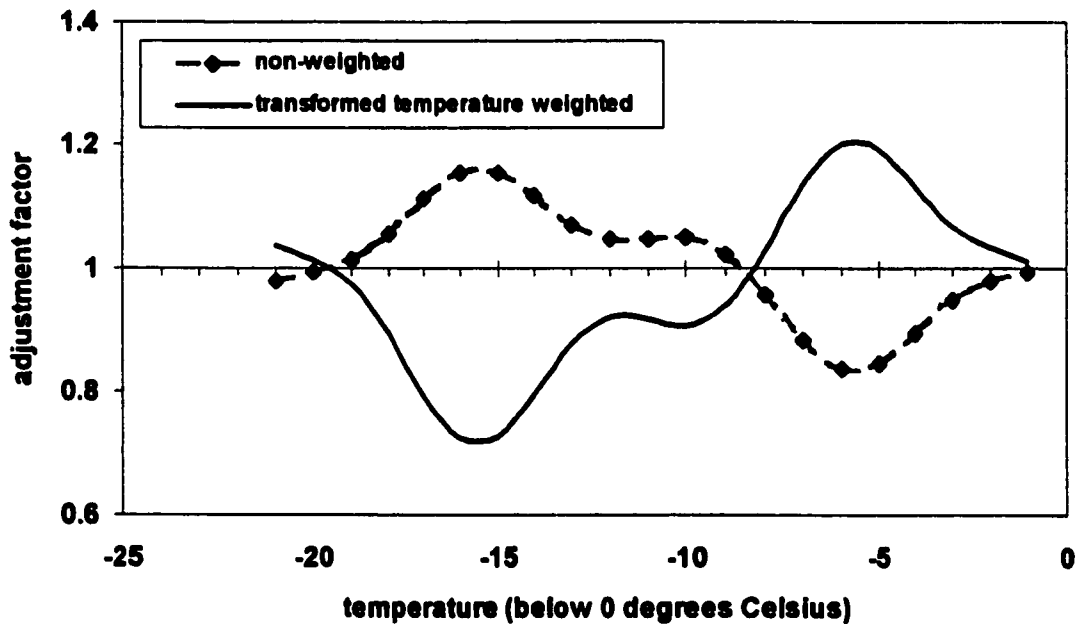


FIGURE 4-2c. Comparison of the initial non-weighted particle shape adjustment curve (same as  $PS_{proposed}$  in Figure 4-2b) to the transformed temperature weighted PS curve.

While the dry adiabatic lapse rate is  $9.8\text{ }^{\circ}\text{C}/\text{km}$  (Oke, 1987), and the average (wet) lapse rate is in the order of  $6.25\text{ }^{\circ}\text{C}/\text{km}$ , the lapse rate varies with location, season and height, as it is a function of the atmospheric condition. Hasenrath (1968) illustrated that there can be limited to no variation in the average monthly lapse rate for warmer climates, yet the annual variation

can be as much as 26 °C/km, from -18 °C/km in December to +8 °C/km in May and June for Eastern Siberia. For colder climates, Lautensach and Bogel (1956) illustrated that in the lowest 1000 to 1500m the winter lapse rate can be 0 °C/km or less. Schaefer and Day (1981) illustrated that the winter lapse rate in mid latitude areas can be close to zero. Personal observations have also shown that particles at near surface temperatures are close to the expected temperatures of formation. Since lapse rate data were not available, the winter lapse rate is assumed to be zero and the transformed temperature weighted particle shape adjustment curve can be applied directly to radar estimates without a temperature shift.

#### *4.1.4d Other Factors*

There are other factors such as synoptic storm type that can be considered to adjust the weather radar winter precipitation estimates. However, to date this method has only been applied to rainfall. Specifically, rainfall *Z-R* relationships have been developed for the tropics, such as the various relationships summarized by Stout and Mueller (1968). In developing the *Z-R* relationship for Southern Ontario, Richards and Crozier (1983) attempted to distinguish between synoptic type and rainfall type. The improvements by stratifying the data by synoptic or storm type were considered insignificant. Further adjustment is beyond the scope of this research.

#### *4.1.4e Summary of Alternatives*

In total 17 (plus 2 additional) procedures were used to adjust the radar estimates. The adjustment scenarios together with the base case and the optimal estimate, the short name used in the accumulation comparisons, and the corresponding seasonal, monthly, and weekly accumulation comparison figures are presented in Table 4-3.

From the different adjustment procedures, six radar scenarios were chosen as input for hydrologic modelling, to compare runoff volumes. These scenarios were considered to be representative of the different sets of radar images. As well, the gridded uncorrected, DFIR, and “bush” corrected precipitation gauge data were used as modelling input (Table 4-4).

To consider the possibility of anomalous propagation (AP) at the study sites, the raw radar data at a specific location were compared to an arithmetic average of the centroid and the

eight surrounding pixels, as well to a weighted mean derived from a 50% middle and 6.25% for each surrounding pixel. The monthly difference at each site is a maximum of 2 mm, and is typically less than 1.5 mm, therefore the weighted mean is used in this study.

## **4.2 MODELLING CHANGES AND ADDITIONS**

This section describes the theoretical considerations for the changes and additions to the snow processes within CLASS version 2.6 (CLASS\_2.6). The specific changes or additions to the computer code are outlined in Appendix A.

### **4.2.1 Mixed Precipitation**

In CLASS\_2.6, the air temperature was used to diagnose precipitation as rain or snow. At present, an air temperature of 0°C was used to distinguish between snow and rain, with no provision for the occurrence of mixed precipitation.

To consider mixed precipitation, the fraction of snow and rain was calculated using equation (4-21) and the coefficients listed in Table 4-2. Since the Auer curve was derived from 1000 observations, it is used for determining the percent probability of mixed precipitation for locations where such a function has not been determined (see section 4.1.4b). To consider the occurrence of mixed precipitation in CLASS\_2.6, the fraction of snow is calculated as a function of air temperature. Below the lower temperature limit the fraction is set to one and below the upper temperature limit the fraction is set to zero. This fraction is used to determine the quantity of snow and rain, and the temperature of the precipitation. To avoid additional melting of frozen hydrometeors and the subsequent accumulation of melted snow, the maximum temperature of falling snow is freezing (0°C). The various mixed precipitation curves, presented in Figure 2-5, have been smoothed to yield a deterministic curve for each dataset. This smoothing procedure is outlined in Appendix B.

TABLE 4-3. The 17 adjustment procedures for seasonal, monthly and weekly snowfall accumulation comparisons.

number	description of adjustment procedure	short name
<i>i</i>	Base case of the raw radar images	raw data
<i>ii</i>	Removal of scale, so radar image increment is 0.5 mm/h. (images used in all subsequent radar adjustments )	scaling removed
<i>iii</i>	Fraction of snow calculated using observed gauge temperature and a linear representation of Auer's curve, then equation (2) with $\alpha = 2.03$ , $\beta = 1.0$	linear mixed precipitation (MP) temperature (T) adjustment
<i>iv</i>	Same as <i>iii</i> , but the dewpoint temperature used instead of observed temperature	linear MP adjustment with dewpoint temperature (Td)
<i>v</i>	Equation (1) used with observed temperature to calculate snow fraction, equation (2) used as above.	Auer's curve MP adjustment with T using a constant of 2.03
<i>vi</i>	Procedure same as in <i>v</i> , but dewpoint temperature is used	Auer's curve MP adjustment with Td using a constant of 2.03
<i>vii</i>	Equation (1) used as in <i>v</i> , but equation (2) used with $\alpha = 2.165$ , $\beta = 1.545$	Auer's curve MP adjustment with T using variable precipitation rate (R)
<i>viii</i>	Procedure same as <i>vii</i> , but the dewpoint temperature is used	Auer's curve MP adjustment with Td using variable precipitation rate
<i>ix</i>	Equation (5) is applied to the radar estimates obtained from procedure <i>v</i>	MP (T on Auer using 2.03) and particle shape (PS) adjustment
<i>x</i>	Equation (5) is applied to the radar estimates obtained from procedure <i>vi</i>	MP (Td on Auer using 2.03) and particle shape (PS) adjustment
<i>xi</i>	Equation (5) is applied to the radar estimates obtained from procedure <i>vii</i>	MP (T on Auer using variable R) and snowflake PS adjustment
<i>xii</i>	Equation (5) is applied to the radar estimates obtained from procedure <i>viii</i>	MP (Td on Auer using variable R) and snowflake PS adjustment
<i>xiii</i>	Observed temperature reduced by 1.5°C for equation (5), applied to radar estimates obtained from procedure <i>v</i>	MP (T, Auer, 2.03) and snowflake PS adjustment shifted by 1.5 °C
<i>xiv</i>	Dewpoint temperature reduced by 1.5°C for eq'n (5), applied to <i>vi</i> result	MP (Td, Auer, 2.03) and snowflake PS adjustment shifted by 1.5 °C
<i>xv</i>	Observed temperature reduced by 1.5°C for eq'n (5), applied to <i>vii</i> estimate	MP (T, Auer, R) and snowflake PS adjustment shifted by 1.5 °C
<i>xvi</i>	Dewpoint temperature reduced by 1.5°C for eq'n (5), applied to <i>viii</i> estimate	MP (Td, Auer, R) and snowflake PS adjustment shifted by 1.5 °C
<i>xvii</i>	all radar estimates closest to the gauge	optimal

TABLE 4-4. Summary of precipitation input data for runoff volume comparison.

source	scenario	specific form	short name	uncorrected	corrected
gauge	-	uncorrected nipher-shielded Belfort gauge	uncorrected gauge	X	
	-	gauge data corrected to DFIR gauge	gauge corrected to DFIR		X
	-	gauge data corrected to "bush" gauge	gauge corrected to "bush"		X
radar	<i>i</i>	raw C-band weather radar images	raw	X	
	<i>ii</i>	radar with variable scaling removed	no scaling		X
	<i>v</i>	no scaling radar with mixed precipitation consideration ( $\alpha = 2.03$ , $\beta = 1.0$ )	mixed precip.		X
	<i>ix</i>	no scaling radar with mixed precipitation ( $\alpha = 2.03$ , $\beta = 1.0$ ) and particle shape considerations	mixed/particle shape		X
	<i>vii</i>	no scaling radar with mixed precipitation consideration ( $\alpha = 2.165$ , $\beta = 1.545$ )	mixed with variable R		X
	<i>xi</i>	no scaling radar with mixed precipitation ( $\alpha = 2.165$ , $\beta = 1.545$ ) and particle shape considerations	mixed/part with variable R		X

#### 4.2.2 Fresh Snow Density

In CLASS\_2.6, the density of fresh snow,  $\rho_s(\text{fresh})$ , was set at a constant value of  $100 \text{ kg/m}^3$ . Since  $\rho_s(\text{fresh})$  varies with the meteorologic conditions through which the snow is falling, the function derived by Hedstrom and Pomeroy (1998), presented in equation (2-2), is used to estimate  $\rho_s(\text{fresh})$  using air temperature. Since Hedstrom and Pomeroy (1998) derived an exponential function, an upper limit of  $\rho_s(\text{fresh})$  equal to  $150 \text{ kg/m}^3$  is used for temperatures greater than  $+1.22 \text{ }^\circ\text{C}$ . At temperatures less than  $-15 \text{ }^\circ\text{C}$ , the function approaches a density of  $68 \text{ kg/m}^3$ . For the Alta function (equation 2-1), the upper limit is also set to  $150 \text{ kg/m}^3$  for temperatures greater than  $+0.12 \text{ }^\circ\text{C}$ , while a lower limit of  $50 \text{ kg/m}^3$  is used for temperatures less than  $-15 \text{ }^\circ\text{C}$ .

Most of the data used by Hedstrom and Pomeroy (1998) are concentrated between temperatures of  $-10 \text{ }^\circ\text{C}$  and warmer, especially the observations by Diamond and Lowry (1953).

There were only five observations by Schmidt and Gluns (1991) below -10 °C, with one observation at -16.6 °C. The Diamond and Lowry (DL) temperatures were taken “immediately prior to” or during the density measurements while the Schmidt and Gluns (SG) temperature measurements were an average over the period of each snowfall event. The time elapsed from the end of each event to the time of the density measurement was not included for either dataset.

To examine the density of fresh snow at lower temperatures, and the variation in temperature during and after a snowfall event, additional observations of fresh snow density were taken as part of this research. The following were measured: snow depth, SWE, air temperature at 15 minute intervals, and the timing of the snowfall event (beginning and end). The snow density is the ratio of SWE to snow depth, and the corresponding temperature was averaged over the length of each snowfall event.

### **4.2.3 Maximum Snowpack Density**

In the CLASS\_2.6 model, the maximum density that a snowpack could achieve was 300 kg/m<sup>3</sup>. This maximum is changed to 250 kg/m<sup>3</sup> for forest, as recommended by Gray and Prowse (1993). Equations (2-6) and (2-7) yield the mean density of a snowpack, and Pomeroy *et al.* (1998) recommended the use of equation (2-7) to determine the maximum density of a deep snowpack (depth > 0.6 m). Since use of equation (2-6) for a shallow snowpack (depth < 0.6 m) yields a density of only 250 kg/m<sup>3</sup> and various research has shown a maximum density between 290 kg/m<sup>3</sup> and 500 kg/m<sup>3</sup> (see section 2.1.5), a maximum of 350 kg/m<sup>3</sup> is selected for shallow snowpacks.

### **4.2.4 Canopy Snowfall Interception**

In comparing the canopy interception of coniferous trees modelled using CLASS\_2.6 to measurements taken in the Canadian Boreal Forest, Pomeroy *et al.* (1998) stated that CLASS\_2.6 underestimated snow interception for snowfall events greater than 3 mm SWE. The model used a linear relationship between snowfall and interception, and a maximum interception was set at 20% of the leaf area index (LAI). For rainfall this may be appropriate, but snow can act as a bridge between branches, and between needles for most coniferous trees. For

broadleaved deciduous trees the winter LAI is less than 10% of the summer LAI, and about 30% of the needleleaved LAI, thus snowfall interception is primarily important to coniferous forests.

Hedstrom and Pomeroy (1998) estimated the intercepted snow ( $I$ ) as follows:

$$I = c_{suc} (I^* - I_o) \left( 1 - e^{-\frac{C_{can} R_s}{I^*}} \right) \quad (4-25),$$

where  $c_{suc}$  is a dimensionless snow unloading coefficient,  $I^*$  is the maximum snow load (in kg/m<sup>2</sup>),  $I_o$  is the initial snow load (in kg/m<sup>2</sup>),  $R_s$  is the snowfall for a unit time (in mm SWE or kg/m<sup>2</sup>), and  $C_{can}$  is the canopy coverage fraction. Pomeroy and Hedstrom (1998) estimated  $c_{suc}$  to be 0.697, and the maximum snow load to be a function of the LAI, a tree species coefficient ( $S_p$ ), and the fresh snow density,  $\rho_s(fresh)$ , as follows:

$$I^* = S_p LAI \left( 0.27 + \frac{46}{\rho_s(fresh)} \right) \quad (4-26).$$

Schmidt and Gluns (1991) suggested values of the tree species coefficient of 6.6 and 5.9 kg/m<sup>2</sup> for spruce and pine, respectively.

To incorporate the snowfall canopy interception model into CLASS\_2.6, the winter moisture storage capacity must be increased from 20% of the LAI. The plots of weekly interception versus weekly snowfall by Hedstrom and Pomeroy (1998) illustrate that on average the maximum interception is 50% of the LAI. Subsequently, equations (4-25) and (4-26) are introduced into the snowfall interception component of CLASS\_2.6.

#### 4.2.5 Redistribution and Transport Sublimation

Although a good understanding of the mechanisms for transport of snow exists, the scale at which these processes occur is much smaller than the watershed grid scale (10 by 10 km). A simplistic form of redistribution was used by Donald (1992) that assumes there is a maximum non-transport limit ( $d_{s,NT\ max}$ ) for open areas, above which all excess snow is transported to forested areas (Figure 4-3). The new snow depth in the forest,  $d_{s,(forest)}$ , is defined as a function



of the open area snow depth,  $d_{s(open)}$ , in excess of  $d_{s-NT\ max}$ , and the ratio of land cover areas:

$$d_{s\ (forest)} = d_{s\ (forest)} + \left[ d_{s\ (open)} - d_{s-NT\ max} \right] \frac{A_{(open)}}{A_{(forest)}} \quad (4-27),$$

where  $A_{(open)}$  is the open area and  $A_{(forest)}$  is the area covered by forest. The snow depth in the open area is set to  $d_{s-NT\ max}$ . Similarly the mass of snow in the forested areas  $SWE_{(forest)}$  can be defined as:

$$SWE_{(forest)} = SWE_{(forest)} + \rho_{s\ (open)} \left[ d_{s\ (open)} - d_{s-NT\ max} \right] \frac{A_{(open)}}{A_{(forest)}} \quad (4-28),$$

where  $\rho_{(open)}$  is the density of the snow being transported. The mass of snow left in the open area can be defined as:

$$SWE_{(open)} = \rho_{s\ (open)} d_{s\ (open)} \quad (4-29).$$

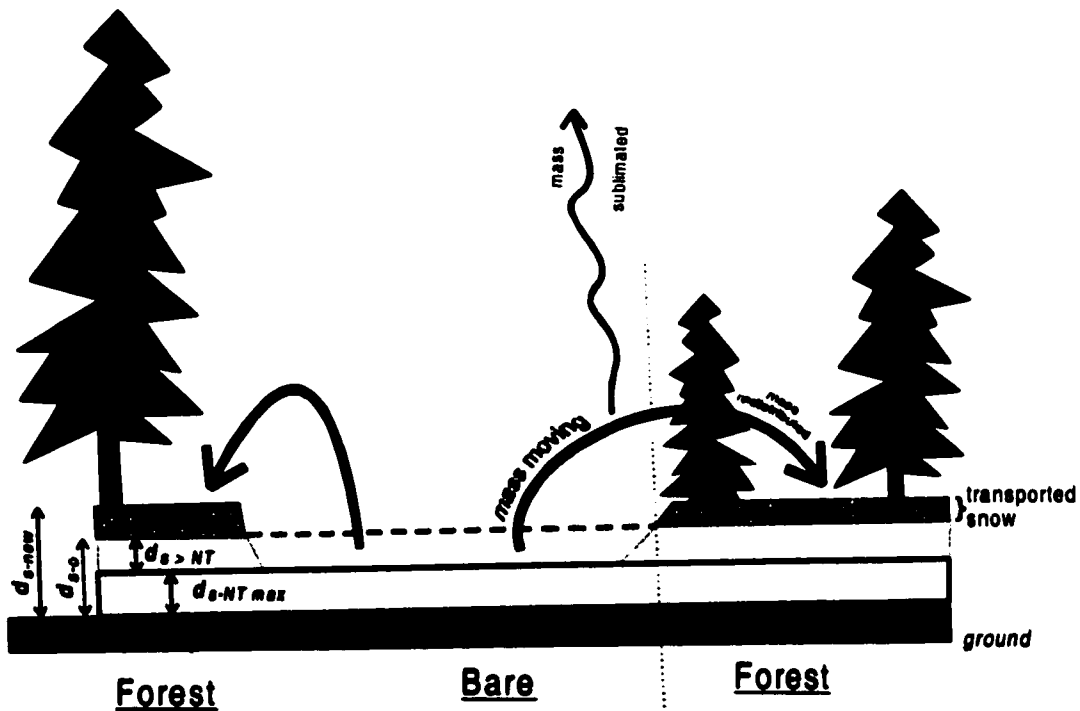


FIGURE 4-3. Schematic of snow redistribution from open areas to forested areas.

A more complex snow redistribution model would consider snowpack characteristics and wind setup potential. Since CLASS\_2.6 only used a single snowpack layer where the mean snowpack density is updated as a function of elapsed time since deposition and the quantity of fresh snow accumulated, the redistribution potential of snow cannot be defined as a function of the age, i.e., density, water content, etc. Blowing snow is typically the movement of fresh snow and not very aged snow, and the initial snow density before blowing will be different than the deposited snow. Fetch length and orientation data were not available, so transport equations (eg., 2-12 and 2-13) could not be used. The parameterized transport equation (2-14) is not applicable as it was derived for a Prairie environment.

To enhance the simple model described above (equations 4-27 through 4-29), a threshold velocity for movement can be assumed to be 5 m/s for falling snow and larger for old snow. A portion of the mass transport can be sublimated (Figure 4-3). Pomeroy and Gray (1995) stated that for different field types in Saskatchewan, over a fetch of 1 km, 15 to 41% of the annual snowfall is lost to sublimation, which was measured to be 1 to 2.6 times the amount of snow transported *by saltation and suspension*. For shorter fetch lengths, the amount blowing snow and transport sublimation is substantially less.

#### 4.2.6 Split State Variables

For each element CLASS\_2.6 used a mosaic of 4 different landcover types, specifically, snow-covered canopy, snow-covered bare ground, snow-free canopy and snow-free bare ground. This was actually just 2 land cover types (canopy and bare ground) under snow-covered and snow-free conditions. To accommodate multiple landcover types, Snelgrove (1996) used multiple subroutine calls for each landcover type, within each grid block. The area of each landcover was known and was used for horizontal flow calculations. Thus the GRU approach was preserved.

The soil properties (temperature, liquid and frozen water content) for each land cover type (snow-covered canopy, snow-covered bare ground, snow-free canopy and snow-free bare ground) were averaged at the end of each time step and these average values were used to initialize the soil properties at the beginning of the following time step. This resulted in a smearing of the soil properties during periods of partial snow-cover, as the warmer temperatures

of the snow-free ground were averaged with the colder ground temperatures below the snow-covered areas, providing additional ground heat for snowmelt.

The disaggregation of the soil properties can be performed external to CLASS\_2.6, such that the snow-covered and snow-free areas for each landcover within each grid cell are considered as individual areas within CLASS\_2.6. This, however, duplicates the call to CLASS\_2.6 by using two columns for each grid cell, and the averaging can be removed. Disaggregation of the soil layer temperatures is a manageable sequence of five steps (see Appendix A.6). However, disaggregation of the soil moisture is in the order of 100 steps. Therefore, to emulate the separation of the soil properties, modelling is performed using the two column approach. Whereas the temperature averaging was removed for one column modelling, the smearing of the temperature is much more important than soil moisture to the smear effect. The saving in computational time, i.e., computer runtime, by using a single column instead of two columns is not enough to justify the effort to remove the averaging of soil moisture.

### **4.3 RESULTS COMPARISON**

This research focusses on improving the radar estimates of winter precipitation and incorporating better representation of winter processes simulated by a physically based hydrologic model, and together the developments are used to improve the peak snowmelt hydrographs.

The results of this research are assessed in terms of snowfall accumulation, the state of the snowpack throughout the winter, and the hydrographs from watersheds of various size. The different radar adjustment schemes are applied to the radar data, and these radar estimates are compared to the winter precipitation quantities that are sampled by several precipitation gauges, in particular, Belfort gauges with Nipher-shields, for different lengths of accumulation. The main assorted radar data adjustment scenarios, i.e., removal of scaling, the occurrence of mixed precipitation, and the variation in snowflake shape, as well as uncorrected and corrected gridded gauge data are used as precipitation input to generate streamflows in order to compare runoff volumes. In investigating the different modelling changes and additions, i.e., the occurrence of mixed precipitation, variable fresh snow and maximum snowpack density, snowfall canopy

interception, redistribution and transport sublimation, and split state soil parameters, the accuracy of the simulated peak flows and timing are assessed. The simulated SWE and snow depths are compared to the snowpack properties measured biweekly at snowcourses to also analyze model improvements. The results are generated from simulating the winter hydrology of five watersheds in central south-western Ontario, with the focus on the upper Grand River basin.

# Chapter 5

## RESULTS AND DISCUSSION

---

*"We will probably come to like snow even less." (Mowat, 1975, p5)*

This chapter describes the use of radar to estimate precipitation over the winter season with an emphasis on the adjustment of the radar data using near surface air temperature, and the implementation of improvements of the snow processes into the CLASS model. The radar data are evaluated using precipitation gauge and radar accumulations, as well as modelled runoff volume comparisons. The validity of the data is discussed in terms of the representativeness, gridding implications, and measurement errors. Next, the effects of modelling improvements on the simulated snowcover and streamflow are discussed. Finally, further considerations for implementation of the data adjustment techniques and model improvements are discussed. This includes comments on the data sources and additional modelling requirements.

### 5.1 RADAR ESTIMATION OF WINTER PRECIPITATION

Monthly radar accumulation estimates of snowfall and winter precipitation can be very similar to the quantities captured by a "bush" gauge, as illustrated at the Wormwood gauge for the month of January 1993 (Figure 5-1). However, this plethograph shows that, although the long term average matches well, accumulation quantities for individual storm events vary considerably. All monthly accumulations at the University of Waterloo (UW) gauges (see Table 3-3 for details) are presented in Appendix C-1. (Temperature data have been included in the plots in Appendix C in order to provide a distinction between rain and snow accumulation estimation using radar data.) The monthly radar-gauge accumulation comparison for the Wormwood site is not always as close as Figure 5-1 illustrates. For example, in February 1994, an event was detected by radar on the 20<sup>th</sup> that was not measured at the gauge (Figure C-1e). The cumulative monthly precipitation for January 1997 at this same site was measured at the

gauge to be 50% more than estimated by the radar (Figure C-1p). At the Euclid site, one event on the 14<sup>th</sup> of March 1997 was 300% more for the gauge than estimated by the radar (Figure C-3b). Resetting of this gauge to correct for observed over-catch yielded improved monthly gauge estimates. While the monthly totals are similar, event discrepancies can also be observed at the Greenoch gauge site (such as Figure C-2d). Since there can be a large difference in the monthly accumulations for various months, a plot of the percentage absolute difference between the raw radar and gauge accumulation over time (Figure 5-2) illustrates that the estimates by the two methods become similar as the length of accumulation increases. It should be noted that while the *y-axis* in Figure 5-2 was limited to a 300% difference, larger differences were observed at shorter accumulation intervals. For the raw radar data, the estimates of accumulated precipitation improved as the length of accumulation increased. The comparison of the radar and gauge winter precipitation estimates for seasonal, monthly, and weekly accumulation intervals is presented in the next section.

### 5.1.1 Winter Precipitation Accumulation

For the comparison between radar and gauge winter precipitation accumulation, the three UW gauges were used, due in part to the location across the study domain, the accessibility to the data, and the setting of the gauges. Since these gauges were located in “bush” gauge type settings, it was assumed that the data collected were very representative of the amount of precipitation that actually fell. Hence the gauge data were not corrected to consider wind undercatchment, unlike the AES gauge data. The gauges were operated for varying periods, up to five years (see Table 3-3), and the comparison to radar considered weekly, monthly and seasonal accumulation periods. The seasonal accumulation period spanned up to four months.

To investigate the improvements in the radar accumulation estimates by the various adjustments, two regression lines were fitted to the seasonal and monthly data, with the second line also fit to the weekly data. The first regression is the line “best fit” through the data that is a standard product form most statistical software and analyses. The slope, the *y-intercept*, the standard error of estimate (SEE) and the coefficient of determination ( $r^2$ ) have been calculated for this line. However, since the radar adjustments are used to improve the snowfall estimates

to approach the observed gauge accumulations, a line with slope of one through the origin, i.e., a “1:1 line” between the x and y axes, has also been fit to the data. The mean difference, SEE and population determination coefficient (unbiased  $r^2$  or  $\rho^2$ ) have been computed for the 1:1 line.

The statistics of the first line (Table 5-1) can be used to illustrate a general trend in the data. The seasonal approximations of snowfall accumulation using radar matches the gauge estimates well, except underestimation for the highest accumulation season. The six main radar datasets have been plotted versus the gauge estimates for seasonal accumulations in Figures 5-3a through 5-3f. These six datasets were chosen from the 17 scenarios, summarized in Table 3.3, since they represent fundamentally different radar datasets. All other scenarios are similar to one of the six “main” radar datasets. The best adjustment procedure is scenario v, the adjustment for mixed precipitation using the observed air temperature with Auer’s curve and a constant rainfall factor of 2.03. The improvement of the radar accumulations for the different time periods is minimal by the subsequent adjustment to consider snow crystal particle shape.

#### *5.1.1a Raw Radar*

One season is overestimated by almost 100% and another is underestimated by more than 30% for the raw radar (Figure 5-3a), which corresponds to a small slope, a high SEE and a small  $r^2$  value for the best fit line (Table 5-1, scenario i). Similarly, the SEE is large and the  $\rho^2$  value is small for the seasonal raw radar 1:1 line (Table 5-2).

For the monthly estimates, there is a larger variation between the raw and gauge accumulations (Figure 5-4a), and the best fit line has a large y-intercept, a small slope and a small  $r^2$  value. While the mean difference is small, the SEE observed for the 1:1 line is large and the  $\rho^2$  value implies almost no relationship; there is a large amount of scatter.

The scatter observed for the monthly accumulations continues to increase for the shorter weekly accumulation comparison (Figure 5-5a). The SEE of the 1:1 line doubles over the monthly comparison while the  $\rho^2$  value is similar.

The raw radar estimates for the three accumulation periods are used as a reference for which to assess the adjustment schemes. Only for the seasonal comparison does the raw radar begin to estimate adequate snowfall accumulations, as compared to the precipitation gauge

estimates. It should be noted however that there are only 8 season-gauge comparisons.

### ***5.1.1b Scaling Removed Radar***

The removal of scaling reduces the large overestimation from the raw radar, but results in underestimation for one season at one gauge (Figure 5-3b); while the slope of the best fit line is the same as for the raw radar, the y-intercept and the SEE decrease whereas  $r^2$  increases substantially. The underestimation is illustrated by the negative mean difference, based on the 1:1 line, with a doubling of the  $\rho^2$  value, and almost a 50% reduction in the SEE.

Similarly for the monthly scaling removed radar estimates, there are more months underestimated than overestimated, as illustrated by the negative mean difference from the 1:1 line, as represented above. The  $\rho^2$  value increases substantially from the raw radar, and the  $r^2$  and SEE values for the best fit line illustrate the best relationship of all radar datasets. However, the slope of this line is 40% less than unity. For an accumulation period of a week, the SEE becomes less, yet the snowfall is generally underestimated using only scaling removal from the raw radar data.

The removal of scaling from the radar images reduces the overestimation during several months. Forced overscaling occurred primarily in the months of December 1994, January 1995 and March 1995. Intermittent clutter was observed in the area of the Toronto downtown, often in the order of 30 mm/h. This forced the scale to increase to 2 mm increments. Since the hourly accumulation in the southern Ontario study region is rarely larger than 10 mm/h, the radar image scale should not be allowed to exceed 13.5 mm/h during the winter. This scaling issue appears to have been corrected after the winter of 1995.

### ***5.1.1c Mixed Precipitation Adjustment***

Six different forms of the mixed precipitation algorithm (scenarios *iii* through *viii*) were applied to the scaling-removed radar data: a linear approximation of the Auer curve with the constant rainfall factor; the Auer curve with the constant rain factor; and the Auer curve with variable precipitation rate factor, in each case using both the air temperature and dewpoint temperature. As can be expected, implementation of each of the six scenarios increased the radar precipitation



estimates for all seasonal accumulations since each winter southern Ontario experiences some mixed precipitation and some rain. Graphical examples of the seasonal accumulation comparisons for the Auer curve with the constant (scenario *v*) and variable (scenario *vii*) rainfall factor using the air temperature are illustrated in Figures 5-3c and 5-3d, respectively. For the best fit line, the slope typically increases, yet so does the y-intercept. With the exception of scenario *vii*, presented in Figure 5-3d, the coefficient of determination increases over the scaling removed scenario. However, the standard error of the estimate is only decreased for the dewpoint - constant rainfall factor (scenario *vi*) adjustment, which corresponds to the maximum  $r^2$ . This improvement is partially a result of the decrease in the number of datapoints from 8 seasonal accumulations to 7, since there were no humidity data for the Euclid gauge for its one season of operation. The greatest  $r^2$  value for the best fit line is from the dewpoint temperature adjustment with the constant factor (scenario *vi*). However, the slope is 9% less and the y-intercept is greater than using the observed temperature (scenario *v*). This corresponds to the greatest 1:1 line  $\rho^2$  value and the smallest SEE. The mean differences were smaller than for the scaling removed dataset. However these mean differences became positive. The  $\rho^2$  value decreased for all considerations of the mixed precipitation. Use of the dewpoint temperature yielded lesser  $\rho^2$  values than use of the observed air temperature, as above due in part to the smaller number of accumulation seasons.

The monthly accumulations plots (Figure 5-4c and 5-4d) present more scatter than the scaling removed plot (Figure 5-4b), yet the plots are more around the 1:1 line, as many of the monthly radar estimates have increased in magnitude. There is more scatter for the variable rainfall factor mixed precipitation adjustment (scenarios *vii* and *viii*), especially for two specific months of significantly more than the scaling removed accumulation (January of 1993 and 1996 at Wormwood). (It should be noted that January 1995 was a problematic month, even after the removal of scaling.) This significant radar overestimation of these two months is illustrated by the smaller coefficient of determination for the variable rainfall factor adjustment in comparison to use of the constant factor. The greatest  $r^2$  values for the best fit line and 1:1 line are from the observed temperature adjustment with the constant factor (scenario *v*). The accumulations from scenario *iii* are very similar to those of scenario *v*, as illustrated by the 1:1 line statistics, since

the linear representation approximates the smoothed Auer curve. The best fit line slopes for all monthly mixed precipitation accumulations are all very similar (0.67 to 0.71), yet there is disparity in the mean difference and SEE based on the 1:1 line.

On a weekly accumulation basis, the coefficient of determination is larger using the variable rainfall factor, but the mean difference and SEE are both less for the constant rainfall factor (Figure 5-5c and 5-5d). When the variable rainfall factor (scenario *vii*) is used to adjust the scaling-removed radar data, there are several weekly accumulations that become highly overestimated, in comparison to use of the constant rainfall factor (scenario *v*). This corresponds to the two months that became overestimated in Figure 5-4d.

The greatest outliers in the weekly dataset are two radar accumulations overestimates from the variable rainfall factor mixed precipitation adjustments (Figure 5-5d). One overestimate is the first week of January, 1993 (Figure 5-1) that included a large rain event. The gauge accumulation was 47.8 mm/week, the scaling-removed radar accumulation was 48.7 mm/week, the constant rainfall factor adjustment increased this to 78.4 mm/week, while the variable rainfall factor increased the accumulation to 111.0 mm/week. Although the gauge was in a 'bush' setting, a Nipher shield is still required for adequate catch of solid precipitation and one was not installed until the second week of January. This may have resulted in an underestimation of the gauge precipitation. The other large overestimation was the third week of January, 1996 (Figure C-11). The gauge accumulation was 34.9 mm/week, the scaling removed radar accumulation was 32.7 mm/week, the constant rainfall factor adjustment increased this to 58.9 mm/week, while the variable rainfall factor increased the accumulation to 89.5 mm/week. These two overestimation are a result of the mixed precipitation adjustment, especially using the variable rainfall factor since large hourly radar estimates were observed during periods of above freezing temperatures (on January 4, 1993 and January 16-18, 1996). The adjustments are based on the probability of snow at a particular temperature, and at any particular instance in time it is likely either snowing or raining, or some form thereof, such as ice pellets, but not both (Donaldson, 1999, pers. comm.). The state of precipitation is not necessarily constant for beyond one point in time and space. Specifically, from one location to another, as well as from minute to minute, the type and phase of falling precipitation can change. Therefore, it is quite possible that snow occurred

throughout the January 16-18, 1996 precipitation events, and that consideration of mixed precipitation was not necessary. However, without specific storm observations, it is difficult at present to determine the phase of particles that fell.

The adjustment of the radar images for above freezing temperatures used in this research is an attempt to consider the radar signal variability caused by mixed precipitation. The use of a linear approximation of Auer's curve produces radar estimates that are very similar to those derived from the polynomial representation. (In this case, a lookup table could also be used.) However, unless computational constraints deem that the simpler representation must be used, it is recommended that the polynomial approximation of Auer's curve be used to adjust radar data to consider mixed precipitation. If another probability-of-snow curve is more suitable for a particular location (eg. Rohrer, 1989 or US Army Corps of Engineers, 1956), such a curve should be used in place of the Auer curve.

A constant factor of 2.03 and a variable factor based on the precipitation rate have both been applied to the scaling removed radar dataset to provide adjustments for mixed precipitation. Theoretically the above freezing temperature adjustment of the radar images should use the precipitation rate to determine the adjustment factor for any rainfall present. However, the application of a constant rainfall factor of 2.03 has been seen to produce better estimates than the variable factor which yields greater variability in the accumulations. While the variable rainfall adjustment factor significantly increases the radar estimates for precipitation rates larger than 1.5 mm/h, the majority of the observed precipitation in this study was less than or equal to 1.5 mm/h (Figure 5-6). (The modal points at 0.1, 0.5 and 1.0 mm/h in Figure 5-6 exist since the radar images have a minimum increment of 0.5 mm/h, and for each gauge the weighted average of the pixel at the gauge location and the eight neighbouring pixels. Thus the first modal point occurs when one or two of the neighbour pixels observe precipitation, yet there is no precipitation at the centroid pixel. The second modal point is the occurrence of precipitation of 0.5 mm/h at most pixels, including the centroid. Similarly, the third modal point is 1.0 mm/h precipitation at most or all pixels.) The average precipitation rate was 0.505 mm/h for the scaling removed dataset. When the summer *Z-R* coefficients were used on this dataset an average rate of 0.939 mm/h was derived. For the variable rainfall factor to be equal to 2.03, a

precipitation rate of 0.889 mm/h is required for use in equation (4-20), i.e.,  $2.165 R_w^{1.545}$  is equal to  $2.03 R_w^{1.0}$  when  $R_w$  is equal to 0.889. While the observed average precipitation rate is less than 0.889 mm/h, it is the extreme precipitation that causes the significant over-correction and hence skews the radar estimates. Therefore, the use of a constant rainfall-adjustment factor of 2.03 yields better accumulation estimates than use of the precipitation rate to determine the rainfall adjustment factor. As well, the ratio of the refractive/absorptive property (equation 2-25) of rain to snow is in the order of 4, which is close to the original ratio of 4.06 that was subsequently divided by 2 to yield the constant rainfall-adjustment factor of 2.03.

To combine the two methods, such that the variable factor approach is used up to maximum rainfall adjustment factor of 2.03, could yield better results than use of each individually. This combined method could address any over-saturation problems that may occur at higher reflectivities. This method has been applied to the seasonal, monthly, and weekly data, as illustrated in Figures 5-7a, b, and c, respectively (scenario *xviii* in Table 5-3). While the standard error does not improve and the  $\rho^2$  values decrease compared to the use of the 2.03 factor, the mean difference does decrease by almost 50%, and the  $\rho^2$  values are larger than for the variable factor. Overall the combined mixed precipitation factors yields an underestimation of radar snowfall accumulation compared to gauge accumulation.

#### ***5.1.1d Particle Shape Adjustment***

The particle shape adjustment has been applied to the scaling removed radar data after these data were adjusted to consider the occurrence of rain and mixed precipitation while the winter *Z-R* coefficients were in use. The four particle shape adjustment scenarios (*ix* to *xii*) all used the same scheme, i.e., equation (4-24), and built upon the four different Auer's curve mixed precipitation scenarios (*v* to *viii*), specifically to consider the combinations of a constant and a variable rainfall factor plus observed and dewpoint temperature.

Application of the particle shape adjustment provides a small improvement of radar estimates over the associated mixed precipitation adjusted estimates. For the seasonal accumulations, only scenario *x* (particle shape on mixed precipitation using the dewpoint temperature with a constant rainfall factor) resulted in a statistical improvement. While the  $\rho^2$

value and the SEE of the best fit line decreased and increased, respectively (Table 5-1), the slope of this line increased and the y-intercept decreased. Considering the 1:1 line, the  $\rho^2$  value increased substantially as the mean difference became 40% less (Table 5-2). The reference scenarios ( $ix$  and  $xi$ ) were very similar to the corresponding accumulation estimates with consideration of the particle shape (Figure 5-3e vs. 5-3c and 5-3f vs. 5-3d).

The monthly snowfall accumulation estimate from the adjusted radar show the same trends as the seasonal approximations (Figure 5-4e vs. 5-4c and 5-4f vs. 5-4d); the estimates are improved only for scenario  $x$ . The SEE of the best fit line decreases and the  $r^2$  value increases (Table 5-1). More significantly, the mean difference of the 1:1 line decreases by almost 50% while the coefficient of determination increases by 17% (Table 5-2). However, the largest  $\rho^2$  value and smallest SEE is for scenario  $ix$ , which corresponds to the best mixed precipitation adjustment scenario of a constant rainfall factor using the observed air temperature (scenario  $v$ ).

As for the seasonal and monthly particle shape adjusted accumulation estimates, the weekly approximations are very similar to the corresponding mixed precipitation adjusted radar data (Figure 5-5e vs. 5-5c and 5-5f vs. 5-5d). The coefficients of determination increase by 5 and 2.6% for scenarios  $ix$  and  $xi$ , respectively (Table 5-2), while the mean differences increase by 17 and 7%. For a weekly length of accumulation, the difference between using the constant or variable rainfall factor for mixed precipitation, prior to particle shape adjustment, is minimal. Either resultant scenario is statistically the same based on the 1:1 line.

Two large radar underestimates were corrected using the mixed precipitation adjustment, while another was not corrected using either adjustment. The largest gauge estimate occurred during the third week of February, 1997 and was 72.0 mm/week (Figure C-1q). The corresponding scaling removed radar estimate was 30.4 mm/week. This increased to 43.8 and 46.4 mm/week for the mixed precipitation (both constant and variable factor) and particle shape adjustments, respectively. As can be expected, this large measured accumulation was similar at the Euclid site for the same period with  $R_{gauge} = 52.9$ ,  $R_{scaling\ removed} = 27.4$ ,  $R_{mixed\ (constant)} = 47.9$ ,  $R_{mixed\ (constant)\ \rightarrow\ particle\ shape} = 47.1$  mm/week (Figure C-3a). The air temperature was above freezing at both sites for the precipitation event, and the mixed precipitation adjustment improved both weekly estimates. Conversely, neither of the two adjustment methods improved the radar

underestimate of the third week in February at the Greenoch gauge (Figure C-2a). The gauge accumulation for the week was 53.1 mm, while the scaling removed radar estimate was only 8.9 mm. Since the air temperature when there was radar detection of precipitation was usually between -1 and +2°C, the radar adjustment procedures yielded little difference from the scaling removed estimates. Specifically, the mixed precipitation adjustment resulted in 9.5 mm/week for the constant rainfall factor (9.7 mm/week using the variable factor) and 9.2 mm/week for the subsequent particle shape adjustment (9.4 mm/week based on the variable factor mixed precipitation). A detailed examination of the gauge accumulations illustrates that 34.5 mm was measured between 15:00 LST on the 18<sup>th</sup> of February, 1995 and 15:00 on the 20<sup>th</sup>, while only 0.25 mm was sampled by the radar during this same period.. The time series of gauge accumulations was 7 mm over the first day, 12 mm over the next 8 hours, no precipitation for 12 hours, followed by 5, 15, 0, and 4.5 mm/h for the last four hours. While each of these snowfall quantities is possible, no precipitation was observed at the Wormwood site (gauge or radar) during this period, and storm events typically have a large area that results in accumulation at Wormwood and Greenoch (eg. Figure C-1j vs. C-2b). The snowfall in the Greenoch area can be very banded, and there can be large accumulation differences between Greenoch and Wormwood, however, the Greenoch gauge may not have measured the precipitation rate accurately especially the last 4 hours of the event during which time 24.5 mm of precipitation were measured. It is possible that bridging occurred at the mouth of the gauge a sudden release occurred.

Since the relative humidity is usually less than 100%, the observed air temperatures are warmer than the dewpoint temperatures and hence the Auer mixed precipitation adjustment will yield larger radar accumulation estimates. To build upon the mixed precipitation adjustment with variable factor to a maximum of 2.03 (scenario *xviii* described above), used to limit the precipitation accumulation increase and to consider the improvements from the particle shape adjustment using the dewpoint temperature, a new scenario (*xix*) combines these two adjustment procedures. Use of the dewpoint temperature to estimate the particle shape usually results in a temperature less than observed, which provides a small lapse rate based on the vapour pressure deficit. The resultant seasonal, monthly, and weekly accumulations are presented in Figures 5-

8a, 5-8b, and 5-8c, respectively (scenario *xix* in Table 5-3). While the fitting statistics (SEE and  $\rho^2$ ) have become less favourable, the mean differences decrease (Table 5-3 *xviii* vs. *xix*). This is seen since the relative humidity was not measured at the Euclid site. Hence there are one, two and six less data points for the seasonal, monthly, and weekly statistics, respectively. Overall there is no significant improvement when the dewpoint temperature particle shape adjustment is applied to the 'limited' mixed precipitation adjustment.

To illustrate the applicability of the particle shape adjustment curve, the temperature distributions for five months each when the radar precipitation estimates were larger (entitled OVER) and smaller (entitled UNDER) than the gauge estimates were plotted on the same graph (Figure 5-9a). For temperatures between -1 and -5°C, there is a greater occurrence of temperatures for the months of UNDER estimation by the radar, and conversely at lower temperatures there is a lesser probability of occurrence of radar UNDER estimation. When the difference between the radar OVER estimation temperatures and the radar UNDER estimation temperatures was plotted (Figure 5-9b), this difference is the inverse of the weighted snow particle shape adjustment curve (see Figure 4-3c). Therefore, from these monthly temperature data, the particle shape curve appears to be able to improve the radar accumulation estimates. It should be noted that while the temperatures used to calculate the OVER and UNDER distributions were for the entire five months for each distribution, it is assumed that the temperature distribution during periods of precipitation is a subset of the all recorded temperatures during the same periods. It is possible that the lack of significant improvement using the particle shape curve over the mixed precipitation adjustment is due to the misrepresentation of the entire temperature datasets as an indicator of the temperature distribution while there is precipitation.

Particle shape is a difficult parameter to estimate, especially considering the size of an individual particle in comparison to the quantity of snow crystals scanned by a radar swath or captured by a gauge. The particle shape curve provides a relative measure of the surface area of various flakes forming at different temperatures. Similar to the transient nature of mixed precipitation in terms of short term variability, the type of snow crystals that can be observed within an hour, i.e., shape, can vary substantially. As well, riming, aggregation, and sublimation

can alter the shape and surface area of falling snow. These changes can occur above and below a radar beam used to quantify precipitation. Future research needs to quantify the particle shape curve based on specific surface area estimates of different snowflakes, as well as their relationship with temperature. The work of Ohtake and Henmi (1970) can be expanded to develop Z-R relationships for different temperature and include observations of particle shape. Another approach is further discretization of the particle shapes beyond those defined by Ohtake and Henmi (1970).

Polarized radar may be useful to identify different snow particle shapes (an extension of work such as Ryzhkov and Zrnich, 1998). For example, by identifying various particle characteristics, the Z-R relationship could be altered. However, this research focuses on post-processing adjustments, and not the refinement of Z-R relationships.

#### ***5.1.1e Additional Adjustment Variations***

To consider the temperature difference between the height of particle formation and the surface where the air temperature is measured, various lapse rates were considered to shift the particle shape curve, ranging from -3 to +8°C/km. The best single lapse rate of +1.5°C/km was chosen to yield the smallest mean difference for the 1:1 line (scenarios *xiii* through *xvi* in Table 5-2). However, the shifted particle shape adjustment curve does not provide substantially improved radar accumulations, as the SEE and  $\rho^2$  are both very similar for the shifted and unshifted accumulations. The curve is intended to consider a small lapse rate between clouds and the near surface, yet if the lapse rate is not close to zero, it likely varies as a function of the type of precipitation event, as well as from storm to storm. Further investigation is required.

The optimal radar scenario (*xvii* at the bottom of Tables 5-1 and 5-2) is the set of individual seasonal and monthly accumulations that are closest to the gauge accumulation estimates. However, it is not feasible to select the best fitting data *a priori* for each accumulation period. It is appropriate to use one of the unsupervised adjustments to improve the radar estimate of winter precipitation. From the accumulation statistics, such an adjustment would be scenario *v*, *ix*, or *xiii* (see Table 3-3).



**5.1.1f Summary of Winter Precipitation Accumulation**

The seasonal underestimation in Figure 5-3b and overestimation for the mid-range accumulations in Figures 5-3c through 5-3f are statistically illustrated by slopes that are 30 to 40% less than unity and y-intercepts between 56 and 104 mm. For shorter time periods of approximately one month (see Figures 5-4a through 5-4f), the general trend is overestimation for smaller accumulations (up to 60 mm per month), and underestimation for larger accumulations, especially for scenario *ii* (Figure 5-4b). The slopes and y-intercepts for all the monthly adjusted data are very similar ( $0.695 \pm 0.025$  and  $22.6 \pm 1.3$ , respectively) and show the same trend as the seasonal data. Similarly, the weekly snowfall totals more than 30 mm are also underestimated (see Figures 5-5a through 5-5f).

Since the monthly data is a subset of the seasonal data, the most appropriate radar adjustment procedures are the same for the seasonal and monthly accumulation comparison, specifically the three modifications that use observed air temperature with the constant rainfall factor (scenarios *v*, *ix*, and *xiii*). For weekly accumulations, there is more scatter with the temperature adjusted radar estimates than for the 'scaling removed' estimate, however, the underestimates are improved using the constant factor for rain adjustment. While improving the  $\rho^2$  value, use of the variable rainfall factor produces more scatter in the data, as seen by the increased SEE.

The deviations from the gauge accumulation estimates vary with length of accumulation, and the largest differences are the raw radar estimates. For several specific months, the raw radar overestimates gauge accumulation by more than a factor of 2, whereas other months are underestimated by a factor of 2, as illustrated in Figure 5-4a. These differences are reduced for seasonal accumulations (Figure 5-3a), but are still significant. For all scenarios, including the raw radar estimates, the difference between the gauge collection and the radar estimate decreases as the length of the accumulation increases. The improved radar estimates with time are also illustrated by the decrease in the standard error of estimate, which is expected. The best procedure is adjustment for mixed precipitation using the observed air temperature with Auer's curve (scenario *v*). Subsequent adjustment for particle shape does not significantly improve the radar accumulation estimates in comparison to gauge accumulations.

Since snowfall accumulation typically occurs over several months, the next step is to use radar as precipitation input to hydrologic models. Snow accumulation can be integrated across a watershed through hydrograph simulation, and coupled with continuous winter modelling, radar can provide a basin wide improvement over the use of gauge precipitation data.

### **5.1.2 Runoff Comparison**

At each of the eight hydrometric gauges in the Upper Grand River (Table 3-5), for the five winter seasons between 1993 and 1997, streamflow was simulated using the three gauge and six radar datasets (Table 4-4) as the precipitation input to the WAT\_CLS3 model. The simulated runoff volumes and seasonal peak flow over the winter were compared to the observed volumes and flows to present a measure of adequacy of the various datasets and to illustrate seasonal trends. While there are errors associated with the measured hydrographs, especially during the winter periods, the observed hydrographs will be assumed correct. Water Survey of Canada assumes that observed hydrographs are accurate to within 10%, and typically are within 5%.

The observed streamflows at the eight stations within the Upper Grand River basin can be compared to the simulated hydrographs derived from gauge and radar precipitation inputs. The observed streamflows were measured by the Grand River Conservation Authority and Water Survey of Canada and are archived on the HYDAT CD-ROM (Environment Canada, 1997). A sample hydrograph comparison for December 1993 to April 1994 on the Grand River at Galt (gauge 02GA003) is presented in Figures 5-10a through 5-10i. The increased flows at the end of January and mid-February are not simulated well from any of the precipitation modelling inputs (uncorrected gauge, DFIR gauge, "bush" gauge, raw radar or radar adjusted for mixed precipitation and particle shape). Correction of gauge precipitation for wind under-catch improved the estimation of the first peak snowmelt flow in late March, but the subsequent peaks are all still underestimated. For this location and year, the volume of spring meltwater is better estimated using the radar precipitation than the corrected gauge precipitation. Use of the adjusted radar precipitation improved the modelling of the initial snowmelt peak (Figure 5-10e) as compared to the streamflow overestimation by the raw radar (Figure 5-10d).

The observed five winter peak flows at each gauge are compared to the modelled peak

flows for the different modelling inputs in Figures 5-11a through 5-11i. The uncorrected and corrected (DFIR and “bush”) gauge precipitation inputs underestimate the peak flow for most winters at most gauges (Figures 5-11a, b, and c), while there are similar results from all the different radar datasets. The largest overestimate of streamflow results from using the raw radar. Slightly improved flows result from use of the radar adjusted for mixed precipitation using the variable rainfall factor (Figure 5-11h) and from the subsequent adjustment for particle shape (Figure 5-11i).

Statistics that accompany the computed versus observed peak flows are presented in Table 5-4. (While Figures 5-11a through 5-11i are presented as log-log plots to illustrate the trends, the statistics were computed using the normal data). For the best fit line through the origin, the best correlation occurred for the uncorrected gauge precipitation, followed by the two corrected gauge precipitation scenarios. However, these correlations correspond to slopes that are 34.6, 22 and 23.2% less than the optimal slope of unity. The best fit slopes for all the radar datasets are closer to unity. Using a best fit line through the origin with a slope of unity, the correlation for the peak flows generated from the two corrected gauge precipitation scenarios is only slightly less than the mixed precipitation and mixed precipitation with particle morphology considerations (constant rainfall factor). The peak flows from the two corrected gauge precipitation simulations are clustered below the 1:1 line, while the peaks from the two ‘constant R’ simulations are above the 1:1 line. On average, modelling using the no scaling radar scenario yields the peak flows closest to the observed. The computed peak flows are an integration of the WAT\_CLS3 model, however, the total seasonal runoff volumes are a better indication of the adequacy of precipitation dataset. WATFLOOD modelling of the Mackenzie River basin has shown that the model does not store significant quantities of water over a year, as illustrated in the four year water balance plot (Figure 5-12a). For Southern Ontario, WAT\_CLS3 modelling for a four year period (Figure 5-12b) illustrates a better closure of the water balance for this case. Hence almost all precipitation is converted into evapotranspiration or runoff, and seasonal ground water storage does not change, only the state of the storage.

The two sample cumulative runoff volumes presented in Figures 5-13a and 5-13b for the 1993 winter on the Eramosa River above Guelph and for the 1996 winter on the Speed River at

Armstrong Mills, illustrate that the different radar datasets yield similar total runoff volumes that are double the flow volumes modelled using the gauge precipitation input. In 1993, the primary difference between the three radar datasets resulted from a rain-on-ice event that occurred in early January. Similarly, a mid-January 1996 melt event caused the main difference in the runoff volumes modelled with the radar datasets.

The winter season runoff volumes for eight stations using the three gauge precipitation and six radar products are summarized in Table 5-5a through 5-5e for the five winters. For all years and at all streamflow stations, hydrologic modelling with the uncorrected gauge precipitation underestimates flow in comparison to observed flow. The same holds true for the corrected gauge precipitation data, with the exception of the winter of 1995 where the DFIR and "bush" gauge precipitation yielded 8 to 10% more water than observed (Table 5-6).

The various radar adjustment schemes provide improved flow estimates. However, significant seasonal variation exists. For 1993, the computed runoff volumes are 8 to 28% less than the observed flows, partly due to underestimation of the early January storm event. The 1994 and 1996 runoff volumes are overestimated by an average of 18 and 19%, with a range of 7 to 40% and 1 to 50% respectively. The Grand River streamflow stations at Galt and near West Montrose were underestimated for 1994 and 1996. There was, on average, a 70% overestimation of runoff volumes in 1995. The computed 1997 streamflows were less than half of the observed flows. Fassnacht *et al.* (1998) and Hollingsworth (pers. comm., 1999) also saw significant radar snowfall underestimation in 1997.

The volume and the peak flows of the 1995 winter hydrograph are significantly overestimated, with the exception of the Grand River at Marsville (02GA014) and the Speed River at Armstrong Mills (02GA040) using the radar adjustment for mixed precipitation with the variable rainfall factor. These overestimates correspond to the January 1995 overestimates observed for the gauge accumulations. The source of these overestimates is unknown. Hollingsworth (pers. comm., 1999) stated that various lake effect events occurred in Michigan in 1995, and that the radar significantly overestimated snowfall quantities.

As the different adjustment algorithms were applied to the radar data, the simulated runoff volumes more closely approached the observed streamflows. The percent differences for

the individual years and the total differences are summarized in Table 5-6. On average the radar provided good estimates of winter precipitation for use in hydrologic modelling. Over the five winter seasons at the eight streamflow locations, the runoff volume from six different radar datasets was 1.53% less than observed. The differences ranged from 14.7% less total runoff volume for the mixed precipitation with variable rainfall factor and particle shape radar adjustments to 10.5% more for the mixed precipitation with constant rainfall factor and particle shape adjustments to the raw images. Runoff volumes and peak flows are modelled best at the mouth of the entire basin on the Grand River at Galt and for the Speed River at Armstrong Mills.

The Grand River is regulated by three reservoirs: Conestogo Lake, Guelph Lake, and Lake Belwood. Operation of these reservoirs alters the streamflow on the Grand River at Galt and near West Montrose, and on the Speed River below Guelph. Reservoir release data were available for 1993. However these data were sparse for the subsequent years and modelled streamflow may have been underestimated due to a lack of reservoir release data at the three aforementioned gauging sites.

When uncorrected meteorological gauge data are used as precipitation input for hydrological modelling, the resultant modelled streamflow is approximately one-half of the observed streamflow, with the exception of 1995. Runoff volume estimates from the corrected gauge data are 17.6 and 22.2% improved over simulations with the uncorrected data, yet the DFIR and "bush" gauge precipitation yielded 37.5 and 35.1% less runoff than observed. Gauge correction did not yield more water since the three precipitation gauges operated by the University of Waterloo (UW) were situated as to resemble "bush" gauges, and hence were not corrected.

There may be some errors in the meteorological gauge precipitation data; but the gridding of the gauge data using the inverse square distance method smears storm events that approach the study watershed. This is important since the two gauges located within the basin are not operated continuously; one gauge was operated only for part of one winter season and the other gauge is maintained only during business hours (8:00 EST to 17:00 EST). Precipitation events tend to approach the watershed from the west (lake effect storms) or the south-west (jet stream storms), and the gridding of the gauge precipitation data does not observe actual storm

movement while radar data tends to preserve the shape of storm events. While there are problems inherent with the gridding technique used to develop the areal precipitation estimates using a limited number of precipitation gauges, it is doubtful that an alternate gridding technique or the inclusion of more station data will improve the runoff volumes by the deficit 35%. Use of precipitation estimates from additional gauges should nevertheless improve the shape of the storm events and provided gridded precipitation data more closely resembling the pattern illustrated in radar images.

### **5.1.3 Radar Data Assessment**

There are problems with the raw radar estimates of precipitation during the winter. The scaling issue is likely local to the King City Radar, but nevertheless is a potential source of overestimation. For the precipitation accumulation comparison the adjustment for mixed precipitation using a constant rainfall factor with Auer's curve provided the best radar estimation. For the runoff volumes, it is more difficult to chose a best radar dataset: even the raw radar dataset provided decent streamflow volume estimates for certain years. Radar estimates do however provided better estimates of precipitation input to WAT\_CLS3 than gridded gauge data. Use of variable rainfall factor for the adjustment of mixed precipitation does not improve the snowfall accumulation estimates over the use of constant-rainfall factor; the modelled streamflow volumes are underestimated by using the variable-rainfall factor. To refine the adjustments, a site specific probability of snow curve should be derived as a function of air temperature and the local lapse rate between particle formation height and surface air temperature should be examined. Similarly the applicability of the particle shape adjustment factor and the variability of the surface area to mass ratio as a function of crystal formation temperature should be investigated.

In nature, the change in temperature and the variation in particle characteristics during periods of transitional precipitation is quite rapid (eg. Stewart and King 1987). Since the temperature data used to tune the radar images were hourly averages, future research into mixed precipitation temperature adjustment must consider the sub-hourly variations, and must be applied differentially across the region. While at any particular instance in time it is likely either

snowing or raining, or some form thereof, such as ice pellets, but not both (Donaldson, 1999, pers. comm.), the state of precipitation is not necessarily constant for beyond one point in time and space. Specifically, from one location to another, as well as from minute to minute, the type and phase of falling precipitation can change. Therefore using the hourly average temperature is an indicator of the variety of particles that may have fallen in an hour.

The radar product used in this research was developed in 1992, and hence is seven years old. However, it was not until 1999 that Doppler and a new conventional scan products were available from the King City Radar, and in future from other Canadian Radar installations (Environment Canada, 1998b). The improvements presented in this research can be applied to new data. It should be noted that Scott (1999, pers. comm.) stated that the all operating parameters for the King City Radar have been altered between 1993 and 1999. The impact of the changes on the computed hydrographs is unknown and the future alterations should be well documented.

A description of the ideal adjustment procedure follows. With the increased computational and data transmission speeds, the 10 minute CAPPIs have now become available. The CAPPIs are now available as precipitation from use of both the rain and snow Z-R coefficients. Recalling that the rain CAPPI is taken at a height of 1.5 km and the snow CAPPI at a height of 1 km, the CAPPI data for each pixel (currently 1 by 1 km) can be adjusted using gridded temperature data. Since the AES temperature data are archived as hourly averages, the 10 minute temperatures can be linearly interpolated. This should pose minimal problems as the hourly variation in temperature is typically small. Computed temperature data with greater temporal resolution, such as from numerical weather models (eg. MC<sup>2</sup>), can also be used where available. To adjust the radar data, the near surface air temperature at a particular location must be altered to consider the local lapse rate, the location's elevation, the CAPPI height and the distance from the radar. The distance from the radar will determine if the height of the radar signal is beyond the CAPPI height and the actual height of the beam is based on the 0.3° beam, for the King City radar. The distance will also influence the beam width, as the temperature can vary across the swath measured by the radar. Therefore, combining all these considerations with a location specific mixed precipitation curve may provide for improved radar precipitation

estimates. However, the precipitation rates derived using the new CAPPI data versus using the hourly data must be assessed. It is possible that, at present, use of the CAPPIs does not justify the increase in computational effort. The resultant data should be compared using double mass curves of RFA-hourly data versus 10 minute CAPPI data, as well as gauge data versus RFA and CAPPI derived precipitation estimates.

One potential problem with using the radar estimation at a point is the drifting of the hydrometeors from the location of radar observation, at a 1 km height for snow, to the ground where the gauge is located. As the snow particles have significantly greater drag due to their increased surface area per unit mass, the particles can be moved a substantial horizontal distance during descent. For the accumulation comparison, an centroid weighted average of the nine 2 km radar pixels surrounding each gauge was used. This alleviated the problem of precipitation movement during vertical drop. For hydrological modelling, a single precipitation quantity is computed for the 25 pixels within the 10 by 10 km modelling cell. This average precipitation over the 100 km<sup>2</sup> area helps overcome particle movement during descent. When smaller spatial and temporal scales are used for radar, the movement during vertical dropping must be further considered. This will be a component of the movement of atmospheric contaminants.

Simulating runoff volumes can be adequately accomplished by using various forms of adjusted radar, however, as mentioned above, peak flows are not simulated as accurately. While the vertical water and energy modelling by CLASS\_2.6 represents most of the physical processes associated with snow and winter hydrology, additional modelling developments may improve the streamflow simulation, specifically this can improve the timing and quantity of the peak flow.

## **5.2 METEOROLOGICAL DATA IMPROVEMENTS**

Once the precipitation data were examined and the optimal dataset selected, the remaining meteorological data were investigated. The modelling results presented in this research used forcing meteorological data derived from gridded climate station data. There are issues with the data gridding, such as discussed in the previous section, and future work with WAT\_CLS3 will



tap into modelled forcing data that use station data for calibration and/or verification, such as results from the mesoscale community climate (MC<sup>2</sup>) model. However, improvements to the gridded meteorological data are possible, especially for the derived parameters. In particular, improvements to the longwave radiation estimates are discussed in this section.

The initial assumption was that there was an average of 50% cloud cover throughout the year (Snelgrove, 1996). However, the validity of this assumption is unknown for the southern Ontario study site. Therefore the effects of different constant cloud cover fractions were examined. The use of measured shortwave radiation to estimate a cloud cover fraction during daylight hours was also investigated, and this will be discussed first. It will be seen that when there is incoming shortwave radiation, the average cloud cover is slightly greater than 50%.

As outlined in section 4.1.3, the observed shortwave radiation ( $K_{meas}$ ) can be compared to the theoretical or computed clear-sky shortwave radiation ( $K_{inc}$ ) for a location where solar radiation is measured in order to determine the cloud coverage fraction, for use in estimating longwave radiation. Figures 5-14a, b, and c illustrate this comparison for the CARE, Elora, and Toronto stations during the winter of 1993. The ratio of  $K_{meas}$  to  $K_{inc}$  was computed using the assumption that the incoming solar radiation was measured at local apparent time (Environment Canada, 1999). The maximum ratio values correspond to clear-sky observations. For most periods of the winter, this maximum ratio is less than unity, due in part to extinction of a small portion of the solar radiation from atmospheric particulates. The low maximum morning ratios are explainable by the fact that there is division using small numbers (numerator and denominator), however, there appears to be an overall increase in the maximum ratio as the day progresses. The division using small number, i.e., around the times of sunrise and sunset, would indicate that the maximum ratio in these hours could be from very small to very large. The maximum ratio for the in-between daylight hours should be relatively constant. Since the three stations (Figures 5-14a, b, c) are located at approximately 79.5 to 80.5° longitude, or 4.5 to 5.5° west of the reference longitude (75°W), and the equation of time is less than zero from January to mid April, the local apparent time is between 14 and 36 minutes before the local standard time. From the maximum shortwave radiation ratios in Figures 5-14a, b, and c, it is likely that the clear-sky radiation was computed for an apparent time later than observed. This would yield

larger morning and smaller afternoon values than the corresponding measurements. Therefore, the observed to theoretical shortwave radiation ratios were recomputed assuming that the station data were collected at LST, instead of LAT (Figures 5-15a, b and c). A distinct pattern is presented that is approximately symmetrical about solar noon. While the shape of the maximum ratio curves are similar for the three stations, the maximum solar noon ratios for CARE and Elora are 0.84 and for Toronto is 0.79. It is likely that this 5% decrease is more absorption of solar radiation by atmospheric particulates due to increased pollutant levels above Toronto. Thus the  $K_{meas}$  to  $K_{inc}$  ratio for the Toronto station was computed separately from the other two stations. As well, the set of ratios was divided into different time periods to consider the variation in the length of a day, in particular, November 3<sup>rd</sup> to December 21<sup>st</sup> (late fall), December 22<sup>nd</sup> to February 7<sup>th</sup> (early winter), February 8<sup>th</sup> to March 19<sup>th</sup> (late winter), and March 20<sup>th</sup> to April 30<sup>th</sup> (early spring). It was assumed that the pattern of maximum  $K_{meas}$  to  $K_{inc}$  ratios for each of the four periods at each station repeated annually.

For the late fall period, the maximum ratio of measured to computed (clear-sky) shortwave radiation was unity at the CARE and Elora stations (Figure 5-16a), as well as the Toronto station (Figure 5-17a). The smallest maximum ratio was for the early winter period (Figure 5-16b for CARE and Elora; Figure 5-17b for Toronto). While the sunrise and sunset ratios approached unity for several days for the late winter period (Figures 5-16c and 5-17c), large morning ratios were not calculated for the early spring period (Figures 5-16d and 5-17d). These maximum ratios of unity were considered anomalies, as a distinct pattern of maximum ratios can be seen at the top of each  $K_{meas}$  to  $K_{inc}$  ratio versus time of day plot, especially Figures 5-16d and 5-17d. The three non-unity maximum ratios (early winter, late winter and early spring) are summarized in Figures 5-18a and b for the CARE and Elora stations and for the Toronto station. The maximum ratio increased as the length of day increased. A third order polynomial was fitted to each set of data, as listed in Tables 5-7a and 5-7b. The curves fitted the hourly data well, as the  $r^2$  values ranged between 0.9746 and 0.9922.

These polynomials were used to adjust the  $K_{meas}$  to  $K_{inc}$  ratios to correspond to the assumption that the maximum non-unity ratio is the clear-sky value. Without use of the polynomials, the average five winter cloud cover fraction (called unadjusted) for the periods of

shortwave radiation observations was 0.67, 0.68, and 0.75 for CARE, Elora, and Toronto (Table 5-8). Using a default fraction of 0.5 for the night and period of no observations, these fractions reduced to 0.57, 0.57, and 0.60, respectively. The overall seasonal variation was less than 10%. When the computed clear-sky shortwave radiation was reduced by the maximum ratios (to consider clear-sky observations when the maximum ratio was less than unity), the average cloud coverage for all the observations was 0.54, 0.55, and 0.60, with a maximum variation of 0.11. When the default value of 0.5 was used for missing data and during the nights, the average cloud cover fractions reduced to 0.52, 0.52, and 0.54, for CARE, Elora, and Toronto, with maximum variations of 0.04, 0.08, and 0.01, respectively. These cloud cover fractions approach the initial assumption of 50% cloud cover on average. However daytime variations may still not be represented, and the cloud cover fraction at the onset of melt and throughout the melt season is crucial to snowmelt modelling.

The effect of different constant cloud cover fractions, and use of the variable cloud cover derived from the shortwave radiation observations (with the default of 0.5) is illustrated in the initial spring snowmelt hydrographs in Figures 5-19a (March 24<sup>th</sup> through April 9<sup>th</sup>, 1993). If 100% cloud cover existed, too much longwave radiation would be retained by the clouds, and snowmelt would occur too fast. Conversely, no cloud cover (0%) would result in too much longwave radiation being lost to the atmosphere and snowmelt would occur too slowly. While the 30% cloud cover yields a hydrograph most similar to timing of the observed hydrograph, the volume of the first peak is too low, and hence the snow is initially not melting fast enough. The hydrographs derived from the 50% and variable cloud coverages are very similar. There is slightly less water initially, in the order of 10%, and more water during the recession of the first major snowmelt peak on March 30<sup>th</sup>. There are other issues that have resulted in modelled hydrographs that were more than 2 days prior to the observed hydrograph rise. Considering the subsequent snowmelt hydrograph peaks (Figures 5-19b and 5-19c), the trends presented for the first peak continue: when the snow melted too fast (100% cloud cover), there was too little snow left later in the season to generate large enough streamflow peaks. Conversely, when the snow melted too slowly, too much snow remained and the later hydrograph peaks were too large. The timing and peak flows from the simulated hydrographs using 50% and variable cloud cover

corresponded closest to the timing and peak flows of the observed streamflow.

Since future modelling with the linked WATFLOOD/CLASS model will use regional climate model data as input, the quantity of cloud cover derived from the comparison of theoretical to observed shortwave radiation should not be investigated future. Hamlin (1996) used various models such as MAC to compute the net radiation for input to a temperature-radiation index snowmelt model. However, regional climate models should provide the meteorological data required for CLASS. At present the regional climate model data should be used with caution. A comparison of the average temperature across the Southern Ontario study area (Figure 5-20) illustrates that, at the onset of melt when the initial rising limb of the snowmelt hydrograph occurred in late March 1993 (Figure 5-21), the computed temperatures at the critical time period were warmer than the gridded temperatures.

### **5.3 MODELLING IMPROVEMENTS**

The separation of the soil state variables, as described in section 4.2.6, improves the spring snowmelt hydrograph significantly (Figure 5-21) and will be used as the default for all subsequent changes. Hence it will be discussed as the first change to CLASS\_2.6. With the exception of the redistribution, the remaining four enhanced snow processes (mixed precipitation, fresh snow density, maximum snowpack density, and canopy snowfall interception) do not significantly influence the streamflow hydrograph. For different maximum snowpack densities and canopy snowfall interception formulations, the snow depth can vary significantly, and subsequently the properties of the top soil layer. However, the SWE is not altered markedly.

The 1993 winter streamflow in the Grand River at Galt is used for the comparison hydrograph. Modelled snow depth, SWE, top soil layer temperature, liquid water content, and ice content are compared for each set of different process representation scenarios. These parameters are simulated for the grid block represented by the Grand River snowcourse 2007 near Elmira. The output is for either the crop/low vegetation or for the forest land class.

### **5.3.1 Split State Variables**

The “out-of-the-box” hydrograph presented in Figure 5-21a uses the average soil state variables and the initial meteorological data files. These initial data files were derived using a combination of MC<sup>2</sup> computed data and station data from Toronto (Pearson) and London, only. Incorporation of the Hamilton, Waterloo-Wellington and Warton meteorological data (see Table 3-1) into the gridding procedure resulted in a decrease of the average temperatures (Figure 5-20) and a better representation of the physical climate across Southern Ontario. After the non-precipitation dataset was improved, the complete removal of the averaging of the soil parameters yielded a hydrograph that approached the characteristics of the observed streamflow hydrograph and the rising limb was only one day early (Grand River at Galt in Figure 5-21a). As well the second modelled snowmelt peak was almost exactly the same as observed.

The initial snowmelt streamflow peak is delayed since the ground heat is no longer smeared between the snow covered and snow free areas. This is illustrated in the top soil layer (Figure 5-21b) where the temperature is warmer from the snow covered component of the decoupled model than the original averaging model. Similarly, the water in the top soil layer melts faster for the separated snowfree area and slower for the separated snowcovered area than for the averaged snowfree/snowcovered area (Figure 5-21c).

### **5.3.2 Mixed Precipitation**

Mixed precipitation for dataset development was previously mentioned in section 5.1.1c. When there is precipitation at one particular location in time and space, it will either be raining or snowing, but not both. The hydrometeors may have a solid core and be water covered. However, the state of the precipitation can change rapidly in time, depending upon changes to local atmospheric conditions up to the cloud base. Therefore, the use of a probability-of-snow versus air temperature curve should better represent the state of the precipitation that fell over an hour, and should illustrate the fact that at a particular temperature near 0°C both snow and rain may be possible. The base case used in CLASS2.6 is 100% snow occurs at colder temperatures and 100% rain occurs at temperatures of 0°C or warmer (0°C division). From the Auer curve, the 50% probability of snow occurs at 2.2°C. This is the second scenario tested

(2.2°C division for 100% snow or 100% rain but not a mixture of both, as per BATS (Yang *et al.*, 1998)). Subsequently the Auer curve, Rohrer's DAVOS curve and the US Army Corps of Engineers' (USACE) curve.

Considering mixed precipitation, the different 1993 Grand River winter streamflow simulations are all very similar (Figure 5-22a). [Note that these modelled hydrographs Figure 5-22a) are different than the full soil partitioning hydrograph because these are mean daily flows, only soil temperature decoupling has been included and a different radar precipitation dataset has been used.] Examining the snowmelt portion of the hydrograph, from March 20<sup>th</sup> to April 30<sup>th</sup> (Figure 5-22b) illustrates some small differences in the first end-of-March peak. Inspecting only this peak (Figure 5-22c) shows that there is a difference between the different mixed precipitation schemes. The 0 degrees division yields the earliest peak, while the 2.2 degrees division yields the latest peak. Use of the Auer curve yields a hydrograph similar to the 2.2 degrees division, except slightly earlier. This occurred since more heat in the form of more liquid precipitation is layered onto the snowpack using the 0 degrees division, as compared to the other schemes. As well, the air temperatures during this period is generally warmer than freezing (Figure 5-20). The 2.2 degrees division allows only snow to be present at the warmest temperatures of all schemes; and the Auer curve has the warmest occurrence of snow. The Davos curve is colder than the USACE curve, but warmer than 0, yet colder than +2.2. Hence the simulated hydrograph produced using the Davos curve occurs slightly prior to the USACE curve, but after the 0 degrees division curve.

The differences in the simulated streamflows for the initial snowmelt peak are a result of the snowpack properties. With the occurrence of snow at warmer temperatures, the snowpack is deeper after precipitation events near freezing (Figure 5-23a). For example, at the beginning of the fourth week of January, a precipitation event occurred that resulted in a deeper snowpack for almost a week. However, the total quantity of water (liquid and solid) that fell was the same and the SWE was thus the same (Figure 5-23b). After a week, the depths became essentially the same, as the new snow consolidated. Twice to three times the depth of new snow was added to the snowpack in mid-March when another precipitation event occurred at near freezing temperatures. For the colder mixed precipitation expressions, in particular 0 degrees division,

water was added to the pack which ripened the pack, and yielded an earlier streamflow contribution.

The results of the variation in the snowpack depth is illustrated by the top layer soil temperature (Figure 5-24a) and the top layer liquid and ice water content (Figure 5-24b). For a deeper snowpack (late January), the soil has more insulation from incoming radiation and hence is slightly warmer. In mid-March the addition of liquid water to a mature pack results in more heat added to the pack, and the subsequent warming of the underlying soil.

In general, while there are differences resulting from variation in the temperature distinction between snow and rain, the effect on streamflow is small. The addition of mixed precipitation to the CLASS model improves the modelling efforts, especially in areas that encounter periods of mid-winter melt. The use of mixed precipitation adds less energy to the earth's surface systems, since a portion of the precipitation at temperatures warmer than freezing is be consider as snow. It is recommended that where data are available a specific probability of snow versus temperature curve should be developed.

### **5.3.3 Fresh Snow Density**

#### *5.3.3a Fresh Snow Density and Air Temperature Relationship*

During the winter of 1999, fresh snow density samples for 14 snowfall events were collected in Waterloo. These data were collected on a 0.2538 m<sup>2</sup> snowboard with a depth measurement density of at most 0.02 m<sup>2</sup>/measurement, except for very homogeneous accumulations where the variation in depth was less than 0.1 cm. (The collection area for sample 6a was 0.192 m<sup>2</sup>, for sample 12 was 0.245 m<sup>2</sup>, and for sample 13 was 0.1491 m<sup>2</sup>.) The size of board and method of sampling are consistent with snow accumulation experiments performed by Pfister and Schneebeli (1999) using a board 72 cm in length with widths varying from 3 to 30 cm and 3 sampling depths. The snow was allowed to accumulated on the board in an area where the exposure to wind was minimal during each snowfall event; no horizontal snow movement was observed. The timing of the events, temperature statistics, and raw density measurement data are summarized in Appendix D. The fresh snow density and the average temperature over which

the snow fell are presented in Table 5-9. The maximum and minimum density limits shown in this Table are based on a net mass measurement error of  $\pm 5\%$  and a  $\pm 0.1$  cm error for the depth measurements.

Samples 6, 9 and 11 have been divided into two subsets since distinct layering was observed for these events, typically the presence of a hard top surface between the *a* and *b* layers. For sample 6 and 11, the top crust on the bottom (*a*) layer was either a result of the densification due to the mass of the overlying layer, melting, or variation in the form of the falling snow crystals. The overlying mass for these samples (layer *b*) was small and the temperature was at least 2.6 degree below freezing, so it is improbable that melting occurred and the *b* portion of the events began prior to dawn, so no solar radiation metamorphosis occurred. It is most likely that the interface between the layers underwent a rapid metamorphosis in the crystal structure due to an interaction between different particle forms, i.e., snow crystal shape. The density for sample 6*b* was too low since the depth was computed from deducting the 6*a* average depth from the total depth after the 6*b* layer was scraped off the top, possibly yielding too much depth. As well, 7 and 5.75 hours elapsed from the end of the *a* portion of event 6 and 11 until sampling. The variation in temperature observed at the surface was small, so it cannot be taken as an indicator of different particles. There was minimal variation in the other measured atmospheric parameters. Melting occurred both at the snow surface and during descent of the snow crystals during event 9, thus large densities were observed, and the samples were not 100% snow.

The 1999 Waterloo fresh snow density data have been plotted against air temperature in Figure 5-25a together with the particle shape adjustment curve that was derived to adjust the radar data (the transformed temperature weighted curve in Figure 3-2c). This curve has been multiplied by the depth-weighted average density ( $\bar{\rho}_r(\text{fresh}) = \Sigma SWE / \Sigma \text{depth}$ ), which was determined to be  $90.7 \text{ kg/m}^3$ . While density measurements were not taken at all the intervals of temperature, i.e., there are gaps from -20 to -14 °C and from -6 to -3 °C, the particle shape curve fits the general variation of fresh snow density with near surface air temperature. Samples 10 and 12 are significant outliers, however the air temperature at the end of event 12 was approaching melting. This is to be expected since melted snow precipitation can be observed at air temperatures below freezing, as illustrated in the mixed precipitation curves in Figure 2-5.



Only one snowfall event occurred at a very cold temperature; sample 5 was observed at an average temperature of  $-20.6^{\circ}\text{C}$ . The density of the 5.4 cm accumulation was  $115\text{ kg/m}^3$ , and because there was 8.5 hours elapsed between the end event and sampling, it is possible that the accumulated snow underwent metamorphosis, the degree of which is however uncertain.

The Waterloo data are within the range of the other observed data (Figure 5-25b), with the exception of *6a* and *6b*, as noted above. Waterloo sample 5 and the Schmidt and Gluns (1991) measurement at  $-16.6^{\circ}\text{C}$  are the two very cold temperature samples; they correspond to the variation in the particle shape curve. In general, the density predicted by the particle shape curve as the temperature decreases from  $-15$  to  $-20^{\circ}\text{C}$  is quite possible since the crystals that form at such colder temperatures are smaller and more concentrated. However, more data are required in this temperature range. The particle shape curve fits the Waterloo data better than the data from the literature. At temperatures warmer than  $-1^{\circ}\text{C}$ , the fresh snow density is underestimated by the particle shape curve, the Diamond and Lowry equation, and the Hedstrom and Pomeroy equation (Figure 5-25b). With the exception of the Rohrer (1989) mixed precipitation data from Arosa (Figure 2-5), liquid precipitation can be observed at air temperatures as low as  $-1^{\circ}\text{C}$ . At Arosa liquid precipitation can be observed at colder temperatures.

Diamond and Lowry (1953) initially plotted the 500 and 700 mb height temperature against the measured fresh snow density to investigate the relationship between upper air conditions and density, since they stated that "the density of new snow is probably a function of the size and type of snow crystal." They elaborate on this by summarized preliminary results relating the air temperature and the degree of saturation to the shape of ice crystal formed. Since then growth rates and directions, and hence type of crystal, have been measured as a function temperature and degree of water vapour saturation (summarized in section 2.1.1 and Figures 2-2a through 2-2e). While no relationship was found between 500mb air temperature and fresh snow density, one was found using the 700mb temperature (Diamond and Lowry, 1953). The linear relationship found between the surface temperature (at an elevation of 2100 m) and density ( $\bar{\rho}_s(\text{fresh}) = 119 + 6.48 T_a$  illustrated in Figure 5-25b) was attributed to the relationship between the surface and 700mb air temperature, 1000 m higher (Diamond and Lowry, 1953).

Based on the observation of Diamond and Lowry, the particle shape curve should be applied at cloud height, or at least using the temperature at the 700 mb height. It should be noted that at non-melting conditions, i.e., below an air temperature of  $-2^{\circ}\text{C}$  throughout the atmospheric column through which a hydrometeor falls, snow crystals can be significantly modified, but Diamond and Lowry (1953) noted that this primarily affects the crystal size. If the particle shape curve is applicable for use with atmospheric temperatures, it would require adjustment at warmer temperatures (likely above  $-2^{\circ}\text{C}$ ), as well as information on the conditions below the 700 mb height to consider the potential for partial or complete melting as the hydrometeors fall. This leads to the possible use of the curve with atmospheric modelling.

Densification of the snowpack was not considered for any of the datasets, and for the Diamond and Lowry (1953) data, the temperatures were measured at the time of sampling, not during the snowfall events. For the Waterloo samples, up to nine hours elapsed from the end of the snowfall event and the density measurement for samples. Since the degree of densification is unknown, future sampling should consider the densification, such as illustrated in Figures 2-6a, and 2-6b ( from Goodison *et al.*, 1981). For measurement of the fresh snow density from samples on the ground, the densification of the snowpack must be considered as a function of the depth of snowfall, the time of accumulation (from the beginning of the event), and the time lapsed since the end of the event (if any).

### ***5.3.3b Fresh Snow Density Influence on Modelling***

Instead of a fresh snow density constant of  $100\text{ kg/m}^3$ , the following three other variable fresh snow density functions were tested: the function derived by Hedstrom and Pomeroy (1998), the Alta function derived by LaChapelle (1961) and the particle shape curve outlined in section 4.1.4c. The constant fresh snow density of 100 yielded a slightly later rise limb of the 1993 initial snowmelt hydrograph than the other variable densities (Figure 5-26a). In the second rising limb, hydrograph simulated using the constant fresh snow density occurred earlier. The depth of snowpack (Figure 5-26b) was influenced by the fresh snow density for colder period such as early February, with less depth change. However, for warmer periods, such as late March, the temperatures are warmer and the variable fresh snow density is larger than  $100\text{ kg/m}^3$ .

Conversely, there was limited impact on the SWE (Figure 5-26c), as the same quantities of precipitation fell in each of the scenarios. After several weeks of limited accumulation, the metamorphosis of the pack results in a convergence of the different simulated snowpack depths (see early February in Figure 5-26b). However, the initial change in depth influenced the top layer soil temperature (Figure 5-26d) and to a lesser extent the liquid water content (Figure 5-26e).

Use of a variable fresh snow density should better represent the characteristics of snowfall and hence the snowpack. However, as stated in the previous section, more data are required to properly represent the fresh snow density as a function of air temperature. An understanding of the initial crystal shape, i.e., formation conditions, and the metamorphosis during descent, i.e., the atmospheric conditions between the cloud and the surface, are the key components necessary to quantify the near surface shape characteristics and hence the fresh snow density.

#### 5.3.4 Maximum Snowpack Density

Different maximum snowpack densities are achievable for different land cover types as well as different climatic regions. A maximum of  $300 \text{ kg/m}^3$  for all land cover types was originally used in CLASS. Increasing this maximum to  $350 \text{ kg/m}^3$  yielded a later onset of melt, while using  $250 \text{ kg/m}^3$  for the forest and  $350 \text{ kg/m}^3$  elsewhere yielded an earlier melt (Figure 5-27a). While the differences in the start of melt were seen in the first snowmelt hydrograph peak (both rising and falling limb), as with the incorporation and the use of a variable fresh snow density, these differences in streamflow were small. However, as can be expected, the snow depth varied inversely as a function of maximum density (Figure 5-27b) and the SWE quantities were identical until the pack started to melt (Figure 5-27c). Underlying the denser but shallower snowpack, the soil was colder (Figure 5-27d) than for the deeper, less dense pack. At colder than freezing temperatures, the transfer of heat through the pack by the radiation density flux, which in CLASS\_2.6 is a function of the depth, dominates, while at warmer temperatures the heat is conducted thermally, which in CLASS\_2.6 is represented as a function of the snowpack density. However, at the onset of melt by mid March, the heat gradient between the snowpack and the

underlying cold soil of the denser snowpack dictated that more heat is transferred to the soil. For the deeper snow pack with the warmer underlying snow, the smaller snow-soil temperature gradient resulted in more snow being melted. There was a small increase in the liquid water content below the less dense snowpack (Figure 5-27e). Therefore more snow melted from the deeper pack, contributing more water to streamflow, resulting in more snow remaining in the denser snowpack. The depths for the different scenarios were almost the same by the time the top soil layers warm to the same temperature. Due to the maximum density differences, the denser snowpack retained more SWE than the less dense snowpacks.

The soil water began to melt rapidly on the 29<sup>th</sup> of March, but colder temperatures and an additional snowfall added frozen mass to the pack (Figure 5-27c), subsequently refreezing the soil water (Figure 5-27e). The soil temperature was lowered slightly (Figure 5-27d) once the water was refrozen. Ensuing warmer air temperatures and incoming radiation fluxes melted the a majority of the pack and then melted the frozen water in the soil. This yielded a more rapid second streamflow peak for the dense pack because more snow was available to melt and contribute to runoff. There was approximately a day delay between the thawing of the remaining frozen water for the denser snowpack scenario as the soil stayed colder on average.

More data are required to quantify the maximum density attainable. However, a different densification formulation that does not use a maximum density, such as the original Anderson equation (similar to equation 2-7) or the Pomeroy equations (2-5 and 2-6), should also be modelled and compared to CLASS\_2.6 (equation 2-4).

### 5.3.5 Canopy Snowfall Interception

To consider the increased interception on the canopy by snow over rain, the maximum holding capacity for the canopy was increased from 20% of the precipitation that fell (rain interception) to 50% of the precipitation that fell (holding capacity = 0.5). Subsequently, the Hedstrom and Pomeroy (1998) formulation was used to determine the actual amount of snowfall interception in the canopy. Since the leaf area index (*LAI*) decreases substantially for deciduous trees and shrubs during the winter, yet remains relatively constant throughout the year for coniferous trees, the composition of the forest is important. For a 100% deciduous forest, increased the holding

capacity resulted in a small decrease of approximately 1% in the maximum SWE below the canopy (Figure 5-28a). By increasing the representation of coniferous trees in the forest, the *LAI* is increased for the winter. Hence for 65% deciduous and 35% coniferous, the holding capacity increase results in a greater decrease in snowpack SWE accumulation of approximately 3% less snow (Figure 5-28b). Furthermore with a 100% coniferous forest, the snowpack below the canopy received even less snowfall (approximately 10% less), as the holding capacity was increased (Figure 5-28c). There were no noticeable changes in the snowpack SWE when the Hedstrom and Pomeroy function was introduced.

The decrease in the maximum snowpack SWE under the canopy did not influence the simulated streamflow (Figure 5-28d). Similarly, the streamflow hydrographs for the different canopy fractions, using the Hedstrom and Pomeroy formulation, were almost identical (Figure 5-29a). The simulated forest SWE quantities from the different canopy fractions were different, as expected (Figure 5-29b). This resulted in a more rapid warming of the top soil layer as the pack melted (Figure 5-29c) and more liquid water in the soil for the initial snowmelt and an earlier melt of the remaining frozen water content (Figure 5-29d).

While the streamflow is not noticeably influenced by the different snowfall canopy interception schemes, nor the fraction of coniferous trees in the forest, these factors do affect the quantity of snow on the ground and subsequently the properties of the soil during snowmelt. It is recommended that the Hedstrom and Pomeroy formulation should be used to represent snowfall canopy interception. Although not examined in this research, the heat fluxes from the canopy will also be different when the canopy interception is increased. The characteristics of the canopy, in terms of distribution and type, i.e., *LAI* and the seasonal variation in *LAI*, are crucial to accurate modelling of the interception of precipitation by the canopy.

### 5.3.6 Redistribution

As a simplification to a complex physically based redistribution model (eg. Prairie Blowing Snow Model) that requires detailed topography and location information, such as fetch length and orientation, the use of a snow capacity limit or maximum non-transport snow depth limit has been used to move snow from possible areas of erosion to possible areas of deposition. This

moves snow from one land class to another. To consider transport within a particular land class, different minimum snow depth for complete snowcover ( $D_{100}$ ) were used. Movement of snow between land classes had a substantial impact on streamflow while transport within a particular land class had a much smaller impact.

### 5.3.6a Redistribution of Snow from Open Areas

Schroeter (1988) and Donald (1992) have illustrated that a simple redistribution model can be effective for hydrological modelling. To illustrate the impact such a model in CLASS\_2.6, redistribution was considered from the bare and the crop/low vegetation land classes. (It should be noted that in the Upper Grand River study basin, there is approximately 8% bare, 59% crop/low vegetation, and 14% forest). As well the maximum non-transport snow depth limit ( $d_{s,NT\ max}$ ) was altered for redistribution from the crop/low vegetation land class. The focus is on the initial peak of the Grand River at Galt hydrograph.

When the simple between land class redistribution is introduced into CLASS\_2.6, the size of the first snowmelt peak was lowered and to a lesser extent timing of the peak was later (Figure 5-30a). Melting occurs later in the forest, hence the initial peak is less as there is less snow in the open area. The subsequent peaks resulting from melt in the forest, results in increases to later streamflow peaks. Since the bare land class only covered a small area of the basin, use of the simple redistribution from bare ground did not alter the peak substantially because only a small quantity of snow was moved from the bare area to the forest. As expected, as the  $d_{s,NT\ max}$  is decreased the initial snowmelt peak is decreased, since less snow is present in the crop/low vegetation (low veg) land class. The snow in excess of the  $d_{s,NT\ max}$  is deposited in the forest. The additional snow accumulation in the forest through this method is not realistic (Figure 5-30b). For redistribution from the bare area, there is a three fold increase in the forest snow depth by the time of maximum accumulation since the forest represents only 2% of the modelling grid block presented in Figure 5-30b, whereas the bare area comprises 8%. Since the crop/low vegetation covers 80% of this particular grid block, redistribution from this land class can result in almost 10 m of accumulation. This is a result of a snowpack threshold of 5 mm. This results in maintaining snowfree areas throughout the winter. Although it is very unrealistic, the resultant

streamflow is only slightly less than 150 mm limit, which yielded a forest snowpack depth maximum of almost 5 m.

A timing of movement was examined. This did not move all the snow as soon as the  $d_{s,NT_{max}}$  was reached, rather it moved a percentage of the snow at each time step. Figure 5-30c illustrates the implication of this stepwise transport. If only 1% is moved at a time, then over several days, almost all of the excess snow can be moved. However, pack compaction is occurring and the stepwise movement is cumulative such that the each subsequent stepwise movement actually moves less snow if no snow is lost from the pack due to other processes. When only 0.1% of the excess snow is moved from the crop/low vegetation area, snow is still transported, but much slower. The resultant snowpack depth in the forest was more realistic when the 0.1% movement per time step was used, but was still an overestimation (Figure 5-30d). A more appropriate method would be to redistribute the snow to an "edge" land class that represented the border between the bare ground and the forest, individual tree lines, fence lines, and ditches. Such a land class would have the combined land cover properties of the forest and crop/low vegetation areas. However, the addition of an "edge" land class would increase the computation time by near 20% and the differentiation between such a class and the other surrounding classes is only important for snowmelt periods. In locations where the quantities of blowing snow are small, such as southern Ontario, the additional computation time may not be justified.

### *5.3.6b Minimum Snow Depth for Complete Snowcover Variation*

The transport within a particular land class by using different  $D_{100}$  values (0.1 m; 0.15 m; and 0.15 m everywhere except 0.06 m in the forest) influences the exposure of snowfree areas. While Donald (1992) observed different  $D_{100}$  values for different land cover types, 0.1 m is commonly used as the default (eg. Verseghy, 1991). Use of a  $D_{100}$  of 0.15 m everywhere yields a lower value of streamflow at the initial snowmelt peak (Figure 5-31a) than use of the other scenarios. A greater snow depth existed for the larger  $D_{100}$  (Figure 5-31b) which corresponded to a larger SWE in the snowpack (Figure 5-31c). The soil temperature from January 15 to 22 was colder (Figure 5-31d) while there was more liquid water in the top soil layer (Figure 5-31e).

This occurred since the snowpack metamorphosized to less than the  $D_{100}$  for the 0.15 m everywhere scenario, and the open areas allowed heat transfer from the soil to melt frozen water, and subsequently refreeze the water. Below the  $D_{100}$ , the the snow depth remains constant, while the snowcovered area is depleted. These differences resulted in less initial snowmelt for a larger  $D_{100}$  during the early January melt, where the daily maximum peak was 4% less. The rate of accumulation was subsequently the same for the different scenarios, after the early January melt. For the initial spring snowmelt, there was more snow in the pack and less initial snowmelt, as for the early January melt, and hence the initial streamflow is less. Afterward there is more water available for the larger  $D_{100}$  and slightly more streamflow.

The  $D_{100}$  also influences the accumulation of snow, particularly in terms of the snowcovered area after a fresh snowfall on top of a partial snowcover. Luce *et al.* (1999) have examined using an alternate approach for snow accumulation using the  $D_{100}$ , but no field data were presented. Therefore, the accumulation of snow using the  $D_{100}$  concept should be examined with field observations in order to better model the accumulation. This is especially important for the atmospheric modelling using CLASS, as the albedo is in part a function of the snowcovered area and the albedo directly influences atmospheric feedback.

A linear relationship between snowcovered area and depth is assumed. The effect of snowcover depletion curves should be investigated compared to the linear relationship. While Kouwen (pers. comm., 1998) illustrated that the linear representation is sufficient for the WATFLOOD index model, the physical model CLASS may show differences, especially due to atmospheric fluxes related to albedo. The further variation of the  $D_{100}$  for different land cover types should also be investigated.

### 5.3.7 Other Cold Processes

Beyond the incorporation of a physically based blowing snow transport and sublimation model into CLASS2.6, a better representation of the infiltration into frozen soil is required. While Zhao and Gray (1999) have developed a comprehensive model for this process, the model would require a much finer discretization of the soil layers. Further parameterization of the process could lead to incorporation into CLASS2.6.



While the separation of the soil properties between snowcovered and snowfree areas provides a more realistic physical representation of a partial cover snowpack than the averaging of the two areas, the advection of heat (mass and energy fluxes) between the two areas are assumed not to exist. There are fluxes of mass and energy between the snowcovered and snowfree area that were overestimated using the original averaged CLASS model, and not considered using the decoupled model. However, Neumann and Marsh (1998) have shown that these fluxes can be significant. These fluxes may be difficult to measure due to the patchiness of partial snowcover, which is a function of the variation in the snowcover depth prior to melt. The distribution of snow depth is considered to be fractal at small scales (sampling distances of approximately 25m) and random at larger scales (Shook and Gray, 1996). An important intention of the GRU approach to hydrologic modelling is to overcome the need to spatially represent the location of land cover types, as well as snowcovered/snow free areas, within a grid cell, thus if future research finds that the horizontal transfer of heat and water fluxes between snowcovered and snow free area is important, then these fluxes can be modelled using four separate areas. Specifically, the snowcovered area would be divided into a non-interacting ( $A_{SC,N}$ ) and an interacting subarea ( $A_{SC,F}$ ). Similarly the snow free area would be divided into non-interacting ( $A_{SF,N}$ ) and interacting ( $A_{SF,F}$ ) subareas. Fluxes would be modelled between the interacting areas, but not between the non-interacting subareas. The portion of the snowcovered area within each subarea would be a function of the size (area and perimeter) of the exposed snow free patches. More data are required, however, to estimate these fluxes and subarea portions. This is beyond the scope of this project and should be investigated in further studies.

## 5.4 OTHER CONSIDERATIONS

To examine the success of the WAT\_CLS3 model with radar precipitation input on all the study basins for the five study years, the model was run for a continuous simulation. The radar data were adjusted to consider both mixed precipitation and particle shape (scenario *xi* as illustrated in Table 4-3). Since the radar data were not continuously available prior to the start of 1993,

the impact on the early January 1993 streamflow peak from two different initial conditions was investigated.

#### 5.4.1 Multi-year Simulations

A continuous simulation of the five watersheds within the southern Ontario study region was undertaken for the five year study period. For the Grand River at Galt, the trends, as illustrated by the runoff volume comparison, is obvious (Figure 5-32). The streamflow for 1993 is simulated quite well, while the timing for 1994 is good, but the size of the snowmelt peaks is not quite correct. The March 1995 snowmelt streamflow is substantially overestimated. However, the mid-April peak is estimated well. The timing of the 1996 peaks are estimated well, as is the total runoff volume, but some of the peak flows are poorly estimated. The 1997 streamflow is notably underestimated. In general, the streamflow for four other hydrometric stations are poorly simulated for some years (Figure 5-33a), but well simulated for 1993 (Figure 5-33b).

For each hydrometric location in the five study watersheds, the simulated and observed cumulative runoff volumes were compared over time (Figures 5-34i) and to show the annual differences, as double mass curves (Figures 5-34ii). As illustrated in Figure 5-34, the 1993 and 1994 Grand River at Galt streamflow was simulated well (Figures 5-34ai and 5-34aaii). Similarly for the upstream station on the Grand River near West Montrose 1993 was simulated well (Figure 5-34b), but the subsequent years were underestimated. Further upstream at Marsville, 1993 was also simulated well (Figure 5-34c), but 1994 through 1996 were overestimated. The streamflow for the fall of 1996 and early winter 1997 were underestimated while the late winter and early spring 1997 were overestimated. Other sub-basins within the Upper Grand River were better estimated over most or all of the five years simulated. The Eramosa River above Guelph (Figure 5-34d) was simulated well until the end of 1996. Over the five years, the runoff volume at the Conestogo River above Drayton was simulated almost exactly as observed (Figure 5-34e). However, only 1993 was simulated well as an individual year. The Speed River at Armstrong Mills (Figure 5-34f) and below Guelph (Figure 5-34g) were simulated well for the first four years. The runoff volume at the Canagagique Creek near Elmira was simulated to be almost the same as observed over the entire five year period, but only 1993 and 1994 were simulated well

as individual years (Figure 5-34h). For the Pine River near Everett sub-basin, within the Nottawasaga River watershed, 1993 through 1996 were simulated well (Figure 5-34i). The streamflow at the Saugeen River near port Elgin was slightly underestimated every year (Figure 5-34j). However, near Walkerton (Figure 5-34k) and near Hanover (Figure 5-34l), the first four years were simulated well and the fifth year streamflow was underestimated. For the Maitland River below Wingham and, upstream, above Wingham (Figures 5-34m and 5-34n, respectively), only one-half of the observed runoff volume was simulated, yet on the Middle Maitland near Belgrave (Figure 5-34o), the five year simulated streamflow volume was almost the same as observed. There are deviations within each year. In general, the first four years of streamflow simulated at the five locations with the Upper Thames River basin are simulated well ((Figures 5-34p through 5-34t). Near Ealing (Figure 5-34p) and the Middle Thames at Thamesford (Figure 5-34q) are both almost identical for the observed and simulated streamflows for each of the first four years. Streamflow was underestimated for the North Thames River near Mitchell (Figure 5-34r) and for 1996 and 1997 near Northdale (Figure 5-34s). On the Thames at Ingersoll, the simulated streamflow was more than observed for 1994 and 1995 (Figure 5-34t), but the 1997 underestimation resulted in a five-year simulated total runoff that was the same as observed.

In general, the streamflow for the first four years (1993 to 1996) were well simulated with respect to the observed runoff volumes. The 1993 year was well simulated for almost all stations. When subsequent years were overestimated, the underestimation for the 1997 year often yielded a net good estimation of runoff volumes. Streamflow was underestimated for most years at other stations. The annual variation in the runoff volumes is a function of the radar precipitation estimation., as the same general trend was illustrated in the accumulation comparison. Scott (pers. comm., 1999) stated that various operation parameters were altered for the King City Radar between 1993 and 1997, however the specifics were not correlated to the variation in precipitation estimation. As well, there were annual variations in the storm types, as suggested by Hollingsworth (pers. comm., 1999). Since the general trend was a good correlation between the 1993 to 1996 simulated runoff versus observed runoff, the King City weather radar provided good precipitation estimates for hydrological modelling. There is a

variation with location of the basin, but there is no obvious relationship. New radar products at finer resolution (1km and 10 minute time steps) and derived from Doppler (up to a range of 120km) have just been released in the fall of 1999 from the King City radar. If the operating parameters are held constant, the accuracy of these new products to estimate precipitation can be assessed and any systematic errors can be removed. Innes *et al.* (2000) are currently assessing these new products.

#### **5.4.2 Initial Conditions**

The 1993 winter season actually started at the end of November. However, warm temperatures in late December resulted in a majority of the snow melting by the end of the month. Personal observation and the snowcourse data from December 31<sup>st</sup> 1992 illustrated that some snow was present at the beginning of January 1993. The streamflow for January 1993 was simulated with WAT\_CLS3 using no snow on the ground and using a depth of 10 cm and a SWE of 20 mm everywhere throughout each basin. In reality there was a variation in the depth and SWE for different land cover types and at different locations, in particular, more snow in the north and less in the south, but the intention was to illustrate the influence of snow versus no-snow. The differences in streamflow are presented in Figures 5-35a through 5-35t for the same hydrometric stations presented in Figures 5-34a through 5-34t. Obviously more streamflow was generated when snow was assumed to be on the ground and, in general, a better streamflow estimated was produced. For the Grand River at Galt (Figure 5-35a), the Eramosa River above Guelph (Figure 5-35d), downstream at the Speed River below Guelph (Figure 5-35g), on the Pine River (Figure 5-35i), and at the Middle Maitland River near Belgrave (Figure 5-35o) the assumption of snow on the ground yielded an overestimation of streamflow. All other stations were better estimated assuming snow on the ground. The overestimation of the Grand River stations (Galt, Eramosa, Speed below Guelph) occurred because there was less snow 20 mm SWE in the southern and eastern portions of the Upper Grand River basin. There was likely no snow on some of these areas, as observed by Kouwen (pers. comm. 1998). For the Pine River (Nottawasaga basin) and Middle Maitland (southern Maitland basin), there was also less snow than 20 mm SWE.

The initial conditions do not influence the spring snowmelt peak and the subsequent

streamflow, as the soil and snowpack properties were almost identical by mid-March since the early January rain-on-snow event saturated the soil on top of which the snowpack accumulated. However, the initial SWE distribution and soil properties are important for the establishing the conditions of the underlying soil if modelling is started at the beginning of snow accumulation without any complete midseason melting.

### **5.4.3 Comparison to WATFLOOD results**

The streamflow for the five years across the five study basins have been simulated using the standalone index model WATFLOOD. The simulated results from WAT\_CLS3 are significantly close to the observed streamflows (Figure 5-36 illustrates the five years of continuous flows for the Grand River at Galt). The results from WATFLOOD do not match the observed hydrographs as well. In particular the summer flows produced by WATFLOOD are much higher than observed. Kouwen (pers. comm., 1998) has seen these overestimations with WATFLOOD, and research is currently ongoing to examine scaling of the summer radar precipitation estimates using the rising limb of individual hydrograph peaks. The winter and snowmelt streamflow simulated by WATFLOOD are improved compared to summer streamflows, but WAT\_CLS3 yielded better results for throughout the year. The hydrographs for the remaining stations are presented in Appendix C (Figures C-8a through C-8s), and illustrate the same trends as on the Grand River at Galt. It should be noted that while both models used the same precipitation and temperature data, WAT\_CLS3 requires five other meteorological parameters. Therefore, while the streamflow estimates are improved through the incorporation of CLASS into WATFLOOD, the data requirements are also increased.

## **5.5 SUMMARY OF RESULTS**

Ground-based weather radar data are shown to be a useful estimate winter precipitation, in terms of snowpack accumulation, with respect to corrected gauge accumulation, and as input for hydrological modelling. Adjustments to the radar data using near surface air temperature

resulted in improved snowfall estimates. The longwave radiation estimates for modelling were also improved. The additional model development for CLASS snow processes yielded improvements to the streamflow hydrograph estimations. Five-year streamflow simulations were additionally generated with varying results.

TABLE 5-1. Summary of seasonal (columns 3 through 7) and monthly (8 through 12) comparison statistics for raw radar and various adjustment schemes versus gauge estimation. The statistics are weighted by the length of each record to account greater errors occurring at shorter intervals. The standard error of estimate (SEE) and coefficient of determination ( $r^2$ ) are based on the best-fit regression lines with the slope and y-intercept. The standard errors are normalized to values of mm/d.

adjustment method	seasonal					monthly				
	n	y-int	slope	SEE	$r^2$	n	y-int	slope	SEE	$r^2$
<i>i</i> raw data	8	89.0	0.61	1.30	0.308	27	29.8	0.56	1.38	0.246
<i>ii</i> scaling removed	8	56.2	0.61	0.53	0.725	27	17.8	0.60	0.64	0.633
<i>iii</i> linear mixed precipitation (MP) temperature (T) adjustment	8	72.8	0.69	0.56	0.753	27	22.2	0.68	0.77	0.605
<i>iv</i> linear MP adjustment with dewpoint temperature (Td)	7	85.6	0.63	0.51	0.773	25	21.5	0.68	0.80	0.592
<i>v</i> Auer's curve MP adjustment with T using a constant of 2.03	8	73.4	0.70	0.56	0.760	27	22.6	0.69	0.78	0.607
<i>vi</i> Auer's curve MP adjustment with Td using a constant of 2.03	7	97.3	0.61	0.43	0.819	25	23.9	0.67	0.87	0.543
<i>vii</i> Auer's curve MP adjustment with T using variable precipitation rate (R)	8	86.5	0.66	0.60	0.709	27	23.2	0.71	0.97	0.516
<i>viii</i> Auer's curve MP adjustment with Td using variable precipitation rate	7	104	0.60	0.50	0.758	25	22.7	0.71	0.98	0.510
<i>ix</i> MP (T on Auer using 2.03) and particle shape (PS) adjustment	8	74.2	0.70	0.57	0.756	27	22.7	0.70	0.79	0.605
<i>x</i> MP (Td on Auer using 2.03) and particle shape (PS) adjustment	7	82.6	0.65	0.51	0.784	25	21.3	0.69	0.80	0.595
<i>xi</i> MP (T on Auer using variable R) and snowflake PS adjustment	8	87.3	0.67	0.61	0.707	27	23.4	0.72	0.98	0.517
<i>xii</i> MP (Td on Auer using variable R) and snowflake PS adjustment	7	102	0.60	0.51	0.757	25	22.6	0.71	0.98	0.509
<i>xvii</i> optimal	8	51.2	0.72	0.33	0.903	27	14.2	0.71	0.44	0.841

TABLE 5-2. Summary of seasonal (columns 3 through 6), monthly (7 through 10), and weekly (column 11 through 14) comparison statistics for raw radar and various adjustment schemes versus gauge estimation. The statistics are weighted by the length of each record to account greater errors occurring at shorter intervals. The mean difference (mean diff.), standard error of estimate (SEE) and coefficient of determination ( $r^2$ ) are based on the 1:1 line with a slope of unity through the origin (i.e., using an intercept of 0). The mean difference and standard errors are normalized to values of mm/d.

adjustment method	seasonal				monthly				weekly			
	n	mean diff	SEE	$\rho^2$	n	mean diff	SEE	$\rho^2$	n	mean diff	SEE	$\rho^2$
<i>i</i> raw data	8	0.16	1.23	0.178	27	0.12	1.46	0.089	103	0.16	2.82	0.081
<i>ii</i> scaling removed	8	-0.33	0.72	0.335	27	-0.34	0.87	0.272	103	-0.32	1.69	-0.008
<i>iii</i> linear mixed precipitation (MP) temperature (T) adjustment	8	0.14	0.63	0.582	27	0.11	0.87	0.462	-	-	-	-
<i>iv</i> linear MP adjustment with dewpoint temperature (Td)	7	0.10	0.64	0.500	25	0.08	0.90	0.434	-	-	-	-
<i>v</i> Auer's curve MP adjustment with T using a constant of 2.03	8	0.18	0.62	0.595	27	0.16	0.87	0.470	103	0.18	1.88	0.326
<i>vi</i> Auer's curve MP adjustment with Td using a constant of 2.03	7	0.20	0.63	0.442	25	0.17	0.97	0.381	-	-	-	-
<i>vii</i> Auer's curve MP adjustment with T using variable precip (R)	8	0.26	0.70	0.474	27	0.25	1.03	0.405	103	0.28	2.25	0.342
<i>viii</i> Auer's curve MP adjustment with Td using R	7	0.26	0.70	0.348	25	0.24	1.05	0.395	-	-	-	-
<i>ix</i> MP (T on Auer using 2.03) and particle shape (PS) adjustment	8	0.21	0.63	0.593	27	0.19	0.88	0.472	103	0.21	1.87	0.341
<i>x</i> MP (Td on Auer using 2.03) and particle shape (PS) adjustment	7	0.12	0.62	0.549	25	0.09	0.90	0.446	-	-	-	-
<i>xi</i> MP (T on Auer using R) and snowflake PS adjustment	8	0.30	0.71	0.471	27	0.28	1.04	0.406	103	0.30	2.25	0.351
<i>xii</i> MP (Td on Auer using R) and snowflake PS adjustment	7	0.25	0.69	0.371	25	0.22	1.05	0.393	-	-	-	-
<i>xiii</i> MP (T, Auer, 2.03) and PS adjustment shifted by 1.5 °C	8	0.20	0.63	0.598	27	0.17	0.88	0.466	-	-	-	-
<i>xiv</i> MP (Td, Auer, 2.03) and PS adjustment shifted by 1.5 °C	7	0.10	0.62	0.544	25	0.07	0.90	0.426	-	-	-	-
<i>xv</i> MP (T, Auer, R) and PS adjustment shifted by 1.5 °C	8	0.28	0.70	0.480	27	0.26	1.04	0.403	-	-	-	-
<i>xvi</i> MP (Td, Auer, R) and PS adjustment shifted by 1.5 °C	7	0.23	0.69	0.369	25	0.19	1.05	0.379	-	-	-	-
<i>xvii</i> optimal	8	-0.09	0.46	0.756	27	-0.18	0.60	0.678	-	-	-	-



TABLE 5-3. Summary of seasonal (columns 3 through 7), monthly (8 through 12), and weekly (column 13 through 17) comparison statistics for combination adjustment schemes versus gauge estimation. The statistics are weighted by the length of each record to account greater errors occurring at shorter intervals. The mean difference (mean diff.), standard error of estimate (SEE) and coefficient of determination ( $r^2$ ) are based on the 1:1 line with a slope of unity through the origin (i.e., using an intercept of 0). The mean difference and standard errors are normalized to values of mm/d.

adjustment method	seasonal				monthly				weekly			
	n	mean diff	SEE	$\rho^2$	n	mean diff	SEE	$\rho^2$	n	mean diff	SEE	$\rho^2$
<i>xviii</i> mixed precipitation (T, Auer) with minimum of R or 2.03	8	-0.10	0.65	0.518	27	-0.12	0.83	0.405	103	-0.10	1.72	0.158
	FIGURE 5-7a				FIGURE 5-7b				FIGURE 5-7c			
<i>xix</i> MP (T Auer: min[2.03, R]) and PS adjustment with Td	7	-0.09	0.69	0.402	25	-0.12	0.89	0.275	97	-0.07	1.72	0.166
	FIGURE 5-8a				FIGURE 5-8b				FIGURE 5-8c			

TABLE 5-4. Summary of peak flow statistics for all the five winters of peak flow data. The nine precipitation input data are as summarized in Table 3-4.

statistic	precipitation gauge data			radar data					
	uncorrected gauge	gauge corrected to DFIR	gauge corrected to "bush"	raw	no scaling	mixed precip	mixed / particle shape	mixed with variable R	mixed/ part with variable R
slope (y-int. = 0)	0.654	0.78	0.768	1.01	0.956	1.09	1.105	0.835	0.853
$r^2$	0.806	0.717	0.714	0.58	0.596	0.65	0.65	0.54	0.556
$r^2$ (slope = 1, y-int. = 0)	0.452	0.639	0.62	0.6	0.619	0.66	0.663	0.518	0.545
average difference (m <sup>3</sup> /s)	-38.1	-22.3	-23.1	7.9	2.7	14.1	16.1	-7.6	-5.6

**TABLE 5-5a. January 1993 to April 1993 winter runoff volumes (mm) at eight streamflow gauges (column 1) for the observed (column 2) and simulated runoff volumes based on the precipitation inputs summarized in Table 3-4.**

stream flow gauge [1]	observed runoff (mm) [2]	simulated runoff volume from different precipitation inputs (mm)								
		precipitation gauge data			radar data					
		uncorrected gauge	gauge corrected to DFIR	gauge corrected to "bush"	no raw	mixed scaling	precip	mixed / particle shape	with variable R	mixed/part with variable R
G1	205	127	129	130	171	169	182	185	157	160
G2	207	136	136	137	156	156	161	163	151	152
G3	241	92	98.1	99.2	152	150	174	177	133	135
G4	212	77.1	81.3	82.2	154	148	174	180	129	133
G5	235	113	119	120	211	209	243	248	183	187
G6	231	81.4	85.5	86.7	164	160	187	193	139	144
G7	192	139	141	142	191	187	204	208	174	177
G8	188	87.3	90.7	91.7	175	172	196	203	150	156

**TABLE 5-5b. December 1993 to April 1994.**

G1	153	72.1	81.9	84.1	136	134	144	146	123	125
G2	145	51.6	56.2	57.3	82.9	81.5	86	86.7	76.2	76.6
G3	157	102	115	117	199	193	212	214	175	178
G4	149	87.7	103	106	194	190	210	211	169	170
G5	180	137	158	162	299	292	316	319	267	271
G6	170	98.9	117	120	220	215	237	238	190	191
G7	123	79	89.3	91.7	148	145	158	159	131	132
G8	187	112	131	135	260	255	275	279	229	241

**TABLE 5-5c. November 1994 to April 1995.**

G1	182	156	200	205	360	294	344	350	247	254
G2	182	158	197	201	341	281	325	331	241	248
G3	205	154	188	191	345	283	326	333	245	253
G4	164	140	175	178	408	321	401	406	254	259
G5	267	207	264	269	479	391	451	459	342	351
G6	207	157	200	205	339	281	337	342	232	238
G7	149	148	189	193	372	301	367	372	242	249
G8	179	172	222	228	352	287	333	337	243	249

**TABLE 5-5d. November 1995 to April 1996.**

G1	307	119	155	164	323	320	354	358	292	296
G2	331	108	126	139	268	266	296	298	241	244
G3	385	155	171	205	382	381	403	406	363	365
G4	285	120	160	173	376	375	412	416	352	358
G5	465	195	240	273	574	570	603	609	530	539
G6	373	138	184	206	413	410	455	463	370	379
G7	245	114	148	159	326	325	364	367	297	302
G8	282	158	214	237	456	453	488	497	420	426

**TABLE 5-5e. December 1996 to April 1997 winter runoff volumes, as in Table 5-5a.**

		simulated runoff volume from different precipitation inputs (mm)								
		precipitation gauge data			radar data					
stream	observed	gauge		gauge	no		mixed	mixed /	mixed	mixed/part
flow	runoff	uncorrected	corrected	corrected	raw	scaling	precip	particle	with	with
gauge	(mm)	gauge	to DFIR	to "bush"				shape	var. R	variable R
G1	328	171	192	195	167	166	196	201	142	146
G2	354	167	185	188	159	158	184	188	136	140
G3	381	158	173	177	148	147	171	175	128	131
G4	332	133	152	155	146	145	170	175	125	130
G5	521	229	253	257	218	216	253	259	185	191
G6	465	162	185	188	165	164	193	197	141	145
G7	280	149	170	173	157	156	184	189	134	138
G8	346	198	224	227	191	190	224	229	160	165

**TABLE 5-6. Average percent difference between the computed and observed runoff volumes at all hydrometric stations for the individual five years (8 datapoints), for all stations for the five years (40 datapoints), and for the total volume over the five winters (8 datapoints). The standard deviations are included for all runoff volumes and for the total station volumes.**

		precipitation gauge data			radar data					
		uncorrected	gauge	gauge	raw	no	mixed	mixed /	mixed	mixed/part
period		gauge	corrected	corrected		scaling	precip	particle	with	with
			to DFIR	to "bush"				shape	var. R	variable R
1993		-49.5	-47.8	-47.4	-19	-20.4	-10.5	-8.4	-28.2	-26.6
1994		-41.9	-33.3	-31.6	19.7	17.1	27.5	28.6	5.9	7.8
1995		-14.8	7.9	10.2	99	61.8	91.9	94.9	35.1	38.7
1996		-58	-46.7	-41	18.3	17.6	28.4	29.9	8.6	10.3
1997		-53.7	-48	-47.1	-54.1	-54.4	-46.5	-45.2	-60.9	-59.7
$\mu$ of all runoff volumes		-43.6	-33.6	-31.4	12.8	4.3	18.2	20	-7.9	-6
$\sigma$ of all runoff volumes		18.4	24.7	24.9	56.6	44.9	52.9	53.4	38.2	39
$\mu$ of 5 winter total		-46.9	-37.5	-35.1	2.7	-3.7	8.8	10.5	-14.7	-12.8
$\sigma$ of 5 winters		6.68	8.31	8.38	14.8	13.8	16	16.4	11.8	12.25

TABLE 5-7a. Equations and for the third order polynomial fits of the form  $K_{obs}/K_{comp} = a_3t_m^3 + a_2t_m^2 + a_1t + b$  for CARE and Elora, corresponding to the curves in Figure 5-18a.

range of application (Julian dates)	sunrise before hour	sunset after hour	polynomial coefficients				
			$a_3$	$a_2$	$a_1$	b	$r^2$
356 to 38	8:00	16:00	0.001010	-0.046396	0.68939	-2.540217	0.9985
39 to 79	7:00	17:00	0.000416	-0.020303	0.326111	-0.862821	0.9790
80 to 121	6:00	18:00	0.000717	-0.031159	0.448264	-1.309011	0.9769

TABLE 5-7b. Equations and for the third order polynomial fits of the form  $K_{obs}/K_{comp} = a_3t_m^3 + a_2t_m^2 + a_1t + b$  for Toronto, corresponding to the curves in Figure 5-18b.

range of application (Julian dates)	sunrise before hour	sunset after hour	polynomial coefficients				
			$a_3$	$a_2$	$a_1$	b	$r^2$
356 to 38	8:00	16:00	0.002046	-0.085097	1.170065	-4.551558	0.9922
39 to 79	7:00	17:00	0.001439	-0.060256	0.826533	-2.945268	0.9859
80 to 121	6:00	18:00	0.000592	-0.026519	0.391736	-1.090355	0.9746

TABLE 5-8. Average cloud cover fraction at the AES CARE, Elora and Toronto meteorological stations as derived from the difference between measured shortwave and clear-sky shortwave radiation, using all data and daytime data. The adjusted method considers the fact that typically less than 100% of the theoretical clear-sky radiation reaches the earth's surface and that there are low morning and late afternoon short-wave measurement encountered during the winter and early spring.

	unadjusted cloud cover fraction						adjusted fraction					
	all data			no night or missing data			all data			no night or missing data		
	CARE	Elora	Toronto	CARE	Elora	Toronto	CARE	Elora	Toronto	CARE	Elora	Toronto
winter	0.59	0.61	0.63	0.74	0.75	0.79	0.53	0.57	0.55	0.58	0.58	0.61
1993	0.59	0.61	0.63	0.74	0.75	0.79	0.53	0.57	0.55	0.58	0.58	0.61
1994	0.59	0.60	0.61	0.71	0.72	0.76	0.52	0.53	0.54	0.56	0.57	0.58
1995	0.57	0.57	0.59	0.67	0.68	0.71	0.53	0.53	0.54	0.56	0.57	0.59
1996	0.54	0.54	0.59	0.58	0.59	0.81	0.49	0.49	0.54	0.47	0.48	0.63
1997	0.56	0.56	0.60	0.68	0.66	0.72	0.52	0.51	0.54	0.56	0.53	0.59
all	0.57	0.57	0.60	0.67	0.68	0.75	0.52	0.52	0.54	0.54	0.55	0.60

TABLE 5-9. Fresh snow density data collected in Waterloo during the winter of 1999, including the average temperature during the each snowfall event, the average depth, the average SWE, and the maximum and minimum fresh snow density limits.

measurement number	average temperature (°C)	average depth (cm)	average SWE (mm)	average $\rho_s(\text{fresh})$ (kg/m <sup>3</sup> )	maximum $\rho_s(\text{fresh})$ (kg/m <sup>3</sup> )	minimum $\rho_s(\text{fresh})$ (kg/m <sup>3</sup> )
1	-8.94	3.6	3.55	98.5	106	91.3
2	-12.28	6.04	5.32	88	94	82.5
3	-7.1	2	2.27	113	125	103
4	-11.54	14.16	9.22	65.1	68.9	61.6
5	-20.58	5.39	6.22	115	124	108
6	-13.09	4.36	3.94	90.4	97.1	84.2
6a	-13.2	2.99	3.56	119	130	110
6b	-12.69	1.37	0.38	27.5	31.1	24.4
7	-1.7	1.96	1.65	84.3	93.3	76.4
8	-2.89	1.79	1.54	85.8	95.4	77.4
9	-0.57	0.7	2.84	405	496	338
9a	-0.63	0.2	1.65	827	1000	525
9b	0.46	0.5	1.18	236	310	188
10	-3.23	1.07	0.49	46	53.3	40.1
11	-3.15	1.93	2.05	106	118	96.4
11a	-3.07	0.93	1.24	134	157	115
11b	-3.23	1.00	0.81	81.1	94.7	70.2
12	-1.2	4.76	7.43	156	167	145
13	-5.82	6.34	4.93	77.7	82.9	72.9
14	-6.99	3	2.56	85.4	92.7	78.7

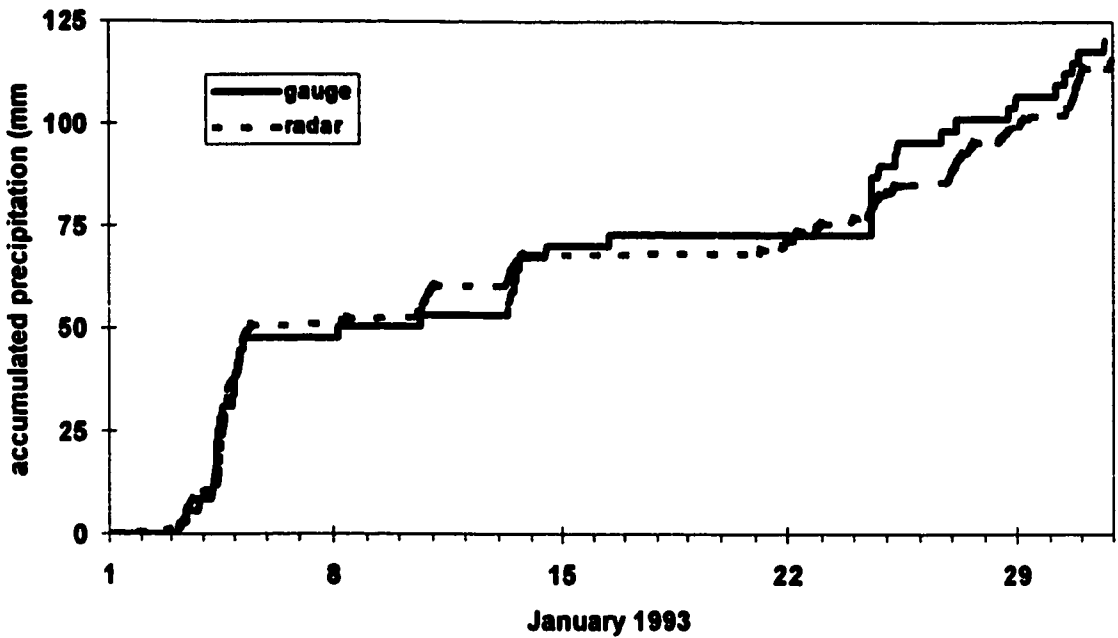


FIGURE 5-1. Snowfall radar versus "bush" gauge accumulation comparison for January 1993 at the Wormwood site.

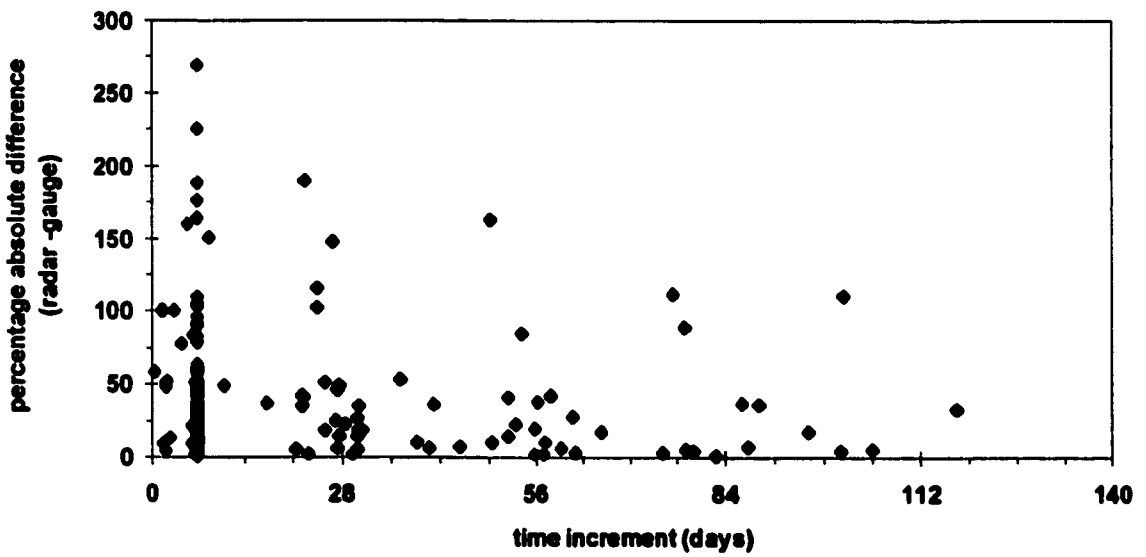


FIGURE 5-2. Percent absolute difference in the raw radar data versus the gauge accumulation as a function of time.

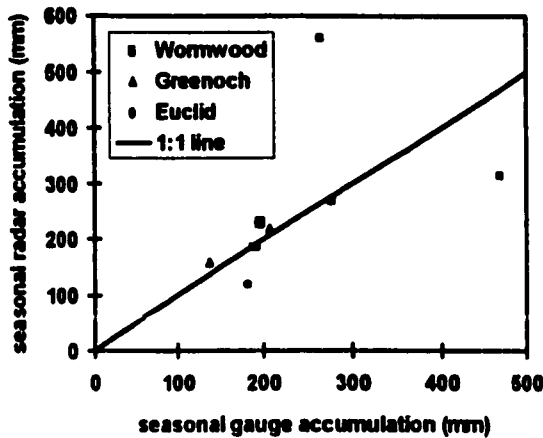


FIGURE 5-3a. Seasonal snowfall accumulation raw radar versus "bush" gauge ( $\rho^2 = 0.178$ ).

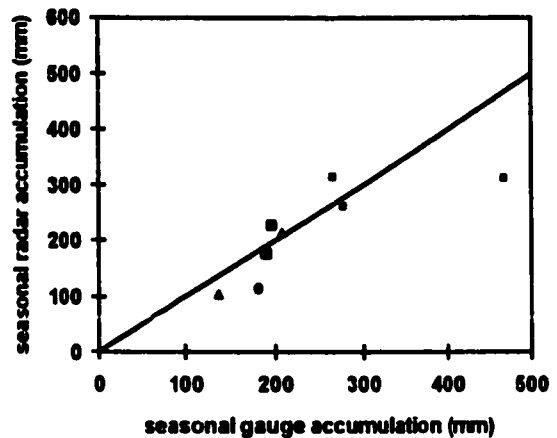


FIGURE 5-3b. Scale adjusted seasonal radar-gauge snowfall comparison ( $\rho^2 = 0.335$ ).

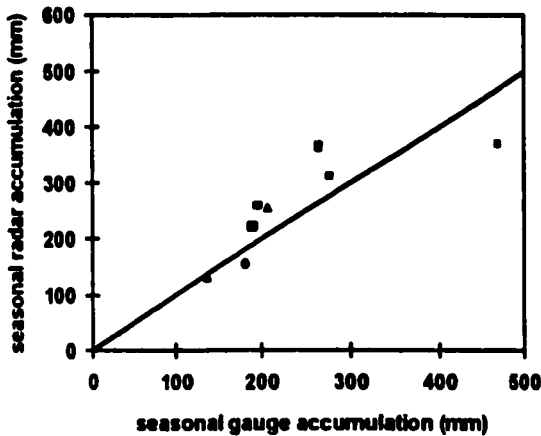


FIGURE 5-3c. Seasonal snowfall adjusted for scale and mixed precipitation using Auer's temperature curve with a constant factor for rain ( $\rho^2 = 0.595$ ).

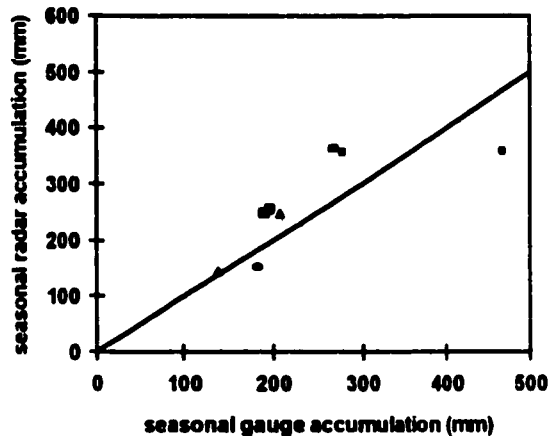


FIGURE 5-3d. Seasonal snowfall adjusted for scale and mixed precipitation using Auer's temperature curve and precipitation rate ( $\rho^2 = 0.474$ ).

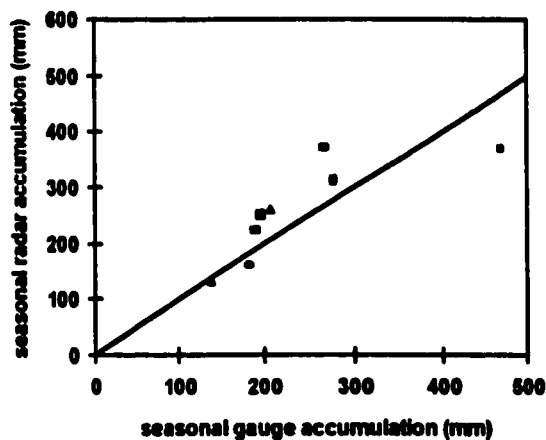


FIGURE 5-3e. Seasonal snowfall adjusted for scale, mixed precipitation (Auer with constant rain factor), and snowflake particle shape ( $\rho^2 = 0.593$ ).

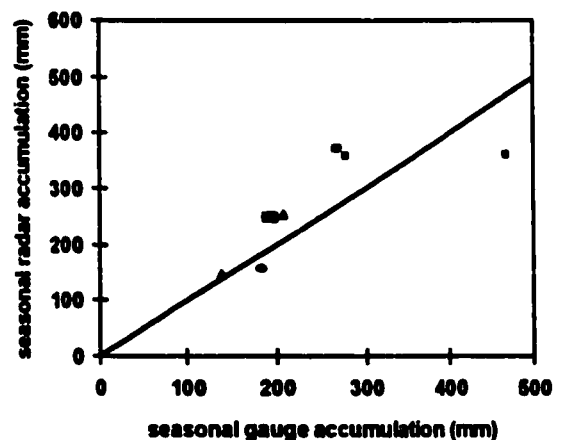


FIGURE 5-3f. Seasonal snowfall adjusted for scale, mixed precipitation (Auer with variable R), and snowflake particle shape ( $\rho^2 = 0.471$ ).

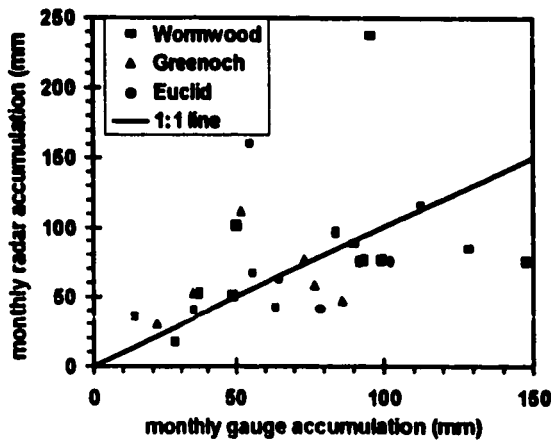


FIGURE 5-4a. Monthly snowfall accumulation raw radar versus "bush" gauge ( $\rho^2 = 0.089$ ).

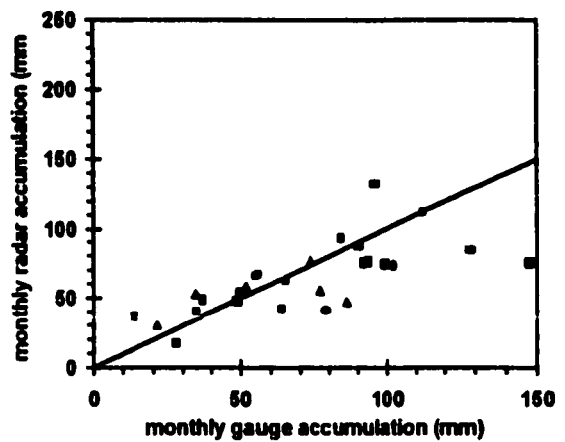


FIGURE 5-4b. Scale adjusted seasonal radar-gauge snowfall comparison ( $\rho^2 = 0.272$ ).

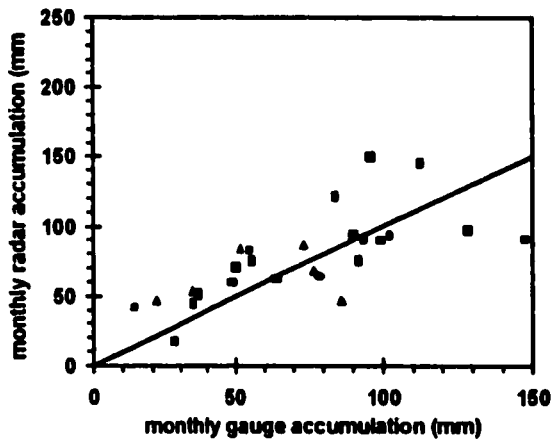


FIGURE 5-4c. Monthly snowfall adjusted for scale and mixed precipitation using Auer's temperature curve with a constant factor for rain ( $\rho^2 = 0.470$ ).

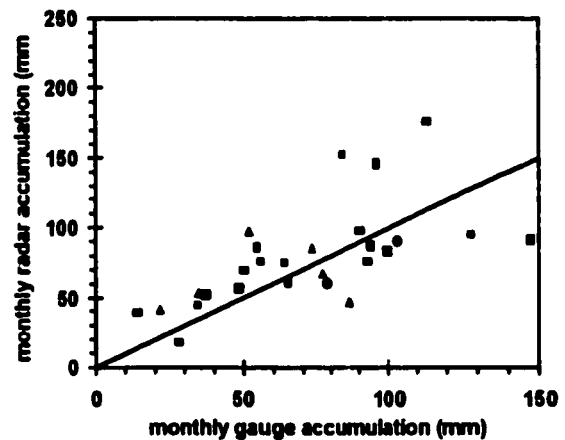


FIGURE 5-4d. Monthly snowfall adjusted for scale and mixed precipitation using Auer's temperature curve and precipitation rate ( $\rho^2 = 0.405$ ).

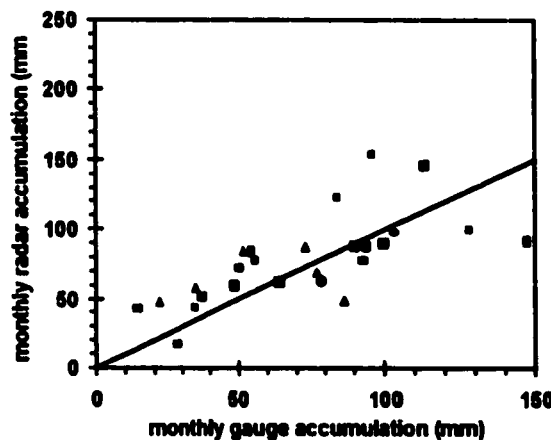


FIGURE 5-4e. Monthly snowfall adjusted for scale, mixed precipitation (Auer with constant rain factor), and snowflake particle shape ( $\rho^2 = 0.472$ ).

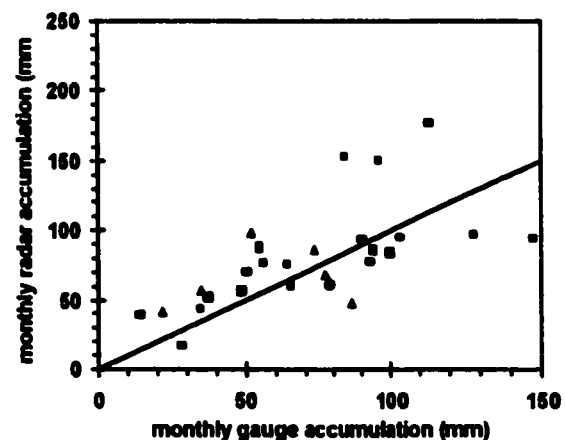


FIGURE 5-4f. Monthly snowfall adjusted for scale, mixed precipitation (Auer with variable R), and snowflake particle shape ( $\rho^2 = 0.406$ ).



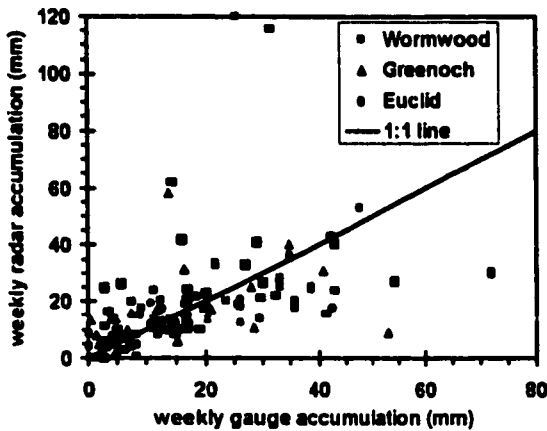


FIGURE 5-5a. Weekly snowfall accumulation raw radar versus “bush” gauge ( $\rho^2 = 0.081$ ).

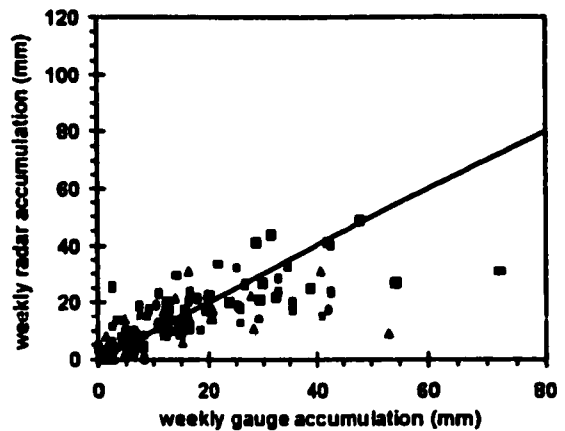


FIGURE 5-5b. Scale adjusted seasonal radar-gauge snowfall comparison ( $\rho^2 = -0.008$ ).

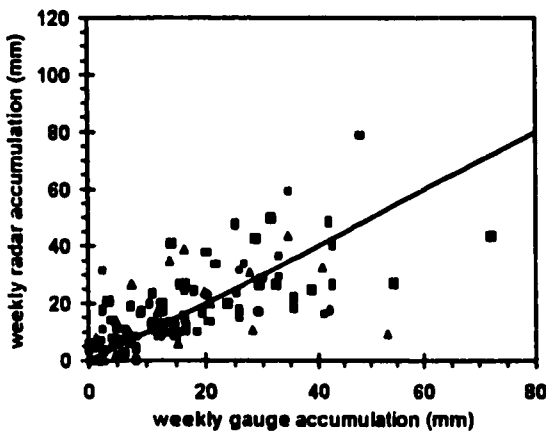


FIGURE 5-5c. Weekly snowfall adjusted for scale and mixed precipitation using Auer's temperature curve with a constant factor for rain ( $\rho^2 = 0.326$ ).

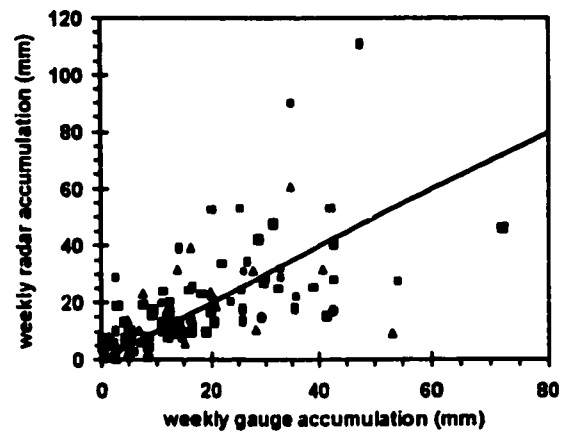


FIGURE 5-5d. Weekly snowfall adjusted for scale and mixed precipitation using Auer's temperature curve and precipitation rate ( $\rho^2 = 0.342$ ).

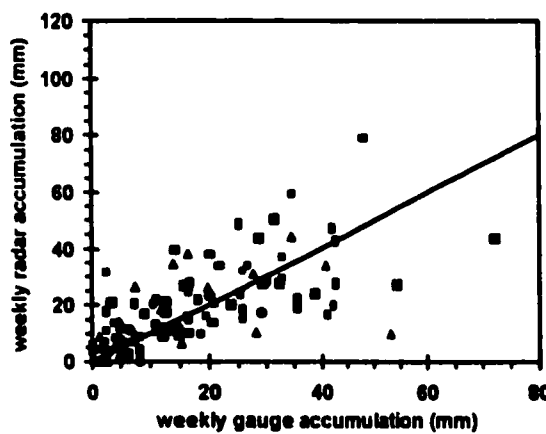


FIGURE 5-5e. Weekly snowfall adjusted for scale, mixed precipitation (Auer with constant rain factor), and snowflake particle shape ( $\rho^2 = 0.341$ ).

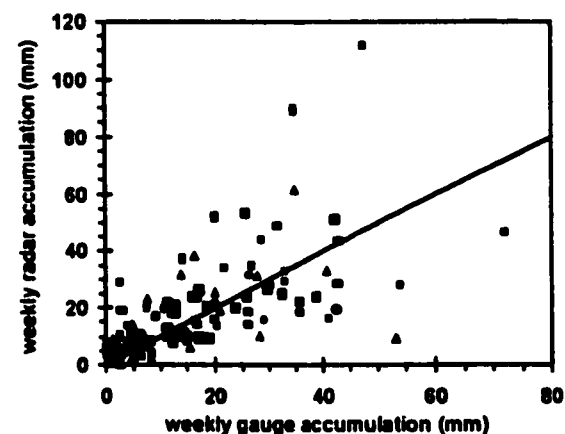


FIGURE 5-5f. Weekly snowfall adjusted for scale, mixed precipitation (Auer with variable R), and snowflake particle shape ( $\rho^2 = 0.351$ ).

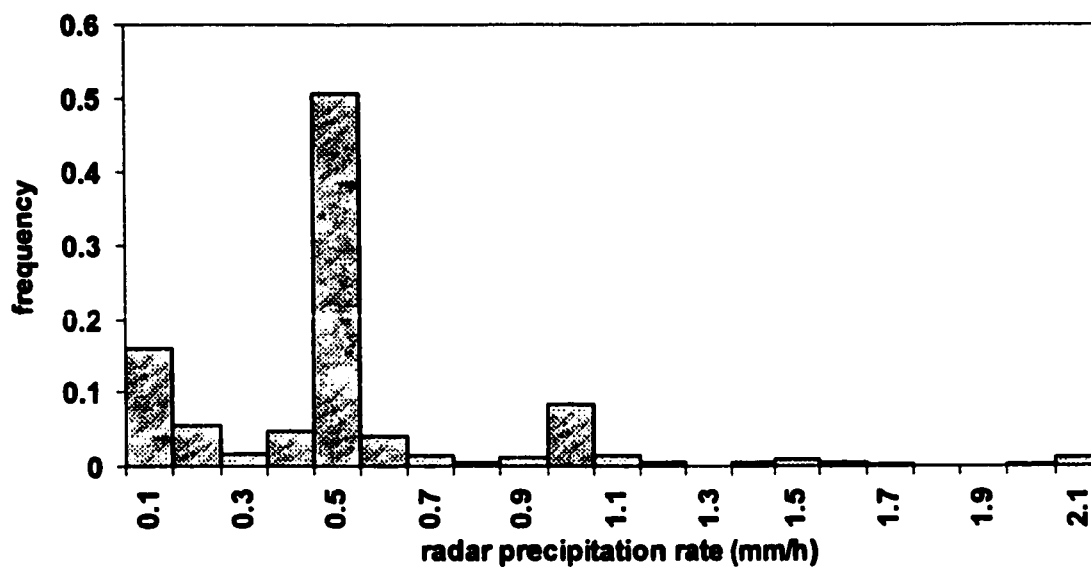


FIGURE 5-6. Histogram of winter radar precipitation rates for the three UW gauge sites. The bin interval is 0.1 mm/h. While the radar rate is measured in 0.5 mm/h increments, the radar data are a weighted average across the 3 by 3 pixels centred above the desired location (see section 3.1.4e).

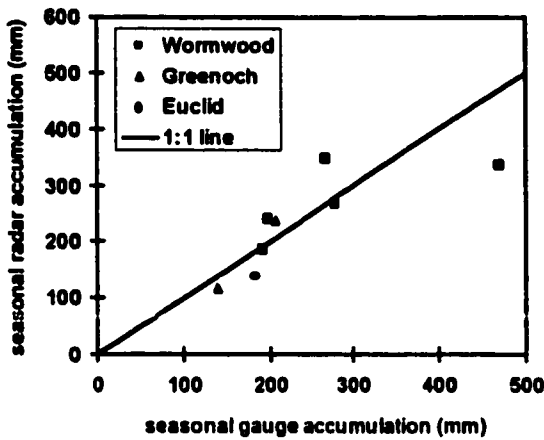


FIGURE 5-7a. Seasonal radar snowfall adjusted for Auer's mixed precipitation with precipitation rate to a maximum rain factor of 2.03 ( $\rho^2 = 0.518$ ).

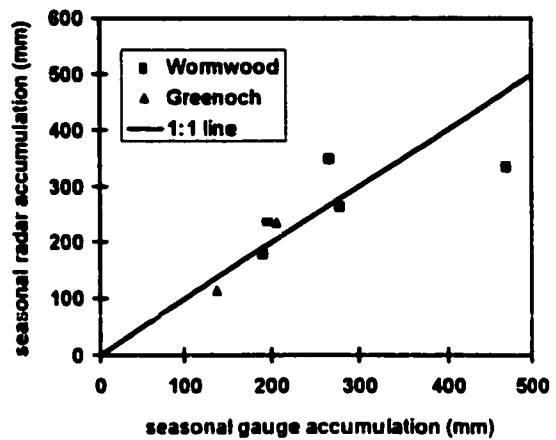


FIGURE 5-8a. Seasonal radar snowfall adjusted for mixed precipitation (variable R to a max. of 2.03) and particle shape using  $T_{dewpoint}$  ( $\rho^2 = 0.402$ ).

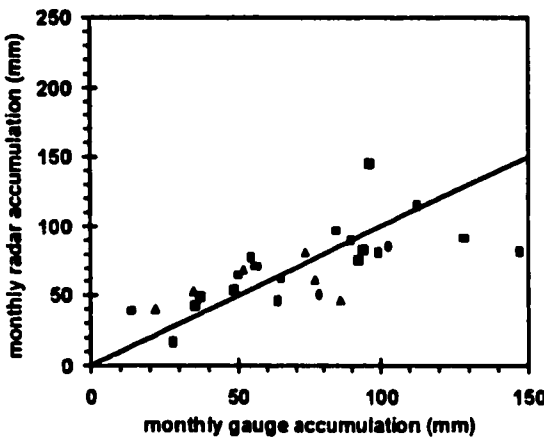


FIGURE 5-7b. As in Figure 5-7a for monthly snowfall ( $\rho^2 = 0.405$ ).

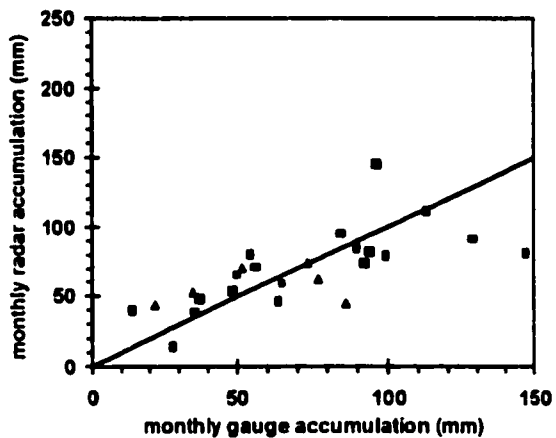


FIGURE 5-8b. As in Figure 5-8b for monthly snowfall ( $\rho^2 = 0.275$ ).

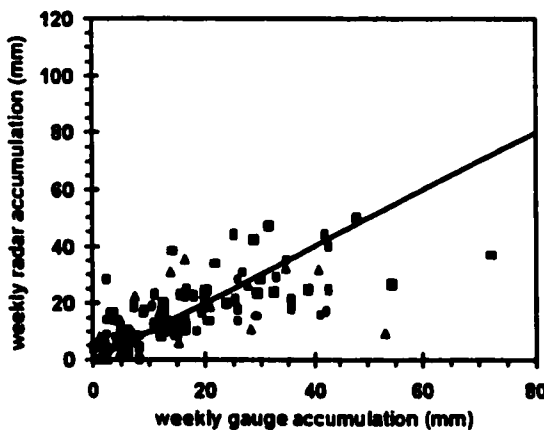


FIGURE 5-7c. As in Figure 5-7a for weekly snowfall ( $\rho^2 = 0.158$ ).

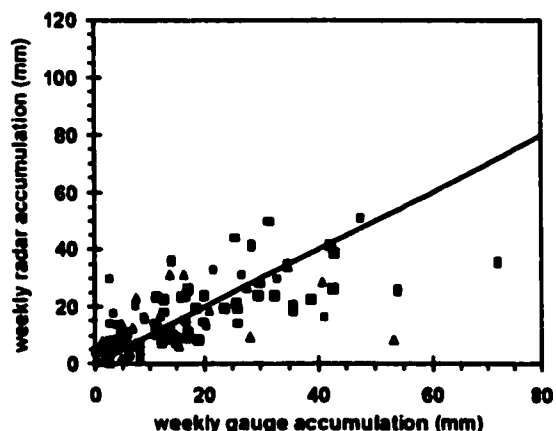


FIGURE 5-8c. As in Figure 5-8b for weekly snowfall ( $\rho^2 = 0.166$ ).

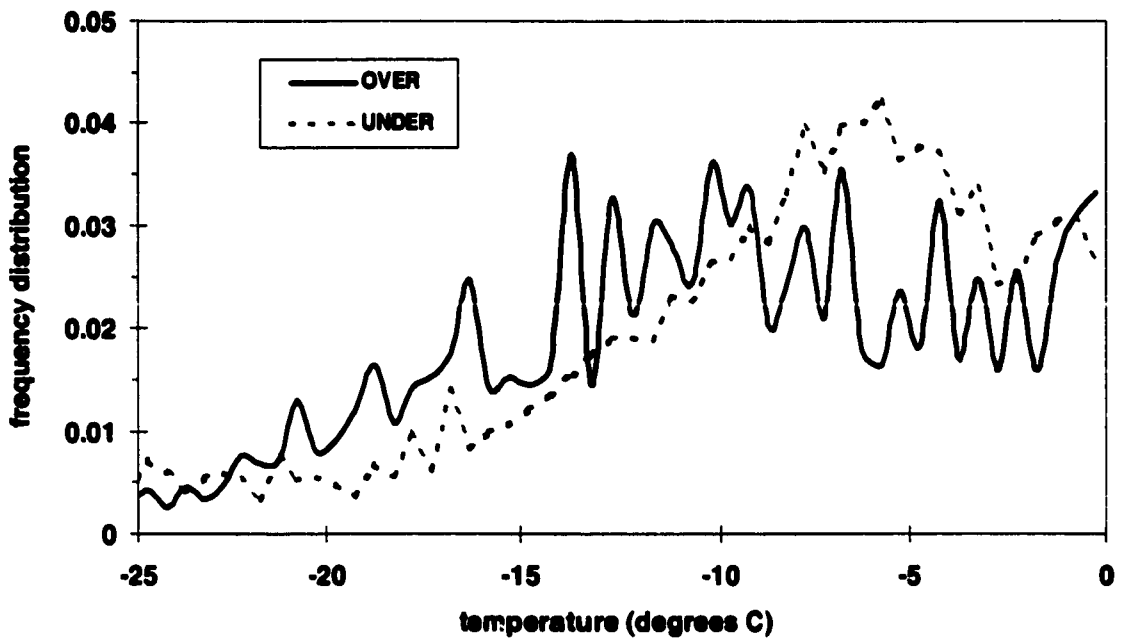


FIGURE 5-9a. The distributions for the OVER and UNDER estimated precipitation data.

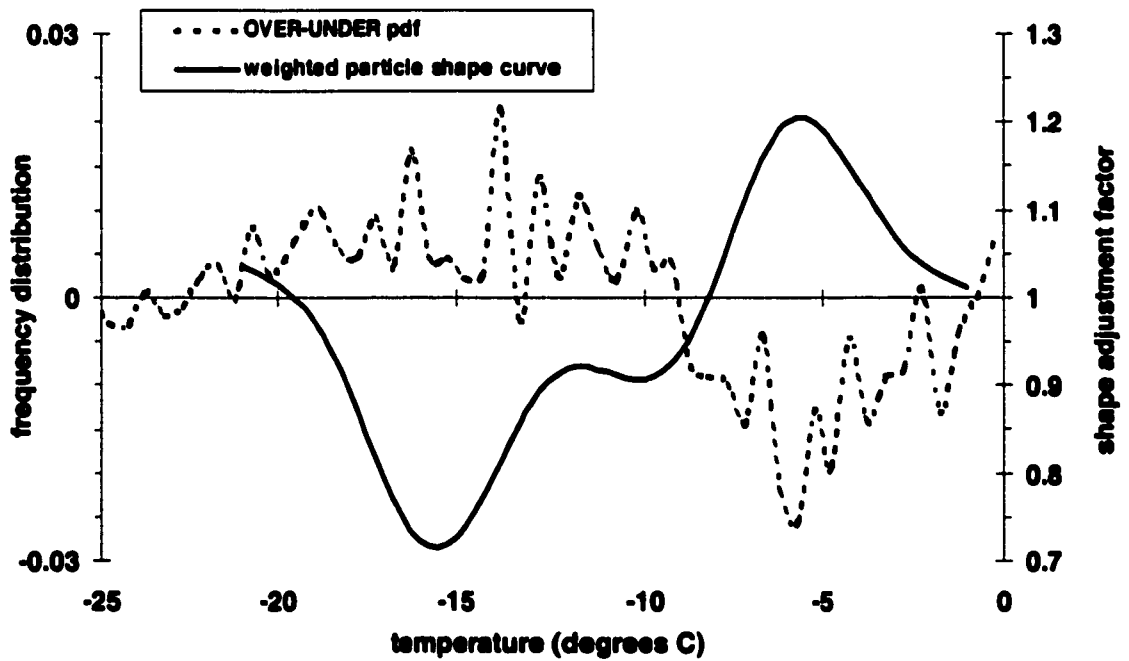


FIGURE 5-9b. The initial non-weighted particle shape adjustment curve and the difference between the OVER and UNDER estimated precipitation data.

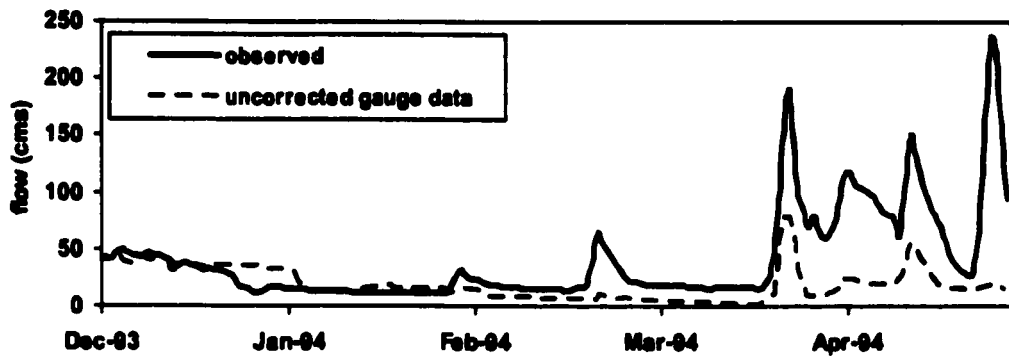


FIGURE 5-10a. December 1993 to April 1994 observed (solid) and simulated (dashed) streamflow at the Grand River at Galt derived from uncorrected gauge data.

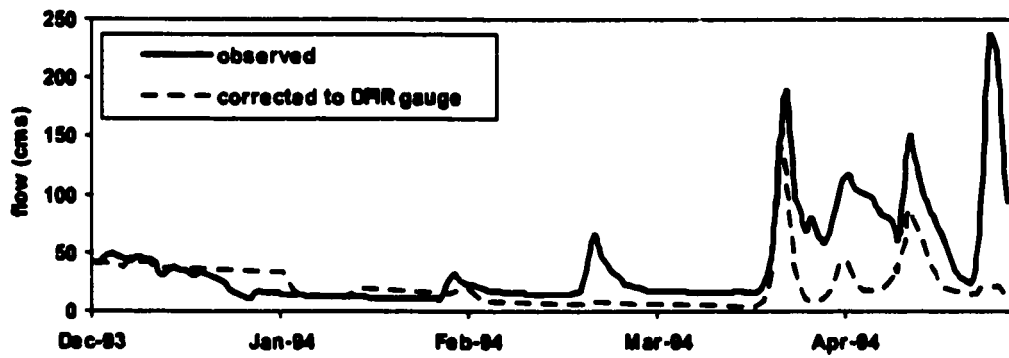


FIGURE 5-10b. December 1993 to April 1994 observed (solid) and simulated (dashed) streamflow at the Grand River at Galt derived from gauge data corrected to DFIR gauge.

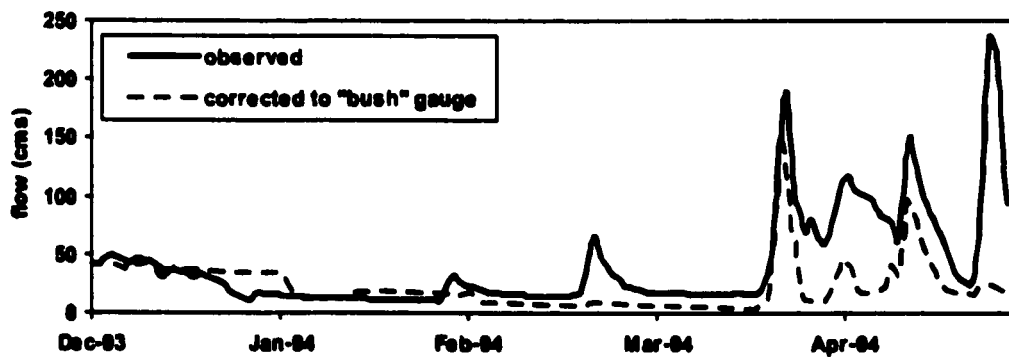


FIGURE 5-10c. December 1993 to April 1994 observed (solid) and simulated (dashed) streamflow at the Grand River at Galt derived from gauge data corrected to "bush" gauge.

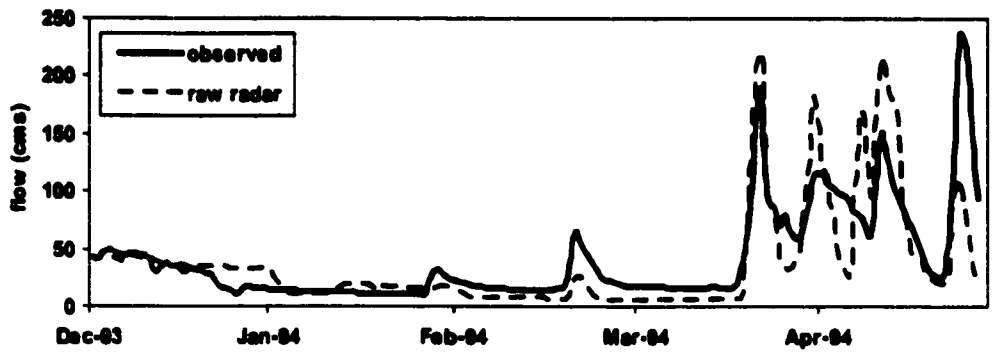


FIGURE 5-10d. December 1993 to April 1994 observed (solid) and simulated (dashed) streamflow at the Grand River at Galt derived from raw radar

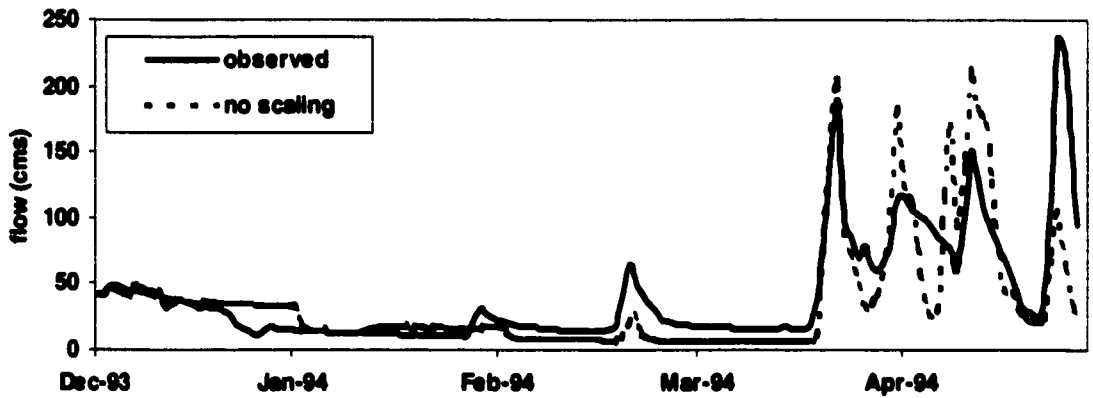


FIGURE 5-10e. Grand River at Galt winter 1993/1994 hydrograph using the "no scaling" radar dataset.

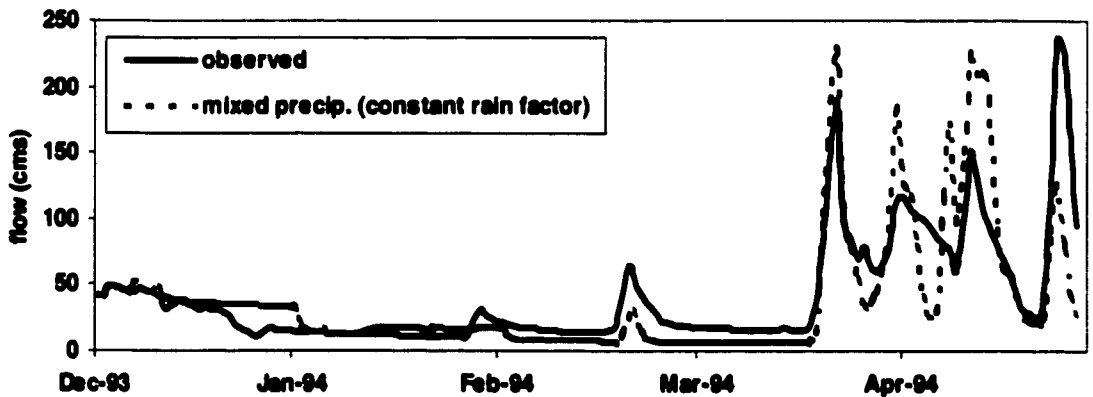


FIGURE 5-10f. Grand River at Galt winter 1993/1994 hydrograph using the "mixed precipitation using a constant rain factor" radar dataset.

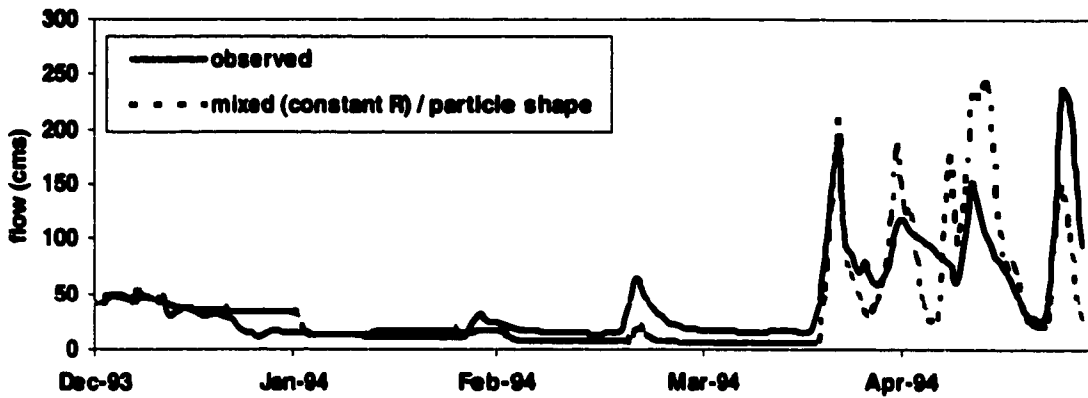


FIGURE 5-10g. Grand River at Galt winter 1993/1994 hydrograph using the "mixed precipitation using a constant rain factor and particle shape curve" radar dataset.

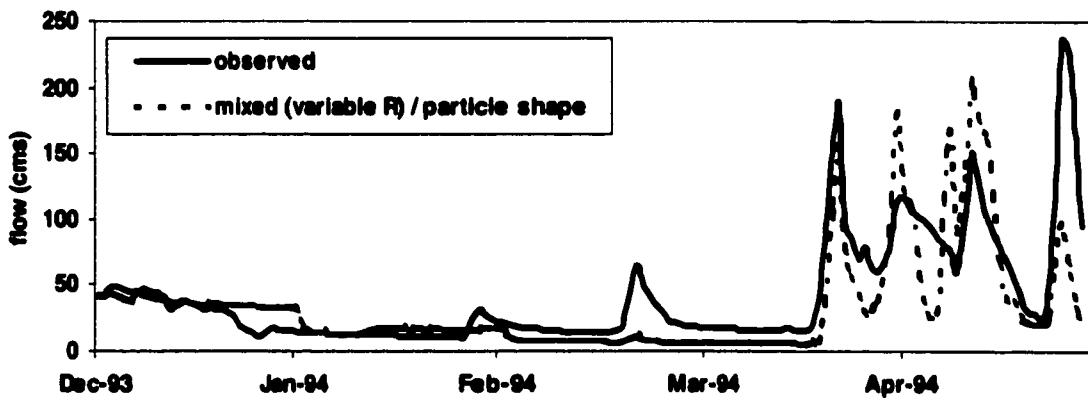


FIGURE 5-10h. Grand River at Galt winter 1993/1994 hydrograph using the "mixed precipitation using a variable rain factor and particle shape curve" radar dataset.

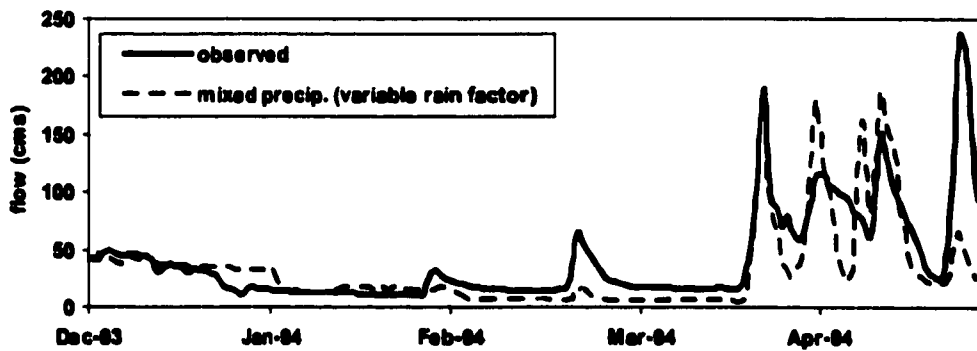


FIGURE 5-10i. December 1993 to April 1994 observed (solid) and simulated (dashed) streamflow at the Grand River at Galt derived from radar adjusted for mixed precipitation (variable rain factor) and particle shape.

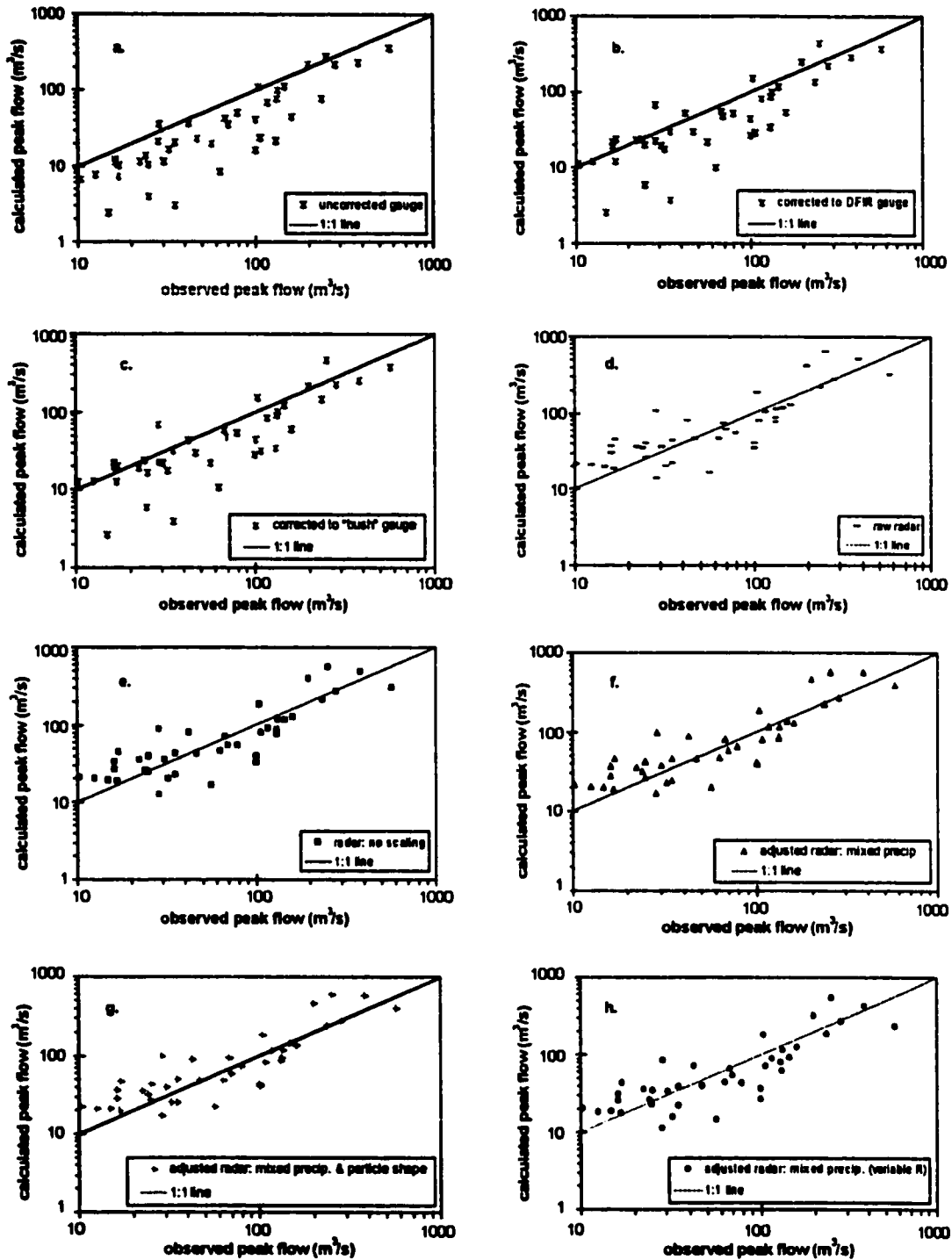


FIGURE 5-11. Observed versus calculated peak flow for the 1993 to 1997 winters using (a) uncorrected gauge data, (b) gauge data corrected to DFIR gauge, (c) gauge data corrected to "bush" gauge, (d) raw radar input, (e) scale adjusted radar, and (f) radar adjusted for mixed precipitation using Auer's curve with a constant rain factor (2.03), (g) radar adjusted for scale, mixed precipitation (constant R), and snowflake particle shape, and (h) radar adjusted for mixed precipitation using Auer's temperature curve and precipitation rate.



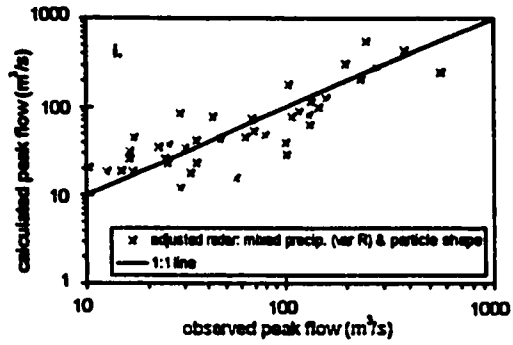


FIGURE 5-11 (continued). Observed versus calculated peak flow for the 1993 to 1997 winters using (i) radar adjusted for scale, mixed precipitation (variable R), and snowflake particle shape precipitation modelling input.

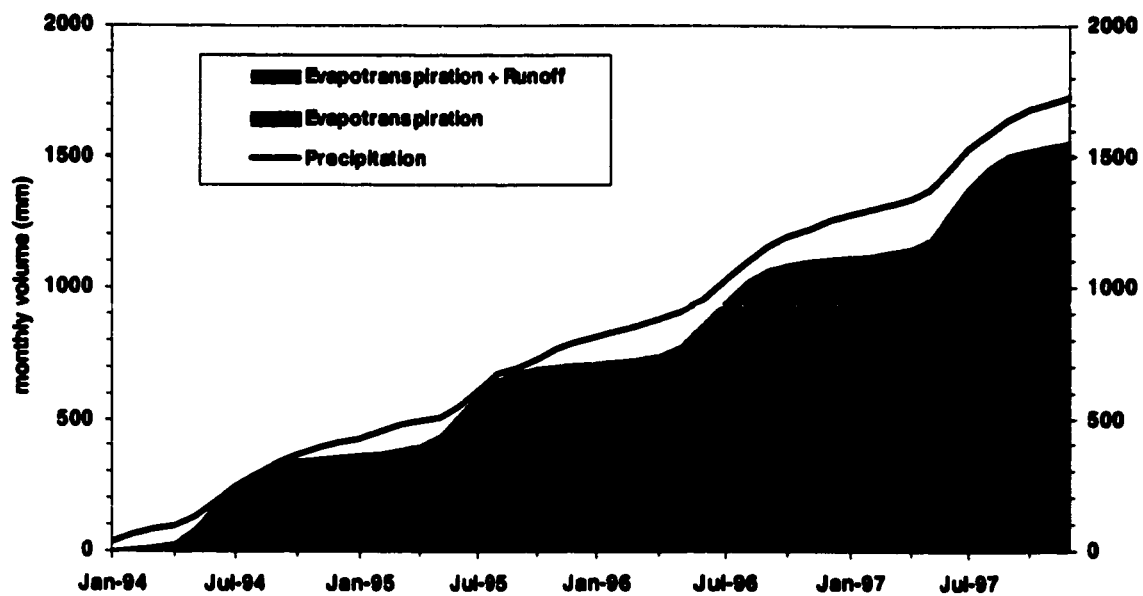


FIGURE 5-12a. Four-year water balance using WATFLOOD (Mackenzie River basin).

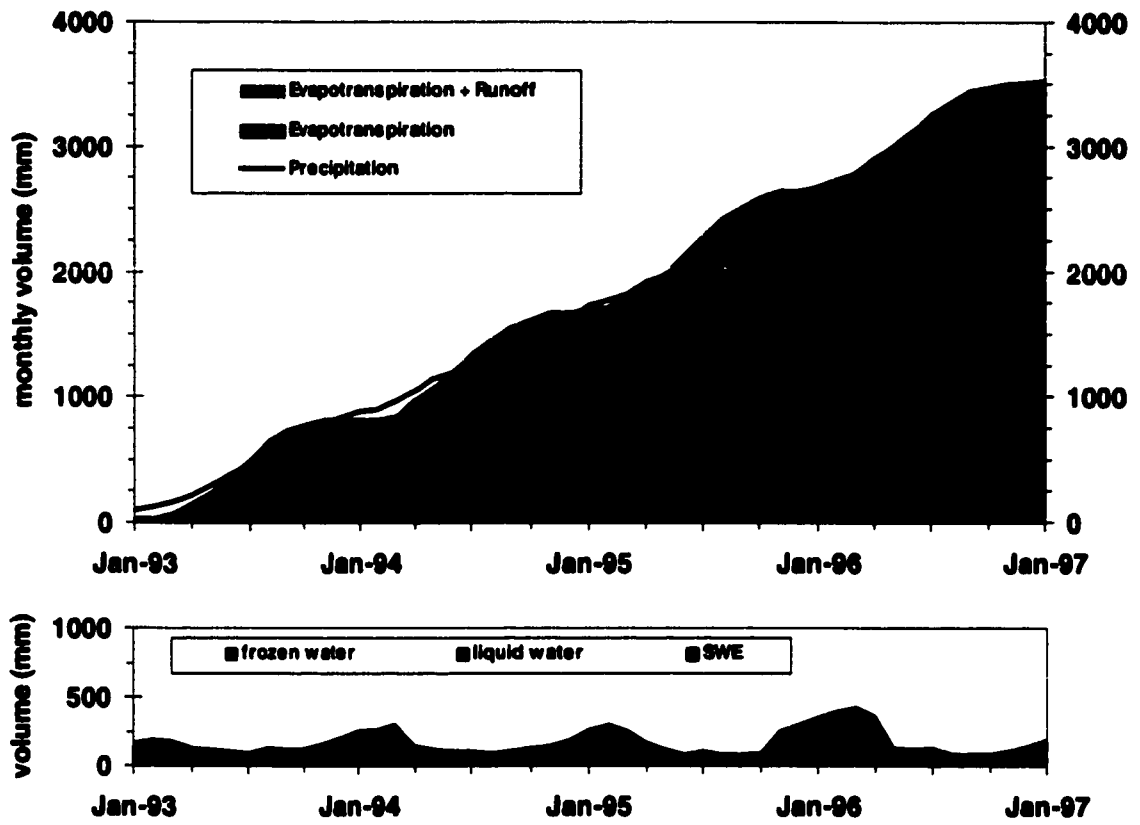


FIGURE 5-12b. Five-year water balance using WAT\_CLS3 at one grid point in the Grand River.

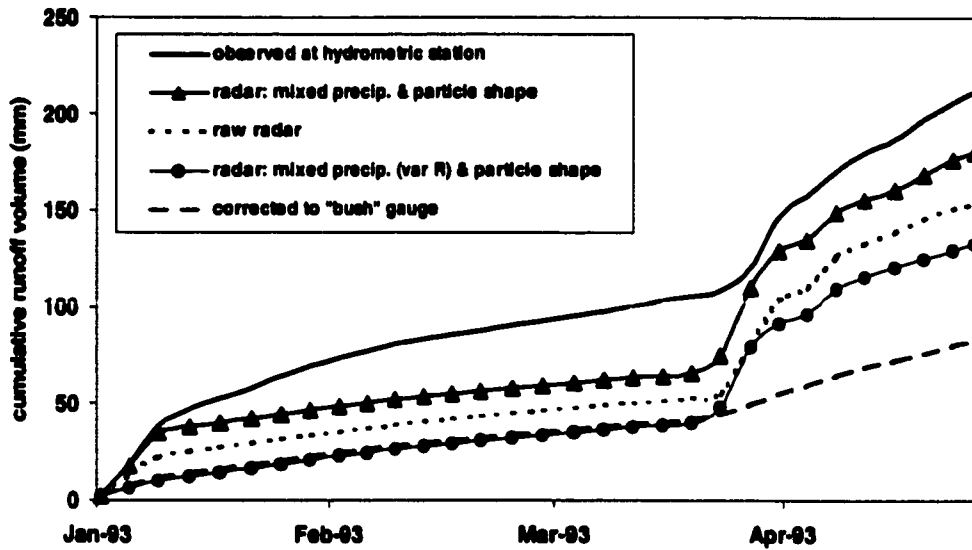


FIGURE 5-13a. Cumulative runoff volume from Jan. 1993 to April 1993 on the Eramosa River above Guelph.

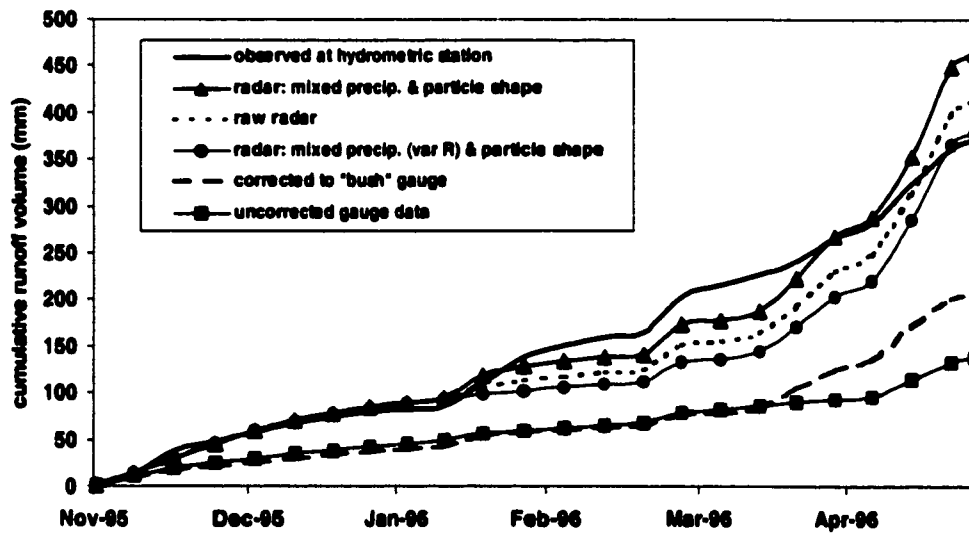


FIGURE 5-13b. Cumulative runoff volume from Nov. 1995 to April 1996 on the Speed River at Armstrong Mills.

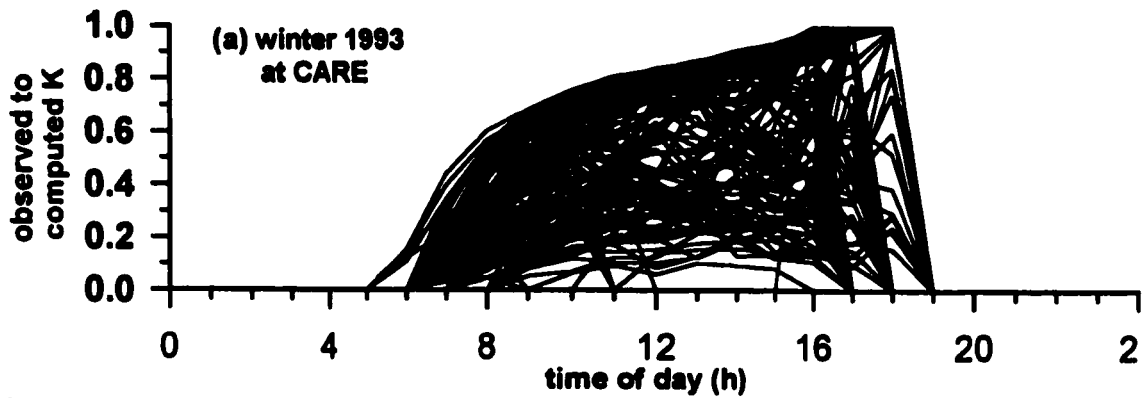


FIGURE 5-14a. Ratio of measured to computed clear-sky hourly shortwave radiation for the AES meteorological station at CARE over the winter of 1993, assuming that station data were collected at Local Apparent Time (LAT).

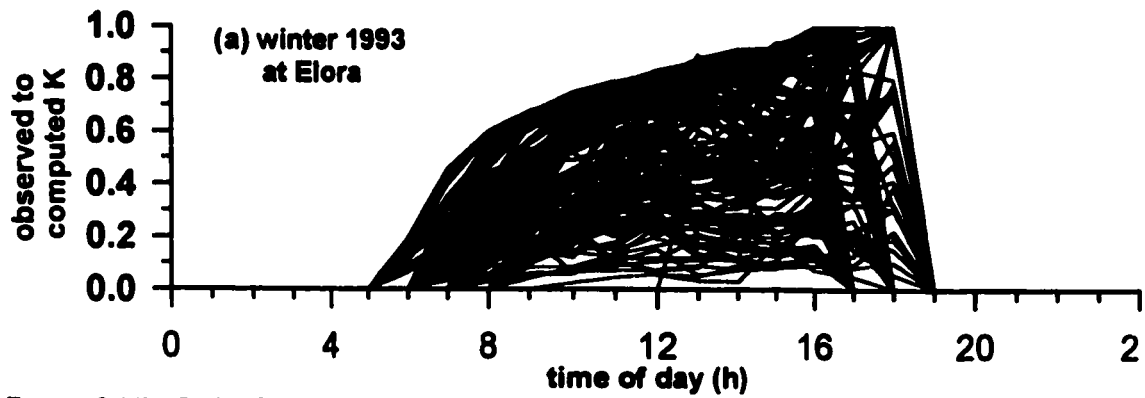


FIGURE 5-14b. Ratio of measured to computed clear-sky hourly shortwave radiation at Elora using LAT.

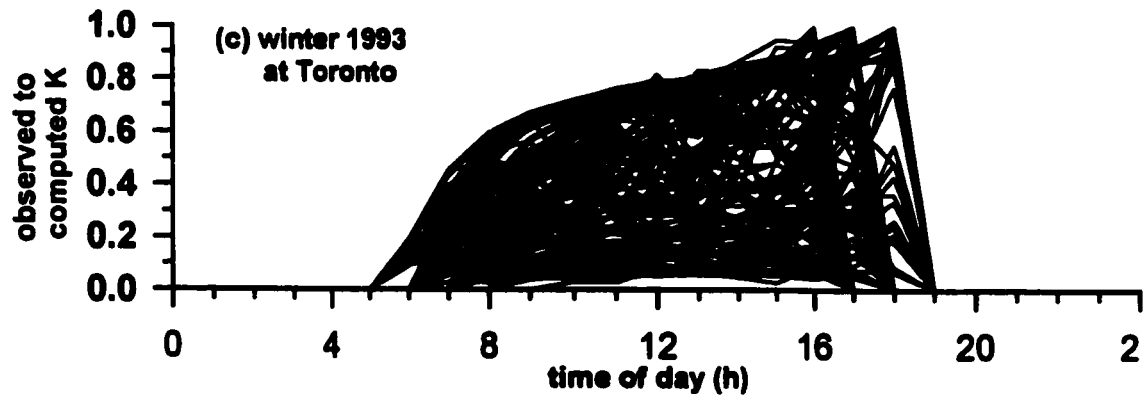


FIGURE 5-14c. Ratio of measured to computed clear-sky hourly shortwave radiation at Toronto using LAT.

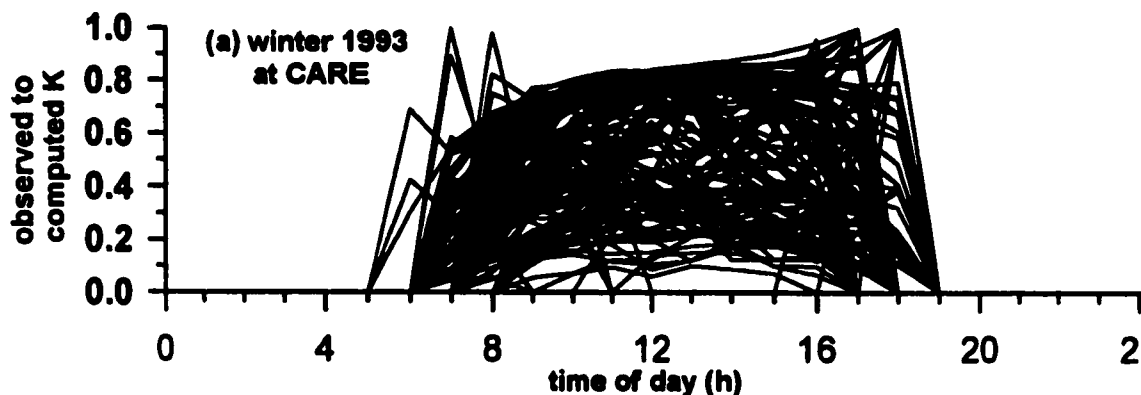


FIGURE 5-15a. Ratio of measured to computed clear-sky hourly shortwave radiation for the AES meteorological station at CARE over the winter of 1993, assuming that station data were collected at Local Standard Time (LST).

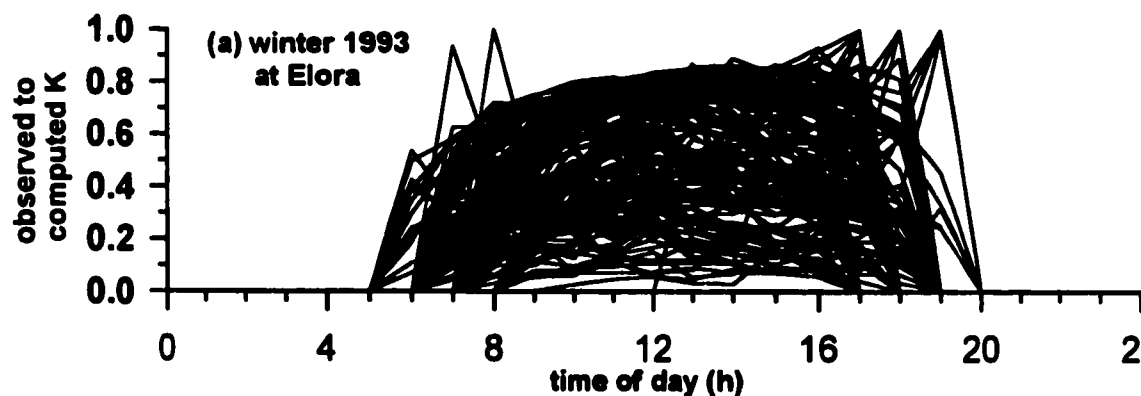


FIGURE 5-15b. Ratio of measured to computed clear-sky hourly shortwave radiation at Elora using LST.

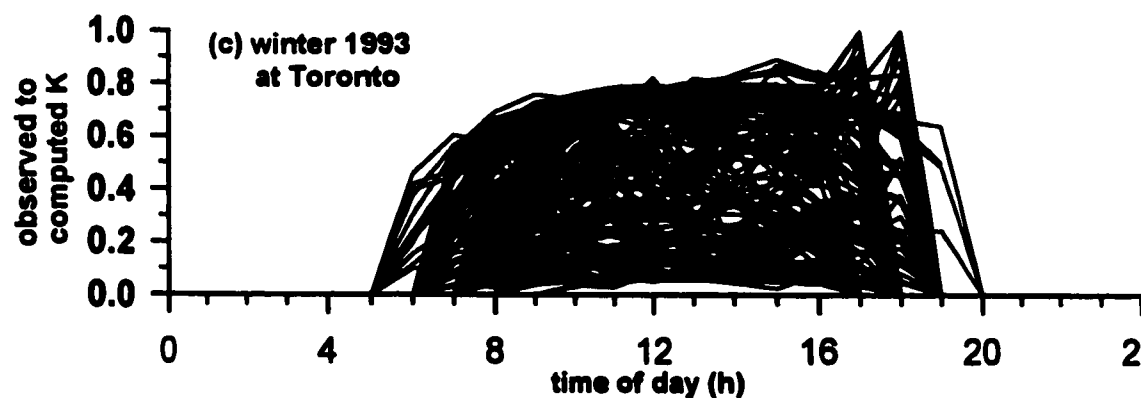


FIGURE 5-15c. Ratio of measured to computed clear-sky hourly shortwave radiation at Toronto using LST.

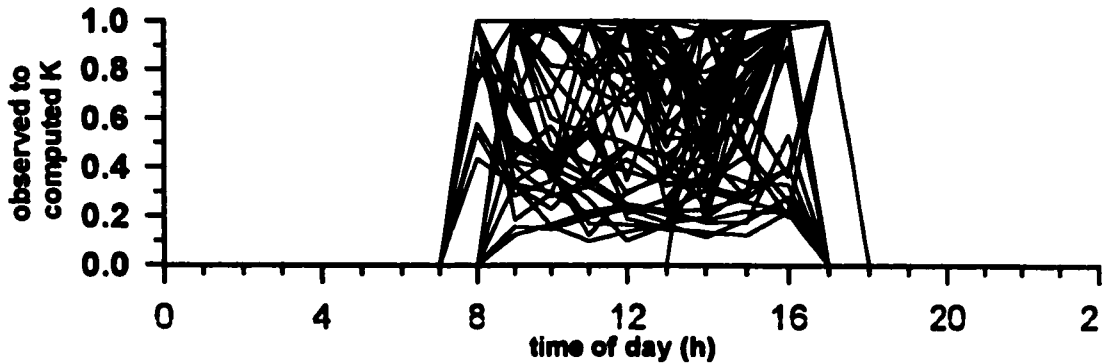


FIGURE 5-16a. Ratio of measured to computed clear-sky hourly radiation at CARE and Elora for November 3 (J=307) to December 21, 1995 (J=355).

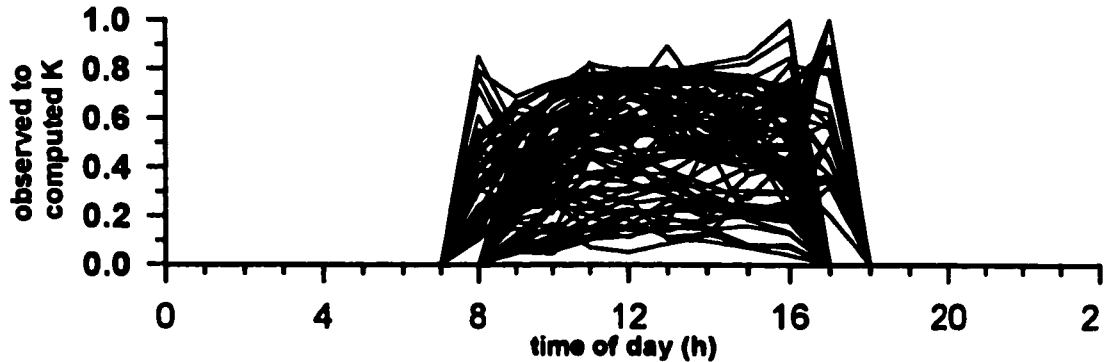


FIGURE 5-16b. As in Figure C-4a, for December 22, 1995 (J=356) to February 7, 1996 (J=38).

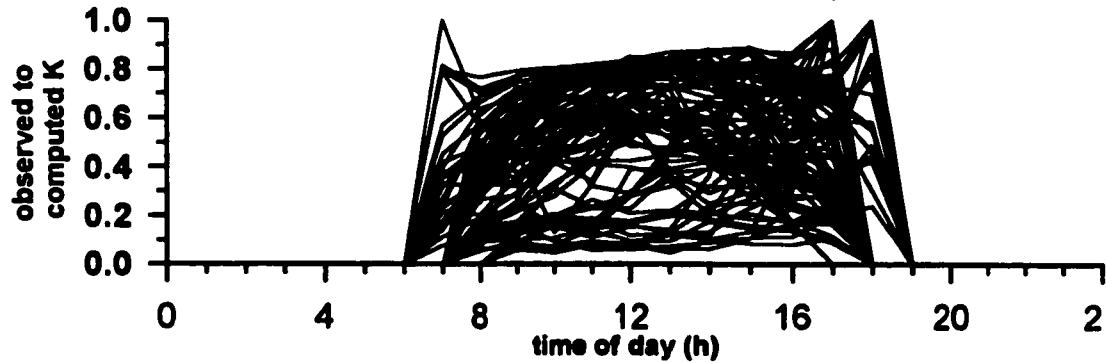


FIGURE 5-16c. As in Figure C-4a, for February 8, 1996 (J=39) to March 19, 1996 (J=79).

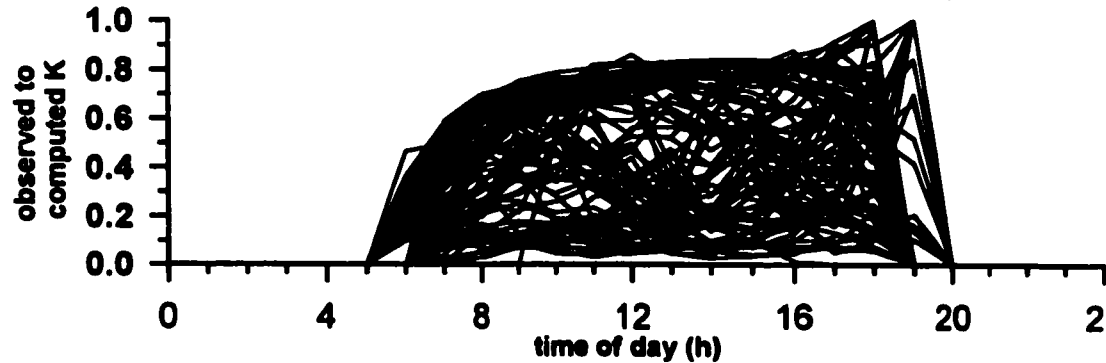


FIGURE 5-16d. As in Figure C-4a, for March 20, 1996 (J=80) to April 30, 1996 (J=121).

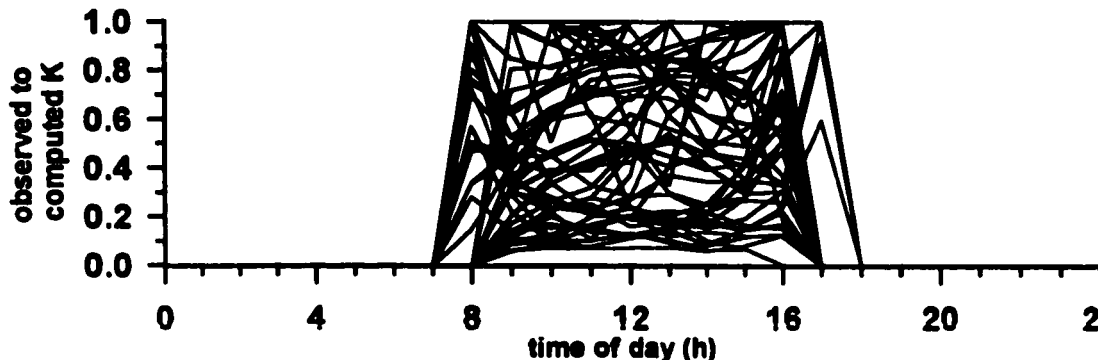


FIGURE 5-17a. Ratio of measured to computed clear-sky hourly radiation at Toronto for November 3 (J=307) to December 21, 1994 (J=355).

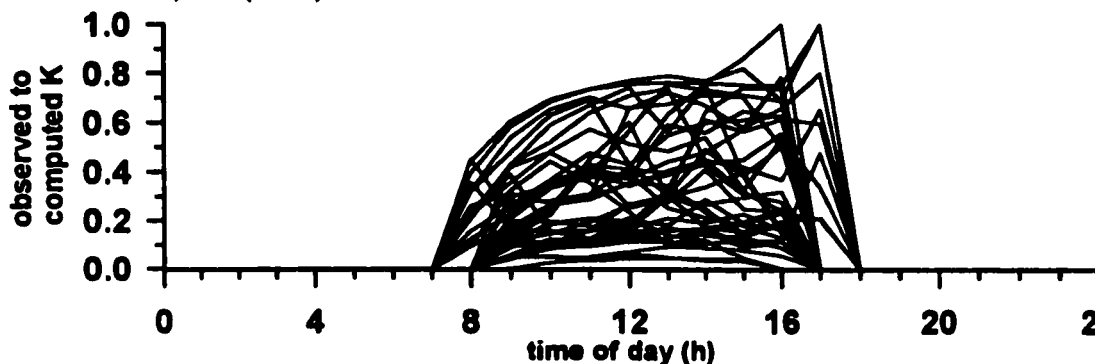


FIGURE 5-17b. As in Figure C-5a, for December 22, 1994 (J=356) to February 7, 1995 (J=38).

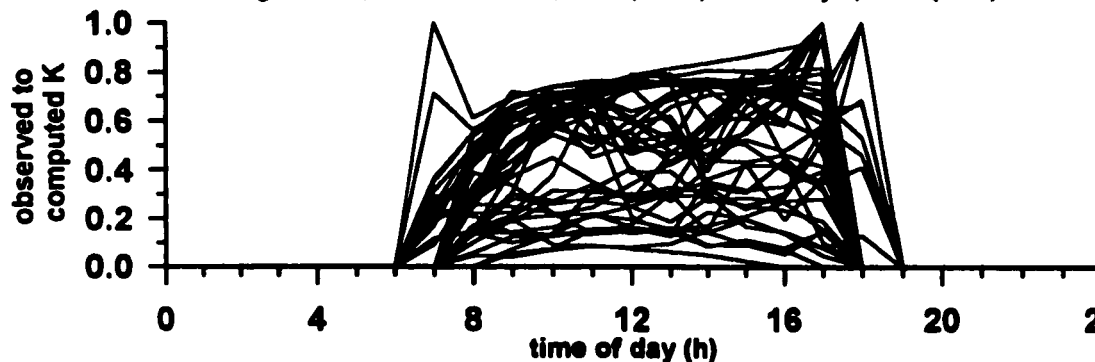


FIGURE 5-17c. As in Figure C-5a, for February 8, 1995 (J=39) to March 20, 1995 (J=79).

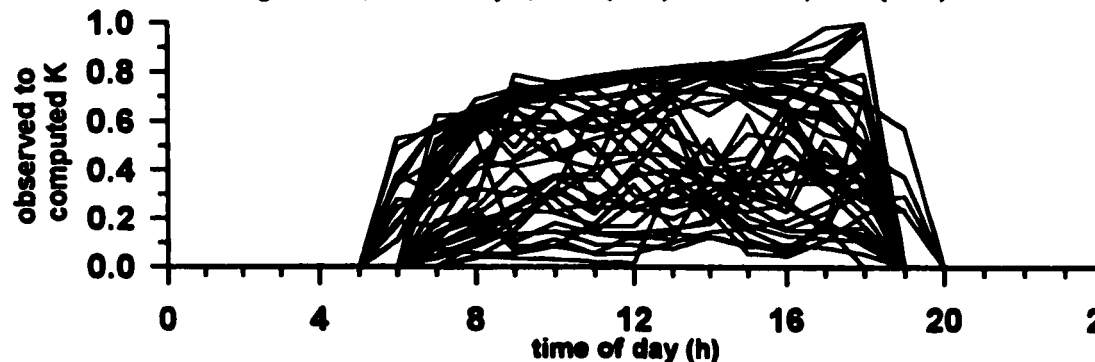


FIGURE 5-17d. As in Figure C-5a, for March 21, 1995 (J=80) to April 30, 1995 (J=120).



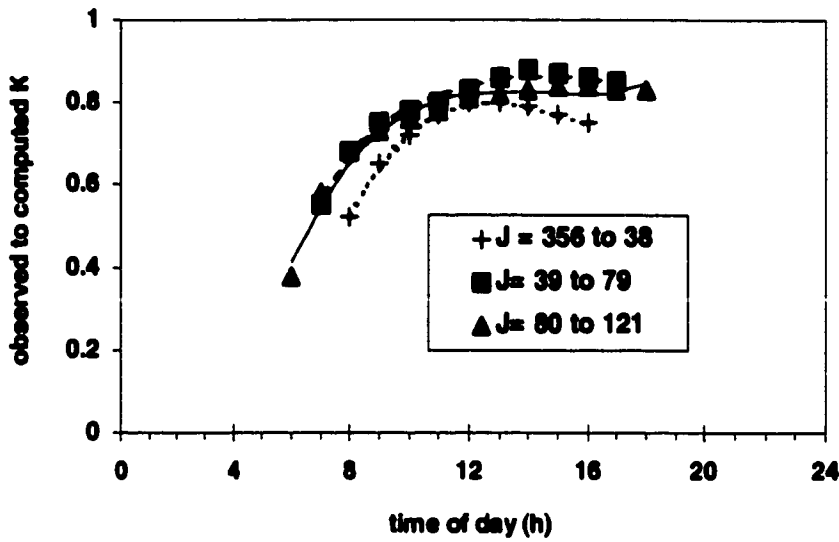


FIGURE 5-18a. Third order polynomial fits for the maximum observed to computed shortwave radiation at the AES CARE and Elora meteorological stations (lower limit of  $K_{obs}/K_{comp} > 0$ ; an upper limit of  $K_{obs}/K_{comp} < 1$ ).

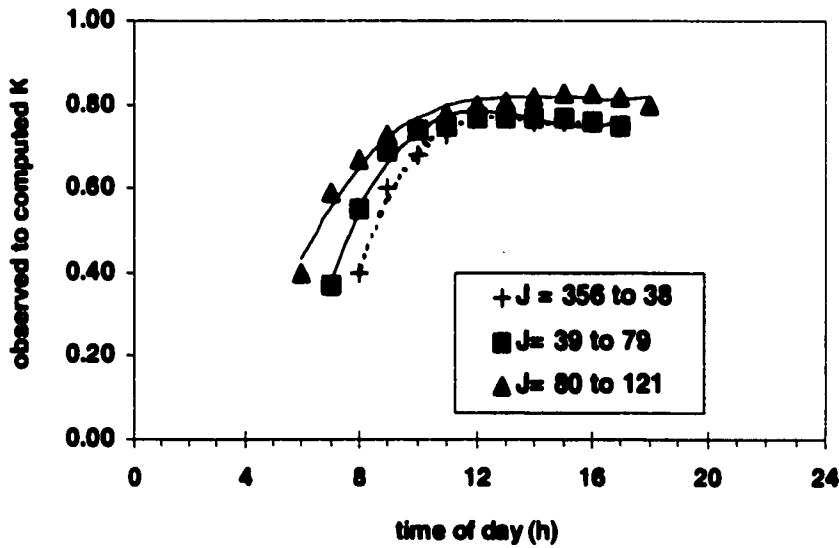


FIGURE 5-18b. Third order polynomial fits for the maximum observed to computed short-wave radiation at the AES Toronto meteorological stations (lower limit of  $K_{obs}/K_{comp} > 0$ ; an upper limit of  $K_{obs}/K_{comp} < 1$ ).

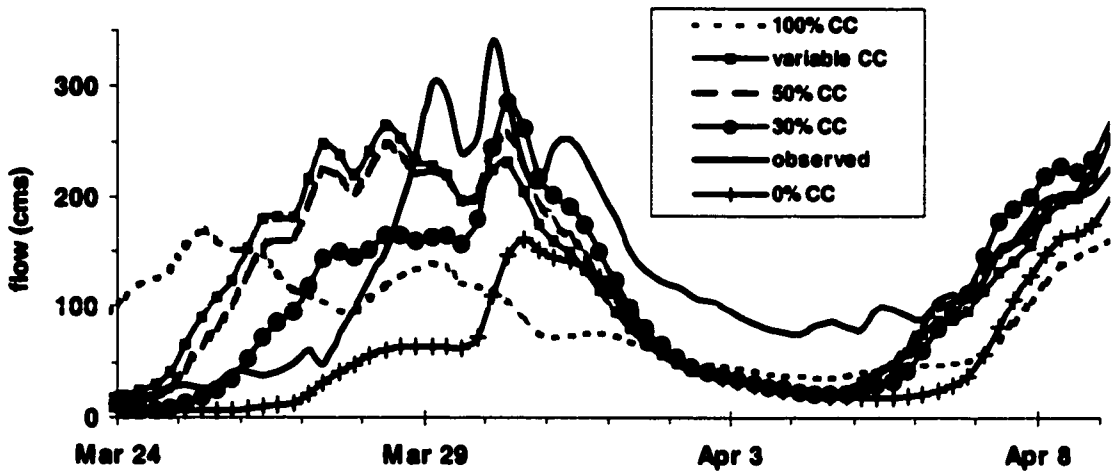


FIGURE 5-19a. Effect of cloud cover percentage used to calculate long wave radiation fluxes on initial spring peak for the Grand River at Galt in 1993 (March 24<sup>th</sup> to April 9<sup>th</sup>).

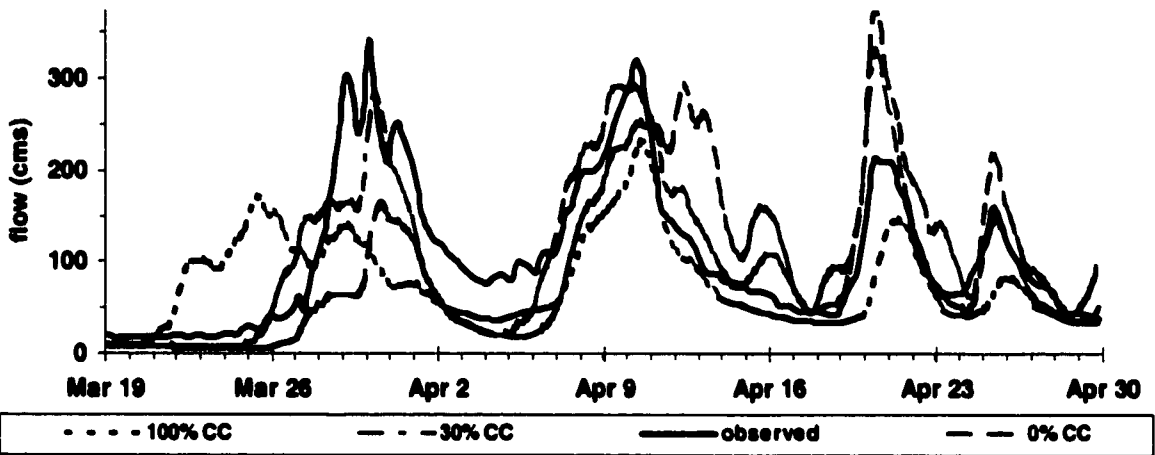


FIGURE 5-19b. As in Figure 5-19a, but for the entire snowmelt period (100, 30 and 0% cloud cover).

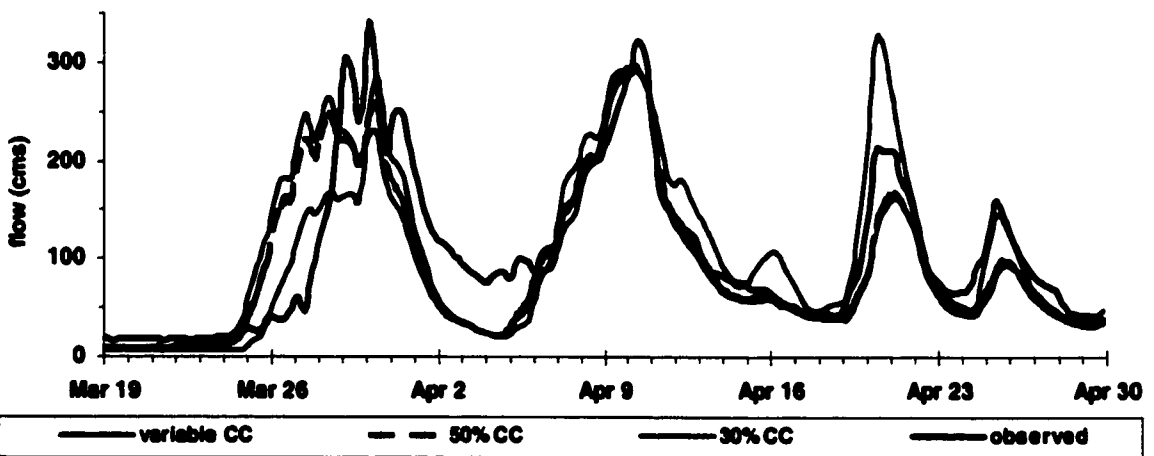


FIGURE 5-19c. As in Figure 5-19a, but for the entire snowmelt period (variable, 50, and 30% cloud cover).

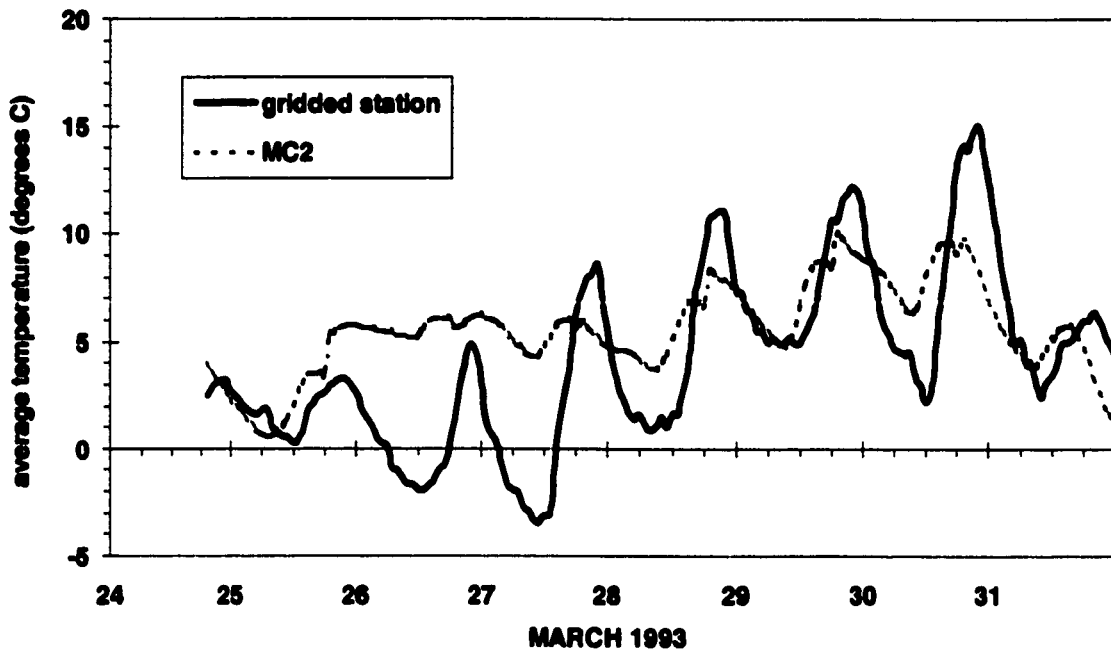


FIGURE 5-20. The difference between the average temperature across the Southern Ontario study area as derived from gridded station data and as computed from the MC<sup>2</sup> model.

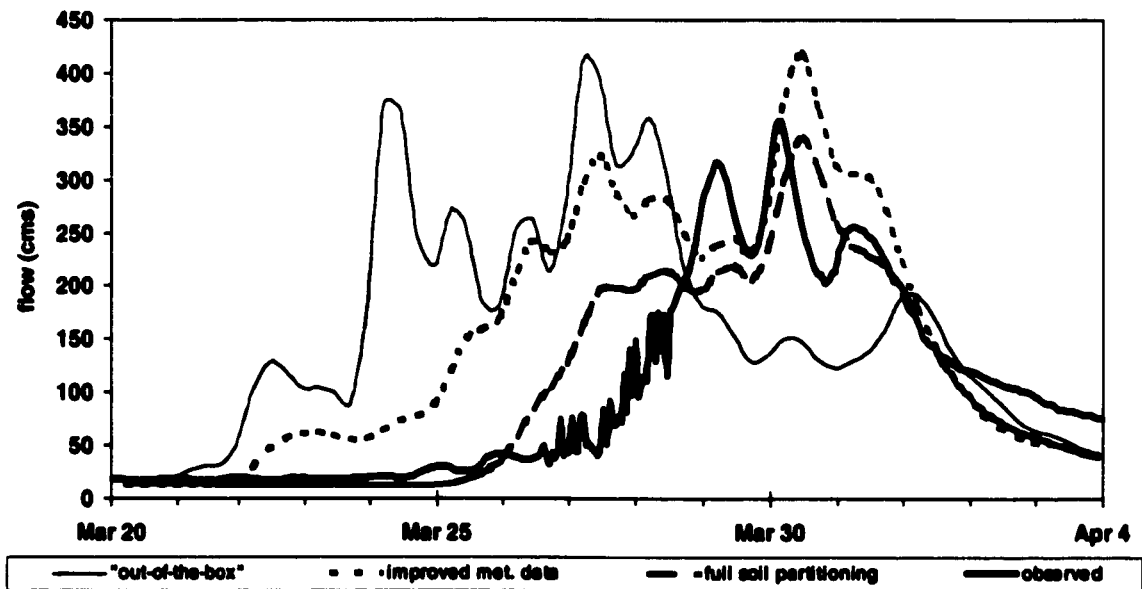


FIGURE 5-21a. Effects of data improvement and partitioning of soil parameters on the 1993 initial spring peak hydrograph (observed and three simulations) for the Grand River at Galt. The simulated hydrographs were modelled using "out-of-the-box" WAT\_CLS3 with a limited meteorological dataset, an improved meteorological dataset, and WAT\_CLS3 modified to differentiate between snow-covered and snow-free areas.

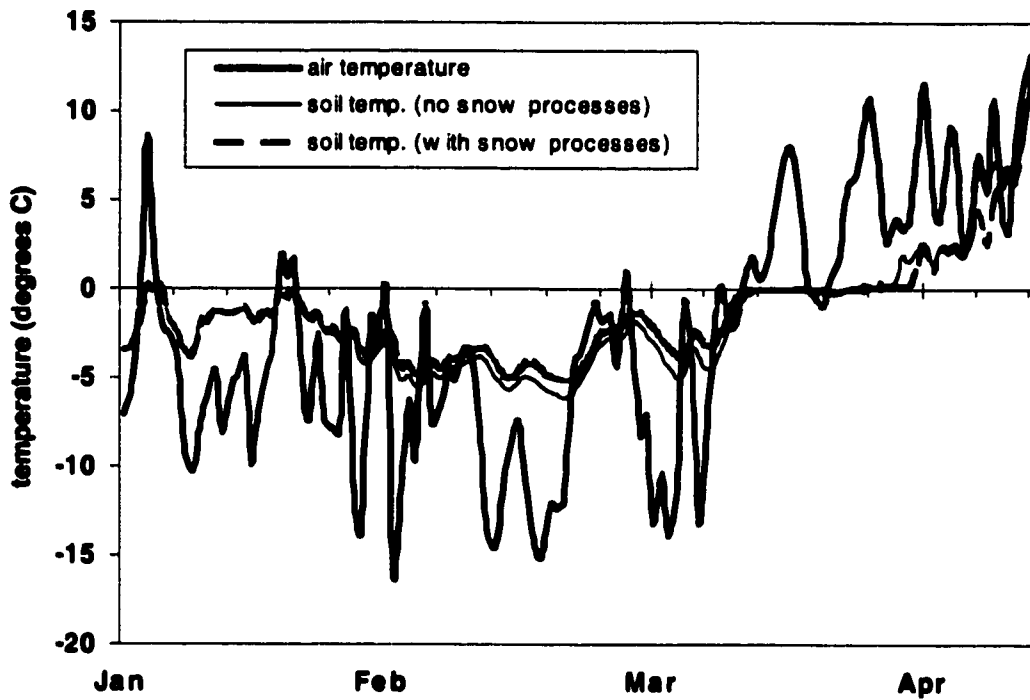


FIGURE 5-21b. Top layer soil temperature for the averaged soil properties (no snow processes) and the snowcovered area from the decoupling of soil properties (with snow processes)

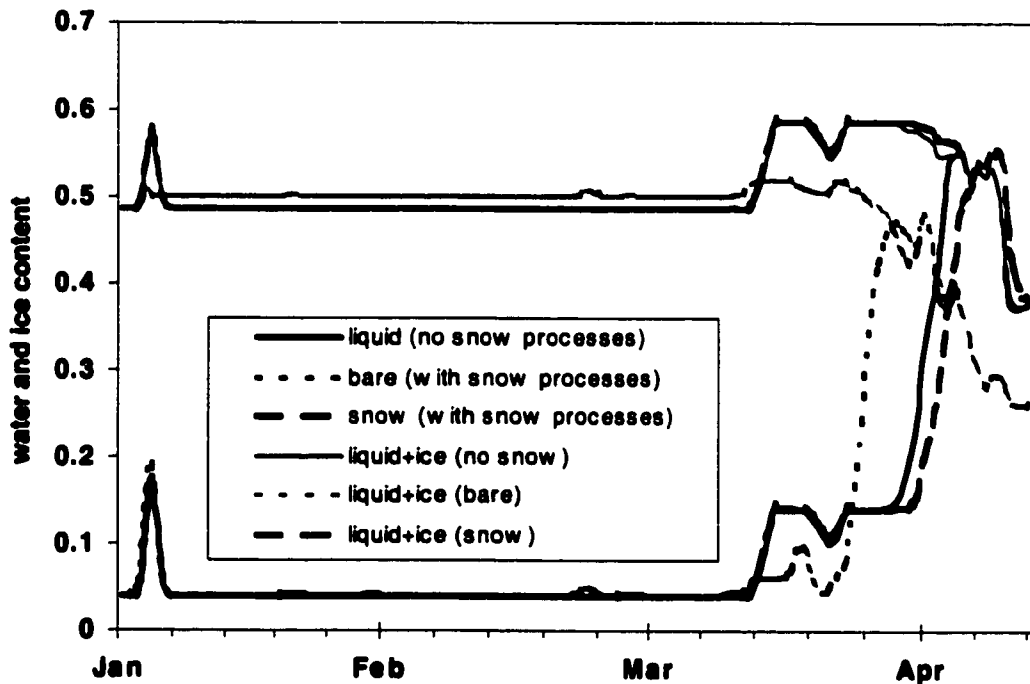


FIGURE 5-21c. Top layer soil liquid and frozen water content for the averaged soil properties (no snow processes) and the decoupling of the soil properties (with snow processes).

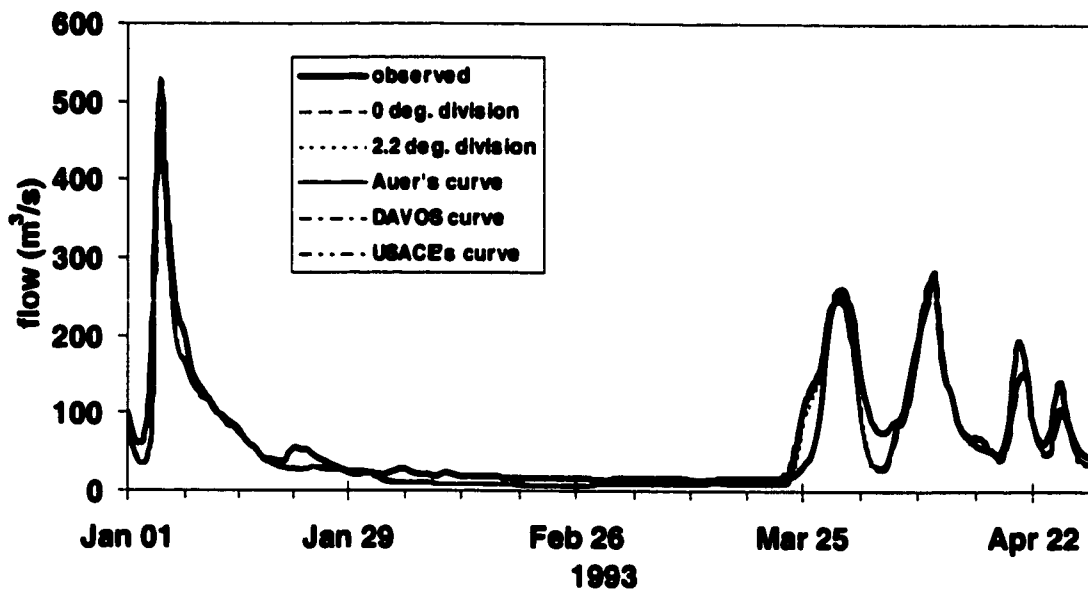


FIGURE 5-22a. January to April 1993 observed streamflow and hydrographs simulated using different mixed precipitation scenarios for the Grand River at Galt.

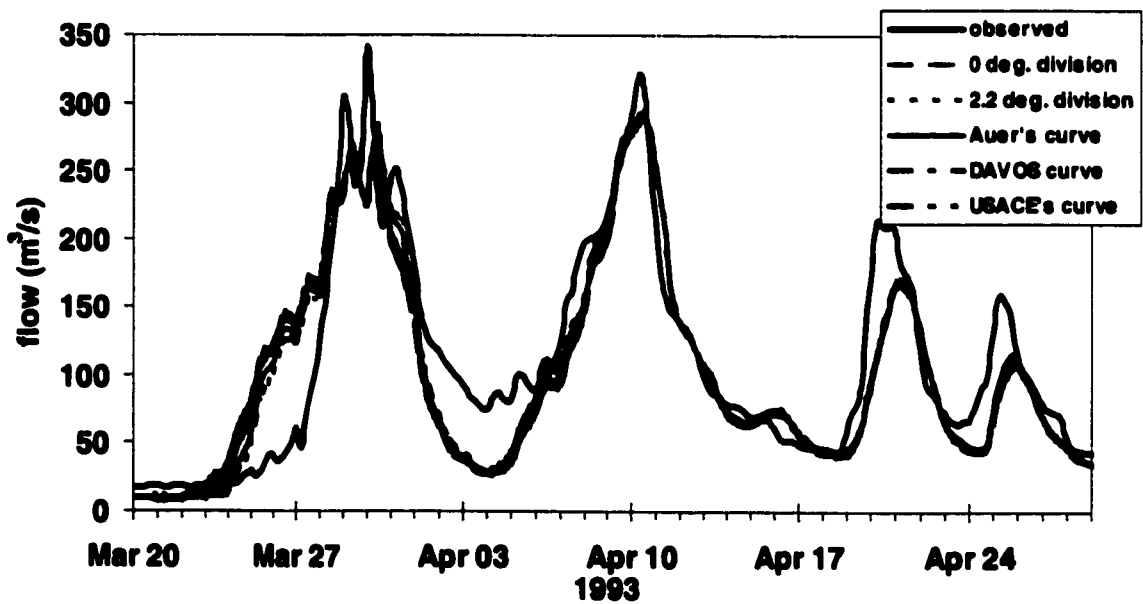


FIGURE 5-22b. As in Figure 5-22a, but for the snowmelt period (March 20<sup>th</sup> to the end of April).

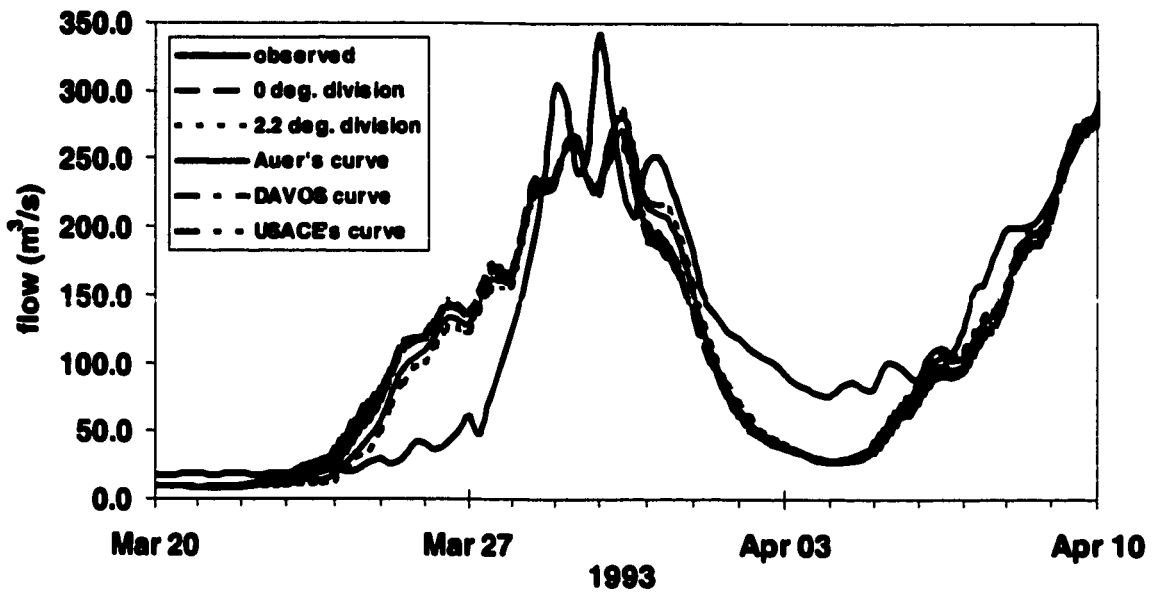


FIGURE 5-22c. As in Figure 5-22a and 5-22b, but specifically only the first snowmelt peak.

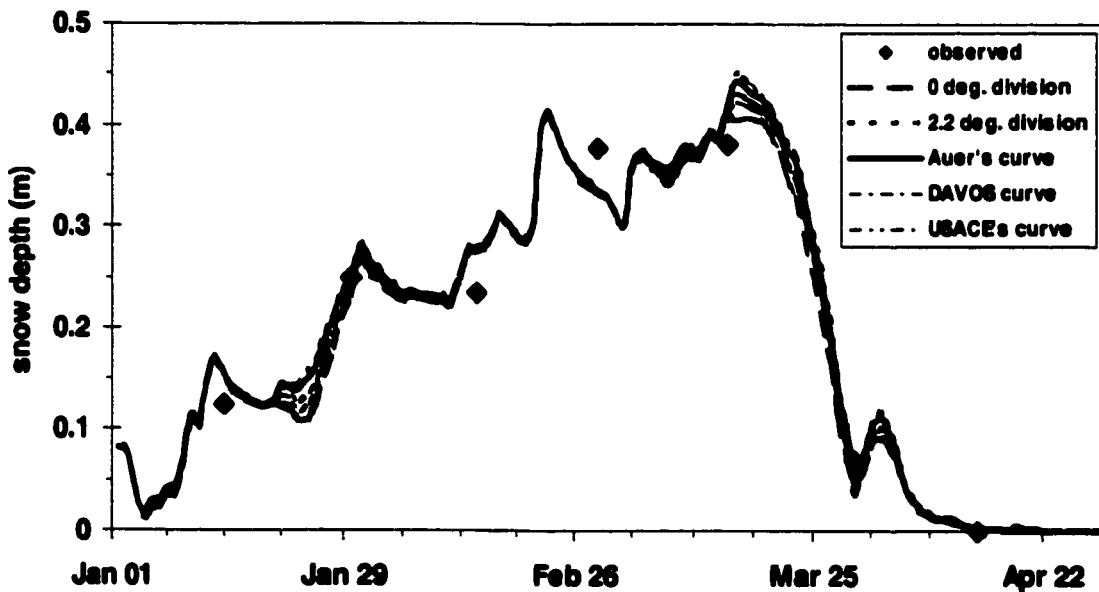


FIGURE 5-23a. Measured and computed snow depths for the mid Grand River snowcourse 2002 (north of Elmira) using different mixed precipitation scenarios for the Grand River at Galt.

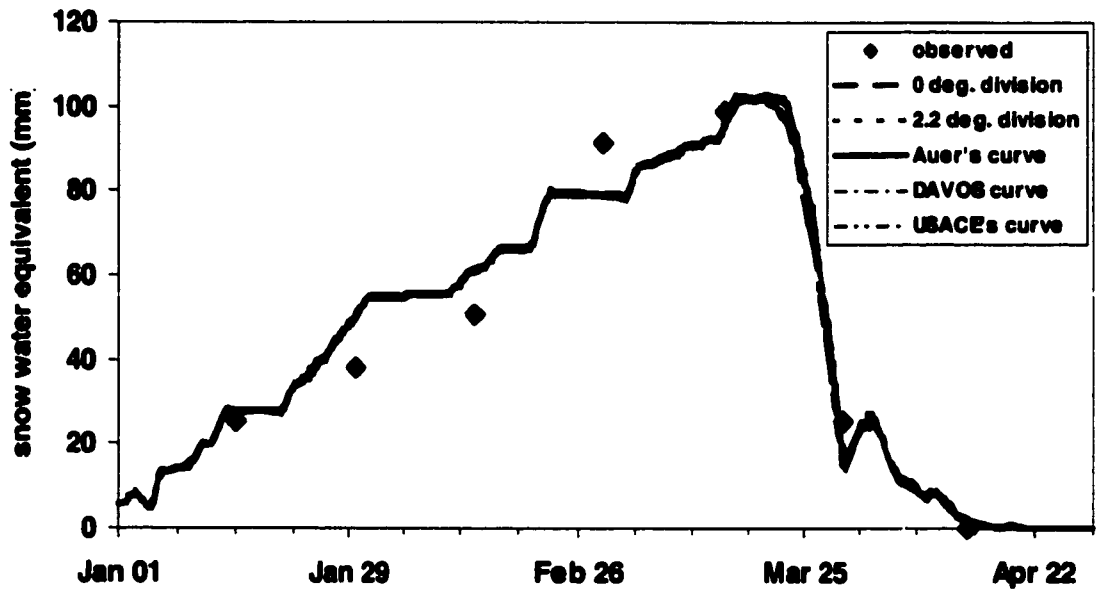


FIGURE 5-23b. Measured and computed SWE, as per Figure 5-23a.

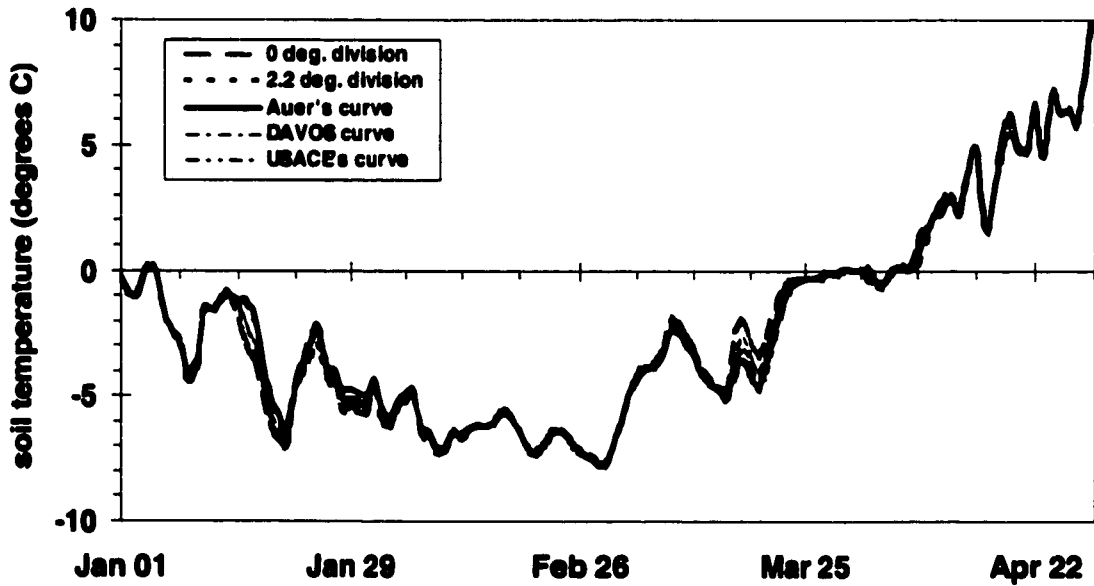


FIGURE 5-24a. Computed top layer soil temperature for the crop/low vegetation land cover type in the vicinity of GRCA snowcourse 2002, simulated using different mixed precipitation scenarios for the Grand River at Galt.

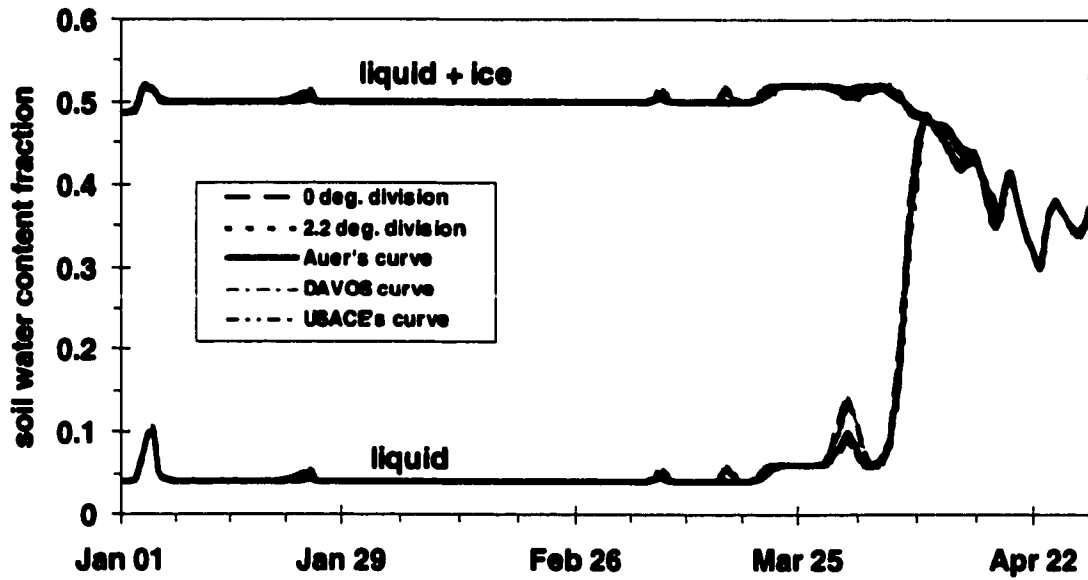


FIGURE 5-24b. Computed soil water content (liquid and liquid + ice), as per Figure 5-24a.

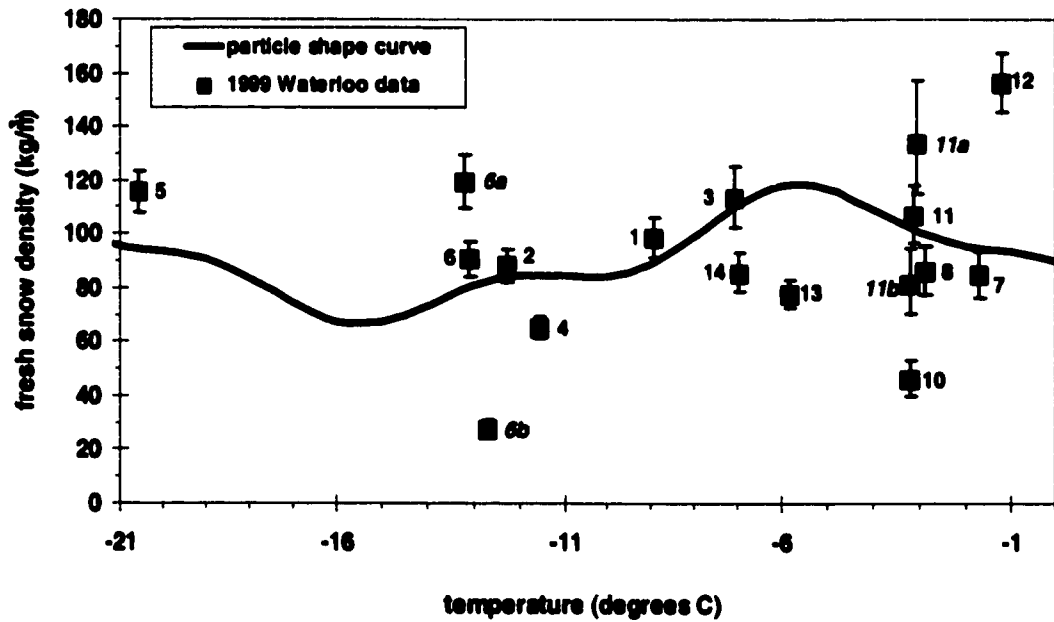


FIGURE 5-25a. Fresh snow density as a function of air temperature for the data collected in Waterloo during the winter of 1999, with the radar adjustment particle shape curve (outlined in section 3.1.4c).



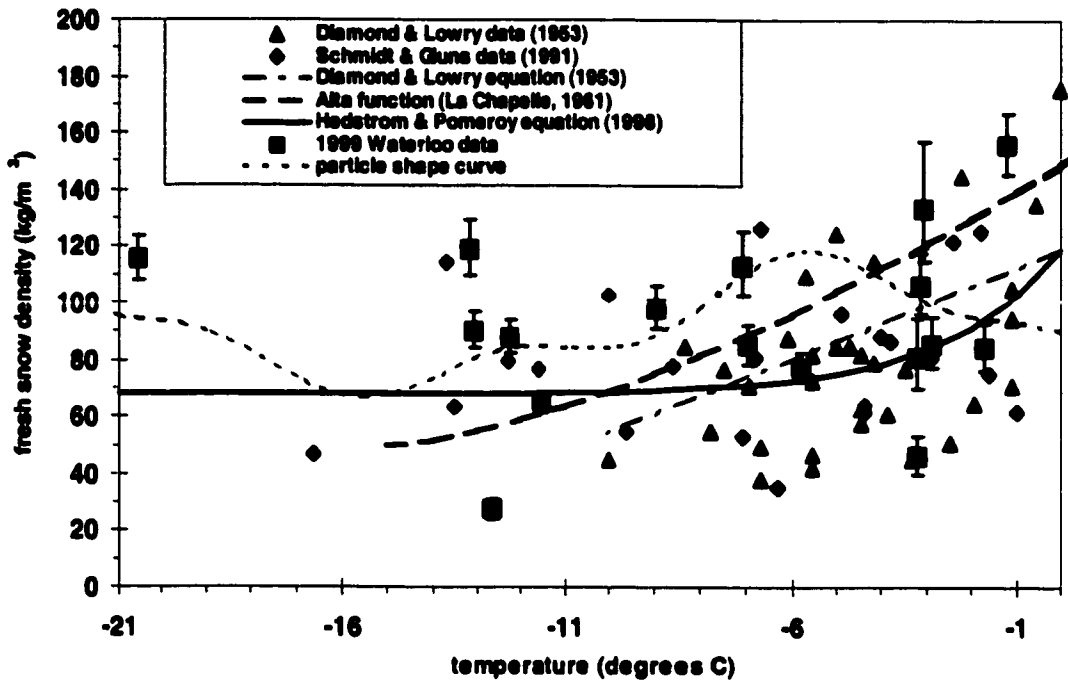


FIGURE 5-25b. Fresh snow density as a function of air temperature observed by Diamond and Lowry (1953), Schmidt and Gluns (1991), and in Waterloo during the winter of 1999. The Hedstrom and Pomeroy (1998) function was derived from the these data, while the Alta function by La Chapelle (1961) was derived from data collected at the Alta Avalanche Study Center. The particle shape curve was used to adjust the radar data, as outlined in section 3.1.4c.

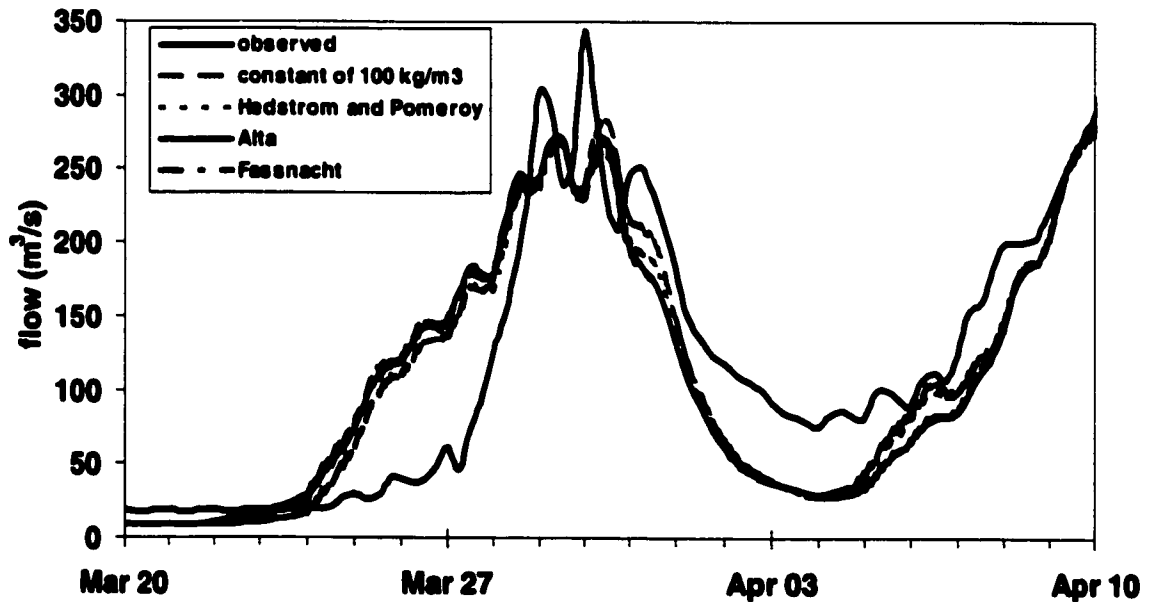


FIGURE 5-26a. Effects of different fresh snow density formulations on the initial snowmelt peak on the Grand River at Galt in 1993.

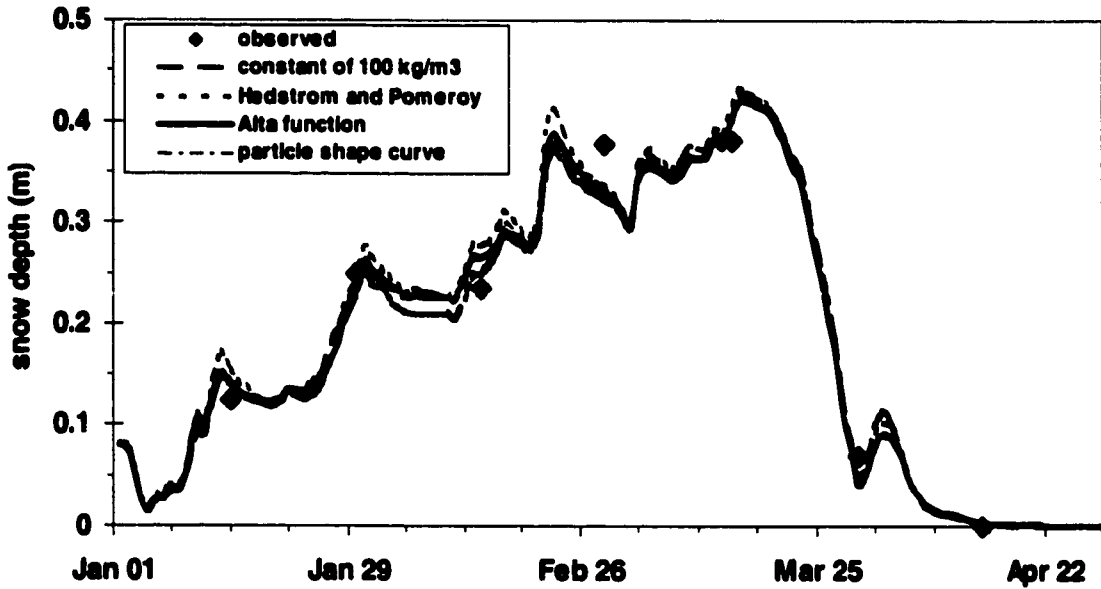


FIGURE 5-26b. Effects of different fresh snow density formulations on the snow depth at snowcourse 2002.

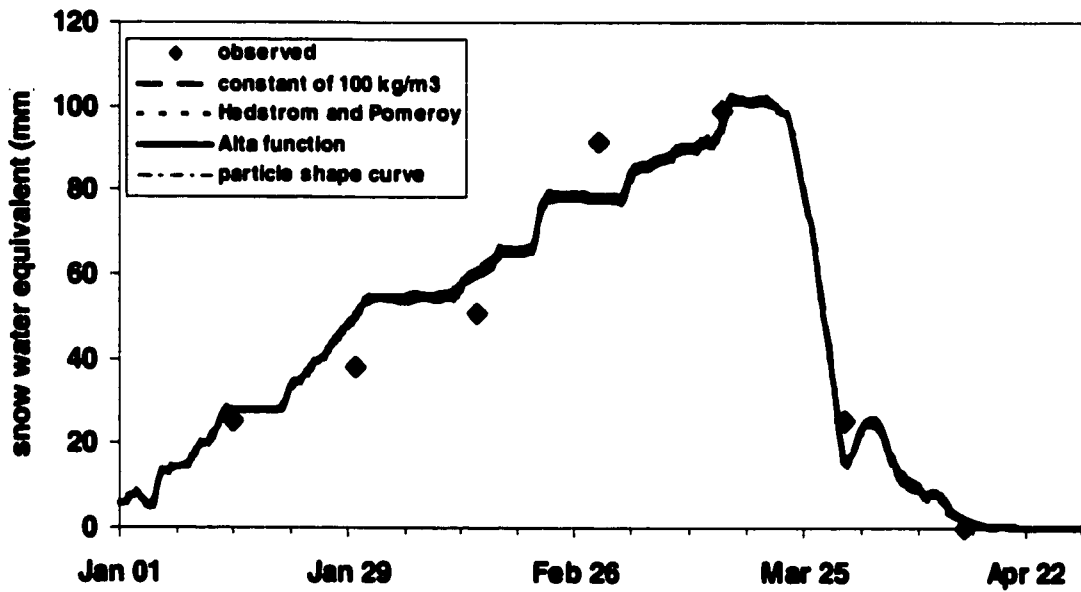


FIGURE 5-26c. Effects of different fresh snow density formulations on the SWE at snowcourse 2002.

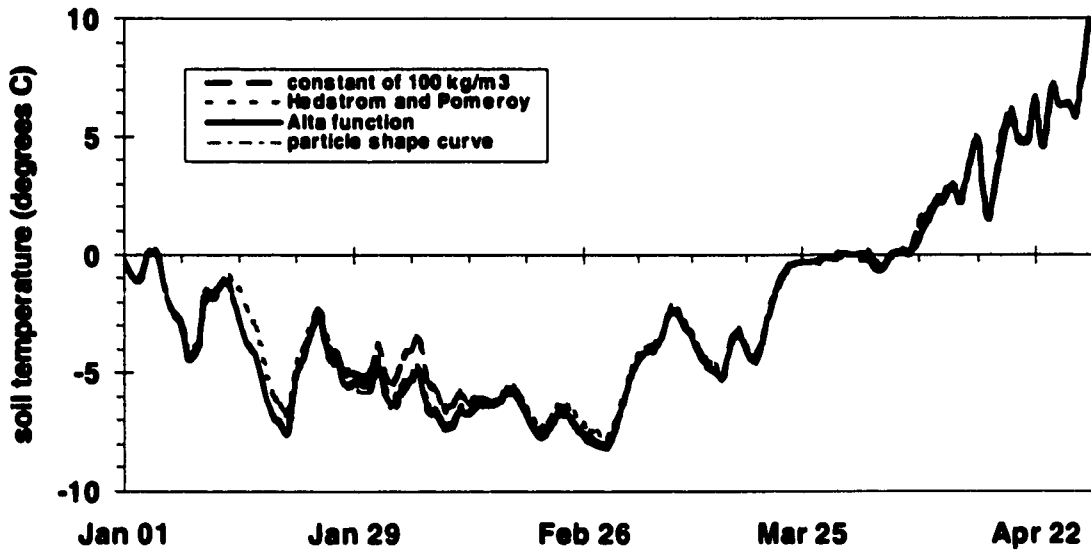


FIGURE 5-26d. Effects of different fresh snow density formulations on the soil temperature.

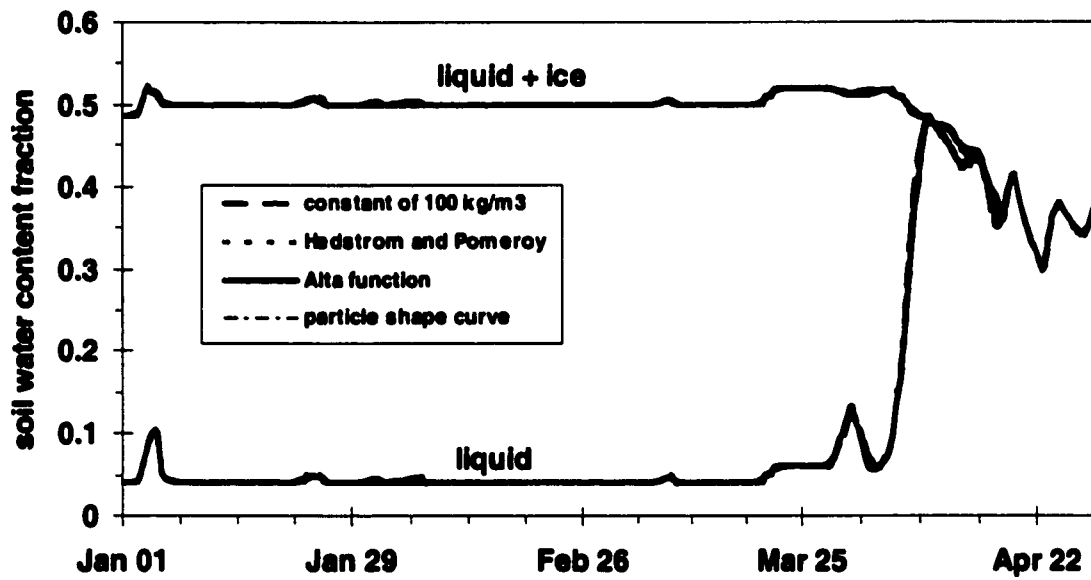


FIGURE 5-26e. Effects of different fresh snow density formulations on the soil water content.

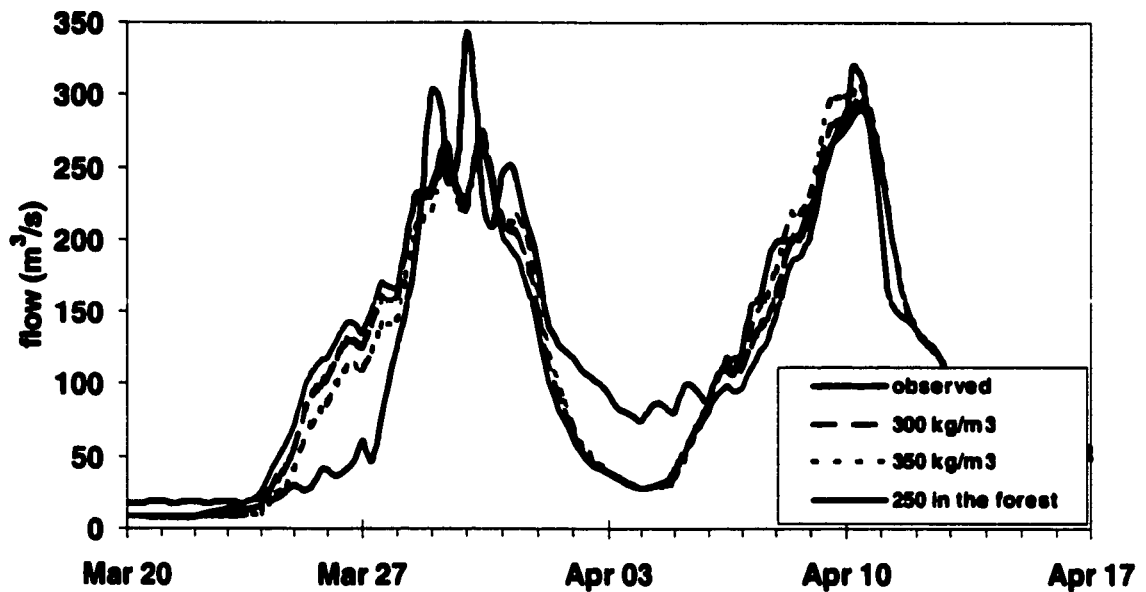


FIGURE 5-27a. Effect of variation in the maximum snow density on the initial snowmelt hydrograph on the Grand River at Galt in 1993.

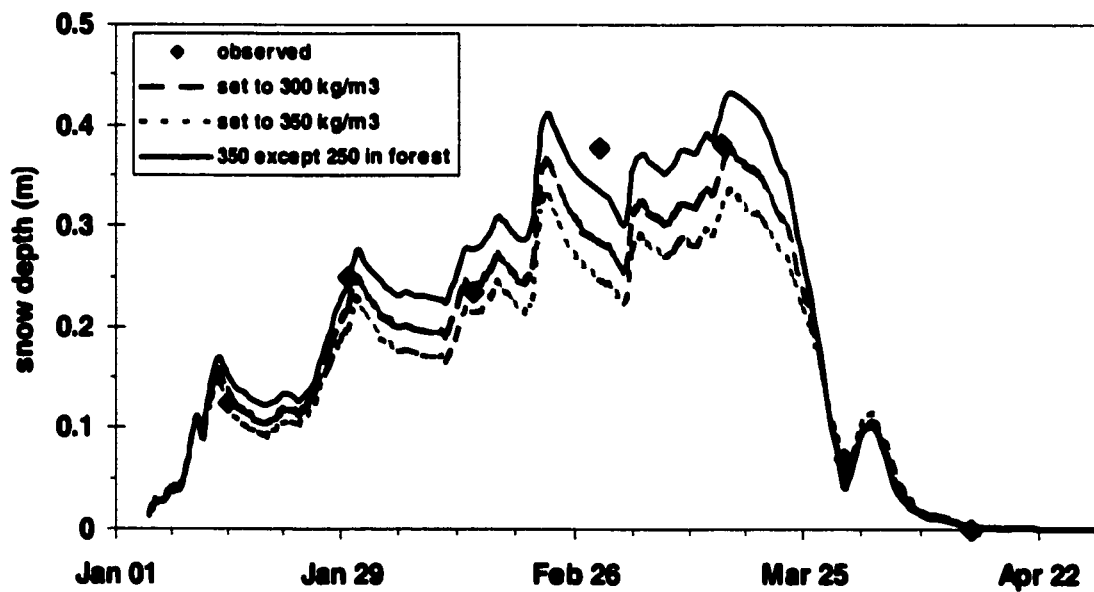


FIGURE 5-27b. Effect of variation in the maximum snow density on the snow depth at snowcourse 2002.

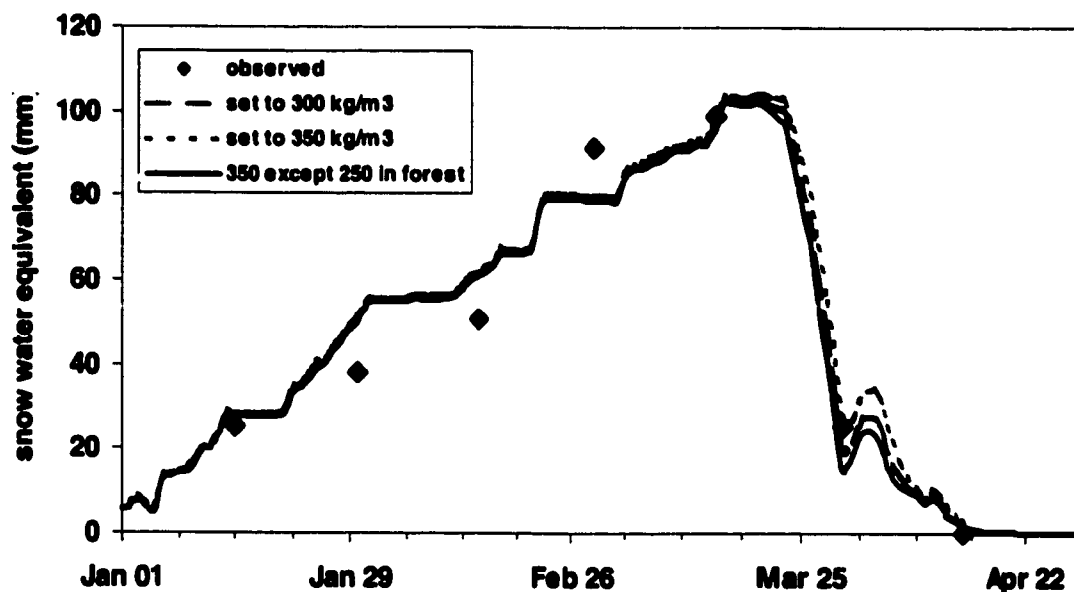


FIGURE 5-27c. Effect of variation in the maximum snow density on the SWE.

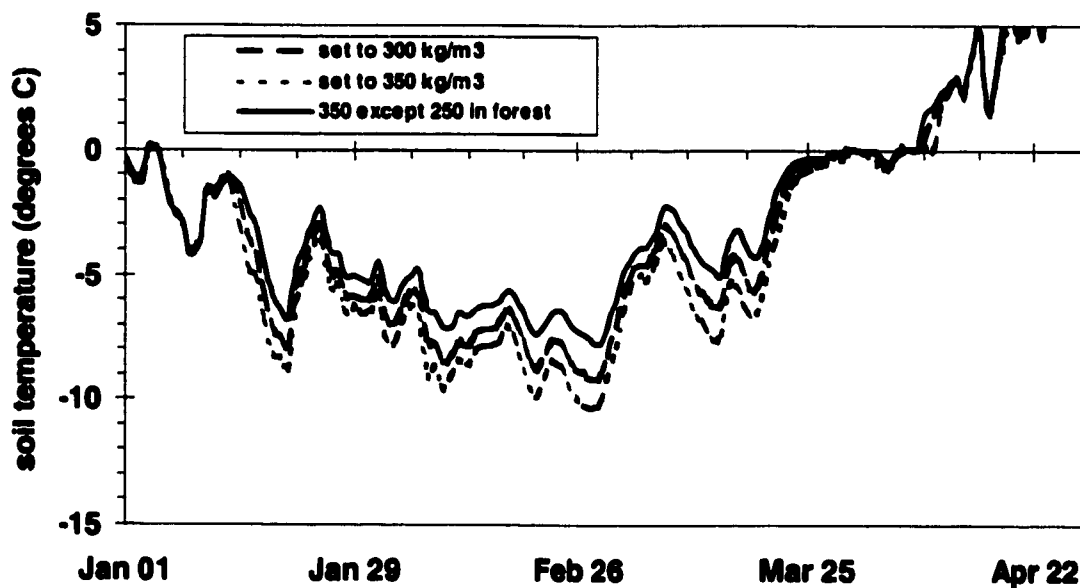


FIGURE 5-27d. Effect of variation in the maximum snow density on the soil temperature.

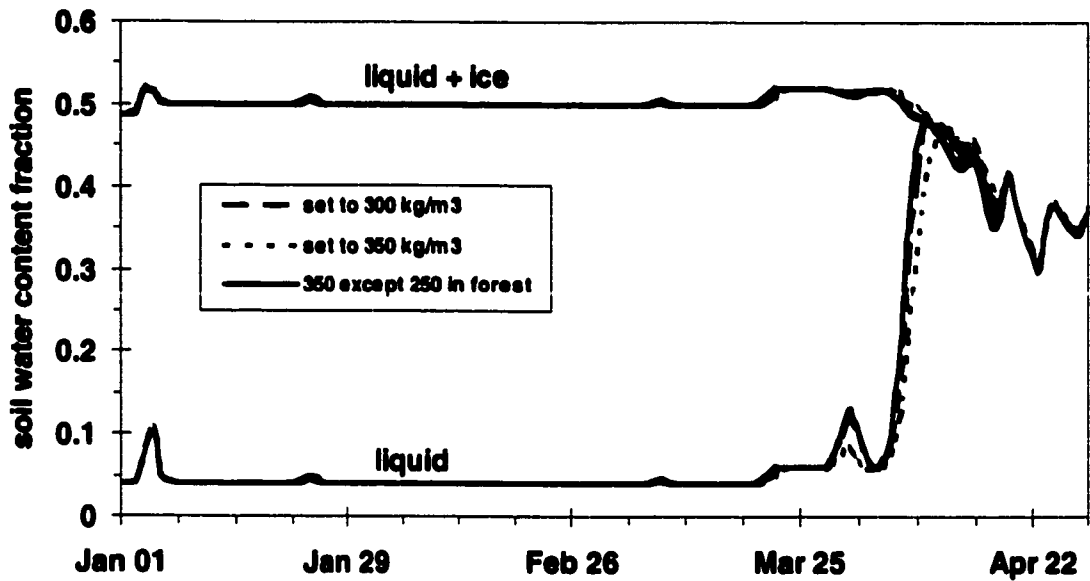


FIGURE 5-27e. Effect of variation in the maximum snow density on the soil water content.

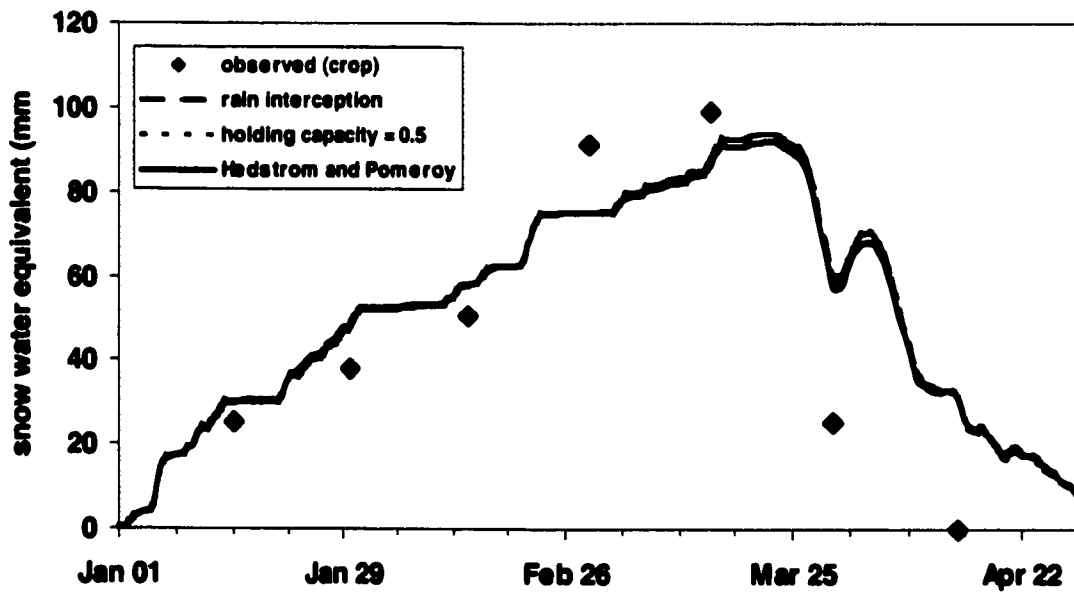


FIGURE 5-28a. Effects of different canopy snow interceptions formulations on the forest SWE, for forests throughout the basin that are 100% deciduous. The observed data are for a nearby snowcourse (2002).

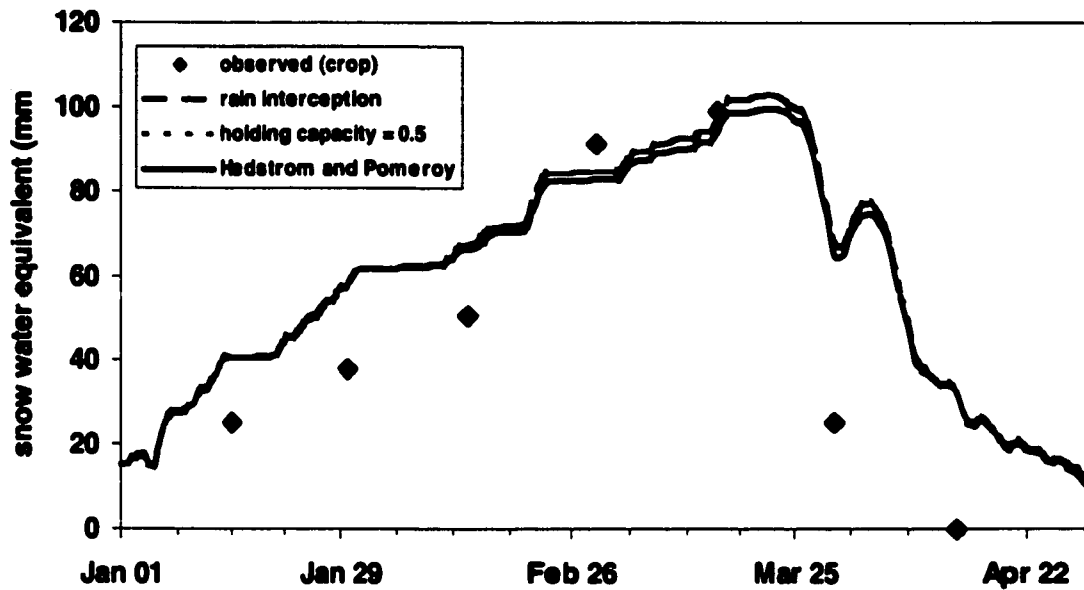


FIGURE 5-28b. Effects of different canopy snow interceptions formulations on the forest SWE, for forests throughout the basin that are 65% deciduous.

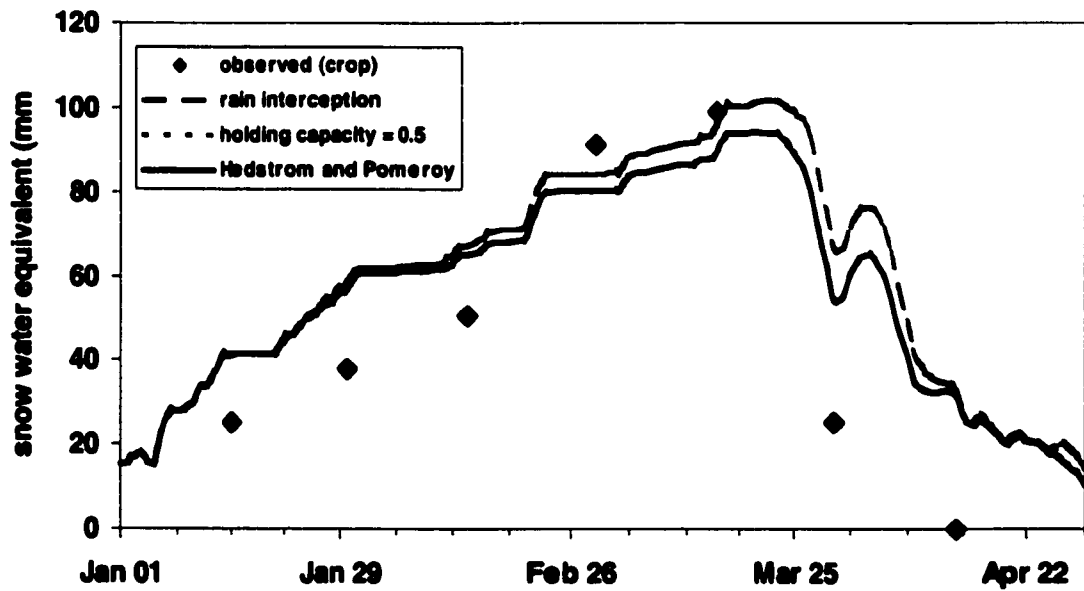


FIGURE 5-28c. Effects of different canopy snow interceptions formulations on the forest SWE, for forests throughout the basin that are 100% coniferous.

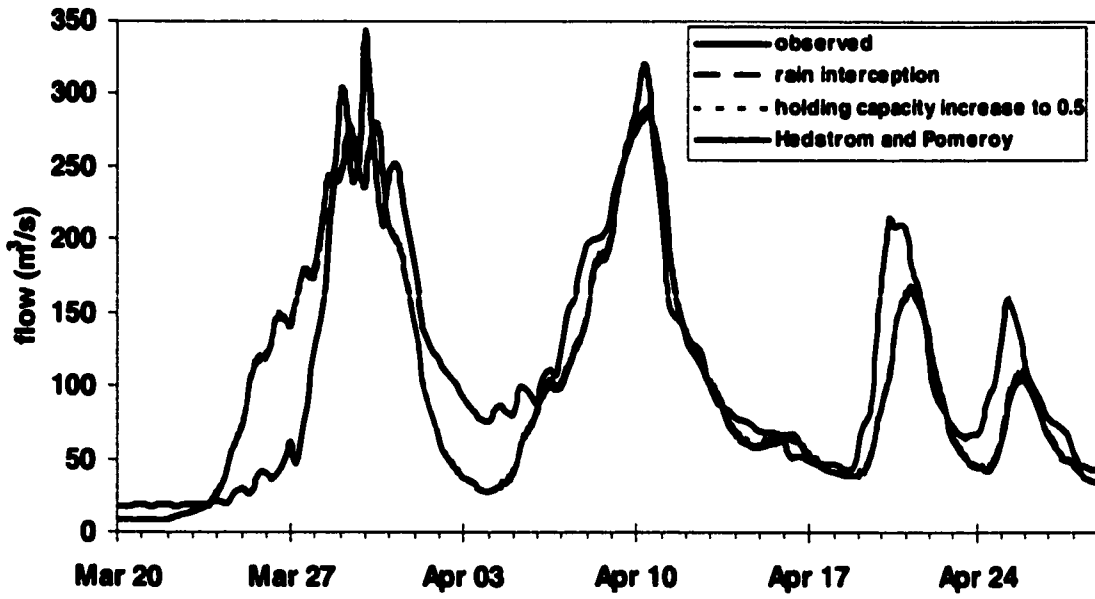


FIGURE 5-28d. Effects of the different canopy snow interception formulations on the simulated streamflow.



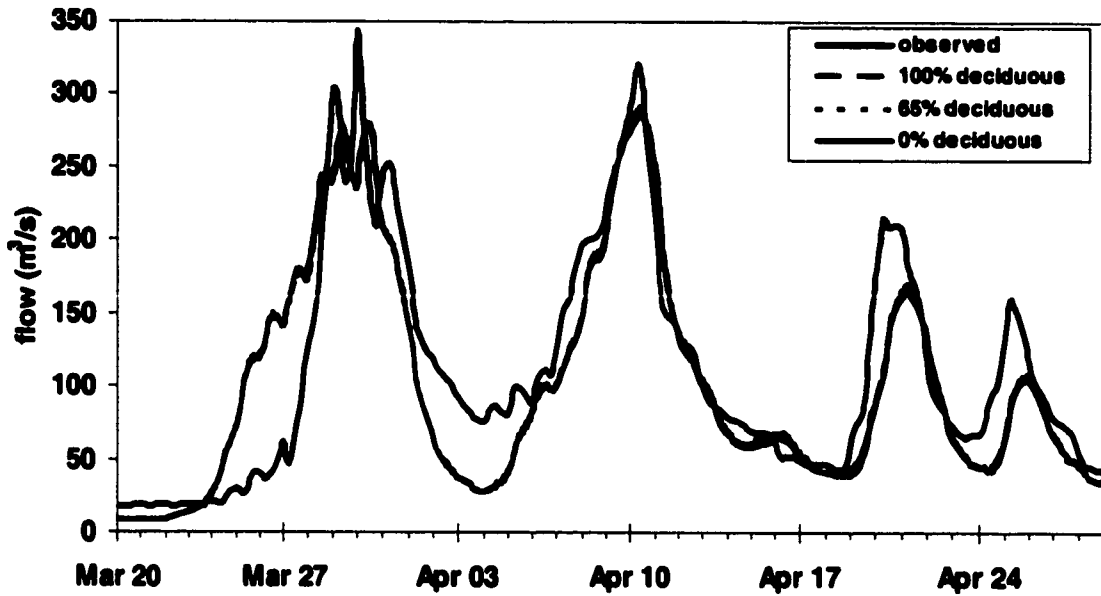


FIGURE 5-29a. Modelled snowmelt flow comparison of different canopy types, using the Hedstrom and Pomeroy (1998) canopy interception formulation.

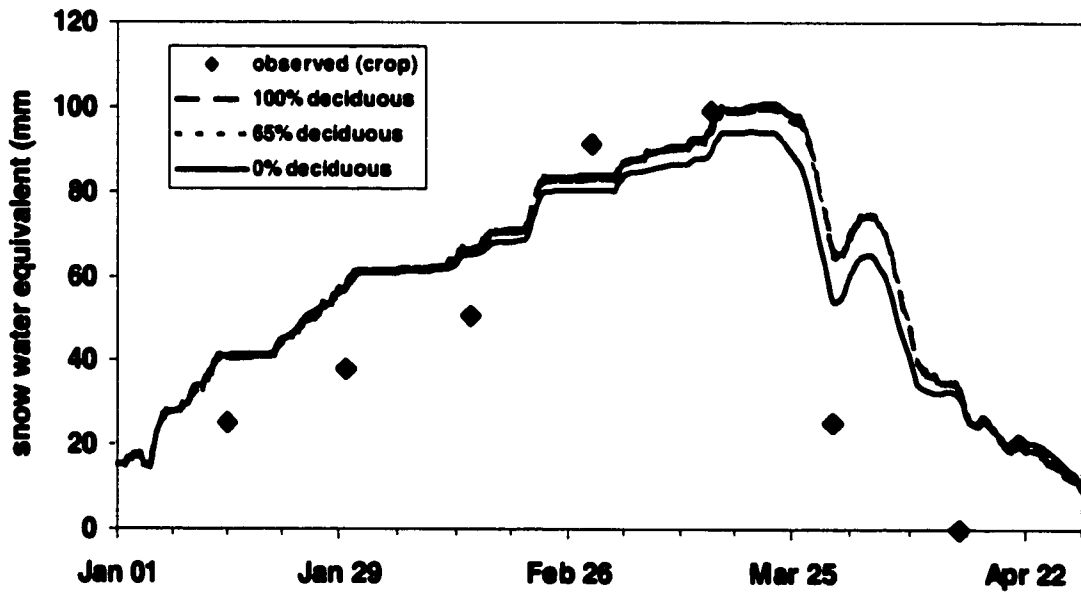


FIGURE 5-29b. Effects of different canopy types throughout the basin on the forest SWE using the Hedstrom and Pomeroy (1998) canopy interception formulation.

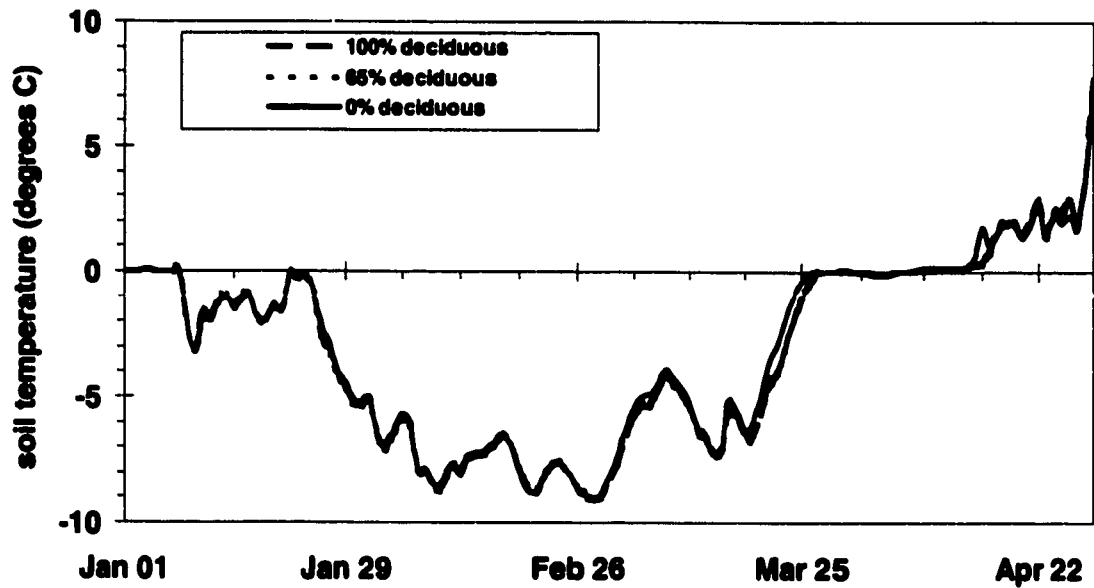


FIGURE 5-29c. Effects of different canopy types throughout the basin on the forest top layer soil temperature using the Hedstrom and Pomeroy (1998) canopy interception formulation.

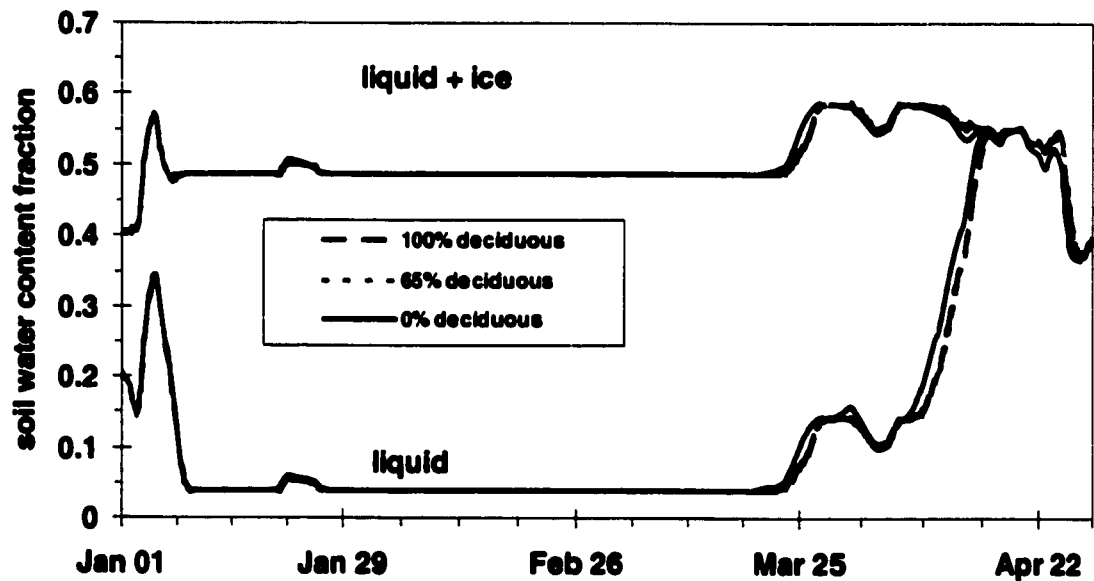


FIGURE 5-29d. Effects of different canopy types throughout the basin on the forest top layer soil water content using the Hedstrom and Pomeroy (1998) canopy interception formulation.

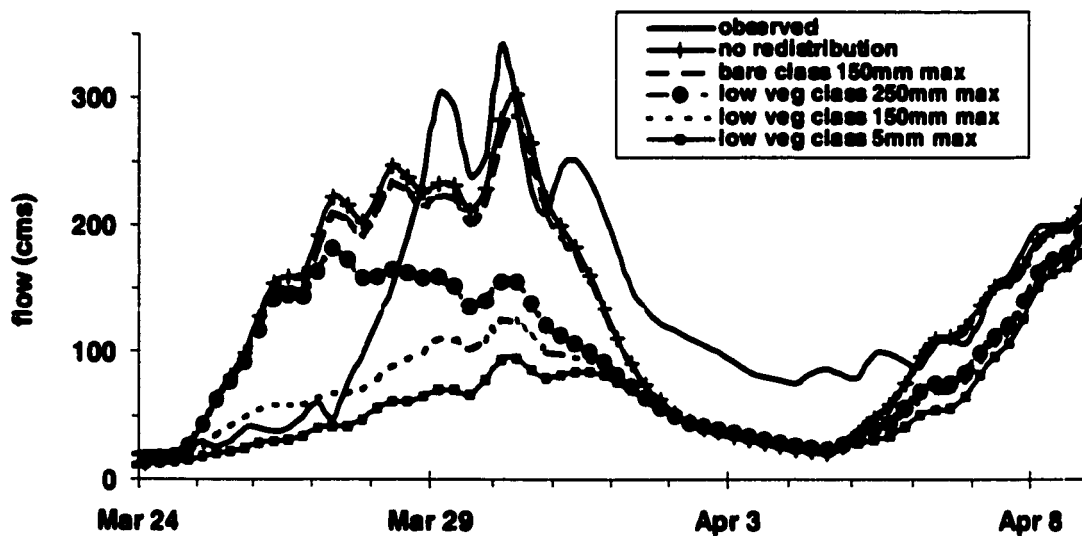


FIGURE 5-30a. Effects of simple redistribution on the 1993 initial snowmelt peak hydrograph (observed and five simulations) for the Grand River at Galt. The simulated hydrographs uses redistribution from the bare or crop/low vegetation land classes with different depth capacity limits.

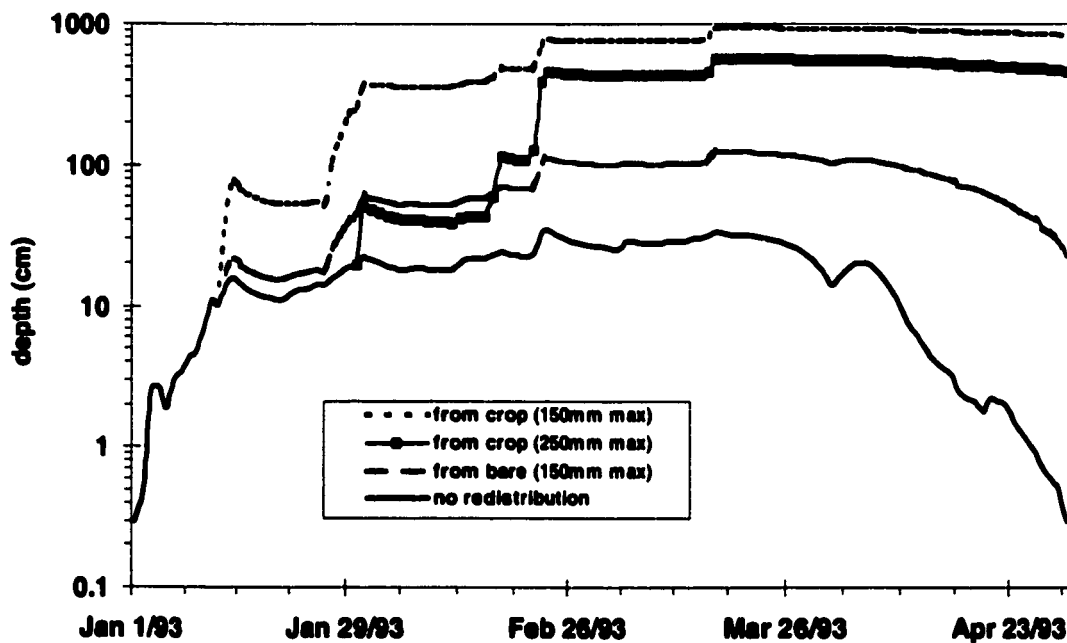


FIGURE 5-30b. Effects of simple redistribution on the forest snowpack depth (near GRCA snowcourse 2002) from bare or crop/low veg. land cover for 150 and 250 mm accumulation limits.

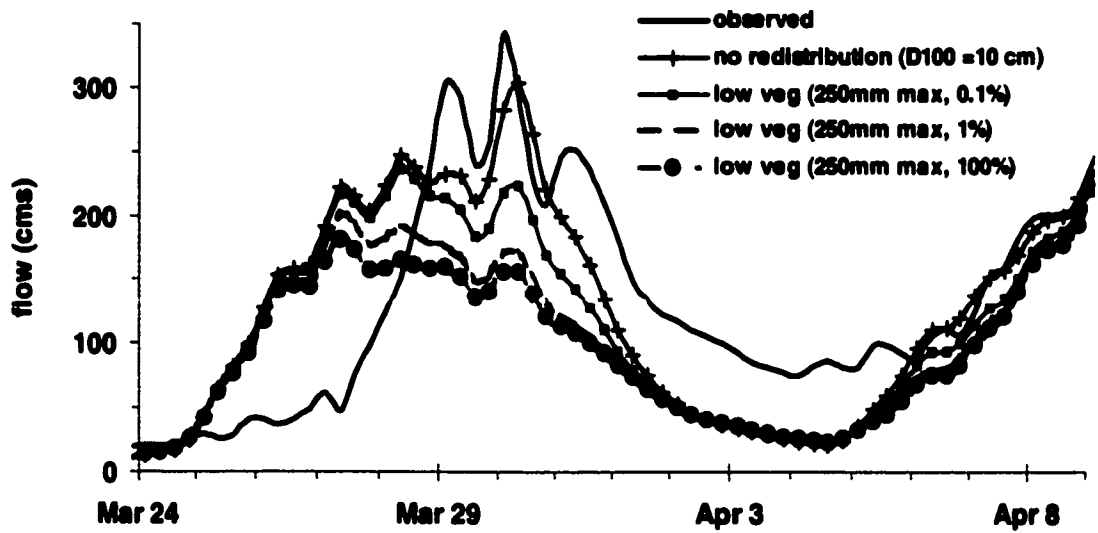


FIGURE 5-30c. Effects of simple redistribution (location, date, and radar data as in Figure 5-29a) with 250 mm depth capacity moving 0.1, 1, and 100% of the redistributable snow at each time step.

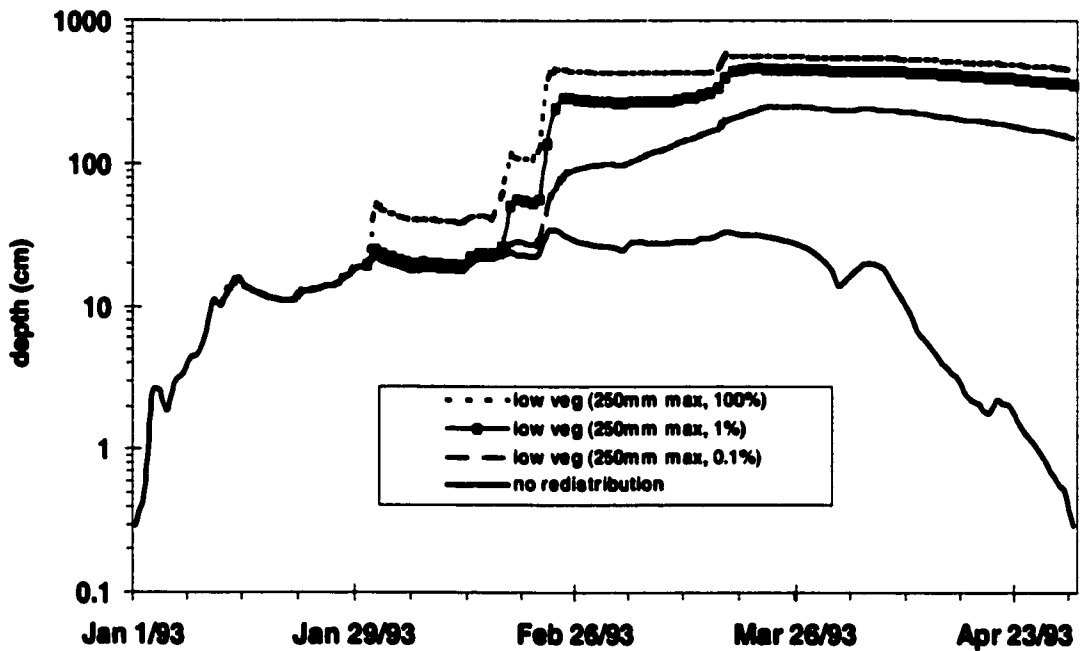


FIGURE 5-30d. Effects of simple redistribution on the forest snowpack depth (near GRCA snowcourse 2002) with 250 mm depth capacity moving 0.1, 1, and 100% of the redistributable snow at each time step.

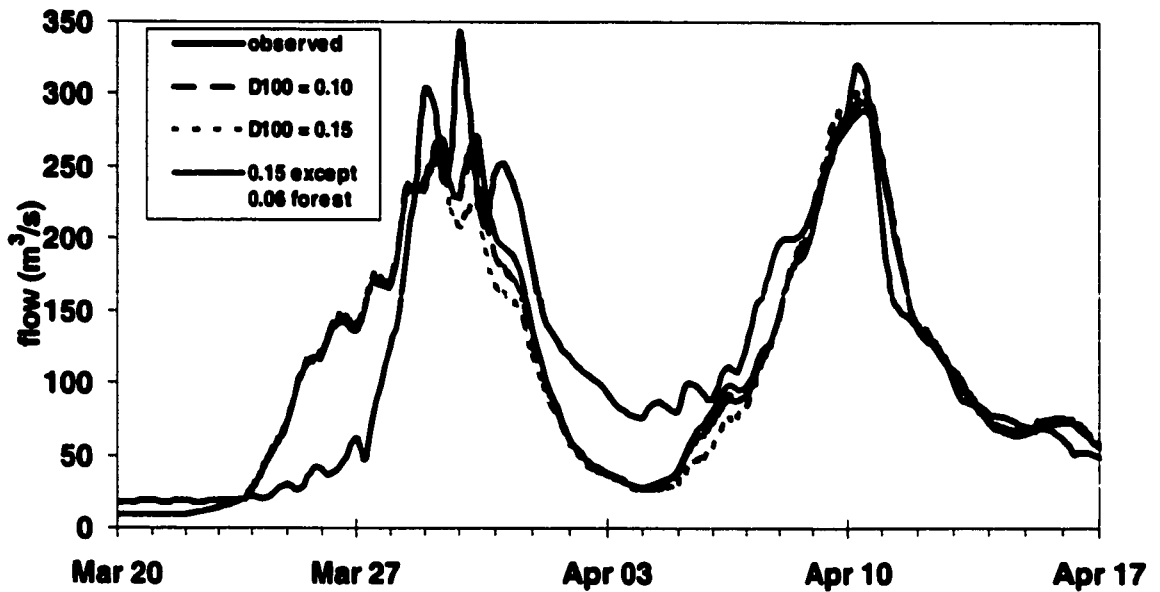


FIGURE 5-31a. Effects of varying the  $D_{100}$  on the 1993 Grand River at Galt streamflow.

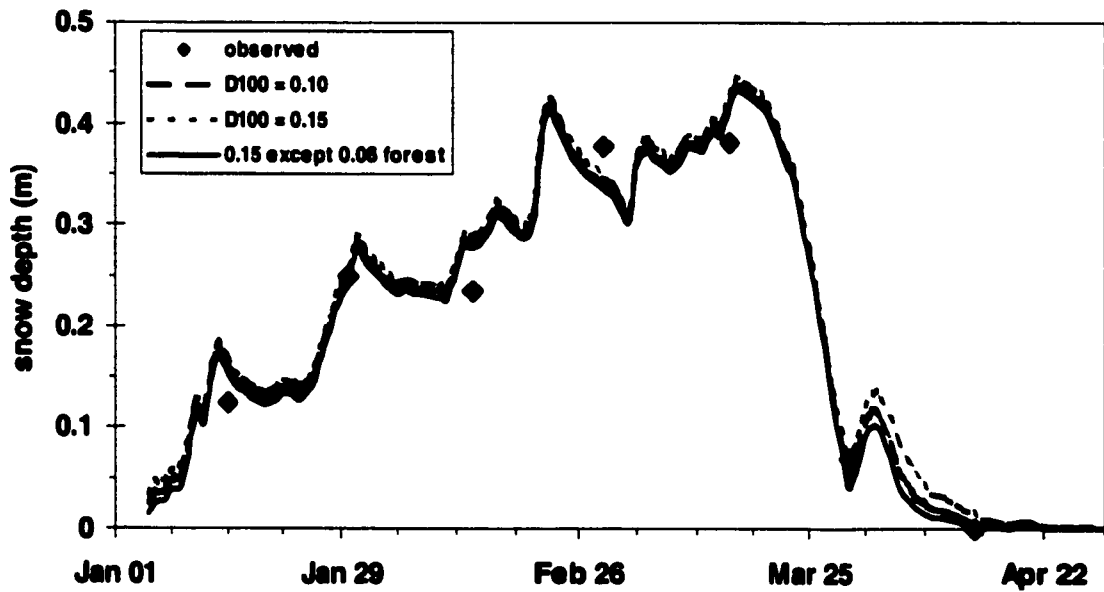


FIGURE 5-31b. Effects of varying the  $D_{100}$  on the snow depth near snowcourse 2002.

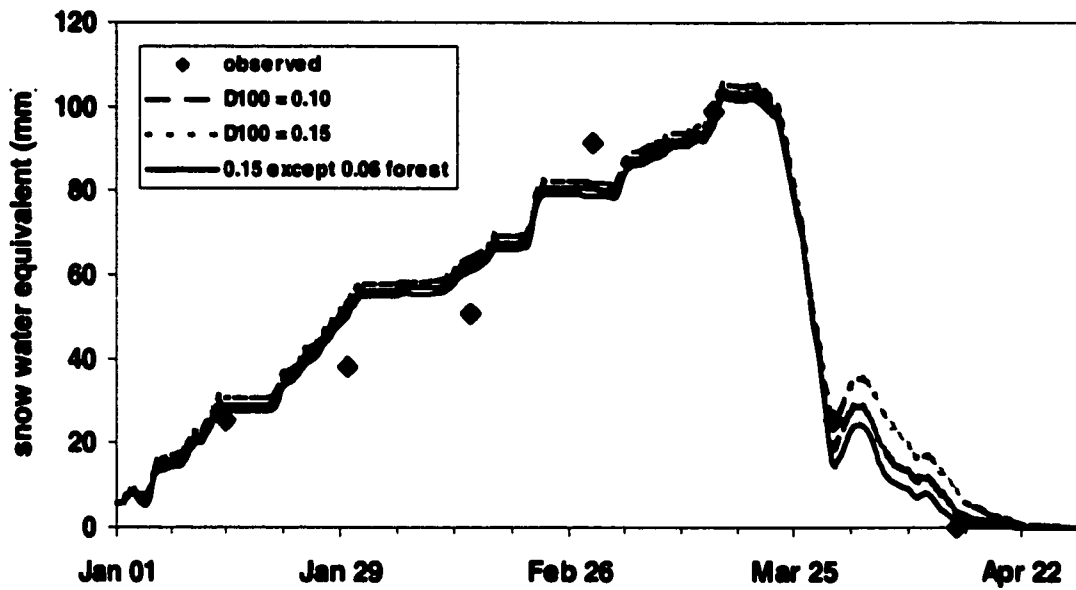


FIGURE 5-31c. Effects of varying the  $D_{100}$  on the SWE.

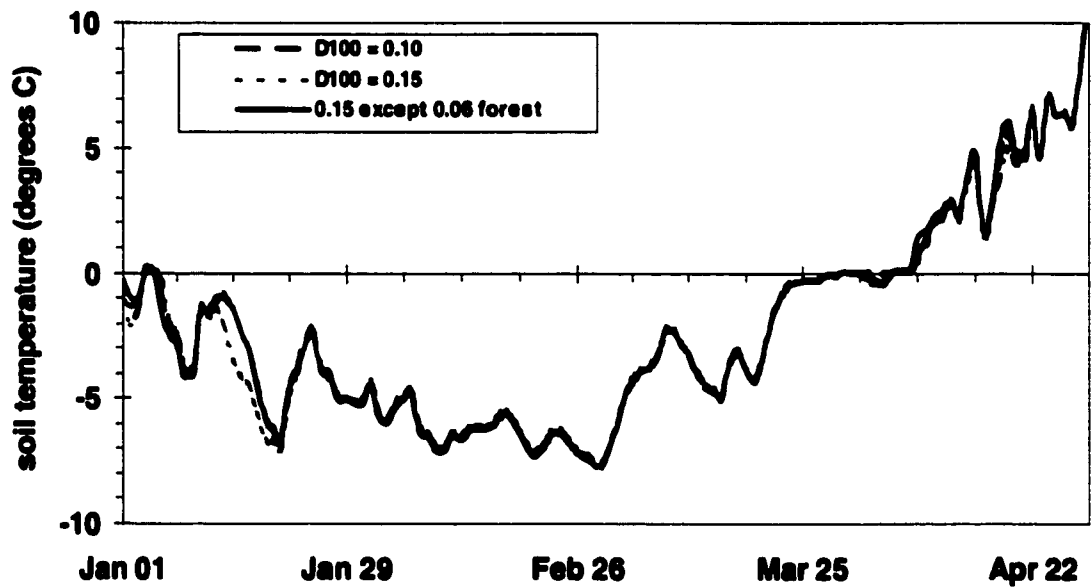
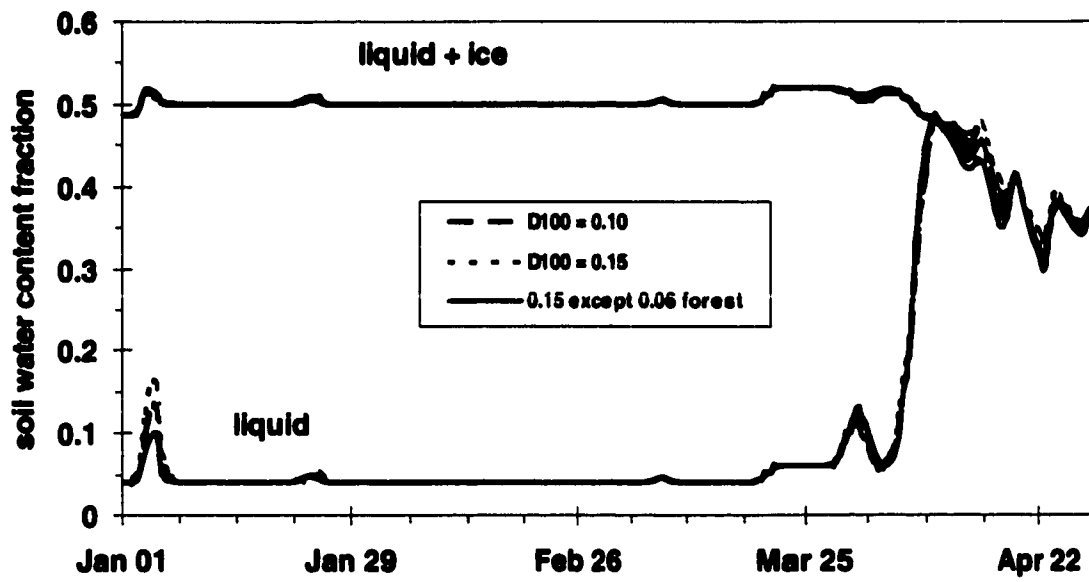


FIGURE 5-31d. Effects of varying the  $D_{100}$  on the soil temperature.

FIGURE 5-31e. Effects of varying the  $D_{100}$  on the soil water content.

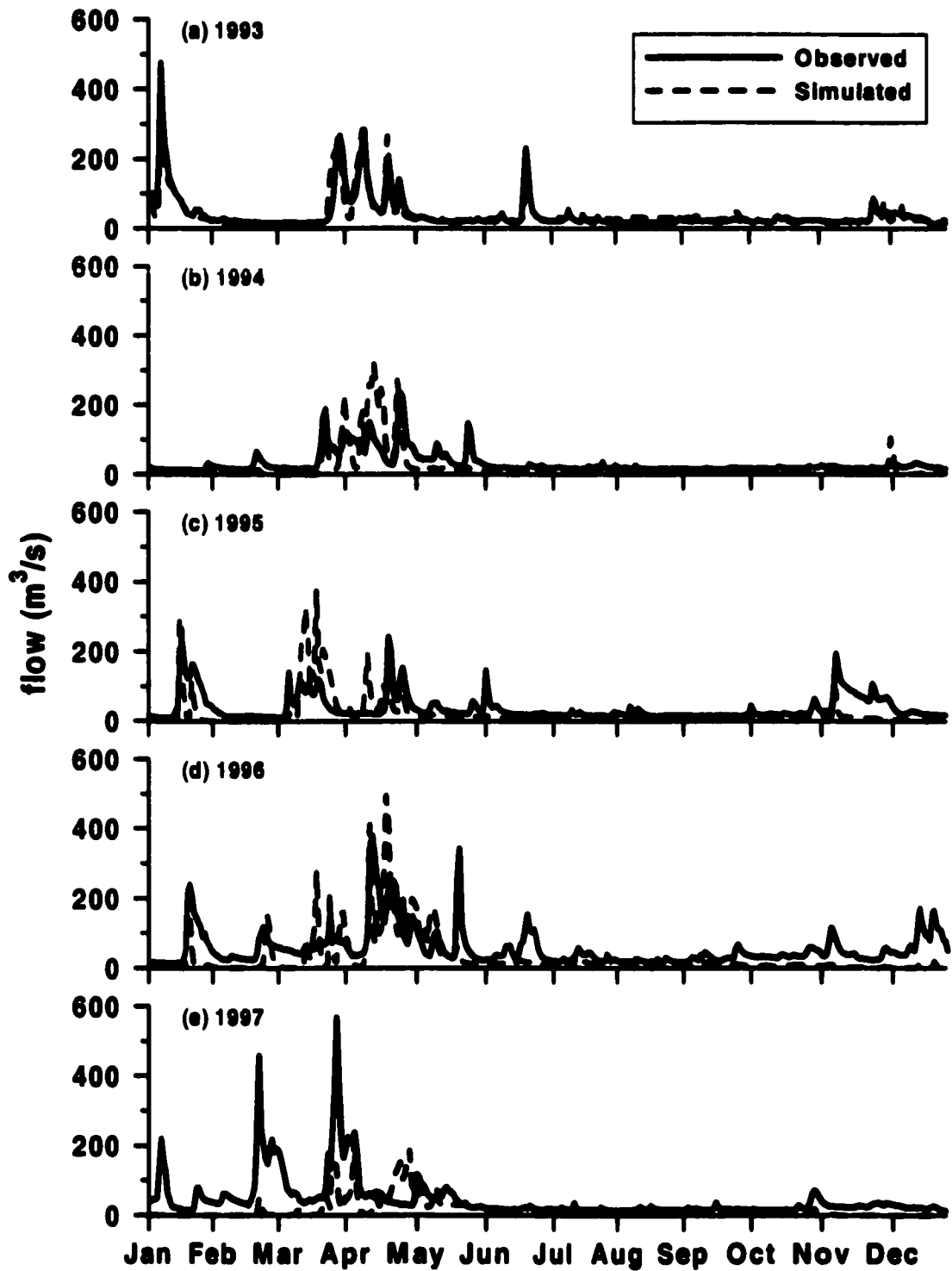


FIGURE 5-32. Five year continuous simulation for the Grand River at Galt.



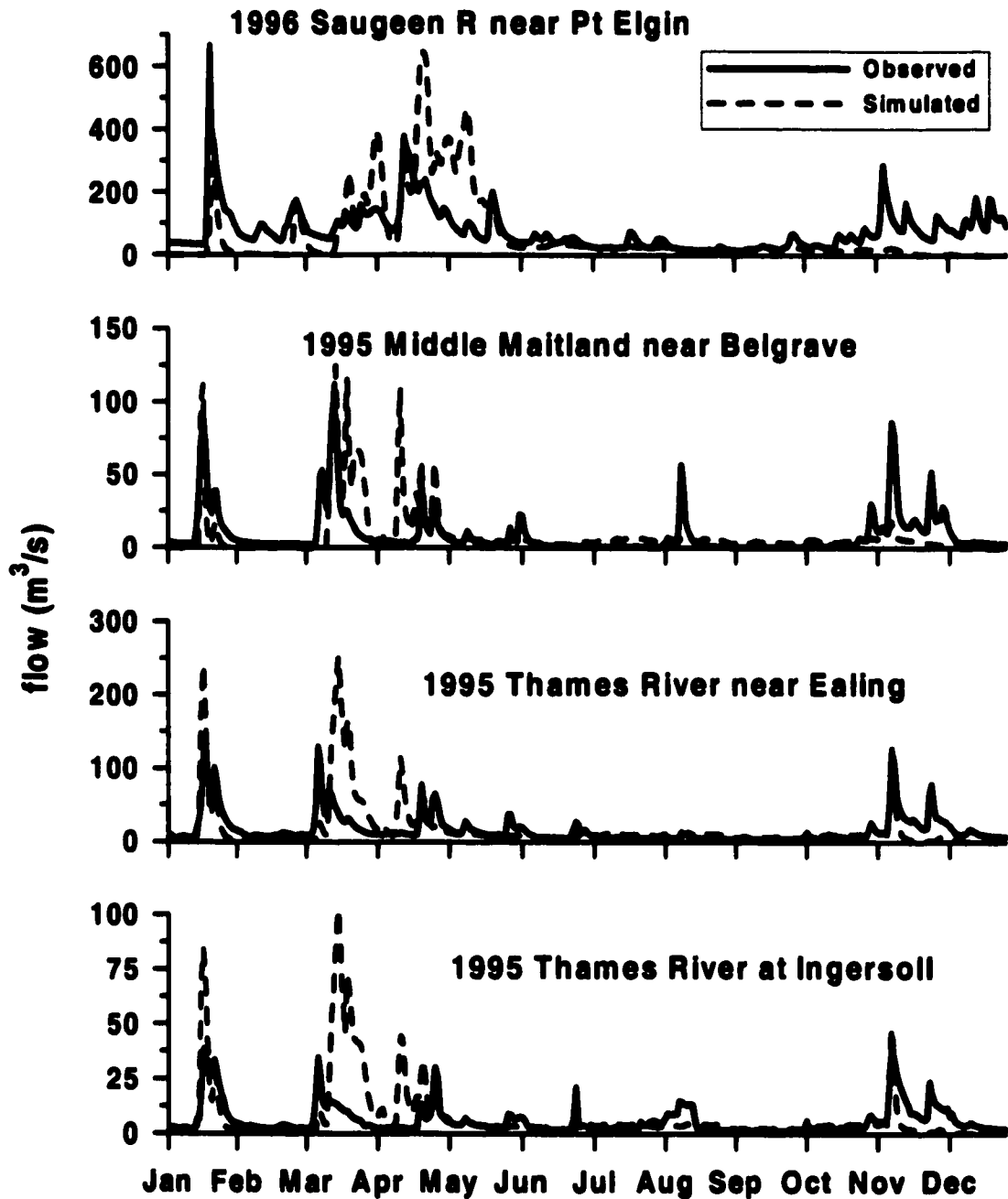


FIGURE 5-33a. Select poorly simulated annual hydrographs from the five year continuous simulation for the entire southern Ontario study area (drainage areas: Saugeen R. near Port Elgin = 3960  $\text{km}^2$ , Maitland R. above Wingham = 528  $\text{km}^2$ , Thames R. near Ealing = 1340  $\text{km}^2$ , and Thames R. at Ingersoll = 518  $\text{km}^2$ ).

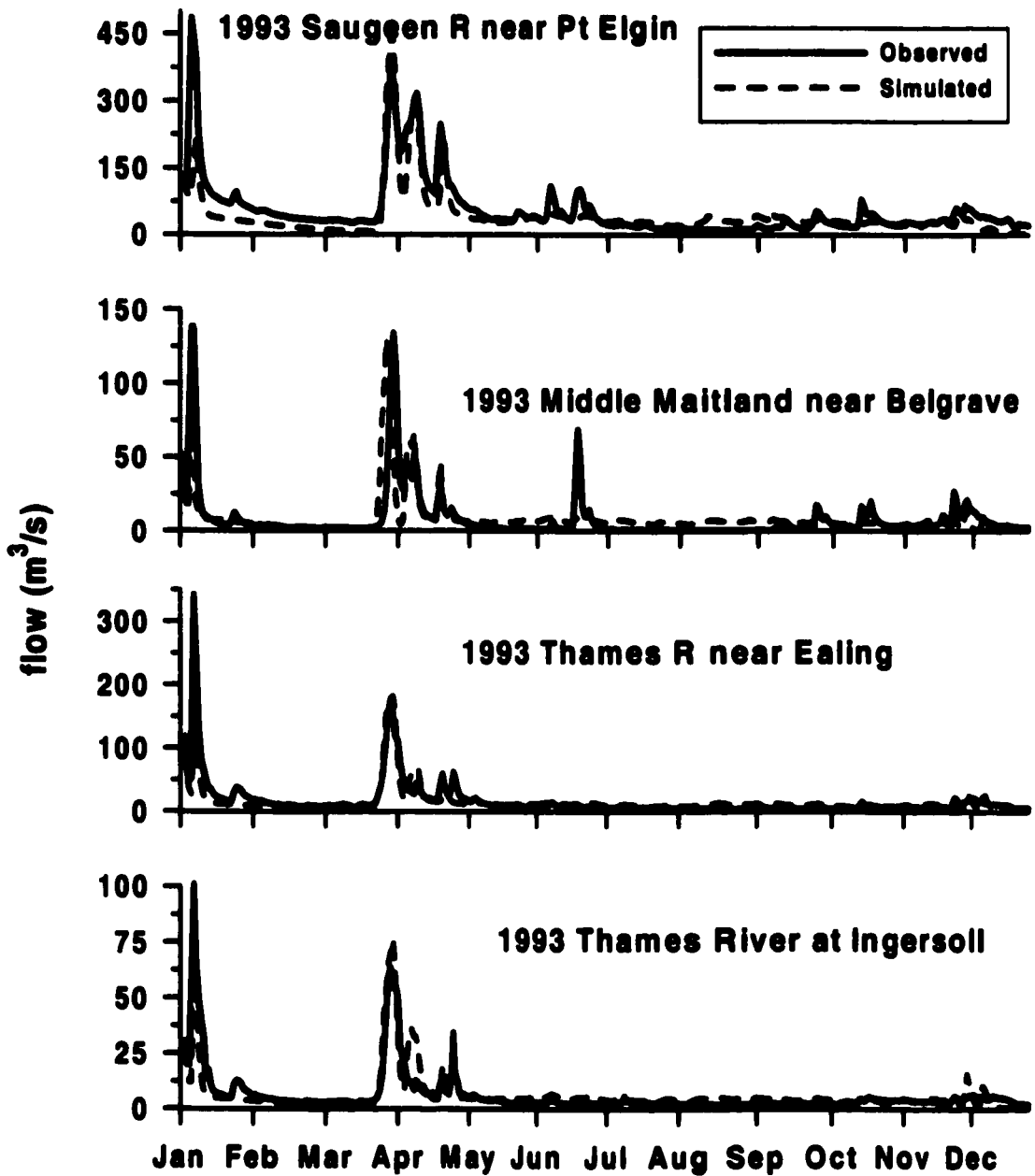


FIGURE 5-33b. The 1993 observed and simulated annual hydrographs from the five year continuous simulation for the entire southern Ontario study area, for the same watersheds as Figure 5-32a.

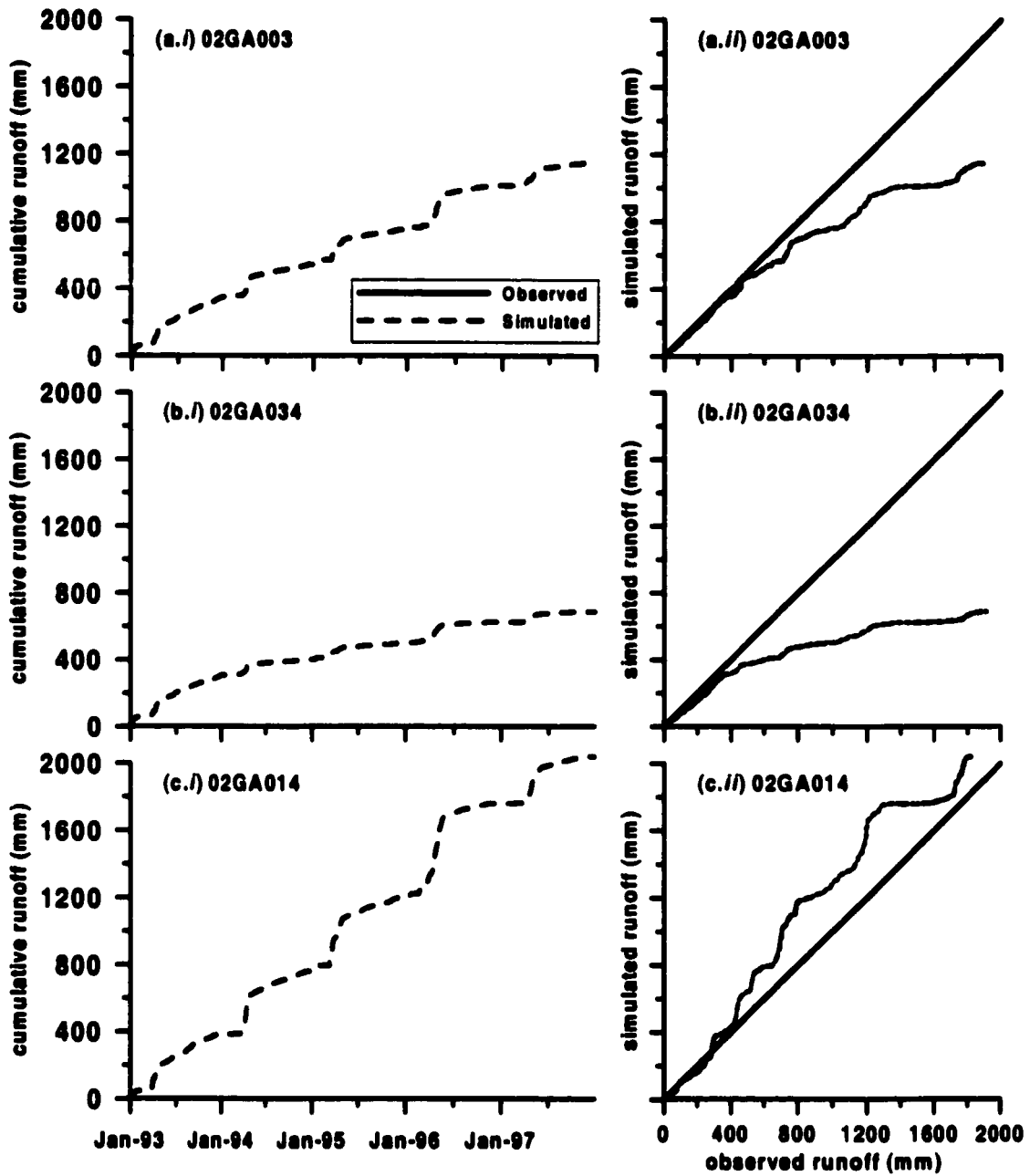


FIGURE 5-34. (i) Simulated and observed cumulative runoff over time from 1993 through 1997, and (ii) simulated versus observed cumulative runoff, for (a) the Grand River at Galt (02GA003), (b) the Grand River near West Montrose (02GA034), and (c) the Grand River at Marsville (02GA014).

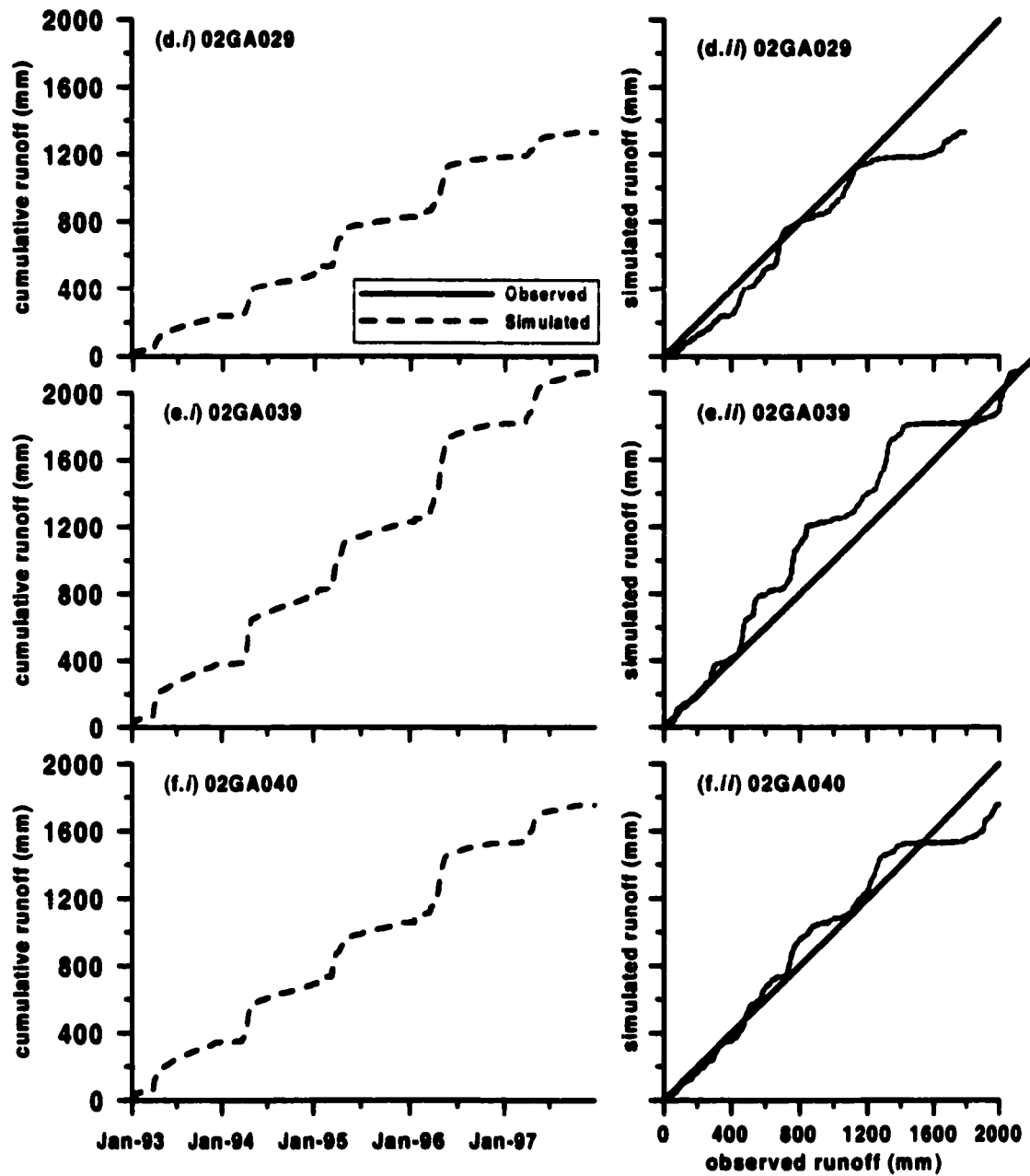


FIGURE 5-34 (cont'd). (d) the Eramosa River above Guelph (02GA029), (e) the Conestogo River above Drayton (02GA039), and (f) the Speed River at Armstrong Mills (02GA040).

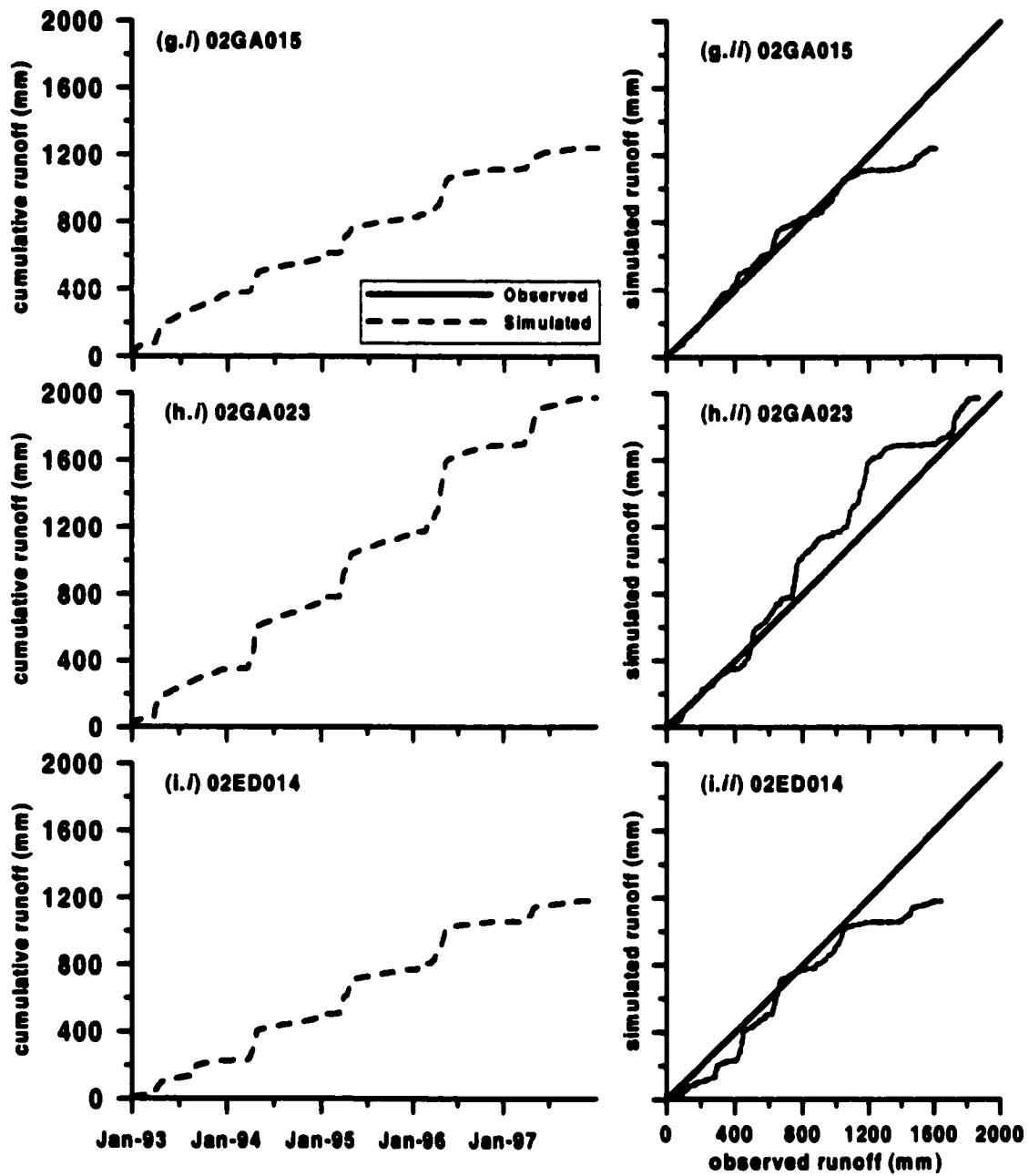


FIGURE 5-34 (cont'd). (g) the Speed River below Guelph (02GA015), (h) Canangagique Creek near Elmira (02GA023), and (i) the Pine River near Everett (02ED014).

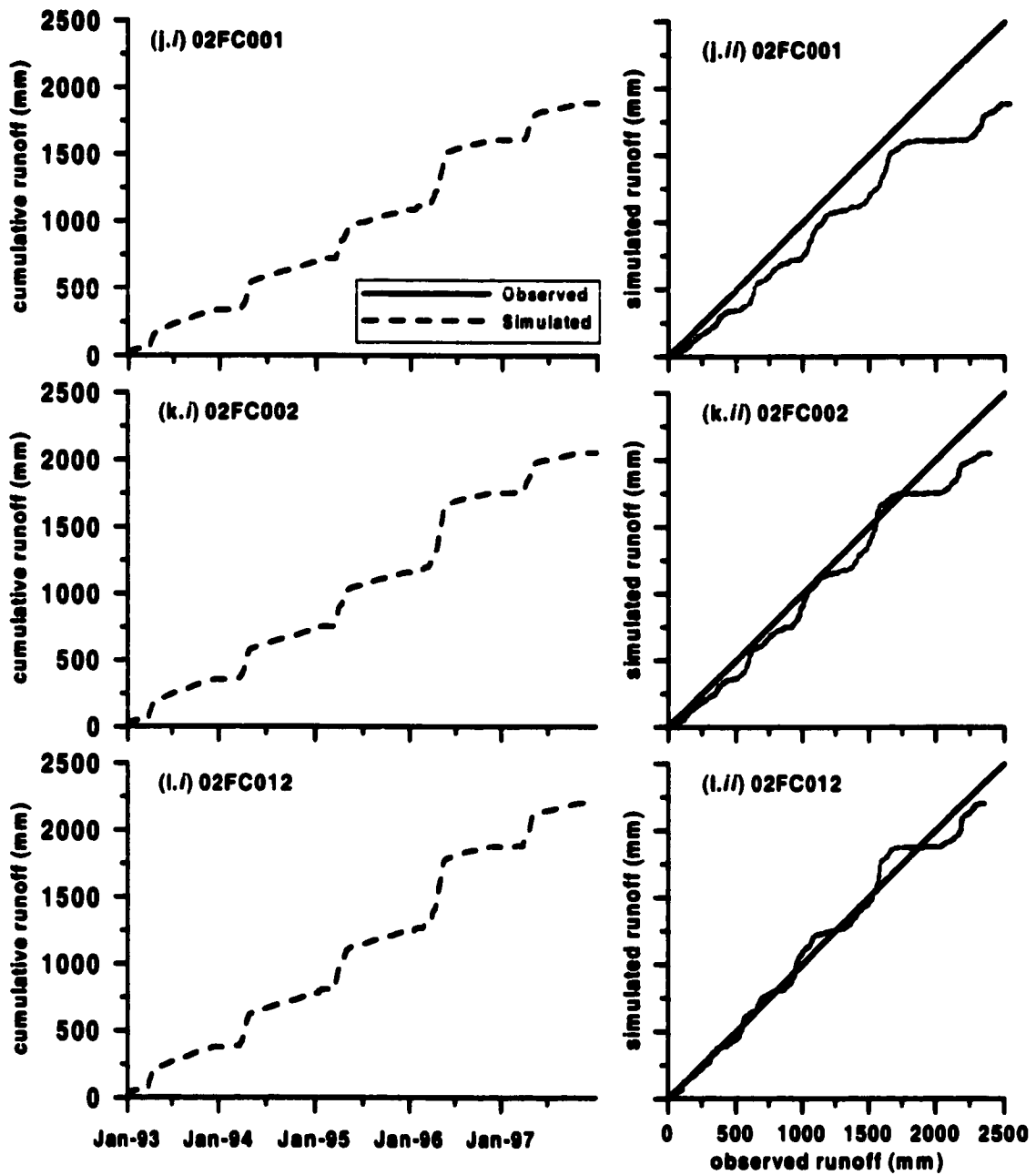


FIGURE 5-34 (cont'd). (j) the Saugeen River near Port Elgin (02FC001), (k) the Saugeen River near Walkerton (02FC002), and (l) the South Saugeen River near Hanover (02FC012).

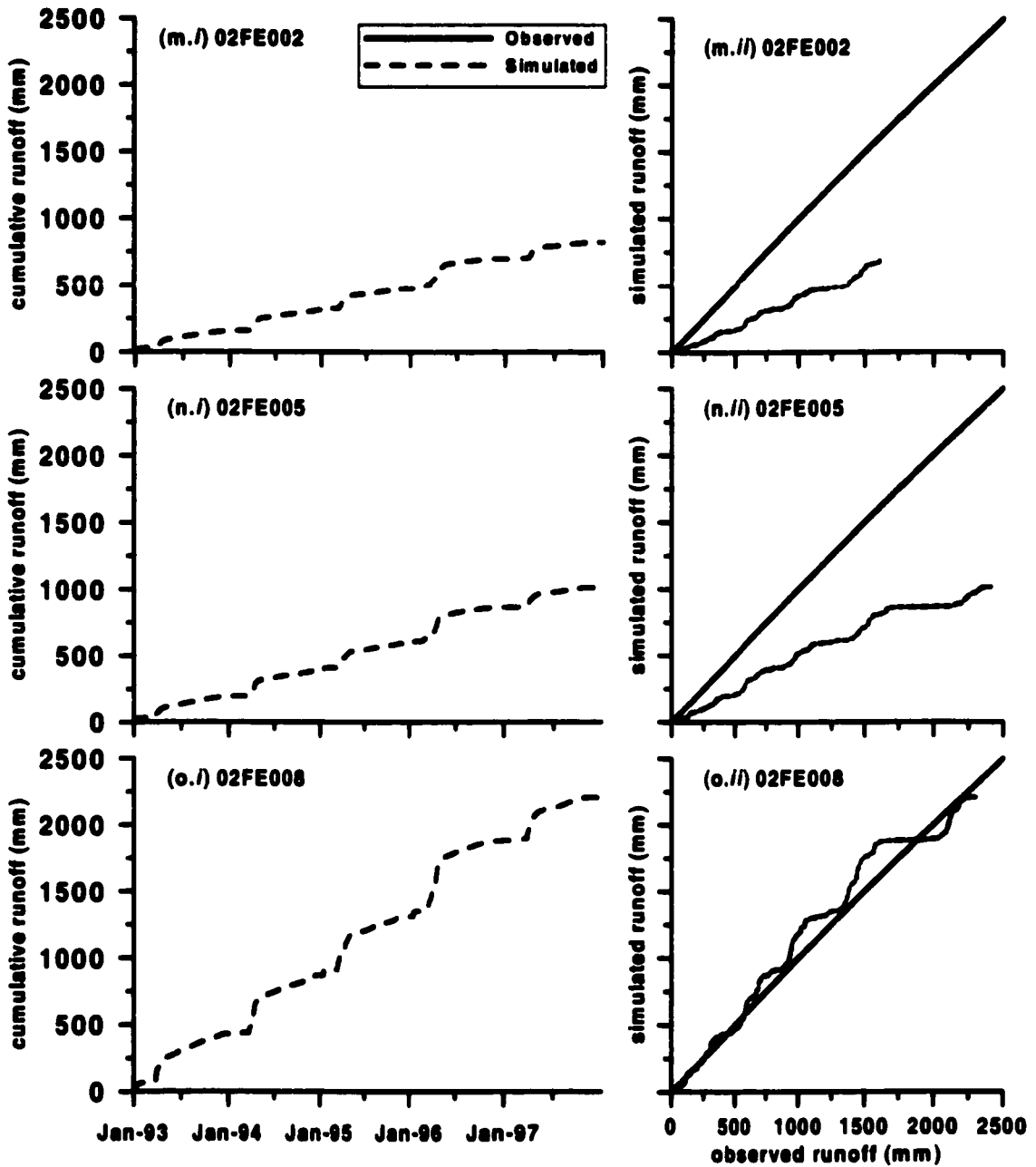


FIGURE 5-34 (cont'd). (m) the Maitland River below Wingham (02FE002), (n) the Maitland River above Wingham (02FE005), and (o) the Middle Maitland River near Belgrave (02FE008).

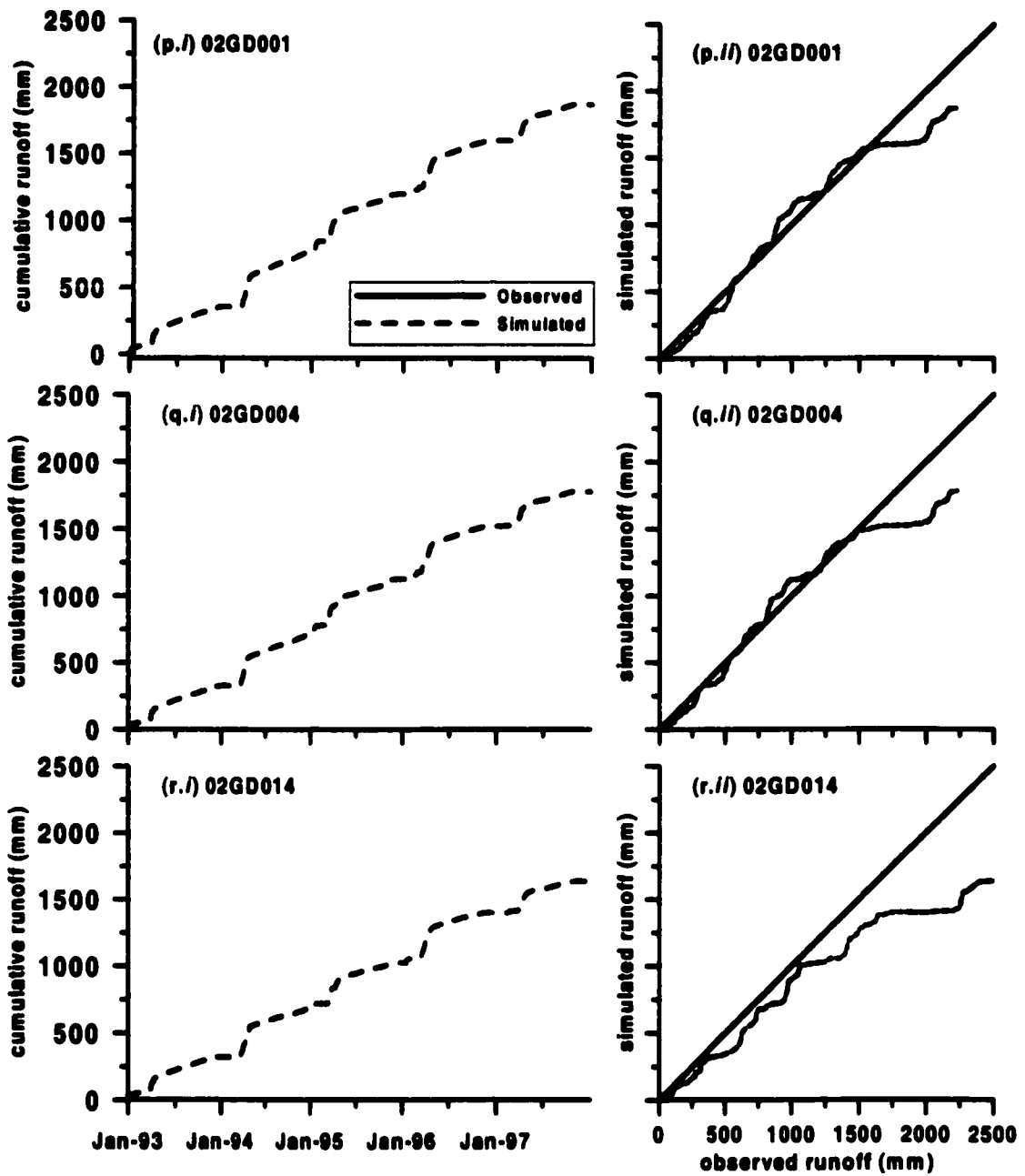


FIGURE 5-34 (cont'd). (p) the Thames River near Ealing (02GD001), (q) the Middle Thames River at Thamesford (02GD004), and (r) the North Thames River near Mitchell (02GD014).



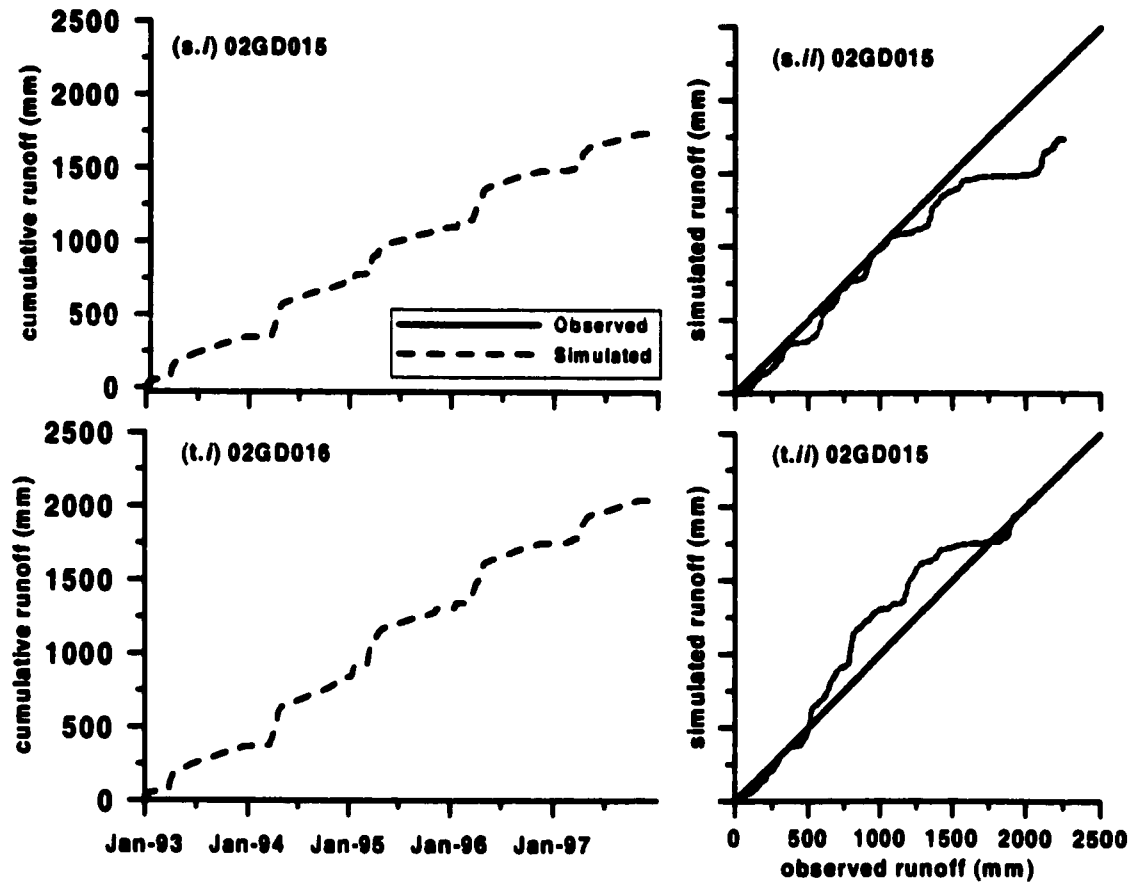


FIGURE 5-34 (cont'd). (s) the North Thames River near Thorndale (02GD015), and (t) the Thames River at Ingersoll (02GD016).

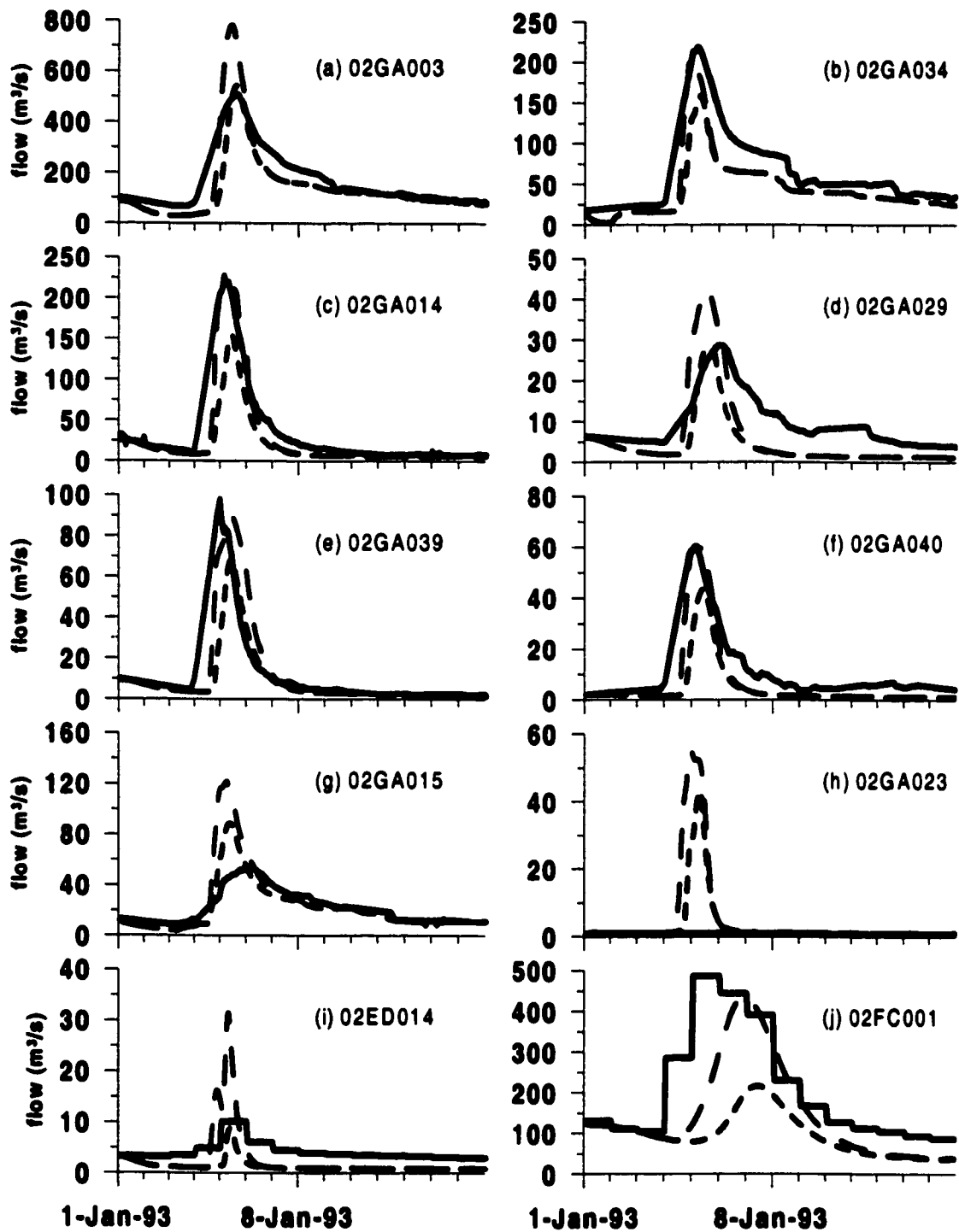


FIGURE 5-35. Variation in the early January 1993 hydrograph peak from the observed (solid black line), modelled assuming no snow on the ground on January 1 (dotted red line), and modelled assuming 10 cm of snow and 20mm of SWE everywhere (dashed green line). The watersheds are as in Figure 5-34.

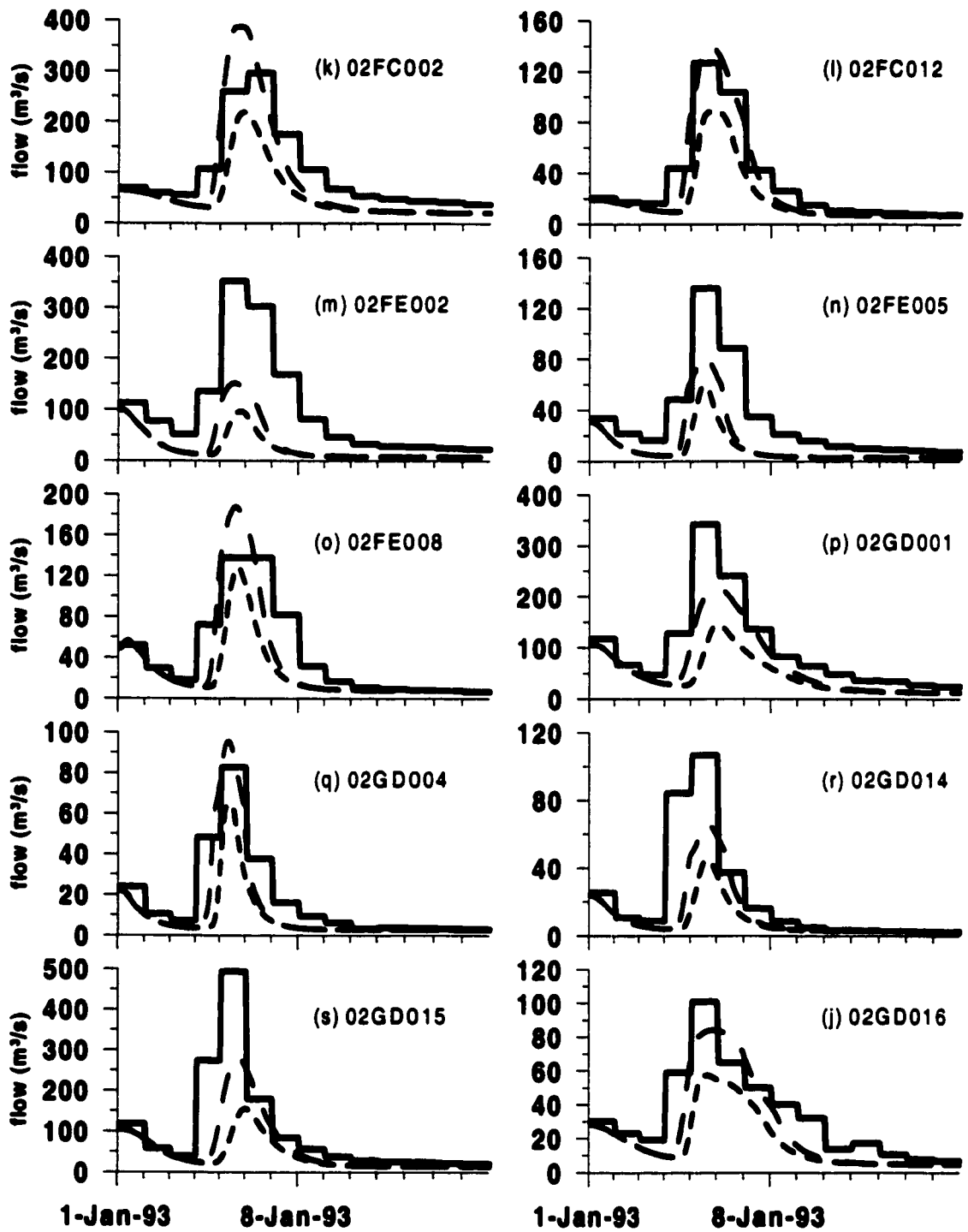


FIGURE 5-35 (cont'd).

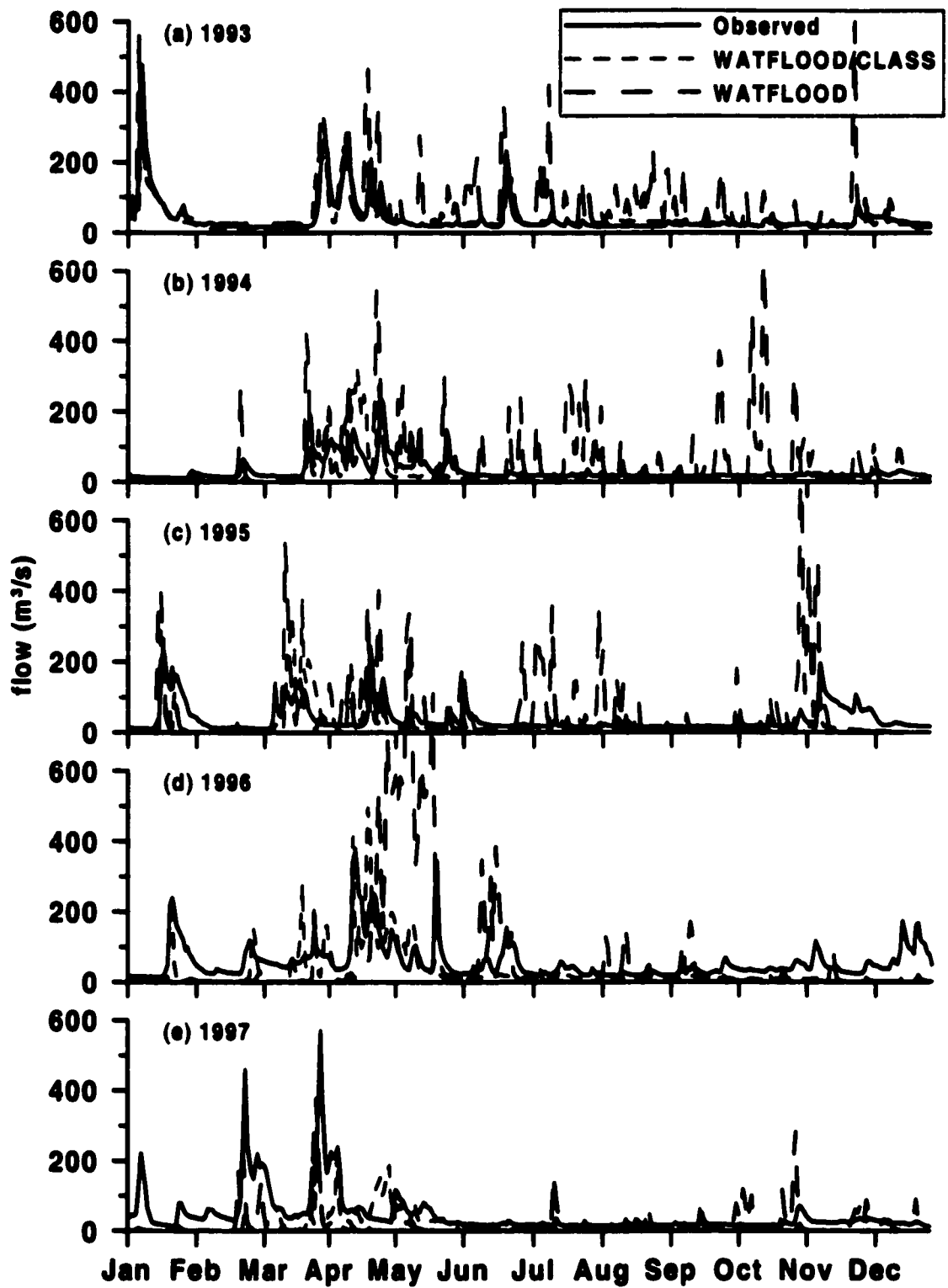


FIGURE 5-36. Comparison of simulated flows using WAT\_CLS3 (short dashes) versus WATFLOOD (long dashes) for the Grand River at Galt.

# Chapter 6

## CONCLUSIONS AND RECOMMENDATIONS

---

*"... in its microscopic forms, snow epitomizes ethereal beauty. It is cliché to say that no two snowflakes are identical, but it is a fact that each single snowflake that has fallen throughout all of time, and that will fall through what remains of time, has been - will be - a unique creation in symmetry and form." (Mowat, 1975, p4)*

The overall objective of this research was to model the snowpack throughout the snow season, using weather radar as the snowfall input, for the purpose of improved streamflow forecasting. Radar data were integrated across a watershed domain to provide winter precipitation, primarily snow, for hydrological modelling using the linked WATFLOOD and CLASS models (WAT\_CLS3). The usefulness of weather radar to estimate winter precipitation was assessed in terms of snowpack accumulation compared to point gauge precipitation estimates, simulated snowpack development compared to observed snowcourse SWE and depth, and simulated runoff compared to observed hydrographs. Various improvements were implemented in the CLASS model to more accurately represent snow processes. The significance of the model changes or additions was assessed using the "best" radar dataset developed from the above comparisons. The method for implementing the changes into the CLASS model was outlined to enable application by non-WAT\_CLS3 users.

## **6.1 CONCLUSIONS**

### **6.1.1 RADAR WINTER PRECIPITATION DATA**

Weather radar is useful in measuring the quantities of precipitation that fall in the winter. However, the raw radar images developed from the radial closest hit to a 2 by 2 km pixel using a conventional scan tend to overestimate in comparison to accumulations measured by Nipher-shielded Belfort gauges. Adjustment of the radar by removal of scaling and the use of temperature corrections to consider mixed precipitations and differences in snowfall shapes can substantially improve radar estimation of cold season precipitation. Figure 6-1 illustrates the improvement in the radar accumulation, with respect to “bush” gauge estimates. As well, the radar estimates are improved as the length of accumulation is increased; the standard error is decreased and the coefficient of determination is increased. In general, the best radar dataset for winter precipitation accumulations is the removal of the scaling followed by mixed precipitation adjustment using the constant rainfall factor.

Weather radar subsequently provides good estimates of winter precipitation for hydrologic modelling. Across the Upper Grand River watershed in southern Ontario the use of radar produces substantially better estimates of runoff volumes than gauge precipitation estimates for 1993, 1994 and 1996 (Figure 6-2a). The 1997 estimates are similar for both datasets, whereas for the simulation of the winter of 1995, the simulated runoff volumes from the gauge precipitation estimates were better than from radar precipitation estimates. However, on average for the five winter radar produced substantially better simulated runoff volumes (Figure 6-2b). While the five-year average runoff volume from the raw radar was very similar to observed, the annual variations from the raw radar were the largest for any of the radar datasets (Figure 6-2a). For three of the five years simulated, the two best radar datasets were derived from the variable rainfall rate adjustment of mixed precipitation, and since the five year average for the particle shape adjustment was better than without, in general, the best dataset for runoff volume modelling using WAT\_CLS3 is derived from the removal of scaling, the adjustment of mixed precipitation using the variable rainfall factor and the adjustment for particle shape.

Removal of scaling resulted in underestimation of radar accumulation and modelled

runoff volume. For southern Ontario, the occurrence of winter precipitation is most often at a rate less than 13.5 mm/h, and thus the incremental scale for the King City radar should remain at the minimum of 0.5 mm or at a smallest increment, when the conventional scan is used.

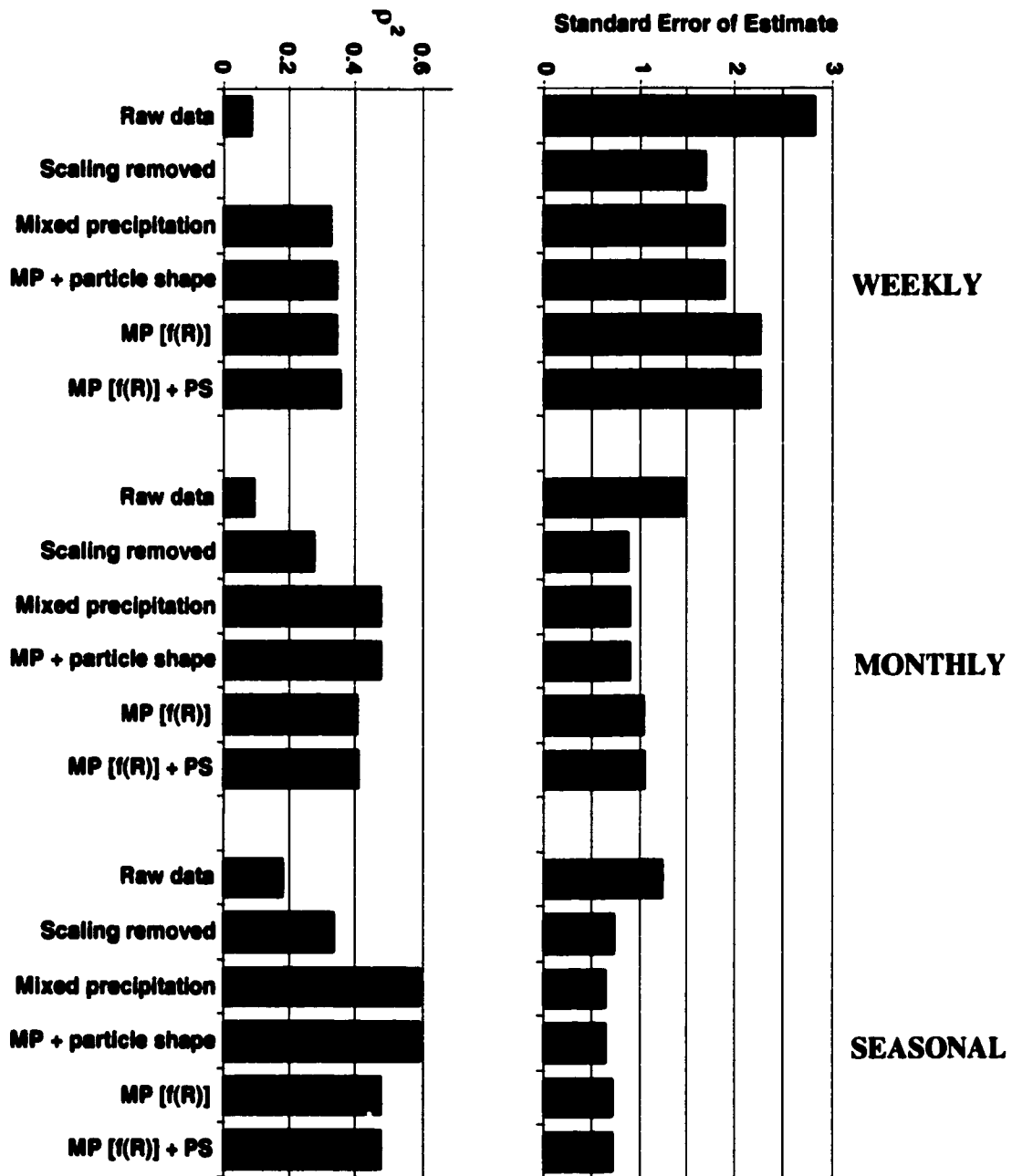


FIGURE 6-1. Summary of gauge versus radar accumulation population coefficient of determination ( $\rho^2$ ) and standard error of estimate (SEE) statistics (MP = mixed precipitation using a constant rainfall factor, PS = particle shape, MP [f(R)] = mixed precipitation using a variable rainfall factor).

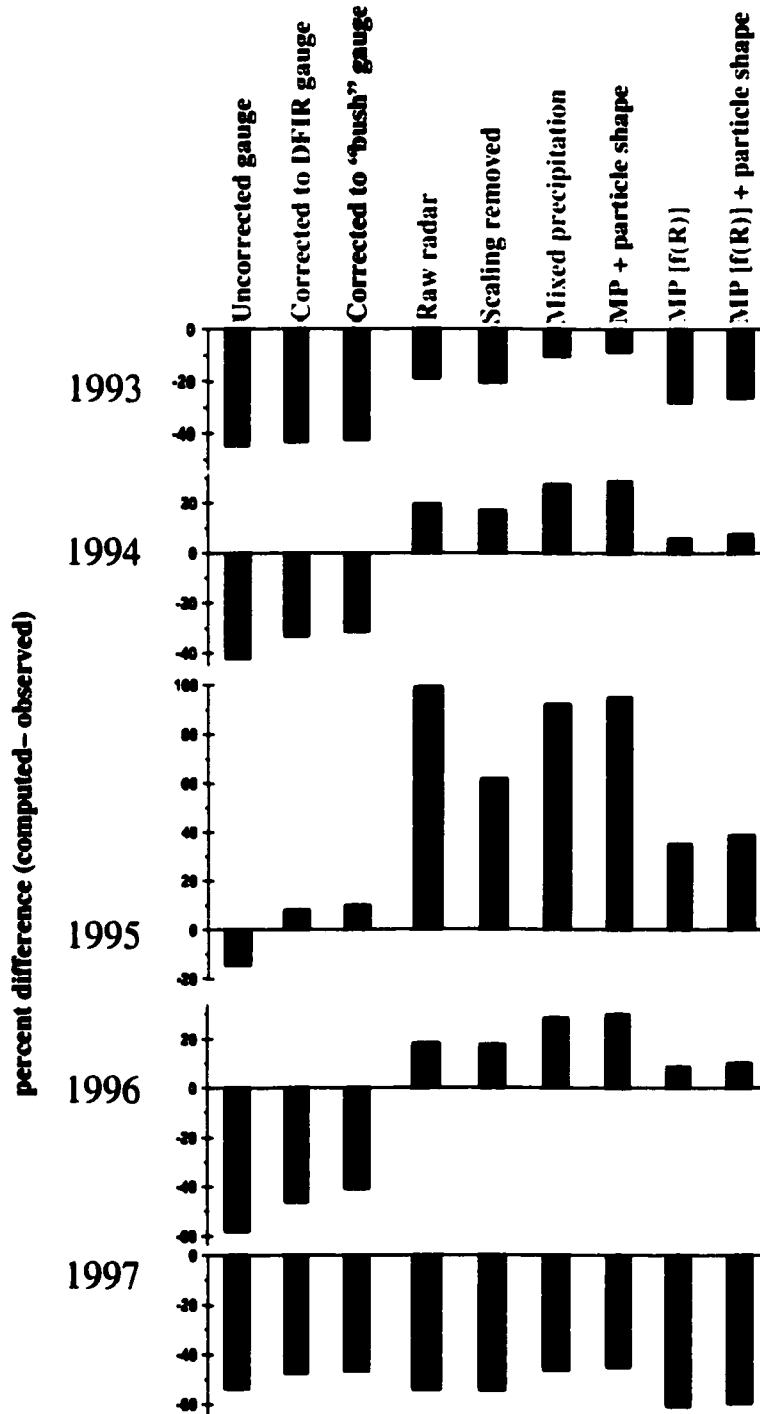


FIGURE 6-2a. Summary of average winter runoff volumes at all sites across the Grand River basin for different precipitation input data using the 'out-of-the-box' WAT\_CLS3 model (MP = mixed precipitation using a constant rainfall factor, PS = particle shape, MP [f(R)] = mixed precipitation using a variable rainfall factor).



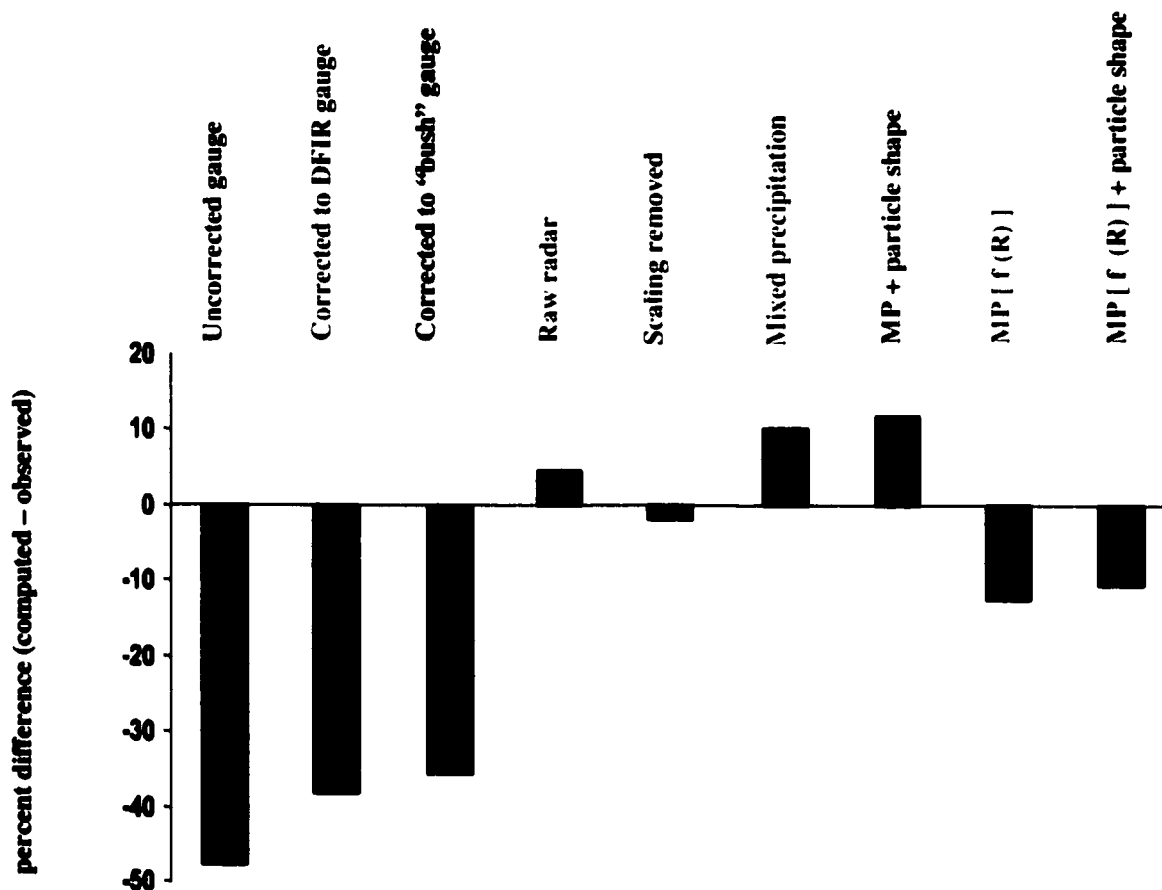


FIGURE 6-2b. Summary of average runoff volumes across the Grand River basin for the 1993 through 1997 winters using different precipitation input data with the 'out-of-the-box' WAT\_CLS3 model (MP = mixed precipitation using a constant rainfall factor, PS = particle shape, MP [f(R)] = mixed precipitation using a variable rainfall factor).

The underestimation of the 'scaling removed' radar accumulations was improved by adjusting the images for the occurrence of mixed precipitation. Specifically the following was observed for the mixed precipitation adjustment for the accumulation data: the linear approximation of the probability of snow versus temperature curve compiled by Auer provides a good adjustment, however, the polynomial representation yields better improvements to the radar accumulation estimates; the observed air temperatures should be used to address mixed precipitation at warmer than freezing temperatures; and while some overestimation resulted, a variable rainfall adjustment factor should be calculated to a maximum, such as 2.03. The

modelled streamflows were improved for some years by adjusting the radar snowfall estimates to consider mixed precipitation using the constant rainfall factor of 2.03 and for other years using the variable rainfall factor as a function of precipitation rate. Consideration of mixed precipitation improves the radar precipitation estimates.

The use of particle shape adjustment at temperatures colder than freezing does not alter the radar precipitation estimates as significantly as the mixed precipitation adjustment. The accumulation estimates are not improved significantly. Simulated runoff volumes increase over the mixed precipitation adjustments. At present the radar data cannot be easily adjusted by air temperature to consider the variation in the shape of falling snow crystals and the resultant reflectivity differences.

While the removal of scale produced better accumulation estimates than the raw radar estimates, only the 1995 simulated runoff volume using the scaling removed data as precipitation input to hydrologic modelling was better than the volume using the raw radar data. Adjustment of the radar for the occurrence mixed precipitation improved the radar precipitation estimates, while use of the snow particle shape curve did not. Including the precipitation rate in the adjustment of mixed precipitation provided worse accumulation estimates but better streamflow estimates than using a constant rainfall adjustment factor for most of the data modelled. As the radar operation parameters were altered through the course of the study (Scott pers. comm., 1999), it is difficult to choose an optimal radar adjustment scheme.

### **6.1.2 SNOWPACK HYDROLOGICAL MODELLING**

The water balance closed within 5% over a four year period using the WAT\_CLS3 model. Therefore, the model can translate precipitation into runoff and evapotranspiration appropriately without losing or storing excess water. Six cold processes were addressed for improvement in CLASS (Table 6-1). While these results are based on simulations for Southern Ontario, they can be generalized for other areas. Once the meteorological data were corrected, the most significant improvement to the streamflow hydrograph occurred as a result of the splitting of the soil state variables (Figure 6-3). Some of the melt was delayed, as heat was not transferred directly from the bare ground to the soil below the snowcover.

TABLE 6-1. Summary of the influence of the incorporation of advanced snow processes on streamflow, snow depth, and snow water equivalence (SWE) in the CLASS model

processes modelled	streamflow	snow depth	SWE
Split state variables	<i>significant:</i> later peak	no averaging: more snow in snowcovered area, no snow in snow-free	no averaging: more snow in snowcovered area, no snow in snow-free
Redistribution	<i>significant:</i> smaller and/or later peak	more in forest, less in open (based on depth limits)	more in forest, less in open
Maximum snowpack densities	<i>small impact:</i> greater density gives later peak	<i>significant:</i> greater density less snow depth	<i>almost negligible</i>
Mixed precipitation	<i>small impact:</i> greater threshold gives later peak	<i>small impact:</i> greater threshold more depth	<i>small impact:</i> greater threshold more snow in pack
Variable fresh snow density	<i>small impact:</i> earlier peak	only immediately after a snowfall	<i>almost negligible</i>
Snowfall canopy interception	<i>almost negligible</i>	more snow held, less in pack	more snow held, less in pack

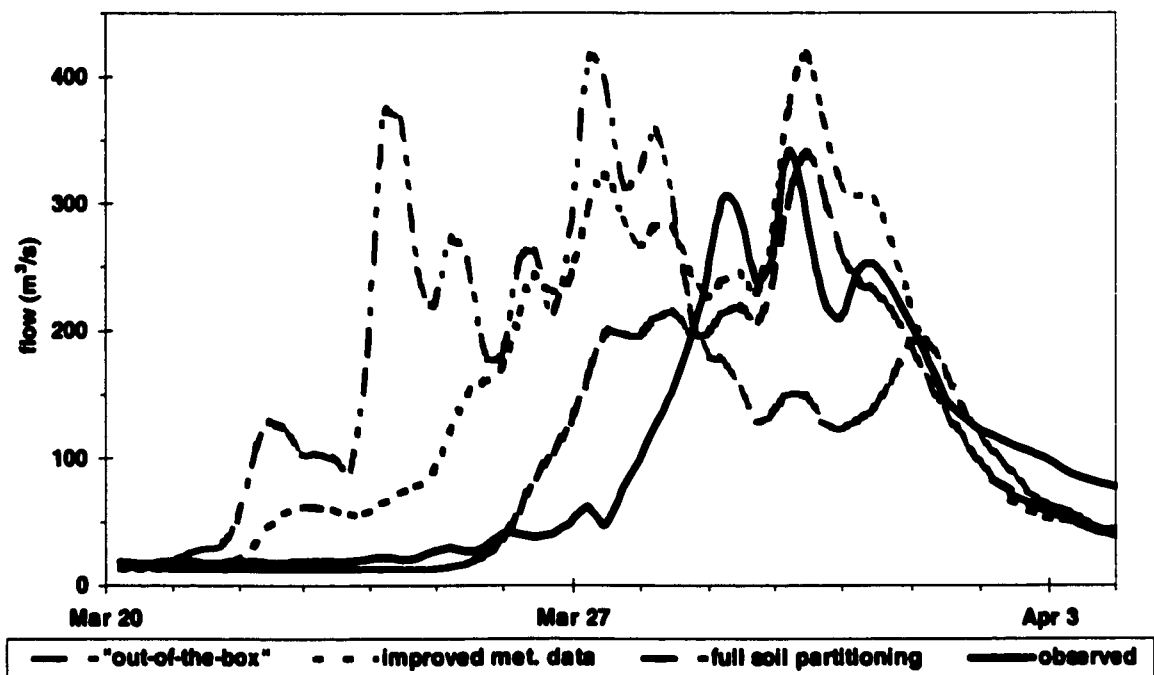


FIGURE 6-3. Initial snowmelt hydrograph improvements (1993 Grand River at Galt).

Redistribution of snow from the bare or crop/low vegetation areas to the forest resulted in a delay in the streamflow snowmelt peak and altered the depth and SWE of each snowpack (Table 6-1). While the delaying of the peak was an improvement in some scenarios, the simple distribution technique did not represent the actual transport of snow, and in most cases overestimated movement.

The movement of snow with a land cover area was explored with respect to variation in the minimum snow depth required for complete snowcover ( $D_{100}$ ) and this had an influence on hydrology.

Variation in the maximum allowable snowpack density altered streamflow and snowpack depth, but not the SWE (see Table 6-1).

The addition of mixed precipitation into CLASS provides for a more realistic representation of the precipitation near the surface, especially in areas that encounter periods of mid-winter melt, since the use of mixed precipitation instead of the 0°C threshold adds less energy to the earth's surface systems. However, the impact on the streamflow was small and yielded a later peak when less energy was in the pack, i.e., more snow and less rain (see Table 6-1). Thus there was more snow in the pack.

The results for the variation in the fresh snow density, instead of a constant value of 100 kg/m<sup>3</sup> yielded the same streamflow results as the use of a lesser maximum snowpack density, however, the actual depth of snow was only different immediately after an event.

The use of a maximum snowfall interception holding capacity of 50% of falling precipitation improves the representation of canopy snowfall interception. The Hedstrom and Pomeroy (1998) snowfall canopy interception formulation provides further improvement. However the impact on streamflow is minimal. Representation of the composition of the forest and estimating canopy parameters has a more significant impact on hydrology.

### **6.1.3 SECONDARY RESULTS**

While the longwave radiation at a location can be computed from the near surface air temperature, an estimate of the cloud cover fraction is necessary. For areas such as southern Ontario the cloud cover fraction can be on average 0.5, however the hour amount can vary from

0.0 to 1.0, resulting in a variation of the longwave radiation estimation of 40% which in turn can significantly alter the energy balance and in particular the rate of snowmelt. For the daytime hours, a method was illustrated to estimate the cloud cover fraction for longwave radiation computation using a comparison of the measured and clear-sky theoretical incoming shortwave radiation. The average daytime cloud cover fraction for three locations in central southwestern Ontario (CARE, Elora and Toronto) for five winters was between 0.54 and 0.60.

A relationship for the relative specific surface area as a function of formation temperature was derived through qualitative means. Data are required to examine the validity of the relationship. However, such a function could be used to adjust radar data and estimate the density of freshly fallen snow.

Fresh snow density data were collected. Existing functions and the particle shape function were plotted with data from the literature and the new data. However a best fit function could not be chosen. More field data are required.

## **6.2 RECOMMENDATIONS**

- Since the radar operation parameters were altered through the course of the study, the implication to the radar estimate of each change to a radar's operation must be determined.
- Further investigation is necessary to illustrate the applicability of hourly averages for sub-hourly physical processes such as mixed precipitation and changes in the shape of falling snow crystals. Localized mixed precipitation curves should be developed for each study area. Field data and supplementary theoretical analysis are needed to justify or further define the particle shape curve. The local lapse rate must be considered to adjust the temperature used with each curve and the shape of each curve. When sub-hour temperature data become available, these data should be used with the finer scale radar data (10 minute CAPPIs), derived from the summer and winter *Z-R* coefficients to adjust for mixed precipitation and the shape of snow particles.

- The local advection of heat and water fluxes between snowcovered and snow-free areas must be further studied. These fluxes must be parameterized to remove the consideration of location to be included in larger-scale physically based hydrologic models.
- It is recommended that if redistribution is modelled in a simplistic form, erosion and deposition of snow should only occur in portions of land covers and not from an entire land cover area to an entire land cover area. Subsequently the sublimation of blowing snow should be incorporated. This can be included if a more physically based blowing snow model, such as a parameterization of the Prairie Blowing Snow Model (Pomeroy *et al.*, 1993) or SnowTrans-3D (Liston and Sturm, 1998), is integrated into CLASS.
- Different  $D_{100}$  values should be assigned to each land cover type. The formulation of a  $D_{100}$  approach for the accumulation of snow should also be further investigated.
- If the exponential decay of the snowpack depth is continued to be used to represent the metamorphosis of the snowpack, then the maximum allowable snowpack density should be assigned for each land cover type. The use of a two- or multi-layer snowpack would enable different metamorphosis and densities based on age and exposure of the layer. However computational time would increase, especially for GCMs.
- As different probability of snow versus temperature curves exist for different geographic regions, specific curves should be investigated. The use of other temperature measures, such as the dewpoint temperature or the ice bulb temperature, could provide a means of developing a generalized mixed precipitation curve.
- The influence of a variable fresh snow density would be more pronounced with the use of a two or multi-layer snowpack model.
- To more adequately represent snowfall canopy interception, the focus should be on evaluating the composition of the forests and estimating canopy parameters.
- Since the comparison of measured to theoretical shortwave radiation for cloud cover estimation (and the subsequent longwave radiation estimation) is only useful for daylight hours and assumptions are required to fill the nighttime and other data voids. The method should be tested with a complete set of energy balance measurements. As regional climate models become more robust, their output can be used directly for physically-

based hydrologic models to overcome the lack of longwave radiation measurements. The meteorological gauge data could be used for validation, as gridding issues related to the spatial distribution of gauge data would have been eliminated.

- Data are required to examine the validity of the relationship between the relative specific surface area and formation temperature. Such a function could be used to adjust radar data and estimate the density of freshly fallen snow.
- The relationship between fresh snow density and near surface air temperature should be reevaluated. It is recommended that the existing methods of collection for fresh snow density data should be reviewed.
- For finer scale spatial and temporal radar data, the horizontal movement of precipitation particles during vertical dropping must be further considered, especially as this influences the movement of impurities within snow crystals and atmospheric contaminants scavenged during descent.

# REFERENCES

---

- Anderson, E.A., 1976. *A point energy and mass balance model of a snow cover*. NOAA Technical Report NWS 19, National Oceanic and Atmospheric Administration, Silver Springs, MD.
- Arnold J.G., and J.R. Williams, 1995. "SWRRB--A Watershed Scale Model for Soil and Water Resources Management." In *Computer Models of Watershed Hydrology*, ed. V.P. Singh, Water Resources Publication.
- Auer, A.H., Jr., 1974. "The rain versus snow threshold temperatures." *Weatherwise*, 27:67.
- Auer, A.H., Jr., and D.L. Veal, 1970. "The Dimensions of Ice Crystals in Natural Clouds." *Journal of Atmospheric Sciences*, 27: 919-926.
- Austin, P.M., 1963. "Radar measurements of the distribution of precipitation in New England storms." Preprints of the *10th Weather Radar Conference*, American Meteorological Society, 10: 247-254.
- Bagnold, R.A., 1941. *The Physics of Blown Snow and Desert Dunes*. Methuen & Co. Ltd., London.
- Boucher, R.J. and J.G. Wieler, 1985. "Radar Determination of Snowfall Rate and Accumulation." *Journal of Climate and Applied Meteorology*, 24(1): 68-73.
- Brown, R.D., 1997. "Historical variability in Northern Hemisphere spring snow covered area." *Annals of Glaciology*, 25: 340-346.
- Bussieres, N. and W. Hogg, 1989. "The objective analysis of daily rainfall by distance weighting schemes on a mesoscale grid." *Atmosphere-Ocean*, 27(3):521-541.
- Carlson, P.E., 1968. "Measurement of snow by radar." Proceedings of the *13th Radar Meteorology Conference*, American Meteorological Society, 13: 384-387.
- Carlson, P.E. and J.S. Marshall, 1972. "Measurement of snowfall by radar." *Journal of Applied Meteorology*, 11(4): 494-500.
- Cole, J.A., C. Wade and R.M. Rasmussen, 1998. "Evaluation of precipitation gauges and wind shielding for the measurement of real-time liquid-equivalent snowfall." *Presentation at the 55th Eastern Snow Conference*, Jackson, New Hampshire, June 3-5, 1998.
- Collier, C.G., and P.R. Larke, 1978. "A case study of the measurement of snowfall by radar: An assessment of accuracy." *Quarterly Journal of the Royal Meteorological Society*, 104: 615-621.
- Collier, C.G., 1991. *Applications of Weather Radar Systems, A Guide to Uses of Radar Data in Meteorology and Hydrology*. Ellis Horwood, Chichester, West Sussex, England.
- Croley, T.E., II, 1989. "Verifiable evaporation modelling on the Laurentian Great lakes." *Water Resources Research*, 25(5): 781-792.
- Crozier, C.L., P.I. Joe, J.W. Scott, H.N. Herscovitch and T.R. Nichols, 1991. "The King City operational Doppler Radar: Development, all-season applications and forecasting." *Atmosphere-Ocean*, 29(3): 479-516.
- Delage, Y., L. Wen, and J-M. Bélanger, 1999. "Aggregation of Parameters for the Land Surface Model CLASS." *Atmosphere-Ocean*, 37(2): 157-178.
- Diamond, M., and W.P. Lowry, 1953. *Correlation of density of new snow with 700mb temperature*. Research Paper 1, Snow, Ice and Permafrost Research Establishment, US



- Army Corps of Engineers, 3pp.
- Dingman, S.L., 1994. *Physical Hydrology*. Maxwell Macmillian Publishing Company.
- Donald, J.R., 1992. *Snowcover Depletion Curves and Satellite Snowcover Estimates for Snowmelt Runoff Modelling*. Unpublished Ph.D. thesis presented to the Department of Civil Engineering, University of Waterloo, ON, 233p.
- Donald, J.R., E.D. Soulis, N. Kouwen, and A. Pietroniro, 1995. "A land cover-based snow cover representation for distributed hydrologic models." *Water Resources Research*, **31**(4): 995-1009.
- Donaldson, N., 1999. *Fractional distribution of snow versus rain as a function of temperature*. King Weather Radar Research Station, Atmospheric Environment Service, Environment Canada, King City, Ontario, **personal communication**.
- Doviak, R.J., and D.S. Zrnich, 1984. *Doppler Radar and Weather Observations*. Academic Press, Orlando, Florida.
- Einstein, H.A., 1950. "The bed-load function for sediment transportation in open channel flows." *US Dept. of Agriculture Technical Bulletin No. 1026*.
- Environment Canada, 1997. *1996 HYDAT Hydrometric Data CD-ROM*. Water Survey of Canada, Ottawa, Canada.
- Environment Canada, 1998a. "Canadian Climate Normals 1961 to 1990: Provincial Normals Index." URL: <<http://www.cmc.ec.gc.ca/climate/normals/eprovwmo.htm>>, Canadian Meteorological Centre, Atmospheric Environment Service, Downsview, Ontario, Canada.
- Environment Canada, 1998b. "Improving Public Safety — Canada's Doppler Weather Radar Network." URL: <[http://www1.tor.ec.gc.ca/doppler/national/network\\_e.htm](http://www1.tor.ec.gc.ca/doppler/national/network_e.htm)>, Atmospheric Environment Service, Downsview, Ontario, Canada.
- Environment Canada, 1998c. "CMC Climate And Water Information: Canadian Climate Station Catalogue." URL: <<http://www1.tor.ec.gc.ca/csc/query.asp>>, Climate And Water Information, Canadian Meteorological Centre, Atmospheric Environment Service, Downsview, Ontario, Canada.
- Environment Canada, 1999. "Documentation for the Digital Archive of Canadian Climatological Data (Surface) Identified by Element." URL: <<http://www.cmc.ec.gc.ca/climate/document.htm>>, Atmospheric, Climate And Water Systems Branch, Atmospheric Environment Service, Downsview, Ontario, Canada.
- Fassnacht, S.R., E.D. Soulis, K.R. Snelgrove, and N. Kouwen, 1998. "Application of weather radar to model the snow hydrology of southern Ontario." *Proceedings of the Eastern Snow Conference* (Jackson, NH, June, 1998), **55**: 115-123.
- Fassnacht, S.R., E.D. Soulis, and N. Kouwen, 1999a. "Shape characteristics of freshly fallen snowflakes and their short-term changes." *Proceedings of the Interactions between the Cryosphere, Climate and Greenhouse Gases Symposium*, IAHS Publication No. **256**: 111-122.
- Fassnacht, S.R., J. Innes, N. Kouwen, and E.D. Soulis, 1999b. "The specific surface area of fresh dendritic snow crystals." *Hydrological Processes*, **13**(18): 2945-2962.
- Fujiyoshi, Y. and G. Wakahama, 1985. "On snow particles comprising an aggregate." *Journal of Atmospheric Sciences*, **42**(15): 1667-1674.

- Fujiyoshi, Y., T. Endoh, T. Yamada, K. Tsuboki, Y. Tachibana and G. Wakahama, 1990. "Determination of a Z-R relationship for snowfall using a radar and high sensitivity snow gauges." *Journal of Applied Meteorology*, 29(2): 147-152.
- Gold, L.W., 1958. "Changes in a shallow snow cover subject to a temperate climate." *Journal of Glaciology*, 3: 218-222.
- Golubev, V.S., 1986. "On the problem of standard conditions for precipitation gauge installation." In *International Workshop on the Correction of Precipitation Measurements*, WMO/TD No. 104: 57-59.
- Goodell, B.C., 1966. "Snowpack management for optimum water benefits." *ASCE Water Resources Engineering Conference*, Denver, CO, Preprint 379, May 1966.
- Goodison, B.E., 1978. "Accuracy of Canadian snow gauge measurements." *Journal of Applied Meteorology*, 17: 1542-1548.
- Goodison, B.E., and J.R. Metcalfe, 1992. "The WMO Solid Precipitation Intercomparison: Canadian Assessment." In *WMO Technical Conference on Instruments and Methods of Observation*, WMO/TD No. 462: 221-225.
- Goodison, B.E. H.L. Ferguson, and G.A. McKay, 1981. "Measurement and data analysis." Chapter 6 in *Handbook of Snow: Principles, Processes, Management & Use* (eds. D.M. Gray and D.H. Male), Pergamon Press, Toronto.
- Goodison, B.E., P.Y.T. Louie and D. Yang, 1998. *WMO Solid Precipitation Measurement Intercomparison Final Report*. WMO Instruments and Observing Methods Report No. 67, WMO/TD No. 872.
- Goodison, B.E., R.D. Brown, M.M. Brugman, C.R. Duguay, G.M. Flato, E.F. LeDrew, and A.E. Walker, 1999. "CRYSYS - Use of the Cryospheric System to monitor global change in Canada: Overview and Progress." *Canadian Journal of Remote Sensing*, 25(1): 3-11.
- Gray, D.M., and T.D. Prowse, 1993. "Snow and floating ice." In *Handbook of Hydrology*, (ed. D.R. Maidment), McGraw-Hill, Toronto, Ontario.
- Gunn, K.L.S. and J.S. Marshall, 1958. "The distribution with size of aggregate snowflakes." *Journal of Meteorology*, 15: 452-461.
- Hamlin, L.P.B., 1996. *Snowmelt Hydrologic Modelling of Northern Wetland Dominated River Basins*. Unpublished MASC thesis, Department of Civil Engineering, University of Waterloo, Waterloo, Ontario, Canada, 212 pp.
- Hamlin, L.P.B., A. Pietroniro, T. Prowse, E.D. Soulis, and N. Kouwen, 1998. "Application of indexed snowmelt algorithms in a northern wetland regime". *Hydrological Processes*, 12: 1641-1657.
- Hastenrath, S.L., 1968. "Der regionale und jahrzeitliche Wandel des vertikalen Temperaturgradienten und seine Behandlung als Waermhaushaltsproblem." *Meteorologische Rundschau*, 1: 46-51.
- Hedstrom, N.R., and J.W. Pomeroy, 1997. "Accumulation of intercepted snow in the Boreal Forest: Measurements and modelling." *Proceedings of the Eastern Snow Conference*, Banff, Alberta, 54: 130-141.
- Hedstrom, N.R., and J.W. Pomeroy, 1998. "Measurements and modelling of snow interception in the boreal forest." *Hydrological Processes*, 12(10-11): 1611-1625.

- Heymsfield, A., 1972. "Ice crystal terminal velocities." *Journal of Atmospheric Sciences*, **29**: 1348-1357.
- Hindman, E.A., M.A. Campbell, R.D. Borys, 1994. "A ten-winter record of cloud-droplet physical and chemical properties at a mountaintop site in Colorado." *Journal of Applied Meteorology*, **33**(7): 797-807.
- Hobbs, P.V., and W.D. Scott, 1965: A theoretical study of the variation of ice crystal habits with temperature. *Journal of Geophysical Research*, **70**(20), 5025-5034.
- Hobbs, P.V., S. Chang and J.D. Locatelli, 1974. "The dimensions and aggregation of ice crystals in natural clouds." *Journal of Geophysical Research*, **79**(15): 2199-2206.
- Hogan, A.L., 1994. "Objective estimates of airborne snow properties." *Journal of Atmospheric and Oceanic Technology*, **11**(2): 432-444.
- Hollingsworth, J., 1999. *Observations of the 1995 and 1997 winter precipitation in Northern Michigan using NEXRAD*. National Weather Service, Northern Indiana, National Oceanic and Atmospheric Administration, Syracuse, Indiana, **personal communication**.
- Hooper, J.E.N., and A.A. Kippax, 1950. "The bright band - A phenomenon associated with radar echoes from falling rain." *Quarterly Journal of the Royal Meteorological Society*, **76**: 125-132.
- Houck, R.E., J. Waldstreicher, J.M. Hassett, and P.F. Blottman, 1995. "Preliminary investigation of WSD-88D data for winter hydrometeorological events in Upstate New York." *Proceedings of the Eastern Snow Conference*, Toronto, Ontario, **52**: 39-50.
- Imai, I., 1960. "Raindrop size distributions and Z-R relationships." In *Proceeding of the 8th Weather Radar Conference*, American Society of Meteorology, p211-218.
- Imai, I., M. Fujiwara, I. Ichimura, and Y. Toyama, 1955. "Radar reflectivity of falling snow." *Papers in Meteorology and Geophysics (Japan)*, **6**: 130-139.
- Innes, J.A.M., N. Kouwen, and J.M.C. Young, 2000. "Assesment of Quantitative Precipitation Estimates using the King City Weather Radar System and the Distributed Model, WATFLOOD." Abstract submitted for the 8<sup>th</sup> Annual *Canadian Geophysical Union - Hydrology Section Conference*, May 23-27, 2000.
- Iqbal, M., 1983. *An Introduction to Solar Radiation*. Academic Press, Toronto, 390pp.
- Jayaweera, K.O.L.F. and R.E. Cottis, 1969. "Fall velocities of plate-like and columnar ice crystals." *Quarterly Journal of the Royal Meteorological Society*, **95**: 703-709.
- Jordan, R., 1991. *A one-dimensional temperature model for a snow cover: Technical documentation for SN THERM.89*. US Army Corps of Engineers, Cold Regions Research & Engineering Laboratory, Special Report **91-16**, 64pp.
- Kirnbaauer, R., G. Blöschl and D. Gutknecht, 1994. "Entering the era of distributed snow models." *Nordic Hydrology*, **25**: 1-24.
- Kitchen, M., and R.M. Blackall, 1992. "Representativeness errors in comparisons between radar and gauge measurements of rainfall." *Journal of Hydrology*, **134**: 13-33.
- Kodairo, N., and M. Inaba, 1955. "Measurement of snowfall intensity by radar." *Papers in Meteorology and Geophysics (Japan)*, **6**: 126-129.
- Kouwen, N., 1988. "WATFLOOD: a micro-computer based flood forecasting system based on real-time weather radar." *Canadian Water Resources Journal*, **13**(1): 62-77.
- Kouwen, N., 1997. *WATFLOOD/SPL 8: Flood Forecasting System*. Users Manual,

- Department of Civil Engineering, University of Waterloo, Waterloo, Ontario, Canada, 142pp.
- Kouwen, N., 1998. *Scaling Weather Radar for Hydrologic Modelling with WATFLOOD*. Unpublished Results, Department of Civil Engineering, University of Waterloo, Waterloo, Ontario, Canada, **personal communication**.
- Kouwen, N., and G. Garland 1989. "Resolution considerations in using radar rainfall data for flood forecasting." *Canadian Journal of Civil Engineering*, **16**: 279-289.
- Kouwen, H., E.D. Soulis, A. Pietroniro, J.R. Donald, and R.A. Harrington, 1993. "Grouped response units for distributed hydrologic modelling." *ASCE Journal of Water Resources Planning and Management*, **119**(3):289-305.
- LaChapelle, E., 1961. *Snow Layer Densification*. Alta Avalanche Study Center, Project F, Progress Report No. 1, US Department of Agriculture Forest Service, Wasatch National Forest.
- Lamb, D., and P.V. Hobbs, 1971. "Growth rates and habits of ice crystals grown from the vapour phase." *Journal of Atmospheric Sciences*, **28**: 1506-1509.
- Langille, R.C., and R.S. Thain, 1951. "Some quantitative measurements of three-centimetre radar echoes from falling snow." *Canadian Journal of Physics*, **29**: 482-490.
- Langleben, M.P., 1954. "The terminal velocity of snowflakes." *Quarterly Journal of the Royal Meteorological Society*, **80**: 174-181.
- Larson, L.W. and E.L. Peck, 1974. "Accuracy of precipitation measurements for hydrologic modelling." *Water Resources Research*, **10**(4): 857-863.
- Lautensach, H., and Bogel, R., 1956. "Der Jahrgang des mittleren geographischem Hohengradienten der Lufttemperatur in den verschiedenen Klimagebieten der Erde." *Erdkunde*, **10**: 270-282.
- Leavesley, G.H., and L.G. Stannard, 1990. "Application of remotely sensed data in a distributed-parameter watershed model." *Proceedings of the Workshop on Applications of Remote Sensing in Hydrology*, February, p 47-68.
- Li, L. And J.W. Pomeroy, 1997. "Estimates of threshold wind speeds for snow transport using meteorological data." *Journal of Applied Meteorology*, **36**: 205-213.
- Light, P., 1941. "Analysis of high rates of snow-melting." *Transactions, American Geophysical Union*, p195-205.
- Linsley, R.K., Jr., M.A. Kohler, and J.L.H. Paulhus, 1975. *Hydrology for Engineers*, 2nd edition. McGraw-Hill Book Company.
- Liston, G.E., and M. Sturm, 1998. "A snow-transport model for complex terrain." *Journal of Glaciology*, **44**(148):498-516.
- Locatelli, J.D. and P.V. Hobbs, 1974. "Fall speeds of solid precipitation particles." *Journal of Geophysical Research*, **79**(15): 2185-2197.
- Longley, R.W., 1960. "Snow depth and density at Resolute, Northwest Territories." *Journal of Glaciology*, **3**: 733-738.
- Loth, B., H.F. Graf, and J.M. Oberhuber, 1993. 'Snow cover model for global climate simulations.' *Journal of Geophysical Research*, **98**(D6):10,451-10,464.
- Luce, C.H., D.G. Tarboton, and K.R. Cooley, 1999. "Sub-grid parameterization of snow distribution for an energy and mass balance snow cover model." *Hydrological*

- Processes*, 13: 1921-1933.
- Lundberg, A., and R.M. Johansson, 1994. "Optical precipitation gauge: Determination of precipitation type and intensity by light attenuation technique." *Nordic Hydrology*, 25:359-370.
- L'vovich, M.I., 1974. *World Water Resources and Their Future*. Translated by R.L. Nace, American Geophysical Union, Washington, DC.
- Mackay, G.A., 1970. "Precipitation." In *Handbook on the Principles of Hydrology* (ed. D.M. Gray), National Research Council, Canada, Water Information Center, Inc., NY.
- Magono C. and C. Lee, 1966. "Meteorological classification of natural snow crystals." *Journal of the Faculty of Science, Hokkaido University, Series VII(2)*: 321-335.
- Marsh, P., 1990. "Snow Hydrology." In *Northern Hydrology: Canadian Perspectives* (eds. T.D. Prowse and C.S.L. Ommanney), National Hydrology Research Institute, Saskatoon, Canada.
- Marshall, J.S. and K.L.S. Gunn, 1952. "Measurement of Snow Parameters by Radar." *Journal of Meteorology*, 9: 322-327.
- Marshall, J.S. and W.M. Palmer, 1948. "The size distribution of raindrops with size." *Journal of Meteorology*, 5: 165-166.
- Marshall, J.S., R.C. Langille, W.M. Palmer, 1947. "The measurement of rainfall by radar." *Journal of Meteorology*, 4: 186-192.
- Mason, B.J., 1955. "Radar evidence for aggregation and orientation of melting snowflakes." *Quarterly Journal of the Royal Meteorological Society*, 81: 262-264.
- Mason, B.J., 1971. *The Physics of Clouds*, 2nd edition. Oxford University Press.
- Mason, B.J., G.W. Bryant, and A.P. Van den Heuvel, 1963. "The growth habits and surface structure of ice crystals." *Philosophical Magazine, Series 8, Vol. 8*: 505-526
- Matrosov, S.Y., 1998: A dual-wavelength radar method to measure snowfall rate. *Journal of Applied Meteorology*, 5: 165-166.
- Mowat, F., 1975. "Snow." In *The Snow Walker* by F. Mowat, McClelland and Stewart Limited, Toronto, Ontario, p1-10.
- Nakaya, U., 1954. *Snow Crystals: Natural and Artificial*. Harvard University Press, 510pp.
- National Research Council, 1954. *The International Classification of Solid Precipitation*. Int'l Assoc. Sci. Hydrol., Tech. Memo. 31, NRC, Ottawa, Canada.
- National Weather Service, 1997a. "NEXRAD." URL: <http://www.nws.noaa.gov/er/mhx/88dt.htm>, US Department of Commerce, National Oceanic and Atmospheric Administration.
- National Weather Service, 1997b. "Health and NEXRAD." URL: <http://www.nws.noaa.gov/er/mhx/88dhltht.htm>, US Department of Commerce, National Oceanic and Atmospheric Administration.
- National Weather Service, 1999a. "NWS Mission Page - defines the mission of the National Weather Service." URL: <http://www.nws.noaa.gov/mission.shtml>, US Department of Commerce, National Oceanic and Atmospheric Administration.
- National Weather Service, 1999b. "National Weather Service Strategic Plan for Weather, Water, and Climate Services 2000 - 2005." URL: <http://www.nws.noaa.gov/modernize/strategic-plan.htm>, US Department of

- Commerce, National Oceanic and Atmospheric Administration. (Also available at <http://www.nws.noaa.gov/pub/sp/stplnall.pdf>.)
- Neumann, N., and P. Marsh, 1998. "Local advection in the snowmelt landscape of arctic tundra." *Hydrological Processes*, 12: 1547-1560.
- Ohtake, T., 1970. "Factors affecting the size distribution of raindrops and snowflakes." *Journal of Atmospheric Sciences*, 27: 804-813.
- Ohtake, T. and T. Henmi, 1970. "Radar reflectivity of aggregated snowflakes." *Preprints 14th Radar Meteorology Conference*, American Society of Meteorology, p209-210.
- Oke, T.R., 1987. *Boundary Layer Climates*, 2<sup>nd</sup> edition. Routledge, New York, 435 pp.
- Ono, A., 1970. "Growth mode of ice crystals in natural clouds." *Journal of Atmospheric Sciences*, 27: 649-658.
- Passarelli, R.E., Jr., 1978. "Theoretical and observational study of snow size spectra and snowflake aggregation efficiencies." *Journal of Atmospheric Sciences*, 35:882-889.
- Peck, E.L., L.W. Larson and J.W. Wilson, 1974. "Lake Ontario snowfall observational network for radar measurements." *Advanced Concepts and Techniques in the Study of Snow and Ice Resources*, National Academy of Science, Washington, DC, p412-421.
- Pfister, R. and M. Schneebeli, 1999. "Snow accumulation on boards of different sizes and shapes." *Hydrological Processes*, 13(14-15): 2345-2355.
- Pomeroy, J.W., D.M. Gray, and P.G. Landine, 1993. "The Prairir Blowing Snow Model: Characteristics, validation, operation." *Journal of Hydrology*, 144: 165-192.
- Pomeroy, J.W., and D.M. Gray, 1995. *Snowcover: Accumulation, Relocation and Management*. National Hydrology Research Institute, Environment Canada, Science Report No. 7, Saskatoon, Saskatchewan, 144pp.
- Pomeroy, J.W., D.M. Gray, K.R. Shook, B. Toth, R.H. Essery, A. Pietroniro, and N. Hedstrom, 1998. "An evaluation of snow accumulation and ablation processes for land surface scheme modelling." *Hydrological Processes*, 12: 2339-2367.
- Quick, M., 1995. "The UBC Watershed Model." In *Computer Models of Watershed Hydrology* (ed. V.P. Singh), Water Resources Publications, Fort Collins, CO, 1144pp.
- Rango, A., and J. Martinec, 1995. "Revisiting the degree-day method for a snowmelt-runoff forecasting technique." *AWRA Water Resources Bulletin* 31(4):657-669.
- Richards, W.G., and C.L. Crozier, 1983. "Precipitation measurement with a C-band weather radar in Southern Ontario." *Atmosphere-Ocean*, 21:125-137.
- Rohrer, M.D., 1989. "Determination of the transition air temperature from snow to rain and intensity of precipitation." *IAHS/WMO/ETH International Workshop of Precipitation Measurement* (ed. B. Sevruk), St. Moritz, Switzerland, 475-482.
- Ryzhkov, A.V., and D.S. Zrnice, 1998: Discrimination between rain and snow with a polarimetric radar. *Journal of Applied Meteorology*, 37(10), 1228-1240.
- Schaefer, V.J., and J.A. Day, 1981. *A field guide to the atmosphere*. The Peterson Field Guide Series, 26, Houghton Mifflin, Boston, 359 pp.
- Schmidt, R.A., Jr., 1972. *Sublimation of Wind-Transported Snow - A Model*. USDA Forest Service Research Paper RM-90, Fort Collins, CO.
- Schmidt, R.A., Jr., and D.R. Gluns, 1991. "Snowfall interception on branches of three conifer species." *Canadian Journal of Forest Research*, 21: 1262-1269.

- Schroeter, H.O., 1988. *An Operational Snow Accumulation-Ablation Model for Areal Distribution of Shallow Ephemeral Snowpacks*. Unpublished Ph.D. thesis presented to the Department of Water Resources Engineering, University of Guelph, ON, 325p.
- Scott, J., 1999. *Operation of the King City Radar*. King Weather Radar Research Station, Atmospheric Environment Service, Environment Canada, King City, Ontario, **personal communication**.
- Seglenieks, F.R., 1994. *Application of Remote Sensing and Ground Measurements to Calibrate the Hydrologic Model WATFLOOD*. Unpublished M.A.Sc. thesis presented to the Department of Civil Engineering, University of Waterloo, ON, 162p.
- Sekhon, R.S. and R.C. Srivastava, 1970. "Snow size spectra and radar reflectivity." *Journal of Atmospheric Sciences*, **27**: 299-307.
- Shook, K. and D.M. Gray, 1996. "Small-scale spatial structure of shallow snowcovers." *Hydrological Processes*, **10**: 1283-1292.
- Singh, V.P., 1995. *Computer Models of Watershed Hydrology*. Water Resources Publication.
- Snelgrove, K.R., 1996. *Hydrologic Computing Modelling using the WATFLOOD Hydrologic Model and the Canadian Land Surface Scheme (CLASS)*. Unpublished M.A.Sc. project presented to the Department of Civil Engineering, University of Waterloo, ON, 162p.
- Solomon, S.I., J.P. Denovilliez, E.J. Chart, J.A. Wolley, and C. Cadou, 1968. "The use of a square grid system for computer estimation of precipitation, temperature, and runoff." *Water Resources Research*, **4**(5): 919-929.
- Solomon, S.I., 1995. "Macro-scale Hydrology." In *Time and the River*, (ed. G. Kite), Water Resources Publications, Fort Collins, CO.
- Soulis, E.D., K.R. Snelgrove, N. Kouwen F.R. Seglenieks, and D.L. Verseghy, 2000. "Toward closing the vertical water balance in Canadian atmospheric models: Coupling of the land surface scheme CLASS with the distributed hydrological model WATFLOOD." *Atmosphere-Ocean*, **38**(1): 251-269.
- Spencer, J.W., 1971. "Fourier series representation of the position of the Sun." *Search* **2**(5): 172.
- Stewart, R.E., 1992. "Precipitation types in transition region of winter storms." *Bulletin American Meteorological Society*, **73**(3): 287-296.
- Stewart, R.E., and P. King, 1987. "Rain-snow boundaries in Southern Ontario." *Monthly Weather Review*, **115**, 1894-1907.
- Stout, G.E., and E.A. Mueller, 1968. "Survey of relationships between rainfall rate and radar reflectivity in the measurement of precipitation." *Journal of Applied Meteorology*, **7**: 465-474.
- Sumner, G.N., 1988. *Precipitation: Process and Analysis*. John Wiley & Sons Ltd.
- Sverdrup, H.U., 1936. "The Eddy Conductivity of the Air over a Smooth Snow Field." *Geofysiske Publikasjoner*, **XI**(7): 1-69.
- Tabios, G.Q., III and J.D. Salas, 1985. "A comparative analysis of techniques for spatial interpolation of precipitation." *Water Resources Bulletin*, **21**(3): 365-380.
- Takeuchi, M., 1980. "Vertical profile and horizontal increase of drift-snow transport." *Journal of Glaciology*, **26**(94): 481-497.
- Tao, T., and N. Kouwen, 1990. "Remote sensing and fully distributed modelling for flood

- forecasting." *Journal of Water Resources Planning and Management*, **115**(6): 809-823.
- Thiessen, A.H., 1911. "Precipitation averages for large areas." *Monthly Weather Review*, **39**(7):1082-1084.
- Thorpe, A.D., and B.J. Mason, 1966. "The evaporation of ice spheres and ice crystals." *British Journal of Applied Physics*, **17**:541-548.
- US Army Corps of Engineers, 1956. *Snow Hydrology: Summary Report of the Snow Investigations*. North Pacific Division, Portland, OR, 437p. (Available through the US Department of Commerce, Washington, DC).
- Verseghy, D.L., 1991. "CLASS - A Canadian Land Surface Scheme for GCMs: I. Soil model." *International Journal of Climatology*, **11**: 111-133.
- Verseghy, D.L., N.A. McFarlane, and M. Lazare, 1993 "CLASS - A Canadian Land Surface Scheme for GCMs: II. Vegetation model and coupled runs." *International Journal of Climatology*, **13**: 347-370.
- Walsh, J.E., 1984. "Snow cover and atmospheric variability." *American Scientist*, **72**: 50-57.
- Walker, A.E. and B.E. Goodison, 1993. "Discrimination of wet snowcover using passive microwave satellite data." *Annals of Glaciology*, **17**:307-311.
- Warner, C., and K.L.S. Gunn, 1969. "Measurement of snowfall by optical attenuation." *Journal of Applied Meteorology*, **8**:110-122.
- Whidden, E.A., 1999. *Distributed hydrological modelling in the Canadian Boreal Forest: Subsurface model development, land surface model improvement and modelling results*. Unpublished M.A.Sc. thesis presented to the Department of Civil Engineering, University of Waterloo, ON, 270p.
- Williams, G.P., 1959. *Evaporation from Snow Covers in Eastern Ontario*. National Research Council of Canada, Division of Building Research, Research Paper No. 73.
- Wilson, J.W., 1974. "Measurement of snowfall by radar." *Advanced Concepts and Techniques in the Study of Snow and Ice Resources*, National Academy of Science, Washington, DC, p391-401.
- Wilson, J.W., 1975. "Measurement of snowfall by radar during the IFYGL." Preprints *16th Radar Meteorology Conference*, Houston, TX, American Meteorological Society, **16**: 508-513.
- Wilson, J.W., and E.A. Brandes, 1979. "Radar measurement of rainfall - A summary." *Bulletin American Meteorological Society*, **60**(9):1048-1058.
- Wood, E.F., M. Sivapalan, K. Bevan, and L. Band, 1988. "Effects of spatial variability and scale with implications to hydrologic modelling." *Journal of Hydrology*, **102**: 29-47.
- Yang, D., J.R. Metcalfe, B.E. Goodison, and E. Mekis, 1993. "True snowfall: An evaluation of the Double Fence Intercomparison Reference gauge." *Proceedings of the Eastern Snow Conference*, **50**: 105-111.
- Yang, D., E. Elomaa, A. Tuominen, A. Aaltonen, B.E. Goodison, T. Gunther, V. Golubev, B. Sevruk, H. Madsen, and J. Milkovic, 1999. "Wind-induced precipitation undercatch of the Hellmann gauges." *Nordic Hydrology*, **30**: 57-80.
- Yang, Z.-L., R.E. Dickinson, M. Shaikh, X. Gao, R.C. Bales, S. Sorooshian and J.M. Jin, 1998. "Simulation of snow mass and extent in global climate models." *Presentation at the International Conference on Snow Hydrology*, Brownsville, Vermont, October 6-9,



- 1998.
- Zhao, L., and D.M. Gray, 1999. "Estimating snowmelt infiltration into frozen soils." *Hydrological Processes*, **13**: 1827-1842.
- Zikmunda, J., 1972. "Fall velocities of spatial crystals." *Journal of Atmospheric Sciences*, **29**:1511-1515.
- Zikmunda, J. and G. Vali, 1972. "Fall patterns and fall velocities of rimed ice crystals." *Journal of Atmospheric Sciences*, **29**:1334-1347.

# Appendix A: CODING SPECIFICS

---

This appendix summarizes the specific changes or additions to the CLASS computer code. The rationale for the changes or additions is presented in Chapter 3.

## A.1 MIXED PRECIPITATION

The rain/snow precipitation diagnosis occurs in the subroutine `wprep.for` that is called from the subroutine `classw.for`. The altered section of the subroutine `wprep.for` is listed below:

```

CCCCC
CCCCC * DIAGNOSE PRECIPITATION AS RAIN OR SNOW
CCCCC *       OR BOTH, BASED ON AUER'S CURVE.
CCCCC
      IF(PCPR(I).GT.0.) THEN
          IF((TA(I).GT.273.61).AND.(TA(I).LT.279.13)) THEN
              FRS=(0.0202*(TA(I)-TFREZ)**6-0.3660*(TA(I)-TFREZ)**5
1              +2.0399*(TA(I)-TFREZ)**4-1.5089*(TA(I)-TFREZ)**3
2              -15.038*(TA(I)-TFREZ)**2+4.6664*(TA(I)-TFREZ)+100)
3              /100.0
              ELSEIF(TA(I).LE.273.61) THEN
                  FRS=1.0
              ELSE
                  FRS=0.0
              ENDIF
              R (I)=PCPR(I)*(1.0-FRS)/RHOW
              TR (I)=TA(I)-TFREZ
              S (I)=PCPR(I)*FRS/RHOSNI
CCCCC *
CCCCC * Cannot have snow at a temperature greater than freezing
CCCCC *
              TS (I)=MIN(TA(I)-TFREZ,0.)
              PCLC(I)=(FCS(I)*(1.0-FSVFS(I))+FC(I)*(1.0-FSVE(I)))*
1              R(I)*RHOW
              PCFC(I)=(FCS(I)*(1.0-FSVFS(I))+FC(I)*(1.0-FSVE(I)))*
1              S(I)*RHOSNI
              PCPN(I)=(FCS(I)*FSVFS(I)+FGS(I))*R(I)*RHOW+
1              (FCS(I)*FSVFS(I)+FGS(I)+FC(I)*FSVE(I)+FG(I))*
2              S(I)*RHOSNI
              PCPG(I)=(FC(I)*FSVE(I)+FG(I))*R(I)*RHOW
              ELSE
                  R (I)=0.0
                  TR(I)=0.0
                  S (I)=0.0
                  TS(I)=0.0
              ENDIF

```

**A.2 VARIABLE FRESH SNOW DENSITY**

The density of fresh snow (*RHOSNI*) is a constant value of 100 kg/m<sup>3</sup>, transferred through various subroutines using a common block. The following steps are required to incorporate a variable fresh snow density:

- 1) *RHOSNI* is removed from the common block CLASS4 in all subroutines (aprep.for, canadd.for, canvap.for, chkwat.for, classa.for, classt.for, classw.for, cwcalc.for, endpnd.for, grdran.for, grinfl.for, icebal.for, runclass.for, sninfl.for, snoadd.for, snoalbw.for, snovap.for, subcan.for, tfreez.for, tmcalf.for, tmelt.for, tnpost.for, tnprep.for, tprep.for, tsolv.c.for, tsolve.for, tspost.for, tsprep.for, twcalc.for, wend.for, wprep.for)
- 2) Definition of *RHOSNI* in the DATA statement is removed (runclass.for).
- 3) *RHOSNI* is initialized as a real array in all subroutines where it is used in calculations and used as an array in calculation steps (canadd.for, classw.for, snoadd.for, snovap.for, subcan.for, wprep.for).
- 4) *RHOSNI* is added to the variable list in 11 CALL statements in classw.for and in the corresponding location of the SUBROUTINE statement in the 5 subroutines (canadd.for, snoadd.for, snovap.for, subcan.for, wprep.for).
- 5) *RHOSNI* is calculated prior to the diagnosis of mixed precipitation for each element, as a function of temperature or as assigned as a constant in wprep.for:

```

CCCCC *
CCCCC * Calculation of fresh snow density,
CCCCC * when there is snow in the canopy or on the ground
CCCCC *
CC      IF((NLANDCS.GT.0).OR.(NLANDGS.GT.0)) THEN
CCCCC *
CCCCC * Remember to use air temperature in degrees celsius for
CCCCC * DENSITY of FRESH SNOW and FRACTION OF SNOW in precipitation
CCCCC *
CC      RHOSNO(I)=0.1E3
CC      RHOSNI(I)=67.92+51.25*EXP((TA(I)-TFREZ)/2.59)
CC      RHOSNI(I)=50+1.7*(TA(I)-258.16)**1.5
CC      ENDIF
CCCCC * -----
CCCCC * DIAGNOSE PRECIPITATION AS RAIN OR SNOW
CCCCC * OR BOTH, BASED ON AUER'S CURVE.
CCCCC
CC      IF(PCPR(I).GT.0.)
CC
CC      THEN

```

### A.3 MAXIMUM SNOW DENSITY

The densification of the snowpack (and decrease in albedo) due to aging is determined at the end of each time step in the subroutine `snoalbw.for`, as follows:

```

CCCCC *
CCCCC * Calculation of increased snow density,
CCCCC * when there is snow on the ground
CCCCC *
      1  IF((FCT(I).GT.0.).AND.(ZSNOW(I).GT.0.).AND.
          (RHOSNO(I).LT.300.)) THEN
          RHOOLD=RHOSNO(I)
          TIMFAC=EXP(LOG((300.0-RHOSNO(I))/200.0)-2.778E-6*DELT)
          RHOSNO(I)=300.0-200.0*TIMFAC
          ZSNOW(I)=ZSNOW(I)*RHOOLD/RHOSNO(I)
          HCPSNO(I)=HCPICE*RHOSNO(I)/RHOICE
      ENDIF

```

For different land classes, the 300 for which *RHOSNO* is compared can be changed as below:

```

CCCCC
CCCCC * Increase snow density as a function of the time increment
CCCCC * Use variable maximum density (RHOSMX) for different land covers
CCCCC
      IF((I.GE.IL2/3+1).AND.(I.LE.IL2/2)) THEN
          RHOSMX=250.0
      ELSE
          RHOSMX=350.0
      ENDIF
      1  IF(FCT(I).GT.0. .AND. ZSNOW(I).GT.0. .AND.
          RHOSNO(I).LT.RHOSMX) THEN
          RHOOLD=RHOSNO(I)
          TIMFAC=EXP(LOG((RHOSMX-RHOSNO(I))/200.0)-2.778E-6*DELT)
          RHOSNO(I)=RHOSMX-200.0*TIMFAC
          ZSNOW(I)=ZSNOW(I)*RHOOLD/RHOSNO(I)
          HCPSNO(I)=HCPICE*RHOSNO(I)/RHOICE
      ENDIF

```

### A.4 SNOWFALL CANOPY INTERCEPTION

To increase the maximum snowfall interception as from 20% of the snowcovered leaf area index (*AILCNS*) to 50%, in the subroutine `aprep.for`, set the moisture storage capacity (*CWCAPS*) to 0.5 of *AILCNS* instead of 0.2.

Subsequently, to introduce the Hedstrom and Pomeroy (1998) canopy interception equations (3-25 and 3-26), the subroutine `canadd.for` is altered and the leaf area index variables (*AILCAN*, *AILCNS*) is carried through `classw.for` to `canadd.for`, as per the following steps:

- 1) In the subroutine `runclass.for`, the canopy leaf area index variables *AILCAN* and *AILCNS* are included in the `CALL` statement to `classw.for`.
- 2) In the same location in the variable list, *AILCAN* and *AILCNS* are included in the `SUBROUTINE` statement in `classw.for`. These variables are dimensioned as single column arrays of size *ILG*. The variable *AILCNS* is added to the 1<sup>st</sup> `CALL` statement to `canadd.for` in `classw.for` for calculation of canopy-over-snow, and *AILCAN* is added to the 2<sup>nd</sup> `CALL` statement to `canadd.for` for calculation of canopy-over-bare ground.
- 3) Within the subroutine `canadd.for`, the variable *AILCAN* is in the `SUBROUTINE` statement. Originally in `canadd.for`, the throughfall was computed from the sky view factor (*FSVF*) and the precipitation quantities, with the remainder of the frozen and liquid water was intercepted, as follows:

```

CCCCC
      IF (FCT(I).GT.0. .AND. (R(I).GT.0. .OR. S(I).GT.0.))      THEN
          RTHRU=R(I)*FSVF(I)
          STHRU=S(I)*FSVF(I)
          RINT=(R(I)-RTHRU)*DELT*RHOW
          SINT=(S(I)-STHRU)*DELT*RHOSNI(I)
          :
      ENDIF

```

In the revised code, the interception is computed first and then the throughfall is computed, as illustrated below:

```

CCCCC
      IF (FCT(I).GT.0. .AND. (R(I).GT.0. .OR. S(I).GT.0.))      THEN
          RTHRU=R(I)*FSVF(I)
          RINT=(R(I)-RTHRU)*DELT*RHOW
          SIMX=6.0*AILCAN*(0.27+46/RHOSNI(I))
          SINT=0.697*(SIMX-SNOCAN)*(1-EXP(S(I)*(1.0-FSVF(I))/SIMX))
1          *DELT*RHOSNI(I)
          STHRU=S(I)-SINT/(DELT*RHOSNI(I))
          :
      ENDIF

```

The Hedstrom and Pomeroy (1998) formulation uses the canopy coverage that is equal to one minus the sky view factor (*FSVF*) for snow or ground underlying the canopy.

## A.5 REDISTRIBUTION

The subroutine `rdstrb.for` is called from `runof5.f` after the vertical hydrology calculations performed through `runclass.for`. The subroutine is listed below:

```

SUBROUTINE RDSTRB(ZSNOW, il1,    il22, aclassD, SNOGAT, issb,
1          SnGSMx,  FCLV)
CCCCC *
CCCCC SUBROUTINE RDSTRB.FOR
CCCCC created: S.R. FASSNACHT 1997.XI.09
CCCCC latest update: SR FASSNACHT 1999.IX.27
CCCCC *****
CCCCC * Subroutine to redistribute snow from a land class that has
CCCCC * reached capacity to an areas that has not reached capacity
CCCCC *****
CCCCC * LIST OF VARIABLES
CCCCC aclassD REAL*8 Percent of land class in element
CCCCC FCLV REAL*8 fraction of crop/low veg. snow to redistribute
CCCCC ide INT total number of grid-subarea elements
CCCCC il1 INT initial index of element loop
CCCCC il22 INT final index of element loop
CCCCC SnGSMx REAL*8 maximum accumulation depth on snowcovered ground
CCCCC ZSNOW REAL*8 depth of snow (from CLASS)
parameter(ide=2400)
CCCCC * Dimension input/ouput array.
REAL ZSNOW(ide),SNOGAT(ide)
CCCCC * Dimension input arrays.
REAL aclassD(ide/12,6)
REAL SnGSMx,FCLV

CCCCC -----
CCCCC * Step over the BARE sub-areas and redistribute the snow deeper
CCCCC * than capacity into the FOREST area within the same element.
CCCCC *
CCCCC * Consider density of the snowpack.
CCCCC *
DO 211, I=il1,il22/6
CCCCC
CCCCC * Initially assume that the snow density is the same
CCCCC * throughout the element
CCCCC
CCCCC * Transfer excess snow from BARE (ii=1) to FOREST (ii=2)
CCCCC
IF((issb.EQ.1).OR.(issb.EQ.2)) THEN
IF((ZSNOW(I).GT.SnGSMx).AND.(aclassD(I),2).GT.0.0) THEN
ZSNOW(I+il22/6)=ZSNOW(I+il22/6)+(ZSNOW(I)-SnGSMx)
1 *aclassD(I,1)/aclassD(I,2)
SNOGAT(I+il22/6)=SNOGAT(I+il22/6)
1 +SNOGAT(I)/ZSNOW(I)*(ZSNOW(I)-SnGSMx)
2 *aclassD(I,1)/aclassD(I,2)
SNOGAT(I)=SNOGAT(I)-SNOGAT(I)/ZSNOW(I)*(ZSNOW(I)-SnGSMx)
ZSNOW(I)=SnGSMx
ENDIF
ENDIF
ENDIF

```

```

CCCC
CCCC * Transfer FCLV of excess snow from CROP/LOW VEG (ii=3) to FOREST
CCCC
      IF((issb.EQ.3).OR.(issb.EQ.2)) THEN
        IF((ZSNOW(I+i122/3).GT.SnGSMx)
1         .AND.(aclassD(I),2).GT.0.0) THEN
          ZSNOW(I+i122/6)=ZSNOW(I+i122/6)
1          +(ZSNOW(I+i122/3)-SnGSMx)*FCLV
2          *aclassD(I),3)/aclassD(I),2)
          SNOGAT(I+i122/6)=SNOGAT(I+i122/6)
1          +SNOGAT(I+i122/3)/ZSNOW(I+i122/3)
2          *(ZSNOW(I+i122/3)-SnGSMx)*FCLV
3          *aclassD(I),3)/aclassD(I),2)
          SNOGAT(I+i122/3)=SNOGAT(I+i122/3)
1          -SNOGAT(I+i122/3)/ZSNOW(I+i122/3)
2          *(ZSNOW(I+i122/3)-SnGSMx)*FCLV
          ZSNOW(I+i122/3)=SnGSMx
        ENDIF
      ENDIF
211 CONTINUE
RETURN
END

```

## A.6 SPLIT STATE VARIABLES

The following steps describe the removal of the averaging of the soil temperature layers in the subroutines of *classt.for*:

- 1) In the subroutine *tprep.for*, the setting of the individual soil temperature layers (*TBARCS*, *TBARGS*, *TBARC* and *TBARG*) to zero is removed.
- 2) In the preliminary temperature solving routines (*tsprep.for* and *tnprep.for*), the individual soil temperature (*TBARPR*) are used to compute the ground heat flux coefficients instead of the average soil temperature (*TBAR*). These changes appear in the SUBROUTINE and the array definition (REAL) statements. These changes also appear in all calculations, where *TFREZ* is added to *TBARPR* to convert to degrees Kelvin.
- 3) In the CALL statements to *tsprep.for* and *tnprep.for* from *classt.for*, the individual soil temperatures (*TBARCS*, *TBARGS*, *TBARC* and *TBARG*) are used instead of the average value (*TBAR*).
- 4) In the calculation of heat flux between the layers subroutines (*tspost.for* and *tnpost.for*), the individual soil temperature (*TBARPR*) are used instead of the average soil temperature (*TBAR*). The variable *TBAR* is removed from the SUBROUTINE and

the array definition (REAL) statements. All uses of *TBAR* are converted to *TBARPR*, and *TFREZ* is added to convert to degrees Kelvin. The setting of *TBARPR* to the *TBAR* at the end of the subroutines is removed.

- 5) In the CALL statements to *tspost.for* and *tnpost.for* from *classt.for*, the average soil temperature (*TBAR*) is removed from the variable list.
- 6) No changes to the liquid and frozen water content calculations are included, as these are a function of the soil temperature and the total water content.



# Appendix B: CURVE FITTING

---

This appendix presents the preparation of data in the literature for use in this thesis, in particular, the smoothing of the mixed precipitation presented in Figure 2-5, and the particle shape curve presented in Figure 4-2b.

## B.1 MIXED PRECIPITATION

### B.1.1 Smoothing of The Data

The curves presented in Figure 2-5 have been smoothed from tabular data, graphically presented data ranges, and stepped curves. Data collected by the US Army Corps of Engineers (1956) illustrated a range of mixed precipitation between 0 and +3°C where the sum of the % rain and % snow was less than 100%. A smoothed curve was fit through these data (Figure B-1).

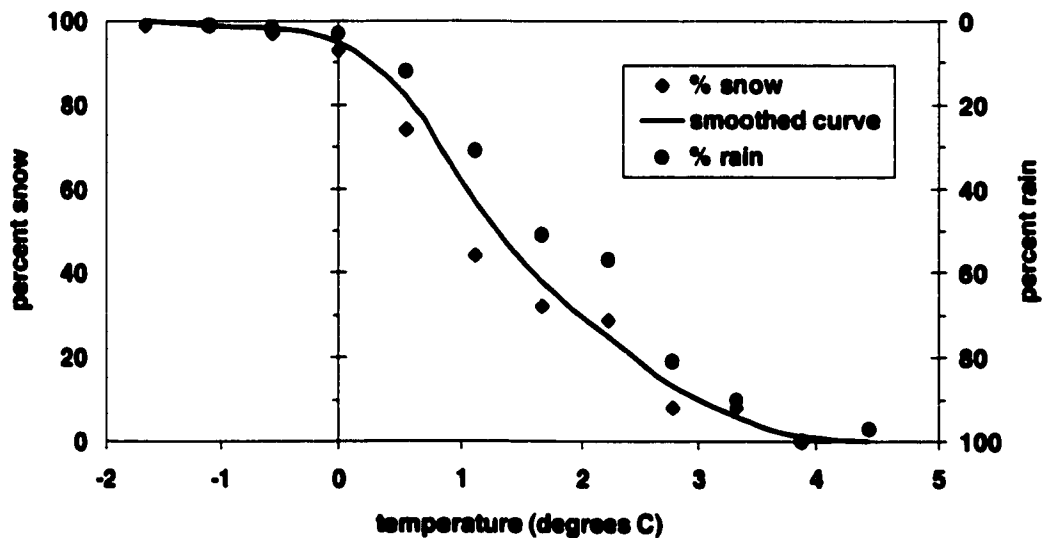


FIGURE B-1. Percent snow, rain and mixed precipitation as a function of air temperature from US Army Corps of Engineers (1956) data. The data were originally presented in tabular form. The *smoothed curve* presented is a smoothed average of the percent snow and percent rain curves.

The data summarized by Auer (1974) were presented as a single curve, but with linear segments connecting the datapoints. The smoothed curve is presented in figure B-2.

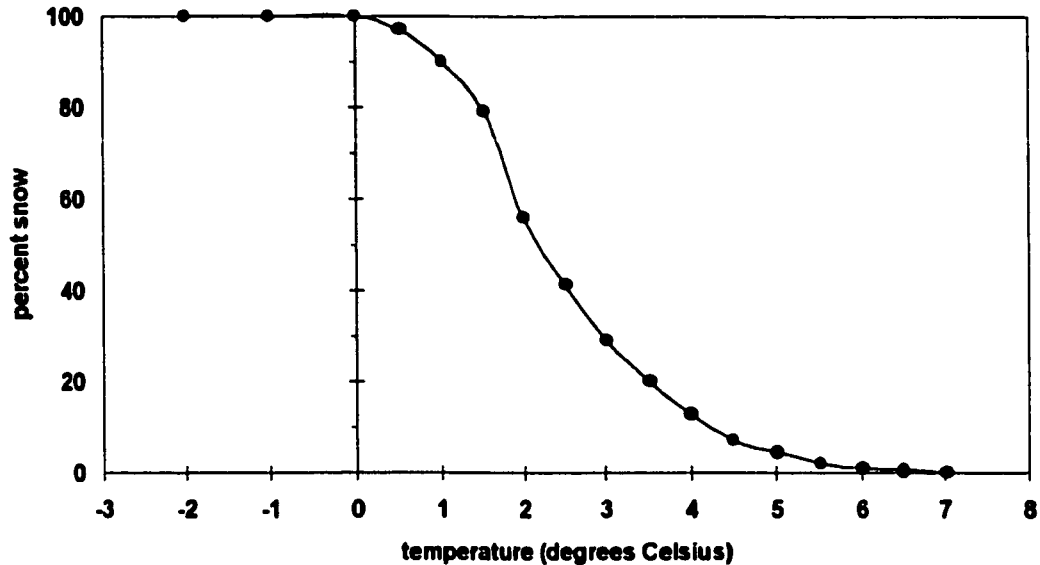


FIGURE B-2. Percent snow as a function of air temperature from 1000 meteorological observations in the US (Auer, 1974). The data were originally presented as a line segments.

The data collected in Switzerland by Rohrer (1989) were illustrated as ranges of % snow and % rain for each temperature interval. At the Arosa site, the average percentage and at Davos, the upper and lower reported limits, for the average temperature interval, has been plotted in Figure B-3 in order to summarize the data.

### B.1.2 Selection of a Suitable Function

To fit functions to the various mixed precipitation curves, several types of functions were considered. Since the Auer curve was selected to adjust the radar imagery, a function was selected fit to it and this same function was then fit to the other mixed precipitation curves. Initially a linear function was chosen for the percent snow ( $y_l$  in Figure B-4), in the form:

$$y_l = 100 - 100 \times \frac{T_a}{6} \quad (\text{B-1}),$$

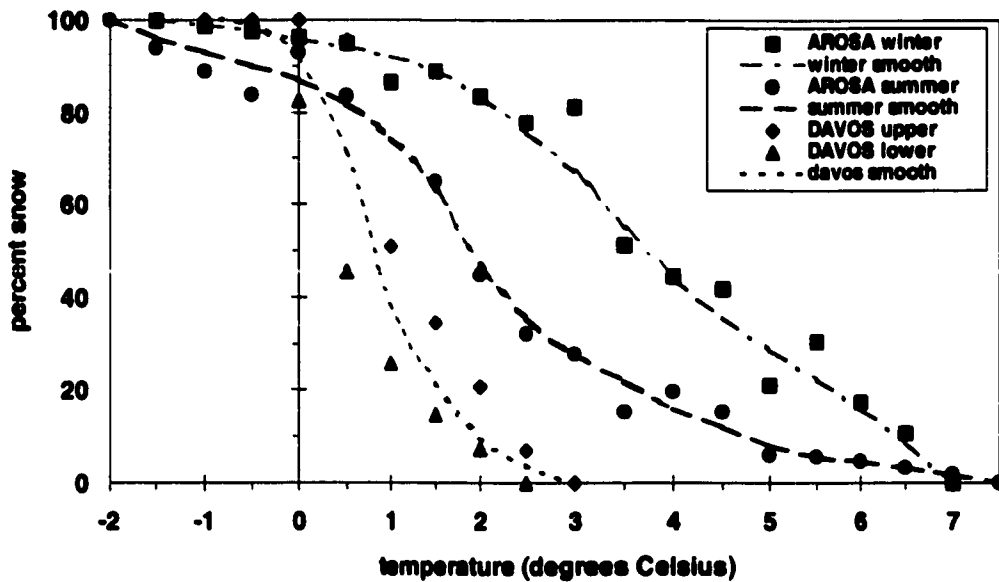


FIGURE B-3. Percent snow as a function of air temperature at two locations in Switzerland (Rohrer, 1989). The summer and winter percent snow curves have been differentiated for the AROSA station. The data were originally presented as a series of bar charts for a temperature increment of 0.5°C. These ranges are presented as the average percent snow within each bin.

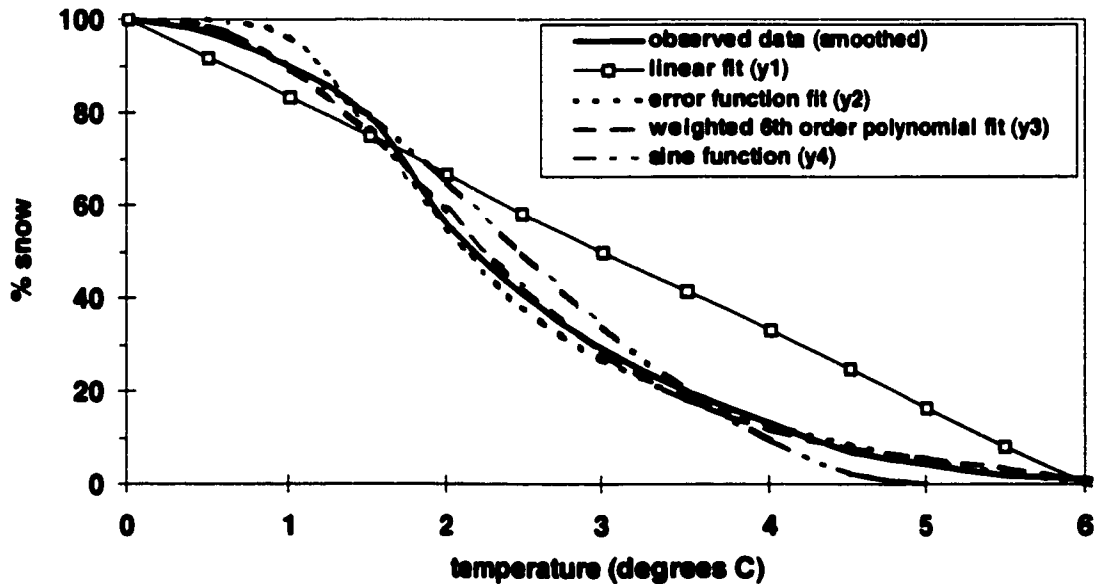


FIGURE B-4. The fit of four functions to the Auer (1974) smoothed curve.

with an  $r^2$  value of 0.871. To improve the fit and considering that the shape of the curve was similar to normalized concentration plots and the inverse cumulative lognormal probability plot, the error function (*erf*) was also fitted to the smoothed Auer curve for the percent snow ( $y_2$ ) as:

$$y_2 = 100 \operatorname{erf} \left[ \frac{1.5}{\left(1 + (T_a / 4.05)^3\right) - 1} - 0.1 \right] \quad (\text{B-2}),$$

with an  $r^2$  value of 0.996. Due to the potential complexity in programming the error function, various polynomials were considered. A four decimal place sixth order polynomial ( $y_3$ ) was found to provide the best fit. To optimize the fit, the polynomial was weighted using the temperature (Figure 3-1b), and the resultant function takes the form:

$$y_3 = 0.02020 T^6 - 0.36602 T^5 + 2.03987 T^4 - 1.50888 T^3 - 15.0376 T^2 + 4.66643 T + 100 \quad (\text{B-3}),$$

as presented in equation 4-8. Equation (B-3) provides a slight improvement over the error function, with the  $r^2$  value increasing to 0.998. For curiosity, a sine function was also fit to the smoothed Auer data. With an  $r^2$  value of 0.983, the best fit sine curve took the form:

$$y_4 = -50 \sin \left( -\frac{\pi}{5} T_a - \frac{\pi}{2} \right) + 50 \quad (\text{B-4}).$$

**B.1.3 Smoothed Curve Representation**

The percent probability of snow from the US Army Corps of Engineers (1956), the US meteorological stations (Auer, 1974), and the two stations in Switzerland (Rohrer, 1989) are summarized as smoothed curves in Figure B-5. In these curves, the percent probability of snow,  $F(T)$ , as a function of air temperature,  $T$ , has been plotted using sixth order polynomial functions of the form of equation (4-10):

$$F(T) = a_1 T^6 + a_2 T^5 + a_3 T^4 + a_4 T^3 + a_5 T^2 + a_6 T + b \quad (\text{B-5}),$$

where  $a_1$  through  $a_6$  and  $b$  are coefficients. The values of these coefficients for the five percent probability of snow curves are presented in Table 4-2. The lower limit of sixth order polynomial curves for the occurrence of 100% snow and the upper temperature limit for the occurrence of 100% rain are presented in Table 4-2, to the nearest one-hundredth of a degree Celsius.

To avoid computational errors that occur as a result of division by a small number, the above lower and upper limits have also been determined for 99% snow (approaching from below, i.e., less than) and 1% snow (approaching from above, i.e., greater than), calculated from temperatures rounded to the nearest one-hundredth of a degree Celsius.

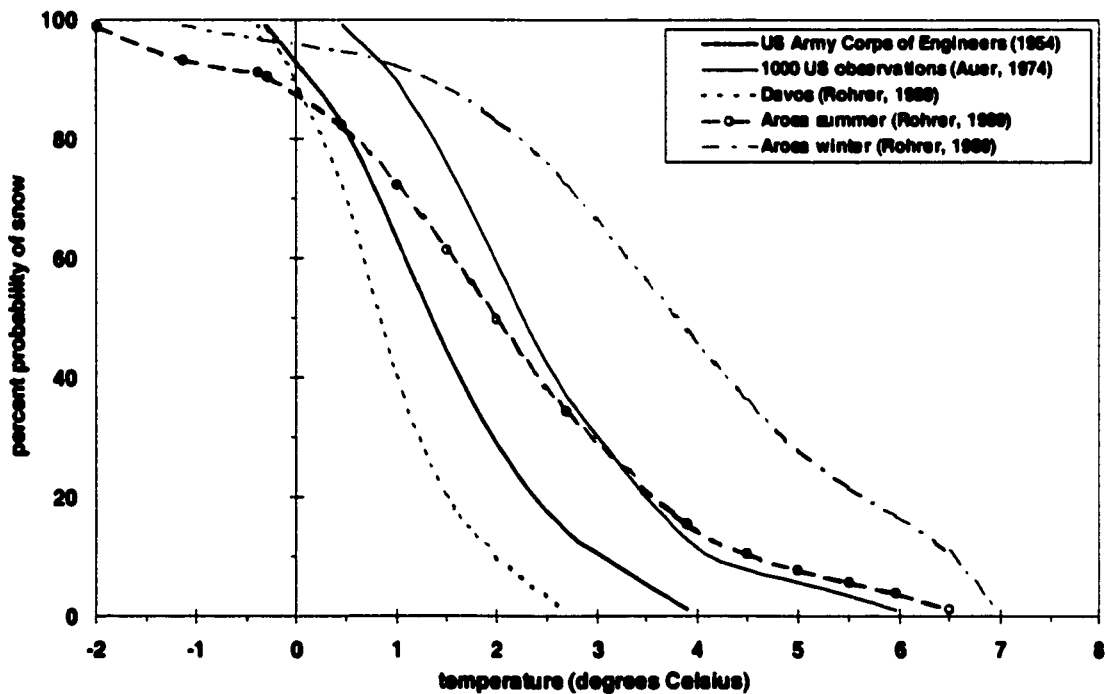


FIGURE B-5. Percent snow as a function of air temperature from the five 6<sup>th</sup> order polynomial curves fitted to the smoothed curves presented in Figures B-1 through B-3.

## B.2 PARTICLE SHAPE CURVE

The particle shape (*PS*) curve presented in Figure 4-2c has been derived from the data compiled by Ono (1970) using various assumptions outlined in section 4.1.4c. The base curve is the average of the maximum and minimum ice crystal growth rates (Figure 2-2c). Considering the

direction of growth, the average ice crystal growth rate curve can be illustrated as a three-dimensional plot (Figure B-6). This plot accentuates the assumptions made in the development of the *PS* curve. The proposed curve, presented in Figure 3-2b, is based on the modified data. Various functions have been fit to these data. Building on the success of the sixth order polynomial fit to the mixed precipitation curves, such a function was examined for use with the *PS* curve (Figure B-7a). For an adequately fit three sixth order polynomials must be used for the temperature ranges from -1 to -9°C, from -10 to -13°C, and from -14 to -21°C. Figure B-7a illustrates that a single *sine* function follows the general trend of the *PS* curve, with an  $r^2$  of 0.934 based on 21 temperature data points from -1 to -21°C. This lead to the use of a Fourier Series. Various Fourier Series, specifically first through sixth as well as tenth order, were applied with varying precision in the terms, in particular, from two to five significant figures. Figure B-7a illustrates the fit of the third and fifth order Fourier Series using three significant figures. While the fifth order Fourier Series (11 terms,  $r^2 = 0.995$ ) and the 3-sixth order polynomial (3 x 7 terms with conditional statements,  $r^2 = 0.998$ ) curves fit the *PS* curve data best, the three significant figure - third order Fourier Series was selected to represent the *PS* curve since it only uses 7 terms while still providing a good fit ( $r^2 = 0.988$ ).

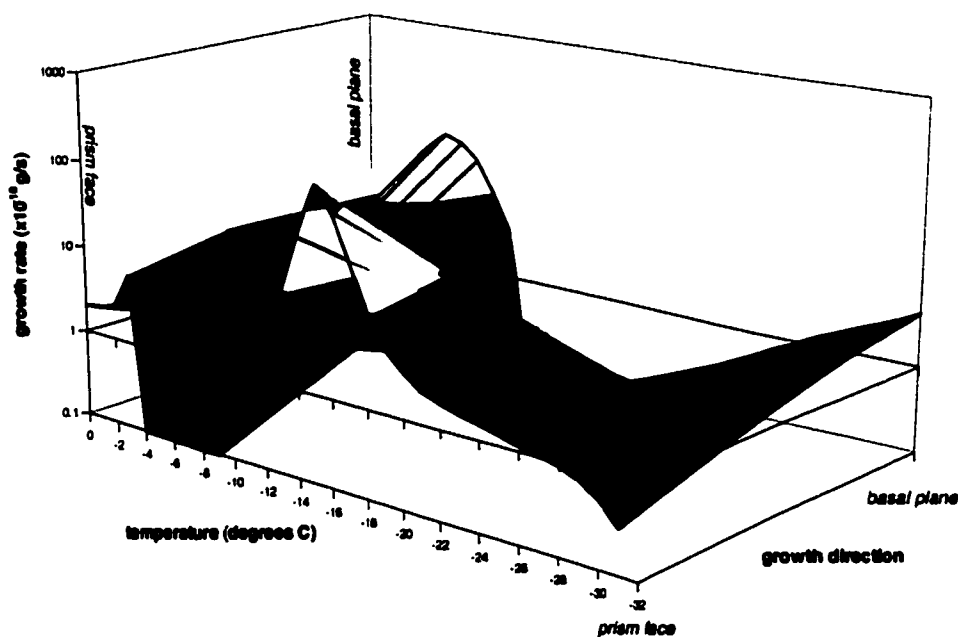


FIGURE B-6. Three-dimensional representation of the directional average ice crystal growth rate as a function of formation temperature, based on the data compiled by Ono (1970).

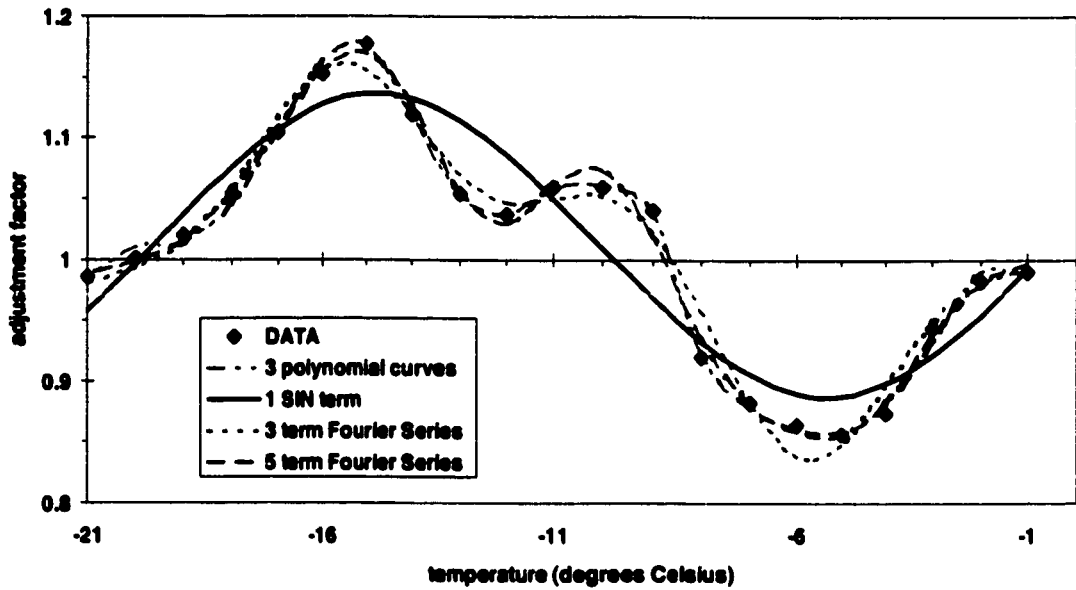


FIGURE B-7a. The fit of four functions to the particle shape curve (non-weighted in Figure 4-2c), across the entire temperature range.

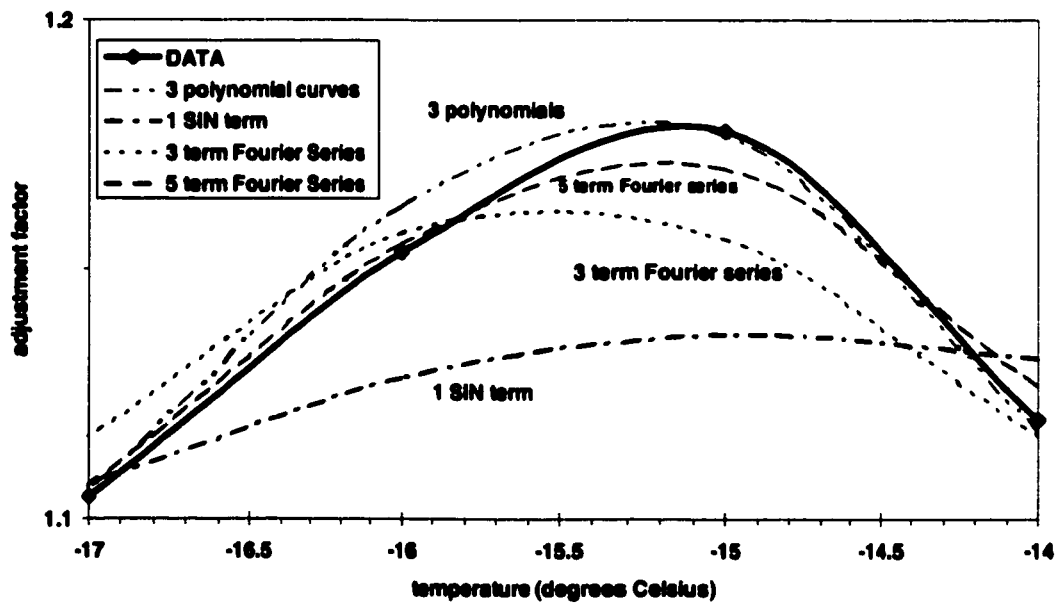


FIGURE B-7b. The fit of the four functions to the particle shape curve (as above) for the maximum dendritic crystal growth range -17 and -14°C.

# **Appendix C: ADDITIONAL RESULTS**

---

This appendix presents supplemental results beyond those presented in Chapter 5 of the main body of the document.

## **C.1 MONTHLY ACCUMULATION COMPARISON**



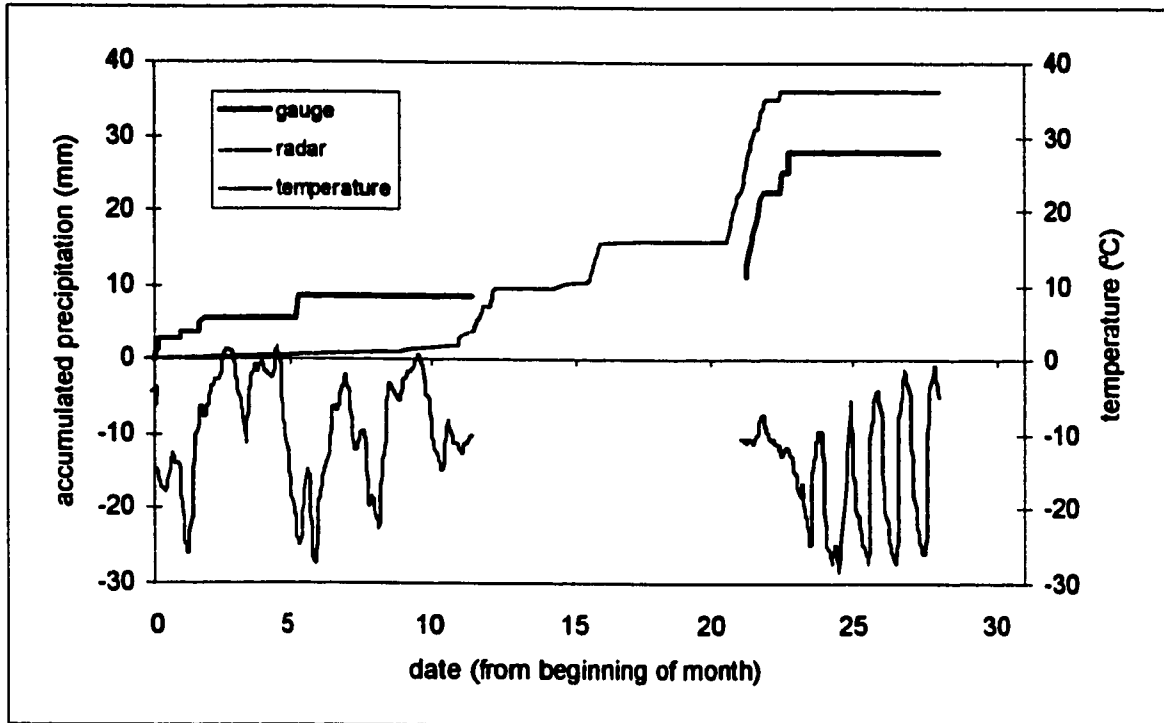


FIGURE C-1a. Snowfall raw radar-gauge comparison for February 1993 at the Wormwood site.

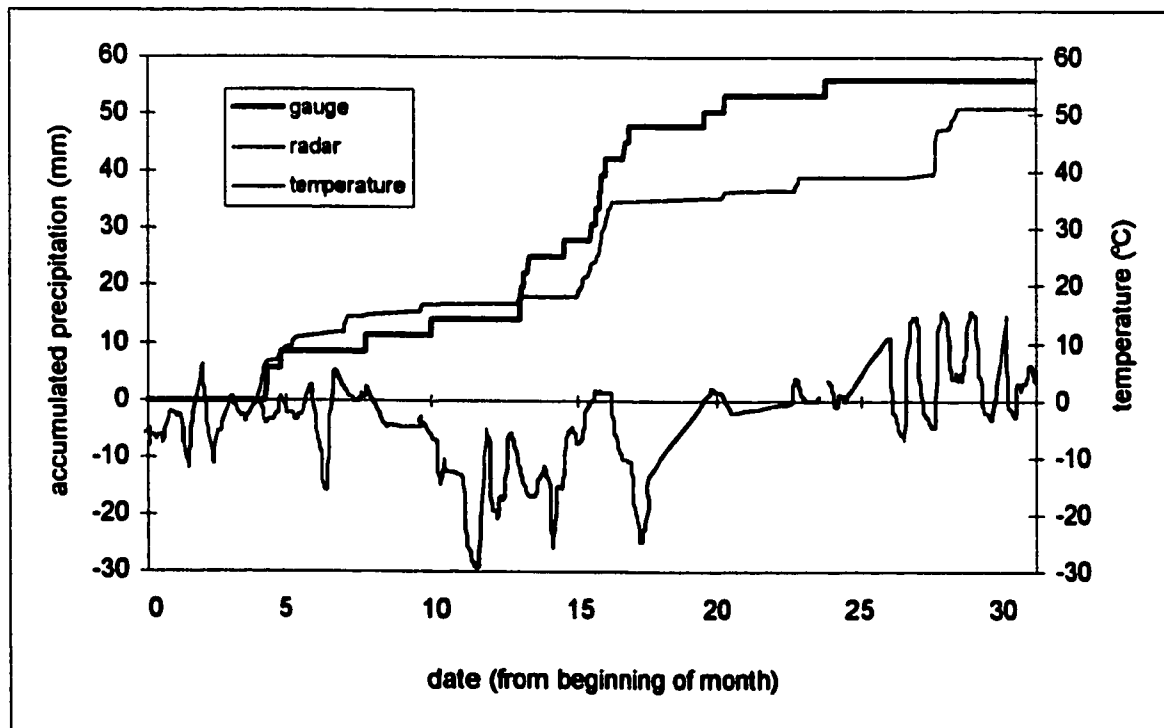


FIGURE C-1b. Snowfall raw radar-gauge comparison for March 1993 at the Wormwood site.

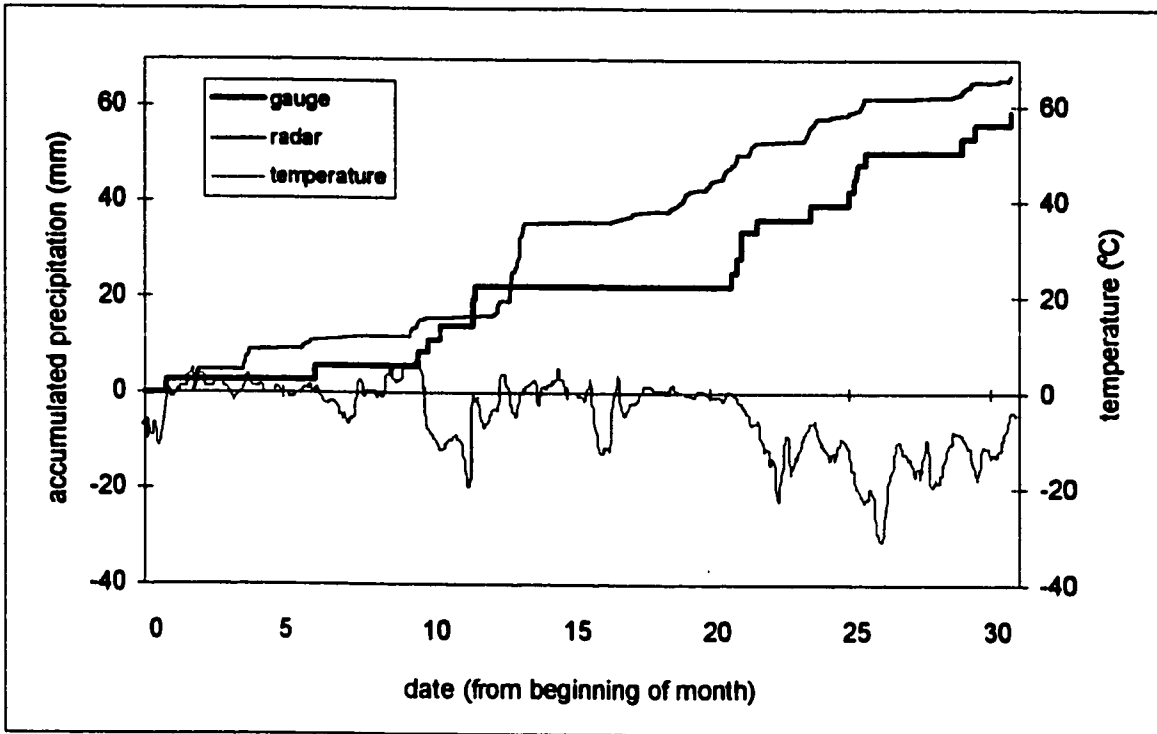


FIGURE C-1c. Snowfall raw radar-gauge comparison for December 1993 at the Wormwood site.

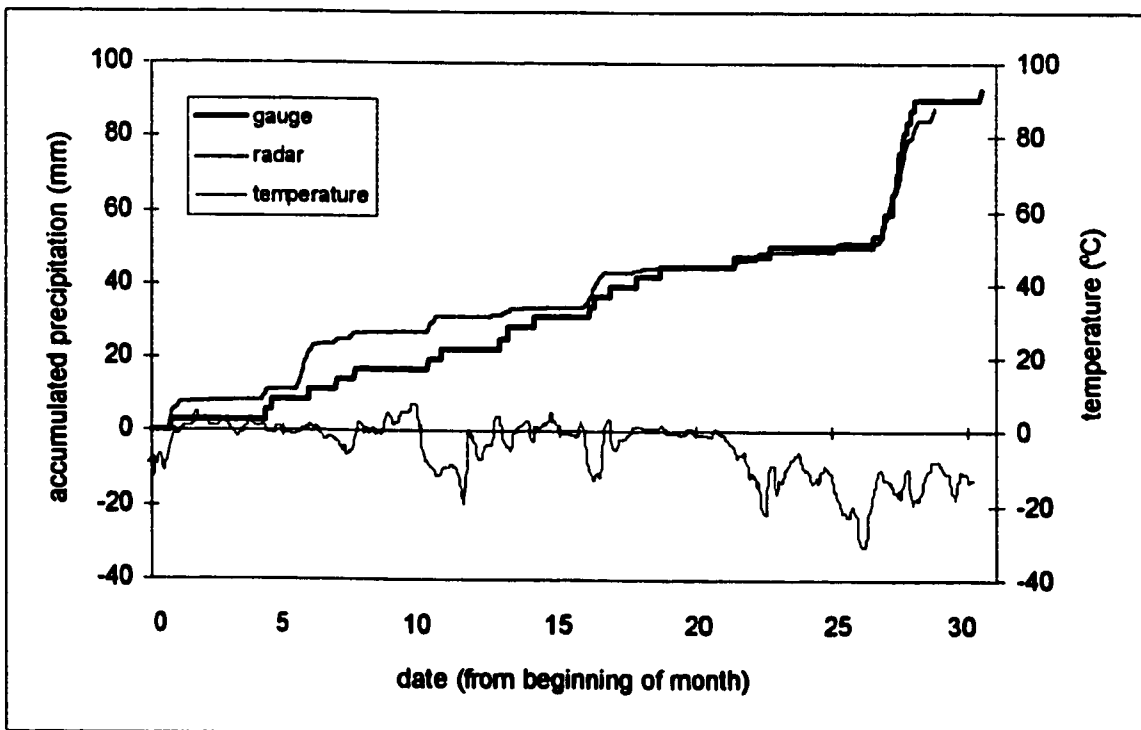


FIGURE C-1d. Snowfall raw radar-gauge comparison for January 1994 at the Wormwood site.

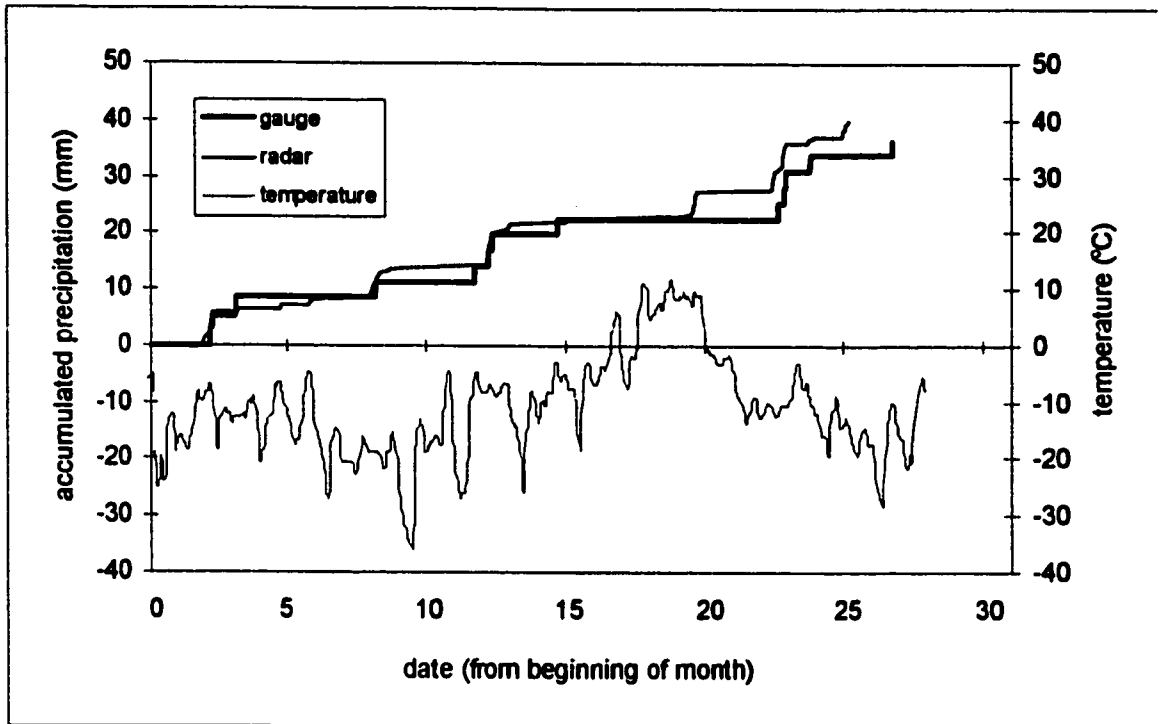


FIGURE C-1e. Snowfall raw radar-gauge comparison for February 1994 at the Wormwood site.

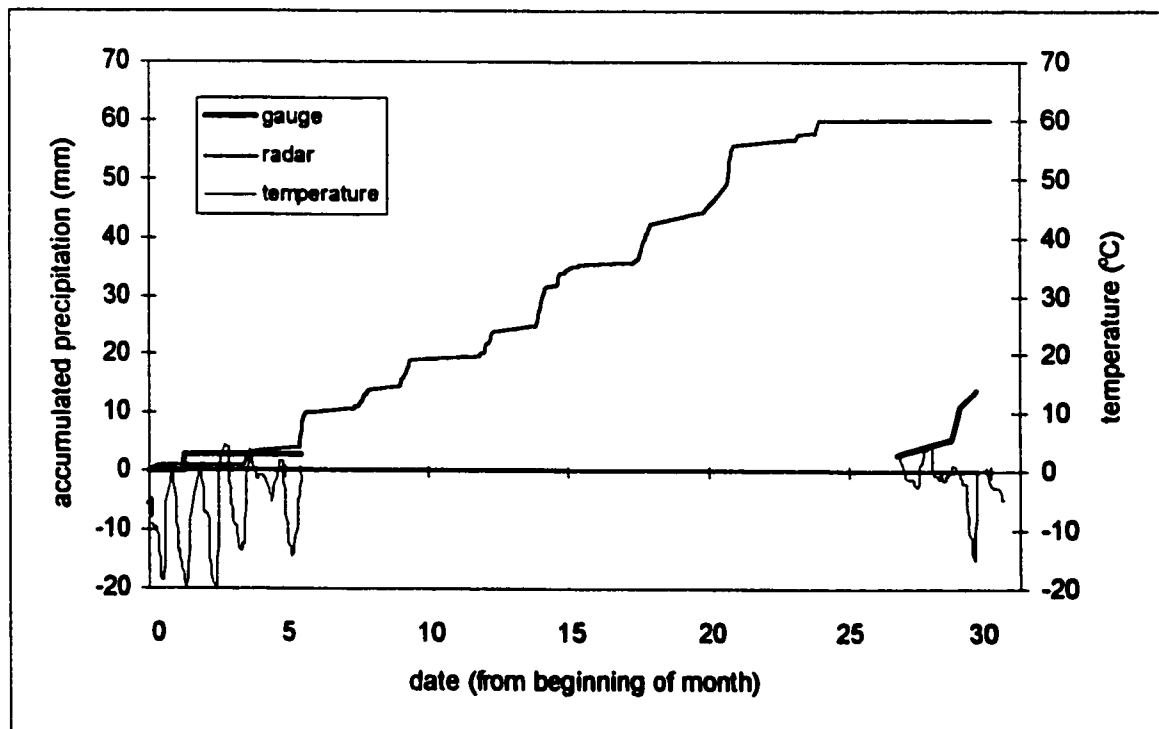


FIGURE C-1f. Snowfall raw radar-gauge comparison for March 1994 at the Wormwood site.

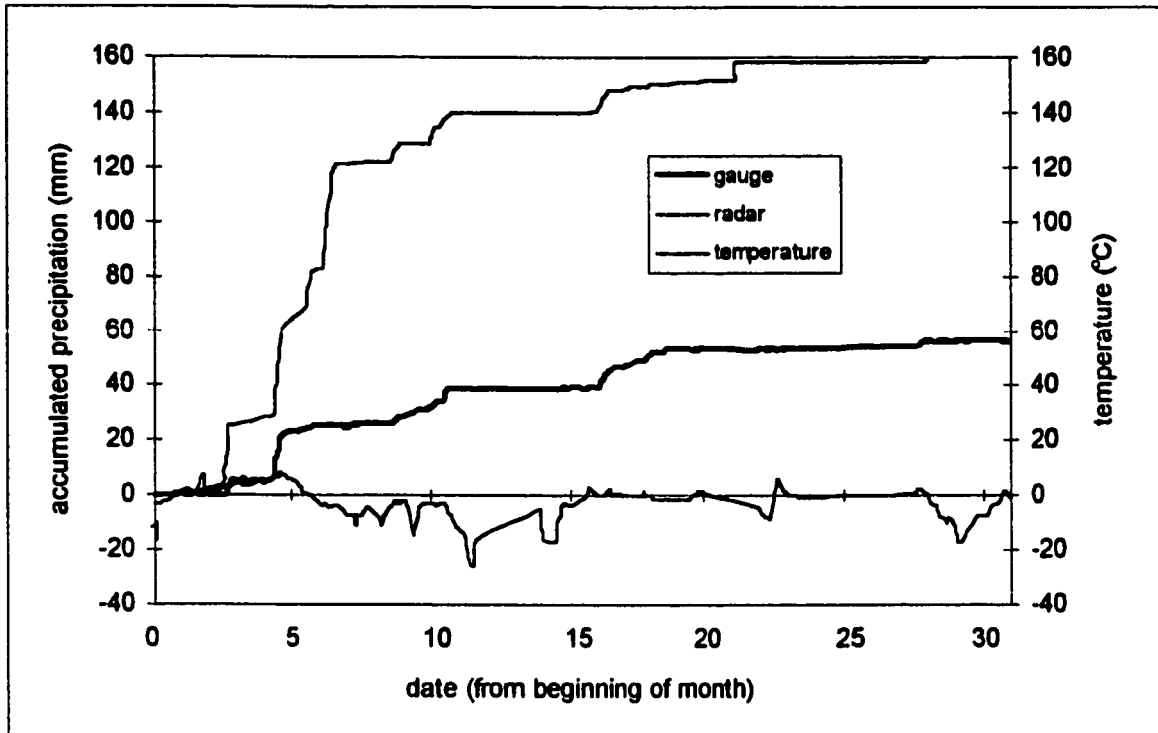


FIGURE C-1g. Snowfall raw radar-gauge comparison for December 1994 at the Wormwood site.

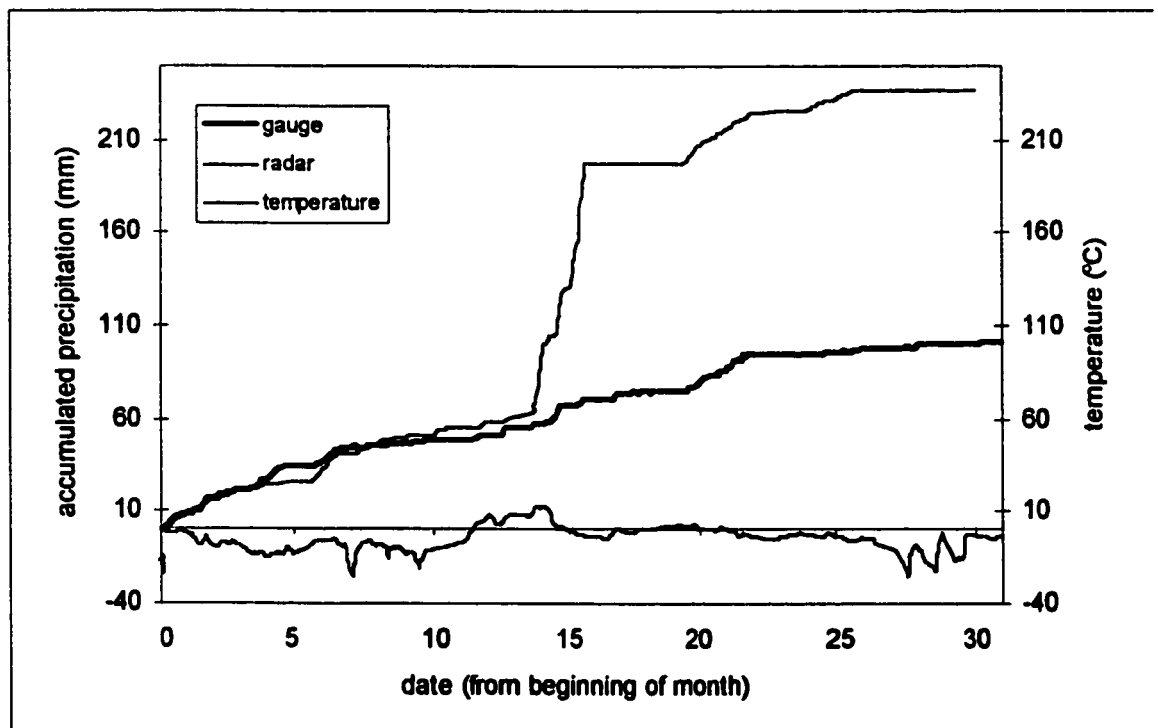


FIGURE C-1h. Snowfall raw radar-gauge comparison for January 1995 at the Wormwood site.

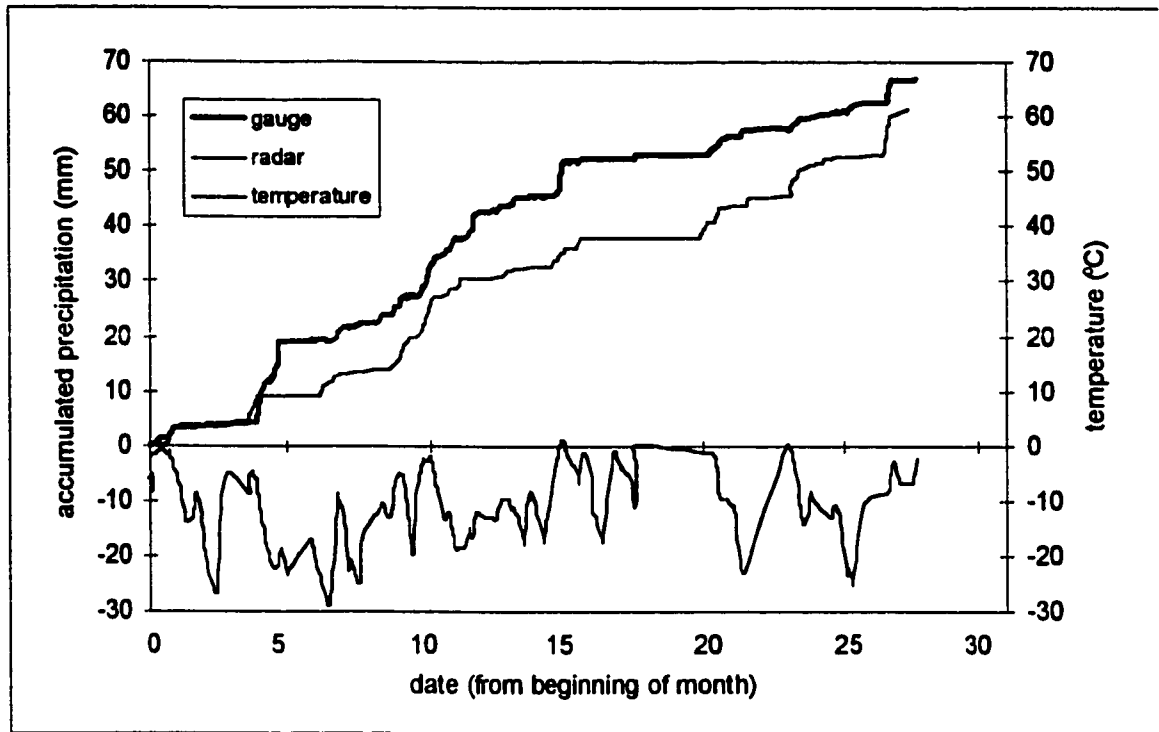


FIGURE C-1i. Snowfall raw radar-gauge comparison for February 1995 at the Wormwood site.

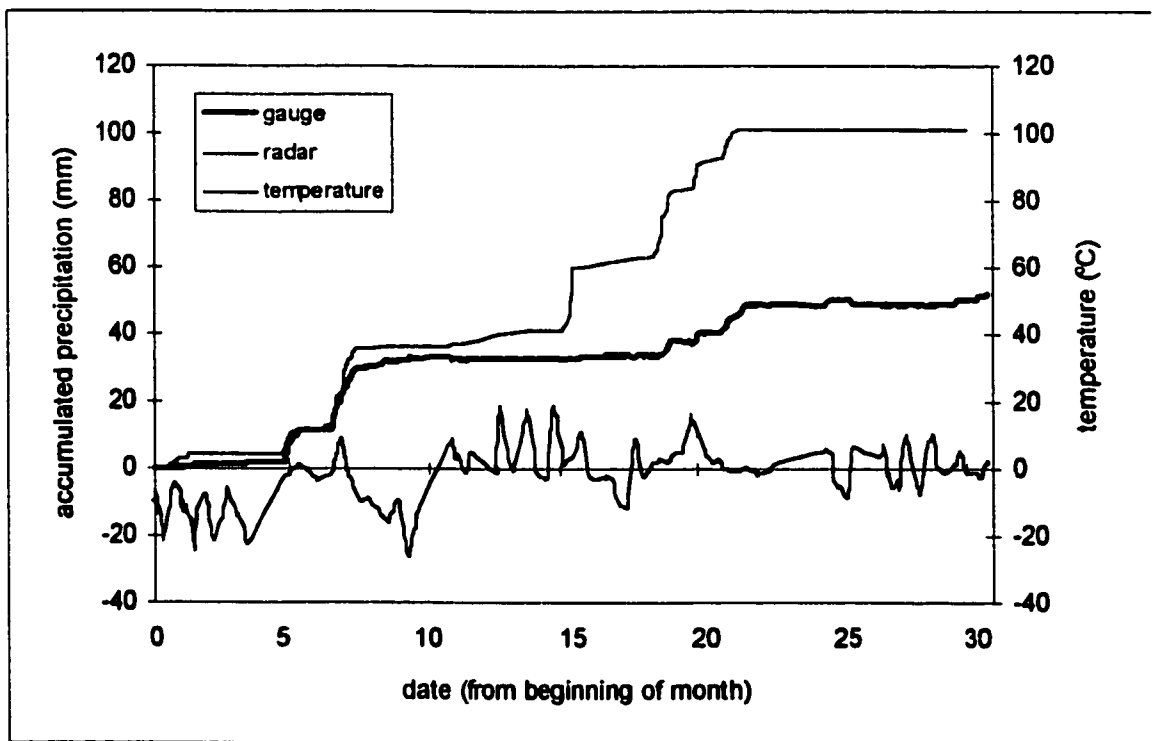


FIGURE C-1j. Snowfall raw radar-gauge comparison for March 1995 at the Wormwood site.

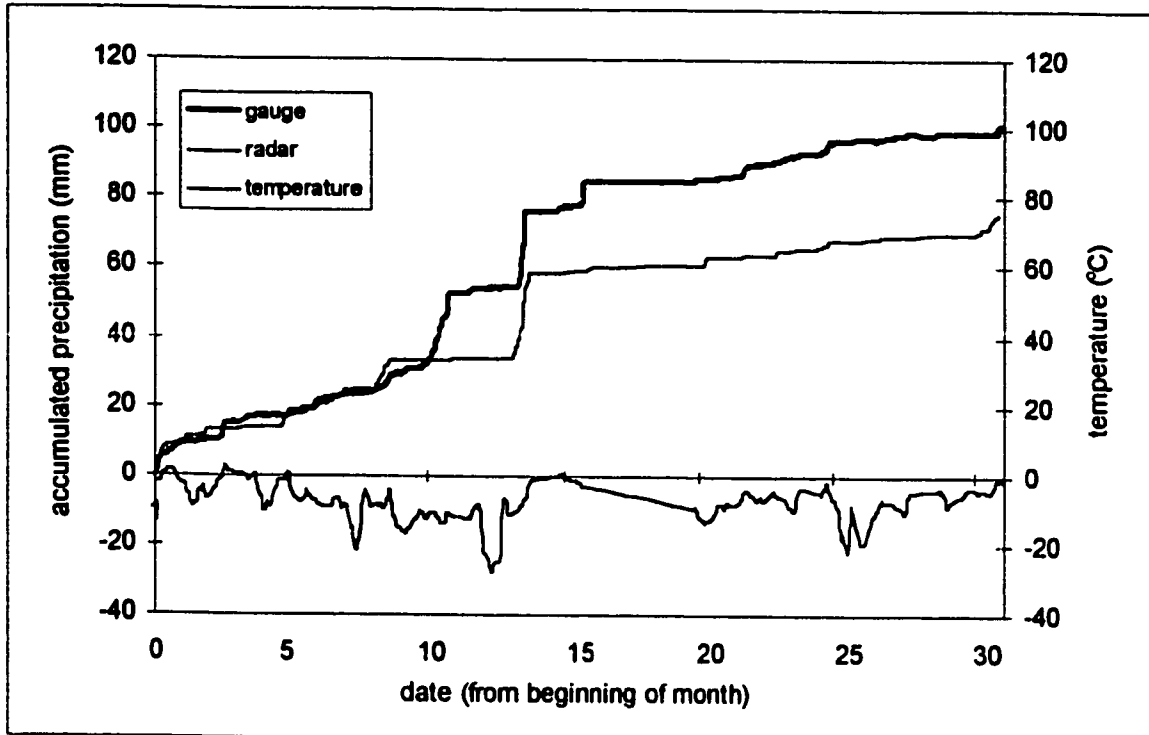


FIGURE C-1k. Snowfall raw radar-gauge comparison for December 1995 at the Wormwood site.

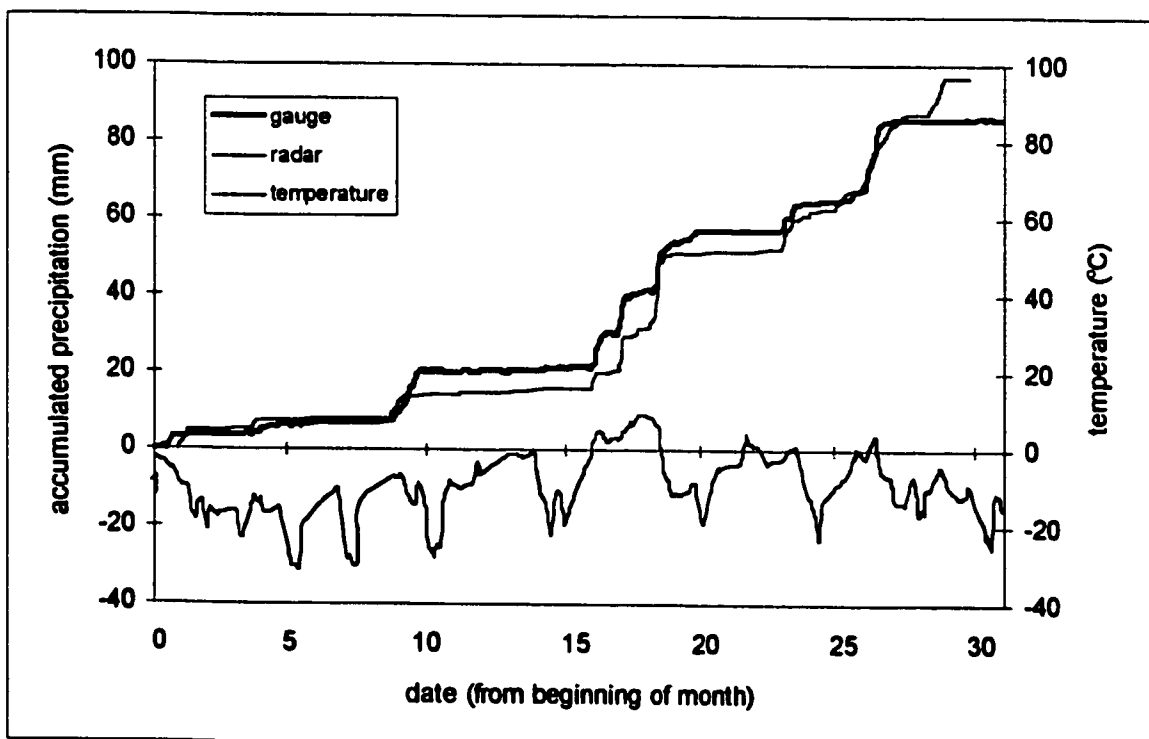


FIGURE C-1l. Snowfall raw radar-gauge comparison for January 1996 at the Wormwood site.

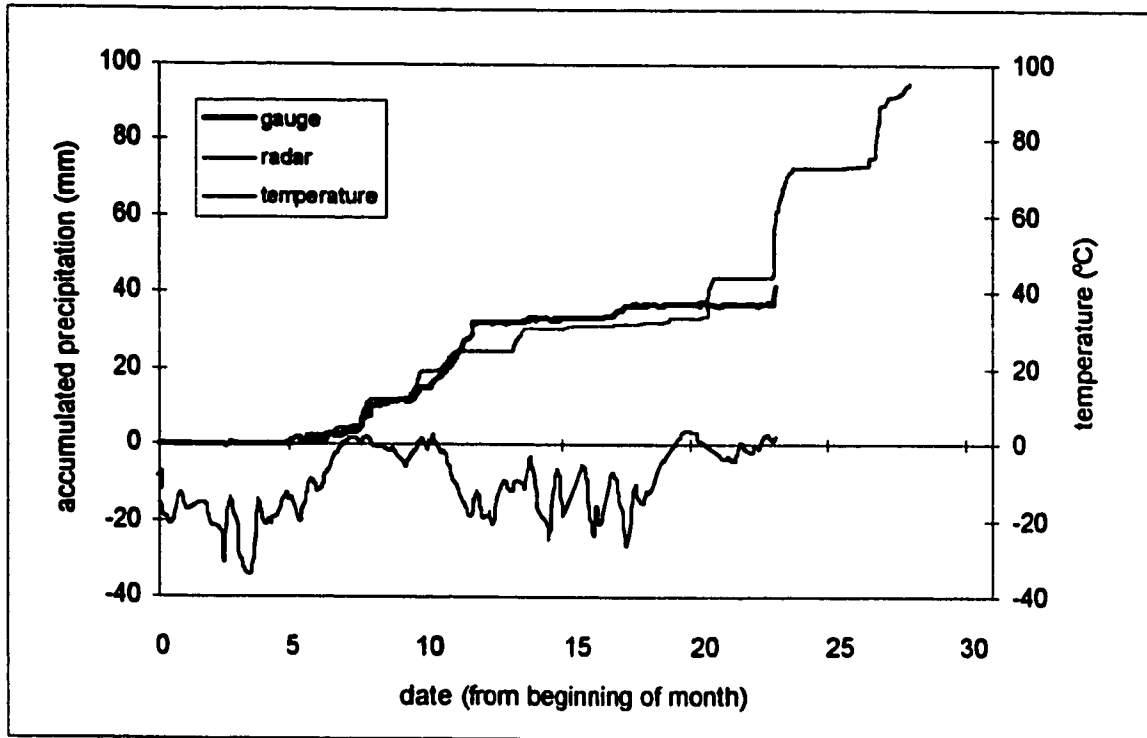


FIGURE C-1m. Snowfall raw radar-gauge comparison for February 1996 at the Wormwood site.

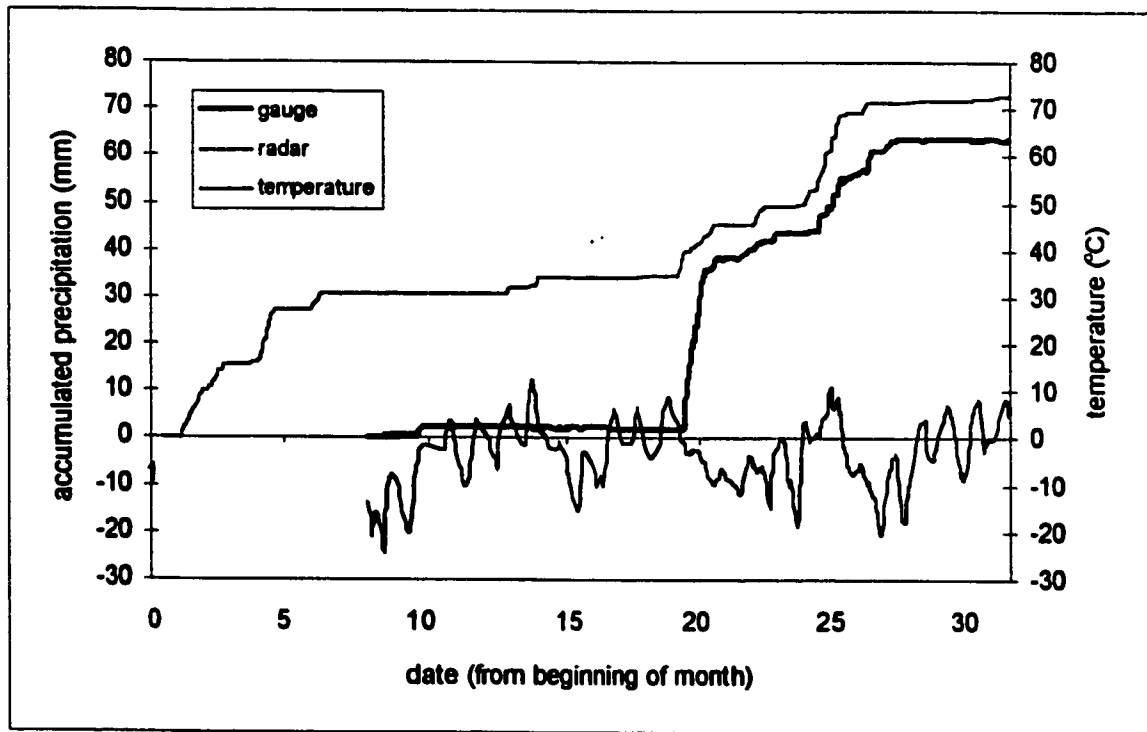


FIGURE C-1n. Snowfall raw radar-gauge comparison for March 1996 at the Wormwood site.

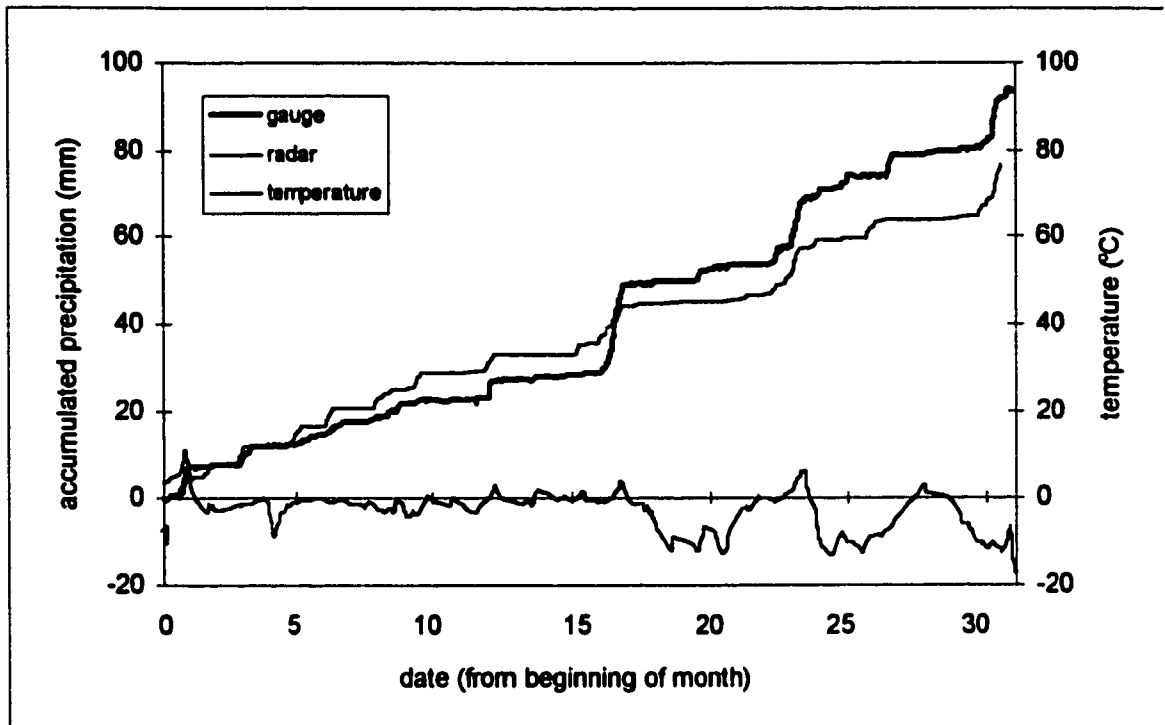


FIGURE C-1o. Snowfall raw radar-gauge comparison for December 1996 at the Wormwood site.

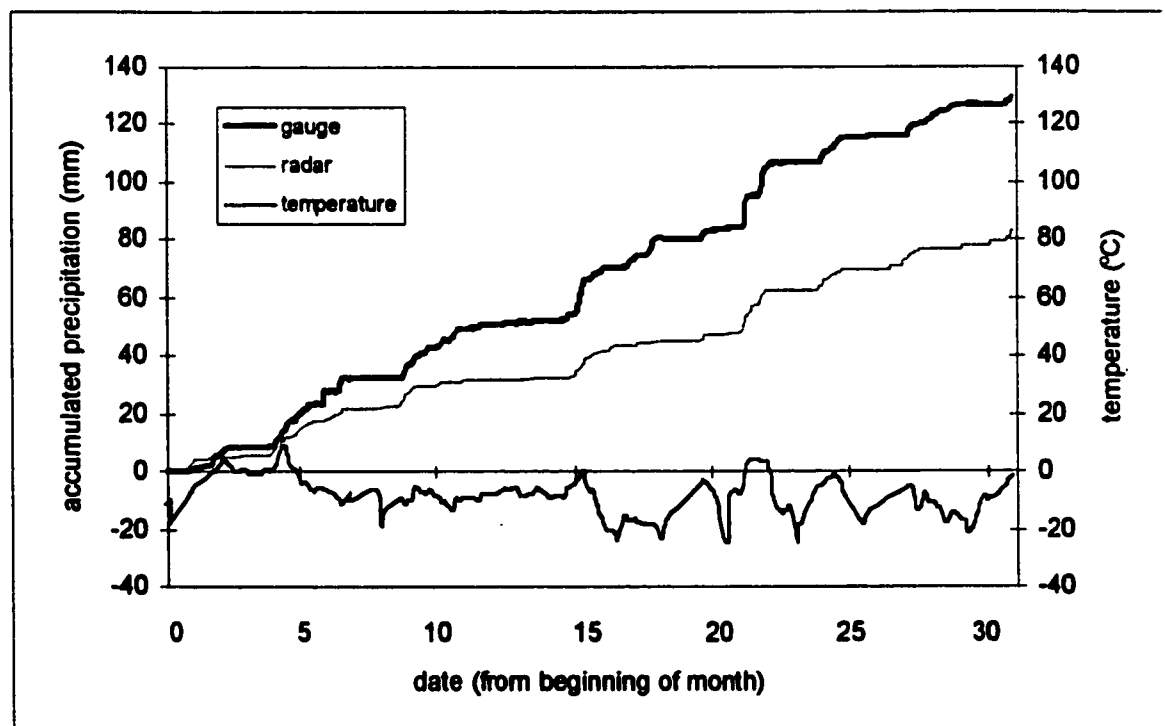


FIGURE C-1p. Snowfall raw radar-gauge comparison for January 1997 at the Wormwood site.



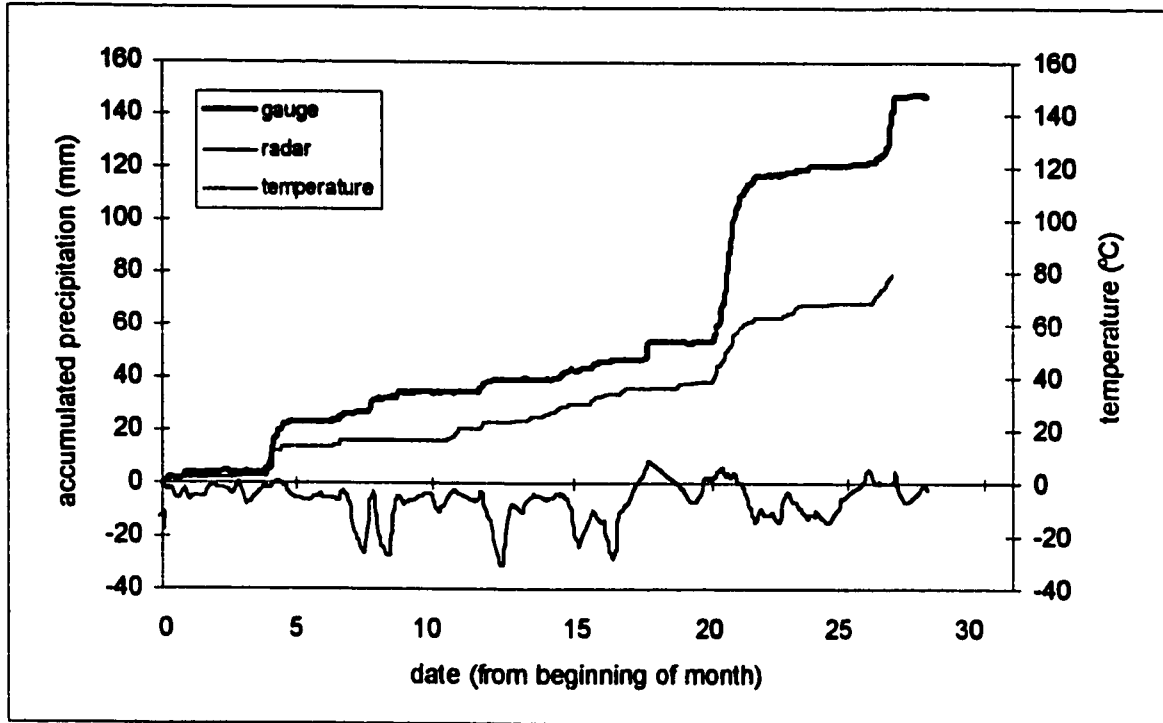


FIGURE C-1q. Snowfall raw radar-gauge comparison for February 1997 at the Wormwood site.

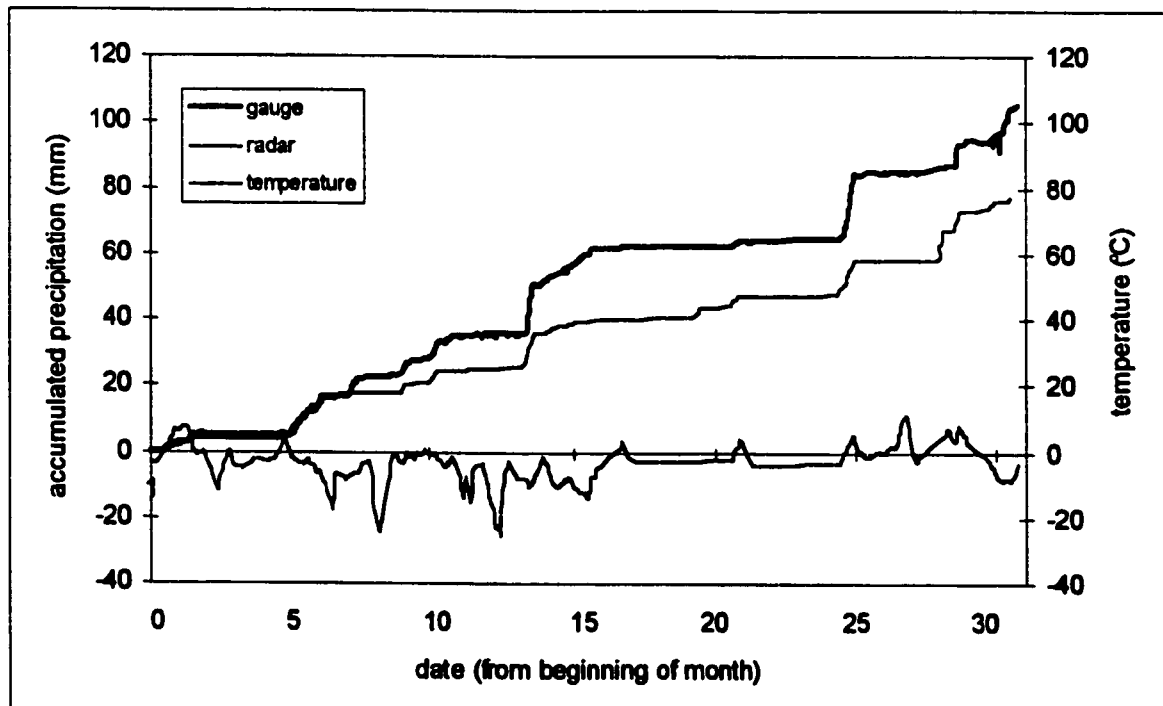


FIGURE C-1r. Snowfall raw radar-gauge comparison for March 1997 at the Wormwood site.

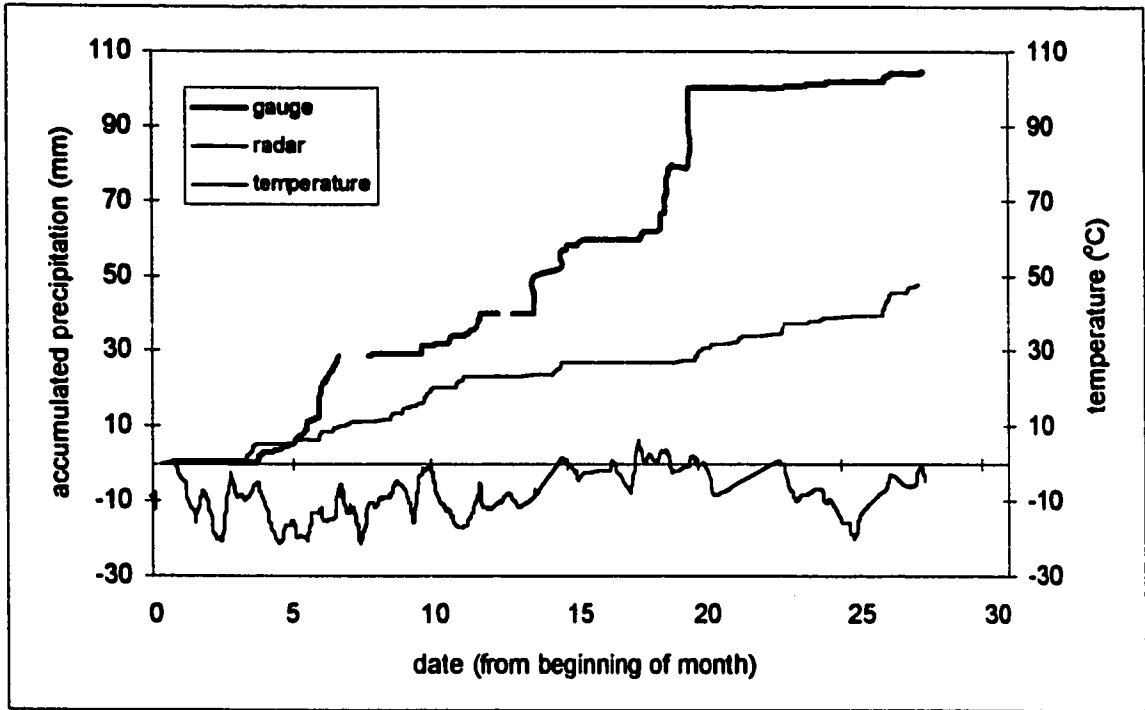


FIGURE C-2a. Snowfall raw radar-gauge comparison for February 1995 at the Greenoch site.

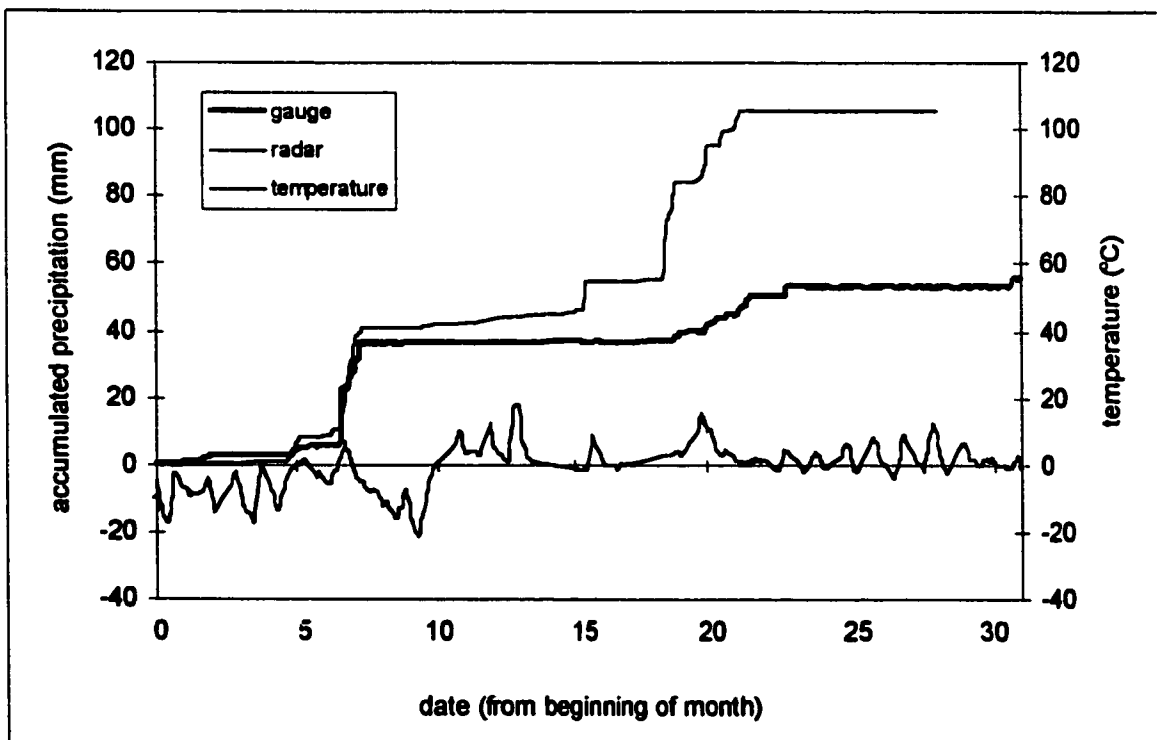


FIGURE C-2b. Snowfall raw radar-gauge comparison for March 1995 at the Greenoch site.

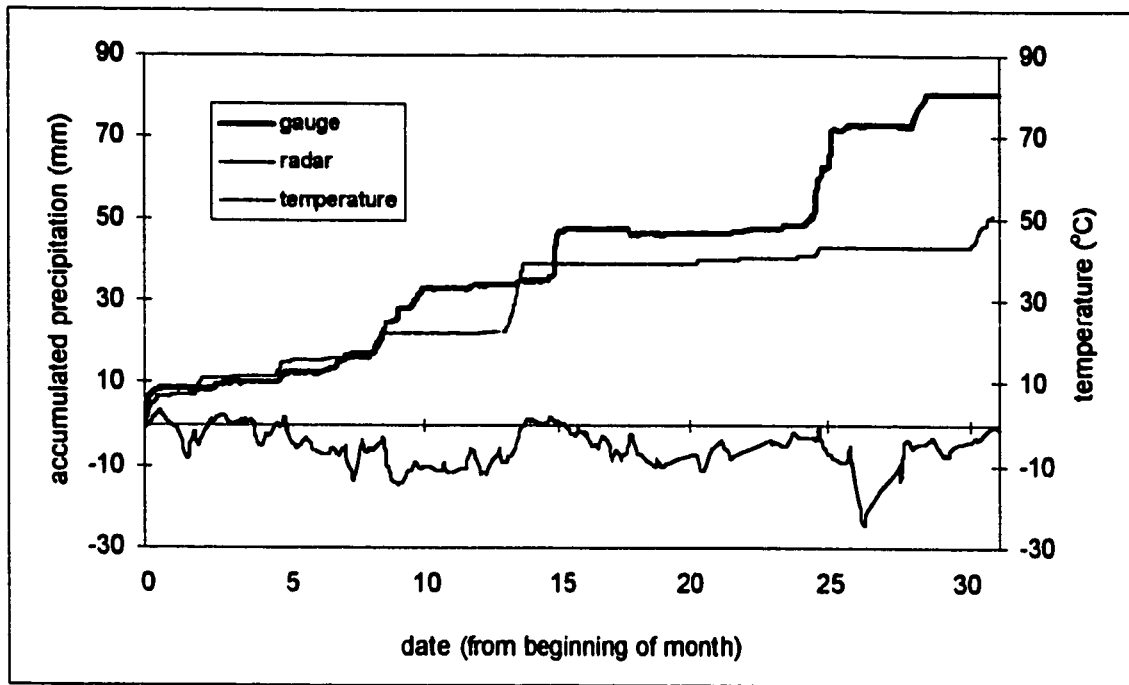


FIGURE C-2c. Snowfall raw radar-gauge comparison for December 1995 at the Greenoch site.

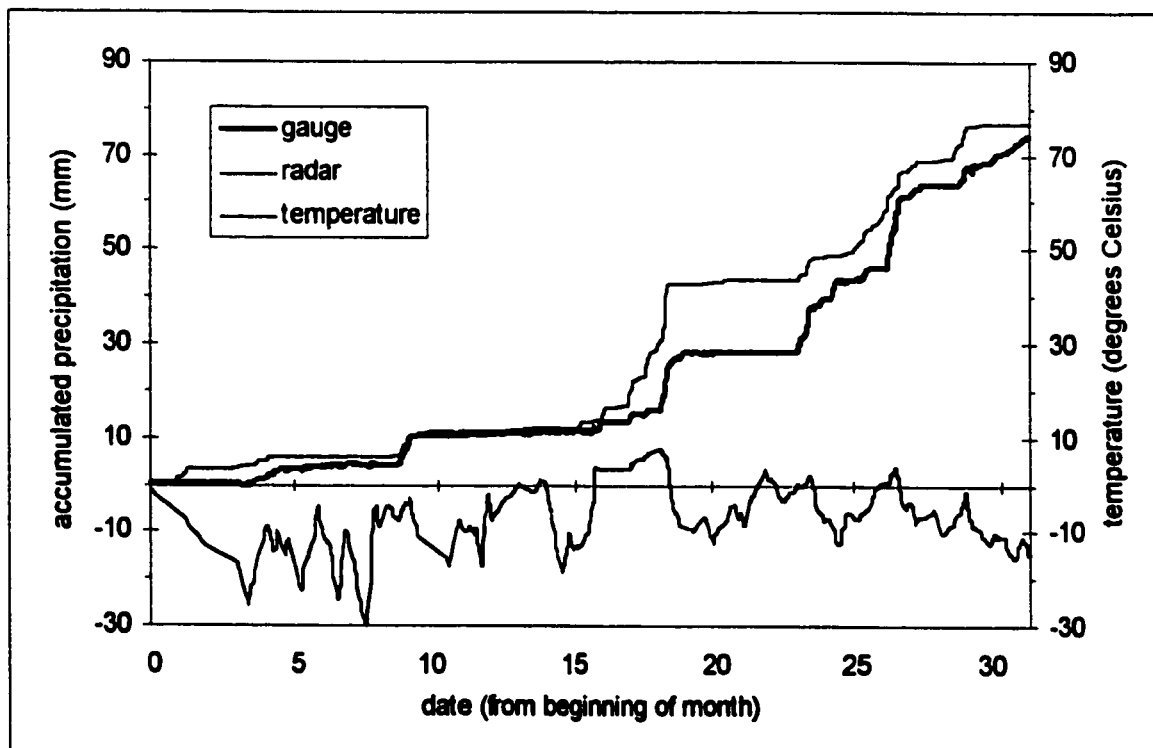


FIGURE C-2d. Snowfall raw radar-gauge comparison for January 1996 at the Greenoch site.

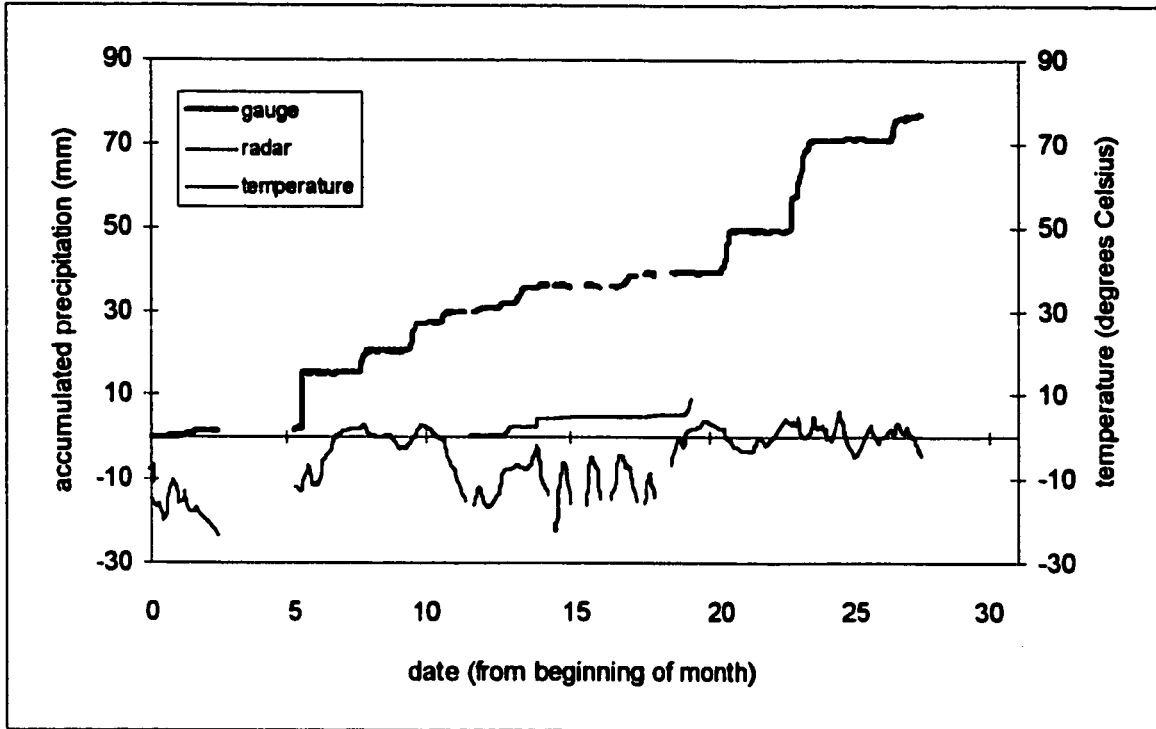


FIGURE C-2e. Snowfall raw radar-gauge comparison for February 1996 at the Greenoch site.

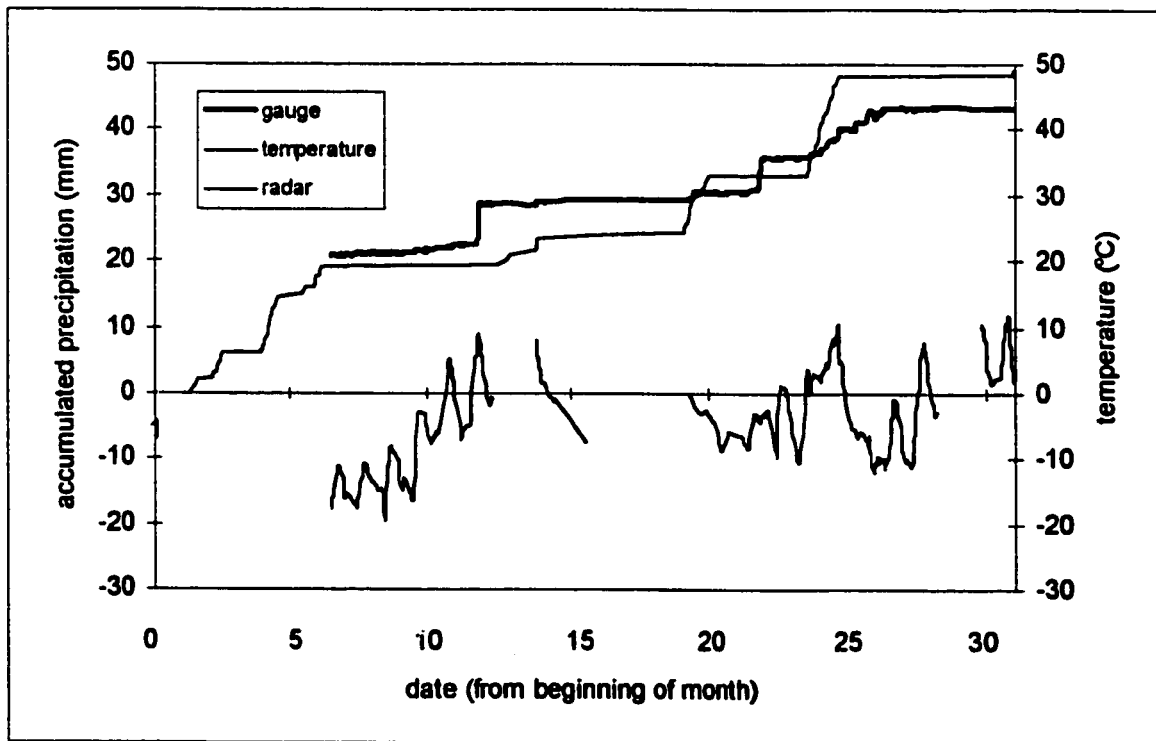


FIGURE C-2f. Snowfall raw radar-gauge comparison for March 1996 at the Greenoch site.

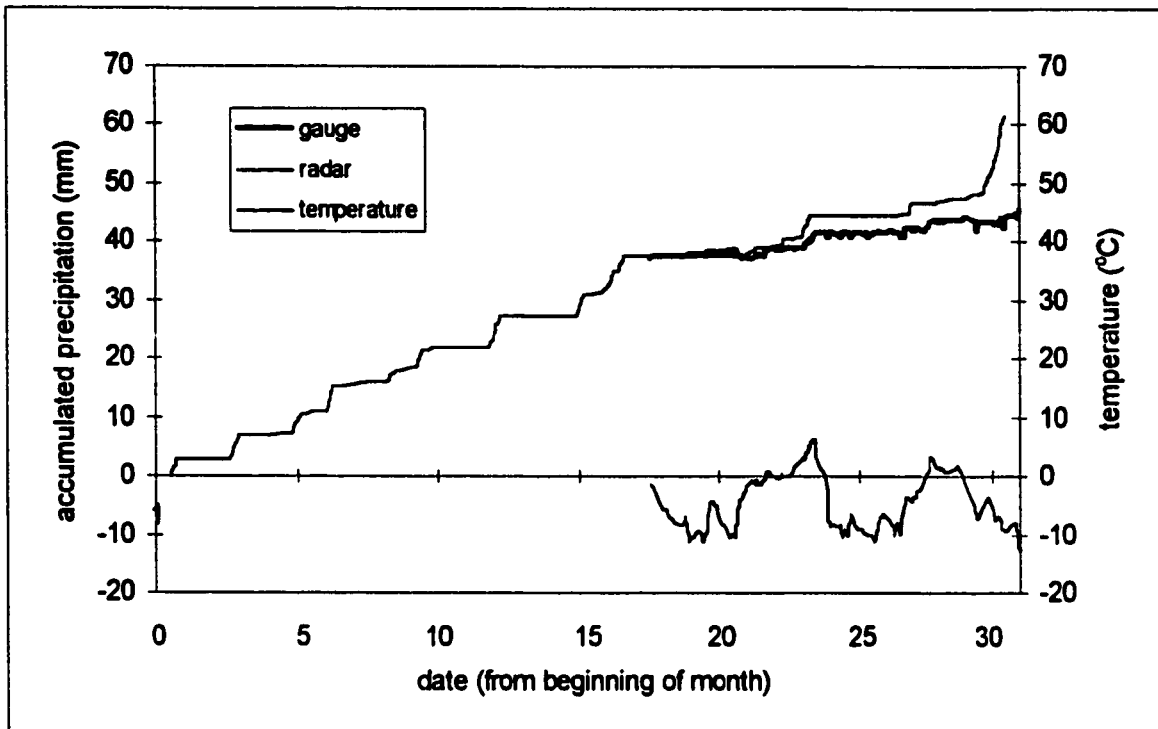


FIGURE C-2g. Snowfall raw radar-gauge comparison for December 1996 at the Greenoch site.

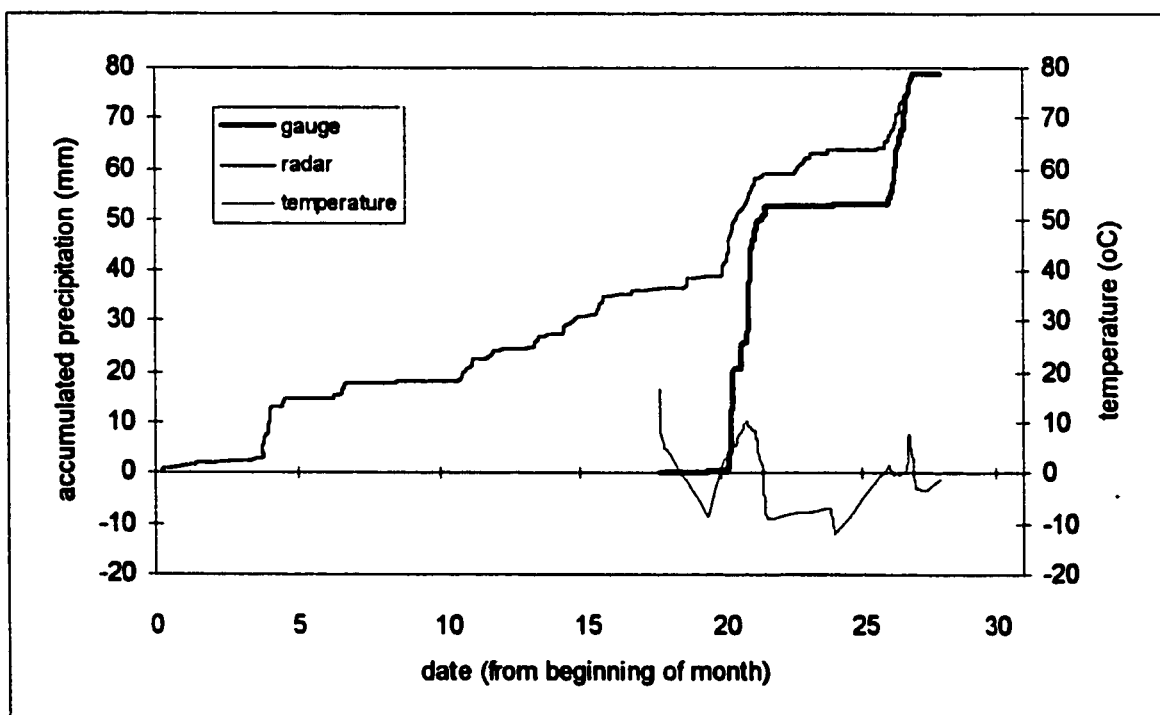


FIGURE C-3a. Snowfall raw radar-gauge comparison for February 1997 at the Euclid site.

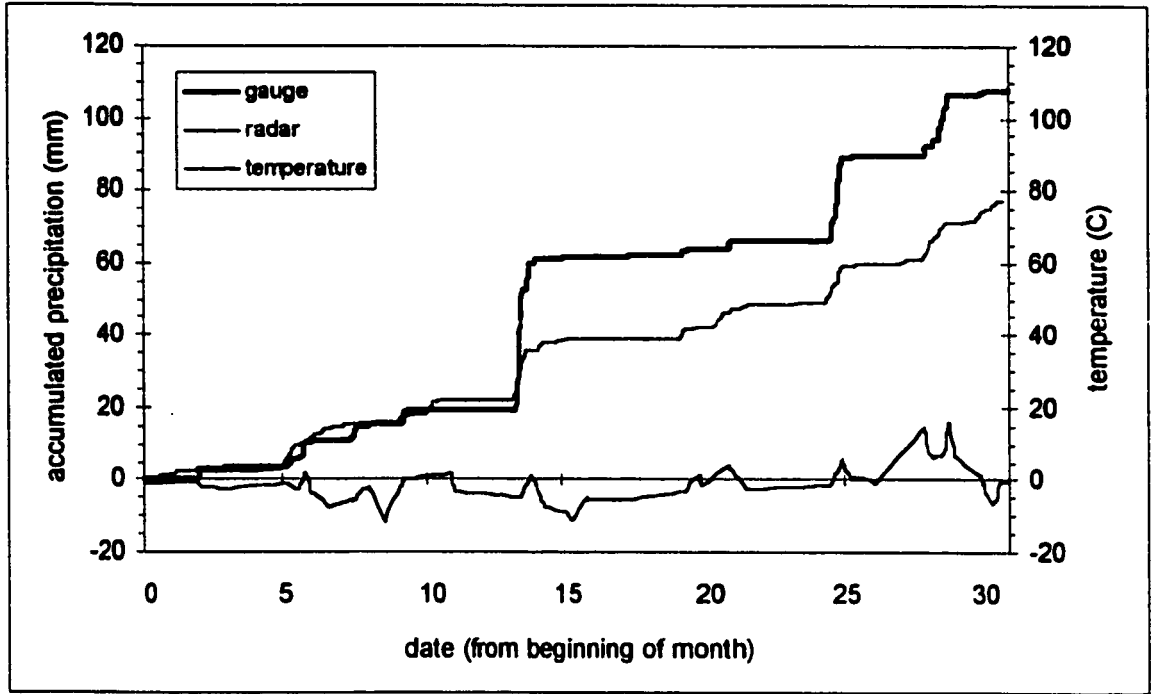


FIGURE C-3b. Snowfall raw radar-gauge comparison for March 1997 at the Euclid site.

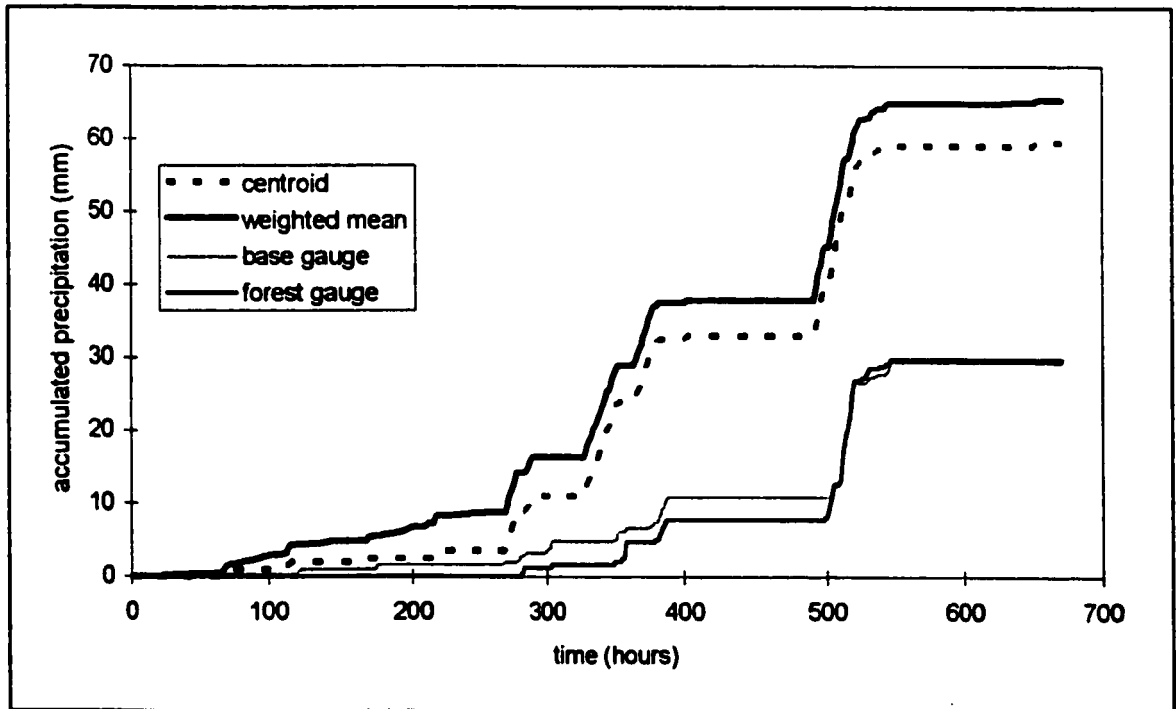


FIGURE C-4a. Snowfall raw radar-gauge comparison for February 1993 at the CARE site.

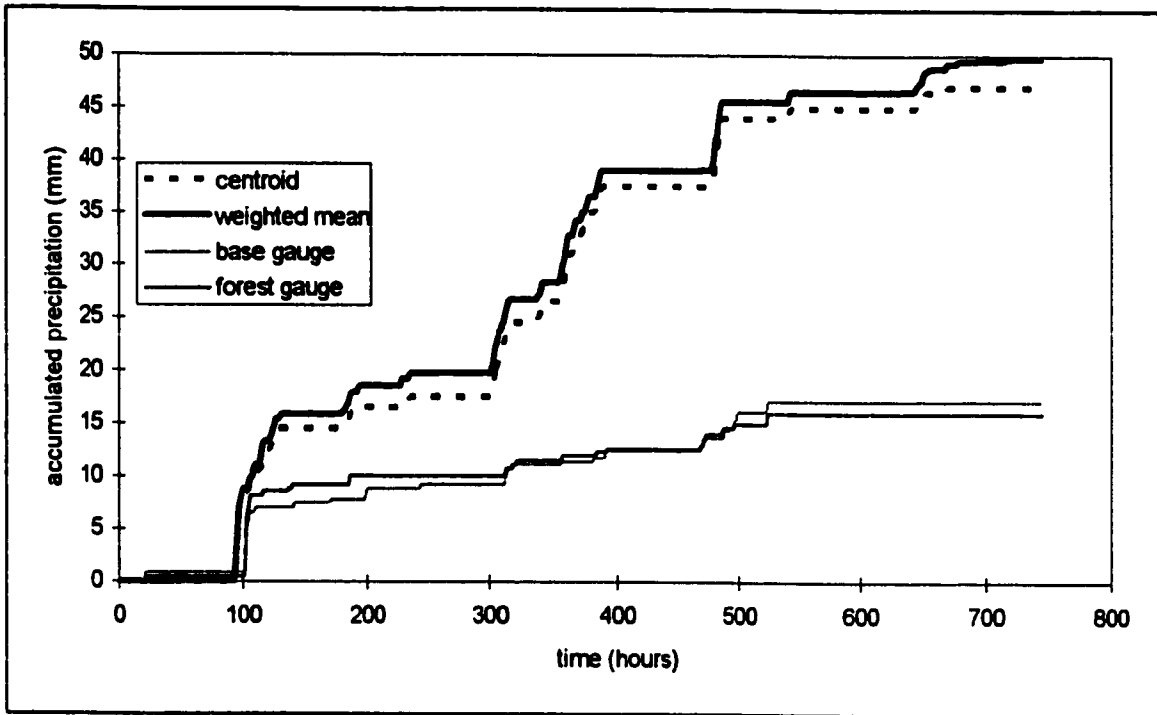


FIGURE C-4b. Snowfall raw radar-gauge comparison for March 1993 at the CARE site.

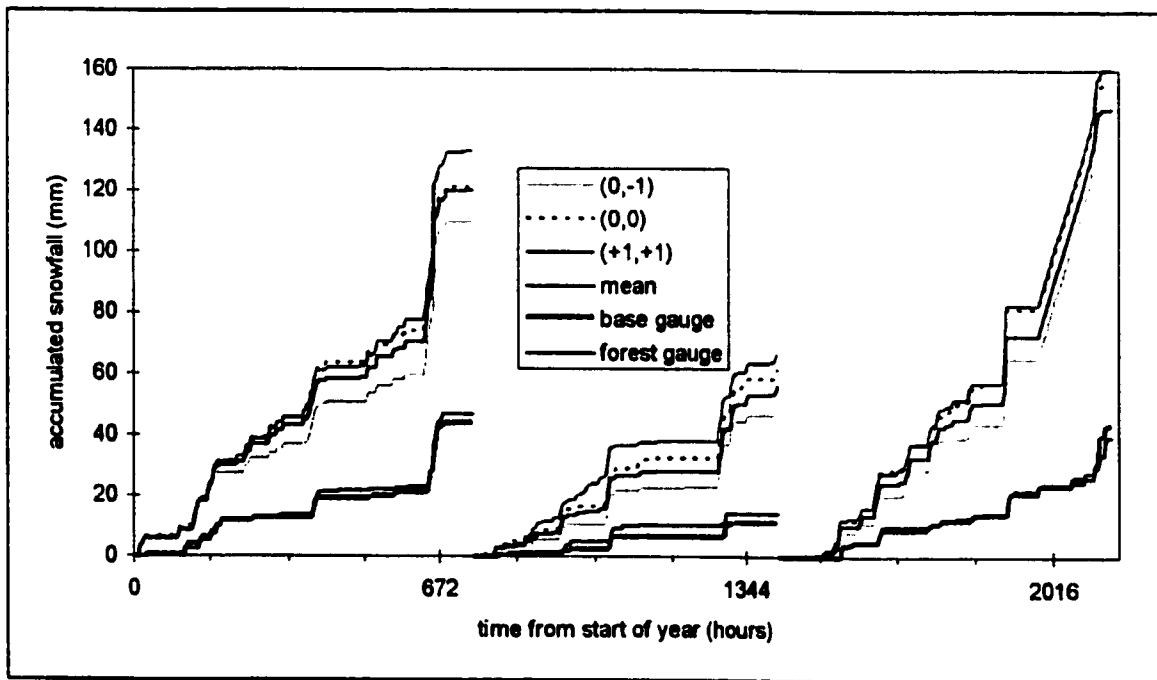


FIGURE C-4c. Snowfall raw radar-gauge comparison for 1994 at the CARE site.

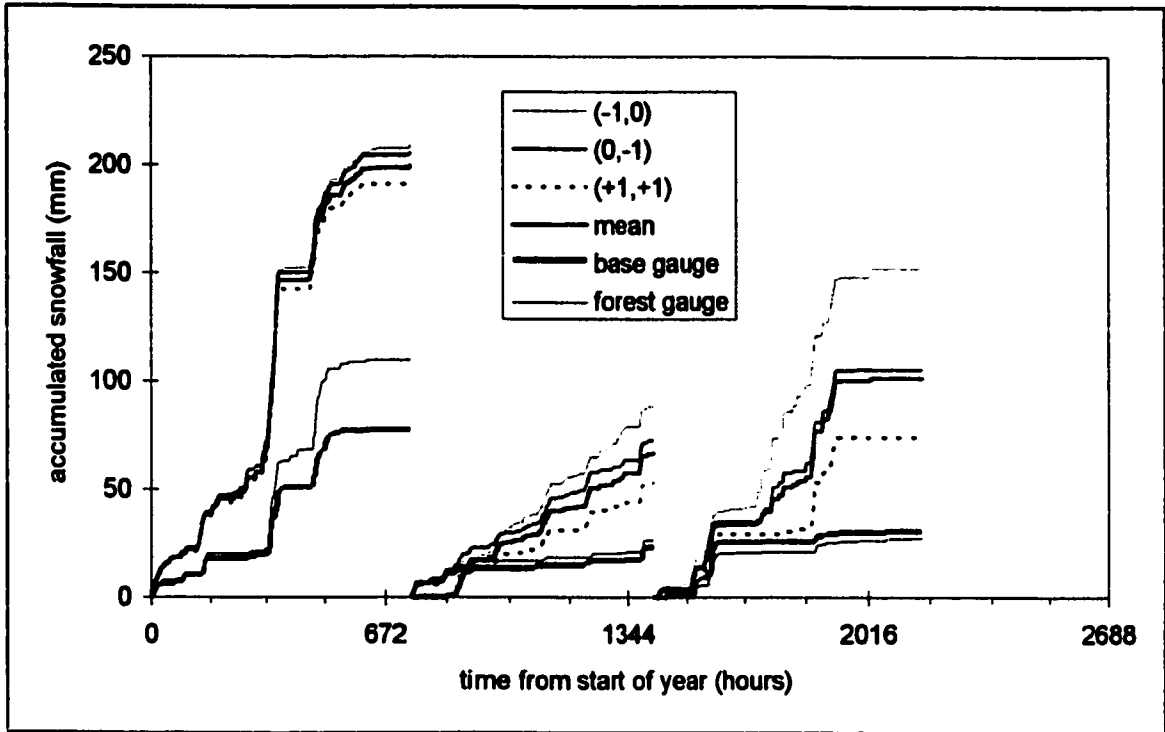


FIGURE C-4d. Snowfall raw radar-gauge comparison for 1995 at the CARE site.



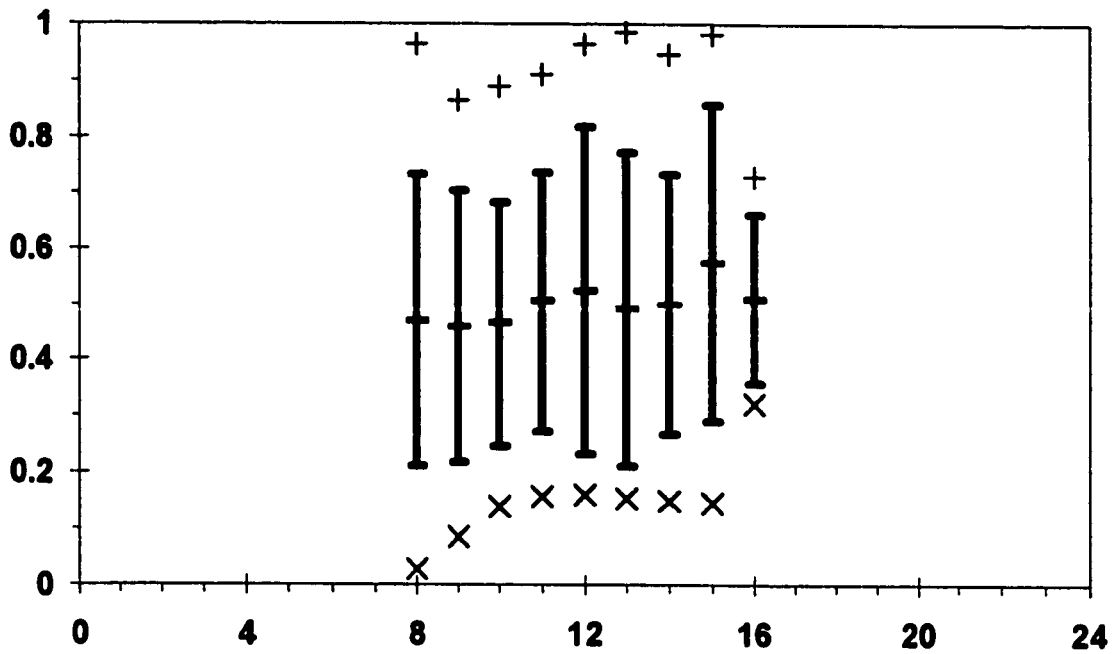


FIGURE C-5a. Average,  $\pm 1$  standard deviation, non-unity maximum, non-zero minimum ratio of measured to computed clear sky hourly radiation at Elora and CARE for November 3 (J=307) to December 21, 1995 (J=355).

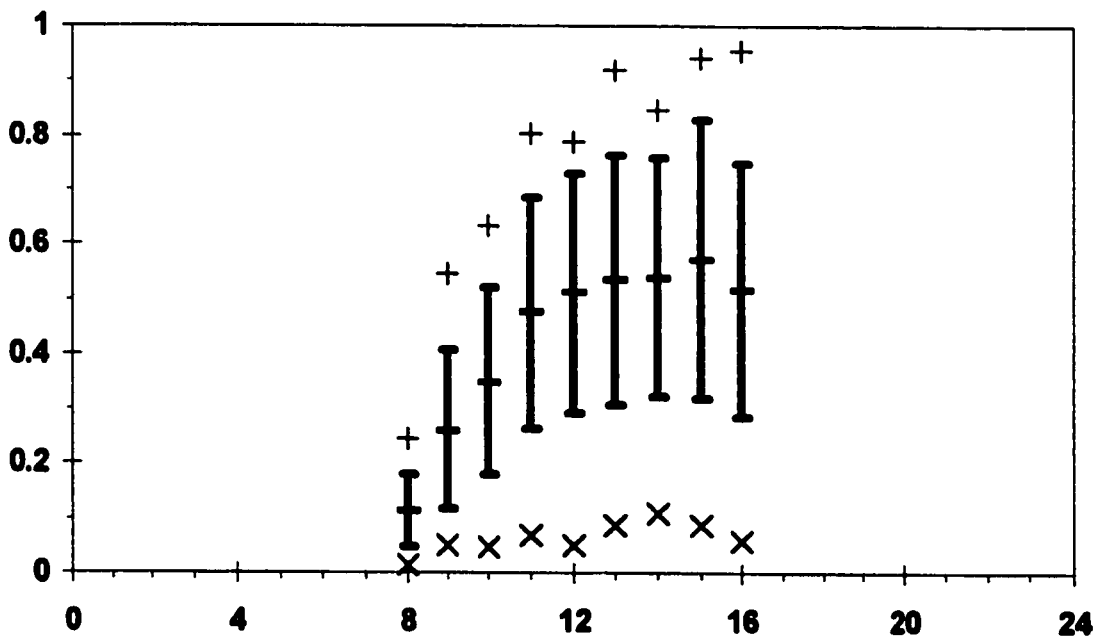


FIGURE C-5b. As in Figure C-7a, for December 22, 1995 (J=356) to February 7, 1996 (J=38).

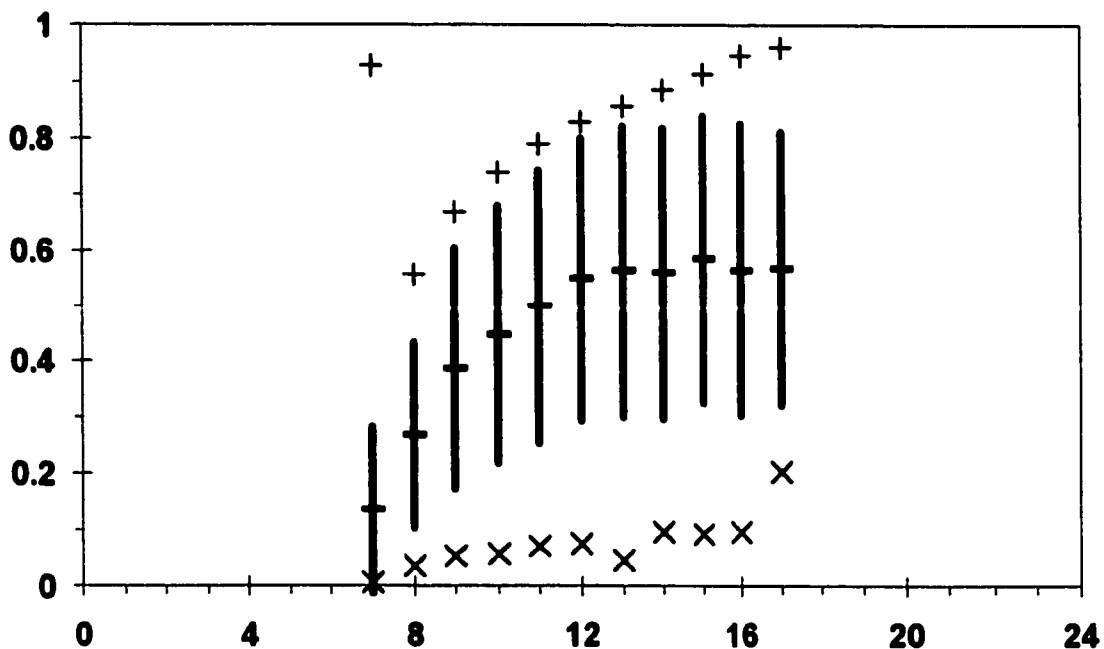


FIGURE C-5c. As in Figure C-7a, for February 8, 1996 (J=39) to March 19, 1996 (J=79).

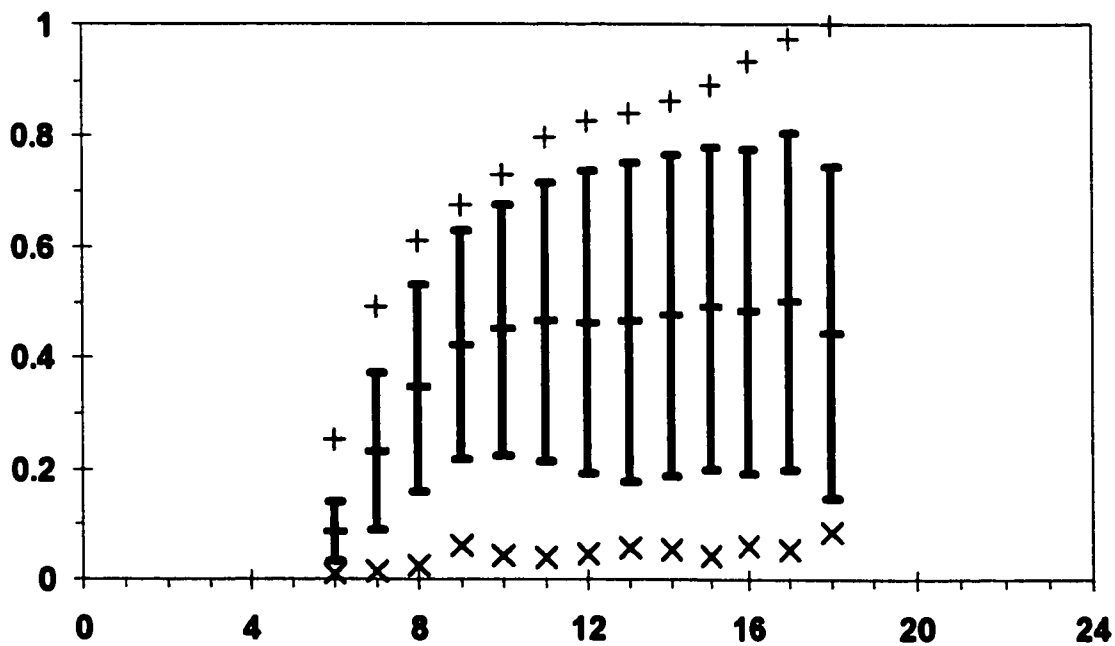


FIGURE C-5d. As in Figure C-7a, for March 20, 1996 (J=80) to April 30, 1996 (J=120).

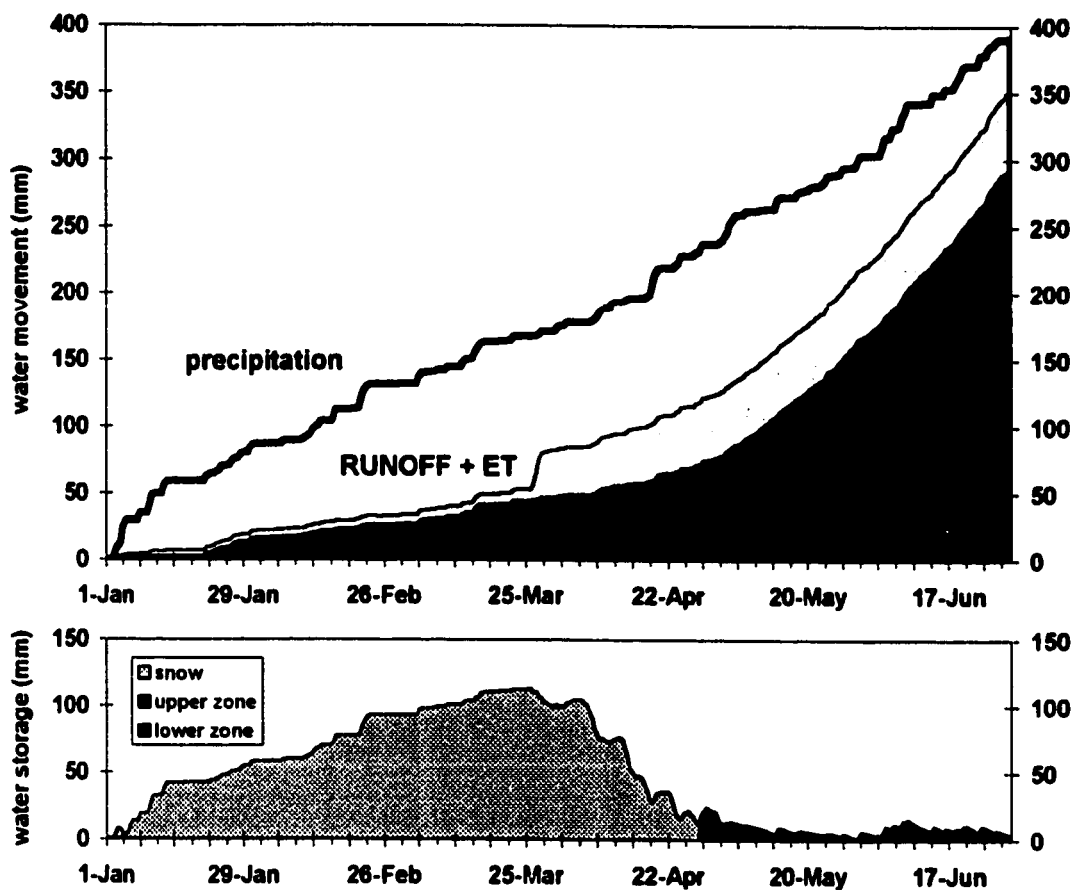


FIGURE C-6a. Water balance at one grid square in the Grand River basin for January to June 1993, before the incorporation of the advanced snow processes.

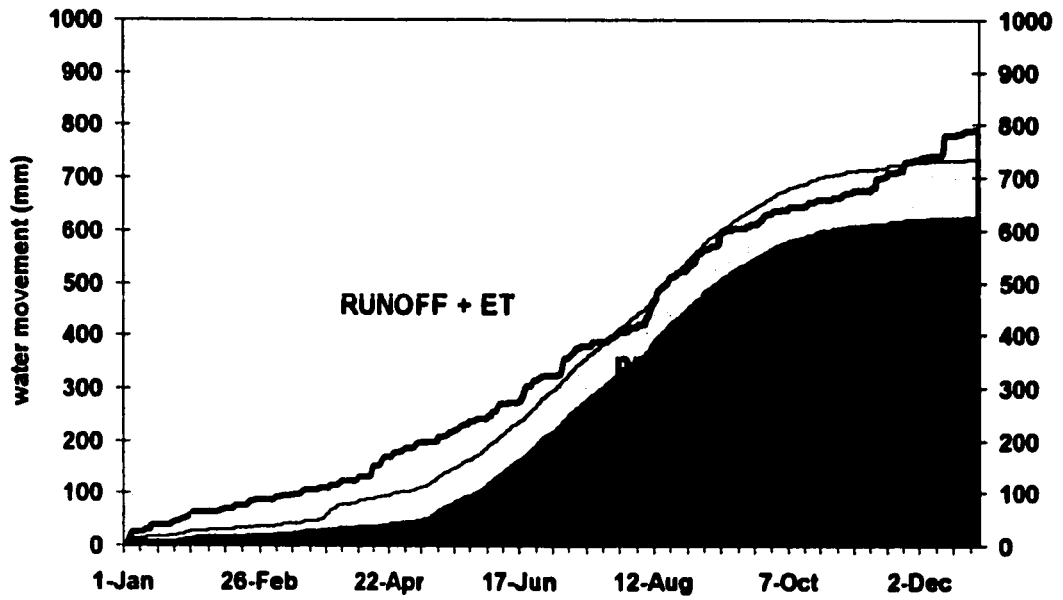


FIGURE C-6b. Annual water balance for 1993 in the Grand River, with snow processes incorporated.

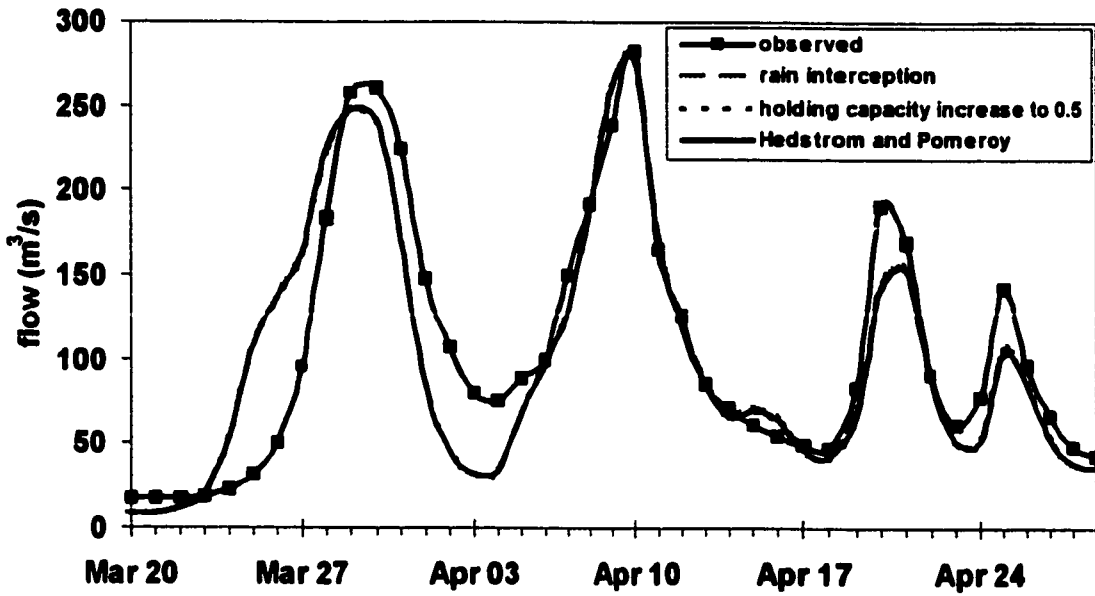


FIGURE C-7a. Effects of different canopy snow interceptions formulations on the 1993 Grand River at Galt streamflow, for the forest that are 100% deciduous throughout the basin.

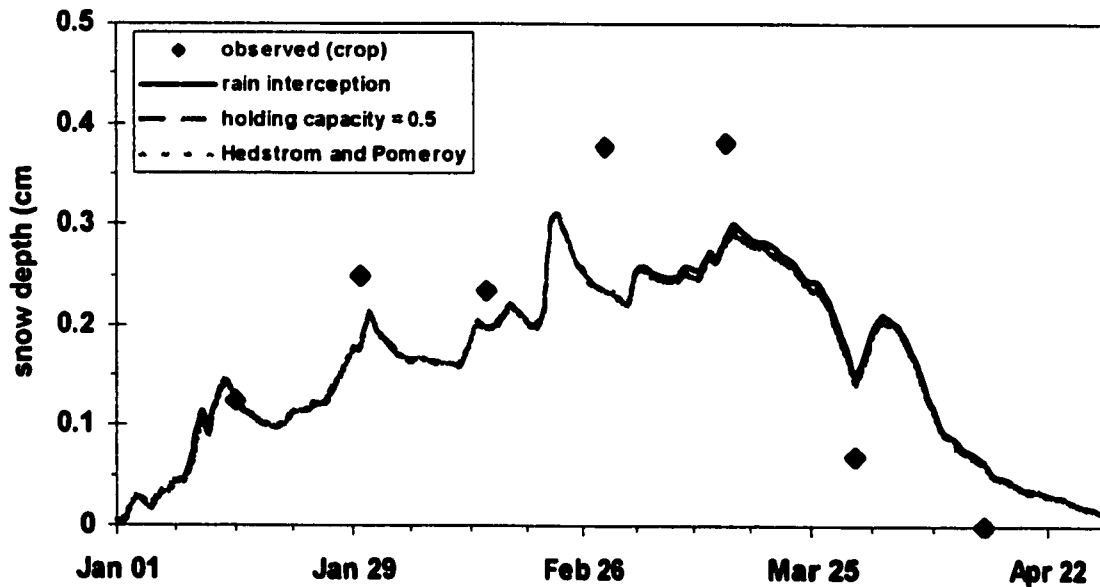


FIGURE C-7b. Effects of different canopy snow interceptions formulations on the forest snow depth near snowcourse 2002, for 100% deciduous forest.

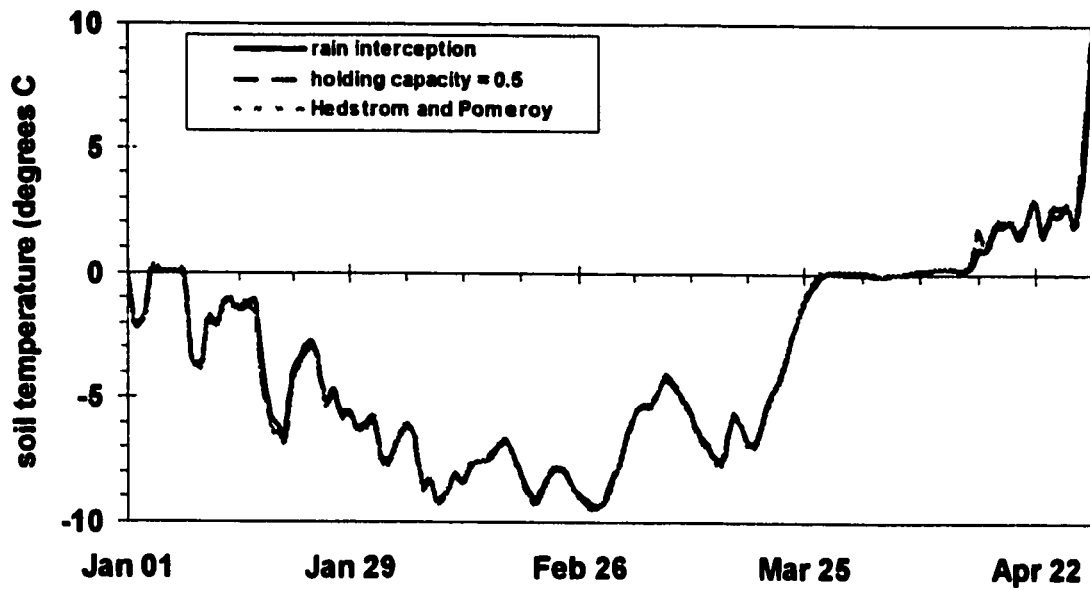


FIGURE C-7c. Effects of different canopy snow interceptions formulations on the forest soil temperature for 100% deciduous forest.

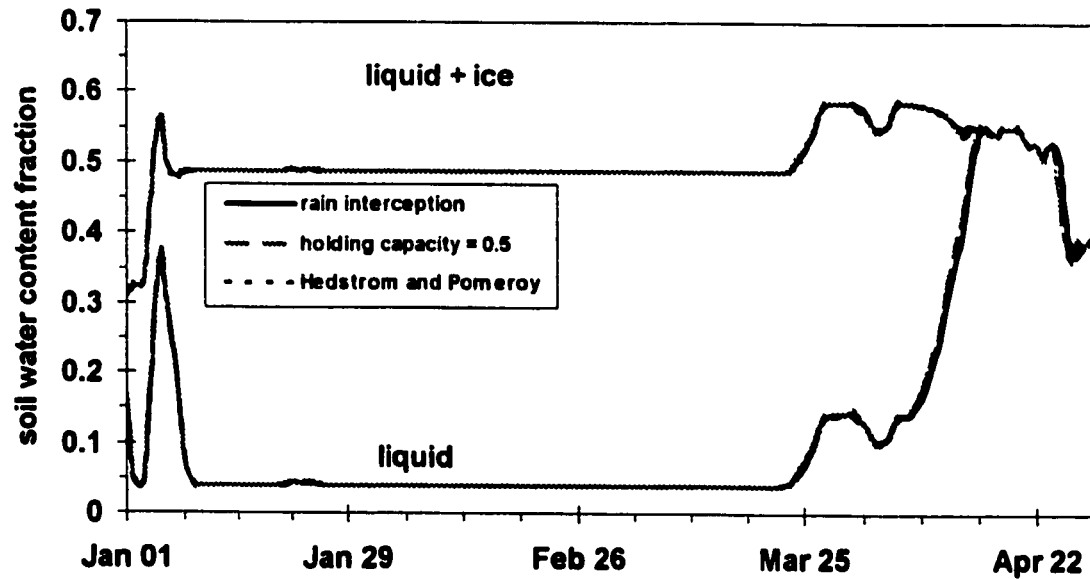


FIGURE C-7d. Effects of different canopy snow interceptions formulations on the forest soil water content, for 100% deciduous forest.

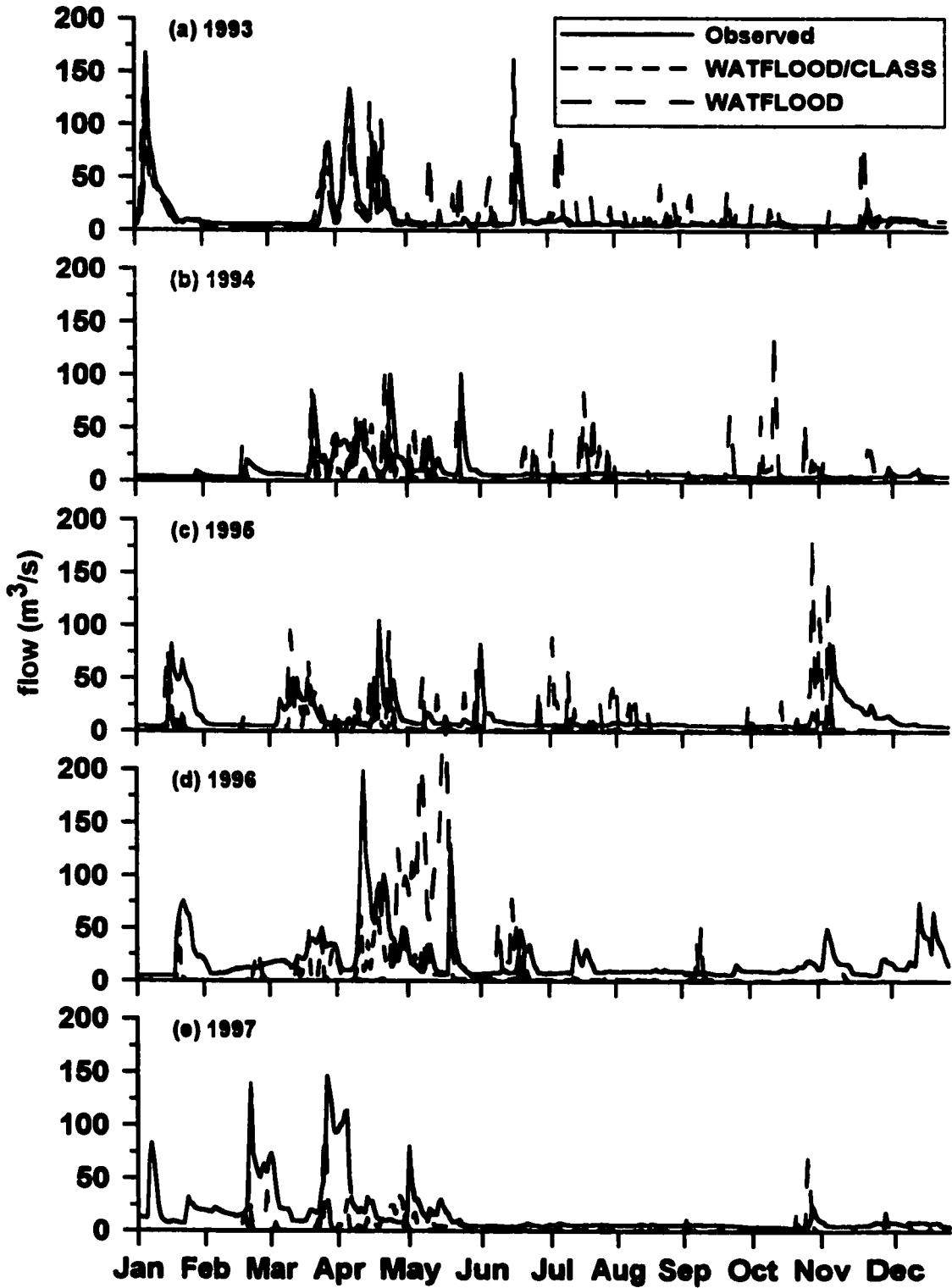


FIGURE C-8a. Comparison of simulated flows using WATFLOOD/CLASS (short dashes) versus WATFLOOD (long dashes) for the Grand River near West Montrose (02GA034).

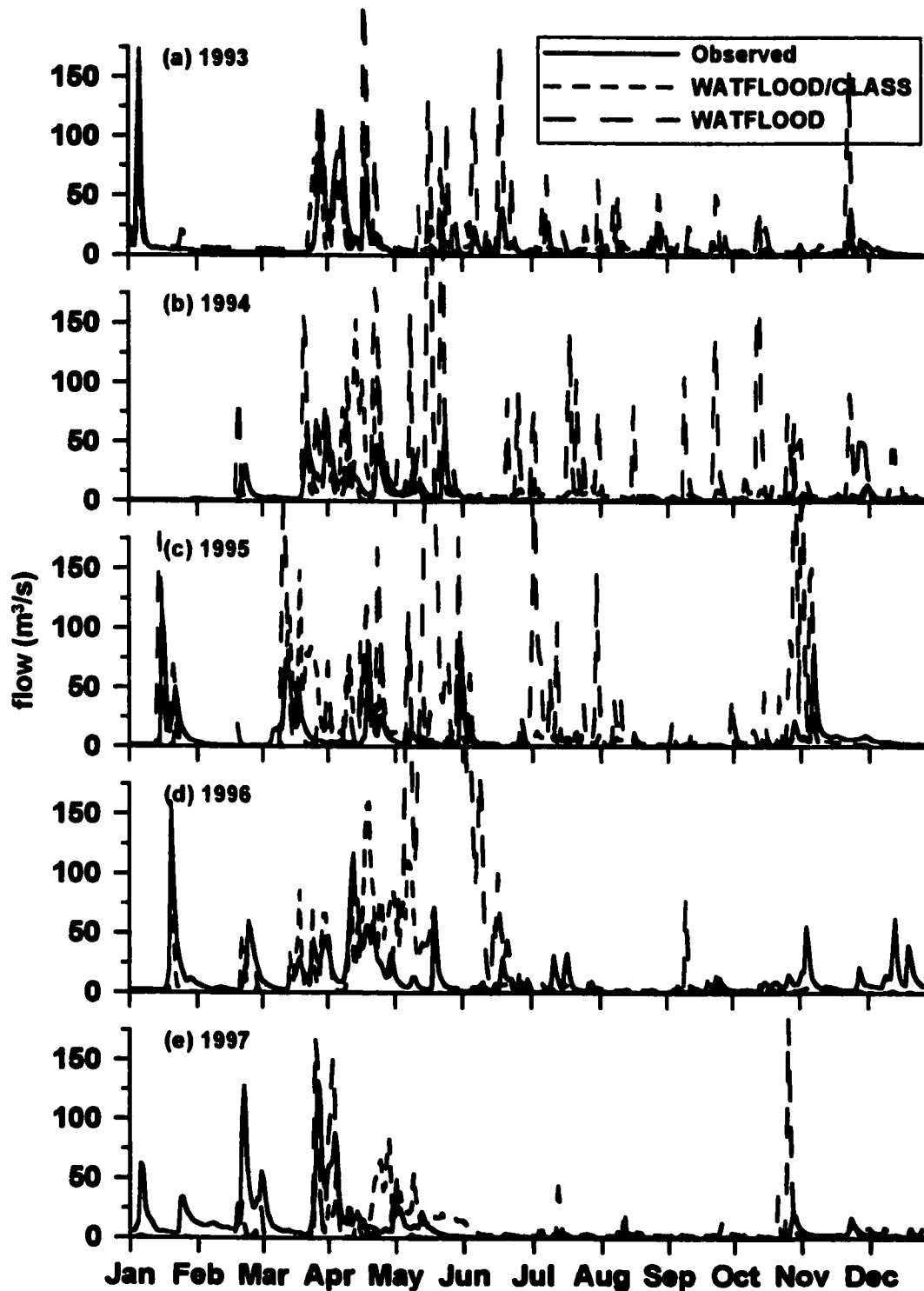


FIGURE C-8b. Comparison of simulated flows using WATFLOOD/CLASS (short dashes) versus WATFLOOD (long dashes) for the Grand River at Marsville (02GA014).



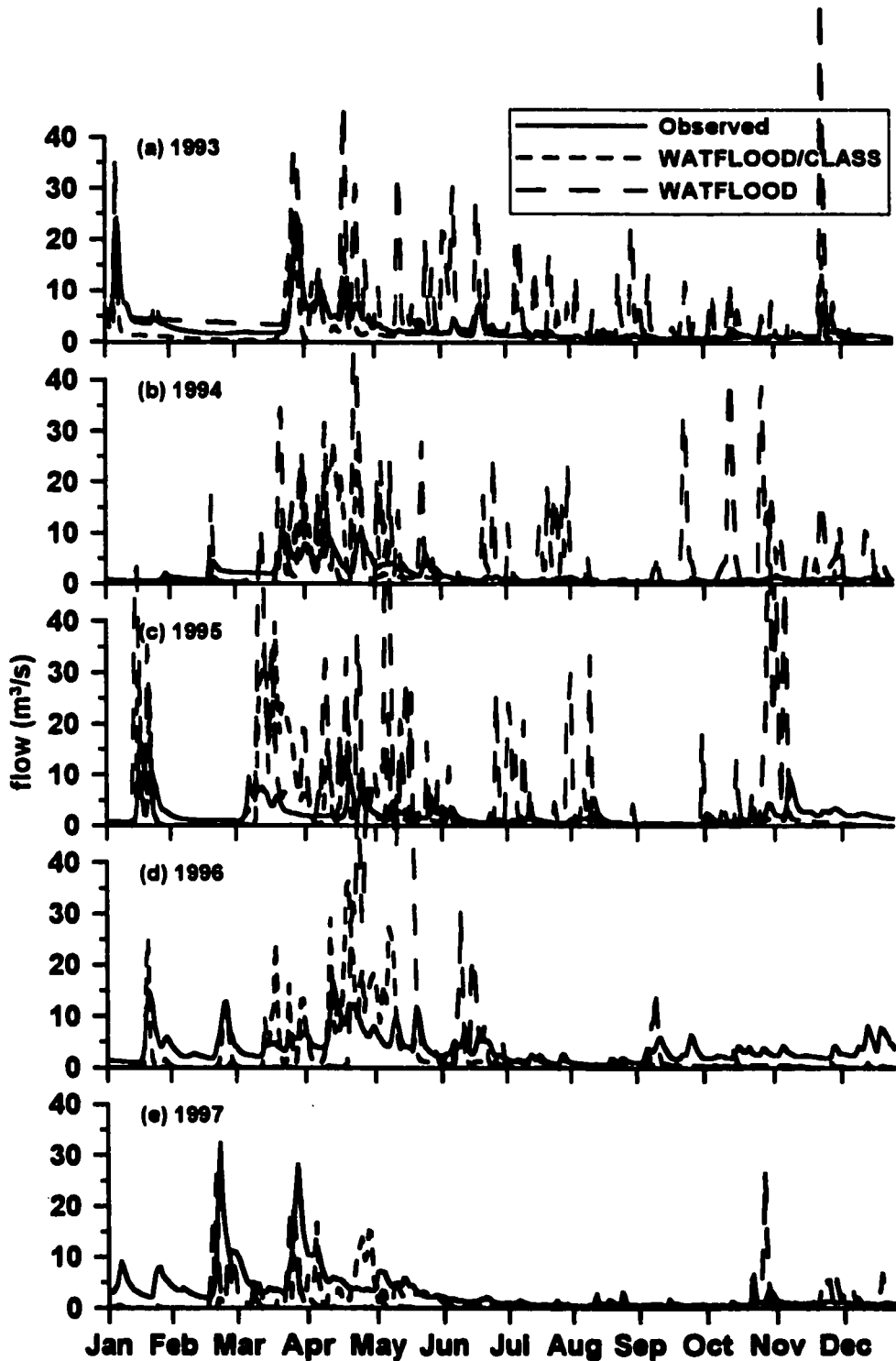


FIGURE C-8c. Comparison of simulated flows using WATFLOOD/CLASS (short dashes) versus WATFLOOD (long dashes) for the Eramosa River above Guelph (02GA029).

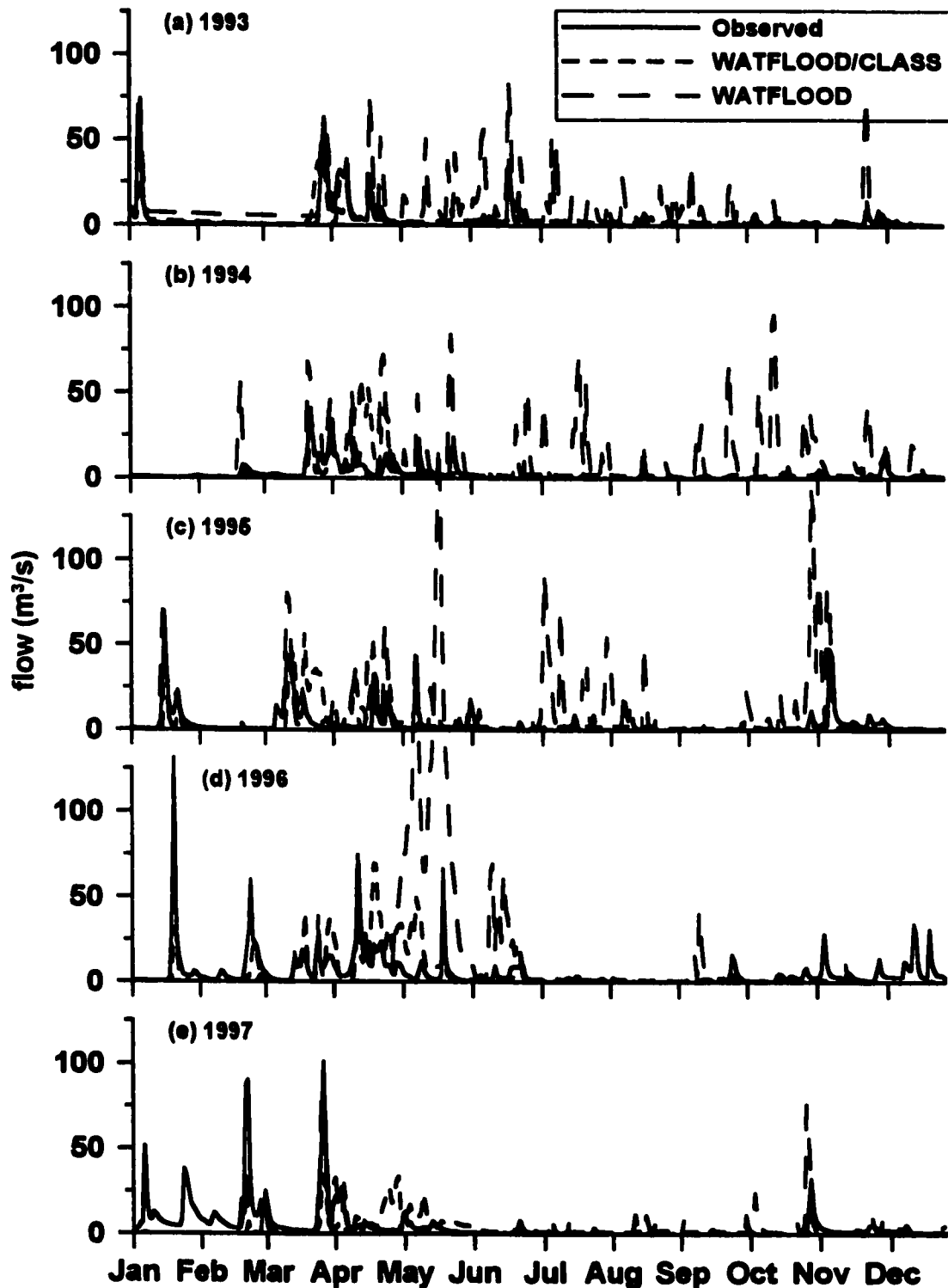


FIGURE C-8d. Comparison of simulated flows using WATFLOOD/CLASS (short dashes) versus WATFLOOD (long dashes) for the Conestogo River above Drayton (02GA039).

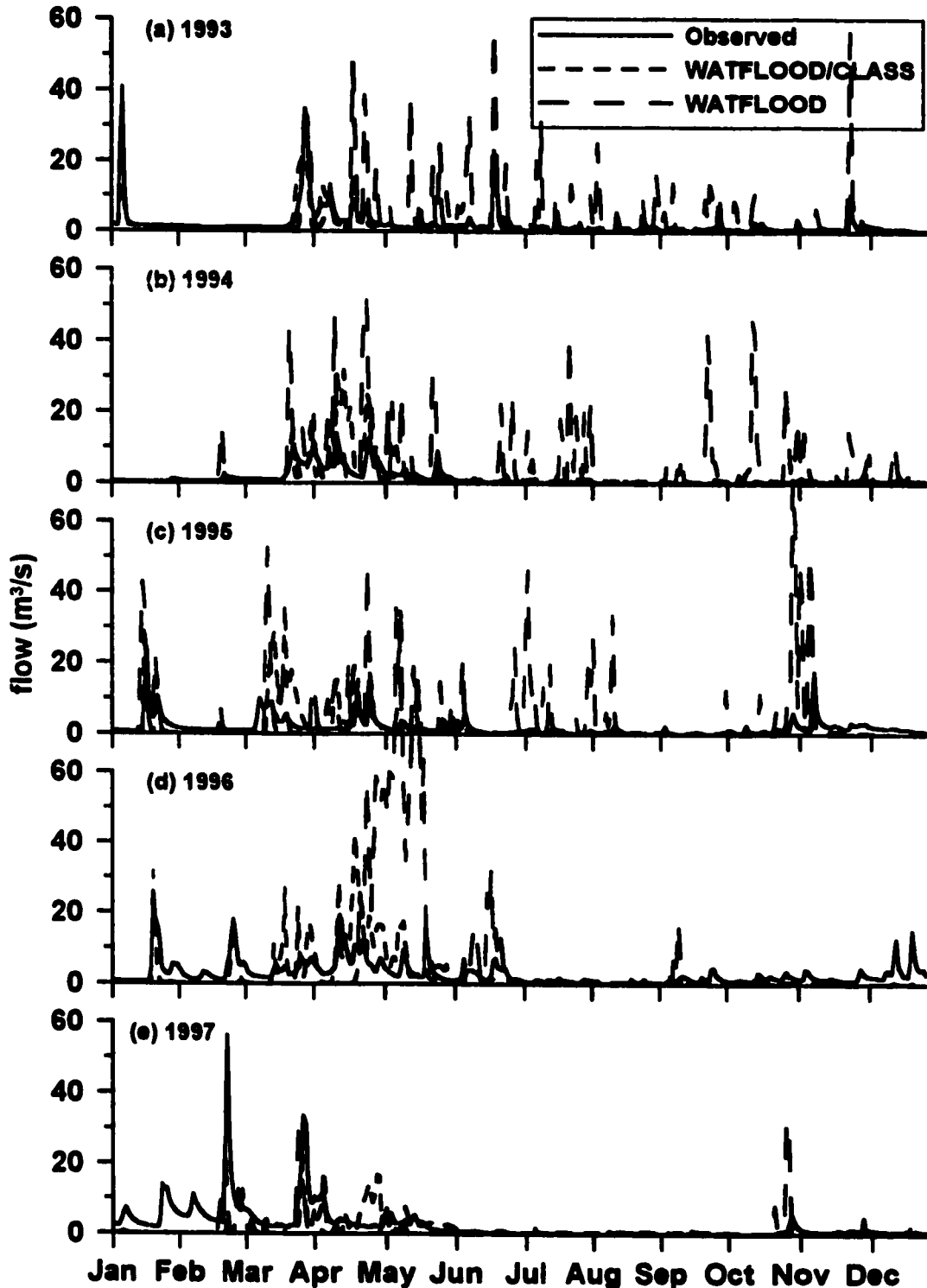


FIGURE C-8e. Comparison of simulated flows using WATFLOOD/CLASS (short dashes) versus WATFLOOD (long dashes) for the Speed River at Armstrong Mills (02GA040).

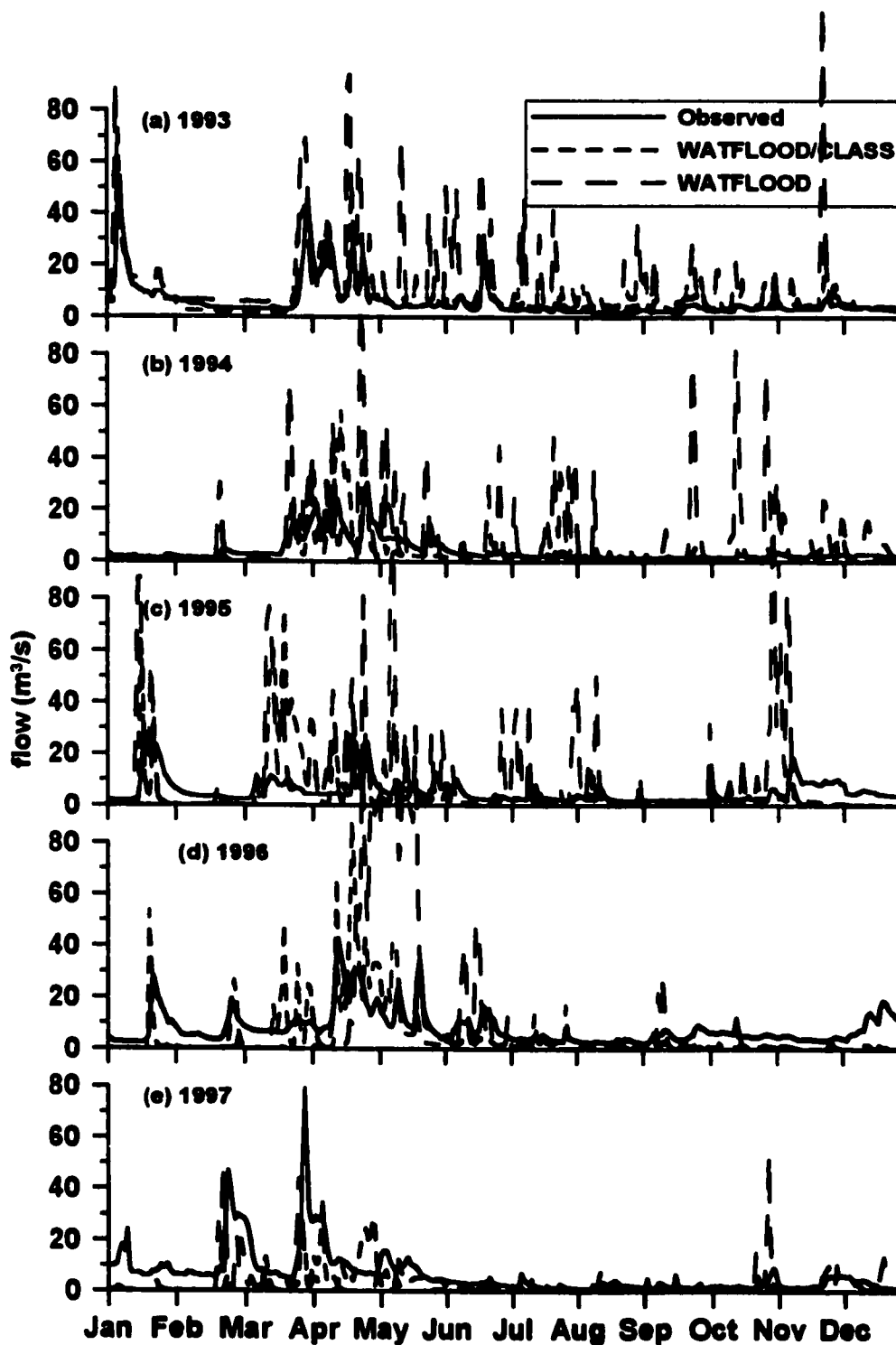


FIGURE C-8f. Comparison of simulated flows using WATFLOOD/CLASS (short dashes) versus WATFLOOD (long dashes) for the Speed River below Guelph (02GA015).

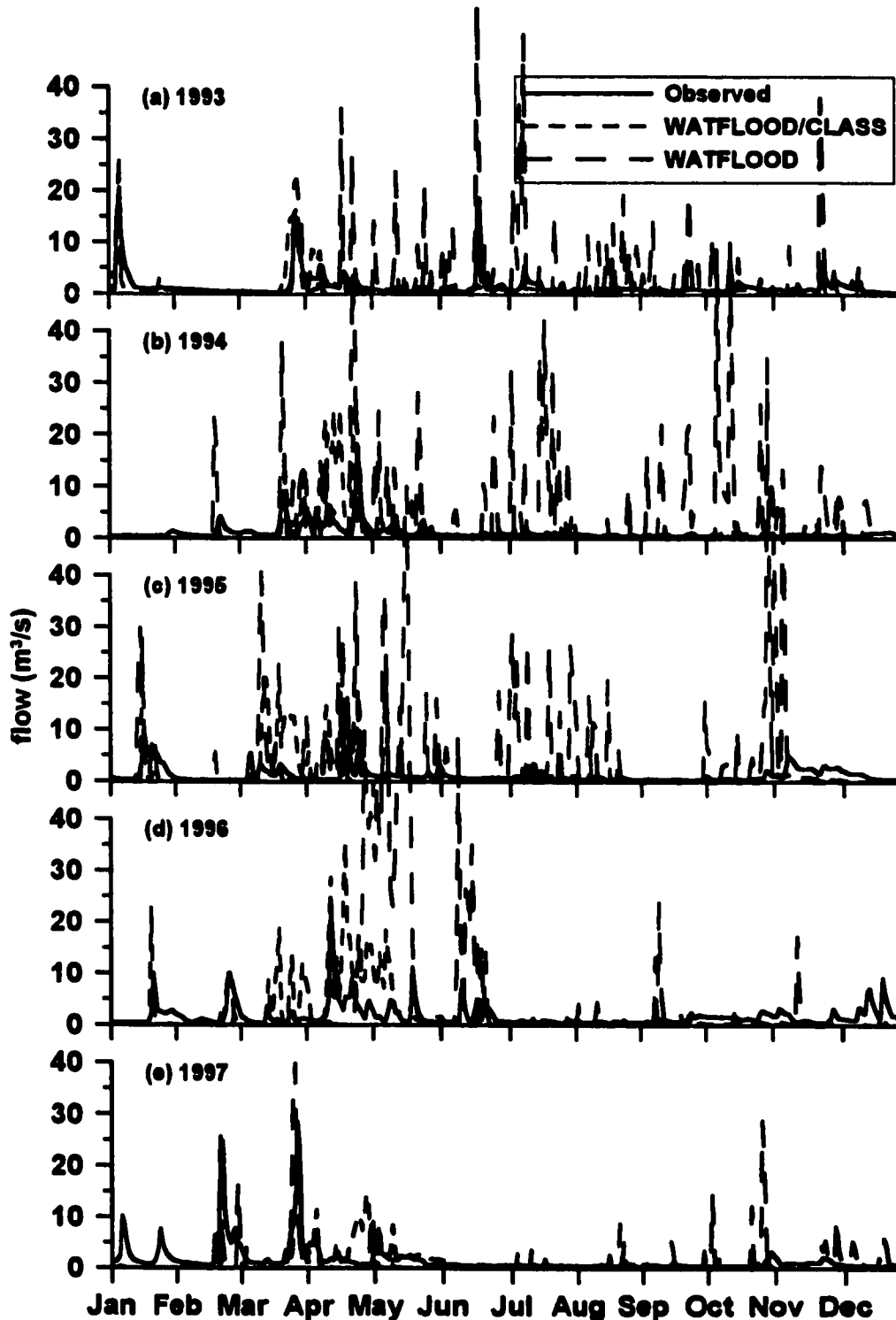


FIGURE C-8g. Comparison of simulated flows using WATFLOOD/CLASS (short dashes) versus WATFLOOD (long dashes) for the Canangagique Creek near Elmira (02GA023).

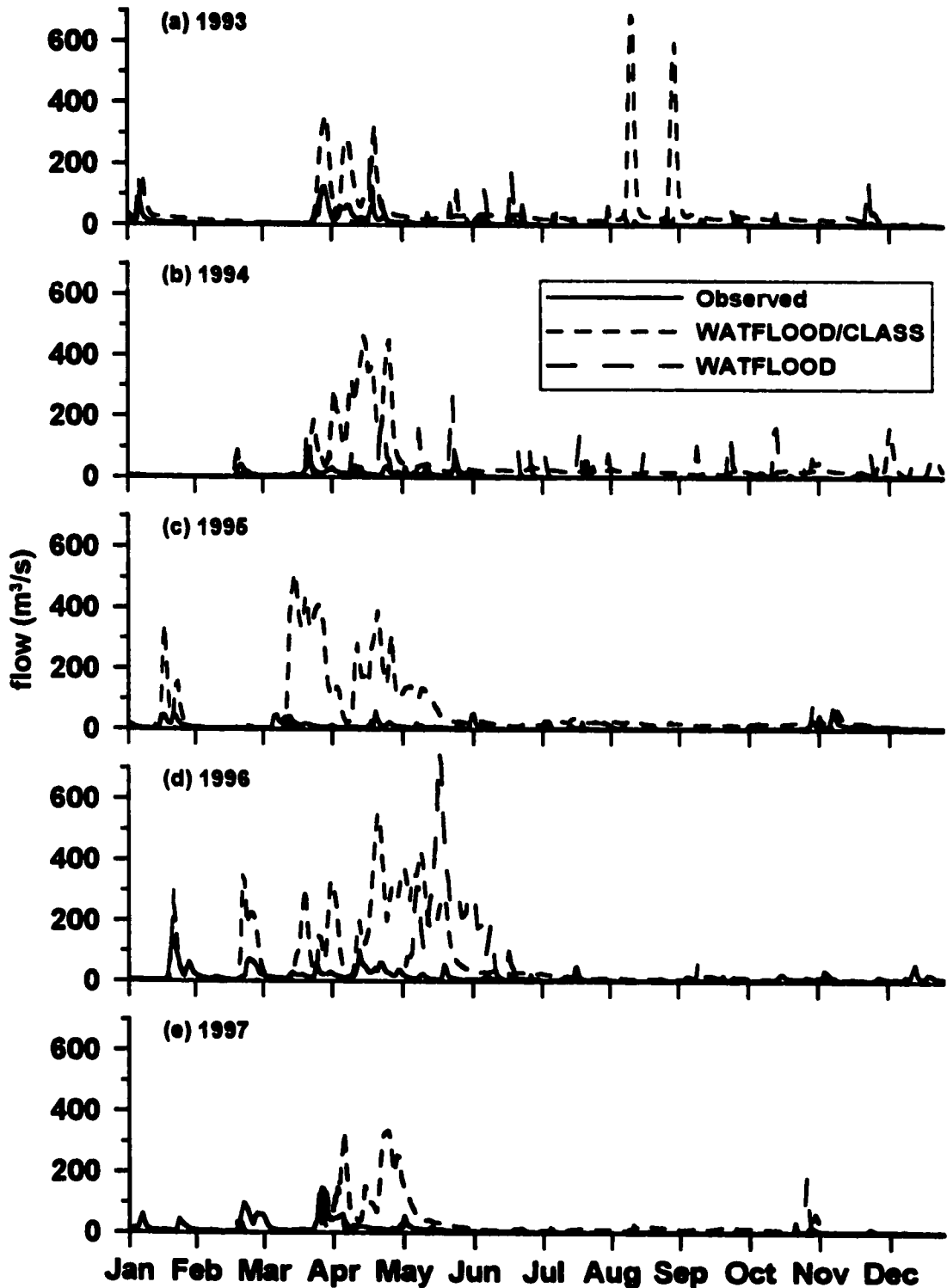


FIGURE C-8h. Comparison of simulated flows using WATFLOOD/CLASS (short dashes) versus WATFLOOD (long dashes) for the Pine River near Everett (02ED014).

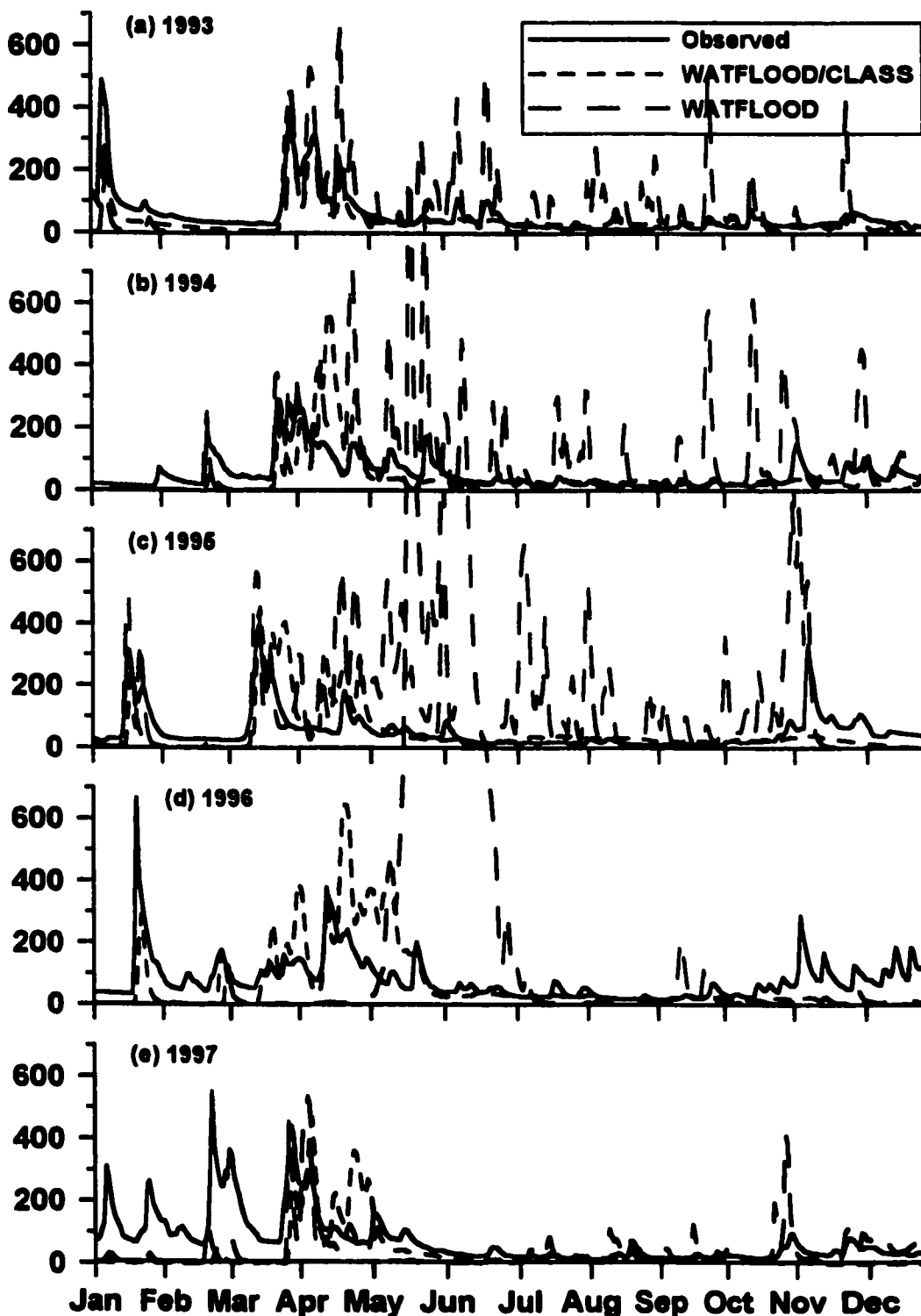


FIGURE C-8i Comparison of simulated flows using WATFLOOD/CLASS (short dashes) versus WATFLOOD (long dashes) for the Saugeen River near Port Elgin (02FC001).

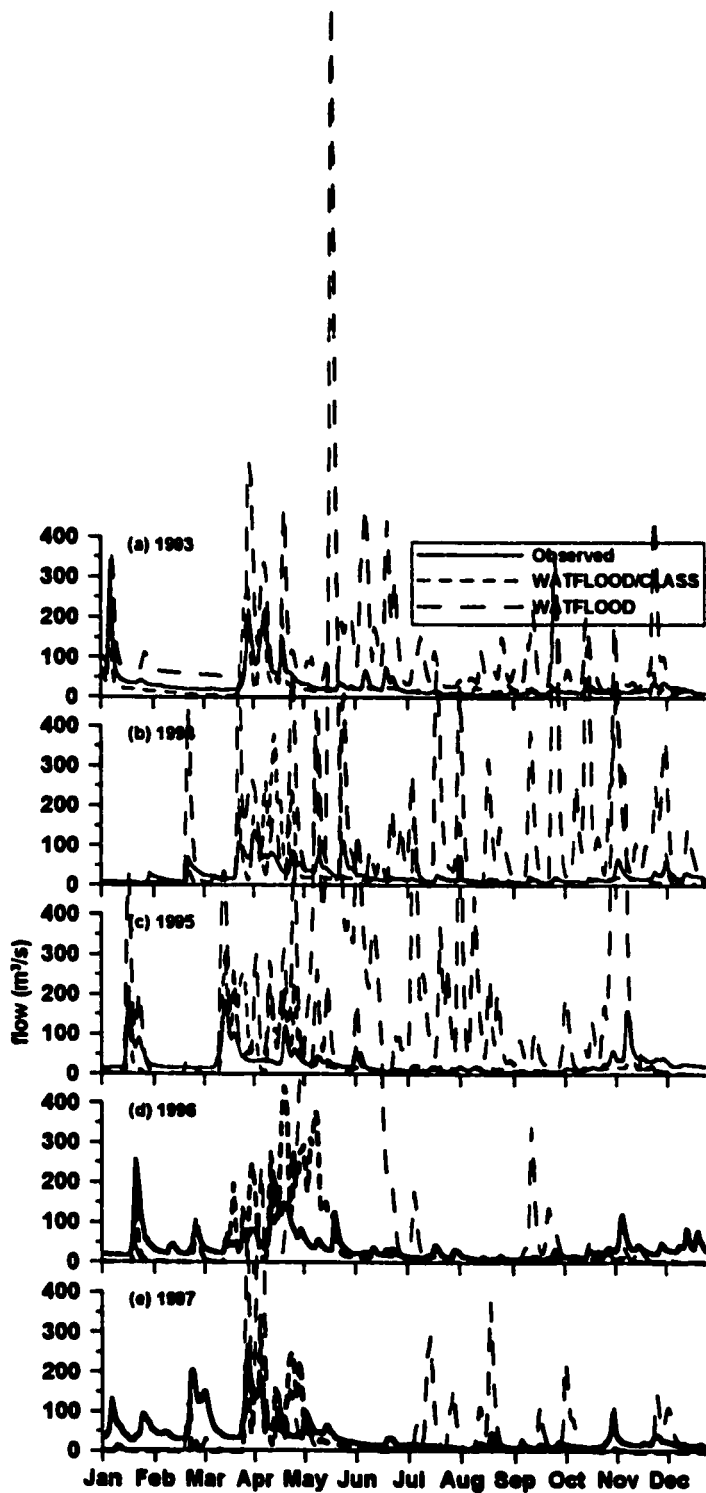


FIGURE C-8j. Comparison of simulated flows using WATFLOOD/CLASS (short dashes) versus WATFLOOD (long dashes) for the Saugeen River near Walkerton (02FC002).



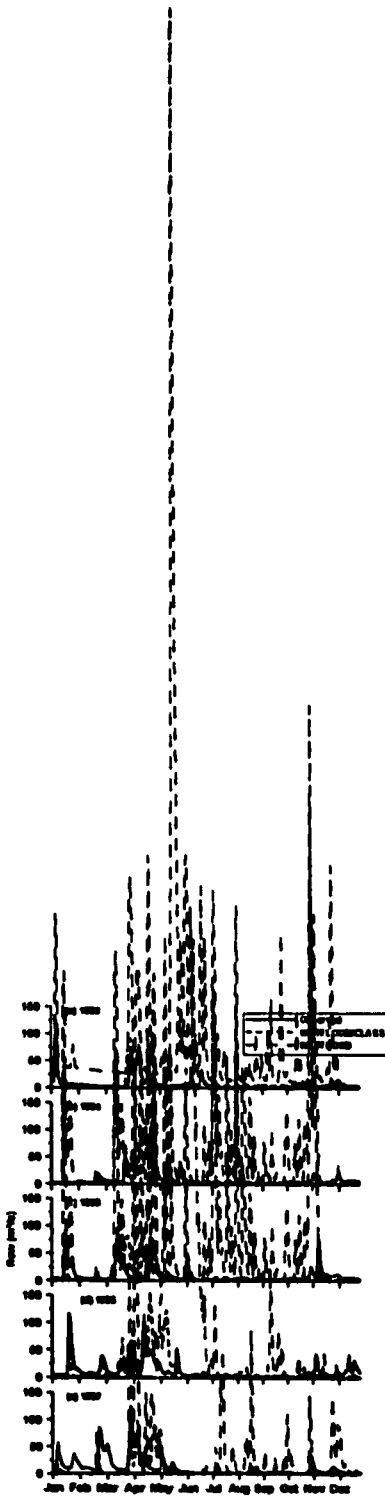


FIGURE C-8k. Comparison of simulated flows using WATFLOOD/CLASS (short dashes) versus WATFLOOD (long dashes) for the South Saugeen River near Hanover (02FC012).

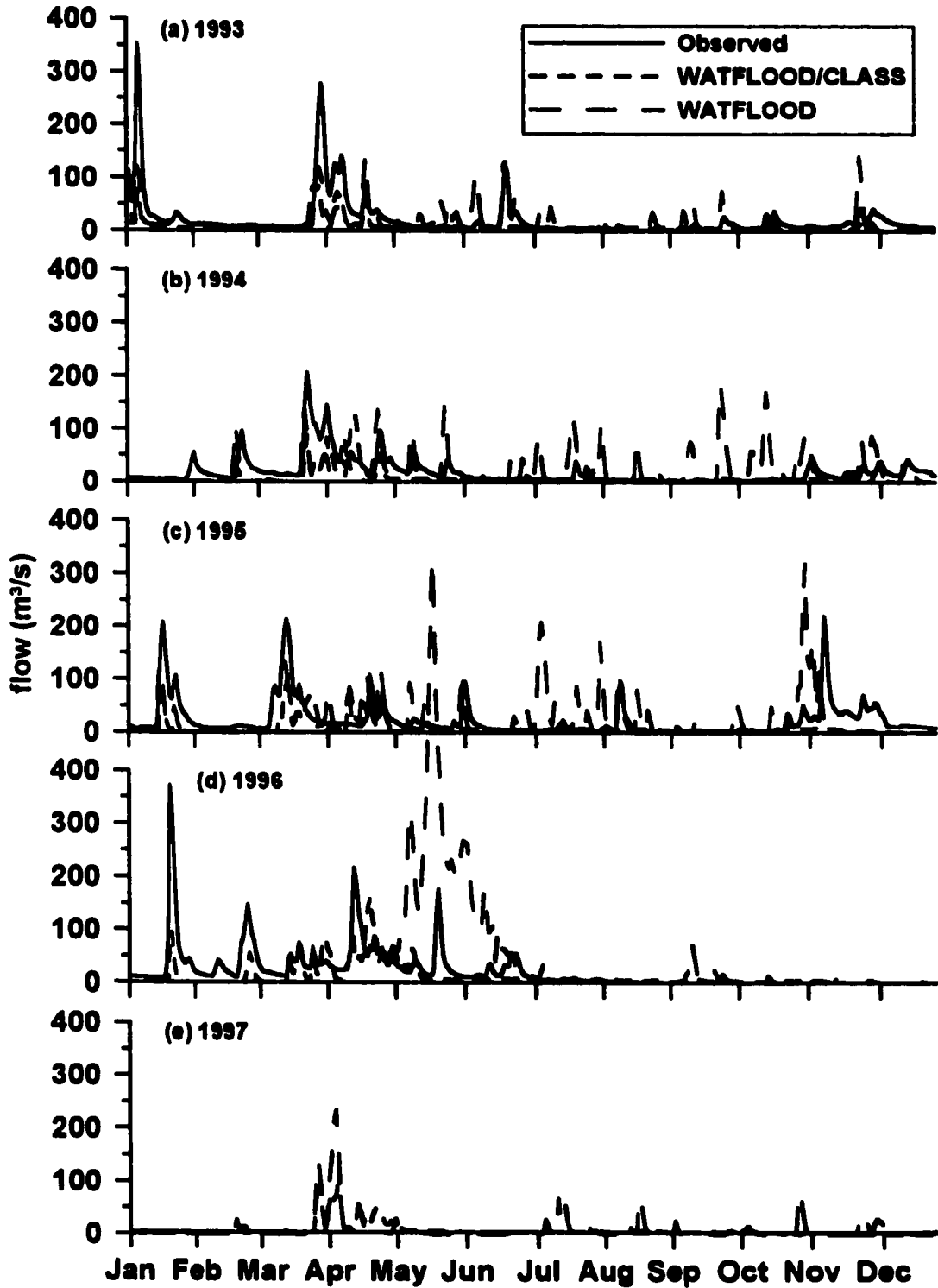


FIGURE C-81. Comparison of simulated flows using WATFLOOD/CLASS (short dashes) versus WATFLOOD (long dashes) for the Maitland River below Wingham (02FE002).

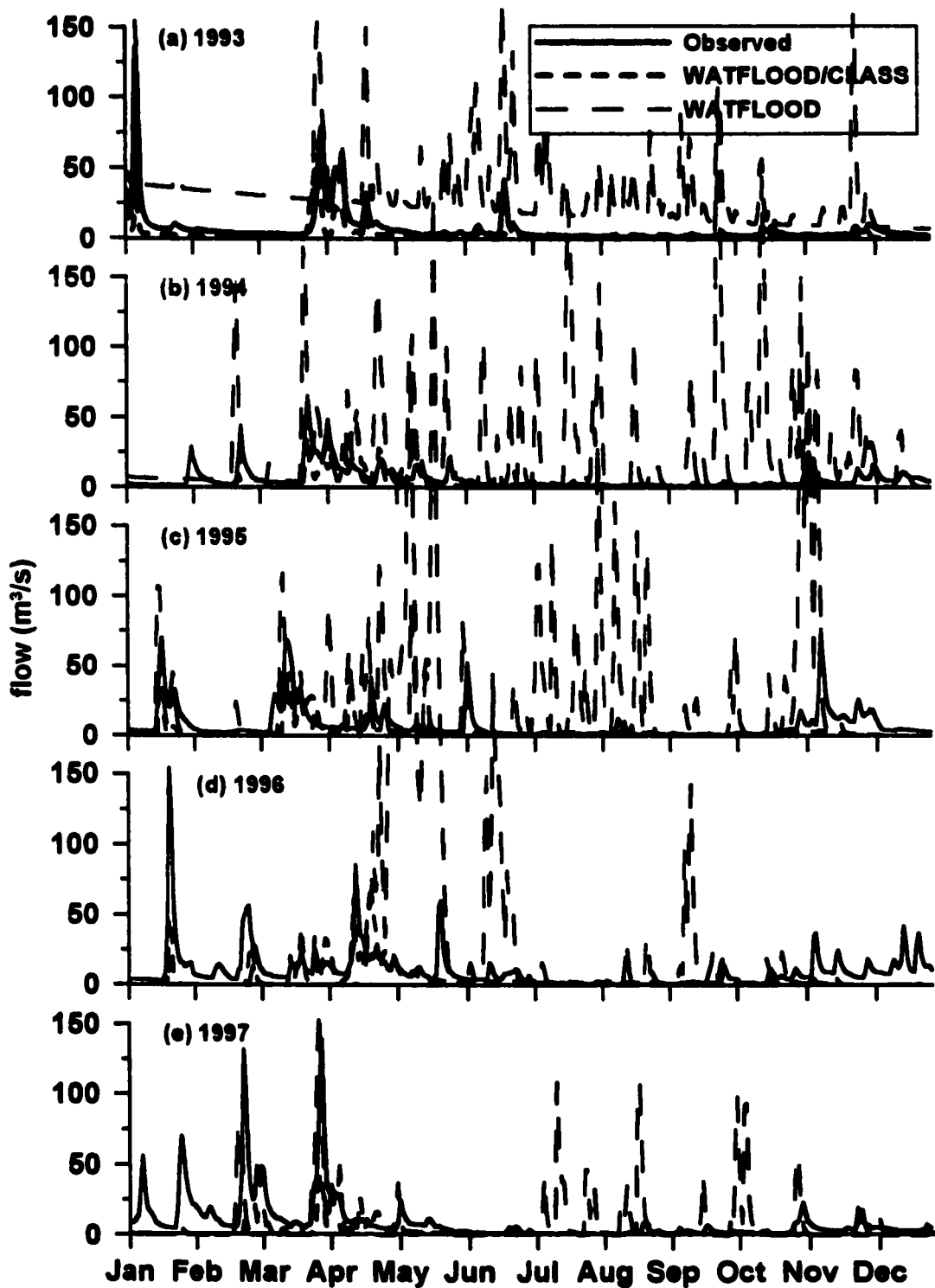


FIGURE C-8m. Comparison of simulated flows using WATFLOOD/CLASS (short dashes) versus WATFLOOD (long dashes) for the Maitland River above Wingham (02FE005).

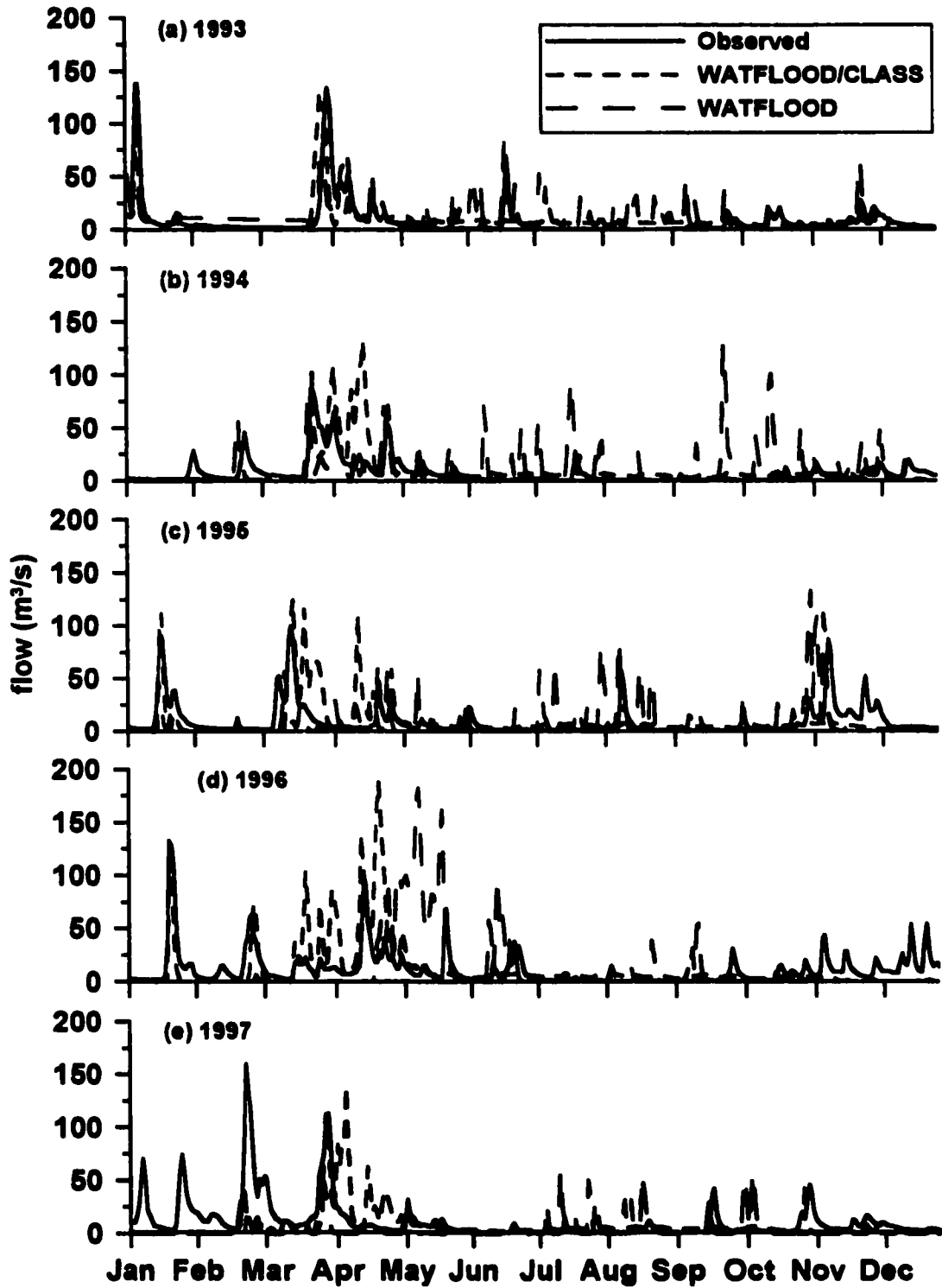


FIGURE C-8n. Comparison of simulated flows using WATFLOOD/CLASS (short dashes) versus WATFLOOD (long dashes) for the Middle Maitland River near Belgrave (02FE008).

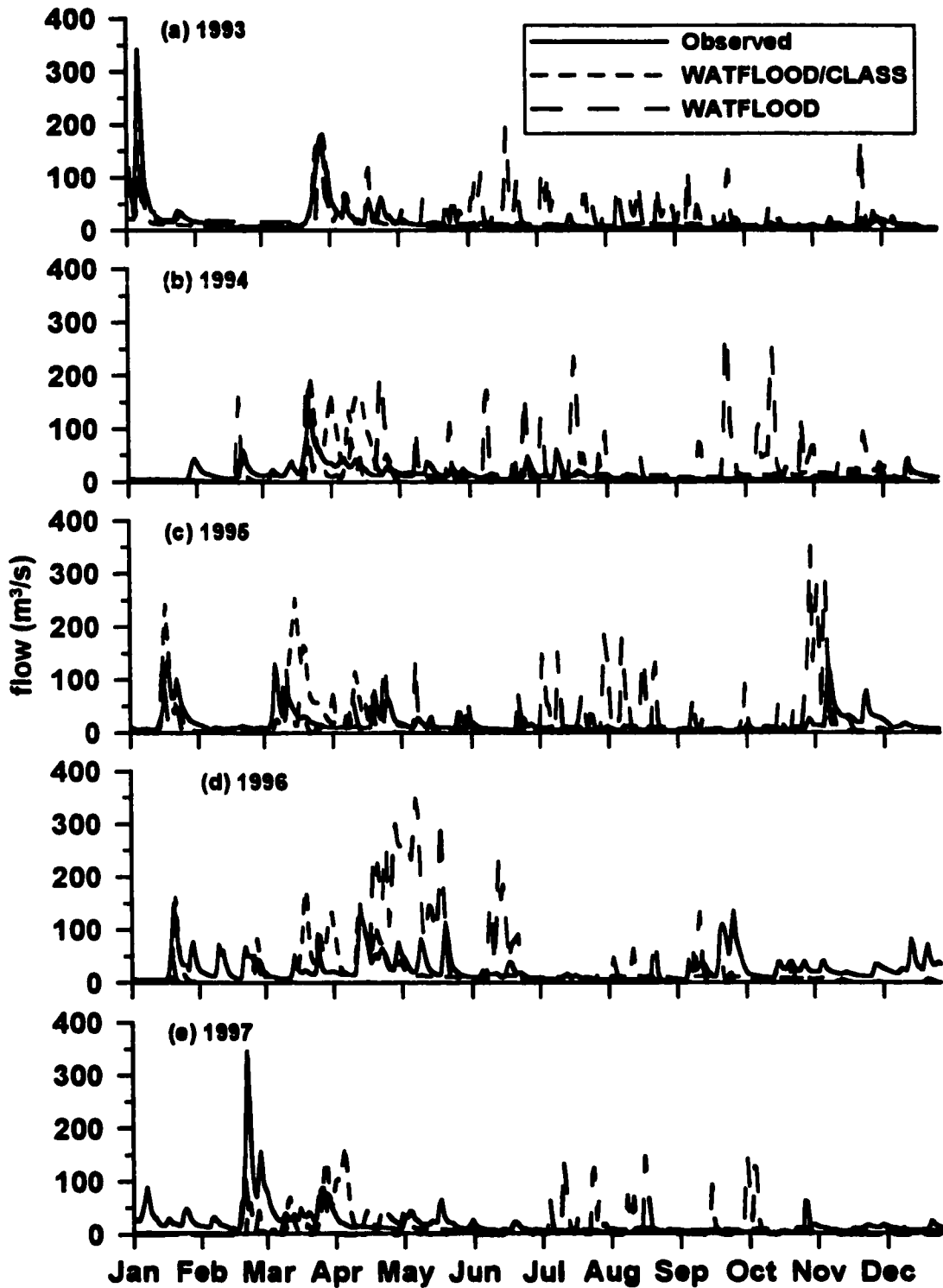


FIGURE C-8o. Comparison of simulated flows using WATFLOOD/CLASS (short dashes) versus WATFLOOD (long dashes) for the Thames River near Ealing (02GD001).

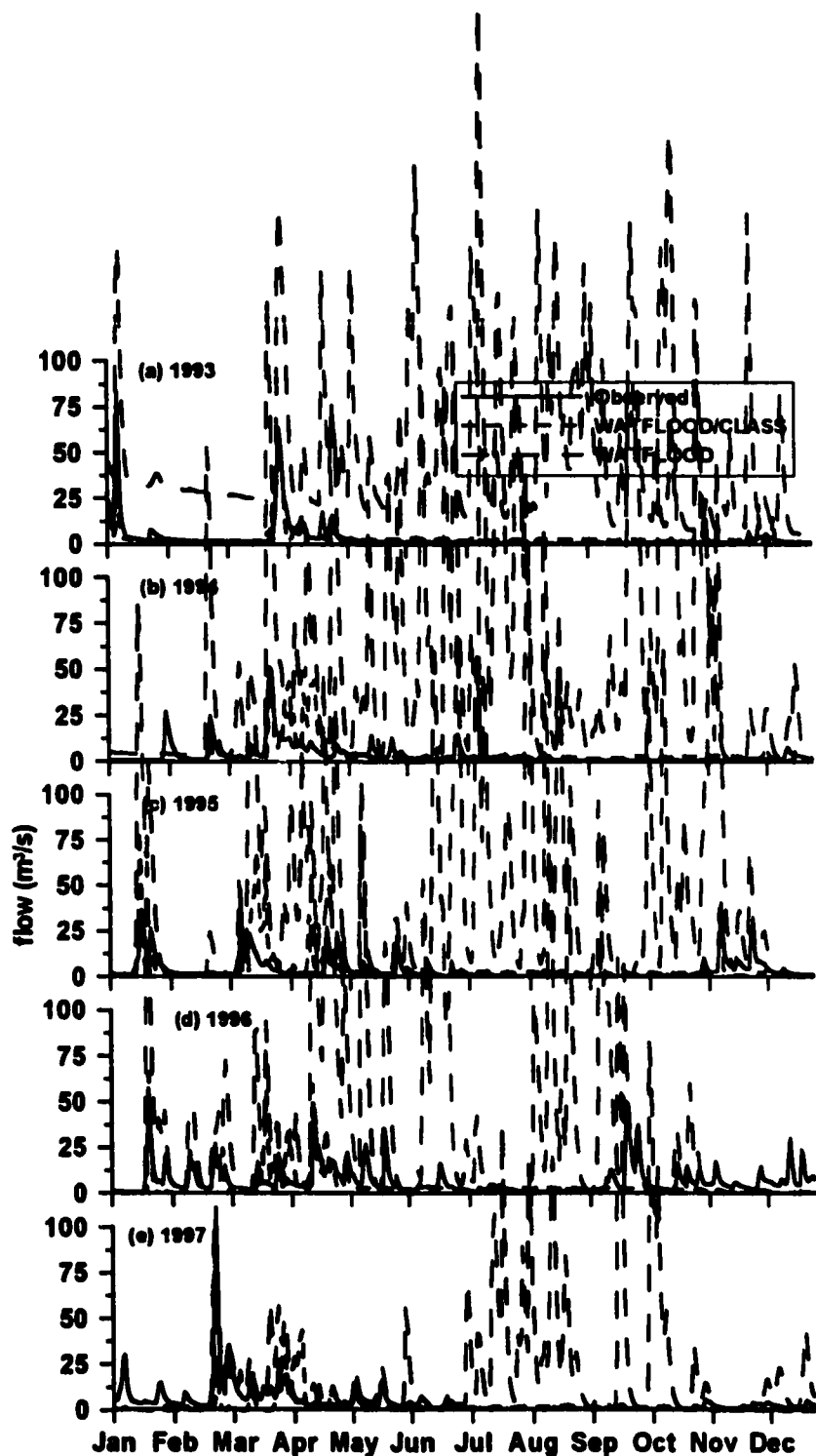


FIGURE C-8p. Comparison of simulated flows using WATFLOOD/CLASS (short dashes) versus WATFLOOD (long dashes) for the Middle Thames River at Thamesford (02GD004).

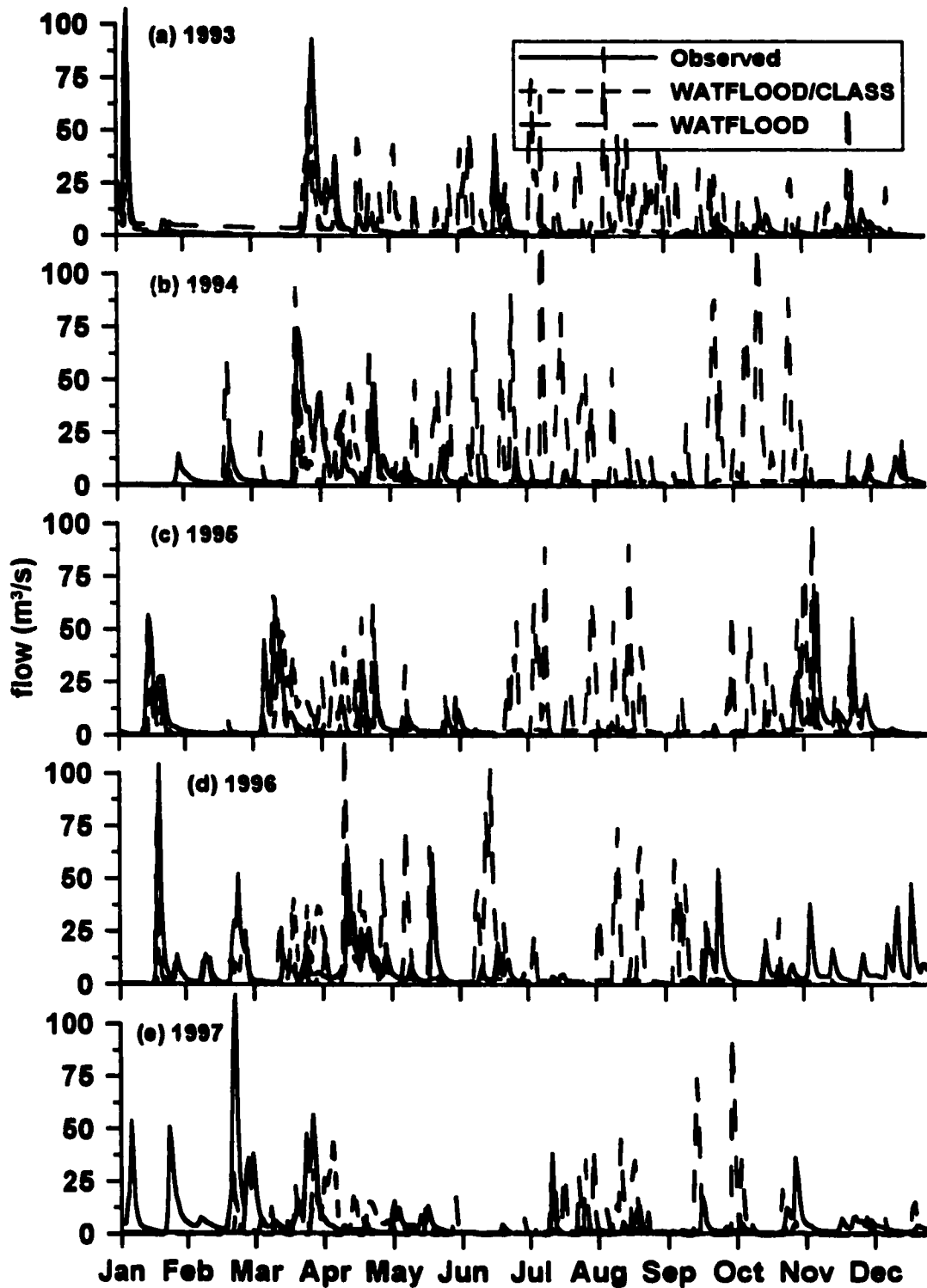


FIGURE C-8q. Comparison of simulated flows using WATFLOOD/CLASS (short dashes) versus WATFLOOD (long dashes) for the North Thames River near Mitchell (02GD014).

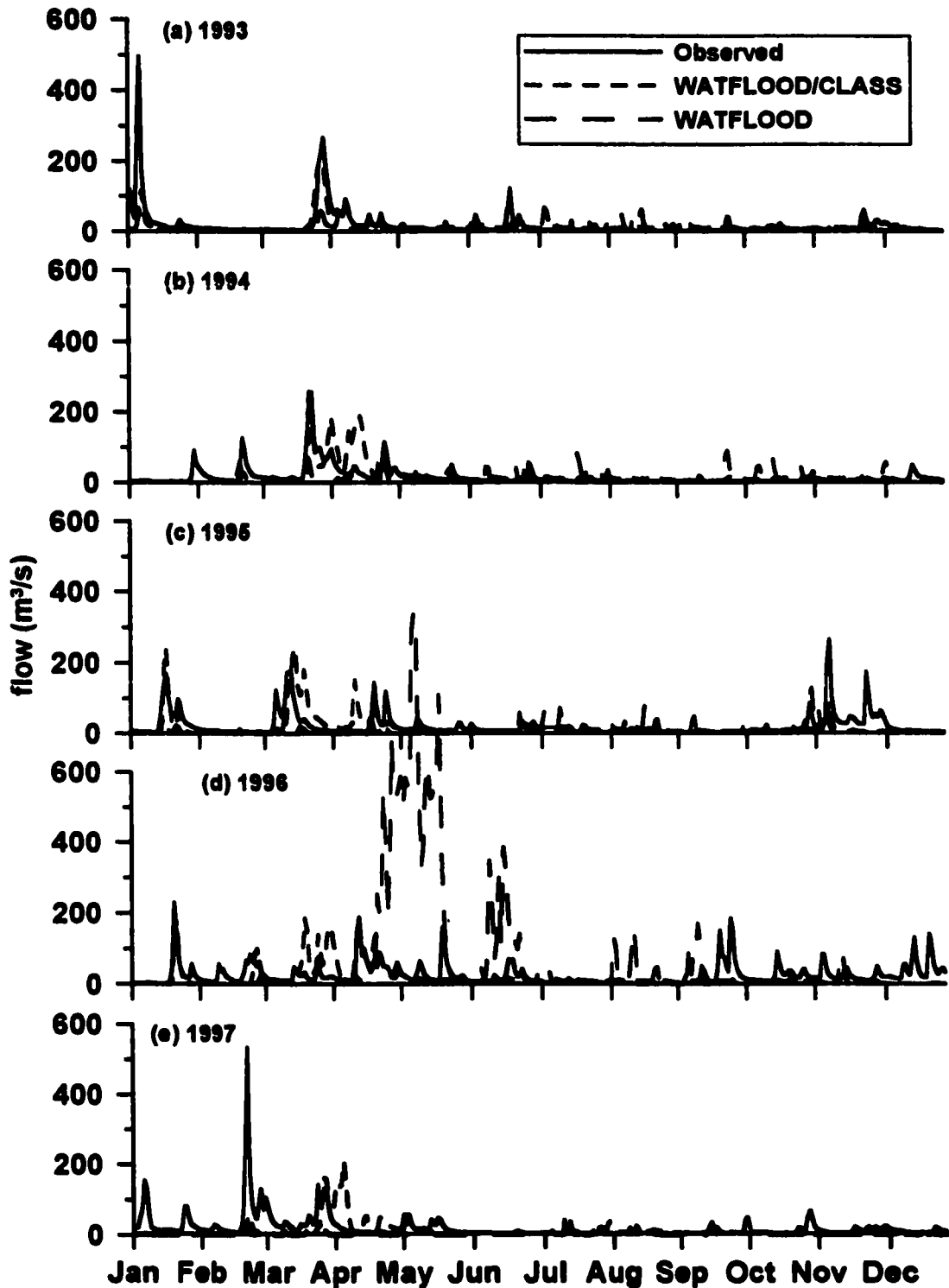
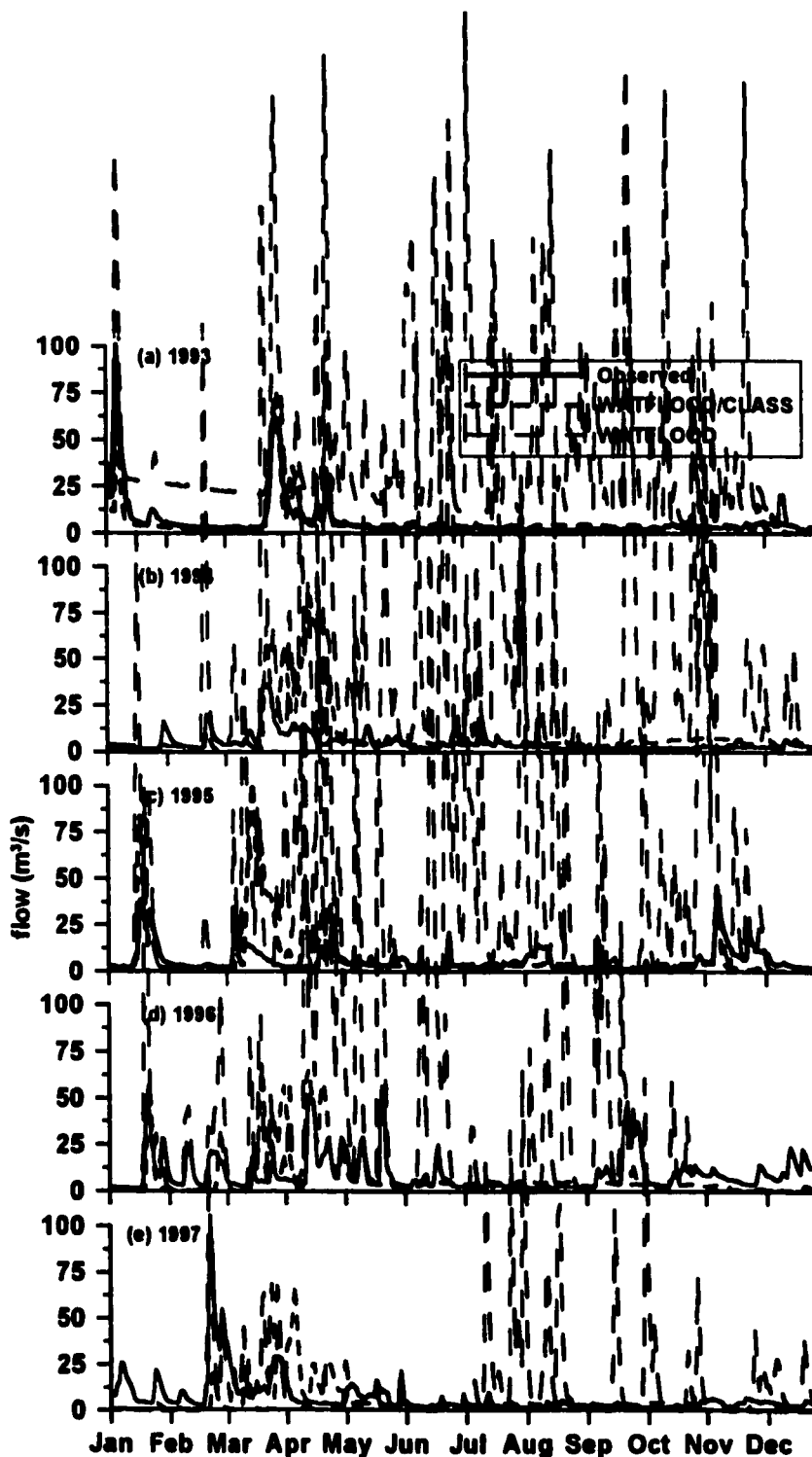


FIGURE C-8r. Comparison of simulated flows using WATFLOOD/CLASS (short dashes) versus WATFLOOD (long dashes) for the North Thames River near Thorndale (02GD015).





Jan Feb Mar Apr May Jun Jul Aug Sep Oct Nov Dec  
 FIGURE C-8s. Comparison of simulated flows using WATFLOOD/CLASS (short dashes) versus WATFLOOD (long dashes) for the Thames River at Ingersoll (02GD016).

# Appendix D: DATA COLLECTED

---

## D.1 FRESH SNOW DENSITY

TABLE D-1a. Raw fresh snow density data: mass, depth and area measurements for samples 1 through 5, with snowfall event start and end dates and times taken from sonic snow depth sampling at the University of Waterloo north campus weather station. Notes that event 2 occurred in 3 periods.

measurement	1	2	3	4	5
start date	1999.I.08	1999.I.09	1999.I.12	1999.I.12	1999.I.13
time	18:00	17:00	10:30	22:00	11:00
end date	1999.I.09	1999.I.12	1999.I.12	1999.I.13	1999.I.14
time	17:00	10:30	22:00	11:00	22:30
gross mass (g)	1400	1850	1070	2850	2110
tare mass (g)	500	500	495	510	530
snow depth (cm)					
1, 13	3.6	5.6	1.9	15.2	8.5, 3.6
2, 14		5.9	2.0	13.8	7.3, 2.9
3, 15		6.1	2.0	13.9	6.1, 8.1
4, 16		5.7	2.1	13.2	5.1, 7.1
5, 17		5.7	2.0	15.2	4.1, 6.2
6, 18		5.9	2.1	14.1	3.2, 5.5
7, 19		6.3	2.1	13.9	2.8, 4.7
8, 20		6.7	2.0	13.6	8.2, 3.5
9, 21		6.6	2.0	15.2	7.1, 3.2
10		6.3	2.0	14.2	6.2
11		5.9	1.9	14.0	5.3
12		5.8	1.9	13.5	4.5
length (cm)	71.5	71.5	71.5	71.5	71.5
width (cm)	35.5	35.5	35.5	35.5	35.5
standard deviation of T	0.189	2.063	0.539	1.464	0.946
maximum T (°C)	-8.77	-8.25	-6.35	-8.34	-18.91
minimum T (°C)	-9.40	-15.12	-8.09	-14.48	-21.83
last T of event (°C)	-9.40	-8.72	-7.93	-14.48	-18.91
average T after event (°C)	-7.61	-8.15	-	-16.09	-16.42
number of hours after event measurement taken	9	3.5	0	3.25	8.5
event start date	1999.I.08	1999.I.10	1999.I.12	1999.I.12	1999.I.14
start time	18:00	12:00	14:00	22:00	10:00
event end date	1999.I.19	1999.I.10	1999.I.12	1999.I.13	1999.I.14
end time	8:00	16:00	22:00	8:00	14:00
sample #2, event 2 start		1999.I.11 4:00			
sample #2, event 2 end		1999.I.11 7:00			
sample #2, event 3 start		1999.I.11 14:00			
sample #2, event 3 end		1999.I.12 7:00			

**TABLE D-1b. Raw fresh snow density data: mass, depth and area measurements for samples 6 through 9, with snowfall event start and end dates and times taken from sonic snow depth sampling at the UW north campus weather station.**

measurement	6	6a	6b	7	8	9	9a	9b
start date	1999.I.14	1999.I.14		1999.I.15	1999.I.24	1999.I.27	1999.I.27	
time	22:30	22:30		11:30	16:00	12:00	12:00	
end date	1999.I.15		1999.I.15	1999.I.19	1999.I.25	1999.I.28		1999.I.28
time	11:30		11:30	8:00	8:00	11:15		11:15
gross mass (g)	1540	1225	1000	960	885	1250	950	1250
tare mass (g)	540	540	905	540	495	530	530	950
snow depth (cm)			4.26 - 3.0					
1	4.4	3.2		4.4	1.7	0.7	0.2	0.5
2	4.4	3.2		2.6	1.8			
3	4.4	3.1		2.2	1.8			
4	4.4	3.0		1.5	1.8			
5	4.3	2.9		1.3	1.7			
6	4.3	2.8		1.2	1.9			
7	4.5	2.9		1.5	1.8			
8	4.4	2.8		3.2	1.9			
9	4.5	3.0		1.8	1.7			
10	4.3			1.6	1.8			
11	4.2			1.1	1.8			
12	4.2			0.8	1.8			
13				1.4				
14				1.5				
15				4.3				
16				2.1				
17				1.9				
18				1.3				
19				1.5				
20				2.2				
21				1.8				
length (cm)	71.5	54.15	71.5	71.5	71.5	71.5	71.5	71.5
width (cm)	35.5	35.5	35.5	35.5	35.5	35.5	35.5	35.5
standard deviation of T	0.327	0.405	0.264	0.292	0.027	0.362	0.272	0.012
maximum T (°C)	-12.62	-12.65	-12.62	-5.38	-2.86	0.52	0.52	0.48
minimum T (°C)	-13.96	-13.96	-13.58	-6.26	-2.92	-1.21	-1.21	0.45
last T of event (°C)	-12.62	-12.89	-12.62	-5.38	-2.86	0.45	0.52	0.45
average T after event (°C)	-12.10	-12.96	-12.10	-4.85	-	-	0.46	-
hours after event measurement taken	1.5	7	1.5	1.25	0	0	1.5	0
event start date	1999.I.15	1999.I.15	1999.I.15	1999.I.16	1999.I.25	1999.I.27	1999.I.27	1999.I.28
start time	1:00	1:00	4:30	5:00	7:00	12:00	12:00	10:00
event end date	1999.I.15	1999.I.15	1999.I.15	1999.I.16	1999.I.25	1999.I.28	1999.I.28	1999.I.28
end time	10:00	4:30	10:00	7:00	8:00	11:15	10:00	11:15

**TABLE D-1c. Raw fresh snow density data: mass, depth and area measurements for samples 10 through 14, with snowfall event start and end dates and times taken from sonic snow depth sampling at the UW north campus weather station.**

<b>measurement</b>	<b>10</b>	<b>11</b>	<b>11a</b>	<b>11b</b>	<b>12</b>	<b>13</b>	<b>14</b>
<b>start date</b>	1999.I.28	1999.II.24	1999.II.24		1999.III.03	1999.III.03	1999.III.05
<b>time</b>	16:00	19:30	19:30		??	23:15	18:30
<b>end date</b>	1999.I.28	1999.II.25		1999.II.25	1999.III.03	1999.III.04	1999.III.05
<b>time</b>	23:45	8:45		8:45	10:45	8:45	22:45
<b>gross mass (g)</b>	710	1020	815	1020	2380	1690	1310
<b>tare mass (g)</b>	585	500	500	815	560	955	660
<b>snow depth (cm)</b>				1.93 - 0.93			
1	1.05	1.9	0.7		4.7	6.6	2.9
2	1.1	2.0	0.7		4.7	6.4	2.8
3	1.1	2.1	0.8		4.6	6.3	2.9
4	1.1	1.8	0.7		4.9	6.4	3.0
5	1.0	2.0	0.8		4.8	6.5	2.7
6	1.0	2.0	1.2		4.8	6.2	2.9
7	1.1	2.0	1.1		4.4	6.6	3.2
8	1.0	1.8	1.0		4.6	6.2	2.9
9	1.0	1.9	1.15		4.8	6.0	3.1
10	1.1	1.9	0.9		4.95	6.6	3.1
11	1.2	1.9	1.0		4.9	6.3	3.2
12	1.1	1.8	1.1		5.0	6.0	3.3
<b>length (cm)</b>	71.5	71.5	71.5	71.5	70.0	42.0	71.5
<b>width (cm)</b>	35.5	35.5	35.5	35.5	35.0	35.5	35.5
<b>standard deviation of T</b>	1.86	0.22	0.244	0.115	0.47	1.06	0.55
<b>maximum T (°C)</b>	-0.94	-2.60	-2.60	-3.00	-0.38	-4.16	-6.33
<b>minimum T (°C)</b>	-6.03	-3.42	-3.39	-3.42	-1.89	-7.37	-7.77
<b>last T of event (°C)</b>	-5.33	-3.06	-2.74	-3.06	-0.38	-7.27	-7.5
<b>average T after event (°C)</b>	-	-	-3.25	-	-	-	-
<b>hours after event measurement taken</b>	0	0	5.75	0	0	0	0
<b>event start date</b>	1999.I.28	1999.II.24	1999.II.24	1999.II.25	1999.III.03	1999.III.03	1999.III.05
<b>start time</b>	17:00	19:30	19:30	3:00	4:45	23:15	18:30
<b>event end date</b>	1999.I.28	1999.II.25	1999.II.25	1999.II.25	1999.III.03	1999.III.04	1999.III.05
<b>end time</b>	23:45	8:45	3:00	8:45	10:45	8:45	22:45